EDDY-CURRENT CHARACTERIZATION OF MATERIALS AND STRUCTURES

Birnbaum/Free, *editors*

ASTM STP 722

AMERICAN SOCIETY FOR TESTING AND MATERIALS

EDDY-CURRENT CHARACTERIZATION OF MATERIALS AND STRUCTURES

A symposium
sponsored by ASTM
Committee E-7 on Nondestructive Testing
AMERICAN SOCIETY FOR
TESTING AND MATERIALS
Gaithersburg, Md., 5–7 Sept. 1979

ASTM SPECIAL TECHNICAL PUBLICATION 722
George Birnbaum and George Free,
National Bureau of Standards, editors

ASTM Publication Code Number (PCN)
04-722000-22

AMERICAN SOCIETY FOR TESTING AND MATERIALS
1916 Race Street, Philadelphia, Pa. 19103

Library of Congress Catalog Card Number: 80-67398

NOTE

The Society is not responsible, as a body, for the statements and opinions advanced in this publication.

Printed in Cockeysville, Md.
February 1981

Foreword

The symposium on Eddy-Current Characterization of Materials and Structures was presented at Gaithersburg, Md., 5-7 Sept. 1979. The symposium was sponsored by the American Society for Testing and Materials through its Committee E-7 on Nondestructive Testing, and was co-sponsored by the National Bureau of Standards and the American Society for Nondestructive Testing. The symposium was held in cooperation with the IEEE Magnetics Society and the IEEE Power Engineering Society. George Birnbaum and George Free, National Bureau of Standards, presided as symposium chairmen and editors of this publication.

Related ASTM Publications

Real-Time Radiologic Imaging: Medical and Industrial Applications, STP 716 (1980), $36.50, 04-716000-22

Computer Automation of Materials Testing, STP 710 (1980), $21.75, 04-710000-32

Acoustic Emission Monitoring of Pressurized Systems, STP 697 (1979), $26.50, 04-697000-22

Nondestructive Testing Standards—A Review, STP 624 (1977), $33.75, 04-624000-22

Practical Applications of Neutron Radiography and Gaging, STP 586 (1976), $25.50, 04-586000-22

Monitoring Structural Integrity by Acoustic Emission, STP 571 (1975), $23.75, 04-571000-22

Acoustic Emission, STP 505 (1972), $22.50, 04-505000-22

A Note of Appreciation to Reviewers

This publication is made possible by the authors and, also, the unheralded efforts of the reviewers. This is a body of technical experts whose dedication, sacrifice of time and effort, and collective wisdom in reviewing the papers must be acknowledged. The quality level of ASTM publications is a direct function of their respected opinions. On behalf of ASTM we acknowledge with appreciation their contribution.

ASTM Committee on Publications

Editorial Staff

Contents

SUMMARY

Introduction

Eddy-current testing in the industrial setting has been a common practice for many years. As industry has become more concerned about cost effectiveness, meaningful design criteria, and the integrity of products, the role of eddy-current testing has become more significant. In response to these concerns, there has been a virtual explosion of activity in all areas of eddy-current nondestructive evaluation (NDE), including theory, instrumentation, data analysis, and applications.

Various conferences have included eddy-current theory and practice as part of a total program, but there has been no conference specifically devoted to the subject. Since only some of the information related to research and development in eddy-current NDE is readily available, and is scattered throughout the literature, it has been difficult to assess the current status of the various eddy-current techniques—their accuracies, repeatabilities, and ranges of application. It has been also difficult to assess the gap between theoretical development and practice and the degree to which the various tests are quantitative. Consequently, a symposium devoted solely to the subject of eddy currents was planned that would deal with all aspects of the subject. Thus this symposium included developments in theoretical models for specific eddy-current problems, the analysis of performance of available instrumentation, and microwave, multifrequency, and pulsed eddy-current methods. Other important areas that the symposium dealt with included automation of experiments, data processing, the properties of materials which can be determined by eddy-current testing, and eddy-current standards.

Analytical approaches to electromagnetic field problems which may be applied to practical eddy-current test situations have been few and far between because of the complexity of dealing with the real boundary conditions. The advent of powerful computers, however, allows the use of approximation techniques, such as finite-element analysis, which can be applied to more realistic situations as discussed in this symposium.

The limitations of using a single frequency in eddy-current testing have been known for many years. Other approaches (using microwave, multifrequency, and pulsed techniques) have been suggested but never fully developed. Many people have lately taken a second look at these techniques, particularly those using multifrequencies, where commercial equipment is now available. The accuracies and repeatabilities of these methods, the types of tests for which they are best suited, and the limits of applicability are discussed in a number of the papers.

Computer technology can be applied to both automating the test apparatus and analyzing the results to significantly improve the range of applicability and the performance of even the simplest techniques. Adaptive learning and pattern-recognition techniques presented here achieve quantitative results far better than can be obtained by point-by-point analyses of the same data.

We feel that the papers in this volume will give the reader some insight into the state of the art in eddy-current research. In particular, these papers may help to answer questions regarding the limitations of present techniques and the possibilities for new areas of research.

George Birnbaum

National Bureau of Standards, Washington, D.C. 20234; co-chairman and co-editor

George Free

National Bureau of Standards, Washington, D.C. 20234; co-chairman and co-editor

Theoretical Analysis of Fields, Defects, and Structures I

W. Lord[1] and R. Palanisamy[1]

Development of Theoretical Models for Nondestructive Testing Eddy-Current Phenomena

REFERENCE: Lord, W. and Palanisamy, R., "**Development of Theoretical Models for Nondestructive Testing Eddy-Current Phenomena,**" *Eddy-Current Characterization of Materials and Structures, ASTM STP 722,* George Birnbaum and George Free, Eds., American Society for Testing and Materials, 1981, pp. 5–21.

ABSTRACT: Eddy-current methods of nondestructive testing rely for their operation on the interaction of induced alternating currents and fields with defects to produce noticeable changes in search coil impedance. To date, analytical techniques have been largely ineffective in providing a model suitable for the basis of a general defect characterization scheme because of the inherent complexity of the field equations describing the phenomena. After an overview of the available analytical models, this paper describes the development of a numerical model that shows promise of providing a solution to the inverse eddy-current problem. Impedance plane trajectories are predicted for a differential probe passing through a tube with axisymmetric inside-diameter and outside-diameter slots to illustrate the use of the numerical approach.

KEY WORDS: nondestructive testing, eddy currents, theoretical modeling, finite element analysis, defect characterization

This paper is concerned with the development of theoretical models describing eddy-current phenomena associated with electromagnetic nondestructive testing (NDT) methods. The authors have limited their comments, for the sake of brevity, to the "intermediate" frequency range [*1*][2] where diffusion equations can be used to describe the behavior of impressed and induced currents and fields, thus avoiding discussion of theoretical modeling developments associated with magnetostatic (active and residual) leakage fields at the lowest end of the frequency spectrum and pulsed eddy-current and microwave methods at the higher frequency ranges. Particular emphasis is placed on those theoretical models that can be used to solve the inverse or defect characterization problem.

[1] Professor and graduate research assistant, respectively, Electrical Engineering Department, Colorado State University, Fort Collins, Colo. 80523.

[2] The italic numbers in brackets refer to the list of references appended to this paper.

Although many eddy-current tests are carried out to determine composition, hardness, dimensions, and other properties of metal parts, the major barrier to further development of eddy current and, indeed, all electromagnetic testing methods at this time, is the lack of a viable theoretical model capable of predicting the complex field/defect interactions which are the very essence of any sound defect characterization scheme.

It is not surprising that solutions to the inverse problem have been slow in developing. Eddy-current NDT methods rely for their operation on an alternating-current excitation that induces secondary currents and fields in the specimen undergoing inspection. Defects in the specimen cause changes in both induced currents and fields, which result in measurable impedance variations in a nearby search coil. The very nature of this NDT technique leads, in general, to three-dimensional, nonlinear, partial-differential equations with very awkward boundary conditions; if the probe is moving, the solutions are functions of both time and position. Nonlinearities occur whenever specimen properties, such as conductivity and permeability, are nonlinear functions of the excitation; the awkward boundary conditions arise because of the rather arbitrary nature of practical defect shapes.

As Hochschild has noted in his overview of eddy-current NDT techniques [*2*], electromagnetic methods of testing metals are of an even earlier vintage than the experimental proof of the existence of electromagnetic waves. Hence the study of eddy-current phenomena is both rich and extensive, especially when one also considers the electrical machinery [*3*], geophysical prospecting [*4*], and communications [*5*] applications, which all rely to some extent on the existence of induced currents for their operation. Classifiers of eddy-current modeling techniques are therefore faced with a plethora of theoretical approaches and testing geometries which, at first sight, seem almost incapable of any logical ordering. For the purposes of this paper, the authors have chosen three model categories: experimental, analytical and numerical.

Experimental models are those based on data obtained from measurements on simulated or actual eddy-current NDT test rigs. As a result, the models are empirical in nature and not readily extendable to the wide variety of test configurations and defect shapes needed for the development of realistic defect-characterization schemes.

Analytical models are those derived from basic field and circuit theory considerations. In general, to obtain an analytical result, simplifying approximations are made with regard to the number of dimensions, linearity of material properties, symmetry, boundary conditions, and defect shape. Even with such simplifying assumptions the mathematics is at best complex and the results tend to be limited to a single geometry.

Numerical and analytical models are both based on the same field equations; however, instead of seeking to solve the equations directly by invoking simplifying assumptions, discretization procedures are used in the numerical model which ultimately leads to a matrix equation whose solution satisfies the original field equations point by point. Such numerical techniques are not limited by material nonlinearities or awkward defect shapes but rather by the core storage available on today's computers. The major disadvantage of numerical models is that one does not end up with an actual equation as the solution but rather with flux, current density, and phase plots or, as we shall see in a later part of this paper, impedance plane trajectories. In many respects the numerical model has much in common with the experimental approach.

It is not the purpose of this paper to rank order these various approaches. There is evidence [*6, 7*] that a combination of modeling techniques may ultimately provide the optimum basis for a defect characterization scheme. In the authors' opinion, however, only the numerical model shows promise of providing a solution to the inverse problem in the immediate future.

In the following sections an overview is given of both analytical and numerical modeling approaches. A specific example of a differential eddy-current probe passing through a tube with axisymmetric inside-diameter and outside-diameter slots is given to show how the numerical model can be used to form the basis of a defect characterization scheme. An extensive reference section is given to provide the reader with all the background work needed for a full understanding of the various eddy-current modeling approaches. Wherever possible, published papers rather than reports and current editions of older textbooks have been cited to aid in the acquisition of a complete bibliography.

Analytical Modeling

Our eddy-current heritage is most definitely experimental in nature. Early work in the nineteenth century by Ampere, Oersted, Faraday, Lenz, Helmholtz, Henry, and Foucault preceded the brilliant theoretical deductions of Maxwell, in many cases by several decades. This is as it should be since theory is most often developed to predict observed fact. Maxwell himself pointed out that Faraday was not a professed mathematician, and that the major reason for the Treatise [*8*] was to express Faraday's ideas in mathematical form.

The first reported eddy-current NDT work of Hughes [*9*], although not preceding publication of the Treatise in 1873, certainly occurred before many of Maxwell's theories had achieved wide acceptance by the scientific community [*2*]. Unfortunately, the rapid strides made in eddy-current NDT developments during the nineteenth century were not continued into our own time. Hochschild's comment, made in 1959 [*2*] on the infancy of electromagnetic testing techniques, still holds today. It is perhaps unkind but nevertheless true to state that our knowledge of electromagnetic fields and their modeling has advanced very little from the state-of-the-art over one hundred years ago. This is not to say that major breakthroughs have been lacking on the road to a fuller understanding of electromagnetic field/defect interactions. The following paragraphs attempt to describe the analytical progress made.

Although not widely heralded in the NDT world, Steinmetz's [10] treatment of alternating-current quantities by the $(a + jb)$ or complex notation in the early part of this century paved the way for Försters pioneering experimental and analytical work on the phase-sensitive method of analysis. Plotting impedance plane (Argand diagram) variations of a test probe has become a widely accepted method for presenting eddy-current NDT data which relates to changes in material properties, probe lift-off, and excitation frequency; it has also been used with success for predicting the presence of defects in metal parts such as tubing [11]. Eddy currents induced in specimens undergoing inspection cause the impedance of the excitation winding (or that of a nearby search coil) to change. The real part of the impedance varies due to the additional resistive loss in the specimen; changes in the reactance occur due to the effect of the induced eddy currents on the magnetic flux set up by the excitation winding.

Analytically these phenomena can be examined after manipulating Maxwell's equations into a form suitable for solving by various partial-differential equation techniques such as separation of variables, Bessel functions, power series, and Fourier transform methods, to name but a few. Invariably the problems are only tractable if simplifying assumptions are made concerning both material properties and test geometry. Förster and Stambke [12] use a Bessel function approach to solve for the complex effective permeability of a metal rod encircled concentrically by a secondary search coil and an a-c excitation winding. The concept of effective permeability, μ_{eff}, is used to express the phasor relationship between magnetic flux density, B, and magnetic field intensity, H, caused by the eddy currents in the test specimen. This is a very useful concept in that the real part of μ_{eff} is related to the change in search coil impedance caused by the resistive losses in the specimen, and the imaginary part corresponds to the change in inductance, the very basis of the Argand or phase plane plot.

Hochschild [2] also examines the case of a cylindrical sample surrounded by a concentric excitation coil, solving the modified Bessel equation of zero order in cyclindrical coordinates

$$\frac{\partial^2 B_z}{\partial r^2} + \frac{1}{r}\frac{\partial B_z}{\partial r} - \gamma^2 B_z = 0 \tag{1}$$

where $\gamma^2 = j\omega\sigma\mu$, a function of the skin depth $\delta = (2/\omega\sigma\mu)^{1/2}$ to give an analytical expression for the magnetic flux density distribution in the cylindrical conductor as a function of the amplitude and phase of the flux density at the conductor's surface. By making use of the expression

$$\Phi = \iint_S B \cdot dA \tag{2}$$

an equation for the magnetic flux, Φ, linking the specimen with the test coil is derived. Subsequent differentiation of the form

$$V = -n \frac{d\Phi}{dt} \tag{3}$$

gives the voltage induced in the n-turn test coil which, on dividing by current and normalizing with respect to the coil reactance in air, X_0, gives the well known "comma shaped" curves of X/X_0 versus R/X_0 describing coil impedance variations as a function of frequency and conductivity.

For the same geometry, Libby [*13*] makes use of the magnetic vector potential, A, defined by the equation

$$B = \nabla \times A \tag{4}$$

to set up the equation

$$\frac{\partial^2 A_\theta}{\partial r^2} + \frac{1}{r}\frac{\partial A_\theta}{\partial r} - \frac{A_\theta}{r^2} + \omega^2\mu\epsilon A_\theta - j\omega\mu\sigma A_\theta = 0 \tag{5}$$

in cylindrical coordinates, solvable again using Bessel functions (note the similarity in form between Eqs 1 and 5). By making use of the expression

$$e_i = -\int_\theta^{2\pi} r \frac{\partial A_\theta}{\partial t}\, d\theta \tag{6}$$

relating the induced voltage, e_i, in a loop of radius r, to the magnetic vector potential A_θ, Libby obtains a closed-form expression for the impedance of the encircling coil. Wait [*4*] extends the study of the coil encircling the rod to include the effects of a nonconcentrically located sample.

Waidelich and Renken [*14*] examine the change in impedance of a circular coil when placed in the vicinity of a conducting medium by use of the image coil concept and show that the results agree with experiment for the case of large lift-off. Vine [*15*] confirms these results as the limiting case of a single loop above a conducting plate of finite thickness. Cheng [*16*] also examines this situation and, assuming the coil to be vanishingly thin, sets up magnetic vector potential equations in cylindrical coordinates, which again yield an expression for the coil impedance, this time in an integral equation form containing Bessel functions.

Dodd [*1*] builds on this concept of a delta function coil and by superposition, obtains impedance expressions in integral equation form for a rectangular cross-section coil both above a two-conductor plane and encircling a two-conductor rod.

An alternative approach to the analysis of eddy-current phenomena appears in the work of Graneau and Swann [17] and Graneau [18] where an attempt is made to avoid the complexities of Maxwell's awkward integral equation solutions by representing metallic objects in which eddy currents exist by an infinite number of filimentary circuits corresponding to the streamlines of current flow. This leads to a coupled circuit theory model and power series representations for the induced currents. Both Vein [19] and Burrows [20] point out shortcomings in this approach related to the transformation of the describing equations from the time domain to the frequency domain, which severely limit the methods generality. Equivalent circuit models based on transmission-line theory can be used for calculating the impedance of coils [21], it is not obvious, however, how such an approach can be extended to include the effects of flawed metallic specimens. Analytically, the presence of specimen defects complicates an already difficult modeling problem. Burrows [22] attacks the situation by postulating that the effects of small flaws can be represented by equivalent magnetic and electric dipoles. This assumption is based on the observation that scattered electromagnetic waves from a body in free space appear, to a distant observer, to be the same as the field of a Hertzian dipole (a similar approach is used by Zatsepin and Shcherbinin [23] to model leakage fields around slots in residually magnetized ferromagnetic materials). By making use of the reciprocity theorem and scattering matrices, Burrows examines the effects of spheroidal flaw shapes on coil voltage and shows that when flaw dimensions are less than skin depth, good agreement is obtained between theory and experiment. Dodd et al [24] utilize Burrows's dipole model to predict the defect induced voltage in a circular search coil, and Hill and Wait [25] examine the effect of a prolate spherical void in a wire rope excited by a toroidal encircling coil.

Work has been reported in the Russian literature describing theoretical models of surface cracks in metals. Domashevskii and Geiser [26] examine the horizontal and vertical components of the field above a surface crack in a ferromagnetic specimen when magnetized with low-frequency alternating current in a direction perpendicular to the crack. The leakage fields emanating from the crack can be likened to those of a "ribbon dipole" having a magnetic surface charge density that decays exponentially with defect depth. Vlasov and Komarov [27] study the eddy-current field above a rectangular slot in a conducting half-space by postulating a network model for the eddy-current flow around the slot based on experimental observation. By assuming a uniform magnetic field applied in the same direction as an infinitely long crack, Kahn et al [28] obtain a solution for the two-dimensional scalar Helmholtz equation describing the field in the metal based on their knowledge of solutions to analogous optical diffraction problems, and hence predict changes in power dissipation due to the presence of the crack. This work has recently been extended to the case of a crack in a conducting cylinder [29] excited axially by a uniform alternating-current magnetic field. Predictions of changes in the complex impedance of a tightly wound solenoid are given as variations from the X/X_0 versus R/X_0 curve.

Numerical Modeling

Computers have had a significant impact on the modeling of eddy-current phenomena both with regard to the numerical solution of the integral equation formulations described in the previous section and in solving finite-difference and finite-element equations. As concerns the former application, Dodd's [30] work on numerically integrating the expressions for vector potential derived for a wide variety of axisymmetric eddy-current testing geometries is widely recognized and used by the NDT community in the design of eddy-current tests. Additional work on the general integral equation approach to solving eddy-current field problems [31,32] shows the wide applicability of the method. However, the integral equation approach still has all the limitations associated with the assumptions made to derive the equations in the first place, before the additional errors relating to the numerical integration techniques are considered. Also, when extending the work to include the effect of flaws, one must seriously examine the range of validity of the dipole approximation. A major drawback with using the integral equation approach as the heart of a defect characterization scheme lies with the basic dipole assumption. How can such a model be used as the basis of the inverse problem solution when one has already assumed *a priori* that the defect has a spheroidal shape?

For defect characterization work a model is required which allows a variety of defect shapes, test geometries, and excitation conditions to be studied, so that parameters can be identified for incorporation into computer-based signal processors [33,34]. Both finite-difference and finite-element analysis techniques appear to have this flexibility.

Dodd [1] used the relaxation or finite-difference approach to find the phase and amplitude of the vector potential of a coil both above a metal plane and surrounding a conducting rod by replacing the partial derivatives in the equation

$$\frac{\partial^2 A}{\partial r^2} + \frac{1}{r}\frac{\partial A}{\partial r} + \frac{\partial^2 A}{\partial z^2} - \frac{A}{r^2} = -\mu J_0 + j\omega\sigma\mu A \tag{7}$$

by appropriate difference approximations. If the material properties are assumed to be constant, the partial differential equation (Eq 7) reduces to a set of algebraic equations that relates the vector potential at any point in a rectangular mesh to that at its four nearest neighbors. Knowing the forcing function current density and appropriate boundary conditions one can iterate the vector potential values at the mesh nodes until they converge to values that are found to satisfy the original partial differential equation. Such analysis techniques were originally developed for the study of pin-jointed frameworks by R. V. Southwell [*35*], then adapted to magnetic-field problems associated with electrical machinery [*36*]. More recently, Erdelyi [*37*] and others have studied nonlinear magnetic phenomena in direct-current machines. The finite-difference method could be applied to the study of three-dimensional, nonlinear eddy-current NDT problems; it has been shown, however, that an alternative numerical approach, finite-element analysis, has significant advantages over finite-difference techniques both with regard to accuracy and economic utilization of computer facilities [*38*].

Finite-element analysis techniques were also originally developed for the design of structures [*39*] and later adapted to the study of electromagnetic field problems associated with electrical machinery [*40–43*]. Such techniques have been used more recently to predict magnetostatic leakage fields around defects [*44*], and a start has been made on applying such methods to the study of eddy-current NDT phenomena [*45–48*]. Because of the potential importance of this technique to the development of defect characterization schemes for electromagnetic NDT methods, the authors describe this approach as it applies to the prediction of impedance plane trajectories for a differential eddy-current probe.

In an axisymmetric geometry such as that shown in Fig. 1 the sinusoidal source current density J_s(amp/m^2) and hence the complex magnetic vector potential A (weber/m) have components along only the positive θ direction. That is, both J_s and A are a function of r and z only. This situation can be modeled by Eq 7, a Poisson type of nonlinear diffusion equation.

From the principles of variational calculus it can be shown that a correct solution of Eq 7 can be obtained by minimizing the nonlinear energy functional

$$F = \iiint \left[\int \frac{1}{\mu} BdB + \frac{1}{2} j\omega\sigma |A|^2 - J_s \cdot A \right] dv \tag{8}$$

where B = flux density (Tesla) over the entire region of interest. The very basis of finite-element analysis is to search for a function A such that the energy functional F of Eq 8 is minimized, instead of solving Eq 7 directly. For this the chosen finite-element region is subdivided into triangles. The number, shape, and size of these triangles are not restricted in any way. Interfaces between different materials must be formed by the sides of the triangles and, in order to ensure a reasonable accuracy of the numerical solution, the triangles must be smaller in a region where the gradient of the

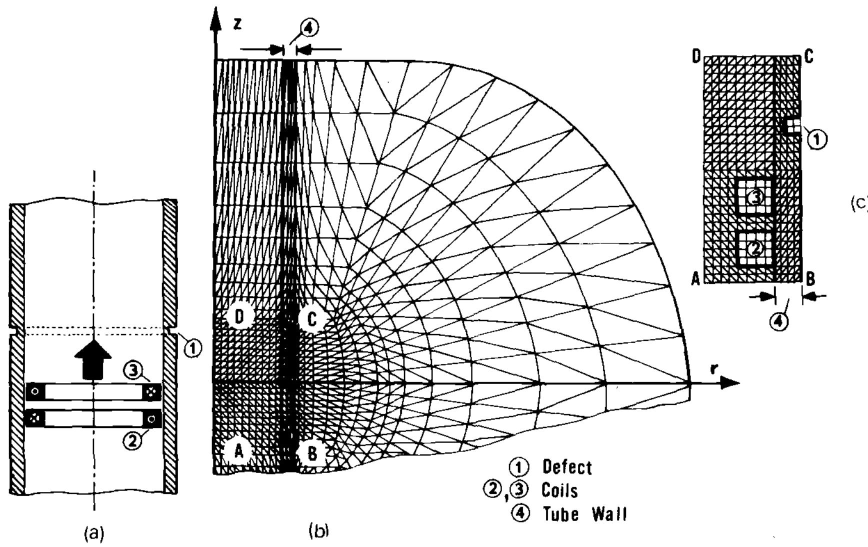

(*a*) Differential eddy-current probe moving inside a nonferromagnetic conducting tube with an axisymmetric slot.
(*b*) Mesh structure in the *r-z* plane,
(*c*) Detailed mesh in probe and slot region.

FIG. 1—*Finite-element discretization.*

magnetic flux density is large. All the elements have the same unit depth of one radian in the θ direction, and the current density, permeability, electrical conductivity, and flux density are assumed to be constant within each triangular element. Along the boundary the magnetic vector potential is assumed to be zero.

Minimization of the energy functional F is achieved by setting the first derivative of F with respect to every vertex value equal to zero. That is

$$\frac{\partial F}{\partial A_k} = 0, \qquad k = 1, 2, \ldots, N \tag{9}$$

where N = total number of nodes in the region. Instead of performing the minimization node by node in sequence, we perform it for convenience, element by element. These individual element equations are then combined into a single "global matrix" equation

$$[G]\{A\} = \{Q\}$$

where $[G]$ is a $(N \times N)$ banded symmetric complex matrix, and $\{Q\}$ and $\{A\}$ are $(N \times 1)$ complex column matrices. Any of the direct solution techniques (for example, Gaussian elimination [*49*]) utilizing the banded symmetry and sparse nature of the global matrix, $[G]$, can be applied to solve for the unknown vector potentials A. Because of the symmetry, it is sufficient to store only the elements in the semibandwidth of the matrix $[G]$, and this brings down the computer storage requirement considerably.

Figure 1 shows the differentially connected coils inside a nonferromagnetic tube having an outside-diameter axisymmetric slot and the corresponding finite-element discretization. The electrical conductivity and relative magnetic permeability of the tube material are assumed to be 1.0×10^6 S/m and 1.0, respectively. The frequency of the current source is 100 KHz. The two eddy-current coils are chosen to be identical in dimensions and are separated by one half the dimension of a single coil measured along the z-axis (axis of the tube). An arbitrary outside-diameter slot having 60 percent depth of the wall thickness and width equal to that of the gap between the two coils is incorporated in the analysis. Contours of absolute value of the magnetic vector potential and eddy-current density are plotted for a defect-free section of the tube in Fig. 2.

The impedance of a filamentary circular loop of radius r_i can be calculated from the magnetic vector potential A_i at r_i and the root mean square value of the impressed current I_s (amps) in the loop (Fig. 3*a*). That is

$$Z_i = -\frac{j\omega \oint A_i \cdot dl}{I_s} \tag{10}$$

$$= -\frac{j\omega 2\pi r_i A_i}{I_s} \tag{11}$$

Integration of Eq 11 over all the turns in the cross section of a circular coil provides the total impedance of the coil. In the absence of distinct values for A_i and r_i for each and every turn in the coil, without much loss of accuracy, we can use the centroidal values A_{cj} and r_{cj} for all the turns in the jth triangular element in the coil cross section (Fig. 3*b*). If N_s is the uniform turn density (turns/m^2) in the source region, the combined impedance of all the turns in the element j, whose area is Δ_j, is

$$Z_j = -\frac{j\omega 2\pi r_{cj} A_{cj} (\mathrm{N_s} \Delta_j)}{I_s} \tag{12}$$

Hence the total impedance of a circular coil whose cross section is discretized into N triangular finite elements is given by

$$Z_{\text{coil}} = -\frac{j\omega 2\pi N_s}{I_s} \sum_{j=1}^{N} r_{cj} A_{cj} \Delta_j \tag{13}$$

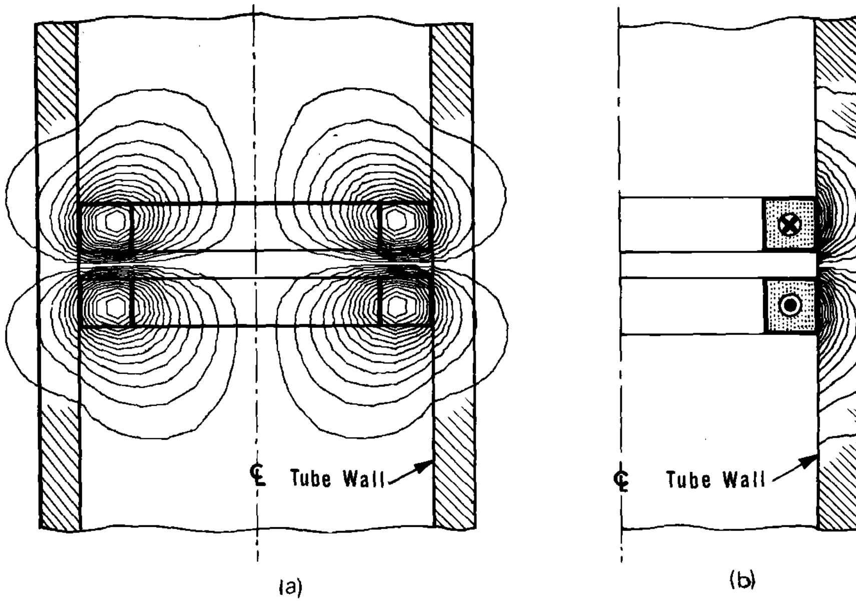

(*a*) Vector potential amplitude ($|A|$) equipotentials (flux lines).
(*b*) Eddy-current density amplitude ($|j\omega\sigma A|$) equipotentials in the tube.

FIG. 2—*Contours of absolute value plotted for a defect-free section of the tube.*

Since $N_sI_s = J_s$, the source density (amp/m^2), Eq 13 can also be written in terms of J_s. That is

$$Z_{\text{coil}} = -\frac{j\omega 2\pi J_s}{I_s^2}\sum_{j=1}^{N}(r_{cj}\Delta_j)A_{cj} \tag{14}$$

When we remember that the currents flow in opposite directions in a differentially connected eddy-current coil system (Fig. 3*c*), the resultant impedance of an eddy-current probe can be calculated by applying Eq 14 to the coils *a* and *b*, and algebraically summing up their individual impedances Z_a and Z_b

$$\begin{aligned} Z_{\text{probe}} &= Z_a + Z_b \\ &= j\omega 2\pi\left[\frac{J_{sb}}{I_{sb}^2}\sum_{j=1}^{N_b}(r_{cj}\Delta_j)A_{cj} - \frac{J_{sa}}{I_{sa}^2}\sum_{j=1}^{N_a}(r_{cj}\Delta_j)A_{cj}\right] \end{aligned} \tag{15}$$

If the two coils are similar in construction and carry the same amount of current, Eq 15 can be written as

$$Z_{probe} = \frac{j\omega 2\pi J_s}{I_s^2}\left[\sum_{j=1}^{N_b}(r_{cj}\Delta_j)A_{cj} - \sum_{j=1}^{N_a}(r_{cj}\Delta_j)A_{cj}\right] \tag{16}$$

For a particular position of the eddy-current probe inside the tube, Eq 16 gives the differential resistance (R) and differential reactance (X). These values can be calculated at desired discrete intervals as the probe moves past the defect along the z axis, and plotted on a complex impedance plane (R-X plane). In this example the magnetic vector potential values were calculated for successive probe positions as the coils moved by the defect using the numerical model, and the resulting differential impedance, Z_{probe}, at each position was calculated by making use of Eq 16. Plots of this calculated probe signal trajectory for both outside-diameter and inside-diameter defects are given in Figs. 4*a* and 4*b*, respectively. The test rig shown schematically in Fig. 5*a* was used to obtain experimental impedance plane trajectories for similar outside-diameter and inside-diameter slots corresponding to those studied numerically. The results are given in Figs. 5*b* and 5*c*.

Discussion

This paper is intended to give a general overview of analytical and numerical techniques for modeling eddy-current NDT phenomena. Emphasis is placed on those models suitable for the development of defect-characterization schemes. It is the authors' opinion that the finite-element analysis method has the necessary flexibility to serve as the basis for such studies. Additional work must be done to extend the techniques to three-dimensions and to take account of nonlinear material properties so that defects (other than those having axisymmetry) can be studied in ferromagnetic materials.

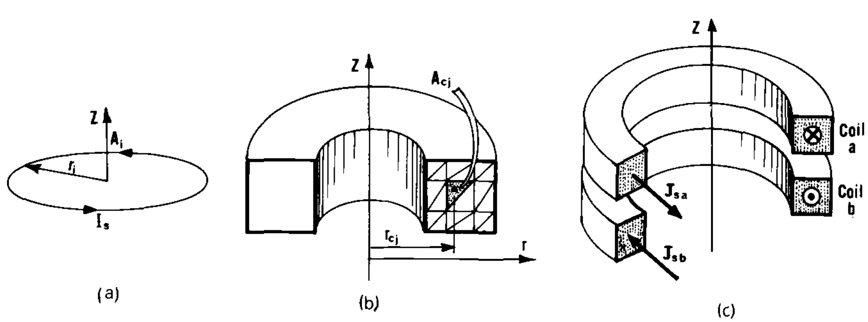

(*a*) Directions of impressed root mean square current, I_s, and magnetic vector potential, A_i, in a filamentary loop of radius r_i.
(*b*) Centroidal values, A_{cj} and r_{cj}, for element j in the coil cross section.
(*c*) Directions of impressed current densities, J_{sa} and J_{sb}, in a differential eddy-current probe.

FIG. 3—*Definition of values used in finite-element impedance calculations.*

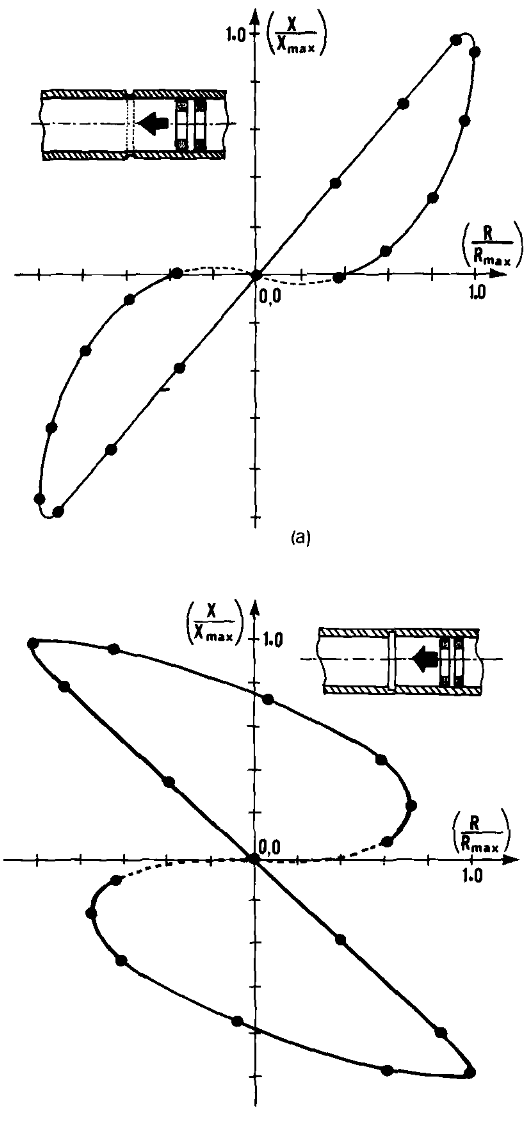

(*a*) Past an axisymmetric outside-diameter slot.
(*b*) Past an axisymmetric inside-diameter slot.

FIG. 4—*Finite-element predictions of impedance plane trajectories for the differential probe as it moves.*

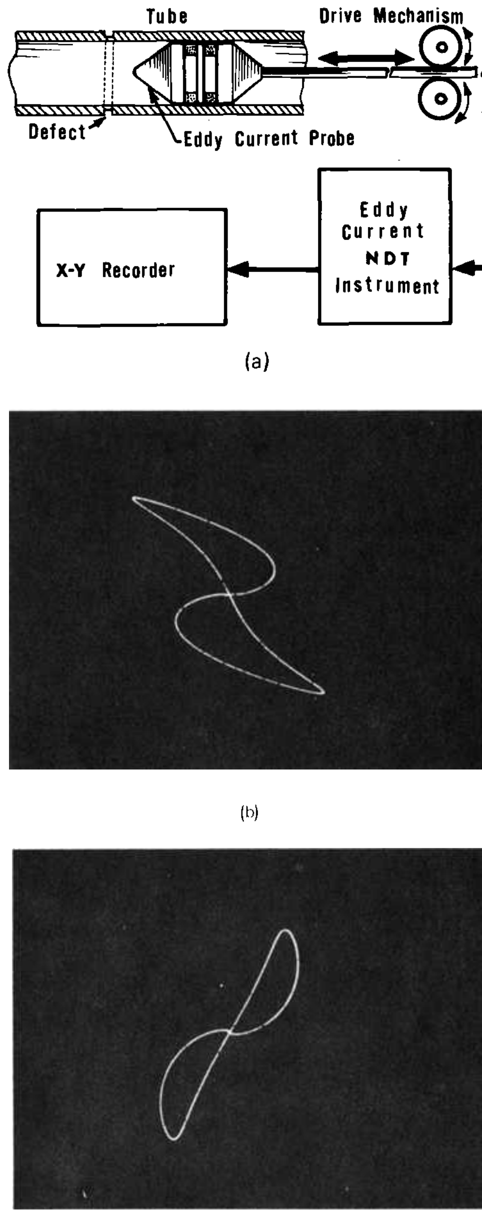

(a)

(b)

(c)

(*a*) Test-rig schematic.
(*b*) Probe response for an outside-diameter slot.
(*c*) Probe response for an inside-diameter slot.

FIG. 5—*Experimental measurement of impedance plane trajectories.*

As with any computer-based modeling, finite-element analysis techniques give results whose accuracy is very much a function of the quality of the input data. In this regard the characterization of material properties, particularly for magnetic materials, must be given more attention.

It is interesting to note that finite-element code developed for the study of electrical machinery problems is already being extended to three-dimensional geometries [50-55] and techniques for handling nonlinear permeability have been developed [56-58].

Certainly one can conclude from this overview that there is considerable activity in the modeling of electromagnetic-field phenomena, much of it directly applicable to the improvement of eddy-current NDT testing techniques.

Acknowledgments

This work has been supported in part by the Army Research Office and the Electric Power Research Institute.

References

[1] Dodd, C. V., "Solutions to Electromagnetic Induction Problems," Ph.D. dissertation, University of Tennessee, June 1967.
[2] Hochschild, R. in *Progress in Non-Destructive Testing,* Vol. 1, E. G. Stanford et al, Ed., Macmillan, New York, 1959, pp. 59-109.
[3] Stoll, R. L., *The Analysis of Eddy Currents,* Clarendon Press, Oxford, 1974.
[4] Wait, J. R., *Proceedings,* Institute of Electrical and Electronics Engineers, Vol. 67, No. 6, June 1979, pp. 892-903.
[5] Wexler, A., *Transactions on Microwave Theory and Techniques,* Institute of Electrical and Electronics Engineers, Vol. 17, No. 8, August 1969, pp. 416-439.
[6] Betzold, K., *Proceedings,* First European Conference on Non-Destructive Testing, Mainz, April 1978, pp. 189-198.
[7] Sukhorukov, V. V. and Ulitin, Y. M., *Defektoskopiya,* No. 1, January-February 1977, pp. 7-14.
[8] Maxwell, J. C., *A Treatise on Electricity and Magnetism,* 3rd ed., Dover, New York, 1954.
[9] Hughes, D. E., *Philosophical Magazine,* Series 5, Vol. 8, 1879, p. 50.
[10] Steinmetz, C. D., *Lectures on Electrical Engineering,* Dover, New York, 1971.
[11] Libby, H. L., in *Research Techniques in Nondestructive Testing,* Vol. 2, R. S. Sharpe, Ed., Academic Press, London and New York, 1973, Chapter 6, pp. 151-184.
[12] Förster, F. and Stambke, K., *Zeitschrift für Metallkunde,* Vol. 45, No. 4, 1954, pp. 166-179.
[13] Libby, H. L., *Introduction to Electromagnetic Nondestructive Test Methods,* Wiley-Interscience, New York, 1971.
[14] Waidelich, D. L. and Renken, C. J., *Proceedings,* National Electronics Conference, Vol. 12, 1956, pp. 188-196.
[15] Vine, J., *Journal of Electronics and Control,* Vol. 16, 1964, pp. 569-577.
[16] Cheng, D. H. S., *Transactions on Instrumentation and Measurement,* Institute of Electrical and Electronics Engineers, Vol. 14, No. 3, September 1965, pp. 107-116.
[17] Graneau, P. and Swann, S. A., *Journal of Electronics and Control,* Vol. 8, 1960, pp. 127-147.
[18] Graneau, P., *Journal of Electronics and Control,* Vol. 10, 1961, pp. 383-401.
[19] Vein, P. R., *Journal of Electronics and Control,* Vol. 13, 1962, pp. 471-494.

[20] Burrows, M. L., *Journal of Electronics and Control,* Vol. 16, 1964, pp. 659-668.
[21] Freeman, E. M. and El-Markabi, M. H. S., *Proceedings,* Institute of Electrical Engineering, Vol. 126, No. 1, January 1979, pp. 135-139.
[22] Burrows, M. L., "Theory of Eddy-Current Flaw Detection," Ph.D. dissertation, University of Michigan, 1964.
[23] Zatsepin, N. N. and Shcherbinin, V. E., *Defektoskopiya,* No. 5, September-October 1966, pp. 50-59.
[24] Dodd, C. V., Deeds, W. E., and Luquire, J. W., *International Journal of NDT,* Vol. 1, 1969/70, pp. 29-90.
[25] Hill, D. A. and Wait, J. R., *Applied Physics,* Vol. 16, 1978, pp. 391-398.
[26] Domashevskii, B. N. and Geiser, A. I., *Defektoskopiya,* No. 2, March-April 1976, pp. 89-95.
[27] Vlasov, V. V. and Komarov, V. A., *Defektoskopiya,* No. 6, 1971, pp. 63-76.
[28] Kahn, A. H., Spal, R., and Feldman, A., *Journal of Applied Physics,* Vol. 48, No. 11, November 1977, pp. 4454-4459.
[29] Spal, R. and Kahn, A. H., *Journal of Applied Physics,* Vol. 50, No. 10, October 1979, pp. 6135-6138.
[30] Dodd, C. V. in *Research Techniques in Nondestructive Testing,* Vol. 3, R. S. Sharpe, Ed., Academic Press, London and New York, 1977, Chapter 13, pp. 429-479.
[31] Biddlecombe, C. S. in *Proceedings* COMPUMAG Conference, Grenoble, September 1978, p. 3.5.
[32] McWhirter, J. H. et al, *Transactions on Magnetics,* Institute of Electrical and Electronics Engineers, Vol. 15, No. 3, May 1979, pp. 1075-1084.
[33] Brown, R. L., "Investigating the Computer Analysis of Eddy-Current NDT Data," Hanford Engineering Development Laboratory Report, SA-1721, Richland, Wash., February 1979.
[34] Stumm, W., *Material Prüfung,* Vol. 19, No. 4, April 1977, pp. 131-136.
[35] Southwell, R. V., *Relaxation Methods in Engineering Science,* Oxford University Press, 1940.
[36] Motz, H. and Worthy, W. D., *Journal,* Institute of Electrical Engineering, Vol. 92, Pt. 2, 1945, pp. 522-528.
[37] Erdelyi, E. A. et al, *Transactions on Power Apparatus and Systems,* Institute of Electrical and Electronics Engineers, Vol. 89, September-October 1970, pp. 1546-1583.
[38] Demerdash, N. A. and Nehl, T. W., *Transactions on Power Apparatus and Systems,* Institute of Electrical and Electronics Engineers, Vol. 98, No. 1, January-February 1979, pp. 74-87.
[39] Desai, C. S. and Abel, J. F., *Introduction to the Finite Element Method,* Van Nostrand Reinhold, New York, 1972.
[40] Winslow, A. M., *Journal of Computational Physics,* Vol. 2, 1967, pp. 149-172.
[41] Silvester, P. and Chari, M. V. K., *Transactions on Power Apparatus and Systems,* Institute of Electrical and Electronics Engineers, Vol. 89, 1970, pp. 1642-1651.
[42] Anderson, O. W., *Transactions on Power Apparatus and Systems,* Institute of Electrical and Electronics Engineers, Vol. 92, March-April 1973, pp. 682-689.
[43] Hwang, J. H. and Lord, W., *Transactions on Magnetics,* Institute of Electrical and Electronics Engineers, Vol. 10, No. 4, December 1974, pp. 1113-1118.
[44] Lord, W. and Hwang, J. H., *British Journal of Nondestructive Testing,* Vol. 19, No. 1, January 1977, pp. 14-18.
[45] Donea, J. et al, *International Journal for Numerical Methods in Engineering,* Vol. 8, 1974, pp. 359-367.
[46] Kincaid, T. G. and Chari, M. V. K., *Proceedings,* ARPA/AFML Review of Progress in Quantitative NDE, La Jolla, July 1978, pp. 120-126.
[47] Palanisamy, R. and Lord, W., "Finite-Element Analysis of Axisymmetric Geometries in Quantitative NDE," to appear in *Proceedings,* ARPA/AFML Review of Progress in Quantitative NDE, La Jolla, July 1979.
[48] Palanisamy, R. and Lord, W., *Transactions on Magnetics,* Institute of Electrical and Electronics Engineers, Vol. MAG-15, No. 6, November 1979, pp. 1479-1481.
[49] Isaacson, E. and Keller, H. B., *Analysis of Numerical Methods,* Wiley, New York, 1966.

[50] Kozakoff, D. J. and Simons, F. O., *Transactions on Magnetics*, Institute of Electrical and Electronics Engineers, Vol. 6, No. 4, December 1970, pp. 828-833.
[51] Arlett, P. L. et al, *Proceedings*, Institute of Electrical Engineering, Vol. 115, No. 12, December 1968.
[52] Zienkiewicz, O. C. et al, *Transactions on Magnetics*, Institute of Electrical and Electronics Engineers, Vol. 13, No. 5, September 1977, pp. 1649-1656.
[53] Guancial, E. and Das Gupta, S., *Transactions on Magnetics*, Institute of Electrical and Electronics Engineers, Vol. 13, No. 3, May 1977, pp. 1012-1015.
[54] Carpenter, C. J., *Proceedings*, Institute of Electrical Engineering, Vol. 124, No. 11, November 1977, pp. 1026-1034.
[55] Preston, T. W. and Reece, A. B. J., *Proceedings*, COMPUMAG Conference, Grenoble, September 1978, pp. 7.4.
[56] Jufer, M. and Apostolides, A., *Transactions on Power Apparatus and Systems*, Institute of Electrical and Electronics Engineers, Vol. 95, No. 6, November-December 1976, pp. 1786-1793.
[57] Demerdash, N. A. and Gillott, D. H., *Transactions on Magnetics*, Institute of Electrical and Electronics Engineers, Vol. 10, 1974, pp. 682-685.
[58] Janssens, N., *Transactions on Magnetics*, Institute of Electrical and Electronics Engineers, Vol. 13, No. 5, September 1977, pp. 1379-1381.

N. A. Demerdash[1] *and T. W. Nehl*[1]

Numerical Solution of Electromagnetic-Field Eddy-Current Problems in Linear and Nonlinear Metallic Structures: The RMS Phasor and Instantaneous Approaches as Potential Tools in Nondestructive Testing Applications

REFERENCE: Demerdash, N. A. and Nehl, T. W., "**Numerical Solution of Electromagnetic-Field Eddy-Current Problems in Linear and Nonlinear Metallic Structures: The RMS Phasor and Instantaneous Approaches as Potential Tools in Nondestructive Testing Applications,**" *Eddy-Current Characterization of Materials and Structures, ASTM STP 722*, George Birnbaum and George Free, Eds., American Society for Testing and Materials, 1981, pp. 22-47.

ABSTRACT: Two numerical analysis approaches for the determination of electromagnetic fields and induced eddy currents in nonmagnetic and magnetic metallic structures are presented. It is demonstrated how these techniques can best serve the purposes of nondestructive testing for material characterization etc. One method is based on instantaneous state-space or Crank-Nicolson discrete-time solution approaches, and is most suited for use with nonsinusoidal excitation wave forms and nonlinear materials. The other approach is based on a root mean square phasor concept and is best suited for sinusoidal excitation cases and linear nonmagnetic materials. Both methods are based on a magnetic vector potential formulation, and can be used in characterization of material conductivities and permeabilities. Results of application of the two methods to magnetic and nonmagnetic materials are reported.

KEY WORDS: nondestructive testing, eddy current, characterization of materials

The concept of magnetic vector potential (MVP) has been used in many previous analogue and numerical solutions of various eddy-current and magnetic-field diffusion problems in nonlinear magnetic and linear nonmagnetic metallic structures [*1-11*].[2] Some of these investigations were based

[1] Associate professor and assistant professor, respectively, Department of Electrical Engineering, Virginia Polytechnic Institute and State University, Blacksburg, Va. 24061.
[2] The italic numbers in brackets refer to the list of references appended to this paper.

on instantaneous discrete-time solution of the governing diffusion equation [*5,6,7,9*], while in other investigations use was made of the concept of MVP in the root mean square (RMS) phasor form and complex-variable formulation [*1,3,4,8,10,11*]. In many of these studies finite-difference (FD) type formulation was used [*1-3,6,9,10*], while in others finite-element (FE) based formulation was utilized [*4,5,7,8,11*].

In this work both instantaneous and RMS phasor based solutions will be used to determine losses, equivalent impedances, etc. In the instantaneous solution, finite differences are used for space-discretization purposes. In the RMS phasor based method, finite elements are used for space discretization. In both applications the main goal of the work is to find the equivalent impedance or losses, or both, induced in metallic structures due to discrete coils which carry time-varying excitation currents. These equivalent impedances are determined as viewed from the side of the excitation coils. Hence, based on the change in equivalent impedances either due to various levels of excitation in nonlinear saturable materials or change in these impedances because of change of materials in the solid metallic structures being considered, material characterization by means of nondestructive testing (NDT) methods can be accomplished. The examples used here are (*1*) equivalent impedances, induced currents, and losses in saturable steel bars, and (*2*) equivalent impedances of excitation coils used to excite metallic slabs for material-characterization purposes.

Electromagnetic-Field Formulation

Formulation of this type of induced eddy-current and flux-diffusion problem using MVP is governed by the following quasi-Poissonian equation [*5-7,9*]

$$\nabla \times \left(\frac{1}{\mu} \nabla \times \bar{A}\right) = -\sigma \frac{\partial \bar{A}}{\partial t} + \bar{J}_e \tag{1}$$

where:

$\bar{A}$ = MVP,
μ = magnetic permeability of the medium under consideration,
σ = conductivity, and
$\bar{J}_e$ = external (excitation) current density.

Equation 1 forms the basis for the instantaneous-type solution which is reported on here for use with nonlinear-type materials subject to general (sinusoidal and nonsinusoidal) type excitations.

In case of use of RMS phasor forms of the MVP in nonlinear problems involving sinusoidally time-varying excitation functions, Demerdash and

Gillott [3] and Demerdash and Nehl [8,11] have utilized the concept of effective permeability, μ_e, detailed in Ref 3, where Eq 1 reduces to

$$\nabla \times \left(\frac{1}{\mu_e} \nabla \times \hat{A}\right) = -j\omega\sigma\hat{A} + \hat{J}_e \tag{2}$$

where $\hat{A}$ and $\hat{J}_e$ are the RMS phasor representations of the MVP and external (excitation) current density, respectively, and ω is the angular frequency of the sinusoidal excitation function $\hat{J}_e$.

In cases involving linear nonmagnetic materials or magnetic materials under low levels of saturation, a constant permeability that is independent of excitation and induction can be used. Equation 2 reduces to

$$\frac{1}{\mu} \nabla \times (\nabla \times \hat{A}) = -j\omega\sigma\hat{A} + \hat{J}_z \tag{3}$$

In the following sections numerical methods based on the previous equations are reported on for use in determination of eddy-current losses, material characterization, etc.

Instantaneous Field Solution

Consider a region that contains metallic structures, current-carrying excitation windings (coils), and nonmetallic nonconducting media, in which the field is basically two-dimensional. Equation 1 yields

$$\frac{\partial}{\partial x}\left(\frac{1}{\mu}\frac{\partial A}{\partial x}\right) + \frac{\partial}{\partial y}\left(\frac{1}{\mu}\frac{\partial A}{\partial y}\right) = \sigma\frac{\partial A}{\partial t} - J_e \tag{4}$$

where A and J_e are z-components of MVP and excitation current densities. Also, in metallic structures $\sigma \neq 0$ while $\sigma = 0$ in nonmetallic portions of the continuum, and J_e is nonzero only in the excitation coils. Within these excitation coils the induced-current term $\sigma(\partial A/\partial t)$ is usually negligible in comparison with the term J_e.

Accordingly, using a space-discretization scheme such as finite differences, coupled with a nodal grid, the set of space partial derivatives in Eq 4 can be replaced by values of MVP at the nodes of a grid multiplied by an appropriate set of algebraic coefficients. For a node, i, in this grid, the corresponding general equation governing the field and induced current is

$$\sum_{j=1}^{N} y_{ji}A_j = \sigma_i\frac{\partial A_i}{\partial t} - Je_i \tag{5}$$

where

y_{ji} = finite difference coefficients,
A_j = MVP at node j,
Je_i = external (excitation) current density at node i, if any,
σ_i = conductivity at node i, and
N = total number of nodes.

Equation 5 can be solved by many discrete-time integration methods [*12*]. Two methods found to be most suitable for this type of formulation are the Crank-Nicolson technique [*12*] and the state-space approach [*13*]. A brief outline of the application of these two techniques to this problem is appropriate at this juncture.

Crank-Nicolson Solution Method

Consider Eq 5 and let time be divided into increments of length τ. Consider the point in time half way between the $(n)^{\text{th}}$ and $(n + 1)^{\text{th}}$ time instants, that is, the $(n + 1/2)$ time instant. At this point in time one can approximate Eq 5 as

$$\frac{1}{2}\sum_{j=1}^{N} y_{ji}(A_j^{\,n} + A_j^{\,n+1}) = \sigma_i\left(\frac{A_i^{n+1} - A_i^{n}}{\tau}\right) - \frac{1}{2}(Je_i^{n} + Je_i^{n+1}) \quad (6)$$

where the superscript indicates the instant of time at which the quantity is evaluated, and τ is the time increment from the $(n)^{\text{th}}$ to the $(n + 1)^{\text{th}}$ instant. Equation 6 can be rearranged as

$$\left[\frac{1}{2}\sum_{j=1}^{N} y_{ji}A_j^{\,n+1}\right] - \frac{\sigma_i}{\tau}A_i^{n+1} = -\left[\frac{1}{2}\sum_{j=1}^{N} y_{ji}A_j^{\,n}\right] - \frac{\sigma_i}{\tau}A_i^{n} - \frac{1}{2}(Je_i^{n} + Je_i^{n+1}) \quad (7)$$

If one applies Eq 7 to every node in the system, one can arrive at a system of algebraic equations that can be written in matrix form as

$$G \cdot A^{n+1} = H \cdot A^{n} + Je^{n+1/2} \quad (8)$$

where

$$Je^{n+1/2} = \frac{1}{2}(Je^{n} + Je^{n+1}) \quad (9)$$

Starting from time = 0.0, where the initial conditions are known, one notices that in the system of Eq 8 the right-hand side (RHS) can be evaluated at all times in terms of the previous history of the problem. One can therefore solve for the MVP forward in time by any of many available solution routines that exploit the sparse and banded nature of the matrix G.

The solution algorithm can be summarized in the following sequence of steps:

Step 1—Set $n = 0$; set all initial conditions.

Step 2—Calculate the excitation current vector $Je^{n+1/2}$ (Eq 9).

Step 3—Calculate the matrices of coefficients G and H (Eq 8).

Step 4—Calculate the product $H \cdot A^n$ and obtain the total RHS of Equation 8 $\{H \cdot A^n + Je^{n+1/2}\}$.

Step 5—Calculate A^{n+1} from Eq 8 using Guassian elimination or another method.

Step 6—Calculate flux densities, induced current densities, etc., throughout the magnetic-field region.

Step 7—Calculate (update) new permeabilities for all the nodes [6,9].

Step 8—Set the increment on the time counter; set $n = n + 1$.

Step 9—Has duration of transient been covered? If NO, go to Step 2.

Step 10—Print results and STOP.

State-Space Solution Method

Equation 5 can be rewritten in matrix form, for a region containing excitation coils, metallic structures, and nonconducting material, after proper node numbering as well as matrix row-and-column permutation operations, as follows

$$\begin{bmatrix} Y_{11}(l \times l) & Y_{12}(l \times m) & Y_{13}(l \times k) \\ Y_{21}(m \times l) & Y_{22}(m \times m) & Y_{23}(m \times k) \\ Y_{31}(k \times l) & Y_{32}(k \times m) & Y_{33}(k \times k) \end{bmatrix} \cdot \begin{bmatrix} A_1 \\ A_2 \\ A_3 \end{bmatrix} = \begin{bmatrix} O \\ O \\ \sigma \dot{A}_3 \end{bmatrix} - \begin{bmatrix} O \\ Je_2 \\ O \end{bmatrix} \tag{10}$$

where

l = total number of nodes in nonconducting media,
m = total number of nodes within the excitation winding (coils) cross section,
k = total number of nodes in solid metallic structures,
Y's = matrices of FD coefficients,
A's = vectors of nodal MVPs, and
$\dot{A}_3$ = vector of time derivatives of nodal MVPs in metallic structures.

By means of matrix manipulation, Eq 10 yields

$$A_1 = L_1^{-1} \cdot L_2 \cdot A_3 + L_1^{-1} \cdot Je_2 \tag{11}$$

$$A_2 = L_3^{-1} \cdot L_4 \cdot A_3 + L_3^{-1} \cdot Je_2 \tag{12}$$

where the matrices L_1, L_2, L_3, and L_4 are all definable in terms of the Y-matrices (Refs *6* and *9* should be consulted for details). It also follows from Eq 10 that A_3 is governed by the following system of ordinary differential equations

$$\dot{A}_3 = G \cdot A_3 + F \cdot Je_2 \tag{13}$$

Here G and F are matrices that are defined in terms of the Y-matrices (in the interest of brevity, Refs *6* and *9* should be consulted for details). In this approach, therefore, Eqs 11 to 13 constitute the basic formulation of any two-dimensional instantaneous eddy-current problem in the state-space form. One realizes by inspection that Eqs 11 and 12 are basically a set of algebraic relationships, while Eq 13 is a set of first-order differential equations. This is the main state-space equation. Solution of Eq 13, followed by the application of Eqs 11 and 12, results in the MVP over the whole region under consideration, and hence all the electromagnetic-field quantities can be obtained.

In any state-space approach [*13*], the solution hinges upon the calculation of the so-called "transition matrices". These matrices allow the calculation of the instantaneous (most recent) values of the state variables (MVP in this case) from their previous values.

In any state-space approach for the solution of a system of ordinary first-order differential equations, such as in Eq 13, one can write a standard recursive relation giving the vector of MVP, $A_3[(n+1)\tau]$, at the $(n+1)^{\text{th}}$ instant of time in terms of the vector of MVP at the n^{th} time instant, $A_3[n\tau]$, as

$$A_3[(n+1)\tau] = \Phi \cdot A_3[n\tau] + \Theta \cdot Je_2[n\tau] \tag{14}$$

where

τ = time increment (sampling time) where time is divided into steps of length τ.

Φ = first-state transition matrix given by Ref *13*

$$\Phi = \exp(\tau G) = U + \tau G + \frac{\tau^2}{2!} G^2 + \frac{\tau^3}{3!} G^3 + \cdots \tag{15}$$

Θ = second-state transition matrix which contributes the influence of the excitation (external) forcing function into the solution. The second state transition matrix, Θ, is calculated directly from a series expansion as

$$\Theta = \left(\tau U + \frac{\tau^2}{2!} G + \frac{\tau^3}{3!} G^2 + \cdots + \cdots\right) \cdot F \tag{16}$$

In Eq 15 and 16, U is the identity matrix. One must also bear in mind that in a nonlinear transient solution the state transition matrices, Φ and Θ, would have to be updated at every time step.

Accordingly, in order to accomplish a solution of the instantaneous magnetic field governed by equations such as Eqs 11 to 13, in a given region one would proceed according to the algorithm outlined by the following steps:

Step 1—Set $n = 0$; set all initial conditions.

Step 2—Calculate the excitation vector $Je_2(n\tau)$.

Step 3—Form the matrix equation (Eq 10), and hence set up Eqs 11 through 13.

Step 4—Calculate $\Phi(n\tau)$ and $\Theta(n\tau)$ using Eqs 15 and 16.

Step 5—Calculate at the $[(n + 1)\tau]$ instant of time the vector of MVPs $A_3[(n + 1)\tau]$ using Eq 14.

Step 6—Calculate the remaining vectors of MVP, $A_1[(n + 1)\tau]$ and $A_2[(n + 1)\tau]$, using Eqs 11 and 12.

Step 7—Calculate flux densities throughout the magnetic-field region as well as other magnetic-field quantities.

Step 8—Calculate (update) new permeabilities for all the nodes (Refs *6* and *9*).

Step 9—Set the increment on the time counter; set $n = n + 1$.

Step 10—Has duration of transient under study been covered? If NO, go to Step 2.

Step 11—Print results and STOP.

The two approaches reviewed were used in practical applications which are presented in a following section of this paper, where induced current densities at the i^{th} nodes are obtained as follows

$$J_i = - \sigma_i(\partial A / \partial t)_i \tag{17}$$

and the flux densities are determined from the relationship $\bar{B} = \nabla \times \bar{A}$.

RMS Phasor Form Field Solution

For steady-state eddy-current problems with predominant a-c sinusoidally time-varying forcing (excitation) functions, the MVP is a periodic function of time, whose fundamental frequency component is predominant. Hence, the MVP can be expressed in two-dimensional problems as

$$A(x,y,t) = \sqrt{2}\,A(x,y)\sin[\omega t + \phi(x,y)] \tag{18}$$

or

$$A(x,y,t) = Im\sqrt{2}\hat{A}(x,y)\epsilon^{j\omega t} \tag{19}$$

where

ω = frequency of the forcing (excitation) function,
$\hat{A}(x,y)$ = complex RMS phasor representation of the MVP, and
$\phi(x,y)$ = two-dimensionally varying phase angle.

In such cases the excitation-current density vector can be also expressed in phasor form as

$$J_e(x,y,t) = Im\,\sqrt{2}\hat{J}_e(x,y)\epsilon^{j\omega t} \tag{20}$$

The induced eddy-current and flux-diffusion problem in metallic structures is governed in this case by Eq 2 for nonlinear materials, and Eq 3 for linear materials with no magnetic saturation. The finite-element discretization and formulation of this class of problems [*14,15*], such as governed by Eq 3, have been developed in detail by Chari in Ref *4* and will not be repeated here. The extension of this formulation to include magnetic characteristic nonlinearity of ferrous structures by use of the concept of effective permeability, μ_e, has been detailed by Demerdash and Nehl in Refs *8* and *11*. The formulation yields a system of complex numbered simultaneous equations in the MVP vector, $\hat{A}$, which can be written in matrix form as

$$S \cdot \hat{A} = \hat{I} \tag{21}$$

where

S = a global FE coefficients matrix, and
$\hat{I}$ = excitation-current vector in complex-variable phasor form.

The matrix, S, is sparse, banded, and symmetric. Equation 21 is therefore amenable to many available efficient solution routines, one of which was chosen for this model.

Flux densities, $\hat{B}$, in complex-phasor form throughout the region under consideration are determined from knowledge of the MVP and use of the discretized form of the vector identity ($\hat{B} = \nabla \times \hat{A}$). At each round of iteration in the search for the proper effective permeabilities in the ferrous regions, one uses the most recent values of elemental flux densities to find a new effective permeability, μe_{new}, for each element. A simple relaxation formula was used to reset the effective permeabilities for the model as

$$\mu e = (\alpha)\mu e_{\text{old}} + (1 - \alpha)\mu e_{\text{new}} \tag{22}$$

where $0.0 \leq \alpha \leq 0.1$.

One calculates the induced eddy-current density, $\hat{J}$, for an element from knowledge of the MVP at the centroid of each element, $\hat{A}_{\text{cn}}$, as

$$\hat{J} = -j\omega\sigma\hat{A}_{\text{cn}} \tag{23}$$

Accordingly, to accomplish a solution of the induced eddy-current problem in applications involving nonlinearity, the following iterative-type algorithm was used:

Step 1—Read all material properties, geometries, finite-element mesh information, etc.
Step 2—Read all excitation magnitudes and all excitation frequencies.
Step 3—Initialize frequency count, NF = 0.0.
Step 4—NF = NF + 1.
Step 5—Initialize permeability (iron set at unsaturated conditions).
Step 6—Initialize excitation count, NE = 0.0.
Step 7—NE = NE + 1.
Step 8—Form excitation-current density vector.
Step 9—Initialize saturation iteration count, NSAT = 0.0.
Step 10—NSAT = NSAT + 1.
Step 11—Form the global matrix, S, and set up Eq 21.
Step 12—Solve for MVP.
Step 13—Find induced-current densities and losses in the elements as well as total power loss.
Step 14—Find new flux densities in the elements.
Step 15—Adjust effective permeabilities assigned to the elements in accordance with new flux densities.
Step 16—If NSAT < 4, go to Step 10.
Step 17—Has total loss stabilized over four consecutive saturation iterations? If NO, go to Step 10.
Step 18—Calculate equivalent impedances and final results, etc.
Step 19—Print results.
Step 20—Have all excitation levels been covered? If NO, go to Step 7.
Step 21—Have all frequencies been covered? If NO, go to Step 4.
Step 22—End.

The same algorithm can be used for cases of linear metallic structures where the iterative process is circumvented and effective permeability becomes the constant permeability of the material under consideration.

Application of the Instantaneous-Solution Approach

The Crank-Nicolson and state-space methods described previously were each applied to the problem of determination of induced eddy currents and flux diffusion in an infinite metallic slab which is excited at its surface by a tangential sinusoidal field intensity function expressed as

$$Hy(0,t) = H_m \sin(\omega t + \gamma) \tag{24}$$

where

γ = initial-phase angle, and
H_m = maximum value of the tangential surface component of the field intensity.

This is essentially a one-dimensional problem in which the MVP is a function of only the depth into the slab, and the induced current density is axial. This is equivalent to a bar which is surrounded on both sides, as shown in Fig. 1, by axially nonconducting material of very high permeability (such as laminations etc.), where the magnetic field is one dimensional due to the low width-to-depth ratio.

Shown in Fig. 1 is the excitation function and the FD grid where the MVP at the bottom node is zero and the top-surface tangential field intensity is known (given by Eq 24). Initially the MVP is zero everywhere throughout the field region at time = 0.0. The resulting formulation for the bar is similar to Eq 4 without the y-component derivatives.

Once a numerical solution has been obtained using either of the Crank-Nicolson or state-space approaches described previously, giving the instantaneous (transient as well as steady state) values of the MVP throughout the cross section of the bar, the following three quantities are obtained:

(1) The induced instantaneous current density, J_i, at a node $i = 1, 2, \ldots, l - 1$ in the bar is obtained using Eq 17, from which RMS steady-state values

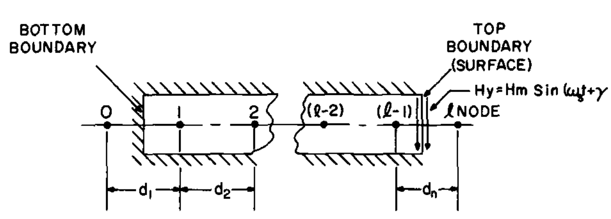

FIG. 1—*FD grid and boundary conditions of bar (infinite slab).*

of induced current densities can be calculated after the solution reaches steady state.

As a means of verification of the results of the computer algorithms developed for the state-space and Crank-Nicolson methods, a linear closed-form solution of the diffusion equation was obtained. With the reluctivity, υ, as a constant, independent of the flux density, $\bar{B}$, the expression for calculating induced-current densities at various depths into the bar becomes

$$J = -\sigma \frac{\partial A}{\partial t} = -\sigma\omega Ao \frac{d\sqrt{2}}{2} \left\{ \exp(-x/d\sqrt{2}) \left[\sin\left(\omega t - \frac{x}{d\sqrt{2}} + \gamma\right) + \cos\left(\omega t - \frac{x}{d\sqrt{2}} + \gamma\right) \right] \right\} \quad (25)$$

where $d = \sqrt{\upsilon/\sigma\omega}$ and $Ao = (1/\upsilon)H_m$.

A simple program was developed by means of which J was calculated for different depths into the bar. For the same set of depths, J was obtained using the state-space and Crank-Nicolson numerical methods. The results of J obtained from both the closed-form solution and the numerical techniques are plotted in Fig. 2. Figure 2 shows the peak-current density as a phasor at various depths into the bar. These curves show, as should be expected, very close agreement between the closed-form solution and the results of the two numerical techniques at hand. Now that the validity of the state-space and the Crank-Nicolson methods has been demonstrated for the linear case, one proceeds to apply the two methods to nonlinear cases.

The state-space and Crank-Nicolson methods were used to determine the induced eddy currents, losses, and flux penetration in the aforementioned damper bar under saturated conditions. The steady-state current density waveforms are given in Fig. 3 for a peak external excitation of 278 386 A/m at various depths into the bar. The solid wave forms are obtained from the state-space method, and the dotted wave forms are obtained from the Crank-Nicolson technique. The results of both methods are in good agreement. The current densities obtained from the Crank-Nicolson model are of slightly lower magnitude. The corresponding RMS current-density distributions versus depth were obtained using both techniques (Fig. 4).

(2) From knowledge of the current densities at the nodes, the total instantaneous power loss, $W(t)$, is obtained as

$$W(t) = \sum_{i=1}^{l-1} \frac{J_i^2}{\sigma}(d_{i+1} + d_i)\cdot w \quad (26)$$

where w is the bar width. Therefore, the average power loss over a cycle becomes

$$P_{av} = \frac{1}{T} \sum_{t=t_1}^{t=t_1+T} \tau \cdot W(t) \tag{27}$$

The average power loss in the bar, P_{av}, was calculated at various levels of RMS excitation from 65 748 A/m to 262 598 A/m for a frequency of 60 Hz. The numerical results obtained from the state-space and the Crank-Nicolson techniques are given in Fig. 5. Corresponding experimental test data for an identical case were obtained in earlier investigations *[16,17]* and are also given in Fig. 5. Good correlation between the calculated results from both methods and the test data is apparent. The results of the state-space method are somewhat closer to the experimental data. This can be partly attributed to the higher degree of accuracy achieved in the representation of the time derivative ($\partial A/\partial t$) in the state-space method in comparison with the first-order approximation used for that derivative in the Crank-Nicolson method.

The equivalent bar resistance, R_{eq}, was obtained as

$$R_{eq} = 2P_{av}/(H_m)^2 \tag{28}$$

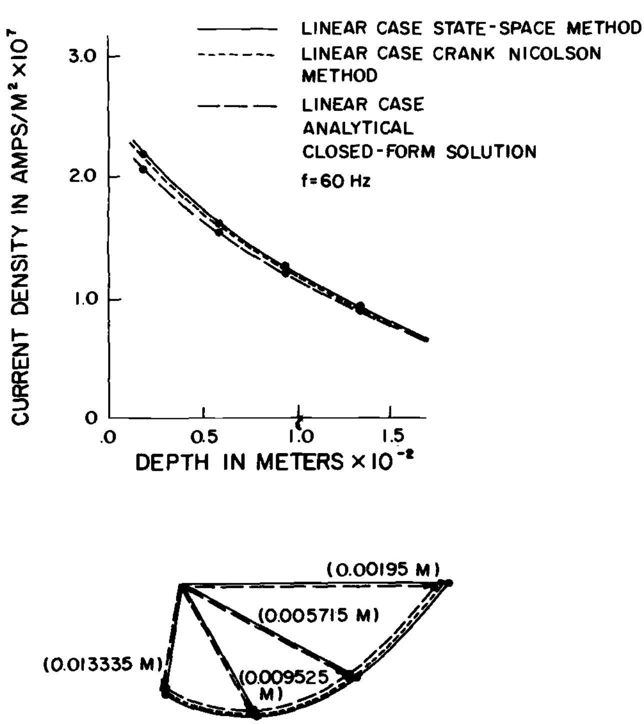

FIG. 2—*Comparison between results of numerical instantaneous solution and closed-form solution in a linear case.*

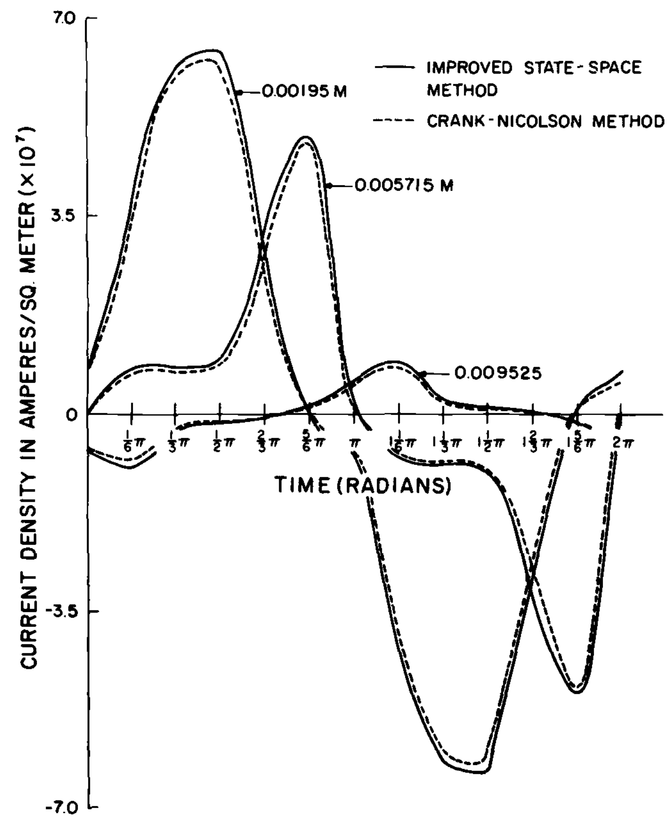

FIG. 3—*Current-density wave forms with impact of distortion resulting from magnetic nonlinearities.*

Accordingly, R_{eq} was obtained at various excitation levels. The results from the state-space and Crank-Nicolson methods are given in Fig. 5.

(3) The instantaneous magnetic energy stored, $Q(t)$, at time, t, is

$$Q(t) = \sum_{i=1}^{I-1} \frac{1}{2} \left(\int_0^{B_i} H\, dB \right) (d_i + d_{i+1}) w \tag{29}$$

from which the average energy storage over a cycle, T, becomes

$$Q_{av} = \frac{1}{T} \sum_{t=t_1}^{t=t_1+T} \Delta t \cdot Q(t) \tag{30}$$

Once Q_{av} is obtained after a steady state has been reached, the reactive power in the bar is obtained in a manner almost identical to the procedure described in Refs *6* and *9*. The reactive power in the given bar was obtained at various excitation levels using both methods and is plotted in Fig. 6.

From the reactive power, the equivalent bar reactance, X_{eq}, follows in a fashion identical to the procedure of determination of R_{eq} (Eq 28). The equivalent bar reactance was obtained at various levels of excitation at 60 Hz and is given in Fig. 6. The effect of material nonlinearities at higher excitation levels is depicted clearly in the reduction of the value of the reactance as the excitation is increased, since at higher excitation levels the bar material has a higher degree of saturation and hence a lower measure of permeance (higher reluctance) along the flux path. Bar reactances are proportional to such a measure of permeance.

Application of the RMS Phasor Solution Approach

This method was also applied to the solution of the induced eddy-current distribution and field-diffusion problem in the infinite ferrous slab with given

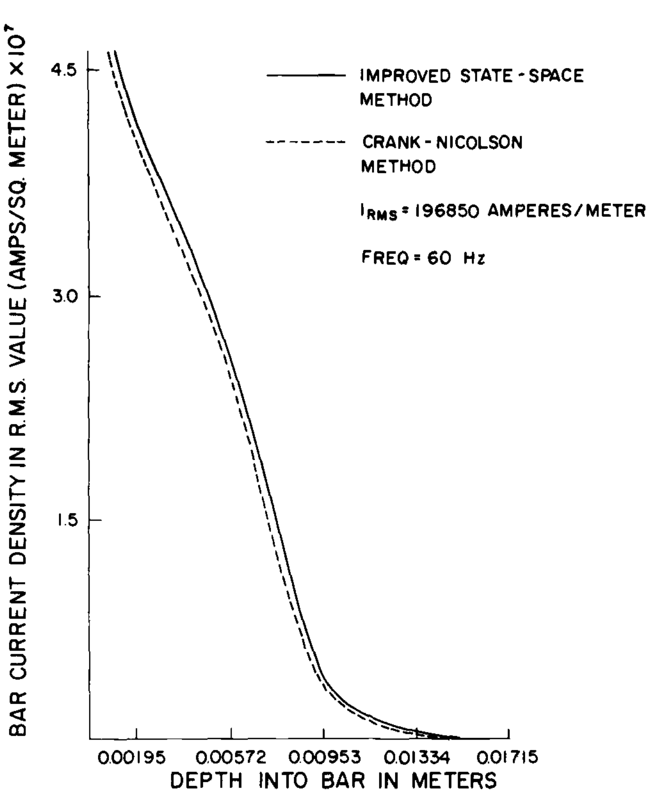

FIG. 4—*RMS current-density distribution in bar (infinite slab).*

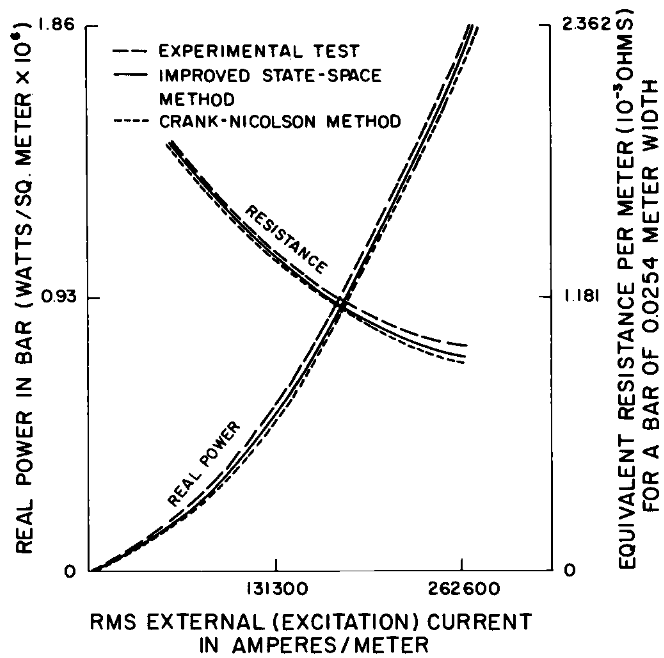

FIG. 5—*Losses per unit surface area of bar (infinite slab) from Crank-Nicolson and state-space methods—compared with experimental test data.*

surface tangential excitation-field density studied previously. As discussed earlier, this is equivalent to the problem of a bar of ferrous material which is surrounded by high-permeability nonconducting material. Experimental loss data per unit surface area of the bar is available for an identical case from Refs *16* and *17*. This problem was also solved using an FE discretization approach whose grid is shown in Fig. 7. This was coupled with the method of effective permeability to account for magnetic nonlinearities. Bar losses were obtained by summing the losses in all the elements of the grid covering the conducting medium as follows

$$P = \Sigma \Delta \cdot |\hat{J}|^2/\sigma \tag{31}$$

The loss results from the FE-effective permeability RMS phasor approach are compared with the experimental test data in Fig. 8. Also included in Fig. 8 are the results of a similar study using FD discretization. An excellent correlation between test and numerical analysis results is clearly demonstrated. This serves to buttress one's confidence in the validity of the method of RMS phasor solution coupled with effective permeability for handling problems involving nonlinear ferrous metallic structures. The effect of phase shift in both the induced eddy-current density, $\hat{J}$, from layer to layer into the bar depth is

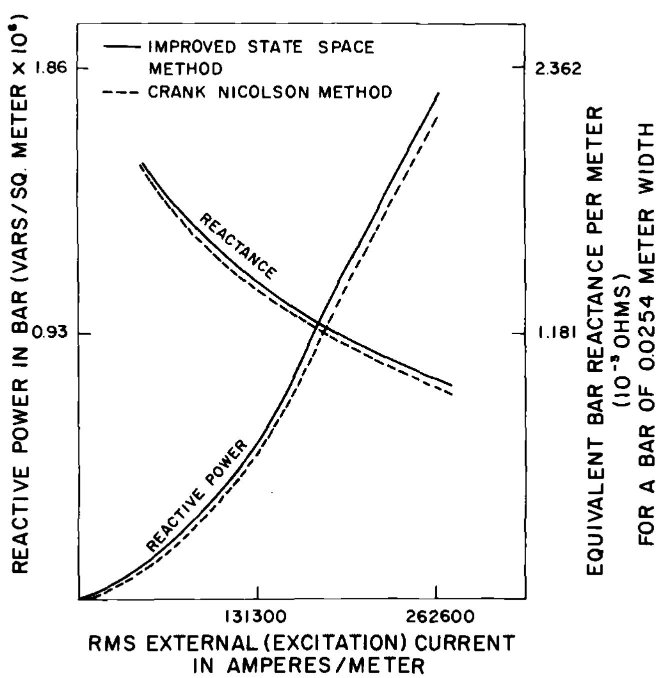

FIG. 6—*Reactive volt-amperes per unit surface area of bar (infinite slab) from Crank-Nicolson and state-space methods.*

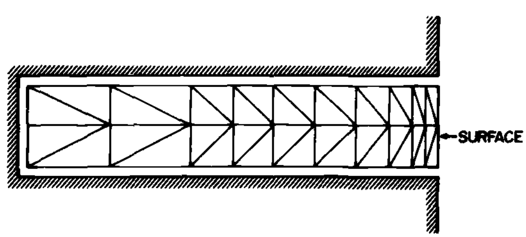

FIG. 7—*FE grid of bar (infinite slab).*

identical to the phase shift in the MVP, $\hat{A}$, from layer to layer. This can be seen clearly upon examining Eq 23, which relates $\hat{J}$ and $\hat{A}$. Results of this phase shift are displayed in Fig. 9 for the MVP inside the bar (infinite slab) at various depths in metres into the material. The exponentially decaying spiral shape of the phasor distribution certainly conforms with classical eddy-current diffusion theorems.

Now that the validity of the phasor approach has been established, we proceed to apply the model for purposes of material characterization.

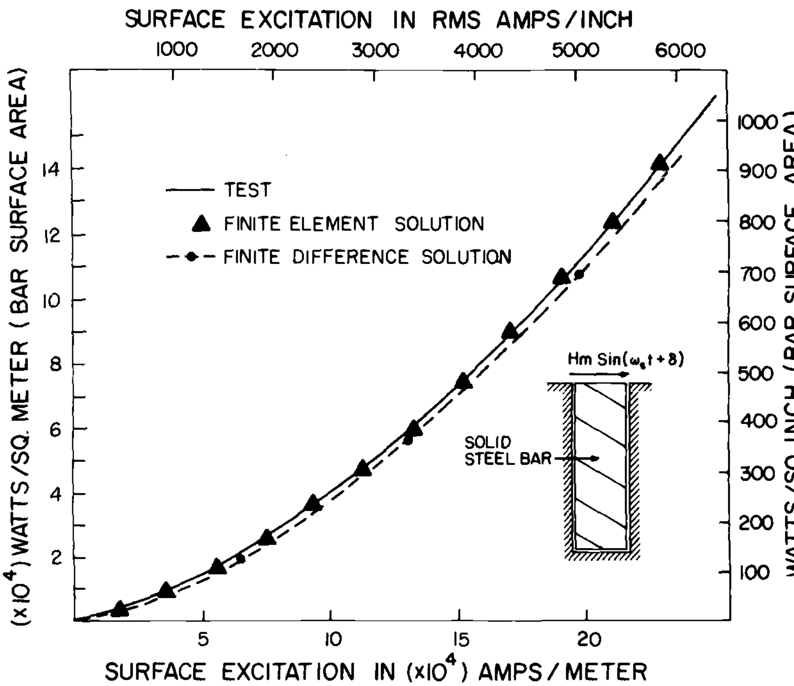

FIG. 8—*Losses per unit surface area of bar (infinite slab) using FE and effective permeability—compared with experimental test data.*

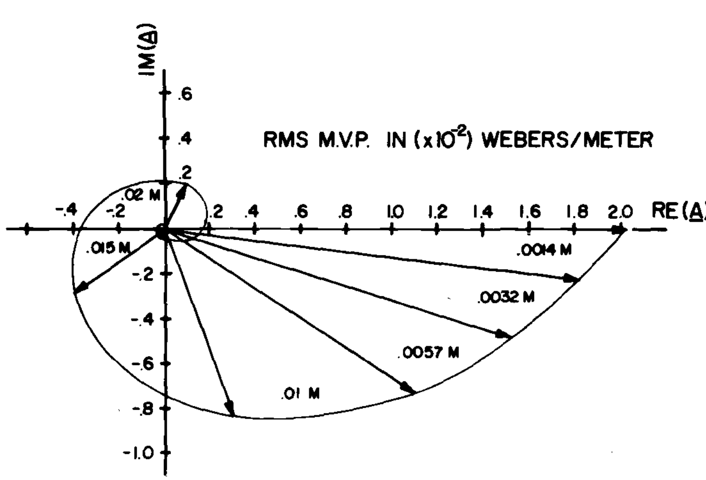

FIG. 9—*MVP phasors at various depths into bar (infinite slab).*

Material Characterization Using Eddy-Current Determination Methods

The RMS phasor approach coupled with the FE method was used to determine equivalent impedances of a coil carrying an alternating current whose magnitude and frequency are adjustable externally. This coil, when placed in the proximity of a metallic slab, will experience a change in its equivalent impedance. This change is caused by the induced eddy currents in the slab which are established by the alternating magnetic field of the coil. In an experimental setup one can measure this change by means of appropriate instrumentation. This change in the impedance of such a coil is a function of many factors related to the slab. Among the most important factors are (*1*) the proximity of the coil to the slab, (*2*) frequency of the excitation current of the coil, (*3*) the geometric configuration of the slab, and (*4*) the conductivity and permeability of the material from which the slab is manufactured.

If factors 1 to 3 are fixed, one can use this scheme to differentiate between various materials from which different slabs are made and perhaps indirectly measure slab conductivities. This can be accomplished numerically using a finite-element grid (such as shown in Fig. 10), in which a coil is placed in the proximity of a slab. The coil was excited in this model by an a-c current, and the electromagnetic-field variable (in this case the MVP) was obtained,

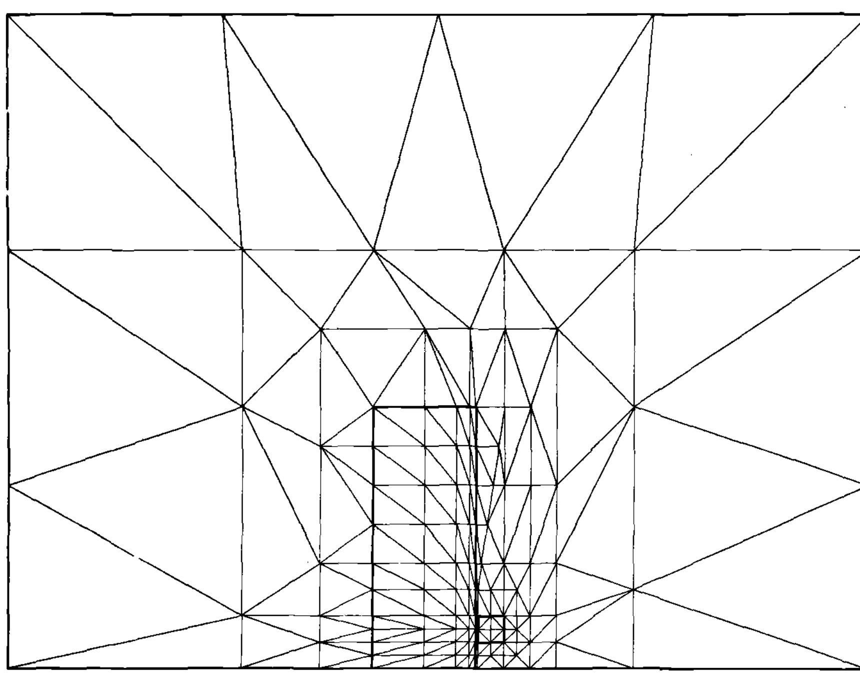

FIG. 10—*FE grid of excitation coil (winding) and metallic slab in a simulation of material-characterization test setup.*

which includes the effect of eddy currents in the slab. This was done by solving Eq 3 subject to the proper boundary conditions.

After determination of the MVP, induced eddy currents in the slab, losses, etc., follow in a manner as given in Eqs 23 and 31. Also, the magnitudes of the resulting RMS phasor MVPs are indicators of flux diffusion and eddy-current penetration into the slab. Pictorial display of these variables are indicators of slab-material conductivity. The larger the conductivity the smaller the depth of penetration of the field into a given slab. This is shown clearly in Figs. 11 to 14 for slab materials of copper, aluminum, lead, and titanium, at a coil-excitation current frequency of 100 Hz. The limit case where there is no slab conductivity, that is, as if slab material was air or free space, is shown in Fig. 15 for the same frequency.

At a higher frequency, one would naturally expect smaller depths of penetration. This can be clearly seen in Figs. 16 to 19 at an excitation frequency of 1000 Hz for slab metals. Figure 20 displays an all-air case at 1000 Hz.

Based on this field solution, the equivalent coil resistances and reactances were calculated in a manner described in Refs *3* and *8*. This procedure is very similar to the one described previously in this paper in conjunction with the instantaneous solution.

This procedure was applied to the coil-slab configuration of Fig. 10 to obtain the coil impedance in the four above-mentioned metallic slab-material

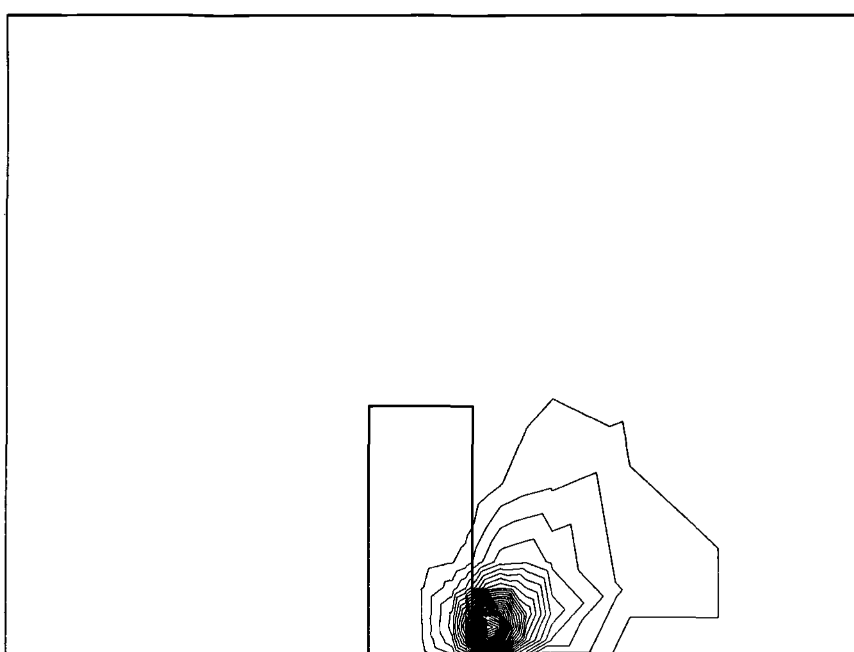

FIG. 11—*Field distribution in copper slab at 100 Hz excitation frequency.*

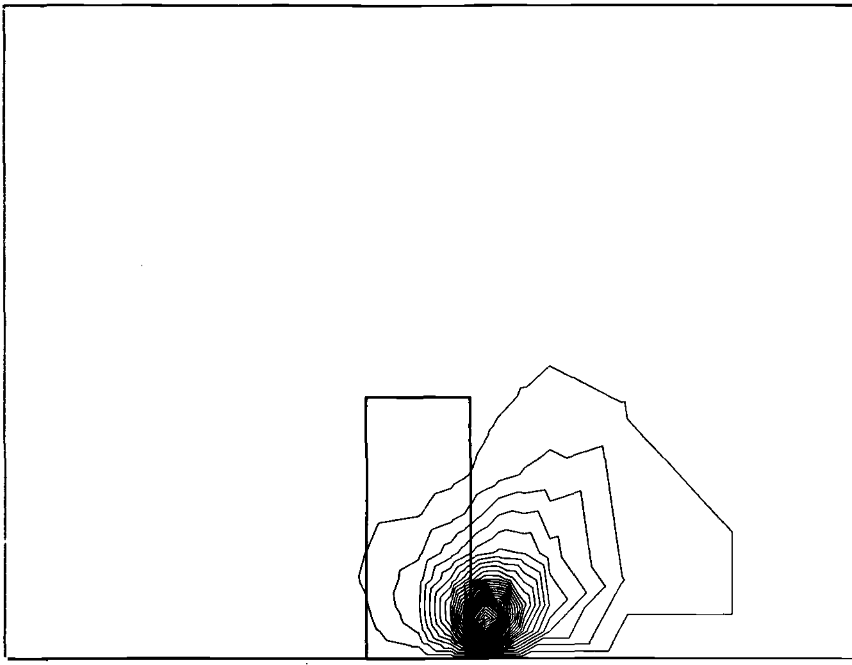

FIG. 12—*Field distribution in aluminum slab at 100 Hz excitation frequency.*

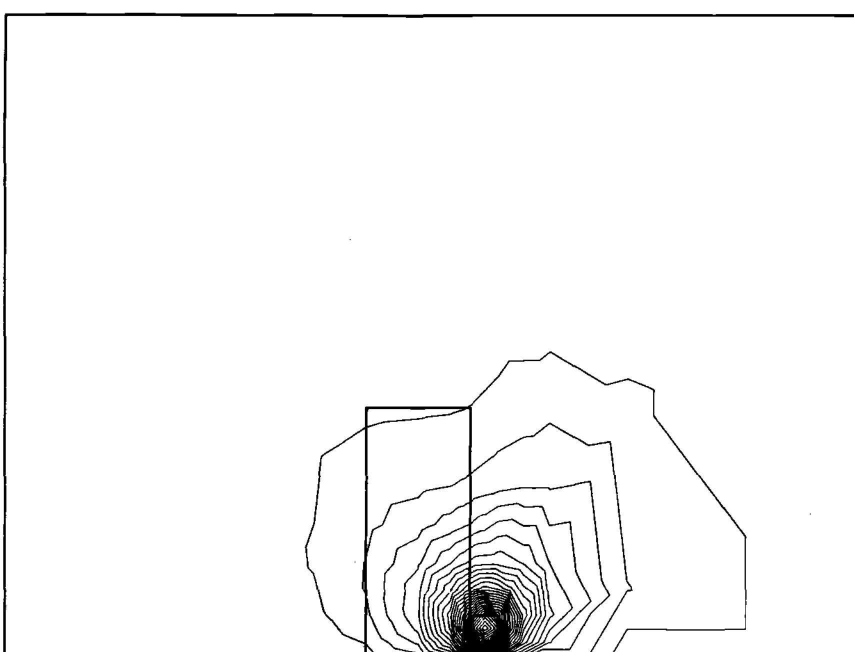

FIG. 13—*Field distribution in lead slab at 100 Hz excitation frequency.*

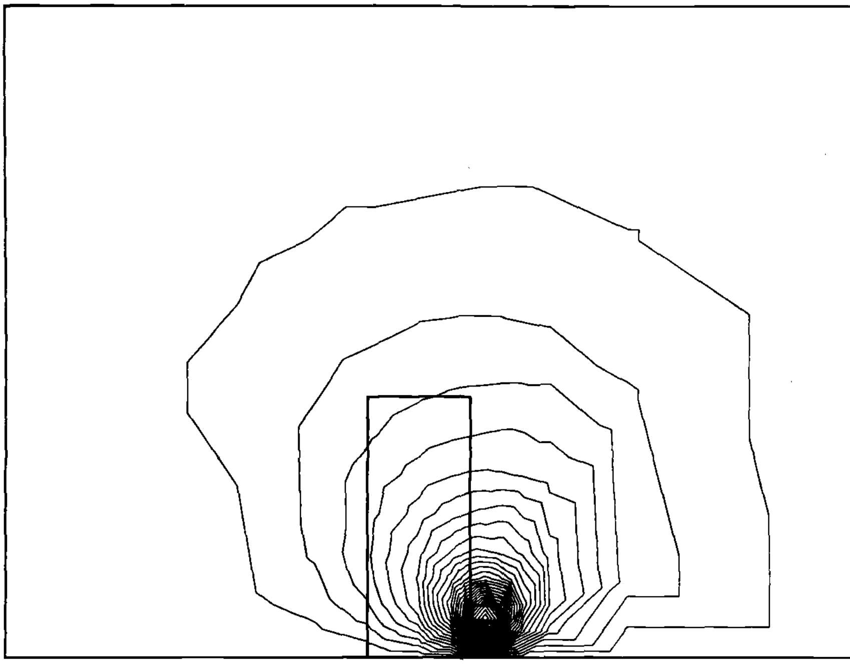

FIG. 14—*Field distribution in titanium slab at 100 Hz excitation frequency.*

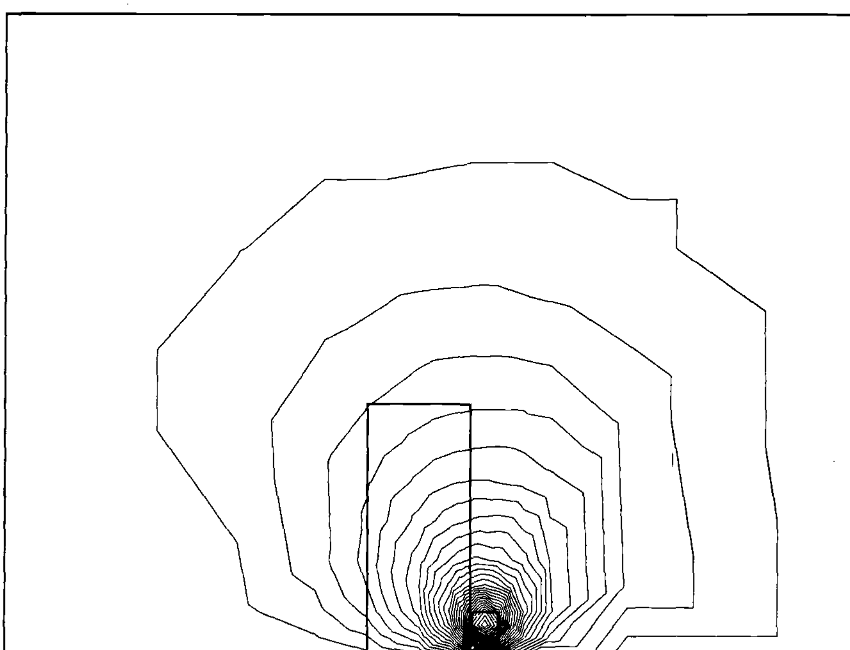

FIG. 15—*Field distribution in an all-air continuum at 100 Hz excitation frequency.*

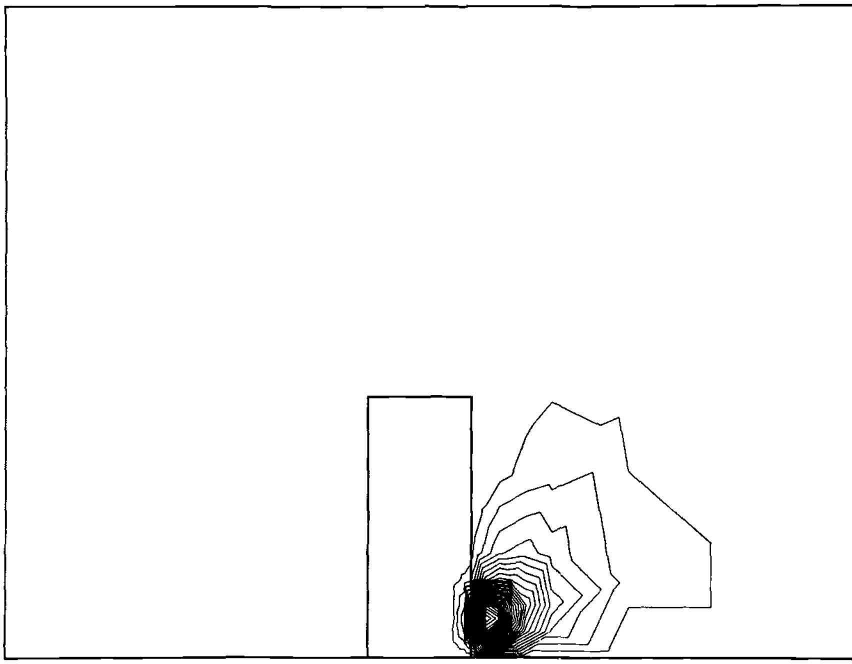

FIG. 16—*Field distribution in copper slab at 1000 Hz.*

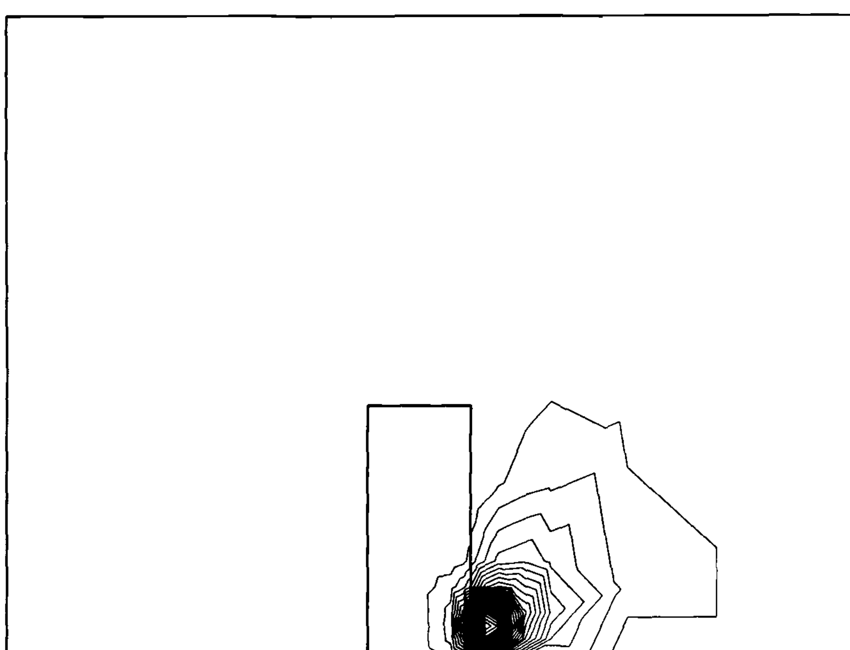

FIG. 17—*Field distribution in aluminum slab at 1000 Hz.*

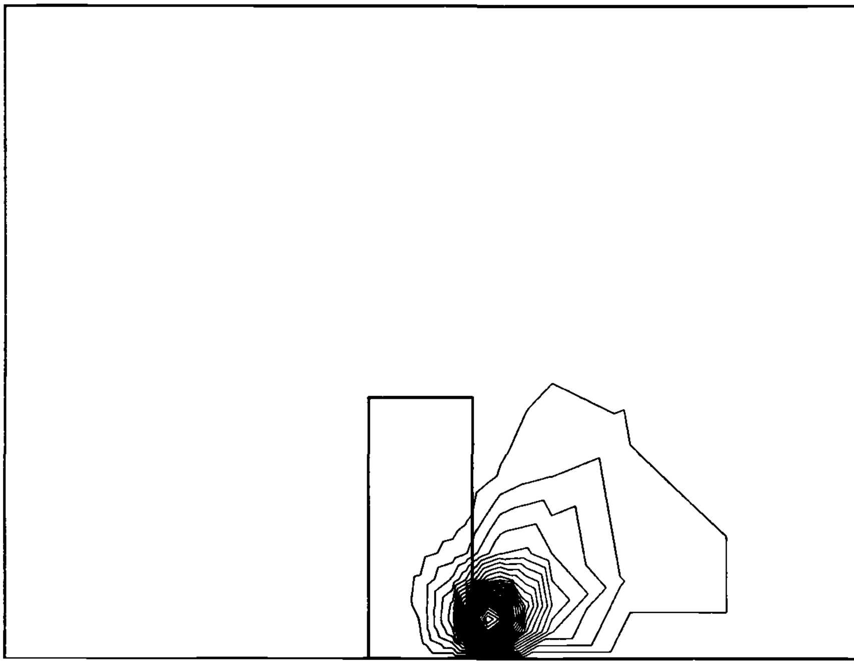

FIG. 18—*Field distribution in lead slab at 1000 Hz.*

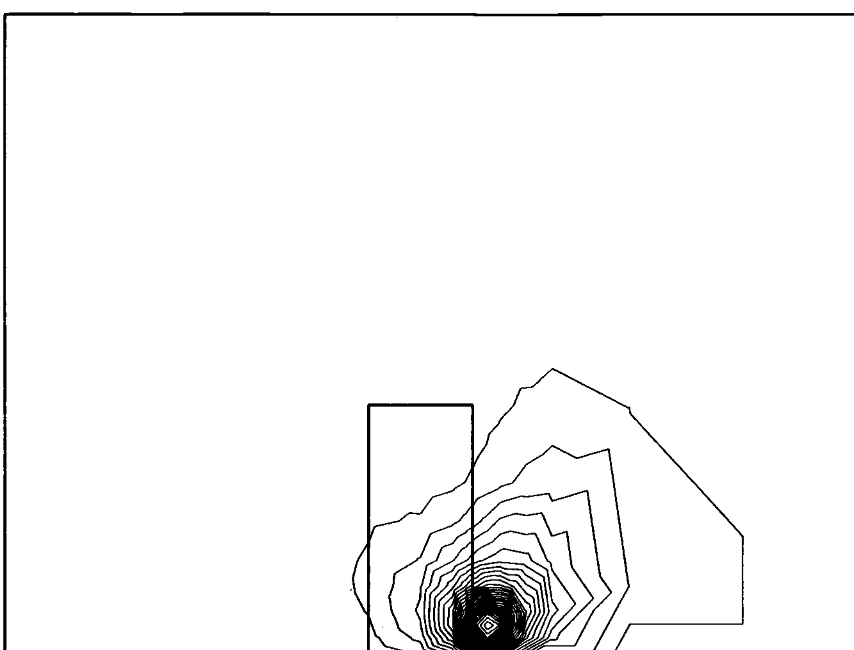

FIG. 19—*Field distribution in titanium slab at 1000 Hz.*

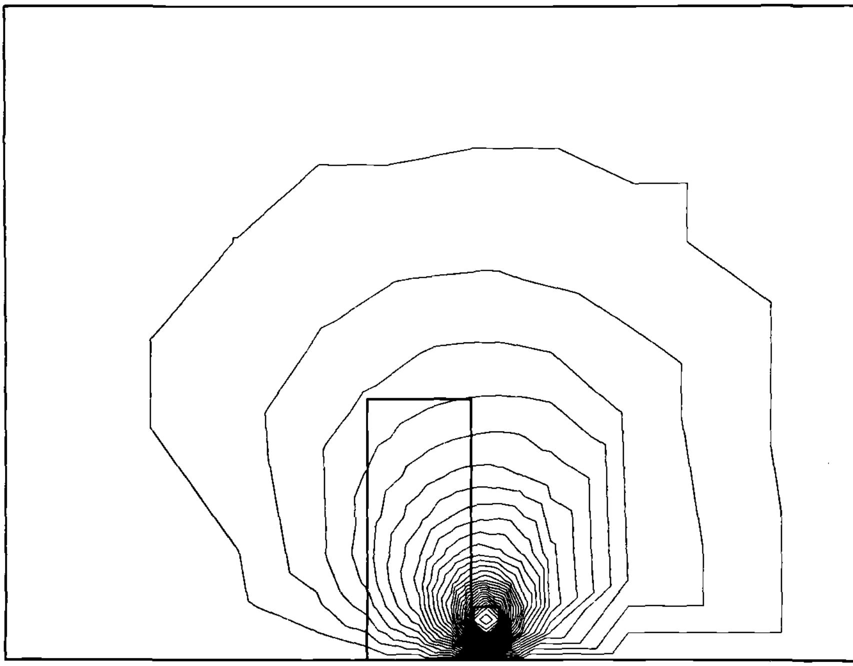

FIG. 20—*Field distribution in an all-air continuum at 1000 Hz.*

cases, at excitation frequencies of 100 Hz, 400 Hz, and 1000 Hz. An *R-X* plot of the equivalent coil impedance in the complex impedance plane for these cases is given in Fig. 21. Once such a figure has been established for all families of materials of interest, experimental measurement of coil impedance can be readily used for material identification and characterization purposes. This is because of the inherent changes of equivalent coil impedance with change of materials, material conductivity, and permeability. These changes are vividly displayed in Fig. 21, which includes the effect of excitation-frequency change.

Conclusions

This paper demonstrates the applicability of numerical eddy-current determination techniques, in both nonlinear and linear metallic structures, to material characterization and NDT applications. These techniques can be readily extended to include crack detection and characterization as well as detection and characterization of material inhomogeneity. This type of analysis can be used for the purposes of optimization of physical geometries etc., of experimental test setups for NDT purposes. These techniques encompass both sinusoidal and nonsinusoidal coil excitation waveforms. The latter can be dealt with by the instantaneous-solution techniques presented.

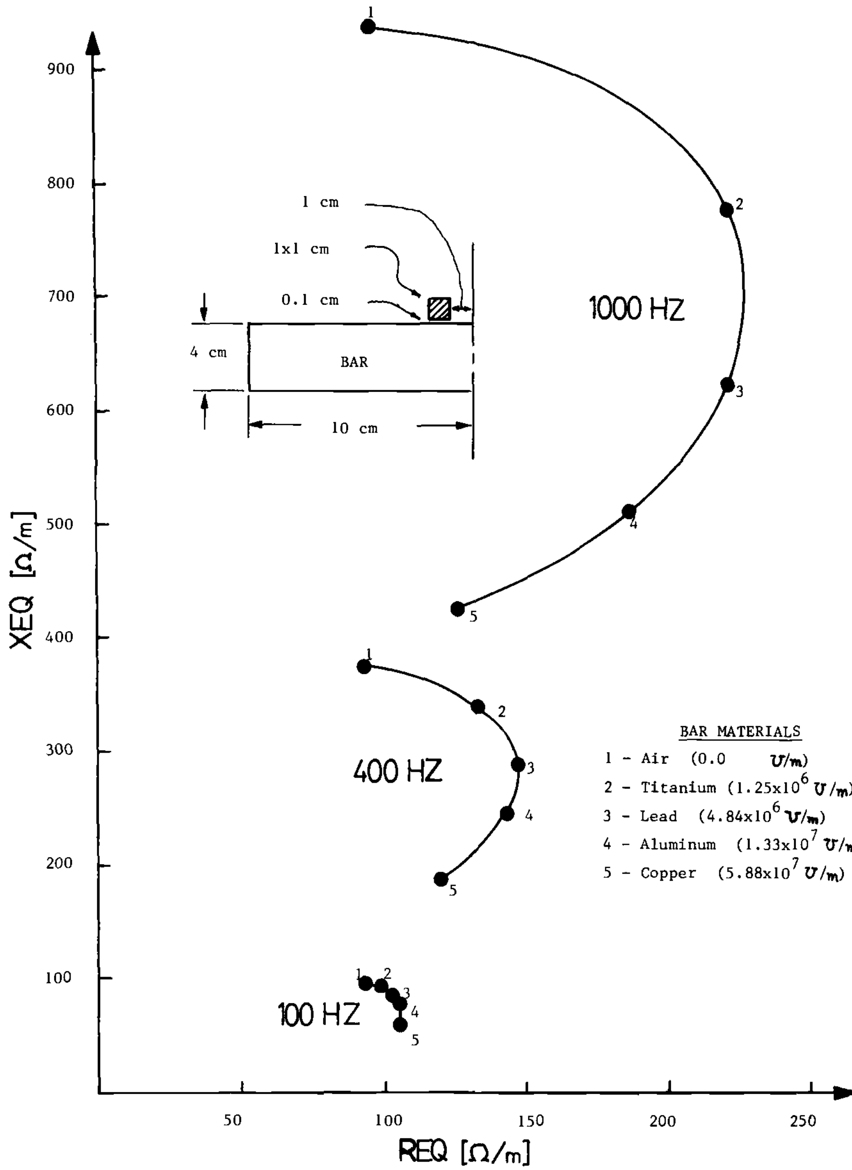

FIG. 21—*Equivalent coil impedances with various slab materials and excitation frequencies.*

References

[*1*] King, E. I., *Transactions on Power Apparatus and Systems,* Institute of Electrical and Electronics Engineers, Vol. 85, 1966, pp. 1646-1657.

[*2*] Oberretl, K., *Transactions on Power Apparatus and Systems,* Institute of Electrical and Electronics Engineering, Vol. 88, 1969, pp. 1646-1657.

[3] Demerdash, N. A. and Gillott, D. H., *Transactions on Magnetics,* Institute of Electrical and Electronics Engineering, Vol. MAG-10, 1974, pp. 682-685.
[4] Chari, M. V. K., *Transactions on Power Apparatus and Systems,* Institute of Electrical and Electronics Engineering, Vol. 93, 1974, pp. 62-72.
[5] Hannalla, A. Y. and MacDonald, D. C., *Transactions on Magnetics,* Institute of Electrical and Electronics Engineering, Vol. MAG-11, No. 5, 1975, pp. 1544-1546.
[6] Demerdash, N. A. and Lau, N. K., *Transactions on Magnetics,* Institute of Electrical and Electronics Engineering, Vol. MAG-12, 1976, pp. 1039-1041.
[7] Hannalla, A. Y. and MacDonald, D. C., *Transactions on Magnetics,* Institute of Electrical and Electronics Engineering, Vol. MAG-13, No. 5, 1977, pp. 1134-1136.
[8] Demerdash, N. A. and Nehl, T. W., "Solution of Nonlinear Eddy Current and Loss Problems in the Solid Rotors of Large Turbogenerators Using a Finite Element Approach," Paper No. A78 312-1, *Power Apparatus and Systems Winter Meeting,* Institute of Electrical and Electronics Engineers, New York, 29 Jan.-3 Feb. 1978.
[9] Demerdash, N. A. and Lau, N. K., *Transactions on Magnetics,* Institute of Electrical and Electronics Engineers, Vol. MAG-14, No. 5, 1978, pp. 557-559.
[10] Salon, S. J. and Hamilton, H. B., *Transactions on Power Apparatus and Systems,* Institute of Electrical and Electronics Engineers, Vol. PAS-97, No. 5, 1978, pp. 1918-1924.
[11] Demerdash, N. A. and Nehl, T. W., "Use of Numerical Analysis of Nonlinear Eddy-Current Problems by Finite Elements in the Determination of Parameters of Electrical Machines with Solid Iron Rotors," *Transactions on Magnetics,* Institute of Electrical and Electronics Engineers, Intermag Issue 1979.
[12] Carnahan, B., Luther, H. A., and Wilkes, J. O., *Applied Numerical Methods,* Wiley, New York, 1969.
[13] Cadzow, J. A. and Martens, H. R., *Discrete-Time and Computer Control Systems,* Prentice-Hall, Englewood Cliffs, N.J., 1970.
[14] Huebner, K. H., *The Finite Element Method for Engineers,* Wiley, New York, 1975.
[15] Strang, G. and Fix, G. J., *An Analysis of the Finite Element Method,* Prentice-Hall, Englewood Cliffs, N.J., 1973.
[16] Gillott, D. H. and Calvert, J. F., *Transactions on Magnetics,* Institute of Electrical and Electronics Engineers, Vol. MAG-1, 1965, pp. 126-137.
[17] Abrams, M. D. and Gillott, D. H., *Transactions on Power Apparatus and Systems,* Institute of Electrical and Electronics Engineers, Vol. 86, 1967, pp. 1077-1083.

L. R. Turner,[1] *R. J. Lari,*[1] *and G. L. Sandy*[2]

Eddy-Current Simulation in Prisms, Plates, and Shells with the Program EDDYNET

REFERENCE: Turner, L. R., Lari, R. J., and Sandy, G. L., **"Eddy-Current Simulation in Prisms, Plates, and Shells with the Program EDDYNET,"** *Eddy-Current Characterization of Materials and Structures, ASTM STP 722,* George Birnbaum and George Free, Eds., American Society for Testing and Materials, 1981, pp. 48-58.

ABSTRACT: The program EDDYNET solves eddy-current problems by means of an integral-equation approach. The conducting material is represented by a network of current-carrying line elements. Consequently, Maxwell's field equations can be replaced by Kirchhoff's circuit rules.

The loop equations for voltages, supplemented by the node equations for the currents, comprise a set of linear equations that can be solved repeatedly to give the time development of the eddy currents. Currents, magnetic fields, and power are calculated at each step.

A TRIM-like mesh generator and internal indexing of lines, nodes, and loops permit solutions with complex geometries incorporating many elements. Results can appear in the form of movies representing currents, field penetration, and power distribution.

Calculations can now be performed for conducting, curved shells acted upon by an applied magnetic field. Changes in the flux through each mesh loop are determined from the normal component of field (both the applied field and the field from the current in each line element). The matrix representing the flux through each loop due to each line can be inverted and the system stepped through time to provide a time history of the currents. Another matrix facilitates calculating the net field over a specified rectangular grid at each time step. Incorporating appropriate symmetry conditions reduces the size of the problem.

Results are presented for field shielding by a thin-walled toroidal shell and for eddy-current effects on a notched tube in a sinusoidal field.

KEY WORDS: eddy currents, computer simulation, nondestructive evaluation, calculation, theory, transient magnetic field

[1] Physicist, Argonne National Laboratory, Argonne, Ill. 60439.
[2] Physicist, New College, University of South Florida, Sarasota, Fla.

The program EDDYNET[3,4] solves eddy-current problems by means of an integral-equation approach. The conducting materials are represented by a network of current-carrying line elements in order that Maxwell's field equations can be replaced by Kirchhoff's circuit rules. The loop and node equations can be solved repeatedly to give the time development of the eddy currents, modified magnetic fields, and power.

The program is reviewed in the next section. The section on Treatment of Curved Shells describes modifications to EDDYNET to treat eddy currents in the thin curved shells of the conductor. We conclude with the results of calculations with EDDYNET.

Review of the Program EDDYNET

Consider the conductor to be a plane figure of arbitrary shape but simply connected, perpendicular to the applied field. The figure is divided into a triangular mesh; the network of mesh lines is used to represent the conductor. The network contains ℓ lines, m loops, and n nodes; ℓ, m, and n obey

$$m + n = \ell + 1 \tag{1}$$

Kirchhoff's node rule holds for each node; the algebraic sum of the currents into each node is zero. If the entire conductor is considered, that is, if symmetry considerations are not explicitly incorporated, then the overall conservation of the current makes one of these n equations redundant; there are $n - 1$ independent node equations.

Kirchhoff's loop rule holds for each loop; the sum of the resistive voltage drops around each loop equals the electromotive force (emf) of the loop. The emf is due to the change in applied flux through the loop plus the change in the flux due to all ℓ currents. The flux through loop j due to the current in line i is given approximately by $G_{ji}I_i$ where I_i is the current in line i and

$$G_{ji} = \frac{\mu_0}{4\pi}\frac{A_j}{r}\left[\frac{gL}{r_2} + \frac{(1-g)L}{r_1}\right] \tag{2}$$

with A_j the area of loop j, and r, g, L, r_1, and r_2 as defined in Fig. 1. Equation 2 is based upon the approximation that the flux through loop j equals the area times the field at the centroid of loop j.

[3]Turner, L. R., *Transactions on Magnetics*, Institute of Electrical and Electronics Engineers, Vol. MAG-13, 1978, p. 1119-1121.

[4]Turner, L. R. and Lari, R. J., "Developments of the Eddy-Current Program EDDYNET," *Proceedings*, COMPUMAG Conference on the Computation of Magnetic Fields, Grenoble, 1978.

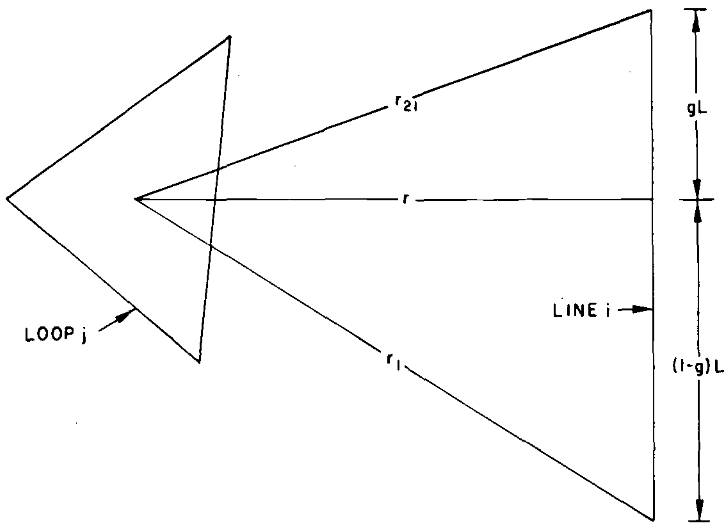

PLATE:

$$G_{ji} = \frac{\mu_0}{4\pi}\,\frac{A_j}{r}\left\{\frac{gL}{r_2} + \frac{(1-g)L}{r_1}\right\}$$

PRISM:

$$G_{ji} = \frac{\mu_0}{2\pi}\,A_j\left\{\tan^{-1}\frac{gL}{r} + \tan^{-1}\frac{(1-g)L}{r}\right\}$$

FIG. 1—*Determination of the flux through loop* j *due to the current in line* i.

For an infinitely long prism or cylinder, I_i represents the current per unit length, and Eq 2 is replaced by

$$G_{ji} = \frac{\mu_0}{2\pi} A_j \left[\tan^{-1}\frac{gL}{r} + \tan^{-1}\frac{(1-g)L}{r}\right] \tag{3}$$

By Eq 1 the total number of equations $m + n - 1 = \ell$, the number of unknown currents.

The emf's which enter the loop equations involve the time derivatives of current and flux.

$$\sum_{k=1}^{3} R_{jk}(I_{jk} + \Delta I_{jk}) = -\Delta\phi_{\mathrm{app},j}/\Delta t - \sum_{i=1}^{\ell} G_{ji}\Delta I_i/\Delta t \tag{4}$$

where

R_{jk} and I_{jk} = resistance and current of side k of loop j, respectively,
$\Delta\phi_{\mathrm{app}j}$ = change in applied flux through loop j, and

I and $I + \Delta I$ = currents at time t and $t + \Delta t$, respectively. Equation 4 can be rewritten in matrix form

$$(G + R\,\Delta t)\,\Delta I = -\Delta\phi_{\text{app}} - (R\,\Delta t)I \tag{5}$$

which is a system of m linear equations for the unknown ΔI. These equations plus the $n - 1$ node equations give the ΔI and thus the currents at time $t + \Delta t$. Fields, forces, and power can also be calculated at each time.

If one or more of the defined boundaries for a problem represent symmetry planes, the number of unknown currents and nodal equations are reduced. Lines that lie in the symmetry plane carry no currents, and nodes that lie in the symmetry plane obey Kirchhoff's node equation automatically. Thus the number ℓ of lines and the number n of nodes are chosen to exclude those in the symmetry planes. Consequently

$$m + n = \ell \tag{6}$$

The number of unknown currents equals the number of loops plus nontrivial nodes.

The mathematical model is described in more detail in Turner.[3]

Figure 2 shows the relations among the programs and datafiles making up the EDDYNET package. FILE 20 contains the input geometrical and

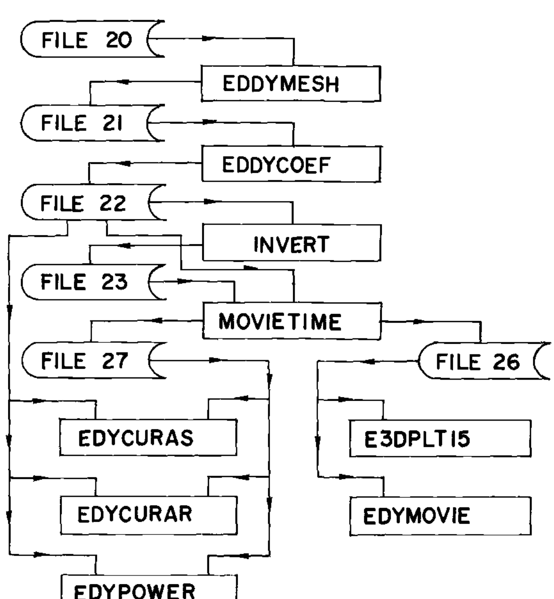

FIG. 2—*Simplified block diagram of the program EDDYNET.*

symmetry data for EDDYMESH, which calculates the triangular mesh. EDDYMESH is a modification of the triangle mesh generator of the magnetostatics program TRIM.[5] It is usually run in the time-sharing mode in TSO or CMS, but can be run in batch as well. The mesh data are written in dataset FILE 21. Figure 3 shows the meshes generated for the two geometries described later.

EDDYCOEF calculates the coefficient matrix G of Eq 5. EDDYCOEF sweeps through the mesh tabulating the ends of each line and calculating the resistances. It skips all mesh points surrounded by air or lying on a symmetry axis. A sweep through the lines locates and tabulates the six lines for each node. Finally, a sweep through the mesh tabulates the three lines for each loop and calculates the centroid of each loop. The G matrix is calculated by sweeping through each line for each loop and is stored on disk in FILE 22. The tabulations, resistances, and geometric information are also written in FILE 22. A standard matrix inversion program, INVERT, is used to invert the G matrix and write the inverse in FILE 23.

MOVITIME calculates the time development of the eddy currents using Eq 5. At each time step the program calculates the current in each line and the magnetic field at each point on the rectangular mesh. These are written in FILE 27 and FILE 26, respectively. In addition the time and instantaneous power are printed out. The desired function for the applied field is specified to this program.

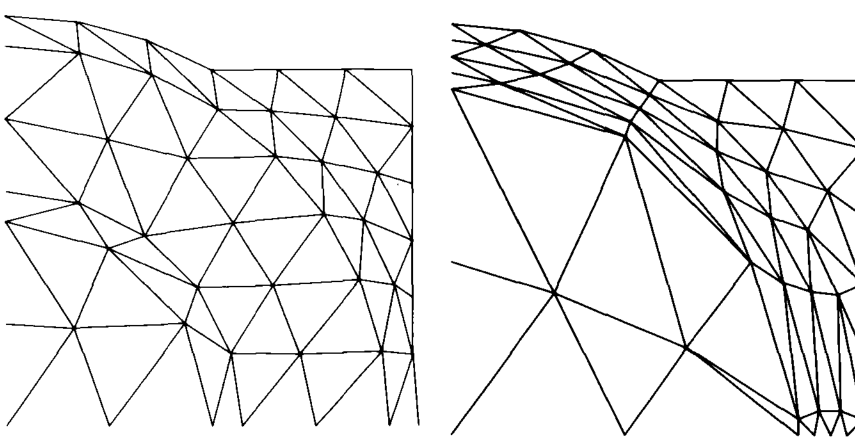

(a) (b)

(*a*) One quadrant of a toroidal shell, projected in the x-y plane.
(*b*) One quadrant of a long thin-walled tube.

FIG. 3—*Mesh for computation of eddy currents and fields.*

[5]Colonias, J. S. and Dorst, J. H., "Magnet Design Applications of the Magnetostatic Program called TRIM," *Proceedings*, International Symposium on Magnet Technology, Stanford Linear Accelerator Center, Stanford, Calif., 1965.

Five other programs create movies of the magnetic field, eddy currents, or instantaneous power using DISSPLA[6] graphic subroutines. E3DPLT15 plots a three-dimensional surface of the field values stored in FILE 26 as shown in Fig. 4. EDDYMOVIE represents the same data by coloring the mesh triangles with colors corresponding to field intensity: low-fields green, intermediate-fields yellow and orange, and high-fields red. EDDYCURAS represents the eddy currents, stored in FILE 27, by the movement of asterisks along the mesh lines, with higher currents represented by more rapid movement. The currents can also be represented by arrows, with the area of the arrow proportional to the vector sum of the currents at each node; this is performed by program EDDYCURAR (Fig. 5). Similarly, program EDDYPOWER represents the instantaneous power associated with each node by an octagon with area proportional to the power.

Turner and Lari[4] describe the operation of the program, including its time and size requirements, in more detail.

Figure 6 illustrates how symmetry considerations permit cases to be calculated using only one quadrant of the geometry.

Treatment of Curved Shells

When treating a curved shell, the same mesh generator is used as for plates. The program is made to specify values of z as a function of the x- and y-coordinates of the mesh point; z must be a single-valued function of x and y, although reflection through the x-y plane is also permitted. If only one octant is modeled and symmetry 8 is specified, reflections through all three coordinate planes are performed.

Modifications to expressions in the programs are required for the applied flux through a loop and the flux through a loop due to a current-carrying line. The expression for applied flux is multiplied by the cosine of the angle between the normal to the loop and the z-axis. The expression for the flux from a line is multiplied by the cosine of the angle between the normal to the loop and the normal to the triangle defined by the line and the centroid of the loop in Fig. 1.

The three-dimensional field plots, as shown in Fig. 4, can be made to represent either the normal component of field over the conducting shell or the z-component of field in the x-y plane.

Results

Two calculations are described here: field shielding by a thin-walled toroidal shell and eddy-current effects on a notched tube in a sinusoidal field. Calculations with simple geometries are described elsewhere.[3,4]

[6] A proprietary software package of the Integrated Software Systems Corporation, P.O. Box 9906, San Diego, Calif. 92109.

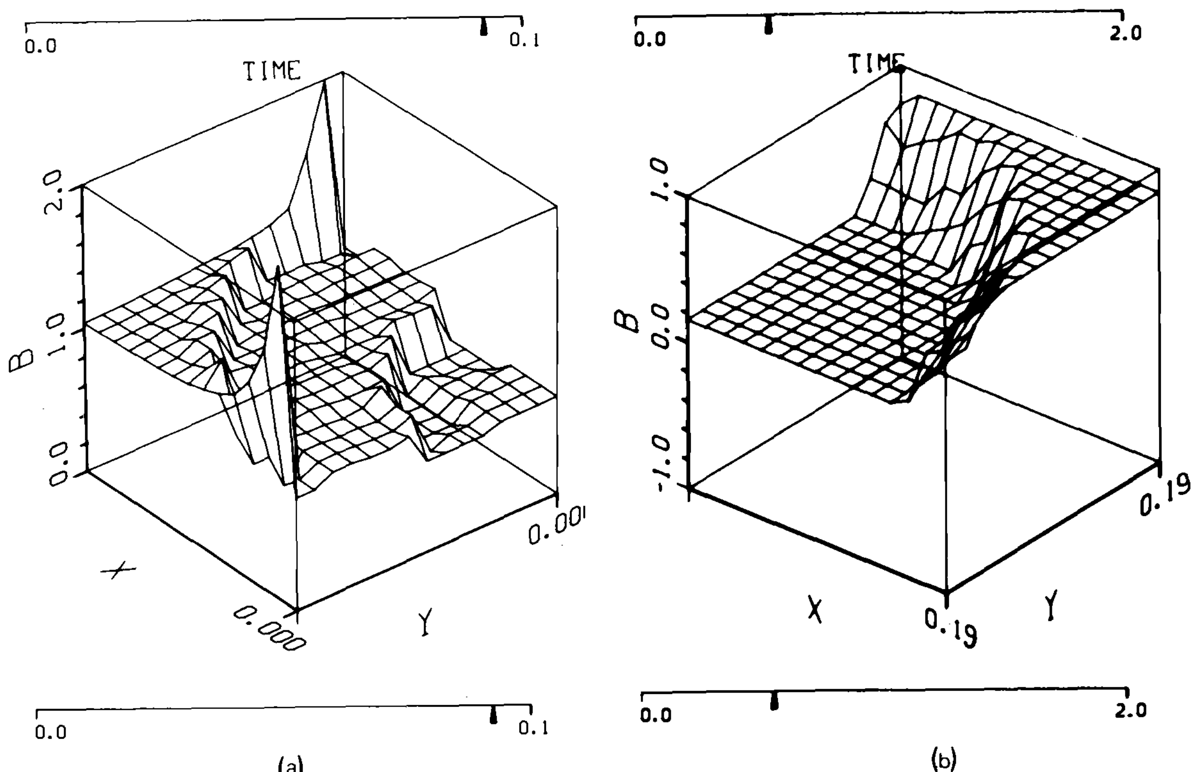

(*a*) Toroidal shell in a ramped field. (See text for details.)
(*b*) Thin-walled tube in a sinusoidal field, with attenuation and phase delay.

FIG. 4—*Three-dimensional plot of magnetic field in the* x-y *plane.*

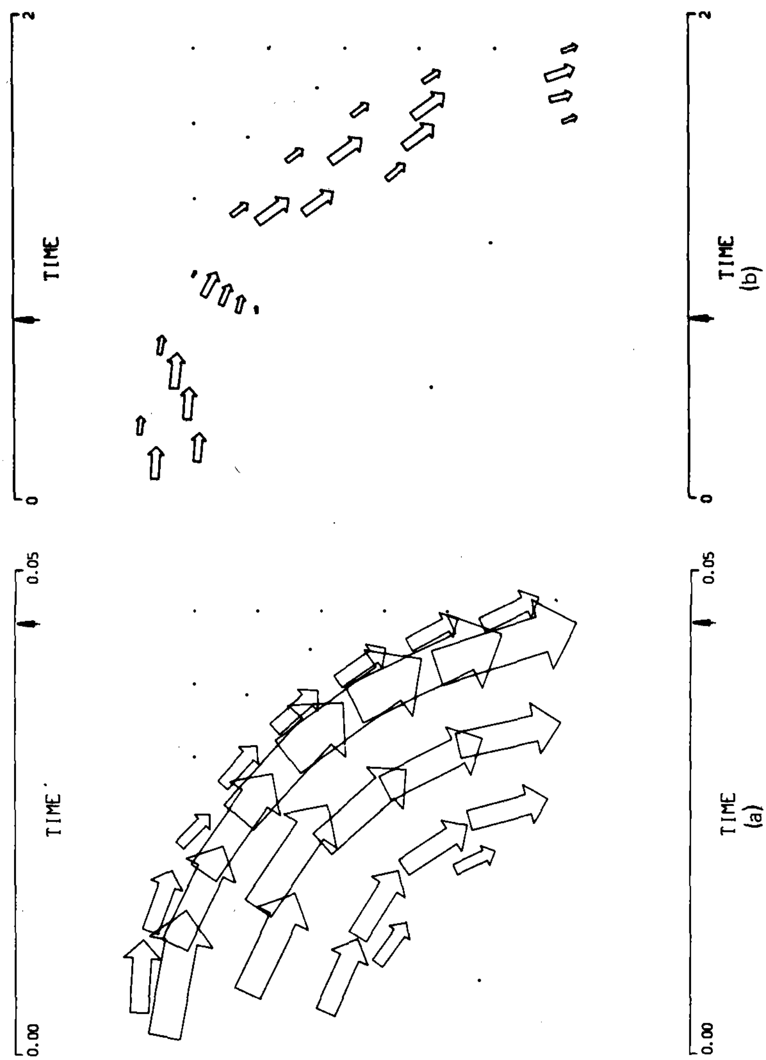

(*a*) Currents on the toroidal shell.
(*b*) Currents in the thin-walled tube.

FIG. 5—*Eddy-current patterns represented by arrows. The area of the arrow is proportional to the magnitude of the current.*

Figure 7 shows the three-dimensional mesh for the torus, and Fig. 3*a* shows the projection of the mesh on one quadrant of the x-y plane over which the calculation was carried out. The torus has a major radius of 7.0 m and an aspect ratio of 3. The wall has a thickness of 0.12 m and a resistivity of $7.0 \times 10^{-6}\ \Omega \cdot \mathrm{m}$. The applied field rises to 1.0 T in 0.02 s, uniform and in the z-direction. Figure 4*a* shows the field in the x-y plane at a time after the field is ramped up. At the left the field outside the torus is falling back to 1.0 T while the field within the torus (center) and in the hole (right) is rising. Note that there is more shielding in the hole than within the torus. This is in accord with the pattern of eddy-current flow in Fig. 5*a*, in which the current on the inside and outside surface of the torus are in the same direction.

Figure 3*b* shows the mesh for an infinitely long, thin-walled tube with

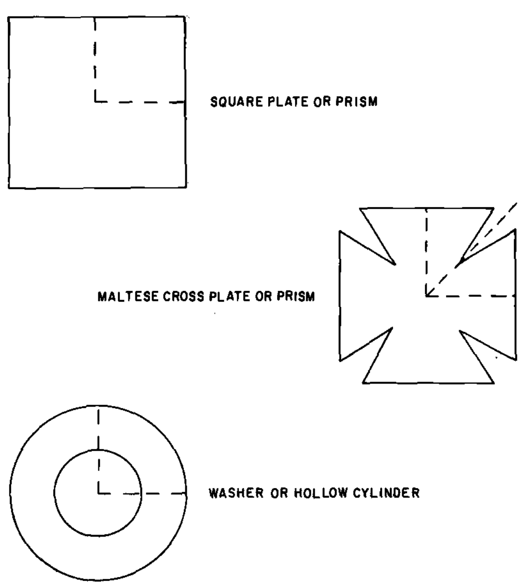

FIG. 6—*One quadrant suffices to solve a geometry with appropriate symmetry.*

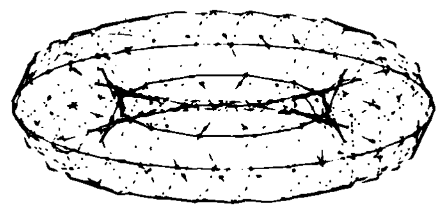

FIG. 7—*Complete mesh for the toroidal shell (isometric view).*

outside diameter 0.38 cm, wall thickness 0.03 cm, and resistivity 0.1×10^{-6} $\Omega \cdot$ m. Three cases were calculated: one with the cylinder unnotched, one with a 0.07 cm deep by 0.016 cm full-width notch on the outside, and one with a 0.008 cm deep by 0.016 cm full-width notch on the inside. For the external notch, the triangle at the lower right of Fig. 3*b* was taken to be air rather than conductor; for the interior notch, the corresponding triangle inside the tube was changed to air. The symmetry of Fig. 3*b* requires that there be a notch where the second and third quadrants meet as well as where the first and fourth meet.

The applied field was taken to be of the form

$$B_{\text{app}} = [1-\exp(-t/0.072\text{ s})] \sin(2\pi t/0.072\text{s} + \phi) \tag{7}$$

with $\phi = 7$ deg. The exponential rise and the phase angle ϕ were chosen to make transient effects disappear as soon as possible.

Figure 4*b* shows the phase delay and shielding of the field inside the

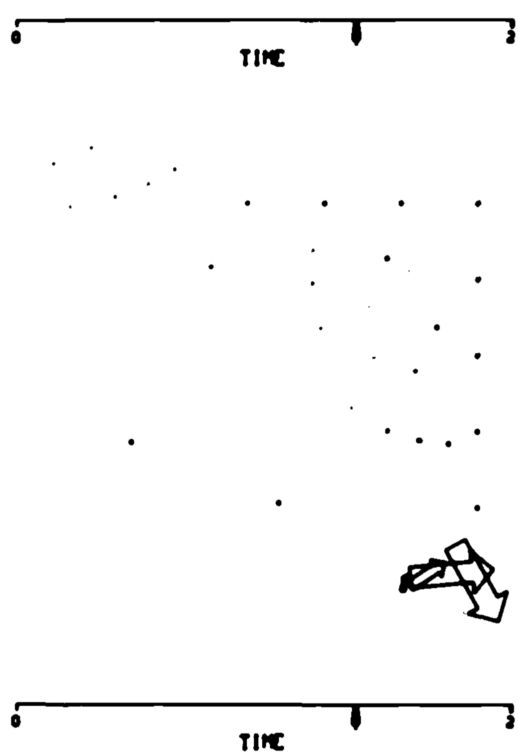

FIG. 8—*Eddy currents in the thin-walled tube. Difference between the current with a notch on the outside and the current with no notch.*

tube relative to that outside; Fig. 5*b* shows the eddy currents at one instant of time. The effects of the notch cannot be seen in Figs. 4*b* and 5*b*. To make them visible, the fields and currents with no notch were subtracted from those with a notch, and the results plotted. Figure 8 shows the difference current for the outside notch. It was observed that the current arrow at each node rotated in time in opposite sense for the inside notch and the outside notch.

Note

These calculations show up much more distinctly in movies which the authors have prepared.

Acknowledgments

This work was supported by the U.S. Department of Energy.

M. V. K. Chari[1] *and T. G. Kincaid*[1]

Finite-Element Analysis of Eddy-Current Flaw Detection

REFERENCE: Chari, M. V. K. and Kincaid, T. G., **"Finite-Element Analysis of Eddy-Current Flaw Detection,"** *Eddy-Current Characterization of Materials and Structures, ASTM STP 722*, George Birnbaum and George Free, Eds., American Society for Testing and Materials, 1981, pp. 59–75.

ABSTRACT: The eddy-current nondestructive evaluation (NDE) inversion problem is to determine flaw parameters from eddy-current sensor impedance changes. Two approaches to solving this problem are discussed for geometries with two components of eddy current. The first is to use the finite-element method of numerical analysis to compute the sensor impedance change for each flaw parameter value. The second approach is to combine the finite-element method with an analytical scattering technique. These two approaches are applied to the problem of an infinitely long coil surrounding an infinitely long conducting bar with an infinitely long surface crack. The calculated impedance changes show good agreement with known analytical and experimental results.

KEY WORDS: eddy current testing, nondestructive testing, nondestructive evaluation, finite-element method

The eddy-current nondestructive evaluation (NDE) inversion problem is to determine flaw parameters from the measured changes in the eddy-current sensor impedance. This is equivalent to determining the transformation between the flaw parameters and the impedance changes of the sensor caused by the flaw. A method of obtaining this transformation is to find the electromagnetic fields induced in the material by the sensor, with and without the flaw, and to use these fields to calculate the change in sensor impedance. The principal difficulty is solving Maxwell's equation in the complex geometries involved. Two approaches to overcoming this difficulty are shown for problems with two-component eddy-current fields, and both are applied to an infinitely long coil surrounding an infinitely long conducting bar with an infinitely long radial surface crack. The results are compared to previous analytical and experimental work.

The first approach is to use the finite element method (FEM) to compute

[1] Manager, Electromagnetics Program, and manager, Nondestructive Testing and Measurement Program, respectively, General Electric Company, Schenectady, N. Y. 12301.

the sensor impedance with and without the flaw. The impedance change can then be found by subtracting the two. An example of the use of this method has been previously reported for a problem with a one-component eddy-current field *[1]*.[2] The FEM approach has the advantages that it can be applied to almost any geometry and that it is capable of very high accuracy. The disadvantage is that a separate computation must be made for each flaw parameter, which can be expensive. In addition, the lack of an analytical transformation equation hinders "understanding" of the relationship between the flaw parameters and the sensor impedance changes.

The second approach is to combine the FEM with analytical scattering theory. In this approach, the eddy-current field in the unflawed material is computed using the FEM. Scattering theory is then used to compute the fields resulting from the introduction of the flaw into this incident field. A formula is then derived for the sensor impedance change as a function of the flaw parameters and the incident field. This combined approach has the advantages that the FEM computation needs only to be made once and that the impedance change formula enhances "understanding" of the relationship between the flaw parameters and the impedance change. The disadvantage is that the formula can be only applied to flaws that fit the scattering model flaw geometry.

Two-Component Finite-Element Analysis

This section outlines the analysis required for computing two-component eddy-current fields by the finite-element method. The two-component eddy-current problem can be formulated directly in terms of a single-component diffusion equation in the magnetic-field intensity H. The formulation thus follows closely that previously presented by the authors *[1]*, requiring only some notational changes.

Assumptions Underlying the Analysis

The following assumptions are made in modeling the eddy-current problem and obtaining the field solution:

1. Displacement currents are neglected and the problem is treated as quasi-stationary.
2. The source current is assumed to be free of eddy current and proximity effects.
3. The resistivity of the conducting parts is constant and single valued.
4. The problem is assumed to be two-dimensional and linear and all field quantities are considered to be harmonic functions of time.
5. The current density is assumed to have components along the x and y

[2] The italic numbers in brackets refer to the list of references appended to this paper.

directions, while the magnetizing field, H, has only one component along the z direction.

Linear Diffusion Equation

For the two-component linear eddy-current field problem, subject to the assumptions stated above, the magnetic-field intensity vector, $\bar{H}$, is a single-component vector given by the solution to the linear diffusion equation

$$\frac{1}{\sigma} \nabla^2 \bar{H} = j\omega\mu\bar{H} \tag{1}$$

where

σ = conductivity,
μ = permeability, and
ω = radian frequency.

Finite Element Representation

Equation 1 can be reformulated in variational terms by energy expressions called functionals. The finite-element method consists of discretizing the field region into subregions or elements and projecting approximations to the solutions $\bar{H}$ that minimize the corresponding functionals. This process results in a matrix equation, which when solved yields the solution to the eddy-current problem. The accuracy of the solution depends largely on the discretization of the field region and the prescription of a good solution approximation. For the sake of completeness, the salient steps of the finite element method are presented next, using a second-order approximation to the field solution.

Representing the diffusion-equation formulation (Eq 1) in terms of a single differential equation

$$D\psi = f \tag{2}$$

where:

D = differential operator,
ψ = potential function, and
f = source or forcing function.

The expression for the energy functional is obtained as

$$F = \langle \psi | D\psi \rangle - 2\langle \psi | f \rangle \tag{3}$$

where the inner product $\langle\ \rangle$, represents volume integration of the dot product of the variables.

We now subdivide the field region into triangular elements as shown in Fig. 1 and prescribe the potential function, ψ, in each element in terms of interpolation polynomials called shape functions, weighted by function values at the nodes. We may thus write

$$\psi = \sum_{k=1}^{n} \zeta_k \psi_k \tag{4}$$

For the second-order approximation, the shape functions are given as

$$\zeta_k = \zeta_k(2\xi_k - 1) \quad \text{for} \quad k = 1, 3, \text{or } 5 \tag{5}$$

$$\zeta_k = 4\xi_p\xi_q \quad \text{for} \quad k = 2, 4, \text{or } 6 \tag{6}$$

with p, q respectively (1, 3), (3, 5), (5, 1), and

$$\xi_k = \frac{(a_k + b_k x + c_k y)}{2\Delta}, \tag{7}$$

where Δ is the element area, and a_k, b_k, and c_k are defined in progressive modulo 3 as

$$a_k = \begin{vmatrix} x_l & x_m \\ y_l & y_m \end{vmatrix}; \qquad b_k = (y_l - y_m); \qquad c_k = (x_m - x_l) \tag{8}$$

The final set of complex linear equations is thus expressed in matrix form in terms of the coefficient matrix, $[S]$, and the related numerical matrix, $[T]$, as

$$K_1[S][\psi] + j\omega K_2[T][\psi] = [T][f] \tag{9}$$

where $K_1 = 1/\sigma$; $K_2 = \mu$; $\psi = \bar{H}$.

Equation 9 is recognized readily as identical to Eq 16 of Ref *1*.

Boundary Conditions and Forcing Function

For the two-component eddy-current field problem described previously, with a single-component magnetic field, H, the field external to the infinitely long coil is zero. Also, the magnetic-field distribution in the coil is unaffected by the circulating currents in the conducting bar.

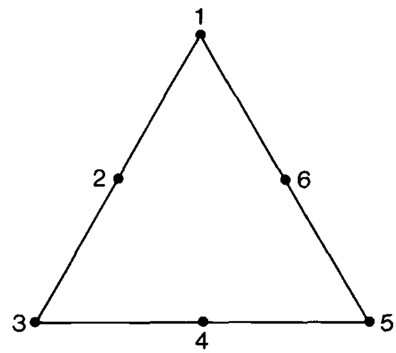

FIG. 1—*Second-order triangular element.*

The value of the forcing function, H, on the inner surface of the coil is related to the coil current density, J, which is uniform such that

$$H_{T1} - H_{T2} = J \tag{10}$$

Winding Resistance and Inductance

The total energy stored in the system is obtained by integrating the product of free-space permeability and the square of the magnetic field, H, over the volume. The energy per unit length is thus

$$W_s/l = 1/2\Sigma\mu_o|H|^2\Delta \tag{11}$$

where l is the length of the bar or solenoid.

Equating the above expression to the well-known stored energy in the terminal inductance, and dividing by the square of the bar coil current, I, we have

$$L/l = \Sigma\frac{\mu_o|H|^2\Delta}{I^2} \tag{12}$$

The power dissipated per unit length in the bar resistance is obtained by integrating the ohmic losses over the volume, giving

$$P_d/l = 1/2\Sigma J_e^2\rho\Delta \tag{13}$$

where the sum is over all triangles, and

J_e = eddy-current density, and
ρ = resistivity of the bar.

Note that J_e can be calculated from H by Maxwell's equation

$$\nabla \times \overline{H} = \overline{J}_e \tag{14}$$

Equating the above power loss to the I^2R product, one obtains

$$R/l = \frac{\frac{1}{2}\Sigma J_e{}^2 \rho \Delta}{I_p{}^2/2} = \frac{\Sigma J_e{}^2 \rho \Delta}{I_p{}^2} \tag{15}$$

The results of applying the FEM analysis to the problem of the infinitely long conducting bar surrounded by an infinitely long coil are shown in Figs. 2 to 7. The eddy-current density profiles in the bar cross section, without and with a crack, are shown in Figs. 2 to 5. The corresponding impedance-plane diagrams are illustrated in Figs. 6 and 7. The test results in Fig. 7 are those of Forster [2].

Two-Component Scattering Theory

The Scattering Model

In the scattering theory approach, the change in sensor impedance is found from the incident and scattered fields of the flaw by using the reci-

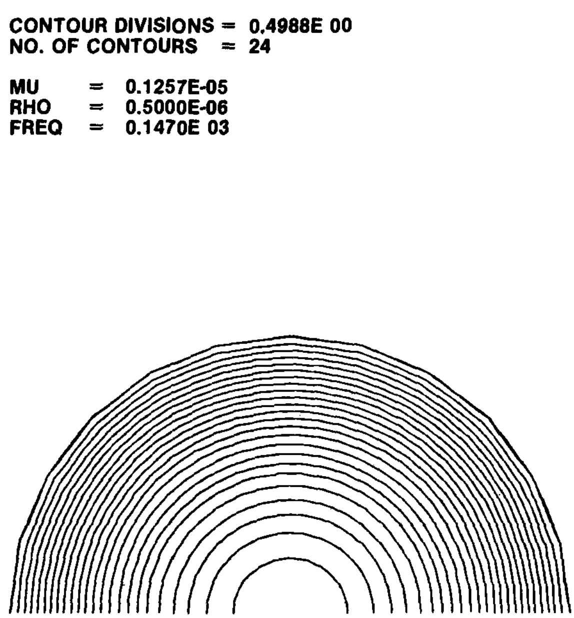

FIG. 2—*Real-part eddy-current profile in cross section of round bar without crack.*

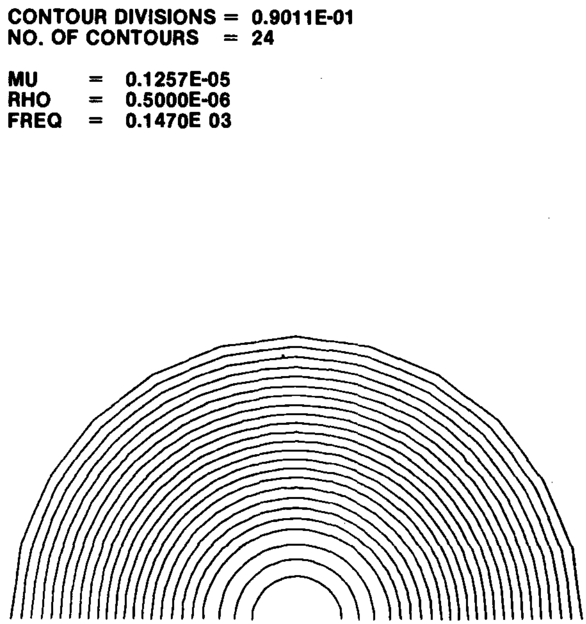

FIG. 3—*Imaginary-part eddy-current profile in cross section of round bar without crack.*

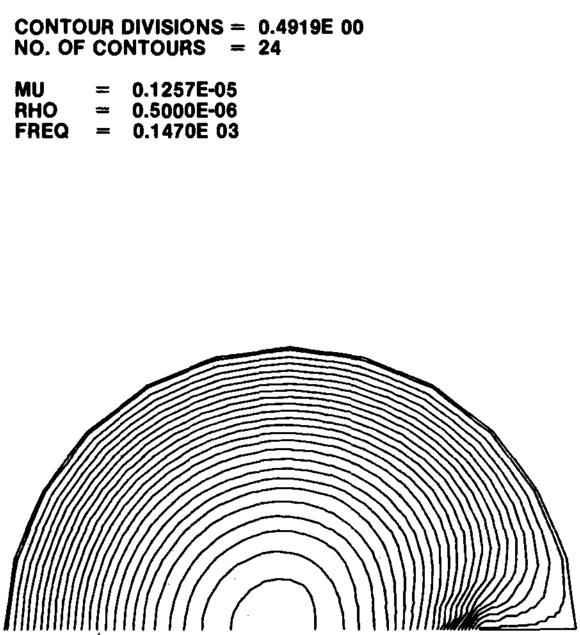

FIG. 4—*Real-part eddy-current profile in cross section of round bar with crack.*

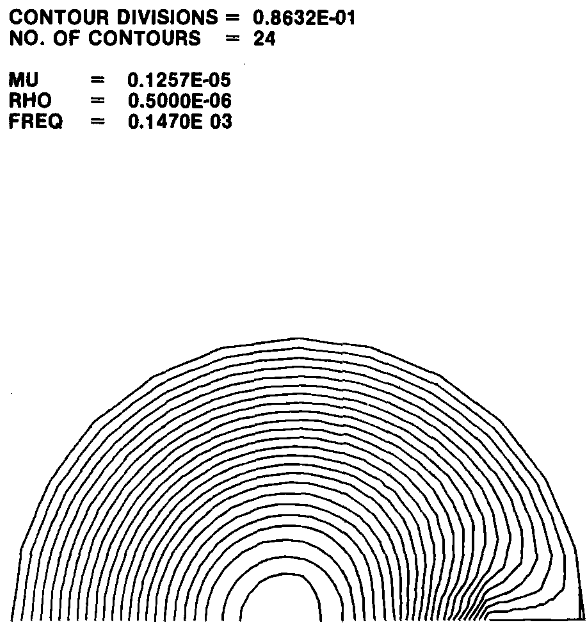

FIG. 5—*Imaginary-part eddy current profile in cross section of round bar with crack.*

procity theorem, as explained by Auld [*3*]. For a void flaw in a homogeneous, isotropic conducting medium with permittivity, ϵ_o, and permeability, μ_o, the change in sensor impedance, ΔZ, is given by

$$\Delta Z = \frac{1}{I^2} \int_{V_f} \sigma(\bar{E} \cdot \bar{E}')dv \tag{16}$$

where:

I = sensor terminal current,
$\bar{E}$ = electric field without the flaw,
$\bar{E}'$ = electric field with the flaw, and
V_f = volume of the flaw.

Therefore, to compute the sensor impedance change it is necessary to compute the electric fields within the boundaries of the flaw both when the flaw is present and when it is not.

The strategy for computing these electric fields is to approximate the incident field (that is, the field without the flaw) by a constant plus a linearly varying component, as shown in Fig. 8. The respective scattered fields can then be computed for an elliptic cylinder flaw by assuming dipole and quadrupole scattered fields, and matching boundary conditions at the flaw.

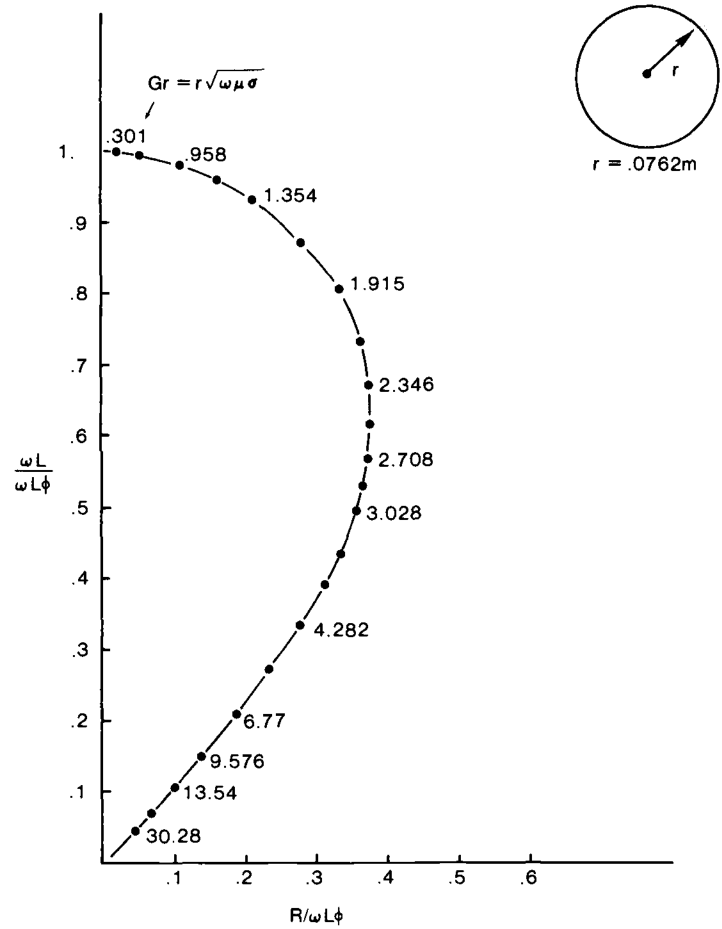

FIG. 6—*Normalized impedance plane diagram for circular cross section.*

The resultant field (that is, the field with the flaw) is then the sum of the incident and scattered fields (Figs. 9 and 10).

In Cartesian coordinates, the constant component of the incident eddy-current field is given by

$$\bar{J}_{ci} = \bar{i}_y J_{ci} \tag{17}$$

The associated scattered current field is a dipole field. The resultant sum field satisfies the static form of Maxwell's equations and matches the current boundary condition for a void, that is, zero current normal to the flaw boundary, $\rho = \rho_o$.

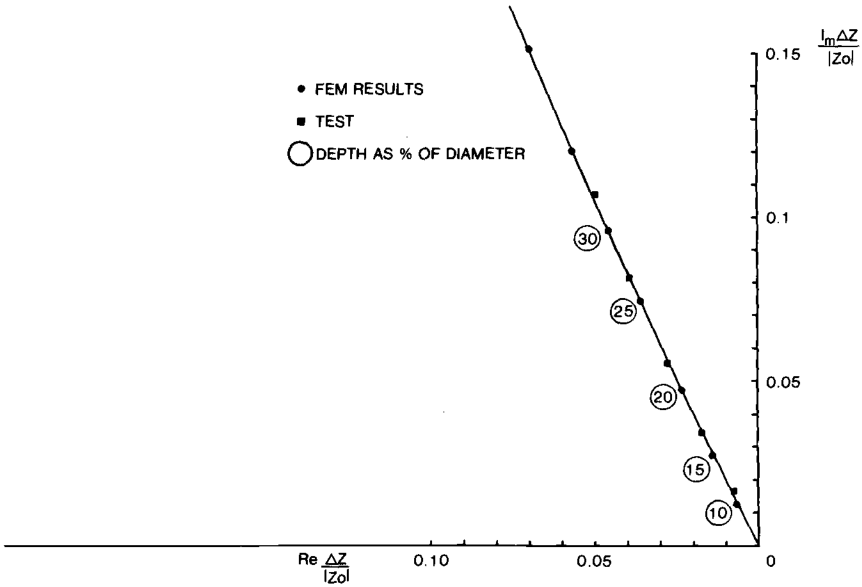

FIG. 7—*Comparison of finite element results with experiment for a crack in a bar with circular cross section.*

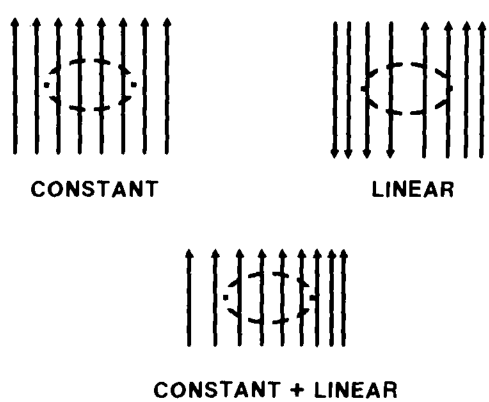

FIG. 8—*Incident eddy-current fields.*

The important field for the sensor impedance change calculation is the electric-field interior to the flaw boundary with and without the flaw. When there is no flaw, the interior electric field is the incident current-density field divided by the conductivity

$$\bar{E}_c = \bar{i}_y \frac{J_{ci}}{\sigma} \tag{18}$$

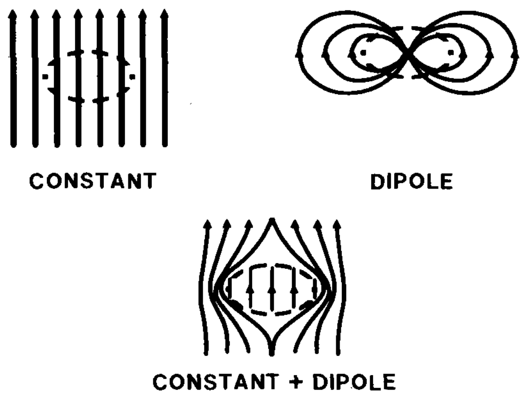

FIG. 9—*Electric fields for dipole scattering.*

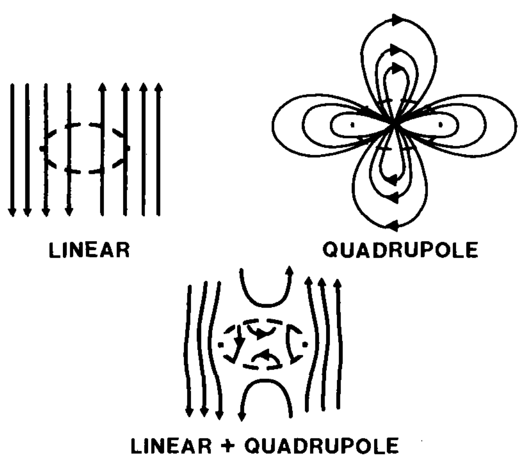

FIG. 10—*Electric fields for quadrupole scattering.*

When there is a flaw, the electric field inside the flaw is the constant field

$$\bar{E}_c{}' = \bar{i}_y \frac{J_{ci}}{\sigma} \frac{a+b}{b} \tag{19}$$

where a and b are the major and minor axes of the ellipse. This field satisfies the static form of Maxwell's equations and matches the boundary condition for the electric field, that is, no change in the tangential electric field across the flaw boundary.

Similarly, the linearly varying component of the incident eddy-current field is given by

$$\bar{J}_{vi} = \bar{i}_y Mx \tag{20}$$

The associated scattered current field is a quadrupole field. When there is no flaw, the electric field interior to the flaw boundary is the linearly varying incident current field (Eq 20) divided by the conductivity.

$$\bar{E}_v = \bar{i}_y \frac{M}{\sigma} x \tag{21}$$

When there is a flaw, the electric field inside the flaw is the sum of a linearly varying and a "saddle" electric field.

In elliptic cylinder coordinates (Fig. 11), this field is given by

$$\begin{aligned}\bar{E}_v = {} & \bar{i}_\rho \frac{M}{2\sigma}\frac{l}{h}\cosh^2\rho \sin 2\theta + \bar{i}_\theta \frac{M}{2\sigma}\frac{l}{h}\sinh\rho \cosh\rho\,(1 + \cos 2\theta) \\ & + \bar{i}_\rho \frac{M}{2\sigma} e^{-2\rho_o}\cosh^2\rho_o e^{2\rho}\sin 2\theta \\ & + \bar{i}_\theta \frac{M}{2\sigma} e^{-2\rho_o}\cosh^2\rho_o e^{2\rho}\cos 2\theta \end{aligned} \tag{22}$$

where h is the metric coefficient for elliptic cylinder coordinates. Note that the first two terms are the linearly varying field, $\bar{i}_y(M/2\sigma)x$, in elliptic cylinder coordinates.

Computation of the Change in Sensor Impedance

The change in sensor impedance due to the flaw can be calculated from Eq 16. For the sinusoidal steady state, the electric fields are complex quantities.

$$\begin{aligned}\bar{E} &= \bar{E}_p + j\bar{E}_q \\ \bar{E}' &= \bar{E}_p{}' + j\bar{E}_q{}'\end{aligned} \tag{23}$$

The dot product in Eq 16 is then given by

$$\bar{E}\cdot\bar{E}' = (\bar{E}_p\cdot\bar{E}_p{}' - \bar{E}_q\cdot\bar{E}_q{}') + j(\bar{E}_p\cdot\bar{E}_q{}' + \bar{E}_p\cdot\bar{E}_q{}') \tag{24}$$

The procedure from here for finding ΔZ is to substitute the expressions for

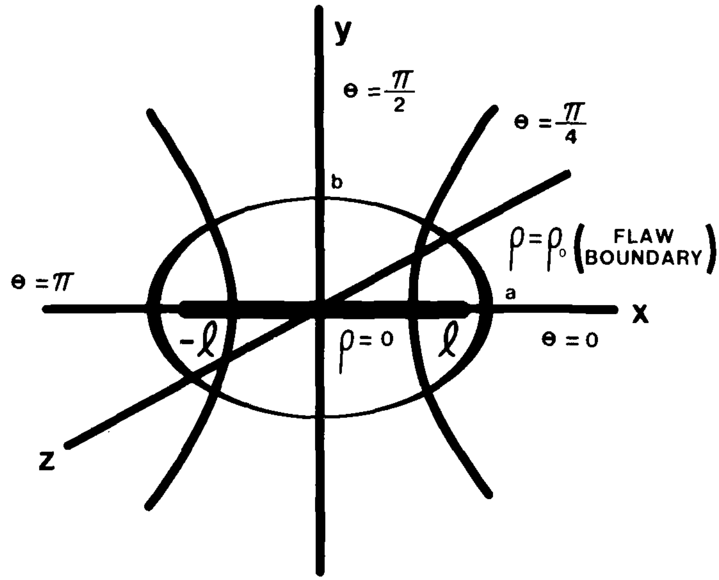

FIG. 11—Elliptic cylinder coordinates.

the various electric fields into the right side of Eq 24, and perform the integration indicated in Eq 16.

The problem to be solved here is shown schematically in Fig. 12. The change in impedance of the lossless coil wrapped tightly around the cylinder is to be found as a function of the tight surface crack depth. The crack cross-section is assumed to be a semiellipsoid as shown. By letting the minor axis b approach zero, the ellipsoid becomes a tight crack.

The distribution of the eddy-current density in a conducting cylinder with no crack is well known [*4*], or can be computed by FEM analysis as shown previously. The real and imaginary parts of this distribution are shown in Fig. 13 for $gr = \sqrt{5}$, normalized to the eddy-current density $J(0)$ at the surface of the cylinder. The constant plus linearly varying approximations to this normalized incident eddy-current field at the surface of the cylinder are shown as dashed lines in Fig. 13. The real part is approximated by the constant 1 plus a linearly varying field with slope A. The imaginary part is approximated only by the linearly varying field with slope B.

Thus, when there is no flaw, the approximations to the real and imaginary parts of the electric field inside the flaw boundaries are given by appropriate combinations of Eqs 18 and 21.

$$\bar{E}_p = \frac{J(0)}{\sigma}\left[\bar{i}_y + \bar{i}_y A \frac{x}{r}\right] \tag{25}$$

$$\bar{E}_q = \frac{J(0)}{\sigma}\left[\bar{i}_y B \frac{x}{r}\right] \tag{26}$$

When there is a flaw, the electric field inside the flaw is given by appropriate combinations of Eqs 19 and 22.

$$\bar{E}_p{}' = \frac{J(0)}{\sigma}\left[\bar{i}_y \frac{a+b}{b} + \bar{i}_y \frac{A}{2}\frac{x}{r} + \bar{i}_\rho \frac{A}{2r} e^{-2\rho_o} \cosh^2\rho_o e^{2\rho} \sin 2\theta + \bar{i}_\theta \frac{A}{2r} e^{-2\rho_o} \cosh^2\rho_o e^{2\rho} \cos 2\theta\right] \tag{27}$$

$$\bar{E}_q{}' = \frac{J(0)}{\sigma}\left[\bar{i}_y \frac{B}{2}\frac{x}{r} + \bar{i}_\rho \frac{B}{2r} e^{-2\rho_o} \cosh^2\rho_o e^{2\rho} \sin 2\theta + \bar{i}_\theta \frac{B}{2r} e^{-2\rho_o} \cosh^2\rho_o e^{2\rho} \cos 2\theta\right] \tag{28}$$

The change in impedance ΔZ can now be found by substituting Eqs 25 to 28 into Eq 24, and performing the integration (Eq 16) over the semielliptical cylinder volume, and letting the crack width b go to zero.

It has been assumed implicitly up to this point that the scattering model is valid for the semiellipse. This is exactly true for the dipole field, since there is no current normal to the y-axis. The quadrupole field, however, does have

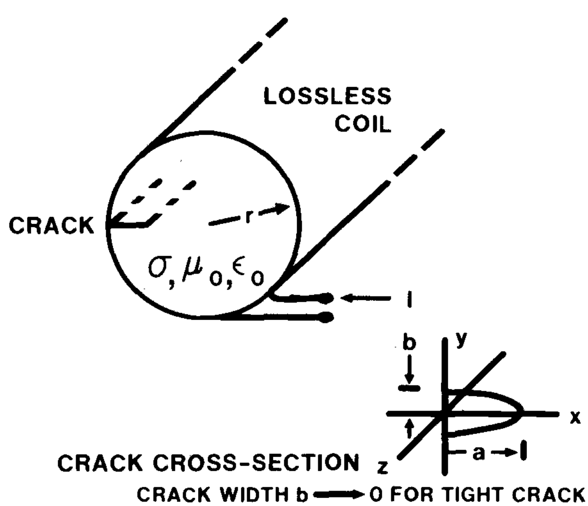

FIG. 12—*Conducting cylinder with tight surface crack.*

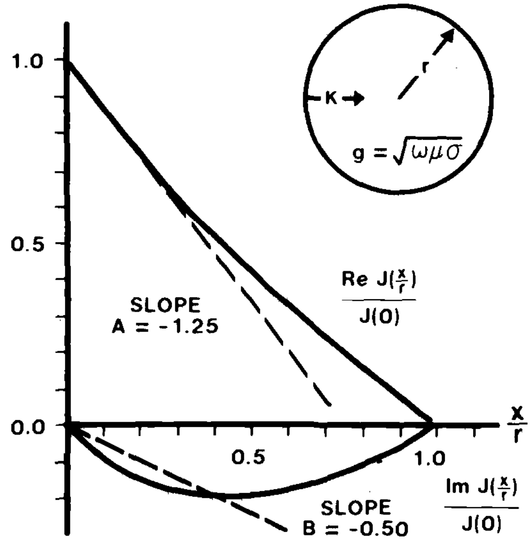

FIG. 13—*Eddy-current density in a cylinder for* gr $\doteq \sqrt{5}$.

a component normal to the y-axis, as shown in Fig. 10. This component is very small compared to the total current density in the region and is simply ignored. The placing of a boundary along the y-axis should not significantly change the distribution of the scattered field.

Carrying out the integration in Eq 16, and letting b go to zero, gives for the change in impedance per unit length

$$\Delta Z = - \frac{J(0)^2}{\sigma I^2} a^2 \left[\left(\frac{\pi}{2} + \frac{2}{3} A \frac{a}{r} \right) + j \frac{2}{3} B \frac{a}{r} \right] \tag{29}$$

It is customary in the literature to normalize this change in impedance to the magnitude of the impedance of the coil with no conducting bar inserted. The magnitude of the impedance per unit length is given by the well-known expression

$$|Z_o| = \omega \mu_o N^2 \pi r^2 \tag{30}$$

where N is the number of turns per unit length, and ω is the radian frequency of the excitation.

The expression for $J(0)$ is given by Hochschild [4] as

$$J(0) = \frac{g}{\mu_o} B_r G e^{j\gamma} \tag{31}$$

where

$$\gamma = \left[\theta_1(gr) - \theta_0(gr) - \frac{3\pi}{4}\right] \tag{32}$$

$$G = [M_1(gr)/M_0(gr)] \tag{33}$$

In these equations, the functions M_0, M_1 and θ_0, θ_1 are respectively the modulii and phases of the Kelvin functions of orders 0 and 1. The constant, B_r, is the magnetic flux density at the surface of the conducting cylinder, and is given by the well-known expression

$$B_r = \mu_o NI \tag{34}$$

Combining Eqs 29 to 32 gives change in normalized impedance of the coil as a function of the crack depth a.

$$\frac{\Delta Z}{|Z_o|} = -\frac{1}{2}(Ge^{j\gamma})^2\left(\frac{a}{r}\right)^2\left[\left(1 + \frac{4}{3}\frac{A}{\pi}\frac{a}{r}\right) + j\left(\frac{4Ba}{3\pi r}\right)\right] \tag{35}$$

Since Z is a single valued function of the crack depth a, this equation is also a solution to the inversion problem for the given conditions.

Comparison With an Experiment and Other Theories

A comparison of the normalized impedance change with an experimental and other theoretical results is shown in Fig. 14 for $ga = \sqrt{5}$. The theoretical results are those of Burrows [*5*] and Spal and Kahn [*6*]. The experimental result is from Forster [*2*]. Burrows's dipole model, as he predicted, shows good agreement with experiment only for crack depths small compared to the skin depth.

The dipole plus quadrupole model derived here compares favorably with experiment for crack depths up to one-half skin depth. The departure of the model from experiment for greater depths is due to the large error in the linear approximation to the imaginary part of the incident field beyond one-half skin depth. The exact theoretical model of Spal and Kahn follows the phase of the experimental result more closely than the others, but has about the same difference in magnitude. This suggests that the experimental conditions deviated from the model assumptions.

Acknowledgments

This work was sponsored by the Center for Advanced NDE operated by the Rockwell International Science Center for the Advanced Research

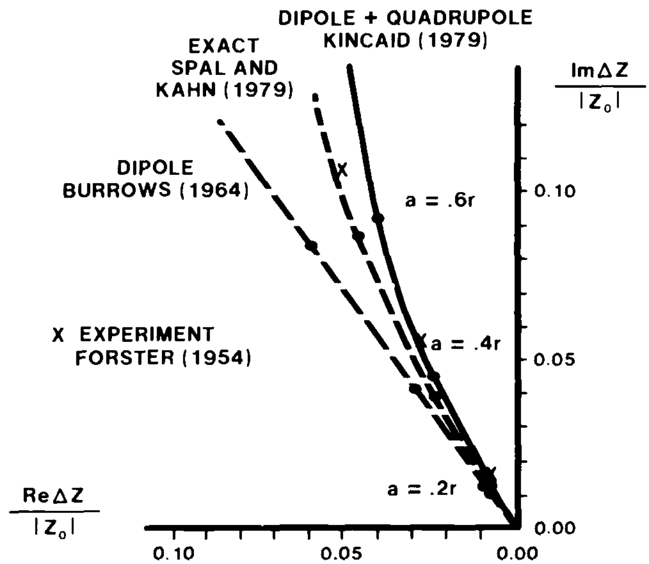

FIG. 14—*Comparison of theory and experiment.*

Projects Agency and the Air Force Materials Laboratory under Contract F33615-74-C-5180.

References

[1] Kincaid, T. G. and Chari, M. V. K., "The Application of Finite Element Method Analysis to Eddy-Current NDE," *Proceedings*, ARPA/AFML Review of Progress in Quantitative NDE, Rockwell International Report to Air Force Materials Laboratory, AFML-TR-78-205, Jan. 1979.

[2] Förster, F., "Theoretische und Experimentelle Grundlagen der Zerstörungsfreiren Werkstoffprüfung mit Wirbelstromverfahren," *Zeitschrift für Metallkunde*, Vol. 45, No. 4, 1954.

[3] Auld, B. A., "Quantitative Modeling of Flaw Responses in Eddy Current Testing," Fourth Monthly Report, Electric Power Research Institute Contract No. RPI395-3, Feb. 1979.

[4] Hochschild, R., "Electromagnetic Methods of Testing Metals," *Progress in Non-destructive Testing*, E. G. Stanford and J. H. Fearon, Eds., Macmillan, New York, 1959.

[5] Burrows, M. L., "A Theory of Eddy-Current Flaw Detection," Ph.D. thesis, University of Michigan, 1964, University Microfilms, Ann Arbor, Mich.

[6] Spal, R. and Kahn, A. H., "Eddy Currents in a Conducting Cylinder with a Crack," National Bureau of Standards, (to be published).

Calibration and Standards

G. Wittig,[1] *M. Beller,*[2] *A. Leider,*[3] *W. Stumm,*[4] *and H. P. Weber*[5]

Application of Reference Standards for Control of Eddy-Current Test Equipment

REFERENCE: Wittig, G., Beller, M., Leider, A., Stumm, W., and Weber, H. P., "**Application of Reference Standards for Control of Eddy-Current Test Equipment,**" *Eddy-Current Characterization of Materials and Structures, ASTM STP 722,* George Birnbaum and George Free, Eds., American Society for Testing and Materials, 1981, pp. 79-85.

ABSTRACT: Within the German Standard Organization a working group was engaged with the task of investigating and specifying methods for testing the essential properties of eddy-current test equipment for application to the inspection of tubes with feed-through coil systems. For this purpose several reference standards are required; these contain artificial defects such as holes, longitudinal and transverse notches, and milled-off segments. Several materials are recommended for use in the usual frequency ranges.

KEY WORDS: eddy current test equipment, tube inspection, feed-through coil systems, reference standards, artificial defect, drilled hole, notch, defect length, defect resolution, end effect, frequency range

Within the German Standard Organization (DIN) the field of nondestructive testing is attached to the Committee for Materials Testing (Normenausschuß Materialprüfung). There are several independent working groups within the committee for particular nondestructive methods. One of them deals with electrical and magnetic methods. For the treatment of precisely defined problems, *ad hoc* groups may be set up; they prepare draft standards that are subsequently discussed and adopted to national standards by the working group.

One *ad hoc* group has been concerned with control methods for determination of the essential properties of eddy-current test equipment with feed-through coils for tube testing. This work and its results are reported here. Because problems related to variations in geometry were recognized, the

[1]Bundesanstalt für Materialprüfung, Berlin, Germany.
[2]Wieland-Werke, Ulm, Germany.
[3]Fa. Schmöhle, Menden, Germany.
[4]Institut Dr. Förster, Reutlingen, Germany.
[5]Mannesmann-Forschungsinstitut, Duisburg, Germany.

initial work was limited to tube testing. Tests were done using artificial control defects and measuring procedures in a simple tube geometry. There is also a commercial aspect. In the field of eddy-current testing, the nondestructive examination of tubes is probably the most important industrial application.

Our objective was to determine for an eddy-current inspection system those properties that are important for the practical performance of nondestructive examination and are independent of the specific test problem. The procedures should be designed to measure the characteristics by the use of reference standards with artificial defects. Therefore the characteristics should not be standardized but only described.

There is a series of requirements for the control defects. They should be machinable in a simple and reproducible manner; the dimensions should be easy to control. Therefore only simple shapes, drilled holes, notches, and milled-off segments were considered. The techniques for machining the control defects into tube pieces had to be chosen so that no inadmissible changes in the material properties could arise. Further, to avoid unreliable measurements, the dimensions of the control defects should be selected so that the signal amplitudes are much higher than the noise signal.

The eddy-current inspection system includes the coil system and the electronic circuitry up to the output which displays the test results in the form of a scope display, an indicating instrument, or a recorder.

Approach

As the working group began, it became apparent that the group's knowledge of the effects of the shape and dimensions of the control defects was insufficient. Provisional tube pieces with specific control defects were used by the members of the *ad hoc* group to make investigations with different test equipment. The results were discussed and new proposals were created.

This procedure may be described by an example. The local resolution of a test equipment is important for the detection of flaws that are situated close together. It is largely dependent upon the applied coil system. The minimum defect separation distance, which may be recognized from the signal shape, is a measure for this characteristic. For the determination of the smallest defect distance, a tube with a series of drilled holes was first proposed. The intervals between the 1.0-mm-diameter single holes were 4, 6, 8, 10, 15, 20, 30, 50, and 100 mm. A sketch of this tube is shown in Fig. 1. Moreover, Fig. 1 shows a recorded result of a measurement with a differential coil system; this result gives the amplitude of the eddy-current signal. The shape of the signal within the region of small separations comes from the superposition of the effect of the single defects. In this region the defect distance is not definitely determinable, and is considered a characteristic of the system.

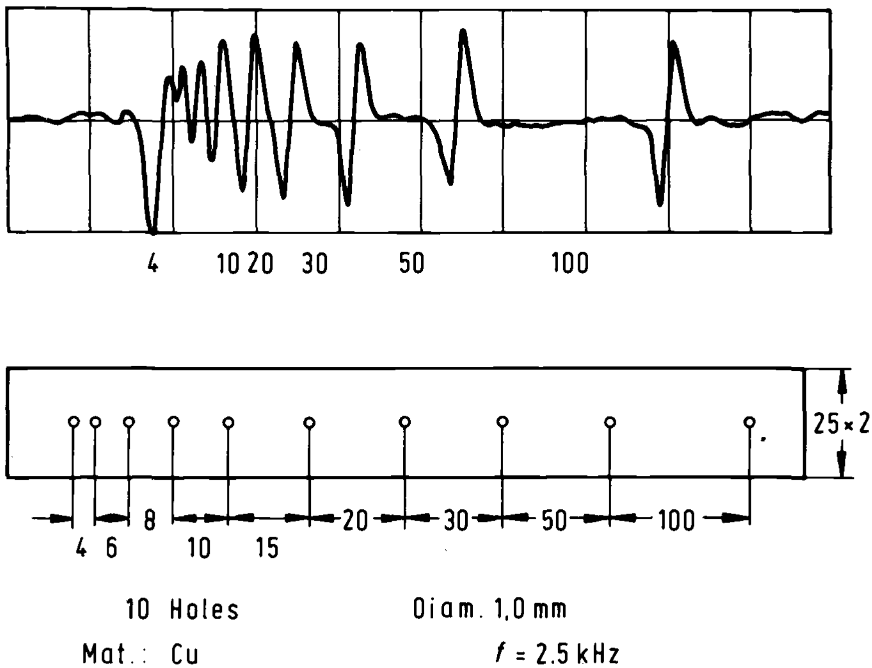

FIG. 1—*Measurement of defect resolution with drilled holes.*

A second model led to a better method. The reference tubes contained groups of three holes each. The intervals between the groups were 50 mm. Intervals of 4, 6, 8, 15, and 20 mm were provided within each group. As demonstrated in Fig. 2, the local resolution of the test system could now be defined as the distance between two holes at which the amplitude of the signal differed by no more than ± 3 dB from those of the holes with intervals of 20 mm.

A similar procedure was performed for other problems.

Characteristics of Eddy-Current Test Systems and Control Defects

As a result of these investigations, a series of procedures to determine system characteristics and the required control defects was proposed.

The reference standards should be fabricated from tubes of 25 mm diameter and 2 mm wall thickness, if possible. A 1.0-mm-diameter hole serves as a reference defect for all measurements. In most cases only the amplitudes of the defect signals are used for the evaluation.

Longitudinal notches with depths of 20, 40, and 60 percent of wall thickness are used to determine the influence of defect depth. Their length is 30 mm and their width is 0.5 mm. The ratio of the amplitudes of outer and

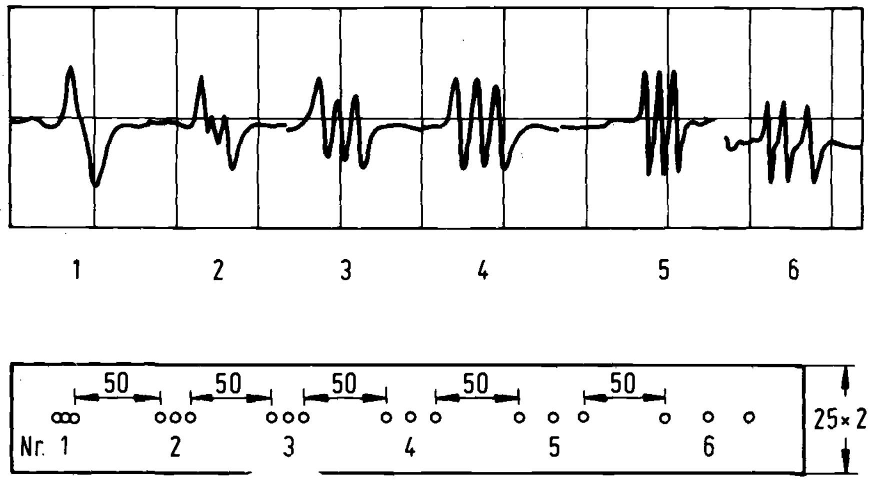

Nr.	1	2	3	4	5	6
Separation in mm	4	6	8	10	15	20

Mat.: Cu $f = 2.5$ kHz

FIG. 2—*Measurement of defect resolution with groups of drilled holes.*

inner surface defects is measured with two annular notches each. Their depths are fixed to 20 and 40 percent of the wall thickness and their widths are fixed to 0.5 mm.

The response to the defect length is found by machining milled-off segments into a tube. It is important to pay attention to the setting of any filter present. Figure 3 illustrates an example of a measurement of this characteristic. The slight increase of the amplitude of the 15-mm-long defect corresponds to a resonance caused by the feed speed and the setting of the filter. A similar behavior may arise even under different conditions.

The effect of the local situation of defects on the circumference of the tube is controlled by three holes, each with a 1.0 mm diameter, that are displaced circumferentially at 120 deg from one another and 50 mm apart from each other axially.

Based on the specific coil construction, an uninspected region at the end of the tube is unavoidable. The so-called end effect can be investigated by a series of 10 holes each with a diameter of 1.0 mm. The intervals between holes and the distance of the first hole to the tube end are uniformly fixed at 20 mm. Measured curves from a differential coil system are given as examples of the end effect and of the defect situation on the circumference in Fig. 4. In this case the end effect is 20 mm.

Testing of ferromagnetic tubes is influenced to a considerable extent by

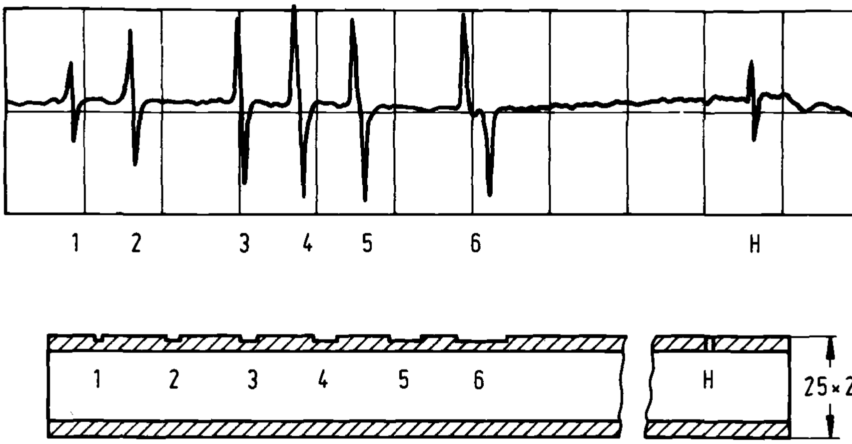

Transversal milled-off segments						depth 0,2 mm
Nr.	1	2	3	4	5	6
Length in mm	2,5	5,0	10	15	20	40

FIG. 3—*Influence of defect length.*

noises caused by the fluctuations of material properties; excessive noise can make a reliable inspection impossible. This problem can be overcome by sufficient magnetization of the test area. A minimum tangential field strength of 1.6×10^5 A/m is recommended.

The characteristic curve of the output or indication of defect signals is determined with a 2.0-mm drilled hole. This measurement is performed by first reducing the sensitivity control to 5 percent of the maximum indication, and then subsequently increasing the setting to 100 percent in five stages. The amplitudes are measured and the mean values of several single values are recorded. From this the characteristic curve of the indication can be determined.

Present eddy-current test equipment is usually provided with devices for phase rotation; the previously mentioned 20 percent outer annular notch is used for checking. The phase angle and the signal amplitude are recorded on a scope dependent on the position of the phase shifter. Also, the phase angle difference between the signals of the 20 percent outer and inner annular notch in dependence of the phase shifter position is evaluated.

Conclusions

These investigations and discussions led to a proposed application of control defects to determine essential properties of eddy-current test equipment

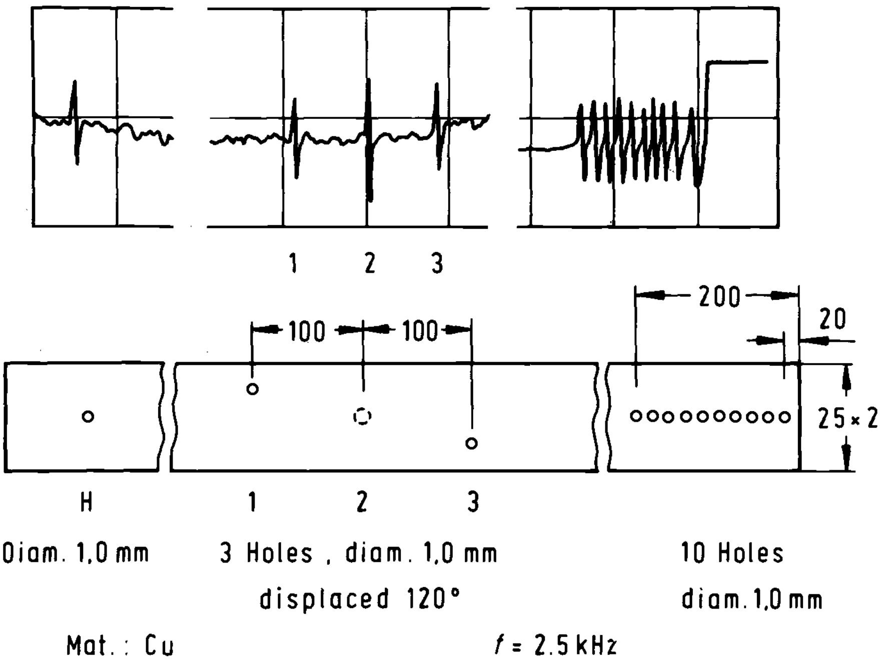

FIG. 4—*End effect and local situation of defects.*

for tube testing. As reference standards for the assigned controls, sets of tube pieces are required in which the necessary control defects are machined. Other diameters should be chosen if coil systems or driving devices for tube feed are used that do not allow the recommended tube diameter of 25 mm. The frequency range of the test equipment may be determined by the material tested. The following series is recommended:

1 to 10 kHz—OFHC copper
25 to 50 kHz—special brass, such as UNS No. (68700 ASTM B 111-80)[6]
>10 kHz—austenitic steel
1 to 100 kHz—ferromagnetic steel, such as ST 35 (German designation)

During the measurements to determine the characteristics, it was observed that the adjustments made to the equipment were customary in inspection applications. The passage of the tube pieces through the coil system is done at a constant velocity. Therefore the filter setting should not be critical.

[6]ASTM Specification for Copper and Copper-Alloy Seamless Condensed Tube and Ferrule Stock.

This standard proposal offers methods to determine the essential properties of eddy-current test equipment with both outer and inner feed-through systems. The procedure also makes possible the comparison of test systems.

There are substantial differences between ASTM Recommended Practice for Electromagnetic (Eddy-Current) Testing of Seamless Copper and Copper-Alloy Tubes (E 243-74) and the scope of the standard mentioned previously. ASTM E 243-74 covers eddy-current testing of specific products, such as seamless tubes of copper and copper-alloys. The procedures are limited to diameters up to 5.08 cm (2 in.) and wall thicknesses of 0.09 to 0.3 cm (0.035 to 0.12 in.). There is also information about the appearance of indications caused by minute dents or tool chatter marks that initiate a reject signal, but that are not relevant to product quality. The artificial discontinuities described are round-bottom transverse notches (fabricated by a prescribed round file) and drilled holes. Their respective dimensions are fixed in a separate ASTM product specification. The sensitivity control settings of the eddy-current apparatus are adjusted with the help of these references discontinuities.

Present experiences with the German document are based on limited investigations within the laboratories and plants concerned with the work. A report on a direct application will be prepared at a later date.

S. Herman[1] *and R. S. Prodan*[2]

A Macroscopic Model of Eddy Currents

REFERENCE: Herman, S. and Prodan, R. S., "**A Macroscopic Model of Eddy Currents,**" *Eddy-Current Characterization of Materials and Structures. ASTM STP 722.* George Birnbaum and George Free, Eds., American Society for Testing and Materials, 1981, pp. 86–93.

ABSTRACT: In many applications only the macroscopic effects of eddy currents (those observable at the electrical terminals of an electromagnetic device) are of interest. In these cases eddy currents, hysteresis, and magnetic saturation are readily modeled using coupled electric and magnetic equivalent circuits.

KEY WORDS: magnetic circuits, eddy currents, magnetic permeability, hysteresis

Many electrical devices utilize magnetic materials. As a consequence, eddy currents are inevitably induced in the magnetic cores. Often, however, the actual microscopic distributions of the eddy currents are not important. They are only of interest because of the effects they have on the electrical performance of the device at its input and output terminals. In transformer design, for example, eddy currents are usually of consequence only in the power loss that they induce and the effect that they have on electrical waveforms.

This paper presents a macroscopic model of eddy currents. This model, in the form of an equivalent circuit, is not derived at all as a representation of the actual eddy currents. Instead, it is a circuit fabricated to make the same mathematical contribution to the voltage and current waveform as the eddy currents. The equivalent circuit has two coupled parts, one in the electrical domain and the other in the magnetic domain. The actual electrical terminals of the device are modeled in the electrical domain; the effects of the eddy currents are generated by an inductor in the magnetic domain.

Since eddy currents are induced by magnetic flux, it is not possible to model eddy currents accurately unless the effects of magnetic saturation and hysteresis on the flux are also represented. The effects of saturation and

[1] Technical staff, Philips Laboratories, Briarcliff Manor, N.Y. 10510.
[2] Columbia University, New York, N.Y.

hysteresis are modeled in the magnetic domain by a nonlinear resistor and a voltage source, respectively. The entire equivalent circuit can be analyzed using the transient analysis feature of commercially available nonlinear circuit analysis programs.

This paper is concerned only with the model of a rectangular parallelpiped carrying flux of uniform density. However, these methods have been generalized to more complicated structures.

Coupled Electrical and Magnetic Circuits

The physical circuit of a simple magnetic reactor is shown in Fig. 1*a*. The voltage E_{source} is imposed on an N-turn reactor. The electrical current is $i_1(t)$ and the induced magnetic flux is $\phi(t)$. The electrical equivalent circuit, Fig. 1*b*, consists of the actual E_{source} and winding resistance in series with the induced voltage, E_{induced}. The magnetic equivalent circuit, Fig. 1*c*, contains a magnetic potential source and the model of the iron core. The development of this model is the subject of this paper. The two circuits are coupled by the usual relationships. Namely, the induced voltage source is set equal to $E_{\text{induced}} = N(d\phi)/(dt)$ and the magnetic potential source is Ni_1. The flux ϕ is the instantaneous "current" in the magnetic circuit, and i_1 is the current in the electrical circuit.

The model of the flux-carrying iron core has three components, which represent magnetic saturation, hysteresis, and eddy currents.

Modeling Magnetic Saturation

The magnetic saturation of flux-carrying iron can be represented in the magnetic circuit by a nonlinear resistor. The resistance is set equal to the

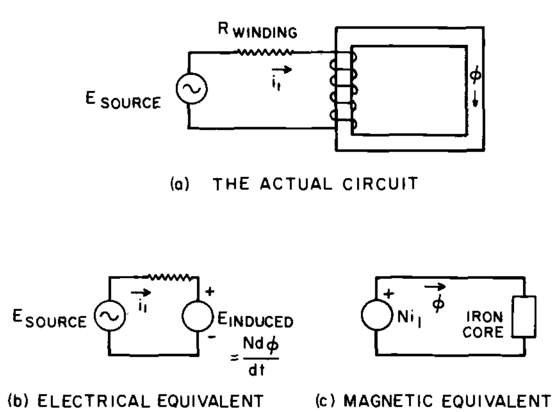

FIG. 1—*Coupled electric and magnetic equivalent circuits.*

reluctance of the iron, reluctance being the ratio of magnetic potential to magnetic flux. In the case of a uniform iron core of constant cross section and uniform flux density, the reluctance is given by

$$R(\phi) = \frac{L}{A\mu(\phi)}$$

where

L = mean flux path length,
A = core cross section, and
$\mu(\phi)$ = instantaneous permeability.

The permeability is defined as $\mu = B/H$. It can be determined from the average path along the hysteresis loop, such as the dotted curve of Fig. 2. Where the iron is driven into deep saturation, not all formulations of the reluctance provide both accuracy and numerical convergence. That topic, however, is outside the intended scope of this paper.

Instantaneous Power Loss Due to Eddy Currents

As mentioned previously, the actual eddy currents are not modeled here. Instead, a magnetic circuit element is derived that will always produce exactly the same instantaneous power losses in the electrical equivalent circuit as the actual eddy currents. As a first step in the derivation, the instantaneous losses generated by true eddy currents are derived.

Consider a thin lamination as in Fig. 3. The length along the flux flow direction is L, the width is W, and the lamination thickness is T, as shown. Let E be the electric field around a closed path normal to the uniform flux ϕ.

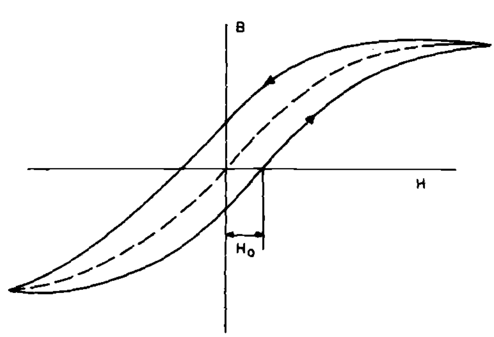

FIG. 2—*Typical* B-H *curve.*

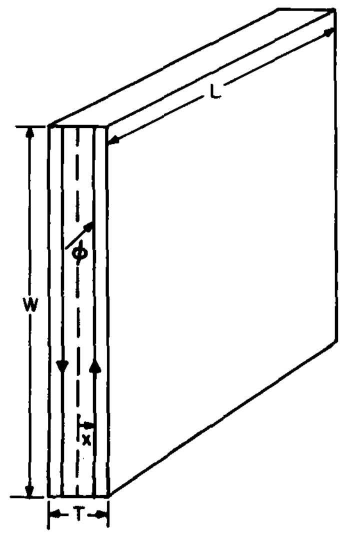

FIG. 3—*Lamination notation.*

This path runs vertically at a distance $\pm x$ from the center of the lamination. The two horizontal portions of this path are very short and may be neglected. Faraday's law states that

$$\oint E \cdot dl = -\frac{dB}{dt}\Delta a$$

where Δa is the area enclosed by the path of integration

$$|E| = \left(\frac{dB}{dt}\right)x$$

The current density, J, is E/ρ where ρ is the resistivity of the iron in ohm-meters

$$J = \frac{E}{\rho} = \frac{dB}{dt}\frac{x}{\rho}$$

Therefore, the eddy current in a path of cross section dx by L is

$$di = \frac{dB}{dt}\frac{x}{\rho}Ldx$$

The voltage along this path is

$$v(x) = xW\frac{dB}{dt}$$

The total instantaneous eddy-current power over the entire lamination thickness, T, is

$$P = \int v\,di = \left(\frac{dB}{dt}\right)^2 \frac{WL}{\rho}\int_{-T/2}^{T/2} x^2 dx$$

$$P = \left(\frac{dB}{dt}\right)^2 \frac{wL}{\rho}\,\frac{T^3}{12}$$

For a stack of M laminations the total instantaneous power is

$$P_T = PM = \left(\frac{dB}{dt}\right)^2 \frac{wL}{\rho}\,\frac{T^3}{12}\,\frac{D}{T}$$

$$= \left(\frac{dB}{dt}\right)^2 \frac{wL}{\rho}\,\frac{T^2D}{12} \qquad (1)$$

where $D = MT$ is the stack height.

Modeling Eddy Currents with a "Magnetic Domain Inductor"

Any circuit element that produces exactly the same instantaneous power dissipation in the electrical circuit as the actual eddy currents produce is defined as being an equivalent representation of the eddy currents.

In any electrical circuit element the instantaneous power is

$$P = vi$$

If a magnetic flux, ϕ, generates a magnetic potential, F, as a result of a current, i, flowing through a coil of N turns, then

$$Ni = F \quad \text{or} \quad i = F/N$$

and the induced voltage is

$$V = N\frac{d\phi}{dt}$$

Therefore, the instantaneous power is

$$P = vi = \left(N\frac{d\phi}{dt}\right)(F/N) = \frac{d\phi}{dt}F \tag{2}$$

If one conceives of a constant valued "inductor" L_M in the magnetic circuit of Fig. 1*c*, with "current" ϕ and "voltage" F, then, by the definition of "inductance"

$$F = L_M\frac{d\phi}{dt}$$

and the instantaneous power, by Eq 2, is

$$P = \frac{d\phi}{dt}F = L_M\left(\frac{d\phi}{dt}\right)^2 = L_mA^2\left(\frac{dB}{dt}\right)^2$$

where A is the cross-sectional area. Using the earlier notation, for the entire stack

$$A = DW$$

Therefore

$$P = L_M D^2 w^2\left(\frac{dB}{dt}\right)^2$$

Comparing this equation with Eq 2 for the total instantaneous eddy-current power, we see that the exact power loss is simulated by using a "magnetic inductor" of value

$$L_M = \frac{LT^2}{12Dw\rho}$$

Hysteresis Model

The magnetic domain equivalent circuit concept can be readily expanded to include a model for iron hysteresis. Such a model must simulate both major and minor hysteresis loop behavior. The complete magnetic circuit model for flux-carrying iron is shown in Fig. 4. The saturation simulating reluctance, $R1$, and the eddy-current inductor, L_M, were discussed previously. The hysteresis is simulated by the magnetic potential source E_{HYST}.

The dotted saturation characteristic of Fig. 2 is generated by the reluc-

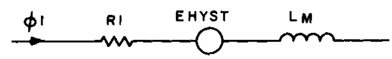

FIG. 4—*Equivalent circuit of flux-carrying iron.*

tance $R1$. To produce the hysteresis effect for a given flux density, B, H is increased by some ΔH if $dB/dt > 0$ and decreased by ΔH if $dB/dt < 0$. An arbitrary offset characteristic that yields satisfactory results is shown in Fig. 5. Here

$$\begin{aligned} \Delta H &= (H_o/\beta)dB/dt \quad \text{for} \quad |dB/dt| \leq \beta \\ &= H_o \operatorname{sgn}(dB/dt) \quad \text{for} \quad |dB/dt| > \beta \end{aligned} \tag{3}$$

where sgn yields the algebraic sign of dB/dt.

An important feature is the fact $\Delta H \rightarrow 0$ as $|dB/dt| \rightarrow 0$. This allows for the simulation of minor hysteresis loops. Each time the flux reverses, $|dB/dt| \rightarrow 0$ and the hysteresis loop is forced to merge to a point. This also avoids the numerical oscillations often associated with simpler approaches to hysteresis modeling.

The magnetic potential across the eddy-current simulating inductor is

$$F = L_M A\, dB/dt$$

which yields a readily available computation of dB/dt. This, combined with the offset formulas (Eq 3), completely specify ΔH. The hysteresis-producing magnetic potential source E_{HYST} is set equal to $L\Delta H$, where L is the mean path length of the magnetic flux. The parameter, β, is determined empirically by matching experimental data and computation.

Concluding Remarks

The use of separate electric and magnetic domain equivalent circuits allows the macroscopic effects of magnetic saturation, hysteresis, and eddy currents to be modeled by the simple circuit of Fig. 4. The three circuit elements are functions of the iron properties and the core dimensions. This allows for the direct modeling of more complex electromagnetic structures, provided they can be decomposed into pieces for which the basic assumptions hold. Among these assumptions is the premise that the core cross section and the flux distribution are uniform over the entire iron-core flux path. This restriction need not apply to leakage flux paths.

This approach has been applied successfully to a variety of fairly complex saturable transformer structures involving deep saturation, iron paths of different cross sections, and a large number of leakage paths. Calculations

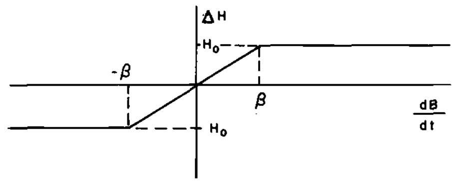

FIG. 5—*The* H *Offset,* ΔH.

and measurements of peak and root mean square voltages, as well as power dissipations, usually differed by less than 10 percent. Owing to the one-to-one correspondence between physical layout and the magnetic circuit, such a model can be rapidly formulated. Solutions of the models can be generated using the transient analysis features of a number of available nonlinear circuit analysis programs. Among the programs that have been used with success are ECAPII and ASTAP, plus PHILPAC, a proprietory product of N. V. Philips Company.

A. R. Jones, Sr.[1]

Secondary Conductivity Standards Stability

REFERENCE: Jones, A. R., Sr., "**Secondary Conductivity Standards Stability,**" *Eddy-Current Characterization of Materials and Structures, ASTM STP 722,* George Birnbaum and George Free, Eds., American Society for Testing and Materials, 1981, pp. 94–118.

ABSTRACT: Calibration values of secondary conductivity standards obtained on a periodic basis, both for the Boeing Company and for commercial customers, have shown various drift patterns. Presently, a 100-kHz bridge used with an H-P 9825 computer compares unknown secondary standards against carefully built, National Bureau of Standards (NBS) traceable, primary bars in an oil-bath environment. Factors affecting the stability of secondary standard values of conductivity include primary conductivity bar value changes, uneven surface wear, environmental contamination, lift-off due to the presence of foreign material on the surface, and aging of the metal crystalline structure. Some secondary standards, which were large physically, exhibited significant conductivity changes across their surface due to the nonhomogeneity of the metal.

Original calibration of secondary standards was accomplished by assigning the same value to a section cut from the primary bar that was given to the primary bar itself. When new alloy metals were obtained, as older metal primary bar material was exhausted for secondary use, an H-P 65 program was developed to utilize a curve-fitting method for replacement secondary-standard material calibration. Some changes in older secondary values resulted from this method. An H-P 9825 computer program was later developed, which resulted in other secondary-value changes. During the last twelve years some significant changes occurred in the primary bars, which further altered the program and the calibration results. New primary bars have been also added from time to time to smooth out the curve-fitting program, which has some effect on the calibration values of the secondary standards.

KEY WORDS: conductivity, standard, percent IACS, titanium, aluminum, alloy, secondary, primary, bar, stability, scatter

Since the Boeing Company began fabricating and calibrating nonferrous secondary conductivity standards in 1966, data from these calibrations have been recorded and periodically reviewed in an attempt to improve the limits of expected error while maintaining the same certified tolerance. Previously presented technical papers [*1,2,3*][2] have detailed the methods used to pro-

[1]Specialist engineer, Boeing Aerospace Company, Seattle, Wash. 98124.
[2]The italic numbers in brackets refer to the list of references appended to this paper.

cure, fabricate, and calibrate the 20 Boeing primary nonferrous conductivity bars that are used to calibrate all secondary conductivity standards. The primary conductivity bars are all indirectly traceable to the National Bureau of Standards (NBS) through dimensional, resistance, and temperature parameters.

After the initial assigning of the same values, in percent International Annealed Copper Standard (IACS), to the secondary conductivity standards that were assigned to the primary conductivity bar from which they were cut, a 100-kHz guarded calibration bridge was designed and built. This bridge is used to calibrate not only nonferrous metals of other than primary-bar conductivities, but to calibrate and track the drift of the original secondary conductivity standards that were exposed to different environmental conditions than the primary-bar metal from which they were fabricated. The following discussion examines the findings of over twelve years of calibrating secondary nonferrous conductivity standards produced by the Boeing Company.

General

The need for a resistance standard for copper wire was recognized early by the electrical industry [*4*]. The British made a significant contribution toward the goal in 1864, but an acceptable international standard had to wait until 1913 at the plenary meeting of the International Electrotechnical Commission (IEC) held in Berlin. Final ratification by 24 nations was given in a report published in London in March 1914. The definition that is relevant to the conductivity program of the Boeing Company is the internationally accepted value for standard annealed copper which states, in part, that "at a temperature of 20°C the resistance of a wire of standard annealed copper 1 metre in length and of a uniform section of 1 square millimetre is 1/58 ohm = 0.017241... ohm". This arbitrary value for 100 percent IACS is used as the basic reference value for all eddy-current measurements that measure the electrical conductivity of many heat-treated aluminum and titanium alloys used in aircraft and missile fabrication.

The relationship between the physical characteristics of heat-treated aluminum alloys (such as tensile strength, corrosion resistance, and hardness) and their conductivity is well documented. Figure 1 shows a typical relationship for one such aluminum alloy where the tensile strength of the alloy is changed appreciably by heat treatment. Electrical conductivity is also changed by heat treatment; tensile strength, therefore, is a function of the measured conductivity values.

Eddy-current meters (direct-reading type) measure the conductivity in percent IACS and, to assure the instrument operator that the conductivity values he measures are accurate, the meter is calibrated against certified secondary conductivity standards. Figure 2 shows a typical eddy-current meter and a set of two Boeing secondary conductivity standards. These standards are cer-

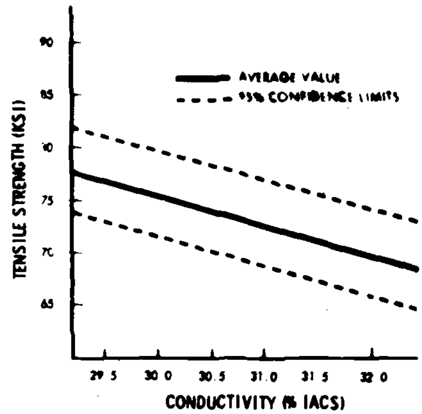

FIG. 1—*General relation between tensile strength and eddy-current conductivity measurements of 2024-T4 aluminum.*

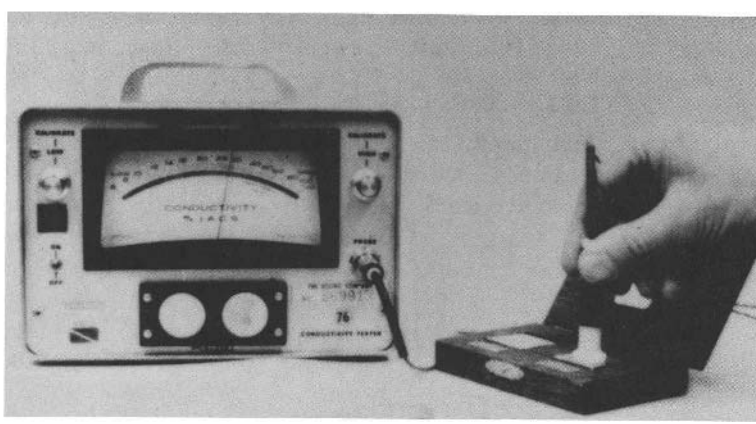

FIG. 2—*Typical eddy-current meter and standards.*

tified to be within ±0.35 percent IACS or ±1 percent of value, whichever is less, at 20°C.

Primary Conductivity Bars

The primary conductivity bars were fabricated by carefully machining the rough-cut metal bars to a predetermined size and surface finish after a thorough inspection for flaws or irregular conductivity due to hard spots, voids, or inclusions. They were then measured dimensionally at 20°C for average thickness and width. Following this, the bars were placed in a temperature-controlled oil bath and the resistance obtained for one fixed laser-interferometer-measured length on each bar. The average volume resistivity in microhm centimetres was determined for 20°C from at least six to as many as eight readings across the width (total for both sides) for the one measured length at several temperatures above and below 20°C. Figure 3 shows a view of the d-c calibration facility. Volume resistivity is converted to percent IACS by means of the formula

$$\% \text{ IACS} = \frac{172.41\, L}{RA}$$

where

R = resistance (corrected for grain direction, stratification, and aging) in ohms $\times 10^6$ at 20°C for
L = centimetres of active length of the bar having
A = an essentially constant cross-sectional area in square centimetres.

The final certified accuracy of the primary standard conductivity bars is ± 0.2 percent IACS or ± 0.5 percent of value, whichever is less, at 20°C.

Secondary Conductivity Standards

The initial sets of secondary conductivity standards consisted of eight secondary nonferrous standards 2.54 by 2.54 cm (1 by 1 in.), approximately 0.508 cm (0.2 in.) thick, made from the excess bar stock of the primary conductivity bars. Figure 4 shows a secondary set consisting of eight square con-

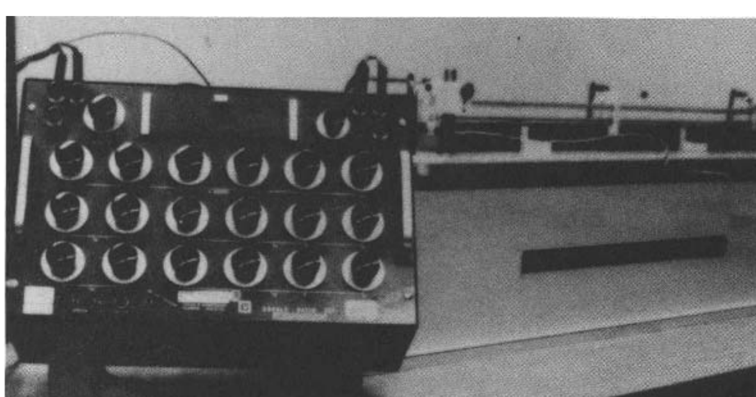

FIG. 3—*Direct-current calibration facility.*

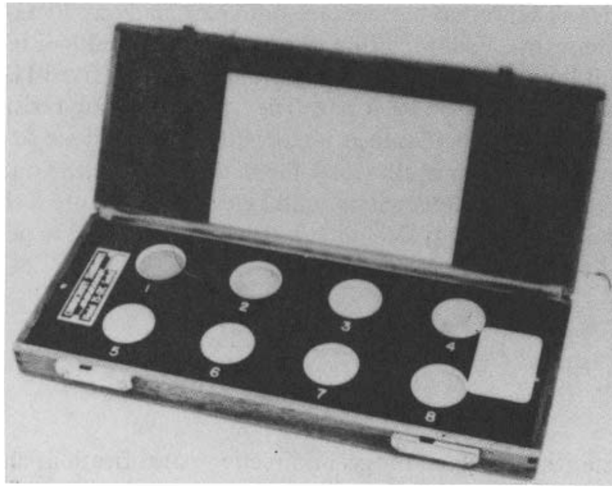

FIG. 4—*Set of eight secondary standards.*

ductivity standards mounted under round panel holes. I selected 15 typical eight-conductivity secondary sets for this investigation; ten are "high" or "aluminum" sets and five are "low" or "titanium" sets. The "high" set consists of 1 titanium, 1 brass, 1 copper, and 5 aluminum standards. The "low" set consists of 5 titanium and 3 bronze standards. Most calibration data reviewed here started to be recorded in 1967, and the recording of these data continued until 1977, 1978, or 1979, depending on when the last calibration of a particular set was made. This analysis, then, gives an overview of the stability of the assigned values for secondary conductivity standards over a 10- to 12-year period.

Significant changes were made in some of the primary bar conductivity values as a result of grain direction and stratification tests. The effect of these changes on the secondary conductivity standards is discussed in detail in Ref *2*. The original single titanium secondary standard that was a part of the "high" set was found to be too thin, which resulted in "punch through," and was replaced with a thicker standard starting in 1969 when the secondary sets came in for their periodic recalibration. The same value titanium primary conductivity bar was retired shortly thereafter for the same reason. The stability analyses of this one standard and its replacement have been omitted from this discussion.

One of the initial nonconductivity-related problems plaguing the secondary conductivity sets was getting the standards to adhere to the underside of the panel on which they were mounted. Several adhesives and under-panel support methods were tried. After much experimentation a thermosetting foam was used to support the secondary standards from the bottom side of the wooden carrying case while an adhesive kept the standards in place laterally. This was important because the panels with the standards attached must be taken out of their wooden carrying cases for recalibration in the oil bath. The foam surface is smooth enough to allow removal of the panels without breaking the adhesive seal which holds the standards to the underside of the panels. Figure 5 shows a view of the secondary-standards panel with the bridge probe used for calibration in a shallow covered oil bath that also contains all of the primary conductivity bars.

Data Analysis

Before the stability of the secondary conductivity standards can be properly analyzed, consideration must first be given to the changes, determined over the past 12 years, in the values assigned to the primary conductivity bars. In 1972 and thereafter, the effect of both stratification and grain direction was incorporated into some of the d-c values to convert them to the more accurate a-c values for eddy-current use. No a-c corrections were made to the d-c values of the copper, brass, bronze, or titanium conductivity bars. The secondary conductivity values are always compared to the values of primary conductivity bars in effect at the time of calibration in the analyses which follow.

The method employed to determine the effective stability of the secondary standards of conductivity was to analyze the "high," or "aluminum," set one value (or alloy) at a time and to compare its value to that of the primary conductivity bar from which it was cut. This analysis was followed by a similar

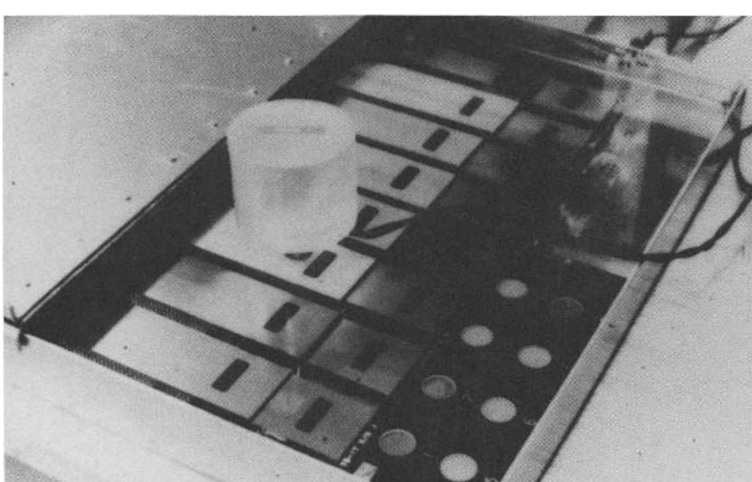

FIG. 5—*Alternating-current calibration oil bath.*

treatment of the "low," or "titanium," set. When this project was begun over 12 years ago, it was expected that surface wear and surface contamination were going to account for most of the differences in causing variations in secondary values of conductivity. No changes in secondary conductivity values, or primary conductivity values for that matter, were expected because of internal or solid-state changes. The data show, however, that for several primary bars internal changes of significant importance did take place that changed values for both kinds of standards, that is, primary bars and secondary standards. These did not necessarily result however, in the same rate of change.

Copper Conductivity Standards

The consecutive calibration values of the copper primary conductivity bar, since its initial calibration in an oil-bath facility in 1967, whose changes are shown in Fig. 6, are as follows:

1967—101.28$_9$ % IACS	1974—101.30$_0$ % IACS
1968—101.27$_6$ % IACS	1975—101.20$_8$ % IACS
1970—101.32$_3$ % IACS	1977—101.16$_3$ % IACS
1972—101.18$_0$ % IACS	10-Year Average—101.24$_9$ % IACS

The largest deviation from the 1967 fiducial value was reached in late 1977 when a total change of −0.126 percent IACS was noted. The difference between the last reading and the 10-year average is −0.086 percent IACS. Curve analysis shows that the measurement system had some built-in bias or

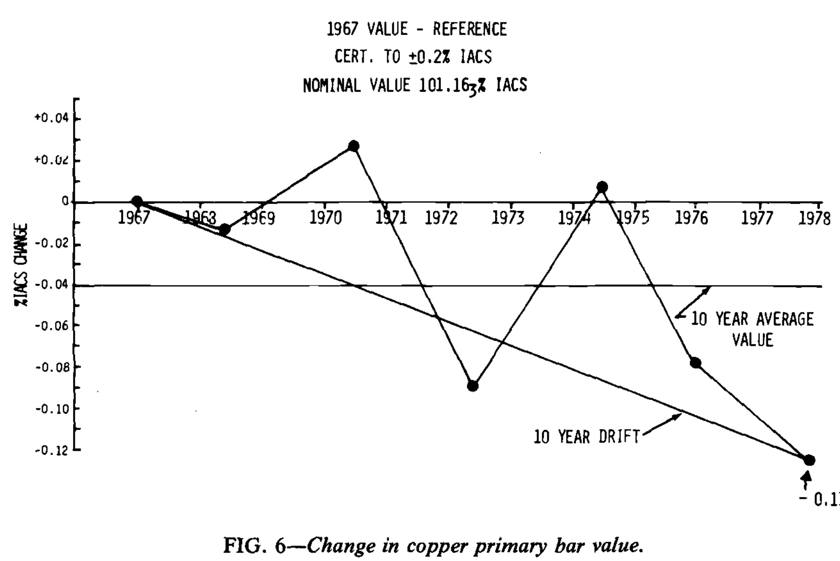

FIG. 6—*Change in copper primary bar value.*

systematic error which masked the slow, time-dependent change in the copper conductivity bar to the latest lower conductivity value, in percent IACS. With its large temperature coefficient of resistivity, the copper primary conductivity bar is particularly difficult to hold to a uniform temperature over its entire length for a period of time long enough to ensure the correct calibrated value within required limits. Uncertainty of all Model 75-17 primary bar values is ± 0.07 percent (approximately) of value [*3*].

The secondary copper conductivity standard analysis is based on the deviation of these standards from the primary copper conductivity bar value in effect at the time of calibration using the values from 1967 to 1977 shown previously. Although this introduces primary bar drift for each analysis, it is indicative of the ability of the 100-kHz conductivity bridge calibration system to utilize primary bar accuracy for secondary standard (or coupon) calibration. Figure 7 shows how ten different secondary copper standards values of conductivity varied from the primary copper conductivity bar value in effect at the time of calibration. Each dot is a separate calibration for this and all similar graphs which follow. The scatter is quite pronounced, with one of the secondary values outside of the lower 0.35 percent certification limit. This does not necessarily mean that this secondary standard is incorrect, but that it probably changed more than the other standards cut from the same bar. The trend of the secondary standards towards lower conductivity is even more pronounced than the trend in the primary copper bar toward a lower value, with time. Uncertainty in these secondary values is approximately ± 0.15 percent IACS.

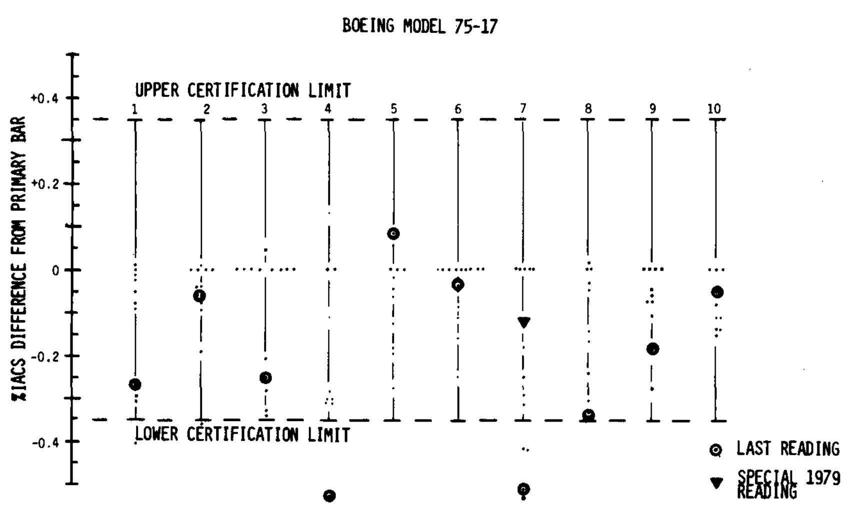

FIG. 7—*Data dispersion of ten different secondary copper conductivity standards.*

Aluminum-Conductivity Standards

Figure 8 shows the changes that occurred in the 1100F aluminum primary conductivity bar. The average value of all readings is 0.02 percent IACS higher than the initial 1967 d-c value and is about −0.005 percent IACS different from the most recent (1978) reading. First (1967) to last (1978) reading difference is +0.015 percent IACS, which indicates a fairly stable metallic structure. The two peaks that occurred in 1970 and 1974 are about one fourth of the certification tolerance of ±0.2 percent IACS and can only be attributed to systematic error in the measurement system, probably due to the lack of tight-enough temperature control during the d-c calibration.

Figure 9 shows the scatter of the data for the secondary conductivity standards of 1100F aluminum when compared to the current primary bar of the same metal. To compare these data directly with the copper secondary standards on a percent-of-value basis would require dividing all the scatter values by 0.6. Since percent IACS is used in actual calibration practice, however, the data can be evaluated as is. The scatter here is less than the scatter of the copper secondary standard; all values are within 0.25 percent IACS, and all of the most recent values are within 0.12 percent IACS except two secondary standards that are almost 0.16 percent IACS.

The 6061-T651 aluminum primary bar percent IACS value is just a little more than −0.02 percent IACS different in over 10 years with only one excursion beyond 0.05 percent IACS (Fig. 10). The secondary conductivity standards made from the same bar material show a mixed trend with the majority of data less than 0.1 percent IACS different from the primary bar and

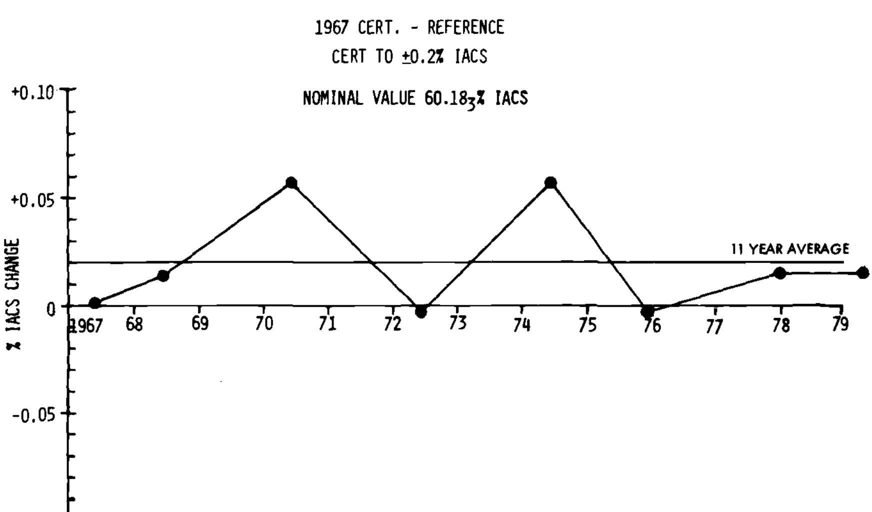

FIG. 8—*Change in 1100F aluminum primary bar value.*

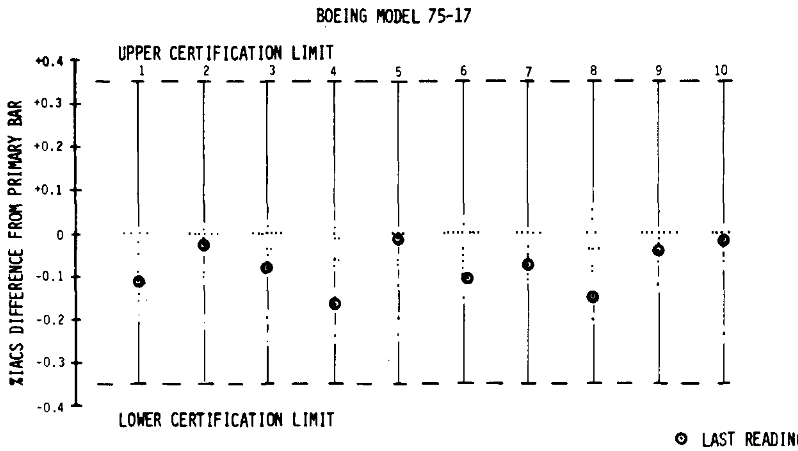

FIG. 9—*Data dispersion of ten different secondary 1100F aluminum conductivity standards.*

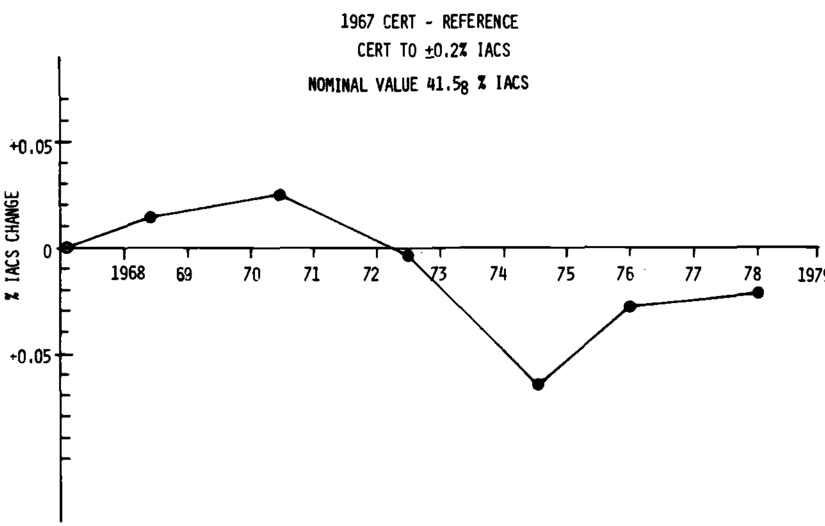

FIG. 10—*Change in 6061 aluminum primary bar value.*

all of the last ten calibrations except two significantly less than 0.1 percent IACS different. The two exceptions are less than 0.13 percent IACS different, which indicates a significant decreasing scatter with time as our system accuracy slowly improves. This trend can be seen in Fig. 11.

The very slight drift of aluminum alloy 5052-0 primary bar is displayed in Fig. 12. The latest calibration (December 1977) indicates a −0.02 percent IACS difference from the original calibration made in March 1967. The

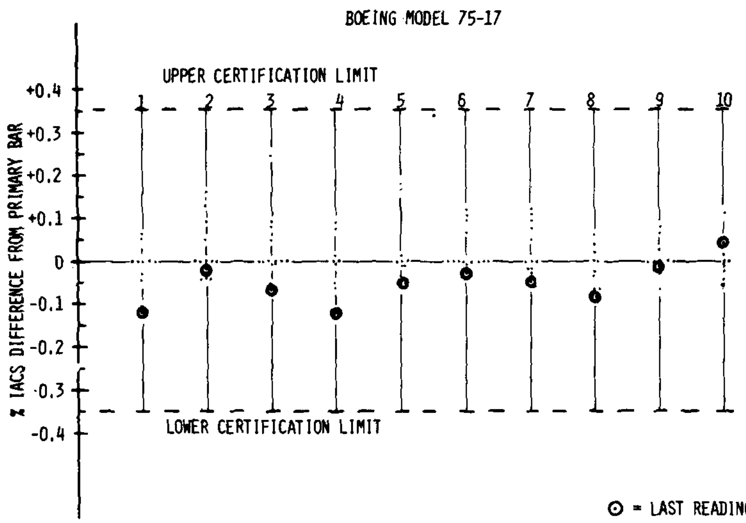

FIG. 11—*Data dispersion of ten different 6061 aluminum secondary conductivity standards.*

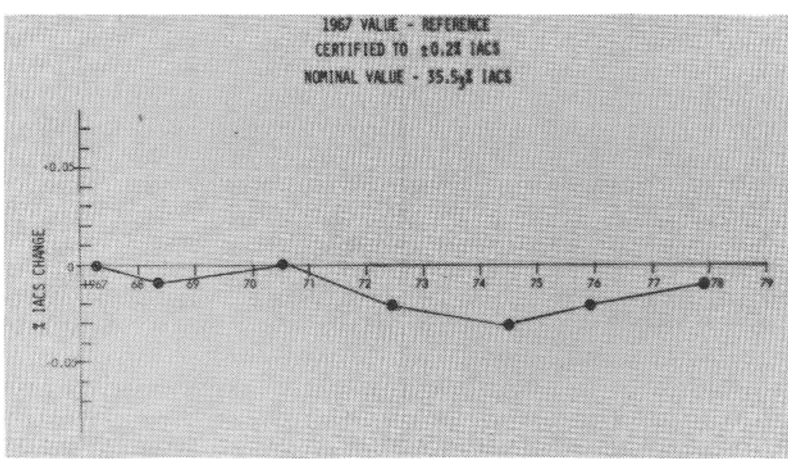

FIG. 12—*Change in aluminum 5052-0 primary bar value.*

maximum deviation resulting from systematic error and calibration temperature drift occurred in 1974 when a −0.03 percent IACS difference was observed. The data scatter shown in Fig. 13 indicates all secondary standard data points less than 0.2 percent IACS different from the primary conductivity bar; eight of the last ten calibration points are 0.05 percent IACS or less different from the primary bar values.

Figures 14 to 17 show the rather large changes in aluminum 2024 alloy with two different heat-treat conditions, T4 and T351. Note that the T4 con-

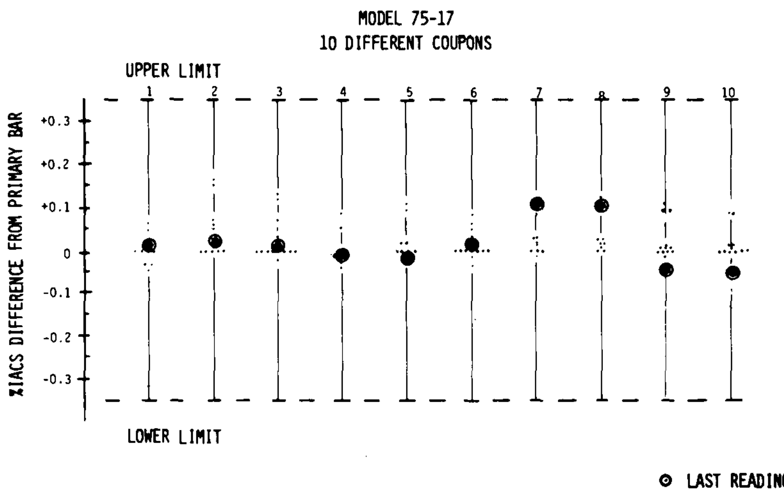

FIG. 13—*Aluminum 5052-0 data dispersion.*

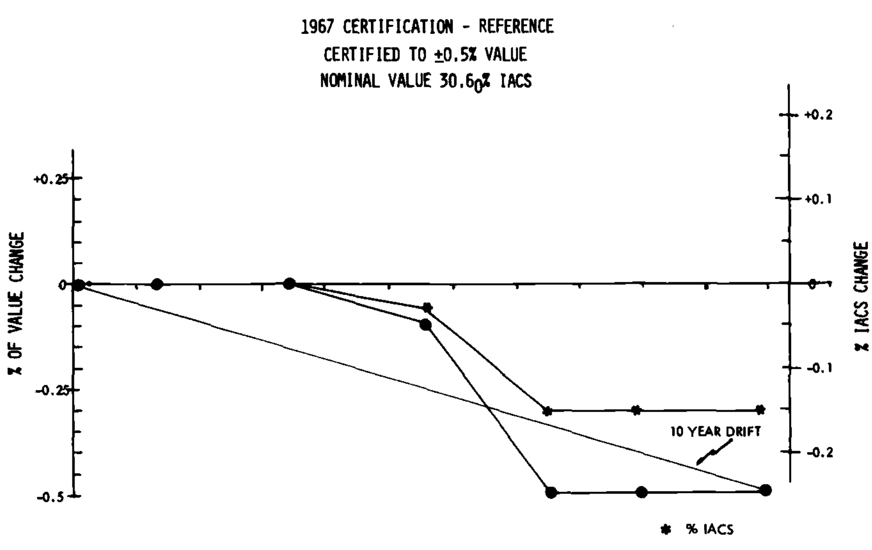

FIG. 14—*Change in 2024-T4 aluminum primary bar value.*

dition changes at a much greater rate with time than the T351 condition. The scatter of secondary data also is greater; the T4 condition shows the differences between secondary and primary values greatly increased. Both percent of value and percent IACS changes are plotted. Note that 2024-T4 primary bar decreased 0.3 percent IACS in 10 years.

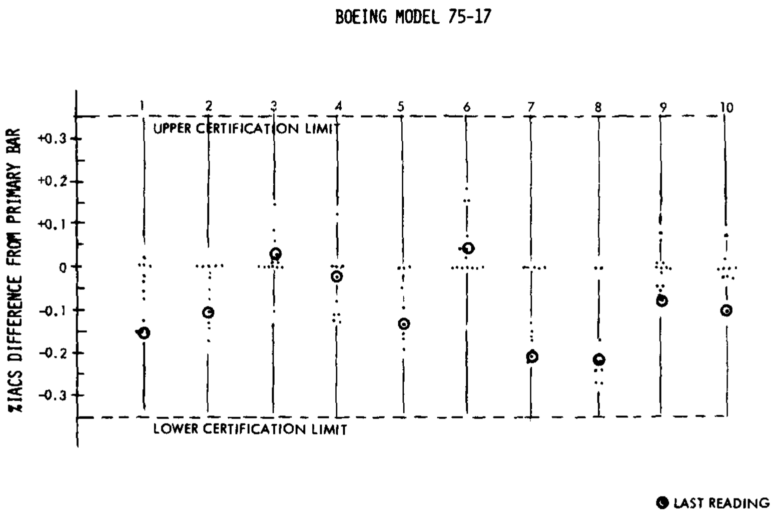

FIG. 15—*Data dispersion of ten different 2024-T4 aluminum secondary conductivity standards.*

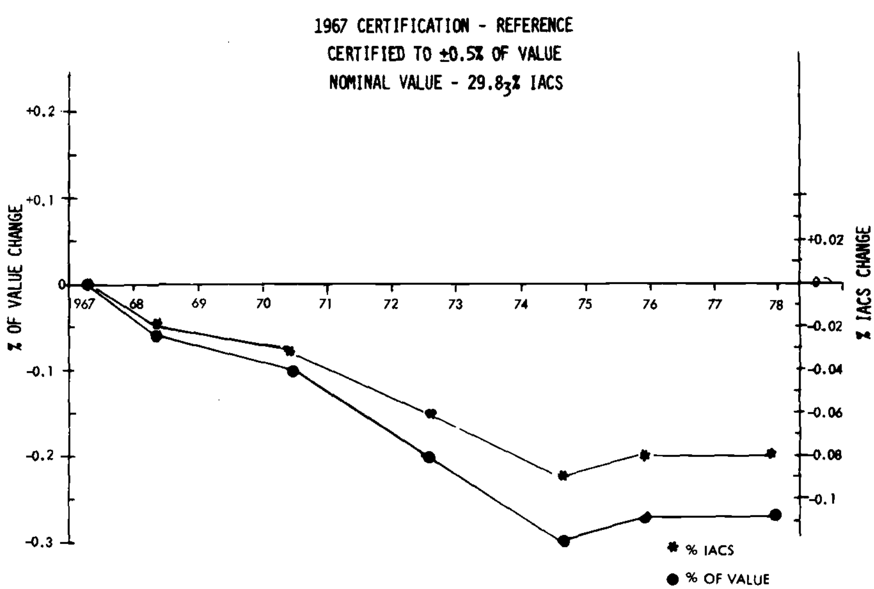

FIG. 16—*Change in 2024-T351 aluminum primary bar value.*

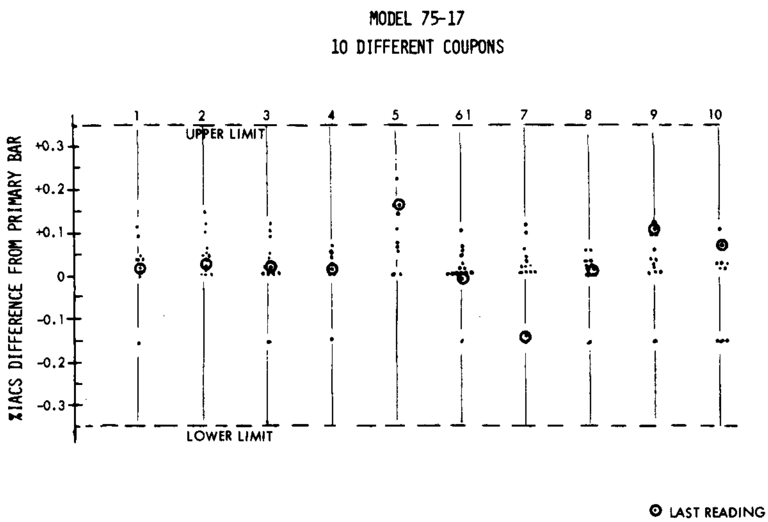

FIG. 17—*Aluminum 2024-T351 data dispersion.*

Brass-Conductivity Standard

As would be expected, yellow brass shows a stable condition with time; it exhibits a final 1978 value only 0.04 percent of value and 0.01 percent IACS change from the original 1967 value (Fig. 18). The secondary scatter is minimal, which reflects more measurement uncertainty than secondary-value changes (Fig. 19). Both percent of value and percent IACS changes are plotted.

"Low"-Set Model 75-17L Standard

The balance of the primary bar changes and secondary-scatter figures belong to the "low", or "titanium", set. The first of these figures, Fig. 20, displays the phosphor-bronze drift which is a significant 0.2 percent of value, or 40 percent of the 0.5 percent of the primary value. Secondary standards of this material also show considerable scatter, which includes the last calibrations of the five sets reviewed (Fig. 21).

An even less stable copper-nickel bronze is shown in Fig. 22; the widely scattered secondary values are displayed in Fig. 23. This paramagnetic standard (μ = 1.00673) is derated to ±5 percent of value because of its lack of stability and the unknown accuracy reduction from d-c calibration to a-c-use as a standard bar.

The improved stability of Everdur bronze is shown in Fig. 24, and the closeness of secondary values to the primary bar, especially the last calibra-

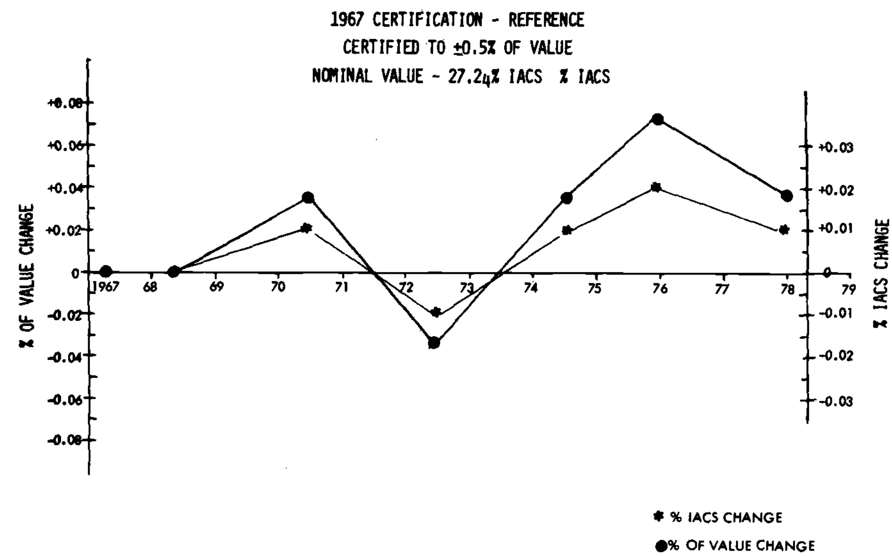

FIG. 18—*Change in yellow-brass primary bar value.*

tion, is illustrated in Fig. 25. All final secondary values are less than 0.1 percent of value different from the primary bar value.

Titanium-Conductivity Standards

Figures 26 to 35 depict the titanium group changes in primary and secondary standard values. Titanium alloy 35A shows only a moderate increase in value, less than 0.1 percent in 10 years, shown in Fig. 26, while the secondary scatter is moderate with all points less than half of the ±1 percent of value limit. The latest values are all less than 0.25 percent of value different from the primary bar of the same value (Fig. 27).

A decrease in percent of value less than 0.1 percent for titanium alloy 431 is shown in Fig. 28; some recent secondary changes approach 1 percent of value limit. The data dispersion of this alloy is shown in Fig. 29.

Figure 30 shows an excursion of over 0.16 percent of value. This is probably owing to slightly blunted potential points, which change the effective length of the bar and the resultant potential drop, when the titanium alloy 64 primary bar was calibrated on dc. The latest value, however, returned to the same value as that originally determined in 1967, as close as the calibration system results indicated. The secondary standard values all were well within the ±1 percent of primary bar value with the latest values within ±0.6 percent of the primary bar value. Figure 31 shows the data presentation.

The final two titanium alloys are both alloy 811, but the first primary bar (811 #1), shown in Fig. 32, varied almost 0.4 percent in ten years while the

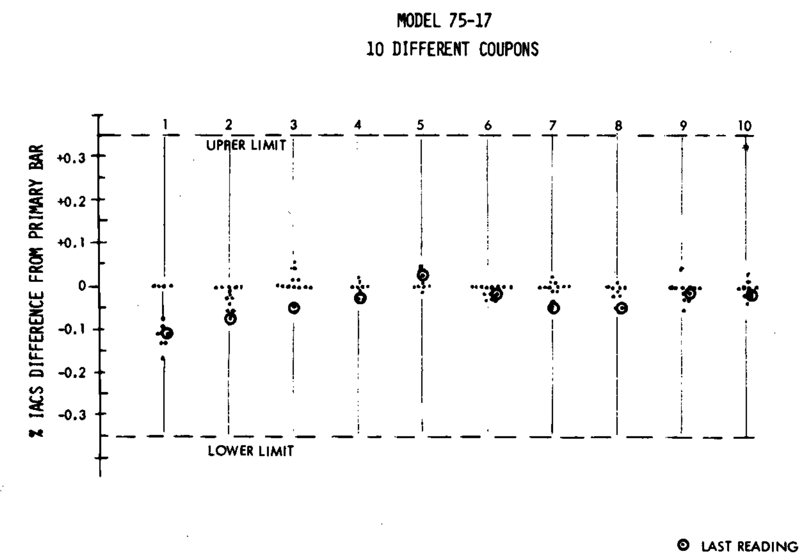

FIG. 19—*Yellow-brass data dispersion.*

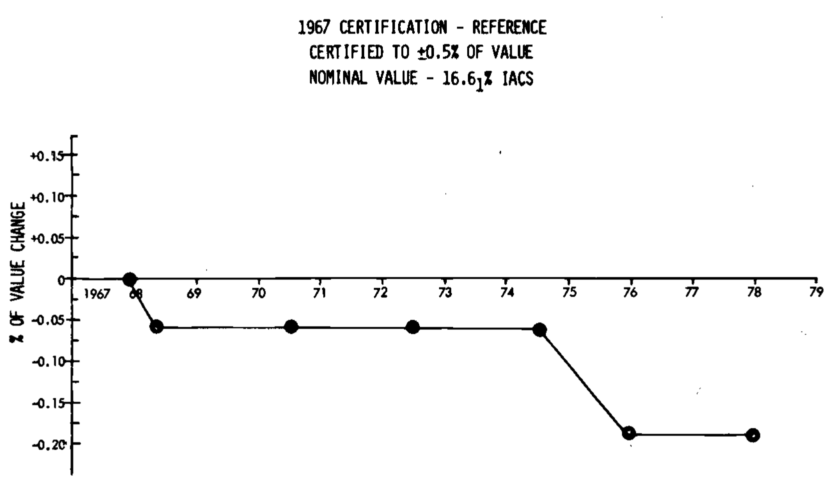

FIG. 20—*Change in phosphor-bronze primary bar value.*

second one (811 #2), shown in Fig. 34, remained fairly constant over this time period. The secondary data dispersion is greater with 811 #1 than with 811 #2, but the latest readings show a very close relationship to each other. (displayed in Fig. 33 and 35). All of the latest readings for both 811 alloys are within 0.5 percent of the value of the primary bar value.

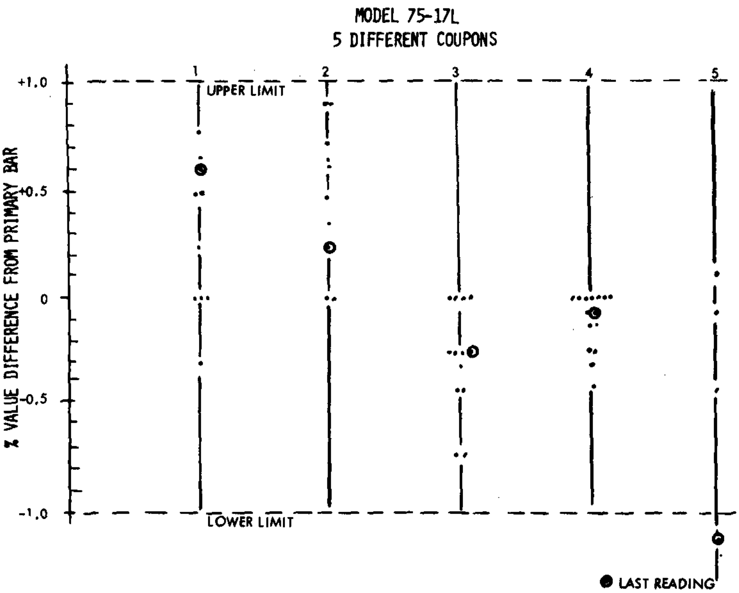

FIG. 21—*Phosphor-bronze data dispersion.*

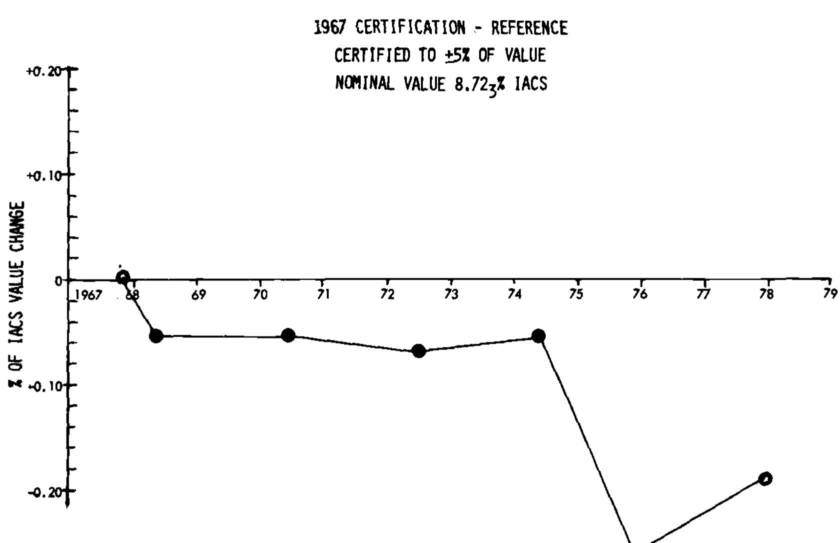

FIG. 22—*Change in copper-nickel primary bar value.*

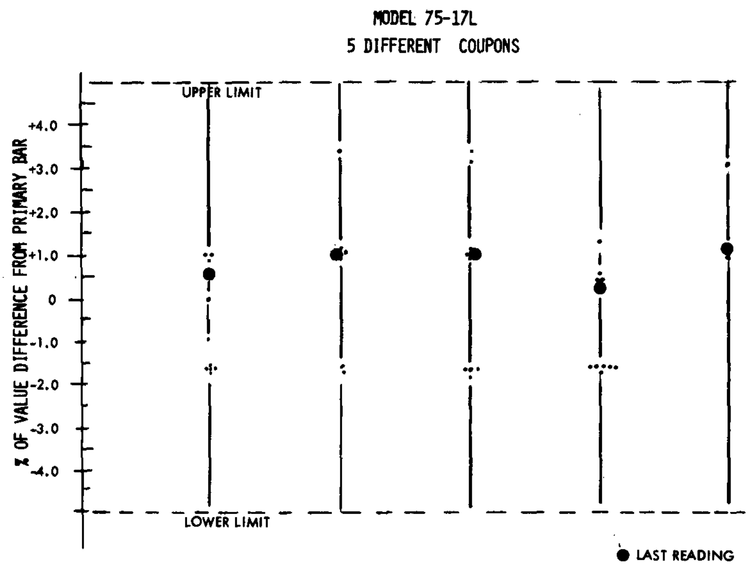

FIG. 23—*Copper-nickel data dispersion.*

Conclusions

Some of the factors that influence the stability of nonferrous secondary conductivity standard values are as follows:

1. The changes in the metallic structure itself due to the large temperature changes of its environment. Both primary and secondary laboratory standards, on the other hand, are usually kept at 23 ± 1°C for years, with only occasional exposure to higher or lower temperature (generally not exceeding ±2°C). The effect of this is shown by the differences in values between certain primary bars and the secondary standards constructed of excess metal from the same primary bar. Copper is a good example of this phenomenon.

2. The methods by which the secondary conductivity standards are calibrated. Several different methods have been used in the past twelve years:

   (*a*) 1966–1970. The identical values were assigned to all secondary conductivity standards that were determined for the primary bar as a result of the d-c calibration for each alloy. As the value of each primary bar changed because of aging, the secondary bar changed with it. When grain direction and stratification corrections were applied to give the a-c values to primary bars, the secondary-bar values were changed accordingly.

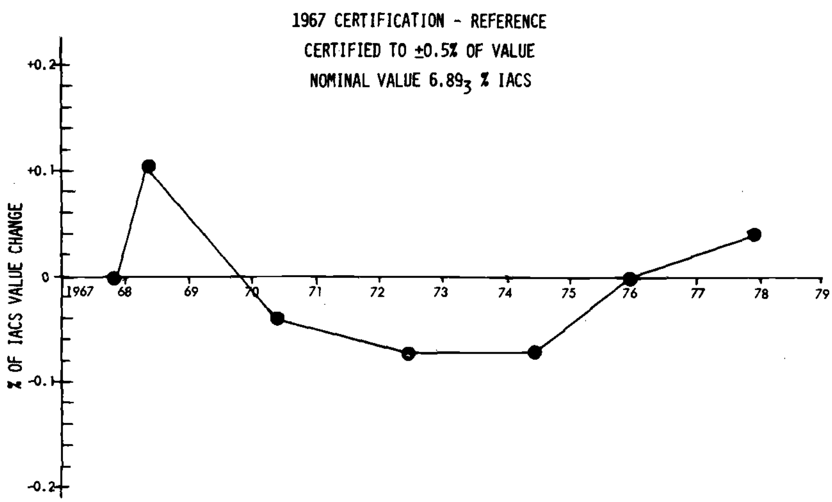

FIG. 24—*Change in Everdur-bronze primary bar value.*

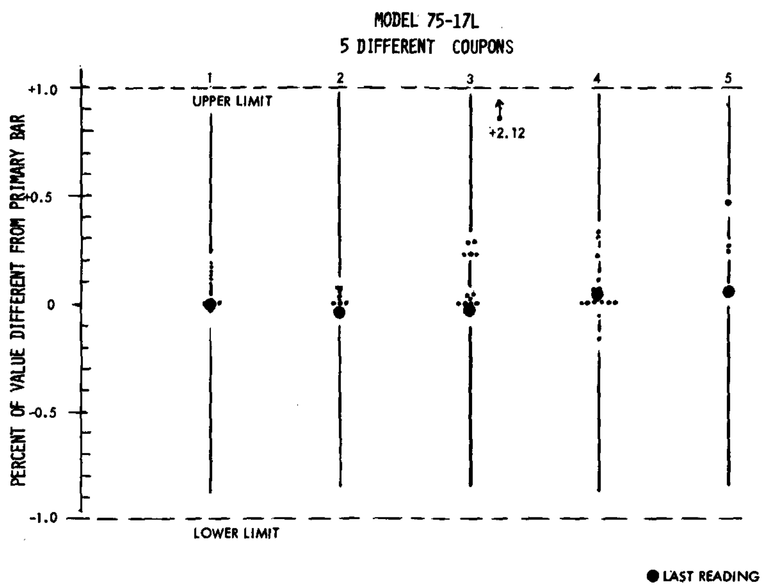

FIG. 25—*Everdur-bronze data dispersion.*

(*b*) 1970–1972. A 100-kHz bridge was built to compare primary and secondary conductivity standards. During this period, two significant problems caused the largest errors to occur between primary and secondary standards values. First, the primary standard bars were kept on top of a lab table in a well-lighted area where air currents occurred from passing personnel and the air conditioning. Significant temperature differences resulted between different parts of primary bars as well as between them and the secondary standards. Second, graphs were used to interpolate results of the calibration where the picofar-

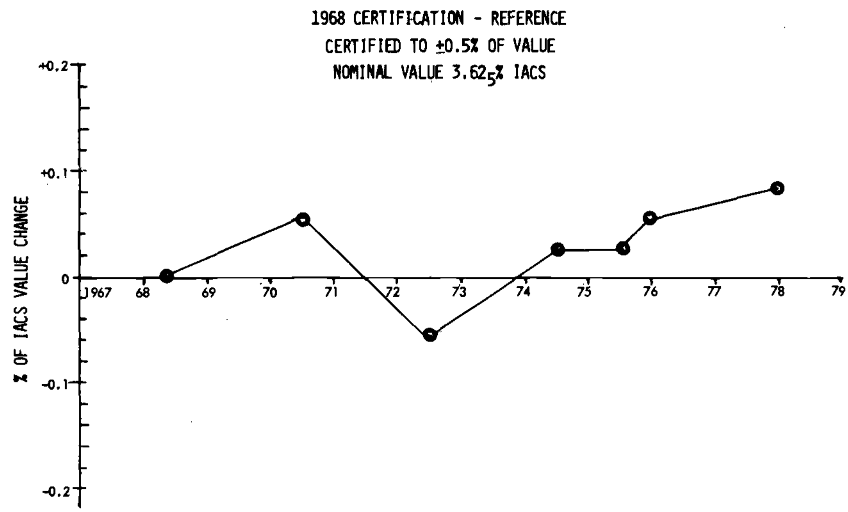

FIG. 26—*Change in titanium 35A primary bar value.*

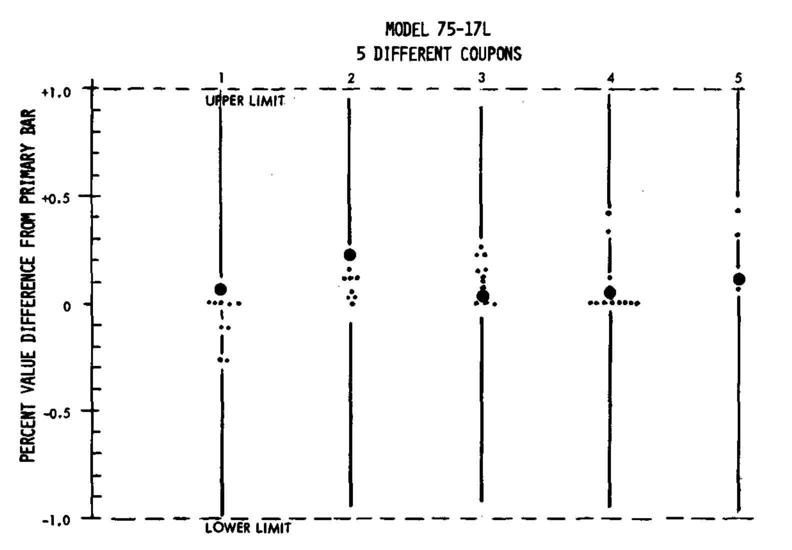

FIG. 27—*Titanium 35A data dispersion.*

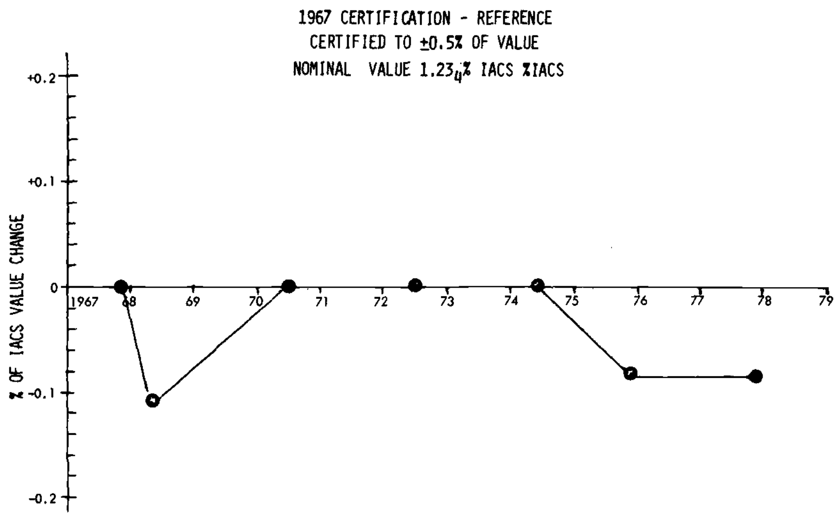

FIG. 28—*Change in titanium 431 primary bar value.*

ads (pF) required for bridge balance were plotted against percent IACS on log-log paper. Almost all of the largest differences in calibrated values resulted from these interpolation errors and temperature differences.

(*c*) 1972–1974. The standards were placed in a shallow oil bath, but the graphs were still in use. A significant improvement in repeatability and some improvement in accuracy resulted immediately.

(*d*) 1974–1976. A segmented program was constructed utilizing an HP-65 to curve-fit the primary bar data to the bridge characteristics. This resulted in still better accuracy and repeatability.

(*e*) 1976–1979. A new program was developed utilizing an HP-9825 programmable computer. Additionally, a raised covered area was added to the shallow oil bath to allow the probe to be operated in the dark, thus avoiding any radiant power absorption or air currents in the area where calibration was in progress. When coupled with meticulous care in the cleanliness of the oil bath, conductivity surfaces, and the probe face, even greater accuracy and precision is now obtainable.

3. Uneven wear on the surfaces of the secondary conductivity standard surfaces due to use in hostile environment, that is, grit from manufacturing processes, chemicals in the air, etc., causes errors similar to lift-off. This can only be corrected by resurfacing the standard or replacing it.

4. Some large-area secondary conductivity standards, that is, 5.08 by 5.08 cm (2 by 2 in.), or larger, if not properly screened for homogeneity, can ex-

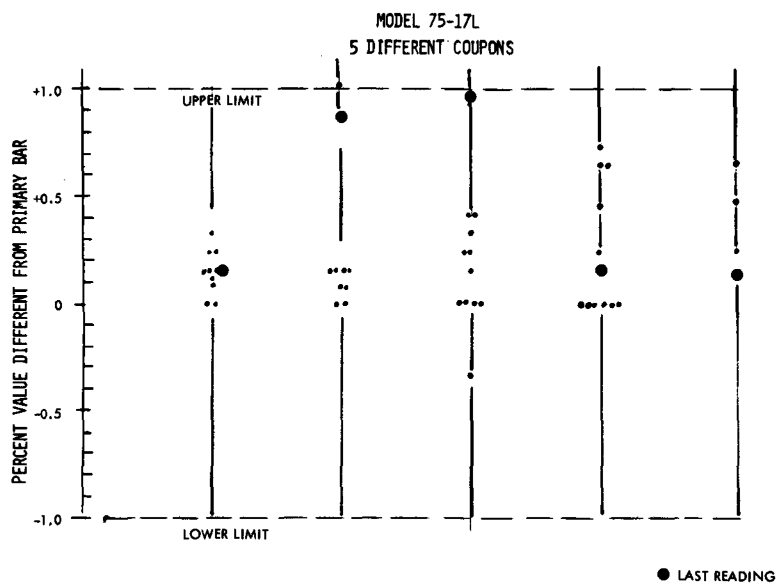

FIG. 29—*Titanium 431 data dispersion.*

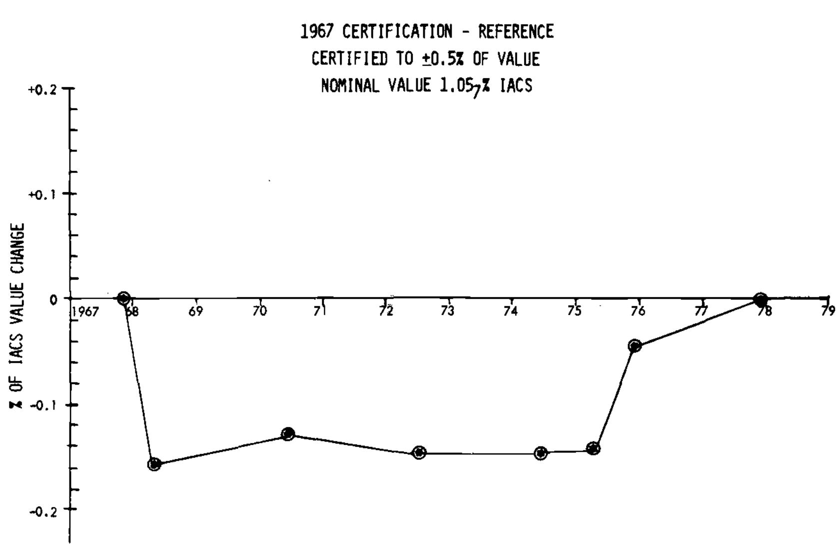

FIG. 30—*Change in titanium 64 primary bar value.*

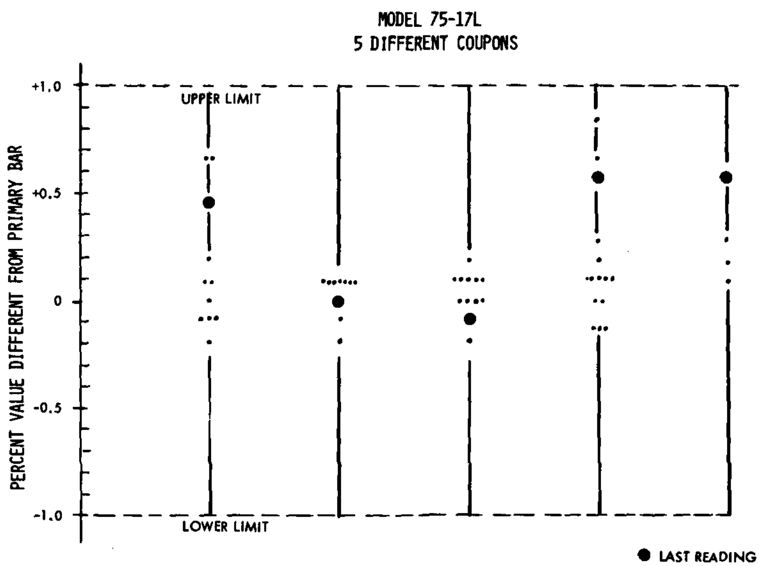

FIG. 31—*Titanium 64 data dispersion.*

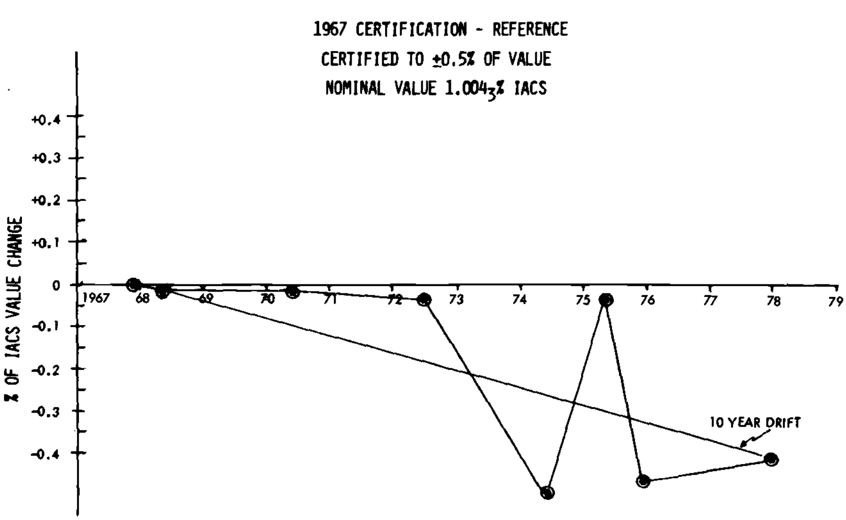

FIG. 32—*Change in titanium 811 #1 primary bar value.*

hibit large differences in conductivity across their surface from one side to the other. Boeing secondary standards are dimensioned 3.175 by 3.175 cm (1.25 by 1.25 in.) to reduce this possibility although all the metal used is checked carefully for nonuniformity before calibrating.

The present values assigned to Boeing-built secondary conductivity standards are indirectly traceable to NBS through resistance, dimensional, and temperature parameters, which themselves are directly traceable to NBS. The care and consistency which is exercised in maintaining Boeing primary conductivity standards as well as the constant improvements constantly being made in the 100-kHz bridge calibration system, such as described previously, give a high confidence factor to the secondary conductivity standard values.

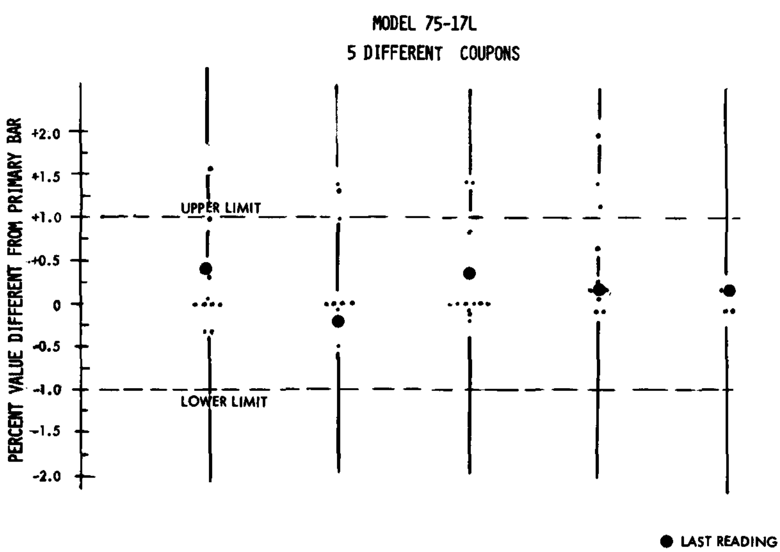

FIG. 33—*Titanium 811 #1 data dispersion.*

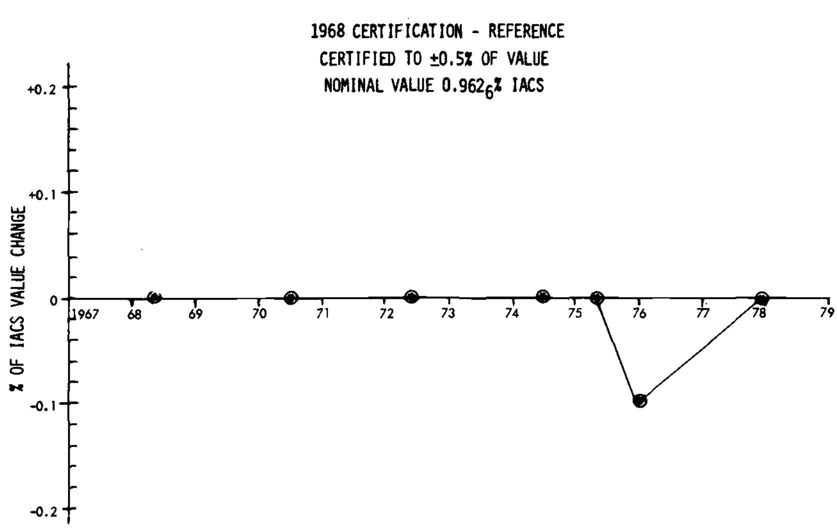

FIG. 34—*Change in titanium 811 #2 primary bar value.*

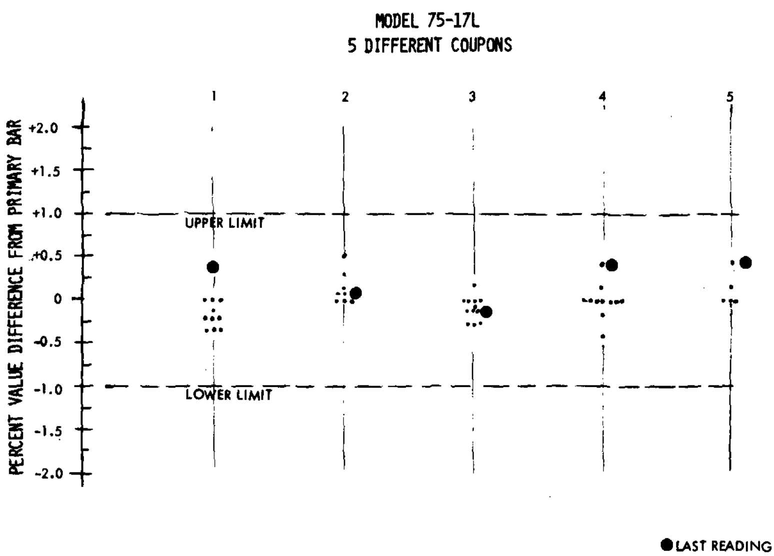

FIG. 35—*Titanium 811 #2 data dispersion.*

It must be expected that the values assigned to some of the secondary standards will change with time, use, and primary bar value changes.

It is my opinion that all of the present values assigned to Boeing-calibrated secondary conductivity standards at present are well within the ± 0.35 percent IACS or 1 percent of value, whichever is less, at 20°C [5]. There have been some calibrations in the past that have slightly exceeded these limits, with a very few more than twice the calibration limits. Additionally, an equation for relative conductivity at other than 20°C is given on all Boeing calibration certificates utilizing temperature coefficients of resistivity determined for all material used. The normal calibration cycle in Boeing calls for annual recertification. It is also recommended to all outside users or purchasers of these standards that they select the annual calibration cycle time of one year unless their usage is such that they can justify cycle extension.

References

[1] Jones, A. R, "Non-Ferrous Conductivity Standards—A 10-Year Review," Paper 76-692, Instrument Society of America Conference, Houston, 1976.

[2] Jones, A. R, "Error Analysis of Non-Ferrous Conductivity Standards," Paper 70-613, Instrument Society of America Conference, Philadelphia, 1970.

[3] Jones, A. R, "Non-Ferrous Conductivity Standards," Paper 68-555, Instrument Society of America Conference, New York, 1968.

[4] Circular of the Bureau of Standards, No. 31, Copper-Wire Tables.

[5] Jones, A. R, *Journal of Materials Evaluation,* American Society for Nondestructive Testing, Vol. 35, No. 11, November 1977.

Applications: Material Properties and Defects

George Free[1]

High-Accuracy Conductivity Measurements in Nonferrous Metals

REFERENCE: Free, George, "**High-Accuracy Conductivity Measurements in Nonferrous Metals,**" *Eddy-Current Characterization of Materials and Structures, ASTM STP 722,* George Birnbaum and George Free, Eds., American Society for Testing and Materials, 1981, pp. 121–128.

ABSTRACT: An eddy-current instrument has been built that measures electrical conductivity with a high degree of accuracy and precision. The instrument measures the electrical conductivity of nonferrous metals at a constant skin depth. By keeping the product $\omega\sigma$ constant in all measurements, a linear relationship between conductivity and frequency can be established. Due to this linear relationship, only one conductivity standard is necessary to calibrate the instrument over the full range of 1 to 100 percent international annealed copper standard (IACS).

KEY WORDS: electrical conductivity, nonferrous metals, skin depth, coil impedance, percent international annealed copper standard, nondestructive evaluation

There are two places in the process of establishing national standards for a-c conductivity that require precision eddy-current measurements. One is in the scanning of the metal bars to be used as primary standards; a conductivity scan is necessary to determine the uniformity of the bar. The second measurement is the comparison of the primary standard and unknowns to be calibrated. Due to the many measurement uncertainties that enter into the total experiment, it was determined that the eddy-current instrument built at the National Bureau of Standards (NBS) should have a total uncertainty of no greater than 0.01 percent in measuring both the resistive and inductive components of the eddy-current probe.

Theory

The impedance of a coil of N-turns at a frequency $f = \omega/2\pi$ with its axis normal to a semi-infinite flat metal surface has been derived as[2]

[1]Research physicist, National Bureau of Standards, Department of Commerce, Washington, D.C. 20234.

[2]Dodd, C. V., Deeds, W. E., and Luquire, J. W., *International Journal of Nondestructive Testing*, Vol. 1, 1969, p. 48.

$$Z_{\text{coil}} = \frac{i\omega\pi N^2 \bar{r}\mu}{(\ell_2 - \ell_1)^2(r_2 - r_1)^2} \int_0^\infty \frac{1}{\alpha_0{}^3\alpha^3} J^2(r_1, r_2) \times \Big\{ 2\alpha_0(\ell_2 - \ell_1) + 2e^{-\alpha_0(\ell_2 - \ell_1)} - 2 + (e^{-2\alpha_0\ell_2} + e^{-2\alpha_0\ell_1} - 2e^{-\alpha_0(\ell_1+\ell_2)}) \times \frac{(\alpha_0 - \beta_1)}{(\alpha_0 + \beta_1)} \Big\} d\alpha \tag{1}$$

where

$$\alpha_0 = [\alpha^2 - \bar{r}^2\omega^2\mu_0\epsilon_0]^{1/2} \qquad \bar{r} = (r_1 + r_2)/2$$

$$\beta_1 = [\alpha^2 - \bar{r}^2\omega^2\mu_0\epsilon_0 + i\bar{r}^2\omega\mu_1\sigma_1]^{1/2} \tag{2}$$

$$J(r_1, r_2) = \alpha^2 \int_{r_1}^{r_2} r_0 J_1(\alpha r_0) dr_0$$

where

α = variable of the integration,
μ_0 = permeability of free space,
ϵ_0 = permitivity of free space, and
J_1 = Bessel function of the first kind.

The probe variables are defined in Fig. 1.

For nonferrous metals μ_1 may be considered equal to μ_0. Furthermore, product $\omega^2\bar{r}^2\mu_0\epsilon_0$ is less than 8×10^{-10} for a coil with a radius of 0.01 m and a frequency of 100 kHz. Thus, it is assumed that the product is zero with little loss in accuracy and $\alpha_0 = \alpha$. Equation 1 can be separated into parts that relate to the coil, the metal, and the coil to metal interaction. Applying Eq 1 to a specific coil so that all geometrical variables related to the coil remain constant, the equation can be separated into parts which are functions related to the electromagnetic interaction as follows:

$$A = \frac{\pi\mu N^2\bar{r}}{(r_2 - r_1)^2(\ell_2 - \ell_1)^2}$$

coil property independent of the variable of integration.

$$B(\alpha) = J^2(r_1, r_2)$$

coil property, a Bessel function and a function only of the variable of integration.

$$C(\alpha) = 2\alpha d_c + 2e^{-\alpha d_c} - 2$$

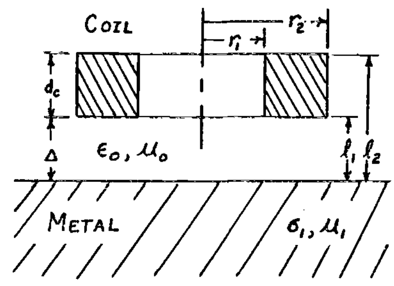

FIG. 1—*Rectangular cross section of coil.*

coil property, which is a function only of the variable of integration.

$$d_c = \text{longitudinal length of coil}$$

that is, $(\ell_2 - \ell_1)$.

$$D(\alpha,\Delta) = e^{-2\Delta}(e^{-\alpha d_c} - 1)^2$$

which is a function of the coil-metal separation distance where Δ = lift-off distance.

$$R(\omega, \sigma, \alpha) + jI(\omega, \sigma, \alpha)$$

metal property, which is a function of conductivity, frequency, and $= (\alpha_0 - \beta_1)/(\alpha_0 + \beta_1)$.

The original equation can thus be rewritten as

$$Z = i\omega A \int_0^\infty \frac{1}{\alpha^6} B(\alpha)C(\alpha)d\alpha + i\omega A \int_0^\infty \frac{1}{\alpha^6} B(\alpha)\, D(\alpha,\Delta)(R + iI)d\alpha \quad (3)$$

All functions are real in the equation. With other variables held constant, the impedance of the coil is a function of lift-off (Δ), frequency (ω), and conductivity (σ). If we assume that both lift-off and the product $\omega\sigma$ are held constant, then

$$L_1 = A \int_0^\infty \frac{1}{\alpha^6} BCd\alpha + A \int_0^\infty \frac{1}{\alpha^6} BDRd\alpha = L_2 \quad (4)$$

where L_1 and L_2 are the inductance of the coil at two different frequencies on metals of different conductivity. The inductance of the coil does not change if the product $\omega\sigma$ is constant. Also for the constant product $\omega\sigma$

$$R_1 = i^2\omega_1 A \int_0^\infty \frac{1}{\alpha^6} BDId\alpha, R_2 = i^2\omega_2 A \int_0^\infty \frac{1}{\alpha^6} BDId\alpha \quad (5)$$

The integral remains constant, but the effective coil resistance changes linearly with frequency.

The resistance of the coil in air has not appeared in the aforementioned equations, but will be discussed later. Using the relationships $\omega\sigma$ = constant, $L_1 = L_2$, and $R_2 = \omega_2/\omega_1 R_1$ a measurement system can be designed to measure conductivity as a function of frequency. Measurements are obtained by varying bridge frequency and bridge resistance. The relationship of conductivities for the two measurements is $\omega_1\sigma_1 = \omega_2\sigma_2$ or $\sigma_2 = \omega_1/\omega_2\sigma_1$. The measurement of conductivity is linearly related to the measurement frequency. Further, since $\sigma_{unknown} = \sigma_{std} \times f_{std}/f_{unknown\ std}$, it is implied that all measurements can be based on one standard of conductivity. There is no need for standards at both the high and low end of the range to calibrate the instrumentation. When measurements are made using these relationships it also implies that all measurements are made at a constant skin depth.

Lift-off Compensation

In all eddy-current measurements there must be some method to minimize errors caused by coil to metal separation. When measurements are made as described previously this is no less a problem. A method of canceling lift-off effects can be seen be referring to Fig. 2, which shows a small section of the impedance plane of a coil. Balance for the first measurement is at the point k_1, k_1'. The coil is then placed on an unknown metal and the impedance changes to the point k_2, k_2'. Before placing the coil on the unknown metal, the reference phase of the detector of the system that has both in-phase and quadrature indications is adjusted so that all change due to variation in coil-metal separation appears only on the quadrature meter, while the in-phase meter remains unchanged. When the coil is placed on the test piece there will

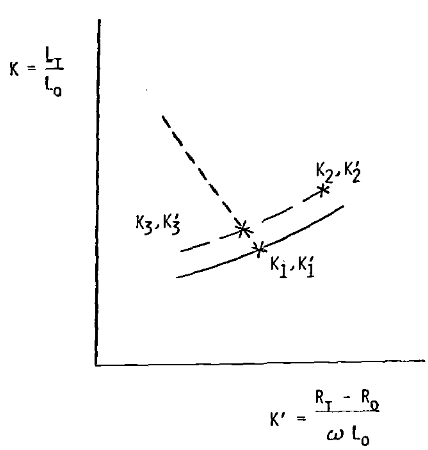

FIG. 2—*Expanded section of impedance plane of a coil.*

be an imbalance in both in-phase and quadrature components. Frequency and bridge resistance are then varied until the point k_3, k_3' is reached. At this point the out-of-balance condition is due only to lift-off and will be displayed on the quadrature meter. The frequency at the point k_3, k_3' is then the frequency used to determine conductivity. Lift-off is compensated for and at the same time becomes a measureable quantity if a correlation is made between lift-off distance and the quadrature meter reading.

Eddy-Current Bridge

Several bridges have been built at NBS using these concepts as the basis for operation. The most important aspect in the design of the bridge is minimizing the frequency dependence. A circuit diagram of the bridge now being used is shown in Fig. 3. The circuit is that of a Maxwell bridge for measuring inductance.[3] To this has been added a grounding network to compensate for capacitance to ground. Instead of using variable resistors and capacitors, in one arm of the bridge inductive dividers driving a fixed capacitor and resistor are used. The balance equation remains

$$Z_{\text{coil}} = Z_1 Z_2 [\beta Y_\beta + \alpha Y_\alpha] \quad (6)$$

where Z_1, Z_2, and $1/Y_B$ are primarily resistances, and Y_α is an admittance. α and β are the settings of the two voltage dividers which have resolutions of 10^{-6}. The voltage dividers drive fixed standards, C_α and R_β, instead of variable elements for several reasons. Switch resistance and capacitance are negligible, increments of resistance as small as $2 \times 10^{-4}\Omega$ can be reproduced accurately, and when calibrating the bridge it is only necessary to calibrate one resistor and one capacitor in this arm of the bridge.

In this bridge, as in any a-c bridge, the actual balance equations are not simple. The impedances Z_1, Z_L, and admittances Y_α and Y_β all have real

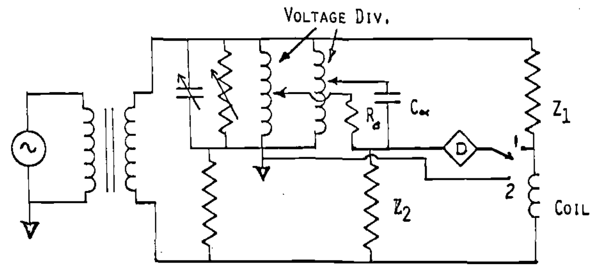

FIG. 3—*Eddy-current bridge.*

[3]Zapf, T. L., "Calibration of Inductance Standards in the Maxwell-Wein Bridge Circuit," Special Publication No. 300, Vol. 3, National Bureau of Standards, December 1968.

and imaginary components. The balance equation must consider second-order effects due to the reactive elements in the resistors, and the conductance of the capacitor must be considered, especially at frequencies above 10 kHz. The performance of the bridge has been enhanced by using bulk metal film resistors. These have series inductance on the order of 0.1 μH and shunt capacitance on the order of 0.5 pF. The capacitance standard used is a parallel-plate capacitor with a dry nitrogen dielectric. The parallel conductance is on the order of 10^{-12} S.

The bridge diagram does not include shielding. In the actual bridge all components are carefully shielded and coaxial cable is used so that all stray capacitance is shunted in parallel with the grounding network. The grounding network is dictated by a-c measurement theory and by the frequency dependence of inductive dividers.

The bridge as constructed measures inductance in the range of 0.1 to 10 mH and coil resistance in the range of 2 to 200 Ω. The frequency range of the bridge is 5000 Hz to 100 kHz. After calibration of the bridge components, and with residual impedance of the leads considered, the uncertainty in making measurements of inductance and series resistance is approximately 0.01 percent. In the comparison measurements that are made when measuring conductivity it is inductance and resistance changes that are determined. Since inductance and resistance changes can be measured more accurately than nominal values, the uncertainty is usually less than 0.01 percent.

To balance the bridge with the coil on a specimen, two sets of adjustments are necessary. Firstly, the detector is connected at Position 1 in Fig. 3, and α and β are varied to achieve balance. The detector is then moved to Position 2 in Fig. 3, and the grounding network R and C is varied for balance. The final balance is achieved when the detector indicates zero at both positions. The bridge converges rapidly to balance; usually two adjustments at each detector position are all that are necessary.

When calibrating specimens, the bridge is first balanced using a conductivity standard. The detector phase is adjusted for lift-off errors. The coil is then placed on the unknown specimen. Since coil resistance follows the equation $R_{\text{coil}} = R_0 + \omega L_0 K'$, and K' is being held constant, the resistance of the coil is predicted at each frequency by

$$R_{\text{coil}} = \left[R_{01} - \frac{L_{02} f_2}{L_{01} f_1} R_{02}\right] + \frac{L_{02} f_2}{L_{01} f_1} R_1 \tag{7}$$

where R_1 is resistance of coil on the standard, and R_{01}, R_{02}, L_{01}, L_{02} are the resistance and inductance of the coil in air at the two frequencies. A slight correction must also be made for L_{coil} owing to the variation of inductance with frequency. Bringing the bridge to balance on the unknown is a matter of varying the frequency and the β voltage divider until a zero reading is achieved on the in-phase meter. The sensitivity of the bridge is a function of the smallest adjustment that can be made to the β resistor. Assuming k' is 0.1,

L_0 = 5 mH, and f = 10 kHz, a change in one hertz is equivalent to a change or resistance of 0.003 Ω. The present bridge measures resistance change of 2 $\times 10^{-4}$ Ω. When translated into percent IACS this means the bridge can detect conductivity changes of 0.001 percent IACS using a 100 percent IACS standard. The noise and frequency drift for the bridge are 0.1 μV for a 2-V input signal and $10^{-7} \times f$, respectively.

The measurement as described would appear to be a matter of holding the phase constant on all test samples. But it is seen from Eq 7 that the resistance of the coil in air must be considered. The phase angle of the coil slowly changes with frequency. If a coil with small resistance is used (that is, 1 to 2 Ω), the error of assuming constant phase is small. If the coils resistance is large (that is, 20 to 50 Ω), this correction term becomes very important.

Measurement Results

The bridge has been used for two types of measurements. Firstly, tests were made using metal specimens of known conductivity. A specimen having a value of 101 percent IACS was used as the standard. The other specimens, with values of 35, 28, and 1 percent IACS, were used as unknowns. The values determined for the unknown standards using the bridge differed from the assigned values by less than the total uncertainty assigned to these standards in all cases. Until more accurate standards are developed it must be assumed that the bridge does measure accurately. The second type of measurement was the scanning of metal bars to be used as NBS Primary Conductivity Standards. The bridge was set at a given frequency, and the coil was mechanically moved back and forth along the bar. At those points along the bar that indicated large changes, the scanning was stopped and measurements were taken. These measurements were repeatable to approximately 0.05 percent σ, where σ is the initial conductivity balance. The change of 0.05 percent was determined to be primarily due to a change in bar temperature. With the bars resting in a temperature controlled oil bath, the repeatability is expected to improve by an order of magnitude. The bars were also scanned using different initial frequencies. The measurements at different frequencies were in agreement with respect to conductivity changes. In two bars, there was a difference of approximately 0.09 percent σ between the lowest frequency scan and the highest. This change is thought to indicate a conductivity variation in the metal that is a function of distance from the surface. Thus measurements at different skin depths would show such a dependence.

Conclusion

The foregoing discussion of the NBS eddy-current bridge does not limit the making of constant skin-depth measurements to this type of instrument. Several bridges built at NBS predicting the present model also achieved similar results. The only criteria are that the bridge measure both components of impedance accurately, and that the bridge components themselves are simple to calibrate. The eddy-current bridge meets the initial design criteria, but in its present form is relatively difficult to operate. The balancing procedure at two detector points is tedious. A voltage-follower network will be built and tested in the bridge. This network would replace the present Wagner ground circuit. If the voltage follower proves feasible, only one set of adjustments to the α and β dividers would be made and the second balance of the detector would not have to be made. The bulkiness of present bridge components (that is, oscillator, detector, and voltage dividers) makes the bridge purely a laboratory instrument. A much smaller bridge could be made if it were dedicated to one or two probes with a limited frequency range. With some reduction in accuracy and precision, a portable bridge could be made.

I. G. Hendrickson[1] *and K. A. Hansen*[1]

High Peak Energy Shaped-Pulse Electromagnetic Crack Detection

REFERENCE: Hendrickson, I. G. and Hansen, K. A., "**High Peak Energy Shaped-Pulse Electromagnetic Crack Detection,**" *Eddy-Current Characterization of Materials and Structures, ASTM STP 722,* George Birnbaum and George Free, Eds., American Society for Testing and Materials, 1981, pp. 129–139.

ABSTRACT: A low-inductance drive coil energized with a shaped high-current drive pulse, together with a separate pickup coil, is used for crack detection in thick multiple-layer aircraft structures. The slow rise time or low-frequency portion of the shaped pulse applied to a solenoid drive coil is used to obtain the required depth-of-field penetration into the structure. The fast fall time or high-frequency portion of the shaped pulse is used to rapidly cancel the slow pulse current and field at the structure surface. This cancellation process causes the collapse of the field within the structure, which reacts with the structure and cracks. The structure/crack eddy-current response is detected at the structure surface with a spiral pancake pickup coil. The pancake pickup coil is used to selectively detect the tangential component of the drive pulse field collapsing from within the structure. An important aspect of this high peak energy testing approach is its saturation of steel fasteners, which highly reduces their permeability variations.

KEY WORDS: crack detection, nondestructive testing, electromagnetic, shaped pulse, aluminum structures, fasteners

Low-frequency eddy-current (LFEC) techniques have been used in the past several years to inspect thick and multiple-layer bolted aircraft structures. The instruments most commonly employed have variable single-frequency, continuous sinusoidal drive waveforms. These instruments employ relatively high-inductance, high-resistance coil probes and are restricted in drive current levels to the milliampere range. Operating frequencies in the 100 to 200 Hz range are employed to obtain the required depth-of-field penetration in the second-layer structure, but produce only relatively low levels of eddy current within the structure. Also, the single-frequency aspect of the present instruments has little capability to discriminate structure response to the eddy-current inspection as a function of thickness increments of the structure.[2] Present capabilities of LFEC instruments for "on-airplane"

[1]Specialist engineer, The Boeing Company, Seattle, Wash. 98124.
[2]Libby, H. L., *Introduction to Electromagnetics Nondestructive Test Methods*, Wiley Interscience, New York, 1971.

inspection of second-layer structure, with 0.635-cm (0.25-in.)-thick upper layer, include the detection of cracks 1.27 cm (0.5 in.) in length and longer. For still thicker upper-layer structures, LFEC crack-detection capabilities deteriorate rapidly; this suggests that possibly new approaches and techniques are required for these thick structures.

Concept

A high peak energy, shaped-pulse, eddy-current (SPEC) technique has been developed and investigated with the objective of improving the inspection of thick multiple-layer aircraft structures. The SPEC approach uses a single, high peak energy pulse to increase the field penetration into the structure and a rapid-drive current cutoff, collapsing-field technique to increase the level of eddy current within the structure. Specifically, the SPEC approach involves applying the high current level slow rise time or low-frequency portion of the shaped pulse to obtain the required depth-of-field penetration into the structure (Fig. 1). The fast fall time or high-frequency portion of the pulse rapidly cancels the slow pulse field at the structure surface; this cancellation process causes the collapse of the field within the structure.[3] This collapsing field then reacts with the structure and cracks, and the associated eddy-current response is detected at the structure surface.

The frequency-spectrum, time-domain aspects of the pulse approach, together with field-orientation response detection techniques, are employed

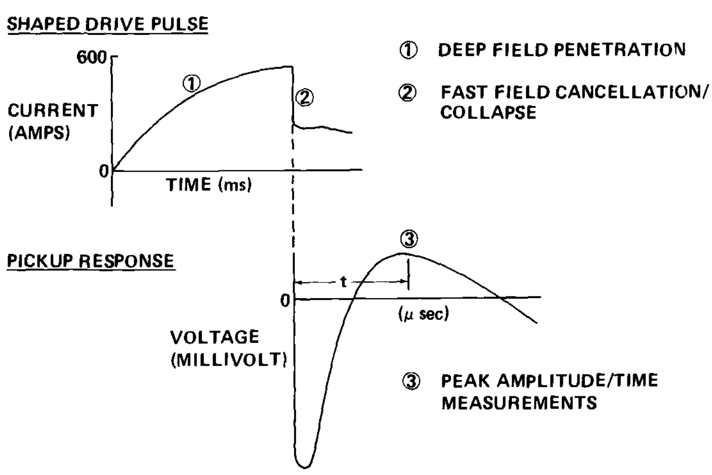

FIG. 1—*Shaped drive pulse and pickup response.*

[3]Hendrickson, I. G. and Hansen, K. A., "Electromagnetic Force Machine Tension Proof-loading and Dent Pulling of Aerospace Structures," Symposium on Nondestructive Evaluation, San Antonio, Tex., 20-22 April 1977.

to selectively monitor crack-response information coming back from within the structure via the collapsing field. The work reported here includes the investigation of the effects of material, structure, and testing variables on the crack-detection capability of the SPEC technique.

Instrumentation

The basic SPEC device is comprised of (*1*) a pulser unit to produce the shaped current pulse, (*2*) a transmit or drive coil to generate the electromagnetic field to be injected into and collapsed out of the structure to be tested, and (*3*) a receive or pickup coil to detect the produced eddy currents/magnetic fields collapsing from within the structure and modified by cracks in the structure. The pulser unit (Fig. 2) contains two capacitor banks: (*1*) a "slow" or low-frequency bank to produce a current pulse with a rise time of approximately 2 ms, and (*2*) a "fast" or high-frequency bank in conjunction with a series resistor, which is used to obtain a 20-μs fall time and to achieve critical damping. The two capacitor banks are connected in opposite polarity to the drive coil. The slow bank is discharged first, followed by the fast-bank discharge which is used to rapidly cancel the slow current pulse. The combined sequence bank discharges, as controlled by

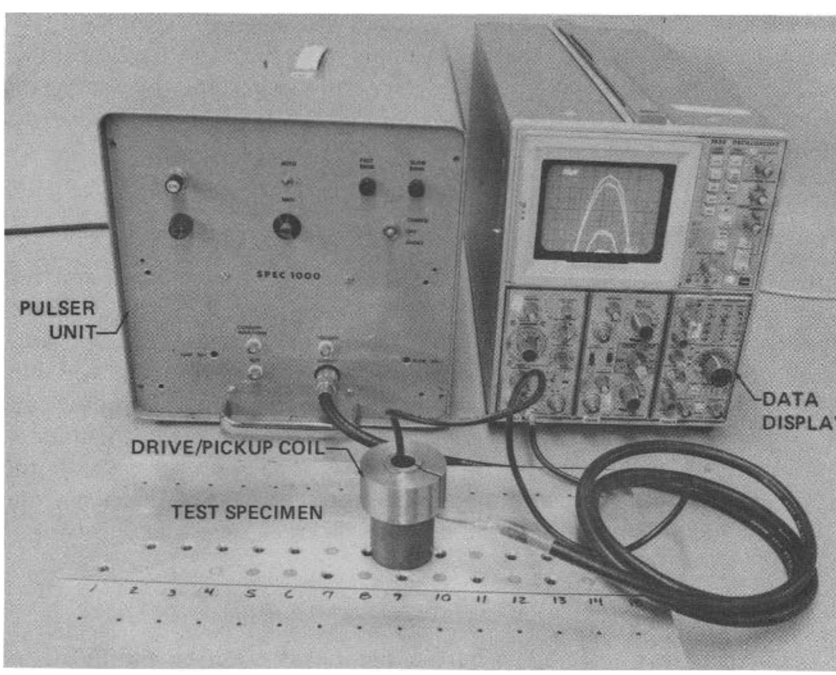

FIG. 2—*Shaped pulse eddy-current (SPEC) system.*

logic circuitry, produce the desired shaped current waveform through the drive coil (Fig. 1).

The pulser unit is then used to supply the shaped current pulse to a low-inductance solenoid drive coil. The solenoid coils used in these experiments have dimensions of 1.91 cm (0.75 in.) inside diameter, 3.81 cm (1.5 in.) outside diameter, and 3.81 cm (1.5 in.) height. The coil has four layers of windings of approximately 60 turns total and has approximately 20-μH inductance and 4-mΩ resistance. The solenoid drive coil produces a high vertically oriented magnetic-field component at the structure surface. This high vertical-component drive field reduces the sensitivity of the system to surface structure variables. The drive field and its tangential field component at depth react with the structure and cracks, and are selectively sensed at the surface with the pancake pickup coil. The pickup coils in these experiments were single layer, spiral wound with outside diameters of 1.91 cm (0.75 in.) and 2.54 cm (1.0 in.), with approximately 20 to 30 turns. The inductance of the coils is from 4 to 6 μH. The pancake pickup coil as used with the solenoid drive coil also provides orthogonal (right angle) decoupling between the two coils. The initial readout for the SPEC system was a storage oscilloscope for the presentation of the structure/crack response data. The voltage signal from the pickup coil was displayed as a function of both signal amplitude and phase, as observed at selected time intervals following the drive current pulse. Also, a digital computer scope, together with a digital printer, was used to investigate the feasibility of employing a digital readout unit. The digital-readout approach is especially important concerning the time/phase portion of the measurement of the pickup coil response in order to compensate for such variables as probe lift-off.

Variables Evaluation

Investigations included the evaluation of material, structure, and test variables. Most of the variables tests were conducted on 0.635-cm (0.25-in.) upper-layer thickness, scarf-joint type structure specimens (Fig. 3). Also, a skin/stringer type specimen was used for the structure-thickness variable. The variables tested and briefly discussed here are base-metal conductivity, fastener variability, edge margin, interface gap, fastener height/countersink depth, upper-layer thickness, and probe lift-off. The approach taken in the investigation included measuring both the overall response level change due to the variables and the effect of the variables on crack-detection sensitivity.

Conductivity

Conductivity was observed to have a significant effect on the SPEC instrument response. For the aluminum-alloy base metal specimens with no

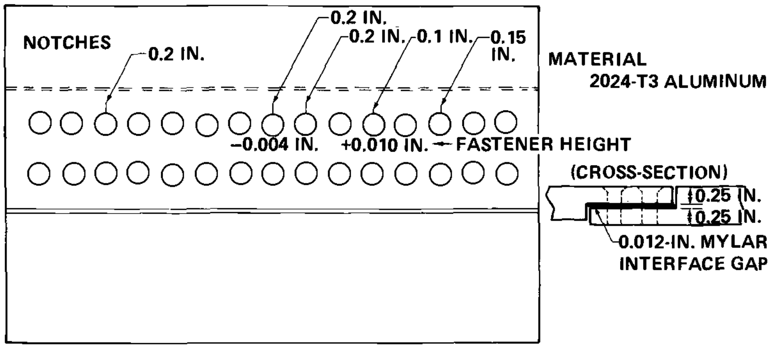

FIG. 3—*Scarf-joint type test specimen (1.0 in. = 2.54 cm).*

holes or fasteners, a 1 percent change in conductivity produced approximately a 1-mV SPEC response change as measured on 1.27-cm (0.5-in.) total-thickness specimens (Fig. 4). For specimens of aluminum sheet material with steel fasteners, the eddy-current response is more complex. For example, a 0.635-cm (0.25-in.)-thick, 2024-T3 aluminum (29.2 percent conductivity) two-layer specimen with 0.635-cm (0.25-in.)-diameter steel fasteners had a 2-mV higher SPEC level response than the same specimen configuration of 7075-T6 (32.3 percent) base alloy (Fig. 5). For these two different conductivity base materials, a significant effect on the notch-crack sensitivity of the SPEC system was also observed: the higher-conductivity material structure caused a lower crack sensitivity than the lower-conductivity material (Fig. 5).

Fasteners

For steel fasteners with the same part number, it was observed that a 0.762-cm (0.3-in.)-long notch crack under a 0.635-cm (0.25-in.)-thick upper-layer skin was not detectable above the fastener's "noise" with the SPEC system operating at 300 peak amperes drive-coil current level. When the peak current was increased to 600 A, the steel fasteners were magnetically saturated to the extent that the permeability variable was nearly neutralized, and a 0.508-cm (0.2-in.)-long crack was detectable over the remaining fasteners' "noise". In production circumstances the next-longer fastener is sometimes used when the normal size is out of stock. This longer-steel-fastener case was also included in the variability test and data are shown in Fig. 6. It was found that magnetic saturation of the steel fasteners also helps to reduce the longer-fastener effect to the extent that a 0.508-cm (0.2-in.) crack is detectable. For titanium fasteners the permeability is one; hence no saturation process is required.

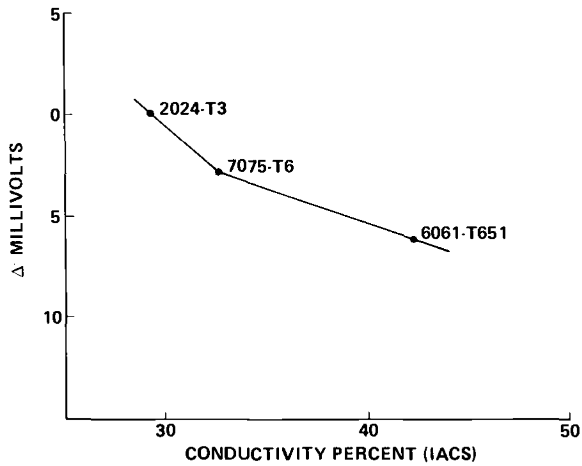

FIG. 4—*SPEC response versus conductivity.*

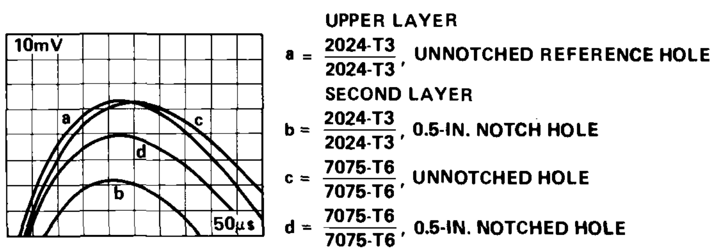

FIG. 5—*SPEC response versus conductivity notch sensitivity, steel fasteners, 0.635-cm (0.25-in.)-thick layers (1.0 in. = 2.54 cm).*

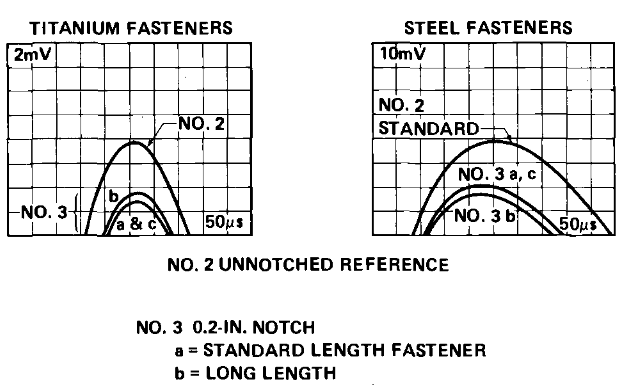

FIG. 6—*SPEC response versus fastener variability 0.635-cm (0.25-in.)-thick upper-layer thickness (1.0 in. = 2.54 cm).*

Edge Margin

Edge margin is an important variable in eddy-current crack detection and involves both upper and lower edges of multiple-layer structures (Fig. 7). The effect of steel fasteners, drawing the magnetic field inward toward the fastener, permits the use of a smaller-diameter pickup coil, which in turn helps to reduce the edge-margin effect. It was found that where the lower-edge margin variation was 0.152 cm (0.060 in.), a 0.381-cm (0.15-in.)-long notch/crack was still detectable.

Interface Gap

Interface-gap variation experiments were made using a similar double row fastener scarf-type joint specimen as used for the edge-margin tests. For the 0.635-cm (0.25-in.)-thick upper-layer structure specimen, a 10 to 15-mV separation between the 0.381-cm (0.15-in.)-long notched hole and unnotched reference hole responses was observed over a 0- to 0.051-cm (20-mil) interface-gap variation; a 0.015-cm (6-mil) gap was used for reference (Fig. 8). Thus the variation of interface gap does not appear to be a problem for the SPEC system for gaps less than 0.051 cm (20 mil).

Fastener Height/Countersink Depth

The fastener height/countersink depth experiments were made with a probe lift-off of 0.030 cm (0.012 in.) in order for the probe to clear the highest fastener height used in the test. The measurements were made on

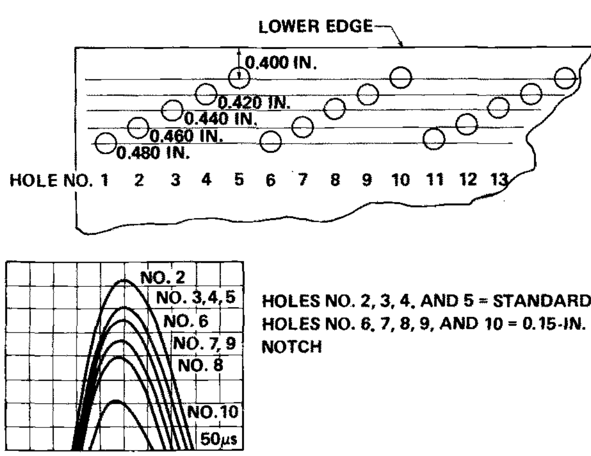

FIG. 7—*SPEC response versus edge margin, 0.635-cm (0.25-in.)-thick upper-layer steel fasteners (1.0 in. = 2.54 cm).*

a specimen using a hole with a flush fastener as a reference, and unnotched and notched holes with various countersink depths. Although the steel fasteners' height was observed to have a significant effect on the SPEC response (Fig. 9), a 0.508-cm (0.2-in.)-long notch crack is readily detectable over the maximum 0.102 to 0.033-cm (0.04- to 0.013-in.) fastener-height variation. Only an insignificant effect of fastener-height variation on crack detection of titanium-fastened structure was observed (Fig. 9).

First-Layer Thickness

A series of skin/stringer structure specimens with 0.635-cm (0.25-in.), 0.787-cm (0.31-in.), 0.953-cm (0.375-in.), and 1.27-cm (0.50-in.) upperskin

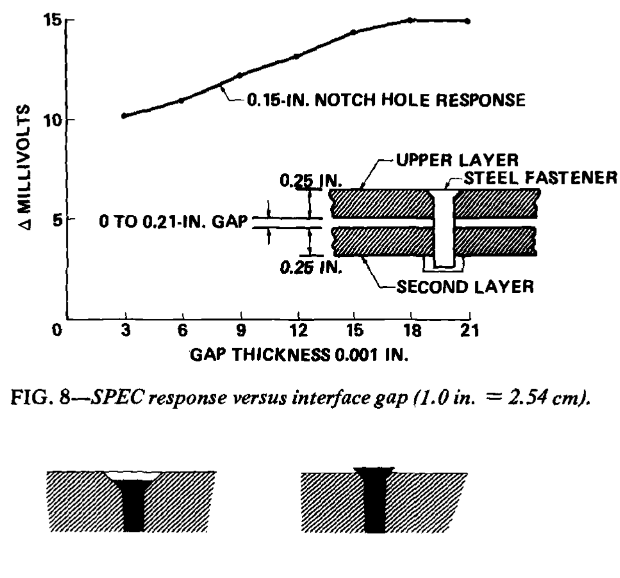

FIG. 8—*SPEC response versus interface gap (1.0 in. = 2.54 cm).*

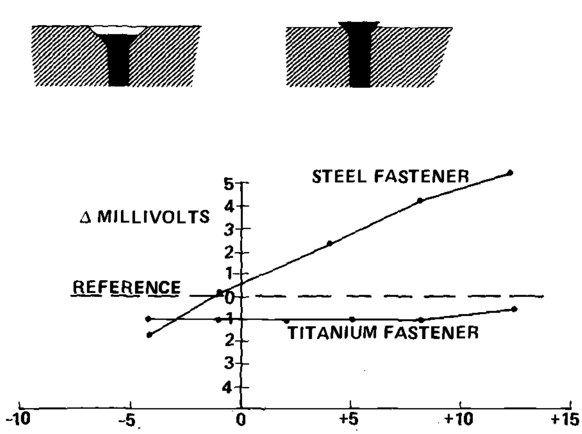

FIG. 9—*SPEC response versus fastener height, 0.635-cm (0.25-in.)-thick upper layer (1.0 in. = 2.54 cm).*

thicknesses with corresponding lower stiffener thicknesses were tested. Fastener sizes included 0.635-cm (0.25-in.) and 0.953-cm (0.375-in.) diameters. SPEC response data for a 1.27-cm (0.50-in.)-long crack versus skin thickness with steel fasteners are plotted in Fig. 10. From these data it can be seen that a 1.27-cm (0.5-in.)-long notch can be readily detected through a 1.27-cm (0.50-in.)-thick upper skin.

Probe Lift-Off

The probe lift-off inspection variable is made up of electrical coil loading, field penetration as a function of distance, and coil distance separation from the fasteners. The coil/fastener separation factor is especially important in the case of steel fasteners. A time/phase relation between probe lift-off amplitude response and probe lift-off distance was measured (Fig. 11). Both the probe mV amplitude response and the time-to-voltage peak response versus lift-off were found to be nearly linear. Thus a direct relationship between SPEC lift-off voltage and time-shift effect can be determined and used for lift-off correction. The lift-off effect as measured for the 0.635-cm (0.25-in.)-thick upper-layer, scarf-joint type structure with steel fasteners is shown in Fig. 12. A 0.015-cm (6-mil) lift-off was used for reference. For example, the lift-off effect over a 0.508-cm (0.2-in.)-long notch was observed to have a significant response change, but still did not obscure the crack response. When the notch response is corrected for lift-off via the time/phase factor, a significant improvement in effective notch sensitivity is obtained (Fig. 12). It is interesting to note, however, that the time/phase correction

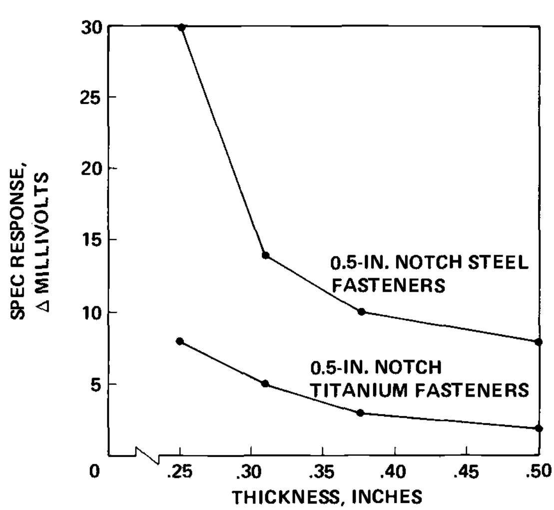

FIG. 10—*SPEC response versus upper-layer thickness (1.0 in. = 2.54 cm).*

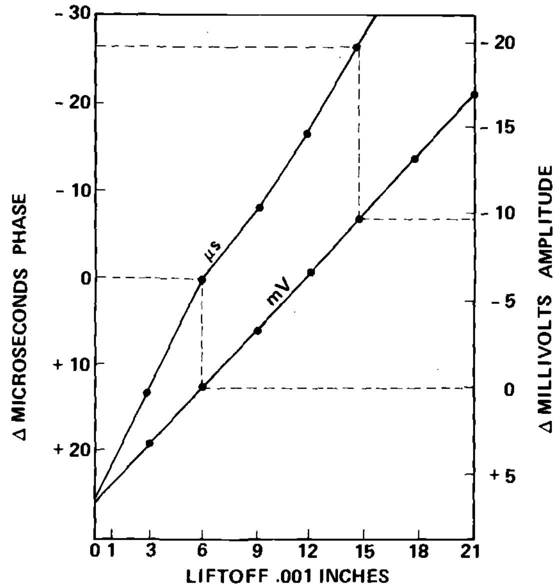

FIG. 11—*SPEC response versus lift-off amplitude versus phase.*

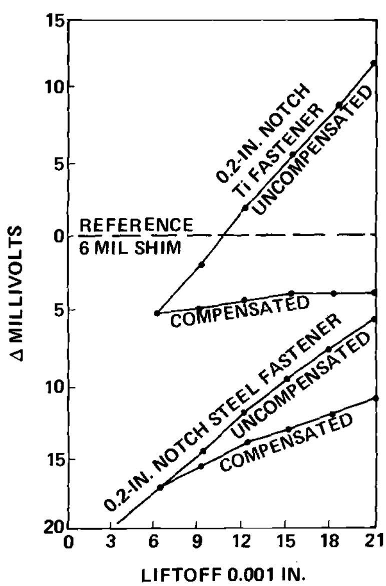

FIG. 12—*SPEC response versus lift-off, 0.635-cm (0.25-in.)-thick upper layer (1.0 in. = 2.54 cm).*

factor does not completely eliminate the total lift-off effect. The uncorrected portion of the lift-off effect for notch detection is believed to be due to the increased distance separation between the probe and the steel fastener.

Conclusions

A high peak energy shaped-pulse eddy-current inspection concept for thick, second-layer aircraft structure has been determined to be feasible. The increased depth of magnetic-field penetration and higher eddy-current levels achieved with the shaped pulse and high peak energy increase inspection capability. The frequency-spectrum character of the pulse approach as used via time-domain response measurements substantially increases crack inspection signal-to-noise ratios; drive pickup coil decoupling and selective drive pickup field orientation detection techniques are also contributing factors. Crack-inspection capabilities of second-layer structures with 0.635- to 1.27-cm (0.25- to 0.50-in.)-thick upper-layer skin, for which conventional eddy-current instruments have limited capability, have been improved significantly with the SPEC inspection system.

Acknowledgments

The authors would like to acknowledge the encouragement and direction of R. D. Whealy, manager, and R. M. Neufeld, senior supervising engineer, of the Boeing Company Quality Control Research and Development organization; also, A. F. Norwood, manager, and S. D. Schneider, senior supervising engineer, of the Boeing Electrical/Electronics Technology organization. The authors would also like to acknowledge the contributions of D. A. Lang and J. K. Bogart of the Boeing Electromagnetics Laboratories.

C. W. Anderson[1]

Eddy-Current Scanning of Graphite-Reinforced Aluminum Panels

REFERENCE: Anderson, C. W., "**Eddy-Current Scanning of Graphite-Reinforced Aluminum Panels,**" *Eddy-Current Characterization of Materials and Structures, ASTM STP 722*, George Birnbaum and George Free, Eds., American Society for Testing and Materials, 1981, pp. 140-153.

ABSTRACT: The application of an eddy-current test technique for the detection of material flaws in graphite-reinforced aluminum panels is discussed. This particular technique involves scanning the specimen and recording both real and imaginary impedance components of the test coil using a format similar to that of an ultrasonic C-scan. The benefits of this approach are discussed and the results are compared with those of X-radiography and ultrasonics.

KEY WORDS: nondestructive tests, metal matrix composites, eddy-current testing

The Naval Surface Weapons Center is currently evaluating the performance of metal-matrix composite materials for lightweight structural applications under a program funded by the Naval Sea Systems Command. As a parallel effort to the development of new materials, the development and evaluation of nondestructive test techniques for these materials is also being pursued. Although several materials are under investigation, this paper deals only with graphite-reinforced aluminum. Specimens of intentionally flawed and unflawed graphite/aluminum have been subjected to a battery of nondestructive examination (NDE) techniques to evaluate their applicability towards detecting material defects. One of these techniques, which is the topic of this paper, involves eddy-current scanning along the material surface.

The material under investigation is composed of Thornel-50 graphite fibers imbedded in a 201-aluminum alloy matrix. The composite material is fabricated as a flat panel of which the fibers occupy approximately 30 percent of the total material volume. A unidirectional fiber orientation is used. Panels fabricated for nondestructive evaluation measured 2.8 mm thick by 152 mm wide by 305 mm long.

The fabrication of the composite material into panel form is a two-stage

[1]Physicist, Naval Surface Weapons Center, Materials Evaluation Branch, White Oak, Silver Spring, Md. 20910.

process (Fig. 1). The first stage involves the formation of precursor wires. These wires are formed by immersing graphite fiber bundles into molten aluminum. Special precautions must be taken during this process to ensure that the aluminum completely infiltrates and wets the fiber bundle. When the aluminum hardens, it is in the shape of a wire whose diameter is between 0.75 and 1.25 mm (Fig. 2). This wire is then cut into equal lengths which are placed side by side and diffusion bonded to form a panel (Fig. 3).

The panels fabricated for this program consisted of three layers and thus three plys of precursor wires. In addition, a thin (0.25 to 0.50 mm) skin of aluminum was diffusion bonded to both surfaces of the panels. This protective layer is required to prevent galvanic corrosion of the graphite/aluminum composite.

The manufacturing process can lead to two basic classes of flaws in the material. These are incomplete infiltration of the aluminum into the graphite bundle and incomplete fusion between adjacent precursor wires. The effects of these flaws on the transverse-strength properties of a composite with unidirectional fiber orientation can be significant.

Previous efforts to detect material defects in graphite-reinforced aluminum panels have principally involved ultrasonics and radiography. A summary of

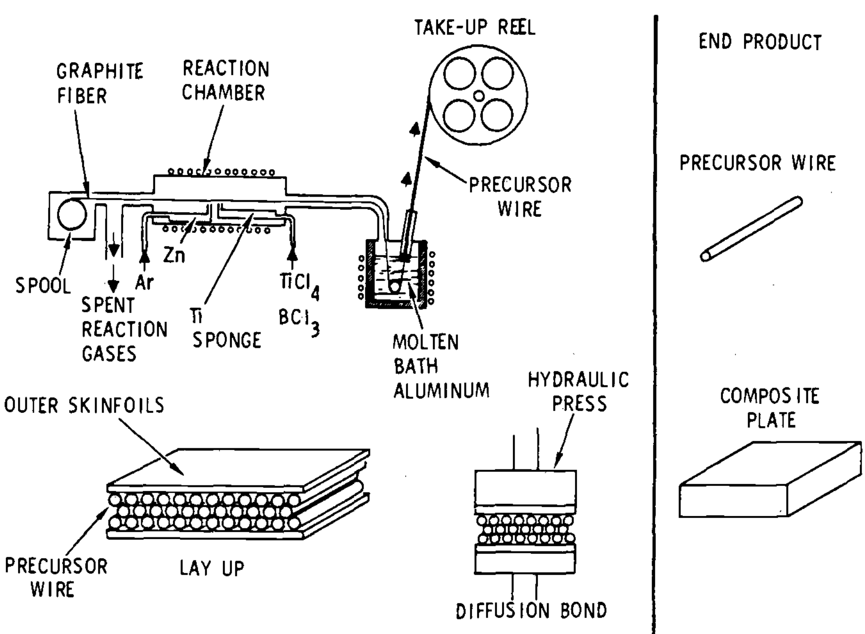

FIG. 1—*Graphite aluminum fabrication process.*

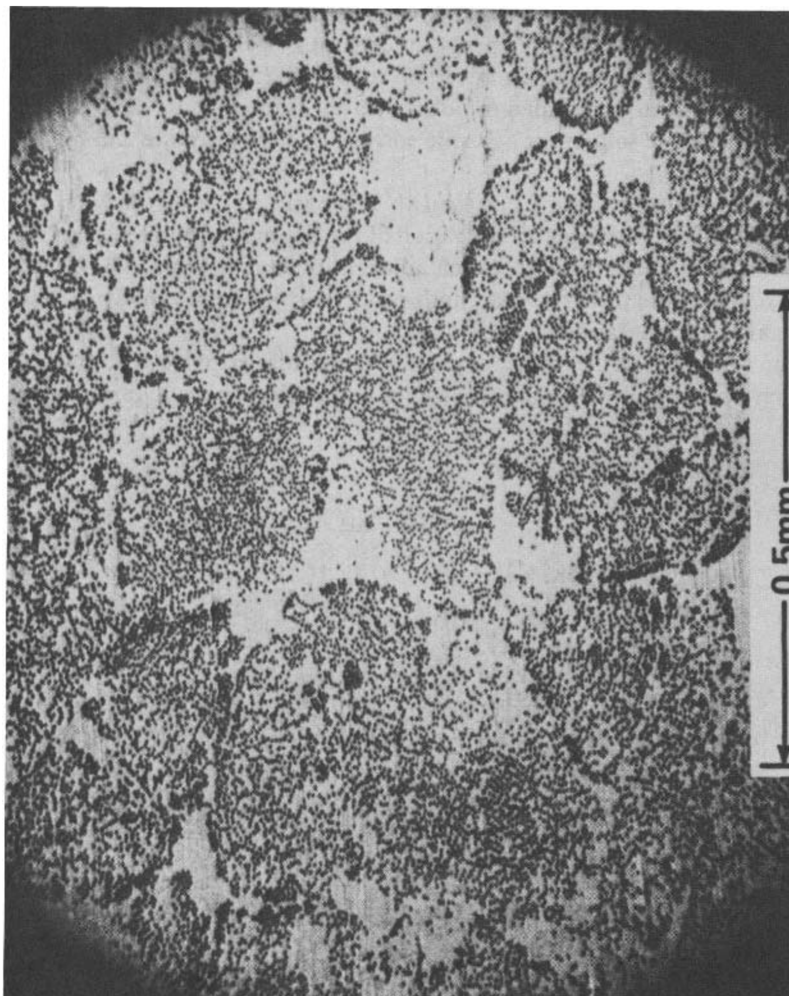

FIG. 2—*End view of a single precursor showing graphite fibers in an aluminum matrix.*

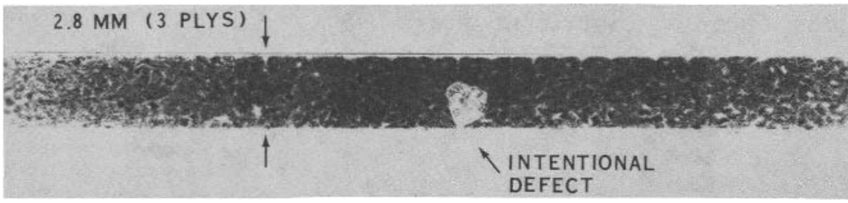

FIG. 3—*Graphite/aluminum panel cross section (sectioned perpendicular to fiber direction).*

much of this work is given by Pfeifer.[2] In addition, Harrigan and Hudson[3] have evaluated the capabilities of pulse-echo ultrasonics on thicker specimens of graphite/aluminum.

Procedure

Preliminary eddy-current testing of a series of graphite/aluminum panels containing intentional manufacturing defects revealed little. The testing was performed at 10 kHz with a hand-held probe and an Automation Industries EM-3300 instrument that has a cathode-ray tube impedance-plane display. It was noted that the illuminated spot on the display changed position in an erratic fashion as the probe was moved. Thus, it quickly became apparent that due to the nonuniformity of supposedly good material the intentionally placed defects were going to be difficult to detect.

Experience in ultrasonic testing has shown that in situations where a fluctuating background signal is encountered, it is often beneficial to create an image or C-scan. A data presentation technique of this sort can often make it easier to notice small signal changes that are superimposed on a varying background. Once an image or mapping is created, the spatial-pattern recognition ability of the human eye can be brought into play to help distinguish signal from noise. Noise in this case refers to signal changes that are not indicative of defective material.

The equipment that was utilized in the eddy-current scanning of the graphite/aluminum test panels consisted of an Automation Industries EM-3300 eddy-current instrument, an Automation Industries 450-series laboratory scanner (Fig. 4) and a Mosely x-y recorder. The test probe had a coil diameter of 2.3 mm and a ferrite core to help concentrate the magnetic flux at the central axis of the probe. The inductance of the test probe as measured in air was approximately 115 μH. It should be noted that the laboratory scanner was slightly modified with the addition of x- and y-axis potentiometers to provide output voltages corresponding to the probe position.

[2]Pfeifer, W. H., "Graphite/Aluminum Technology Development," *Hybrid and Select Metal-Matrix Composite*, American Institute of Aeronautics and Astronautics, 1977, pp. 197–208.

[3]Harrigan, W. C., Jr. and Hudson, S. P., "Inspection of Graphite/Aluminum Composite by Means of Holography," Report Number TOR-0077 (2950-01)-1. The Aerospace Corporation, El Segundo, Calif., 21 June 1977.

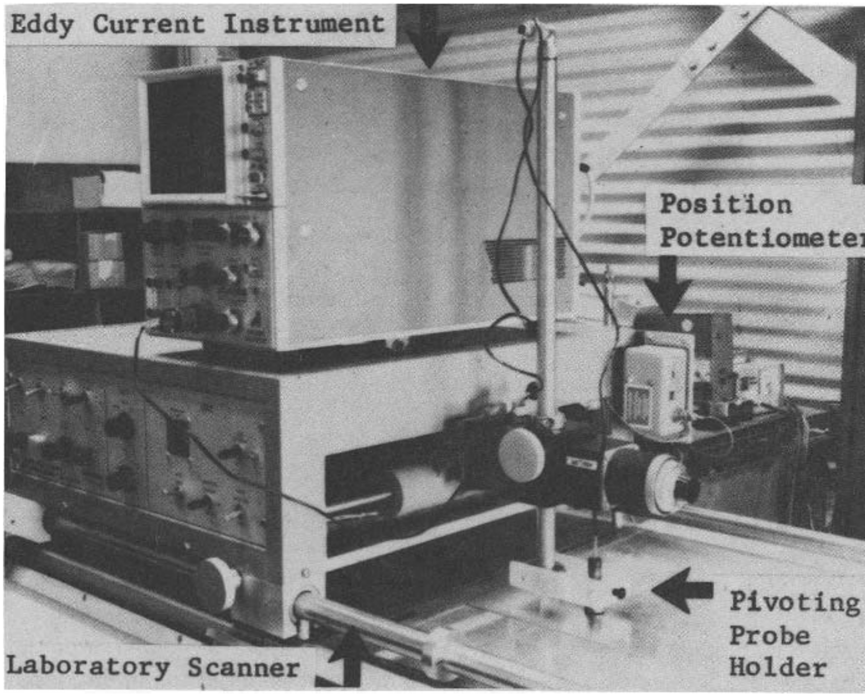

FIG. 4—*Eddy-current scanning apparatus.*

The eddy current instrument provides a cathode-ray tube impedance-plane display of the test coil signal. With the proper phase rotation of the signal, the vertical and horizontal axes of the display can be made to correspond to the imaginary and real axes of the test coil impedance plane. This was accomplished by setting the lift-off line for ferrite in the vertical direction.

Instead of using the conventional black and white or tone shaded C-scan recorder on the laboratory scanner, a modified C-scan output was recorded on an x-y recorder. The y axis of the recorder was driven by the voltage across the y-axis position potentiometer on the laboratory scanner. The x-axis was driven by the sum of the x-axis potentiometer and either the real or imaginary axis outputs of the eddy current instrument. The result is a composite recording of three variables: x position, y position, and either the real impedance component (R) or the imaginary component (X). Separate recordings are required to obtain mappings of each of the real and the imaginary impedance components.

It is important in eddy-current testing to eliminate as many variables as possible. In this case, lift-off or probe-to-specimen spacing is such a variable. To minimize its effect, a pivoting arm was used between the probe and the scanner. This arm was hinged at the connection to the scanner to allow the probe to follow the contours of slight warpages in the test panels.

Defect Modeling

Eddy-current test signals are affected by a large number of variables, some of which include flaw size, flaw depth beneath the surface, specimen conductivity, and specimen thickness. The effect of these and other variables on test indications is complex and sometimes ambiguous. A means of sorting out the effects of certain key parameters is essential for a meaningful interpretation of the test results.

An empirically derived model was used to study the effects of flaw size and flaw depth below the surface for the particular test probe driven at a frequency of 10 kHz. Ideally, an eddy-current model should be fabricated from the actual material being tested, but in this case surplus graphite/aluminum material was not available at the time. Instead, a model was constructed from thin sheets of 7075-T6 aluminum. The aluminum had an electrical resistivity of 5.9 $\mu\Omega \cdot$cm as compared to 11.6 $\mu\Omega \cdot$cm for the graphite/aluminum composite.

The model was constructed by stacking aluminum plates together in a manner similar to that described by Libby.[4] Defects could then be simulated in one layer or any combination of layers by butting the edges of two plates together to simulate a crack in that particular layer. Indications were recorded from simulated cracks of different sizes and different starting depths below the surface.

The difference in the resistivities of the model-development material and that of the actual material being tested required that a scaling function be imposed on the model. At a particular test frequency, material resistivity dictates skin depth which in turn dictates signal amplitude and phase angle. The aluminum-model results, therefore, had to be rotated on the impedance plane in addition to being scaled in amplitude before they could be said to approximate the eddy current response of the graphite/aluminum test specimen. The skin depth at 10 kHz in the aluminum model was calculated to be 1.2 mm, whereas for the graphite/aluminum it was determined to be 1.8 mm. Figure 5 depicts the model results after being corrected to apply to graphite-reinforced aluminum.

One assumption that must be made in this type of model analysis is that the material being tested or modeled is homogeneous and isotropic. This is not the case with graphite aluminum. One would expect slightly greater electrical conduction in the direction parallel to the fibers. In addition, metallo-

[4]Libby, H. L., *Introduction to Electromagnetic Nondestructive Test Methods*, Wiley-Interscience, New York, 1971, pp. 291-292.

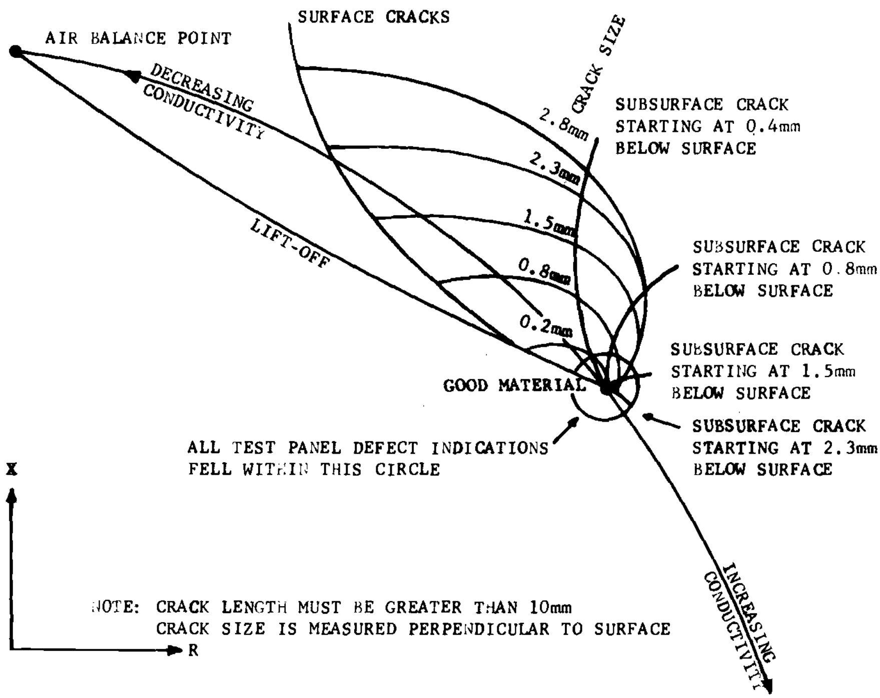

FIG. 5—*Eddy-current model for graphite/aluminum at 10 kHz.*

graphic analysis reveals that the concentration of graphite fibers is not uniform throughout the material. Instead, fibers are still grouped together in somewhat distorted bundles. One could certainly expect these two factors to complicate the localized flow of eddy currents around fiber bundles. It is expected, however, that these highly localized discrepancies will, to a large extent, be averaged throughout the entire volume of material being inspected at any one time. One then has a choice of viewing the problem as that of testing either a uniformly conducting material with varying porosity as simulated by the carbon fibers or a nonporous material with varying conductivity. For the macroscopic first-order approximation, at least, both viewpoints appear equally valid.

Results

A total of four panels were tested by eddy-current scanning, ultrasonics, and radiography. Three of the panels contained intentionally fabricated defects. The results from Panel 1 appear in Fig. 6 to 10. Radiographic and ultrasonic results are presented for comparison.

Figure 6 shows the positions of intentionally fabricated defects in Panel 1.

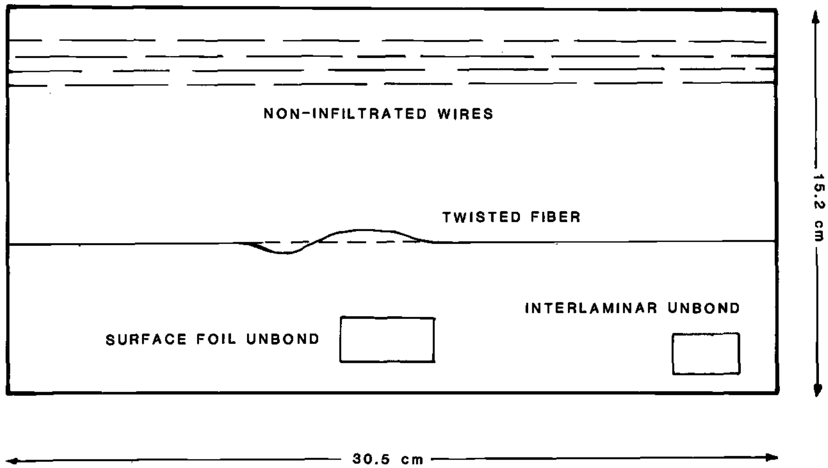

FIG. 6—*Placement of intentional defects in Panel 1.*

The two unbonded regions were intended primarily for ultrasonic detection; however, there is reasonable doubt as to whether they were successfully created.

Figures 7 and 8 are recordings of the real and imaginary components of the test-probe impedance for Panel 1. The imaginary component scan contains most of the useful information. This is not surprising since the eddy-current model predicts that subsurface defects will produce indications with large components in the imaginary direction of the impedance plane. As predicted by the model, the real impedance component scan appears noisy as the result of oversensitivity to insignificant fluctuations near the material surface.

Both the noninfiltrated wire region and the twisted fiber give clear indications of their presence. The surface foil unbond also shows up, but this is most likely due to difficulties encountered in fabricating the defect, and thus one should not conclude that this technique can reliably detect unbonds parallel to the surface. The indication recorded for the twisted fiber points out the fact that the eddy-current model is only partially complete. This indication is in the direction of decreasing reactance from the surrounding material, thus indicating a highly conductive defect. The model, which was adapted from similar models used for homogeneous materials, accounts only for defects such as cracks which decrease the apparent conductivity of the material. An ideal model for a metal-matrix composite would have to also account for defects with apparently higher conductivity than the surrounding material. Such defects could result from improper fiber-to-matrix content or a nonuniform distribution of the two constituents.

The indications received from both the noninfiltrated wires and the twisted fiber are both quite small with respect to the scale of the eddy-current model.

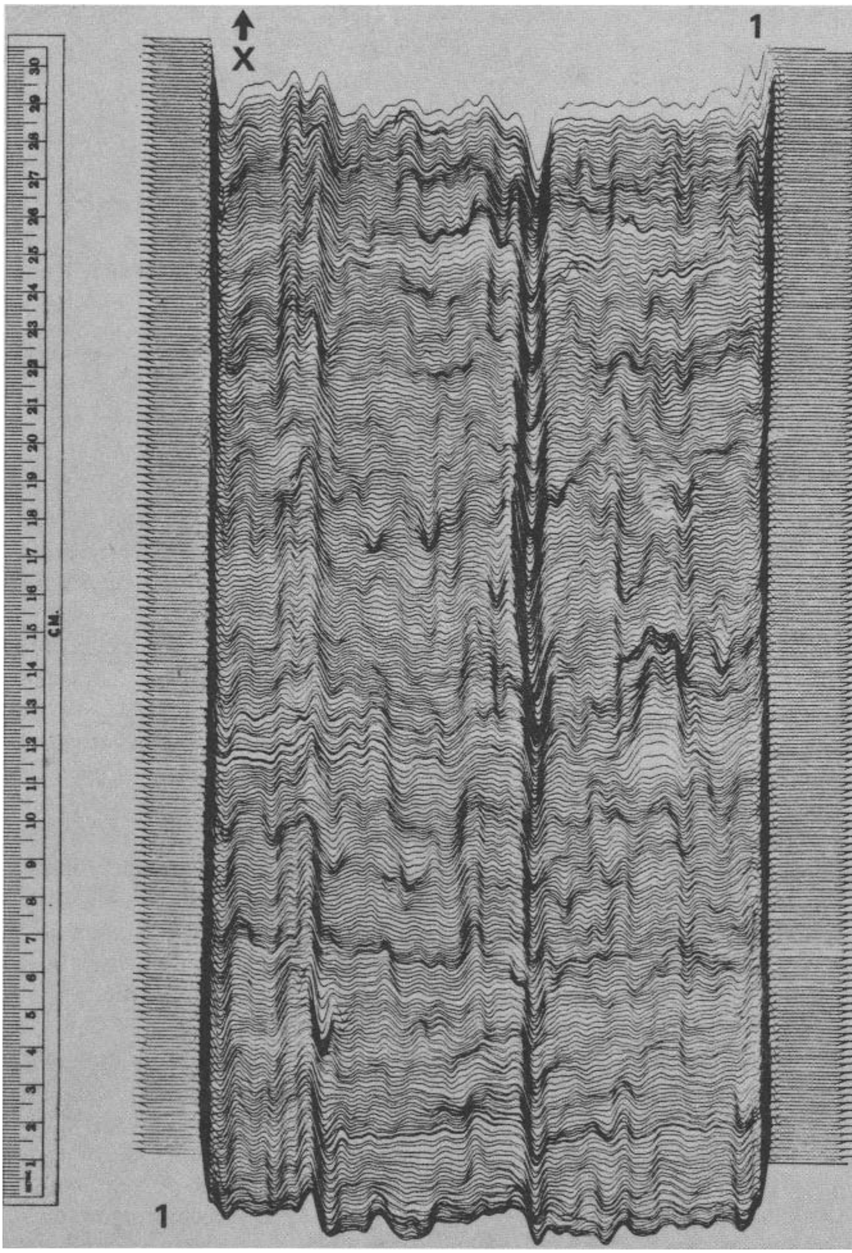

FIG. 7—*Eddy-current scan of Panel 1 showing imaginary impedance component.*

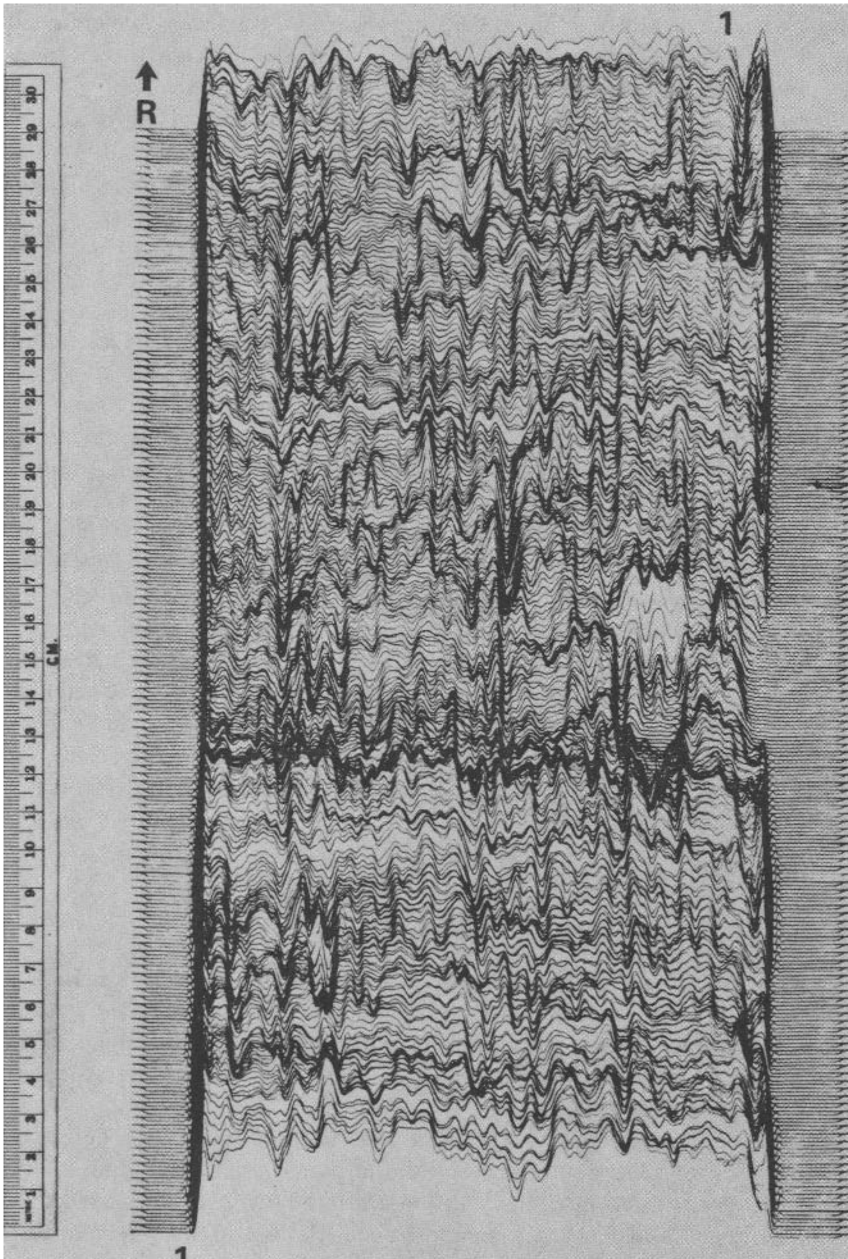

FIG. 8—*Eddy-current scan of Panel 1 showing real impedance component.*

Both indications have magnitudes equivalent to a subsurface crack no greater than 0.4mm deep and starting at 0.75 mm below the surface. As mentioned earlier, however, the twisted-fiber indication is in the opposite direction on the impedance plane as would be expected from a crack.

Radiographic results (Fig. 9) and ultrasonic testing (Fig. 10) give similar indications. For these particular defects, the signal-to-noise ratio of the eddy-current test appears only slightly superior to that of the ultrasonic C-scan. Testing of the other panels containing similar defects gave similar results; however, in certain cases the ultrasonic technique was superior to eddy-current scanning. This seems reasonable since the eddy-current signal is related to the flaw dimension perpendicular to the surface whereas the ultrasonic signal is governed by the flaw dimensions parallel to the surface. Thus, the two techniques are somewhat complimentary.

Perhaps the strongest argument in favor of eddy-current testing of graphite-reinforced aluminum panels is not the fact that the technique can detect certain material-fabrication flaws, but rather that it may be advantageous in the detection of in-service or material-forming flaws, namely, cracks. By viewing the radiograph of Panel 1, one can appreciate how difficult it could be to distinguish the presence of a crack from among the fibers. Cracks in the material are most likely to be perpendicular to the surface and parallel to the fiber direction. This orientation would also make ultrasonic crack detection difficult without resorting to a shear-wave inspection mode. Even this may not be practicable, however, due to high-scattering and ultrasonic-attenuation characteristics of graphite-reinforced aluminum. The eddy-current model reveals that the detectability of cracks by this technique would be greatly enhanced over the detectability of material-fabrication defects such as noninfiltrated wires.

Conclusions

Significant benefit can be achieved by recording eddy-current test indications as an image or mapping of the test item. Such a technique can help to sort out legitimate flaw indications from a varying background signal. This is particularly true for nonhomogeneous materials such as metal-matrix composites.

The use of eddy currents to test for certain material-fabrication defects in 2.8-mm-thick graphite-reinforced aluminum panels appears comparable in signal-to-noise ratio to ultrasonic testing and may serve to complement the ultrasonic technique. Probably the most beneficial use of eddy-current testing lies in its ability to detect cracks resulting from material forming or in-service use. Such cracks would be difficult to distinguish from fiber images by either radiography or ultrasonic C-scan testing.

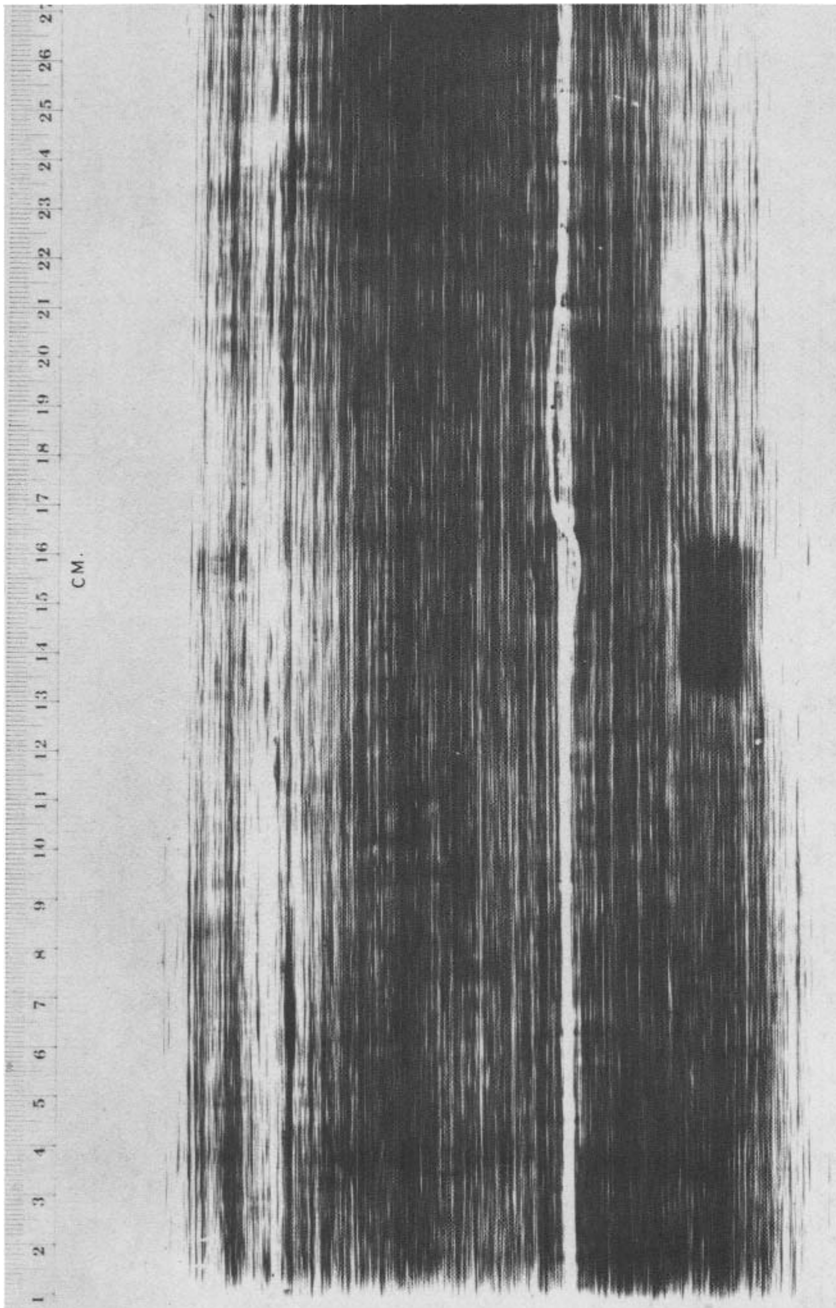

FIG. 9—*Radiograph of Panel 1.*

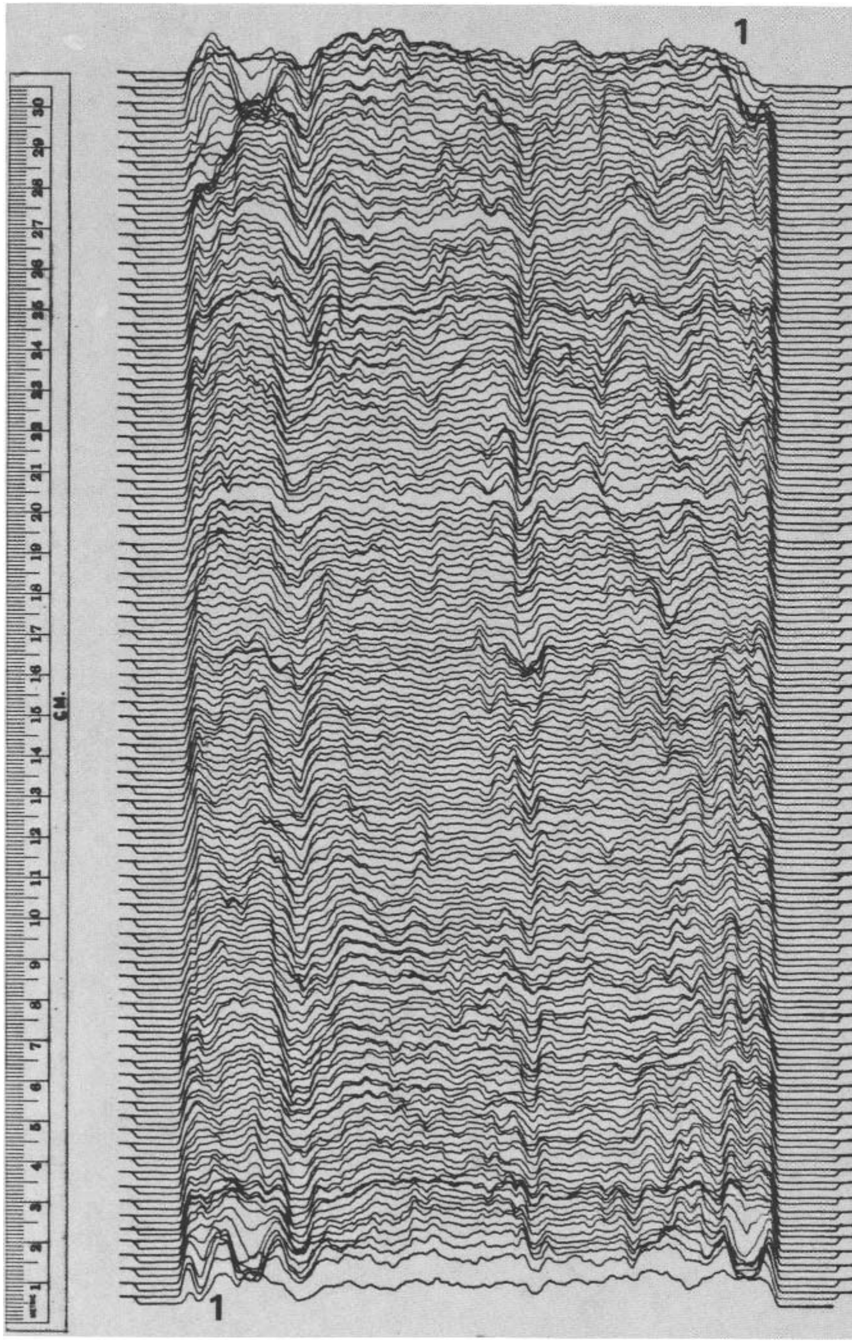

FIG. 10—*Ultrasonic C-scan of Panel 1.*

Acknowledgments

The author wishes to acknowledge the assistance of J. V. Foltz for obtaining material specimens, G. V. Blessing for helpful guidance and discussions, and J. M. Warren for assistance in modifying the scanning apparatus.

Material Properties

K. T. Hartwig[1]

An Eddy-Current Decay Technique for Low-Temperature Resistivity Measurements

REFERENCE: Hartwig, K. T., "**An Eddy-Current Decay Technique for Low-Temperature Resistivity Measurements,**" *Eddy-Current Characterization of Materials and Structures, ASTM STP 722*, George Birnbaum and George Free, Eds., American Society for Testing and Materials, 1981, pp. 157–172.

ABSTRACT: The eddy-current decay technique developed by Bean for resistivity determination is well suited for material characterization studies. The technique is shown to be an excellent method for determining the terminal solid-solution phase boundary in aluminum-gold (Al-Au), for following age hardening in dilute Al-Au alloys, and for detecting anisotropic electrical resistivity in cold-worked aluminum. Rapid and highly accurate resistivities are measured with a basic circuit arrangement incorporating a digital oscilloscope.

KEY WORDS: aluminum, dilute alloy, eddy current, low temperature, phase boundary, precipitation, resistivity, resistance, work hardening

Low-temperature resistivity measurements are relatively easy to take and can provide precise information about the chemical and physical constitution of metals. Such measurements are sensitive to the amounts and types of dissolved impurity atoms, structural imperfections, and phases present, as well as specimen size and surface conditions. Even though resistivity effects from impurities and structural defects are relatively small, the contributions from the various phenomena are independent and can be separated if supplemental structural information is available.

Under low-temperature conditions, measurement of total resistivity can be performed without interference from phonon contributions. Matthiessen's rule states that the total resistivity, ρ_T, is the sum of a residual resistivity, ρ_o, arising from impurities, defects, etc., and the intrinsic resistivity ρ_p

$$\rho_T = \rho_o + \rho_p \tag{1}$$

[1]Assistant scientist, Engineering Experiment Station, University of Wisconsin, Madison, Wisc. 53706.

The rule assumes that each mechanism contributes independently to the measured resistivity. For a well-annealed metal, ρ_o is ρ_{impurity}, which in turn is a sum of contributions from all impurities i

$$\rho_{\text{impurity}} = \Sigma\,(\rho_i/c_i)\,c_i \tag{2}$$

where (ρ_i/c_i) is a measure of the electron scattering by an isolated substitutional impurity atom i, and c_i is the concentration of each specific impurity. The contributions from defects such as vacancies, dislocations, inclusions, and grain boundaries are also considered to be independent and separable and to scale linearly with defect number density. At room temperature, the resistivity of even a relatively pure metal is dominated by the phonon contribution, whereas ρ_p is negligible at temperatures below 20 to 30 K. A measurement of ρ_T at a low temperature will thus reflect principally the impurity, defect, and structural contributions to resistivity.

This paper presents a brief overview of the standard potential difference measurement, the theory of the eddy-current decay (ECD) resistivity measurement, and a description of an eddy-current decay apparatus. The value and suitability of the ECD technique for material characterizations are demonstrated by examples of the assessment of the primary solid solubility phase boundary in the aluminum-gold (Al-Au) system, the measurement of precipitation kinetics in dilute Al-Au alloys, and the establishment of structural anisotrophy in 99.99 percent aluminum and Al-Ni_3Sb alloy rod subjected to cold work by wire drawing. The use of the method eliminates the possibility of specimen damage during tests, allows for measurements on large specimens, and is quick and accurate.

Eddy-Current Decay Resistivity Measurement

Electrical resistivity is often measured by a four-terminal potentiometric (FPP) method. The resistance, R, is computed from measurements of a voltage drop, V, and applied current I. Resistivity is equal to RA/L where R is measured as above, and A and L are the cross-sectional area of the specimen and the distance between voltage contacts, respectively. The ratio of resistivities at two temperatures is frequently desired instead of the resistivity at one temperature, which permits cancellation of the geometric factor A/L. For ratio measurements size is often unimportant and, in fact, the specimen need not be of uniform shape. The potentiometric method is most useful for voltage drops greater than about 1×10^{-8} V. For very pure, large specimens, however, it is difficult to obtain accurate measurements. As an example, the potential drop along a 50 mm long, 6.35 mm diameter, 99.999 percent pure, aluminum rod is on the order of 15 nV for a current of 1 A.

In 1959, Bean [*1*][2] described an eddy-current decay technique for measuring the electrical resistivity of metals that is quite different from standard potential difference methods. When a magnetic field is applied to a conductor, eddy currents flow in the conductor creating a magnetic field in opposition to the externally applied field. With time, the average field in the conductor approaches the value of the applied field after eddy currents have decayed. The rate of change of flux density, B, is governed by a magnetic-diffusion equation

$$\frac{\partial \bar{B}}{\partial t} = D \nabla^2 \bar{B} = \frac{10^9 \rho}{4\pi \mu_r} \nabla^2 \bar{B} \tag{3}$$

where

B = average flux density in gauss,
ρ = resistivity in ohm·cm, and
μ_r = relative permeability (dimensionless).

The magnetic diffusivity D, in a weakly magnetic material for which $\mu_r \simeq \mu_o$, is $10^9 \rho / 4\pi \mu_r$.

Flux diffusion can be measured by a simple circuit arrangement. The specimen is located in a small secondary pickup coil which is in turn located in a larger magnetizing solenoid. A step change in current is applied to the magnetizing coil; the resultant voltage across the pickup coil is noted as a function of time. This voltage is caused by flux penetration into or out of the specimen and is a measure of diffusivity.

If we assume a body of constant cross section and uniform isotropic resistivity, and apply a magnetic field along the Z-directed axis perpendicular to the cross section, then Eq 1 becomes a scalar equation for B_Z. The voltage in the secondary coil will be proportional to the time rate of change of average flux within the material. For a circular cross section of radius r, and after long times, the voltage $V(t)$ across a coil with N turns approaches a simple exponential

$$V(t) = 10N \rho H_o \exp(-t/\tau_r) \tag{4}$$

where H_o is the magnetic field strength in gauss, t is time in seconds, and

$$\tau_r = \frac{2.17 \mu r^2 10^{-9}}{\rho} \tag{5}$$

The $V(t)$ relationship of Eq 4 is plotted in Fig. 1.

There are several distinct advantages to the ECD technique compared with

[2]The italic numbers in brackets refer to the list of references appended to this paper.

conventional current-voltage methods [2,3]. The most significant advantage is that no electrical connections are made to the specimen with the ECD method. For pure specimens, the effects of chemical diffusion of impurities into the metal from a weld or physical damage from the mechanical strain of a probe contact may occur and can affect low-level resistivity values. Another advantage is that the measurement accuracy associated with the ECD approach remains high as the specimen resistivity decreases. In addition, the ECD measurement can be performed quickly and can be also applied to a variety of specimen geometries and resistivities.

Eddy-current decay measurements have a number of limitations [2,4]. For instance, the rate of decay of eddy currents, τ_r, is inversely proportional to the resistivity and directly proportional to the specimen cross-sectional area. As sample resistivity increases or the size decreases, τ_r may approach the response time of the measuring apparatus. Typically, it is difficult to determine τ_r for temperatures above 77 K or for specimen diameters less than a few millimetres. Another difficulty occurs when τ_r is very large since the time rate of change of B is then small, which results in a small induced voltage. Also, end effects may become appreciable for specimen length to diameter ratios of less than eight.

Experimental Procedures

Specimen Preparation

The experimental procedures used for specimen preparation and analysis are outlined in Fig. 2. Alloy preparation involved induction melting 99.999 percent aluminum having a residual resistivity ratio (RRR $= \rho_{273\ K}/\rho_{4.2\ K}$) of greater than 2500 with 99.999 percent gold in high-purity graphite crucibles under argon. The Al-Ni_3Sb alloy was formed in a graphite crucible with an alumina liner and cast in a copper mold. Ingots 25 mm in diameter containing nominally 0.06, 0.1, 0.15, and 0.2 percent by weight gold and 1.0 percent by weight nickel antimonide were extruded hot to 6.35 mm diameter. Specimens were sectioned for composition analysis, metallographic observation, and resistance measurements. All Al-Au specimens were homogenized in air at a temperature above 873 K for at least 2 h and water quenched. Neutron activation analysis and emission spectroscopy were used to determine accurately the solute content of each specimen. The alloy and specimen preparation scheme yielded highly pure alloy. For example, pure aluminum with a RRR in excess of 5000 was melted, cast, and extruded without a noticeable drop in purity as determined by residual-resistivity measurements.

The phase-boundary experiment was performed on specimens containing nominally 0.05, 0.10, 0.15, and 0.20 percent by weight gold that were quenched simultaneously from a vertically mounted furnace. The same specimens were used for all annealing temperatures investigated. The heat treat-

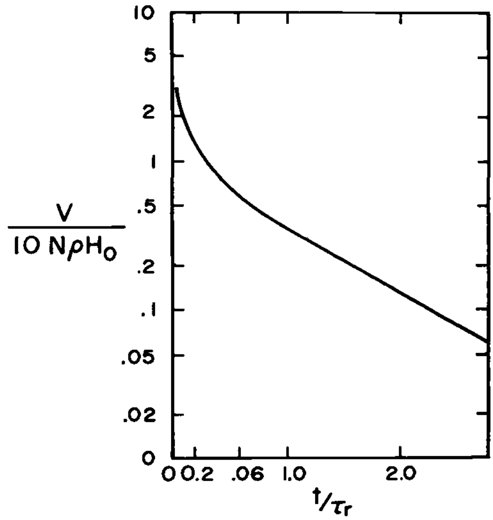

FIG. 1—*Theoretical curve of voltage across an* N*-turn pickup coil versus time after applying a magnetic field,* H_0*, to a cylindrical rod of radius* r *and resistivity* ρ [1]. τ_r *is the relaxation time defined as* $2.17 \times 10^{-9}\ \mu r^2/\rho$.

ment procedure included a 2-h soak at the selected temperature followed by a quench into cold water and a cooling to 4.2 K.

In the aluminum-gold precipitation experiment, all specimens were given a solution heat treatment followed by a quench and a hold at room temperature before artificial aging. Aging was performed in an isothermal bath of oil or molten salt. Room-temperature aging was not observed; therefore, special precautions were not taken to inhibit precipitation during the room-temperature hold.

The wire-drawing reduction experiment was performed on 99.99 percent aluminum and Al-1.0Ni_3Sb. Rod with a diameter of 6.35 mm was drawn progressively in area reduction steps of not more than ten percent to a final wire diameter of 1.6 mm with standard carbide copper wire drawing dies.

Electrical-Resistivity Measurements

Specimens at least 51 mm long were used for all resistivity determinations. Potential-difference measurements were made in the standard fashion and are described in detail elsewhere [5].

An eddy-current decay system was constructed following National Bureau of Standards (NBS) designs [2] and was used for measurement of residual resistivity. Measurements of residual resistivity taken by the ECD method on well-annealed specimens agreed with residual resistivity measurements taken on the same specimens by the conventional potential-difference method.

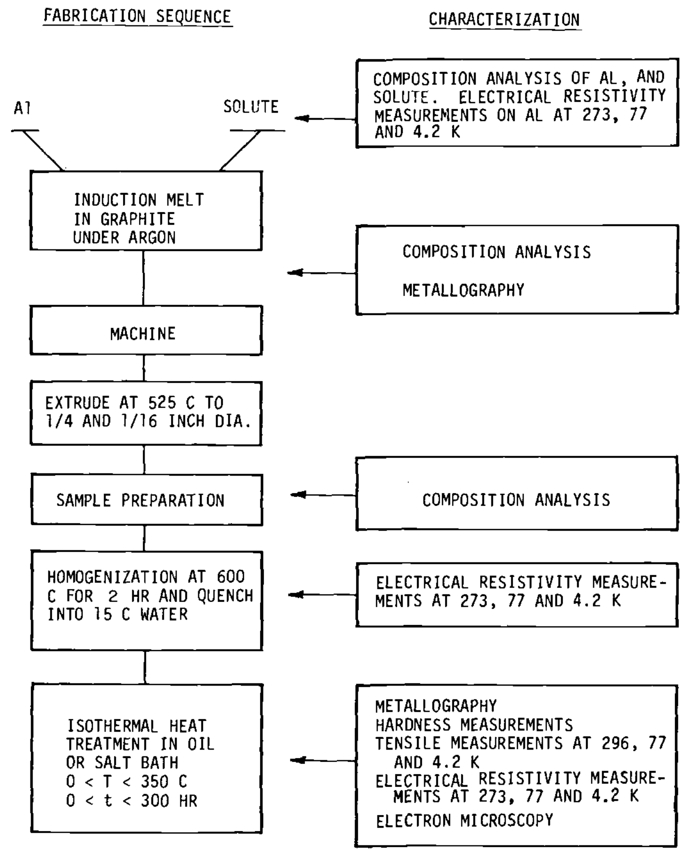

FIG. 2—*Flow chart of experimental procedures.*

The ECD probe was designed to hold specimens no larger than 6.5 mm in diameter. The primary and secondary coils are mounted together so that samples are located within the pair as shown in Fig. 3. The coil forms were machined from linen rod (micarta), wrapped with conventional magnet wire, and held together by a fiberglass-epoxy (G-10) protection sheath. Twisted and shielded leads are connected to each coil. Coil parameters are listed in Table 1.

The components of the ECD primary circuit and apparatus, shown in Fig. 4, are current source, mercury relay set, and primary coil. The ECD pick-up circuit includes the secondary coil, an amplifier, and a display device. Typically, 300 mA dc was passed through the primary for a time sufficient for complete flux penetration of the specimen. Subsequently, the current was interrupted abruptly and the voltage caused by the emergence of flux from the specimen was monitored across the secondary coil. The amplified voltage sig-

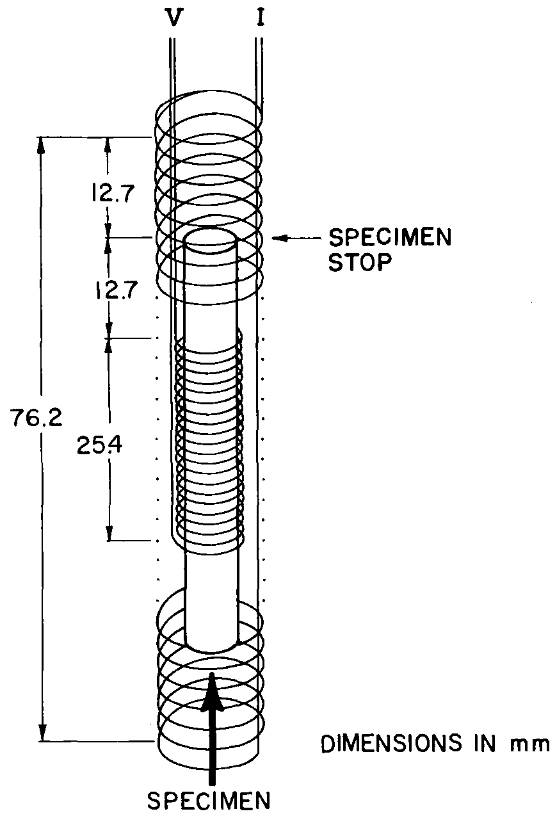

FIG. 3—*Sample and coil geometry for eddy-current decay resistivity probe.*

TABLE 1—*Primary and secondary coil parameters for eddy-current decay resistivity probe.*

	Coil Features	
	Primary	Secondary
Wire	36 gage (6 mil) Cu "magnet wire", formvar insulation	44 gage ($2^1/2$ mil) Cu "magnet wire", formvar insulation
Dimension, mm		
Length	76.2	25.4
OD	13.5	9.9
ID	11.7	8.6
Turns	2900 (even)	4900 (random)
Self-inductance (calculated)	1.5×10^{-2} H	7.62×10^{-2} H
Calculated field and voltage for a primary coil current of 300 mA, specimen diameter = 6.35 mm, $\rho = 2.43$ n$\Omega \cdot$cm, and $\tau = 3\tau_r$	143.6 gauss	0.85 mV

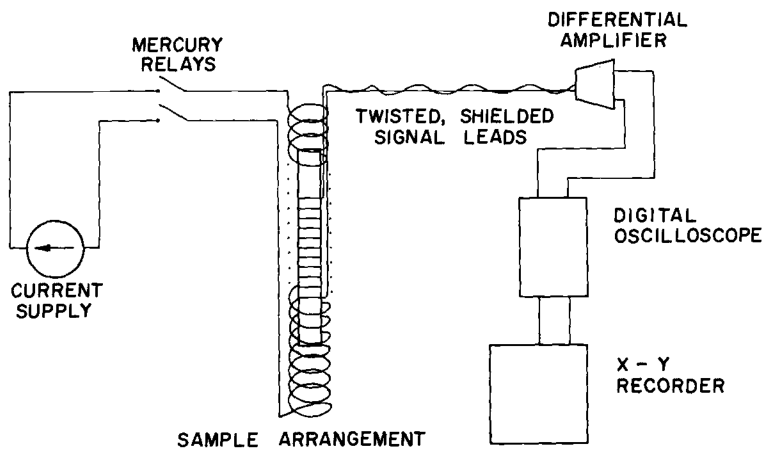

FIG. 4—*Circuit-block diagram for eddy-current decay resistivity measurements.*

nal was recorded in a Nicolet Model 1090 storage oscilloscope that converted the voltage-time information to a maximum of 4096 twelve-bit words. An actual recording of the voltage across the pickup coil for a specimen of zone-refined copper having a RRR of 890 is shown in Fig. 5.

Results and Discussion

Primary Solid-Solubility Phase Boundary in Aluminum-Gold

The compositions of the specimens tested are listed in Table 2. The residual-resistivity values of the various specimens quenched from temperatures between 781 and 880 K are plotted in Fig. 6 against composition. The points at which the curves change slope for the various annealing temperatures indicate the location of the terminal solid-solution phase boundary and are tabulated in Table 3. The solubility limit is defined as the point at which the slope change occurs, because when the solute content of the alloy exceeds the solubility limit, excess solute is rejected by the matrix and precipitates out as Al_2Au. Crystallites of Al_2Au have a much smaller effect on resistivity than does dissolved gold or else the curve to the right of the solubility limit would have a significant positive slope. The curves to the right of the solubility point appear to be horizontal. Up to the solubility limit, dissolved gold contributes to resistivity by an amount proportional to gold concentration.

The location of the solubility limit curve agrees well with Fujikawa's measurements [*6*], but disagrees with the earlier work of Heimendahl [*7*]. Heimendahl's calculations stem from metallographic examination while those of Fujikawa were based on FPP measurements taken at 77 K. Figure 7 de-

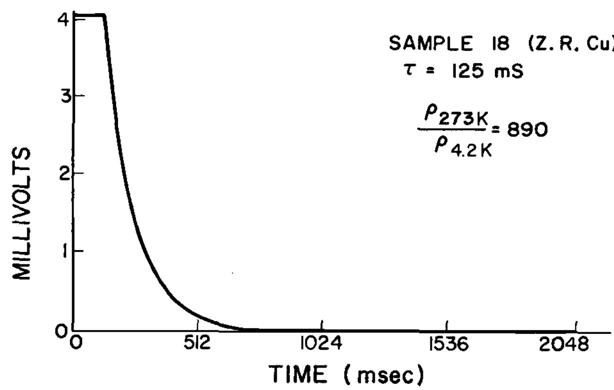

FIG. 5—*Voltage-time trace for eddy-current decay with coils containing a 6.4-mm-diameter specimen of zone-refined copper at 4.2 K.*

TABLE 2—*Chemical composition of phase-boundary experiment specimens.*

Gold Content		
Nominal, percent by weight	Measured, percent by weight	Measured, atom percent
0.05	0.066	90.5 ± 5
0.10	0.11	151.0 ± 15
0.15	0.145	198.0 ± 10
0.20	0.213	290.0 ± 15

picts the aluminum-rich side of the equilibrium-phase diagram over the temperature range studied. Data of Fujikawa and Heimendahl are included for comparison.

Precipitation in Dilute Aluminum-Gold

The amount of gold in dilute aluminum-gold alloys increases resistivity in direct proportion to the quantity of gold in solid solution and alters the time to reach and the magnitude of the final level of resistivity as a consequence of precipitation.

For dissolved gold, the linear relationship defined as $\Delta\rho = 2.1 \pm 0.1\ \mu\Omega \cdot$ cm/atom percent is measured [5] and is in good agreement with the value of 2 $\mu\Omega \cdot$ cm/atom percent reported by Fujikawa [6]. The effect of aging on the residual resistivity (ρ_o) of dilute aluminum-gold is shown clearly in Fig. 8. The dramatic variation in ρ_o with aging contrasts sharply with the tiny change in resistivity measured at room temperature. The resistivity of solution heat treated Al-0.2Au is 2490 n$\Omega \cdot$ cm at room temperature and only 41 n$\Omega \cdot$ cm

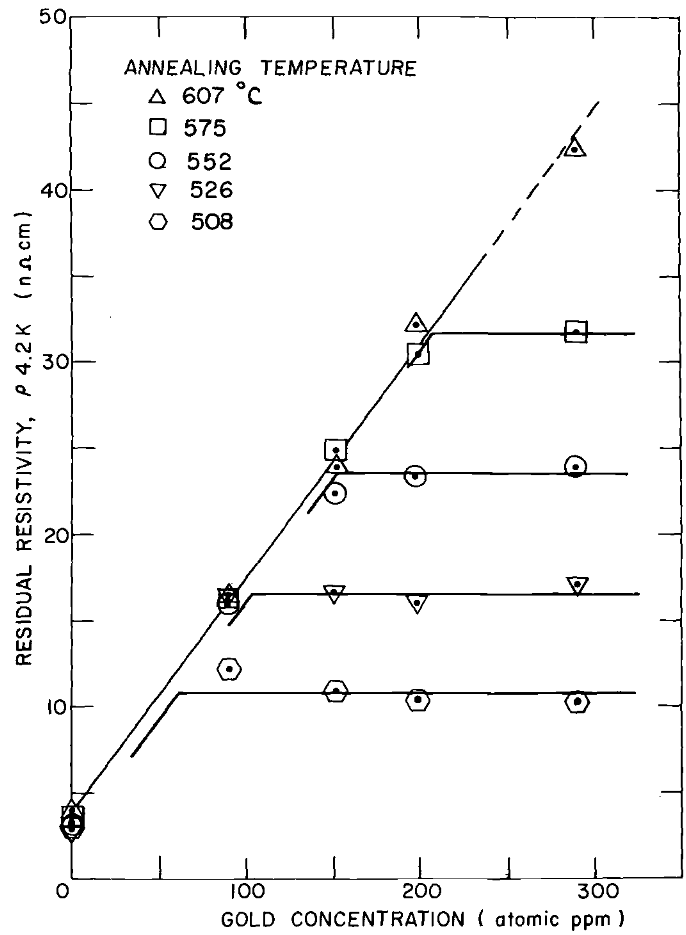

FIG. 6—*Residual resistivity of Al-Au alloys as a function of gold content for different annealing temperatures.*

at 4.2 K. The corresponding values for over-aged material are 2480 and 2.8 nΩ · cm.

An exponential decrease in residual resistivity is observed after long aging times. This stage in the aging process involves slow growth of precipitates and slow matrix purification.

The following principal features are apparent for the residual-resistivity aging-time behavior of dilute aluminum-gold: (*1*) a resistivity decrease always accompanies aging, (*2*) the shape of the aging curve is independent of composition for a given aging temperature, (*3*) an increase in annealing temperature accelerates the aging process, and (*4*) after the initial major drop in resistivity takes place a much slower steady decrease with time is observed.

TABLE 3—*Solid solubility of gold in aluminum.*

Temperature, K	Solubility
781 ± 3	62 ± 8
799 ± 3	103 ± 5
825 ± 3	152 ± 8
848 ± 2	207 ± 5
880 ± 2	...

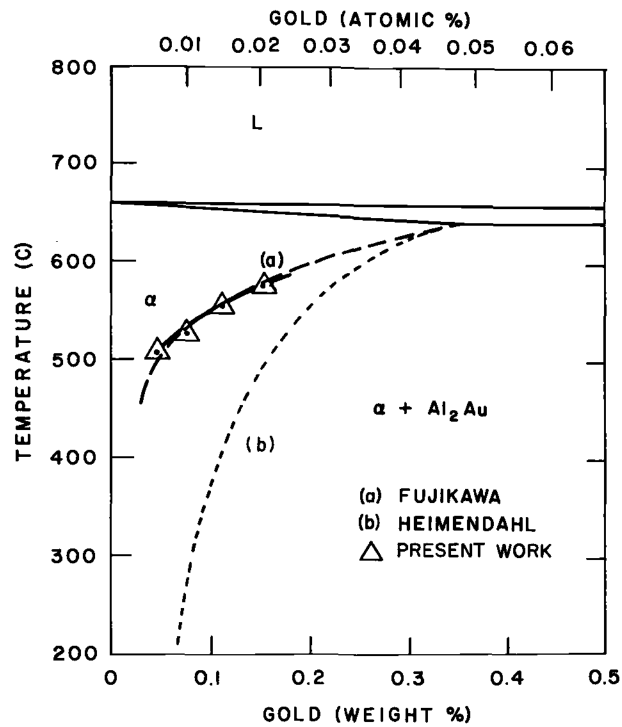

FIG. 7—*Aluminum-rich side of the Al-Au phase diagram.*

The fact that a resistivity increase with time is not observed suggests preprecipitation does not occur in aluminum-gold alloys. To test the possibility of preprecipitation clustering, which would be accompanied by a slight resistivity increase early in aging, a reversion experiment was performed. The results appear in Fig. 9 and give no indication that Guinier-Preston zones form. No resistivity increase is seen with aging at 498 K after preaging 2 h at 398 K.

The outcome of the present reversion experiment conflicts with a similar experiment performed by Fujikawa [*8*]. Fujikawa measured the variation of

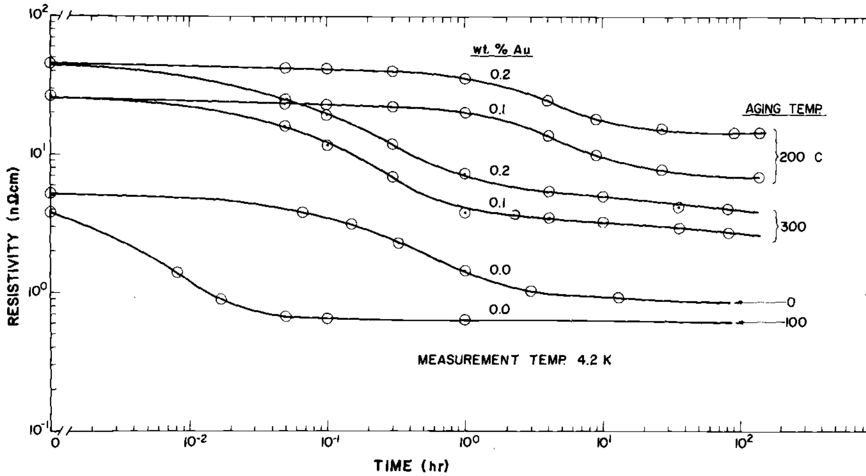

FIG. 8—*Dependence of resistivity at 4.2 K on aging time for aluminum and Al-Au quenched from 873 K.*

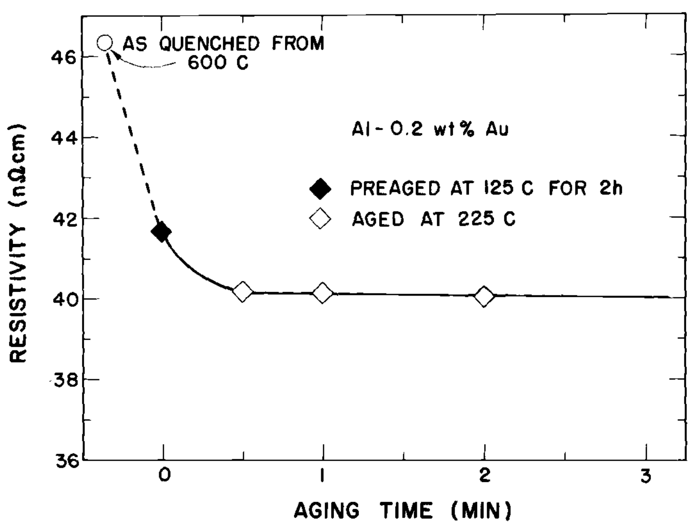

FIG. 9—*Resistivity at 4.2 K versus time for a 6.4-mm-diameter specimen of Al-0.2Au quenched, pre-aged at 398 K for 2 h, then aged at 498 K.*

yield stress with aging at 503 K after preaging 2 h at 393 K in 1-mm-diameter wires of Al-0.2Au quenched from 893 K and saw an initial decrease of about 30 percent in yield stress with a subsequent return to and slow rise from the value at the start of aging. In addition, Fujikawa found a six percent resistivity increase during the early stages of aging 0.5-mm-diameter wire at 273 and

291 K. A possible explanation for disagreement with the present study is that the quench rates were different for the two studies. Fujikawa's smaller specimens received a more severe quench than the 6.35-mm-diameter wires of the present study and thus would have been more susceptible to preprecipitation phenomena.

Structural Anisotropy in Cold-Drawn Aluminum Rod

Aluminum with a purity of 99.99 percent and Al-0.6Ni-0.4Sb alloy were used for the anisotropy study. These materials had initial yield strengths of 2.4×10^7 N/m^2 (3500 psi) and 3.9×10^7 N/m^2 (5700 psi), respectively. The 99.99 percent aluminum was in the annealed condition (1 h at 773 K) before drawing while the Al-Ni_3Sb alloy was drawn from the as-extruded condition.

The results of residual resistivity ratio (RRR) measurements are shown in Fig. 10. For both alloys the RRR decreases with increasing area reduction. The incremental RRR decrease per incremental increase in percent area reduction (ΔRRR/ΔPAR) also decreases as the overall percent area reduction gets larger. On the basis of defect resistivity, ρ_d, however, the 99.99 percent aluminum material exhibits a near linear $\Delta\rho_d/\Delta$PAR of 0.06 n$\Omega \cdot$cm/PAR for the potential-difference measurements. The value of $\Delta\rho_d/\Delta$PAR is not constant for residual resistivities measured by either technique in the Al-Ni_3Sb alloy. From the results listed in Table 4 it is apparent, however, that $\Delta\rho_d/\Delta$PAR is greater in the alloy than in 99.99 percent aluminum and is greater when measured by the ECD method than by the FPP method.

It is noteworthy that the residual resistivity measured by the ECD method is less than that measured by the potential-difference method. In the ECD method resistivity is measured in the direction of eddy-current flow, or the circumferential direction, and is more sensitive to the specimen region near the sample surface than in the sample core. This latter effect arises because of the r^2 dependence of the time constant, which tends to give extra weight to surface material. The potential-difference method, on the other hand, measures the average longitudinal resistivity. Cold-drawn faced-centered cubic (fcc) metals exhibit preferred orientations with grains elongating and line dislocations forming along the drawing axis. Line defects are expected to have a greater apparent density in the radial than in the longitudinal direction. It is likely that a conduction electron traveling in the longitudinal direction will have fewer collisions with line defects than if it were traveling radially outward, or in the circumferential direction. Hence, resistivity should be greater in the radial and circumferential directions than in the longitudinal direction. Furthermore, under these conditions one would expect to observe a homogeneous circumferential resistivity that increases in magnitude from the wire center outward. This latter effect arises because work hardening is greatest near the sample surface and diminishes radially inward for cold-drawn wire.

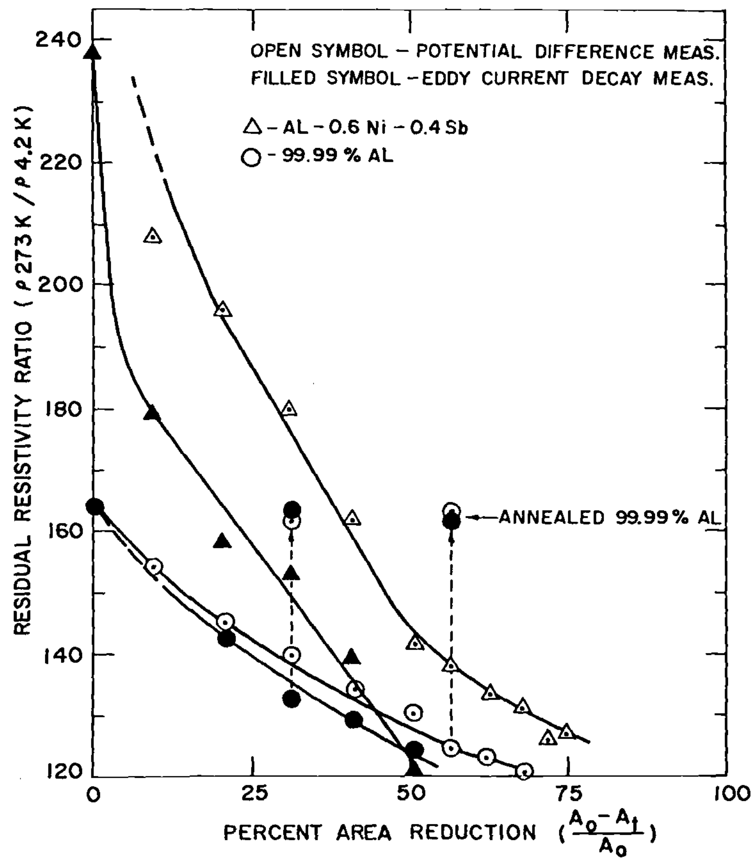

FIG. 10—*Residual resistivity ratio of 99.99 percent aluminum and Al-0.6Ni-0.4Sb as a function of percent area reduction by wire drawing. Measurements are for wire with an initial diameter of 6.4 mm and were taken by a standard potential-difference method and by the eddy-current decay method.*

Benefits of the Eddy-Current Decay Method

The ECD technique proves to be a unique and valuable measurement tool in materials characterization as shown in each of the example studies presented. For the set of phase-boundary and precipitation experiments performed on dilute aluminum-gold, reproducible measurements accurate to better than one percent were taken within seconds of quenching and cooling to 4.2 K on relatively small cylindrical specimens of wire. Study specimens were not mechanically damaged nor contaminated by the handling that is a necessary feature of standard potential-difference methods.

The rapid and accurate means by which a terminal solid solution phase boundary can be determined by use of residual-resistivity measurements

TABLE 4—*Incremental decrease in defect resistivity per incremental decrease in percent area reduction* ($\Delta\rho_d/\Delta PAR$) *for cold-drawn aluminum.*

		$\Delta\rho_d/\Delta$PAR[a]			
		99.99 % Al		Al-1.0Ni_3Sb	
Specimen Diameter, mm	Percent Area Reduction	ECD[b]	FPP[c]	ECD	FPP
5.61	0	0	0	0	0
5.23	13.1	0.092	0.055	0.023	0.086
4.85	25.3	0.067	0.054	0.087	0.104
4.45	37.3	0.067	0.052	0.139	0.131
4.17	44.9	...	0.063	...	0.117
3.86	55.8	...	0.054	...	0.106
3.58	59.3	...	0.059	...	0.105
3.35	64.3	...	0.057	...	0.108
3.15	68.5	...	0.059	...	0.099

[a]In units of $n\Omega \cdot cm$ per percent area reduction (PAR).
[b]Eddy-current decay (ECD) measurement.
[c]Potential-difference (FPP) measurement.

contrasts dramatically with conventional metallographic techniques. A boundary determination by residual resistivity pinpoints temperature and concentration coordinates while tedious metallography provides phase concentration information from which the location of the boundary must be deduced. It is clear that residual-resistivity measurements taken by the ECD technique offer distinct advantages to terminal solid solution phase boundary determinations in dilute alloy systems. With the ECD technique there is little or no risk of specimen damage, the measurement is sensitive to dissolved solute concentration and insensitive to the quantity of second-phase material present, and measurement accuracy remains high even at solubility levels in the part per million range. Highly accurate impurity resistivity measurements cannot be made as easily at higher temperatures.

The anisotropic resistivity present in cold-drawn aluminum rod was easily detected and measured by the combined use of the ECD and standard potential-difference methods. Anisotropy could not have been detected and measured accurately, however, without the ECD measurements. The technique afforded a quick way to determine the material resistivity in a direction perpendicular to the longitudinal (draw) direction. This was possible even in specimens with diameters of 4.5 mm. This circumferential measurement can be made easily on specimens of any diameter provided the time constant for eddy-current decay is greater than about one millisecond.

Conclusions

The eddy-current decay method of resistivity determination has been shown to provide a convenient and often advantageous means for characterizing the properties and structures of dilute aluminum alloys. The examples presented for material characterization are meant to be representative and are by no means complete or limited to dilute aluminum alloys. Similar studies could be performed on any conducting material.

Specific conclusions from the present study include:

1. Residual-resistivity measurements accurate to within one percent are possible with a simple circuit arrangement employing a two-coil sensing probe, a switch, and a digital-storage oscilloscope. An ECD measurement can be performed very quickly without making physical contact with the specimen.

2. The ECD technique provides a highly accurate means whereby terminal solid-solution phase boundaries can be determined in dilute alloy systems. This conclusion is derived from such a measurement in dilute aluminum-gold.

3. Resistivity trends during precipitation reactions can be conveniently studied with the ECD technique. In disagreement with an earlier study [8], the present work suggests preprecipitation may not occur in dilute aluminum-gold.

4. Eddy-current decay measurements provide a simple means to study anisotropic resistivity in cold-drawn aluminum. Such studies can be performed easily on materials with different chemical, structure, and defect makeup.

Acknowledgments

The author wishes to extend thanks to Don McNamara and Pirmin Appius for valuable assistance in carrying out the work reported. Support from the Department of Energy and the Wisconsin Electric Utility Research Foundation is acknowledged.

References

[1] Bean, C. P., Deblois, R. W., and Nesbitt, L. B., *Journal of Applied Physics,* Vol. 30, No. 12, Dec. 1959, pp. 1976–1980.

[2] Clark, A. F., Deason, V. A., Hust, J. G., and Powell, R. L., "Standard Reference Materials: The Eddy Current Decay Method for Resistivity Characterization of High Purity Metals," NBS Special Publication 260-39, U.S. Department of Commerce, National Bureau of Standards, Boulder, Colo., May 1972.

[3] Clark, A. F., Deason, V. A., and Powell, R. L., *Cryogenics,* Vol. 12, Feb. 1972, pp. 35–39.

[4] Arp, V. D., Kasen, M. B., and Reed, R. P., "Magnetic Energy Storage and Cryogenic Aluminum Magnets," Technical Report AFAPL-TR-68-87, Air Force Aero-Propulsion Laboratory, Wright-Patterson Air Force Base, Ohio, Feb. 1969.

[5] Hartwig, K. T., "A Study of Dilute Aluminum-Gold Alloys for Superconductor Stabilizer Applications," Ph.D. thesis, University of Wisconsin, Madison, 1977.

[6] Fujikawa, S., and Hirano, K., *Journal of the Japan Institute of Metals,* Vol. 38, 1976, pp. 929–936.

[7] Heimendahl, M., *Zeitschrift für Metallkunde,* Vol. 58, 1967, pp. 230–235.

[8] Fujikawa, S., Hirano, K., and Hirabayaski, K., *Zeitschrift für Metallkunde,* Vol. 59, No. 10, 1968, pp. 782–786.

J. P. Wallace,[1] D. C. Kunerth,[1] and R. M. Siegfried[1]

An Eddy-Current Study of Casting

REFERENCE: Wallace, J. P., Kunerth, D. C., and Siegfried, R. M., "**An Eddy-Current Study of Casting,**" *Eddy-Current Characterization of Materials and Structures, ASTM STP 722,* George Birnbaum and George Free, Eds., American Society for Testing and Materials, 1981, pp. 173-186.

ABSTRACT: Even though casting technology has a 5000-year history, the understanding and control of the process still has significance to current metal producers. Nondestructive evaluation is usually applied to finished or semifinished product; however, in casting, when the evaluation is moved to the point of production, the testing procedure can be incorporated into the casting control. The metallurgical impetus for such casting control and evaluation cannot be simply stated since the needs are process and product dependent. The main technical advantage of applying eddy-current analysis to the study of solidification is that eddy currents have a reasonable sensitivity to continuous and discontinuous conductivity changes. A drawback in the examination of the liquid-solid interfaces is that the eddy-current signals are integrated over a substantial volume, which averages out detailed information such as dendrite structure. To successfully use the technique of eddy-current analysis, one must utilize postmortem metallographic examination of specimens for standards and detailed mathematical modeling of the solidification response, which cover probable morphologies. Laboratory measurements of freezing of a Pb-20Sn alloy demonstrate that directional solidification can be identified. Finally, two techniques of data analysis for processing eddy-current signals are presented and discussed.

KEY WORDS: eddy currents, solidification, continuous casting, electroslag remelting, vacuum arc melting, control, inclusions, metals, alloys

The efforts of early technicians to produce metals, such as lead and copper, by pyrometallurgical techniques extend back at least to the seventh millennium BC [*1*].[2] Casting as a practice in the regular production of objects of art and commerce followed these discoveries [*2*]. A common limitation for application of cast metal objects is that their strength, toughness, and reliability are often inferior to wrought products. However, production requirements such as cost, volume, and shape often require casting to be the property controlling step in the manufacturing process. The analysis of casting practice, whether it be batch or continuous, begins with the exami-

[1] Assistant professor and graduate students, respectively, Department of Chemical Engineering and Materials Science, University of Minnesota, Minneapolis, Minn. 55455.

[2] The italic numbers in brackets refer to the list of references appended to this paper.

nation of the cast structure. Visual inspection, sectioning, and metallograpic inspection of the microstructure reveal many of the pathologies that can occur when metal freezes within the confines of a mold. Common defects such as porosity [*3*], formation of pipe [*4*], internal cracking [*5*], freckles, and segregation [*6*] are the result of poor casting practice. To relate cast metal properties to the details of solidification is a metallurgical endeavor required to understand and control the final structure. This requires information that describes the existing internal structure during solidification. Dynamic studies of transient solidification phenomena require information that is not available upon final examination. Transients in temperature gradients, dendrite fragments moving through the melt, solid-liquid interface motion (both in velocity and direction), and evolution of gas are phenomena common to solidification. The relative timing between these events during solidification determines much of the final structure of the product.

The utility of such transient information for reconstructing the events during solidification will find use in current solidification practices of continuous casting, electroslag remelting, and vacuum-arc melting owing to the existing direct process controls. In these processes the possibility of producing an undesirable product such as a breakout in continuous casting or a solidification profile that will result in freckles is not currently detectable at the time that the heat is cast. If the dynamic information on the melt condition were available in real time, refined controls could be placed on these casting practices. It is in these processes that a degree of control can be introduced. One may choose, for example, to control the casting rate of a continuous caster or the melt rate and electrode position of an electroslag remelter or a vacuum-arc melter.

Eddy-current detection of melt morphology seems to be an ideal technique to monitor solidification [*7,8*]. The application of eddy-current measurements to solidification, however, presents the basic problem of signal interpretation where a standard does not exist. One is required to depend upon an analytical description of phenomena in order to interpret data directly, and, if applicable, multifrequency data may be usefully inverted to provide a limited description of the spatial conductivity variation. The eddy-current technique of detecting spatial variations in solidification structures depends upon a change in conductivity between the solid and liquid state. This discontinuity between liquid and solid is usually much greater than the conductivity gradients encountered due to the thermal gradients in the macroscopic ingots. Resistivities of some common metals at and around the transition temperature between the solid and liquid are presented in Table 1. The presence of inclusions that are gaseous or nonconducting solids introduces more effective reflecting interfaces than the solid-liquid interfaces of the solidifying conductors. The contribution of the inclusion to the reflected signal as a function of its size and position determines the lower size limit that can be detected. For transient phenomena

TABLE 1—*Resistivities of solid liquid metals at their melting points (μohm · cm).*

Metal	Transition Temperature, K	ρ_{liquid}	$\frac{d\rho}{dT}_{liquid}$	ρ_{solid}	$\frac{d\rho}{dT}_{solid}$
Al[13]	933.2	24.2	1.3×10^{-2}	10.95	1.4×10^{-2}
Cu[14,15]	1356.2	22.9(1100°C)	2.2×10^{-2}	11.5	2.2×10^{-2}
Fe[15]	1808.2	139	...	127.5	...
Pb[16]	600.5	96.7(320°C)	6.7×10^{-2}	54.76(330°C)	34.1×10^{-2}
Sn[15]	505.1	45.0	...	...	...
Zn[15]	692.7	35.3	4.3×10^{-2}	18	6.3×10^{-2}

to be detected, its response signal must have a measurable bandwidth. The eddy-current detection of freezing phenomena works well in the laboratory on low-temperature melts [*8*]; it also has been found sufficiently sensitive to detect the solidification of steel within the molds of continuous steel-strand casters [*9*].

The physical equipment necessary for solidification measurements consists of a calibrated phase detector, signal source, temperature-controlled balance network, and a coil for which the component's combined attenuation and phase shifts of the signal are known. This allows the effects of the signal processing equipment to be removed from the final data. To ascertain what is taking place within the volume of the metal being sampled, however, the eddy-current signals require a detailed analysis.

Reflection of a Plane Wave from a Conductor

An elementary analysis of an eddy-current response begins with the reflection of a plane wave from a conductor [*10*]. This response is assumed to be free of instrument contribution and to carry information on the state of the sample. Two contributions to the conductivity encountered in solidification experiments at high temperatures appear to dominate; they are the temperature dependence of the conductivity and the discontinuous difference in the electrical conductivity between the solid and liquid state. The effects of these conductivity variations are best illustrated graphically for the reflected vector potential, which can be translated directly to the detected voltage. The simplest case is that of a wave reflecting from a semi-infinite conductor (Fig. 1). The indicated plane waves in vacuum and the metal must satisfy two boundary conditions: (*1*) the flux must be conserved at the boundary, and (*2*) the first derivative of this transverse component must be continuous. The eddy-current coils detect the sum of the incoming wave and reflected signal, a_1 and a_2, respectively, which is a function of the propagation vectors in the vacuum metal, k and k^* respectively, where k^* is complex.

$$a_1 + a_2 = \frac{k(k^* - k)}{k^*(k^* + k)} a_1 \quad (1)$$

The dependence of the measured signal on conductivity and test frequency is shown in the plot of Fig. 2. At very low conductivities and high frequencies, one tends to detect little or no reflected signal as $(a_1 + a_2)/a_1$ approaches 1. The values of the propagation vectors during bulk eddy-current measurements are determined by the relative low test frequency, ω, and the high metal conductivity, σ. In this situation $k = \omega\sqrt{\mu\epsilon}$ and $k^* = (1+i)\sqrt{\omega\sigma\epsilon/2}$, where μ is the magnetic permeability and ϵ is the dielectric permittivity. The sum of the fields in free space is then $(a_1 + a_2)/a_1 \approx (1-i)\sqrt{2\omega\epsilon/\sigma}$. As the efficiency of the reflector is increased by the reduction of the test frequency or by a conductivity increase, the signal is forced to move down the 45 deg trajectory towards the origin of the plot in Fig. 2. For most metallic conductors, the eddy-current measurements are taken near the origin where $(a_1 + a_2)/a_1 \approx 10^{-6}$ to 10^{-8} and the large cancellation between a_1 and a_2 provides a degree of rejection allowing easier detection of small conductivity changes within the conductor. It is not the continuous variation in conductivity that is often of interest in solidification; rather it is the position of the solid-liquid interfaces within the sample when it is freezing or melting that is important. The simplest case to model is that of plane-front solidification, where the solidification front is parallel to the free surface of the semi-infinite conductor of Fig. 3. Such solidification could proceed in two ways: (*1*) the higher conductivity solid could extend from the free surface inward to the liquid metal, or (*2*) the liquid metal could start at the free surface with the solid-liquid interface at some

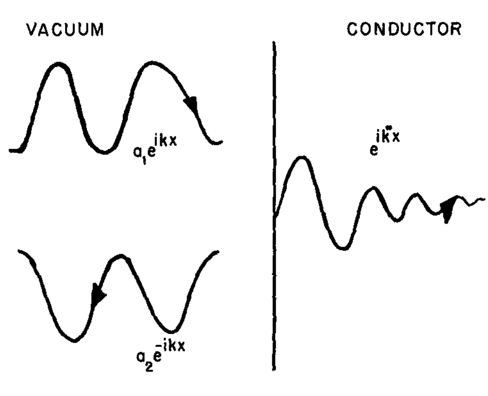

FIG. 1—*Schematic of the boundary-value problem for an electromagnetic wave reflecting from a uniform semi-infinite conductor.*

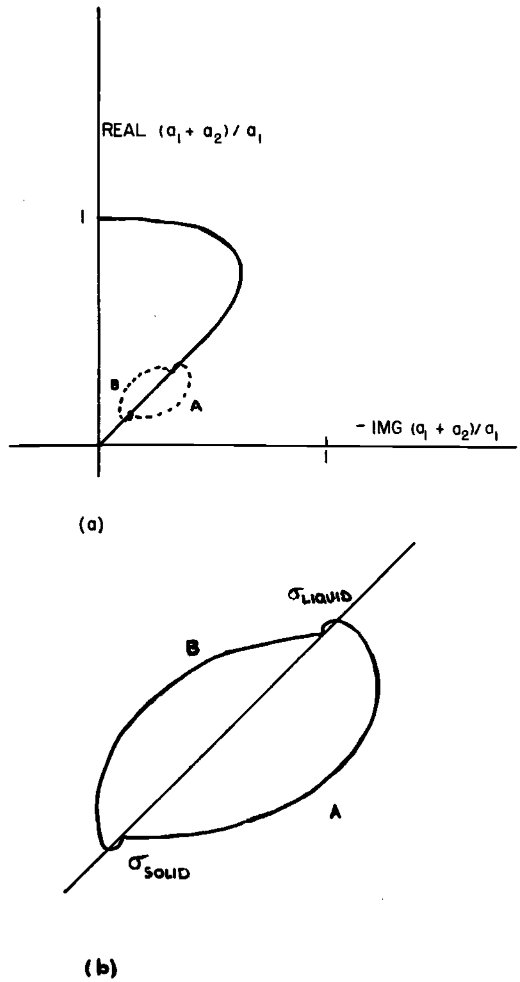

FIG. 2—*(a) The solid line is the calculated reflection response of a conductor. As conductivity varies from 0 to ∞, the normalized signal* $(a_1 + a_2)/a_1$ *varies from 1 to 0. (b) This straight line represents a portion of the curve shown in (a), where the conductivity → ∞ and* $(a_1 + a_2)/a_1 \rightarrow 0$. *This is in the signal range of most metals. Trajectory* A *represents the response of plane-front solidification proceeding from the interior outward. Trajectory* B *represents the response of plane-front solidification from the mold wall inward.*

distance within the melt. The motion of the solid-liquid boundary is simply an extension of the example illustrated in Fig. 1, and the results are shown superimposed upon that solution in Fig. 2 for both cases of plane-front solidification. The two trajectories enclose the straight line that corresponds to a spatially homogeneous change in conductivity between the limiting

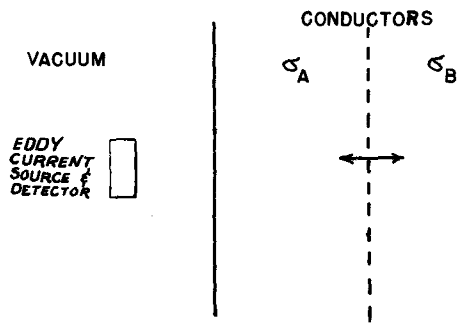

FIG 3—*The movable boundary between two different conductors, such as a solid and liquid conductor, during plane-front solidification.*

cases of a complete solid and liquid metal. This model is confirmed experimentally by the behavior of the eddy-current responses to lead freezing in a near planar manner [*8*].

The high and uniform thermal gradients required to drive plane-front solidification are not common, and solidification in alloys with a finite freezing range proceeds by cellular or dendritic extension of the solid into the liquid melt [*11*]. Such solidification profiles show a monotonic conductivity variation from that of complete solid to complete liquid (schematically illustrated in Fig. 4). This freezing zone is referred to as the mushy zone. In eddy-current measurements of solidification, where the transverse and longitudinal dimensions of structures within the mushy zone are an order of magnitude smaller than the wavelength of the eddy-current signal within the melt, response signals detect the average conductivity of the mushy zone. Segregation effects in freezing of alloys are pronounced and result in compositional variations; their contributions to electrical conductivity variations, however, have not been studied owing to the larger thermal effects that dominate high-temperature conductivity in metals and alloys. The signal trajectory in an eddy-current measurement for a mushy zone of finite thickness moving through the melt will be contained within the limits of the plane-front trajectories illustrated in Fig. 2. An alloy that has a large freezing range of 100°C or more frequently has thin solid dendrites run into the melt many times the skin depth of the sampling electromagnetic radiation, and as freezing proceeds, the dendrites simply coarsen. The result is that the mean conductivity of the alloy being tested is changing uniformly over the sampled volume, and the subsequent signal response is a linear trajectory. The same type of response may be observed if a pure metal is sufficiently undercooled so that homogeneous nucleation occurs with evenly dispersed, equiaxed grains, which could then continue to grow in the supercooled liquid.

The thermal gradients that are required for the extraction of heat during

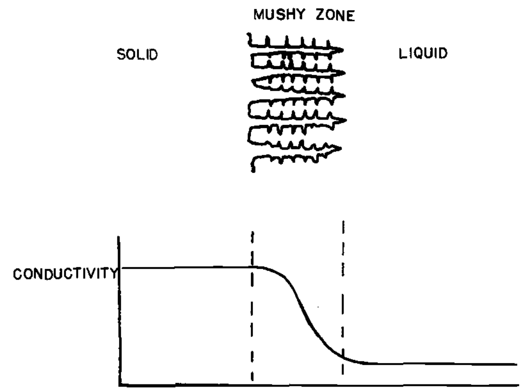

FIG. 4—*An averaged conductivity profile that one would expect to measure through a dendritic mushy zone.*

solidification also contribute to the eddy-current response. Owing to the weak dependence of conductivity upon temperature, however, the thermal gradients are most easily measured through conductivity variations in conducting molds when one face of the mold is at a fixed or a known temperature. This is often the case in chill casting or continuous casting practice.

Inclusions are common in casting. They arise from entrained nonconducting solids, gas formed pores, or through contraction of the freezing metal forming a pipe. The general contraction of the ingot separating itself from the mold wall in conducting molds results in a condition that imitates an inclusion during eddy-current measurements. The one-dimensional treatment of an inclusion as a vacuum layer is a simple extension of what was performed for the single and two-layered conductors. The effect of introducing a vacuum layer can be illustrated by lead solidifying in a copper mold. Figure 5 shows seven signal trajectories which describe both the three extreme forms of solidification previously discussed and the effects of introducing a vacuum layer in the center of the melt and at the boundary between the melt and the mold. The details of geometry, conductivities, and formalism used for these calculations are described in Ref 7. What we note here is the complexity in interpretation that is introduced with the presence of an inclusion and the ambiguity that exists when it falls within the signal domain of the inclusion free metal. In practice the phase response of some inclusions moving by detectors during solidification results in transients that are more rapid than changes in solidification profiles; they can be identified by that characteristic. These rapid transients in signals are particularly noticeable during solidification when gas evolution occurs at the liquid-solid interface for a melt that has been saturated with a gas that is relatively insoluble in the solid state. We have observed these effects in Pb-20Sn through which air was bubbled.

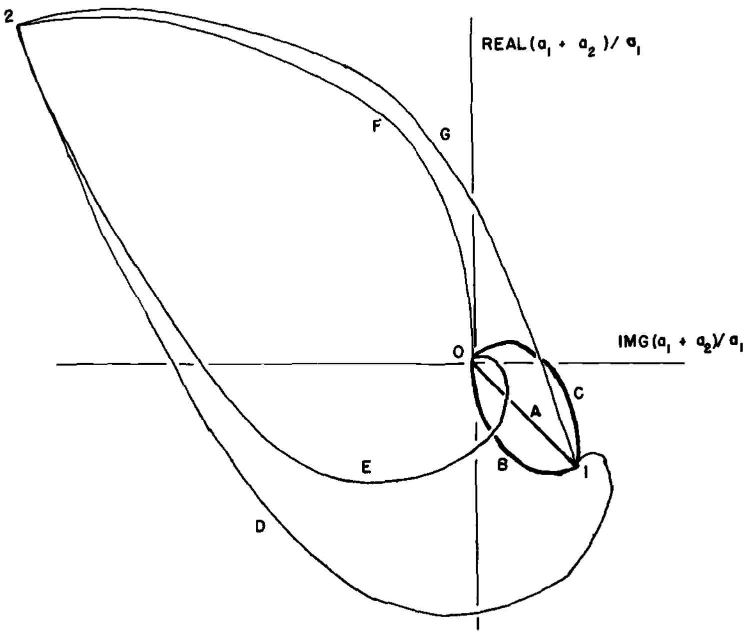

Starting Point		Path		End Point	
1	→	A	→	0	uniform conductivity change $\sigma_{liquid} \rightarrow \sigma_{solid}$
1	→	B	→	0	plane-front solidification starting from wall
1	→	C	→	0	plane-front solidification starting from center
1	→	G	→	2	
		and			plane-front expansion of a void between mold and lead
0	→	F	→	2	
1	→	D	→	2	plane-front expansion of a void which initiates in the center and
		and			
0	→	E	→	2	radially expands eliminating the lead

FIG. 5—*The three fixed points in this calculated eddy-current response* [7] *represent a thin-wall copper mold containing no lead (Point 2), solid lead (Point 1), and liquid lead (Point 0). The table describes what takes place on the individual signal trajectories.*

Differential Solidification Measurements

We have previously reported and discussed the absolute measurements of solidification of Pb-20Sn in a cylindrical copper mold [*8*]. The major solidification features were easily detected and can be summarized from the phase diagram of the alloy and from the eddy-current solidification measurements shown in Fig. 6. Since the primary cooling of this system was through the concentric copper mold, we did not expect much information to be gained by a second identical coil differentially connected and

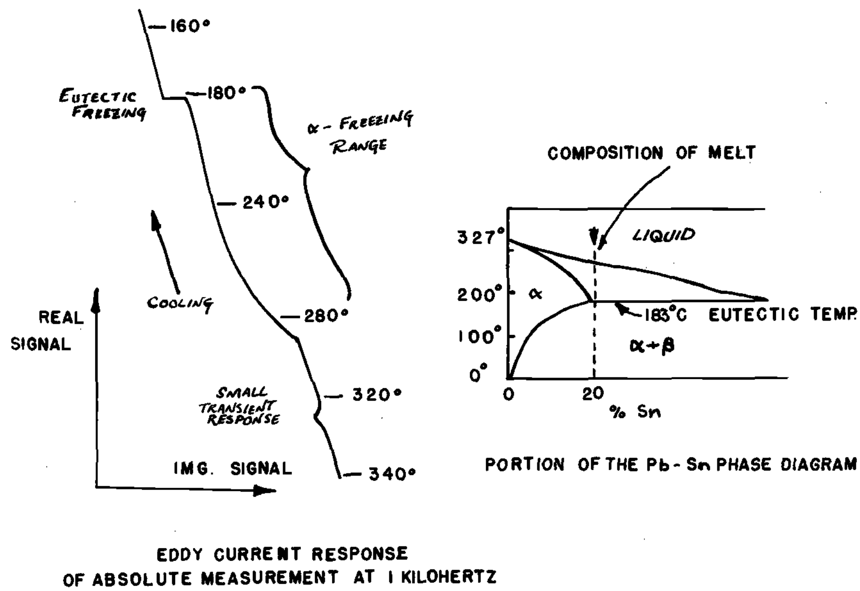

FIG. 6—*The left diagram represents the absolute freezing response of a Pb-20Sn alloy reezing within a copper mold. The major features of this response can be related to the correponding features of the Pb-Sn phase diagram on the right. The onset of freezing, the freezing f the eutectic liquid, and a transient near 230°C are the three main features evident.*

laced 0.2 cm lower than the first coil. With the two encircling coils so lose and the major heat transfer path being radially outward, no signifiant differences would be expected in adjacent segments. Such differential etection would be sensitive to any axial variations in properties where we ould expect most variations to depend upon the radial coordinates. The ata that were taken can be compared to the absolute data because the xperimental systems are identical except for the placement of the second oil. There are three features in this differential data that are identifiable: *1*) the signal transient prior to the liquidus between 330 to 320°C, (*2*) a major change in the direction of the response at 240°C, which does not orrespond with anything in the absolute measurements, and (*3*) the signals hat correspond in temperature and phase to the freezing of the eutectic iquid. Each of these signals corresponds to events taking place at different imes along the axis of the mold. The easiest to identify from these data is he solidification of the eutectic liquid at 183°C, which occurred uniformly nder the coils showing little radial dependence. The differential data indiate that freezing occurred under the lower coil, then the upper coil. The reezing front moved upwards, with the major cooling coming from the ottom of the mold. For the eutectic freezing response to indicate a plane ont moving up the column instead of radially, there had to be a switch from radial cooling to axial cooling (illustrated by the data in Fig. 7). This transition probably occurs when the ingot contracts away from the mold wall.

Contraction occurs in an alloy when unfrozen liquid can no longer be supplied to the expanding void between the mold and the contracting ingot. The supply of liquid alloy must cease to flow freely when the fluid reaches the percolation threshold of the dendritic maze [12]. This limit is probably reached at about 240°C, which corresponds to 40 percent of the liquid alloy remaining. Above this temperature the major effect on the signal is that of the differential freezing and cooling effects within the mold, which are well coupled to the mold. Below this temperature the ingot contracts away from the wall of the mold. The mold is then thermally uncoupled from the ingot and the main cooling comes through the bottom of the ingot, which will alter the thermal gradients and the eddy-current response. Finally, the major effect on the signal before alloy freezing appears to occur over a range of 328 to 320°C and is considered a rapid transient. These transient effects may be due to liquid convection and dendrite fragments moving past the coils from cooler portions of the melt. Unlike the other two described events, the transient signals have large variations in their amplitude during successively monitored solidifications.

Analysis of Eddy-Current Signals

One can model specific freezing responses to compare with measured responses of solidification activity within the coils; the result is that comparison can provide quantitative data on freezing phenomenon. The direct determination of the conductivity profile of the melt, however, is a different consideration than the measurement of isolated solidification events. The question of how well the conductivity profile can be determined from an absolute measurement of the reflected signal requires the consideration of the simple half-space reflector of Fig. 1, where the uniform conductivity has been replaced by spatially dependent conductivity $\sigma(x)$. The solution of the electromagnetic wave equation in the vacuum is represented by the two plane waves a_1e^{ikx} and a_2e^{-ikx} and in the conductor by the power series solution $\Sigma_{n=0}^{\infty} c_nx^n$. The conditions of continuity and a continuous first derivative at the interface, $x = 0$, result in a pair of equations

$$a_1 + a_2 = c_0 \tag{2}$$

$$ik(a_1 - a_2) = c_1 \tag{3}$$

Since a_1 is the amplitude of the prepared signal and a_2 is the reflected signal amplitude, the quantities c_0 and c_1 can be determined. With an arbitrary conductivity profile to the right of the interface, one would like to know how much information about $\sigma(x)$ can be extracted by measuring the phase

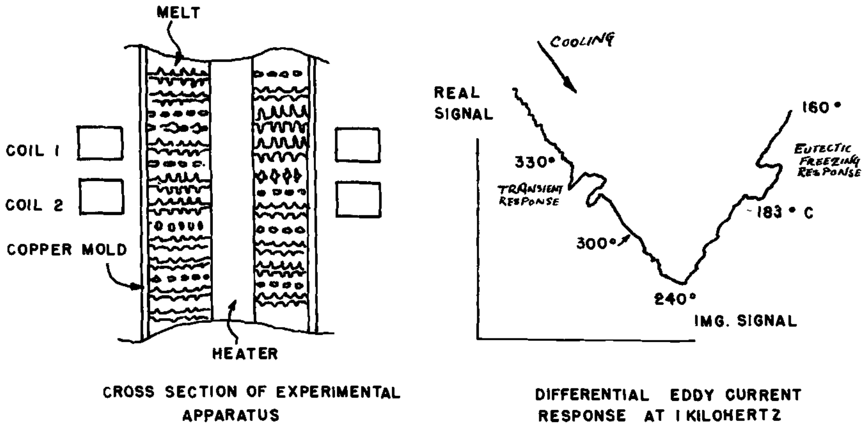

FIG. 7—*The left diagram illustrates the mold and coils in half sections. Sketched in are the dendrites which grow rapidly inward, spanning the melt. As solidification proceeds the dendrite are thought to slowly coarsen, producing a solute-rich interdendritic fluid. A differential eddy-current response of a Pb-20Sn alloy is shown on the right. A rapid transient between 328 and 320°C, a significant change in the direction of the response at 240°C, and a uniform eutectic solidification response at 183°C are evident. The shift in the direction of the response at 240°C is assumed to coincide with the shift from radial solidification to axial solidification due to ingot pull away.*

and amplitude of the reflected signal. Taking the wave equation for the vector potential field within the conductor as

$$\nabla^2 A + [i\mu\omega\sigma(x) + \omega^2\mu\epsilon]A = 0 \tag{4}$$

and substituting the power series for the conductivity

$$\sigma(x) = \sum_{m=0}^{\infty} S_m x^m \tag{5}$$

into the power series solution for the vector potential, the wave equation yields

$$0 = \sum_{n=0}^{\infty} (n + 2)(n + 1)c_{n+2}x^n + i\mu\omega \sum_{m=0}^{\infty} \sum_{n=0}^{\infty} S_m c_n x^{m+n} + \omega^2\mu\epsilon \sum_{n=0}^{\infty} c_n x^n \tag{6}$$

By making the substitution, $m + n = k$, and by dropping the small ω^2 in the limit of low frequencies and high conductivity, the previous series can be written more simply as

$$\sum_{n=0}^{\infty} x_n\{(n + 2)(n + 1)c_{n+2} + i\mu\omega \sum_{k=0}^{n} S_{n-k} c_k\} = 0 \tag{7}$$

One can examine this and determine that in any reflection experiment where we can find c_0 and c_1, even the lowest order terms in S are obscured. Writing out the first few terms, we have

$$n = 0; \qquad 2c_2 + i\mu\omega c_0 S_0 = 0 \tag{8}$$

$$n = 1; \qquad 6c_3 + i\mu\omega(c_1 S_0 + c_0 S_1) = 0 \tag{9}$$

$$n = 2; \qquad 12c_4 + i\mu\omega (c_2 S_0 + c_1 S_1 + c_0 S_2) = 0 \tag{10}$$

This will allow the vector potential field inside the conductor to be written in the form

$$A(x) = A(x, a_1, a_2, S_0, S_1, S_2, \ldots) \tag{11}$$

where all the components of the conductivity must be known to determine the vector potential, and the conductivity profile cannot be exactly determined from the reflected field. To reduce the magnitude of the inversion problem, the case of small changes in bulk conductivity of the medium will be considered. Thus, separate contributions of small conductivity changes can be summed while neglecting the second-order contributions. The contribution of a differential conducting layer with a small change in the conductivity $\delta\sigma(x)$ is shown in Fig. 8, where $\delta\sigma$ results in a corresponding change in the propagation vector, dk, at a depth, x, in the conductor. The amplitude of the reflected signal, da_2, within the conductor can be determined by

$$da_2 = i dk\, dx\, a_1\, e^{2ikx} \tag{12}$$

This result can be summed over all the small changes in the propagation vector within the solid to give the first-order reflected signal

$$a_2 = i\, a_1 \sum_j dk(x_j)\, dx_j\, e^{2ikx_j}$$

For a continuous variation in the propagation vector, an integral expression replaces the above equality:

$$a_2(k) = i\, a_1 \int_{-\infty}^{\infty} dk(x)\, e^{2ikx} dx \tag{13}$$

This can be inverted to yield the spatial dependence for the small conductivity changes in terms of measurable data. It is first necessary to remove the frequency dependence in the quantity $dk(x)$. This is accomplished by dividing by k, the mean propagation vector

$$a_2(k)/ika_1 = \int_{-\infty}^{\infty} \frac{dk}{k} e^{2ikx}dx \tag{14}$$

By using a Fourier transform, the inverse is obtained

$$\frac{dk}{k} = \frac{1}{2\pi}\int_{-\infty}^{\infty} \frac{a_2(k)}{ika_1} e^{-2ikx}dk \tag{15}$$

This can be rewritten in terms of the conductivity variation

$$\delta\sigma(x) = \frac{\sigma}{2\pi}\int_{-\infty}^{\infty} \frac{a_2(k)}{ika_1} e^{-2ikx}dk \tag{16}$$

In order to make this expression more useful, it is helpful to integrate over $d\omega$, the continuous variation in frequency. Such an adjustment changes Eq 16 to

$$\delta\sigma(x) = \frac{\sigma}{2\pi i}\int_{0}^{\infty} \frac{a_2(\omega)}{a_1\omega} e^{(1-i)x\sqrt{2\mu\sigma\omega}}d\omega \tag{17}$$

It is assumed that $a_2(\omega) = 0$ when $\omega < 0$. If data for $a_2(\omega)$ can be taken over a finite frequency range which covers the detectable features of interest, this inversion will provide useful data about the conductivity distribution in these structures. When interpreting experimental data, Eq 17 must be corrected for the effect of phase shift and attenuation of specific molds and conductors between the test coil and the test volume.

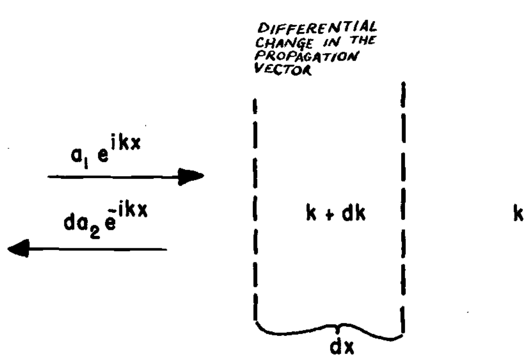

FIG. 8—*This differential reflecting element is used as the basic reflecting element for small conductivity changes. These small contributions to the reflected signal can be summed and consequently inverted to provide an approximate conductivity profile when multifrequency data are available.*

Conclusion

The utility of eddy-current analysis in the study of solidification phenomena depends upon the ability of the investigator to process data from experiments into useful forms. There are presently two techniques that can be employed: (*1*) modeling a system and fitting data to that model, or (*2*) in the limit of small conductivity changes, inverting the data to provide a conductivity profile. The choice and application of these tools will be determined by the particular engineering application.

Acknowledgments

We would like to thank the Magnetic Analysis Corporation of Mount Vernon, N.Y. for their support of this research.

References

[*1*] Todd, I. A., *Catal Huyuk in Perspective,* Menlo Park, N.J., 1976, pp. 89-91.
[*2*] Smith, C. S., *Actes du XIe Congress International d'Historie des Sciences,* Vol. IV, 1963, p. 241.
[*3*] Eastwood, L. W., *Gases in Non-Ferrous Metals and Alloys,* American Society for Metals, Cleveland, Ohio, 1953.
[*4*] Weinberg, F., *Metallurgical Transactions,* American Institute of Mining, Metallurgical, and Petroleum Engineers, Vol. 6A, November 1975, p. 1971.
[*5*] Fujii, H., Ohashi, T., and Hiromoto, T., *Transactions,* Iron and Steel Institute of Japan, Vol. 18, 1978, p. 511.
[*6*] Ridder, S. D., Reyes, F. C., Chakravorty, S., Mehrabian, R., Nauman, J. D., Chen, J. H., and Klein, H. J., *Metallurgical Transactions,* American Institute of Mining, Metallurgical and Petroleum Engineers, Vol. 9B, September 1978, p. 415.
[*7*] Wallace, J. P. and Kunerth, D. C., *Metallurgical Transactions,* Vol. 11B, No. 2, 1980.
[*8*] Kunerth, D. C. and Wallace, J. P., *Metallurgical Transactions,* Vol. 11B, No. 2, 1980.
[*9*] Wallace, J. P., Kunerth, D. C., and Siegfried, R. M., "Eddy-Current Study of Continuously Cast Steel," in review.
[*10*] Dodd, C. V. and Deeds, W. E., *Journal of Applied Physics,* American Institute of Physics, Vol. 39, 1968, p. 2829.
[*11*] Flemings, M. C., *Solidification Processing,* McGraw-Hill, New York, 1974, p. 58.
[*12*] Kirkpatrick, S., *Reviews of Modern Physics,* American Institute of Physics, Vol. 45, 1973, p. 574.
[*13*] *Aluminum,* Vol. I, Kent R. Van Horn, Ed., American Society for Metals, Metals Park, Ohio, 1967, pp. 9-10.
[*14*] *OFHC Brand Copper/Properties and Applications,* American Metal Climax, Inc., New York, 1974, p. 72.
[*15*] *Metals Handbook,* Vol. I, Tayler Lyman, Ed., American Society for Metals, Metals Park, Ohio, 1961, pp. 1203-1209.
[*16*] Hoffman, W., *Lead and Its Alloys,* Springer Verlag, New York, 1970, p. 20.

Measurement Methods I: Multifrequency

S. D. Brown[1]

In-Service Evaluation of Multifrequency/Multiparameter Eddy-Current Technology for the Inspection of PWR Steam-Generator Tubing

REFERENCE: Brown, S. D., "**In-Service Evaluation of Multifrequency/Multiparameter Eddy-Current Technology for the Inspection of PWR Steam-Generator Tubing,**" *Eddy-Current Characterization of Materials and Structures, ASTM STP 722,* George Birnbaum and George Free, Eds., American Society for Testing and Materials, 1981, pp. 189-203.

ABSTRACT: The recent introduction of field-usable multifrequency/multiparameter instrumentation has provided a basis for the development of a near-term system for the inspection of pressurized water-reactor steam-generator tubing. Multifrequency eddy-currents offer benefits in the performance of parallel tests and a readily available data base for the identification of nonunique signals. Multiparameter methods allow for the minimization of extraneous test variables, that is, support plates and small dents, for the more reliable detection and characterization of tube degradation. The suppression of the extraneous variable in real time offers advantages over off-line computer/digital subtraction approaches. Experience with the system based on the in-service inspection of three steam generators is considered.

KEY WORDS: PWR steam generator tubing, multifrequency eddy currents, multiparameter methods

The Electric Power Research Institute (EPRI) Steam-Generator Project Office has initiated Project S-115 with the primary objective of assisting in the technology transfer of multifrequency/multiparameter eddy-current (MFEC/MPEC) instrumentation for the in-service inspection of steam-generator tubing. An important secondary objective is to document utility benefits that are derived from the use of this instrumentation during steam-generator inspections.

The need for MPEC steam-generator tubing inspection methods is not necessarily warranted on an industry wide basis. There are isolated instances, however, in recirculating steam generators (RSG) and once-through steam generators (OTSG) where tube secondary side degradation occurs in

[1]Senior engineer, The EPRI NDE Center Operated by Jones Applied Research, Charlotte, N.C. 28230.

proximity to tube supports/tube sheet precluding reliable defect detection and characterization. The advent of denting has given greater impetus for the in-service use of improved steam-generator inspection methods.

The MPEC method takes a linear combination of in-phase/quadrature eddy-current data at different frequencies to reduce the effect of an extraneous test variable. The extraneous test variable may be ferromagnetic tube supports/tube sheet, tube ID noise, small dents, or combinations of these variables. The linear combination of data is accomplished in what is basically an analog computer for the real-time subtraction of the extraneous test variable or variables.

The MFEC method relies on the analysis of a signal in the impedance plane at different frequencies. The impedance-plane presentation is, in general, nonunique at a given frequency for certain tube conditions. An analysis of signals at two or more frequencies and the monitoring of the rate-of-change of patten-phase angle with frequency can provide information as to the nature of the signal. Thus, from a steam-generator diagnostics standpoint, MFEC offers benefits in identifying secondary side tube conditions.

EPRI MFEC/MPEC System Configuration

The recent commercial introduction of MFEC/MPEC instrumentation (Intercontrole IC3FA in 1977 and Zetec MIZ-12 in 1979) has provided the necessary basis for the assembly of a field-usable system. The EPRI system consists of two parallel subsystems: one based on the conventional Zetec single-frequency system and the other based on the Intercontrole IC3FA technology. A dual differential probe can be used, with each system operating independently. The motiviation for the parallel system is as follows. Conventional single-frequency data can be gathered and compared with independent data from the IC3FA multifrequency system. Use of the dual coil allows for the collection of both data sets in one pull through the tube resulting in no increase in inspection time. The EPRI system is illustrated in Fig. 1. A typical dual-coil configuration is shown in Fig. 2. The system is controlled by a single operator using a Zetec OMB-1 for the start/stop of the magnetic tape and strip-chart recorders. Insertion of a common-voice record on both tape recorders for data documentation is achieved via the microphone mounted on the OMB-1.

The conventional system consists of an EM-3300 for the generation of single-frequency data (usually 400 kHz in RSGs and OTSGs). The in-phase and quadrature components are then recorded on a two-channel TEAC 2300 magnetic tape recorder and Brush two-channel strip-chart recorder. In conventional in-service inspection, data at one frequency are gathered during one pull of the tube. If additional eddy-current data are desired at different frequencies, repetitive probing of the tube must be performed.

The parallel MFEC/MPEC system is a simultaneous three-frequency in-

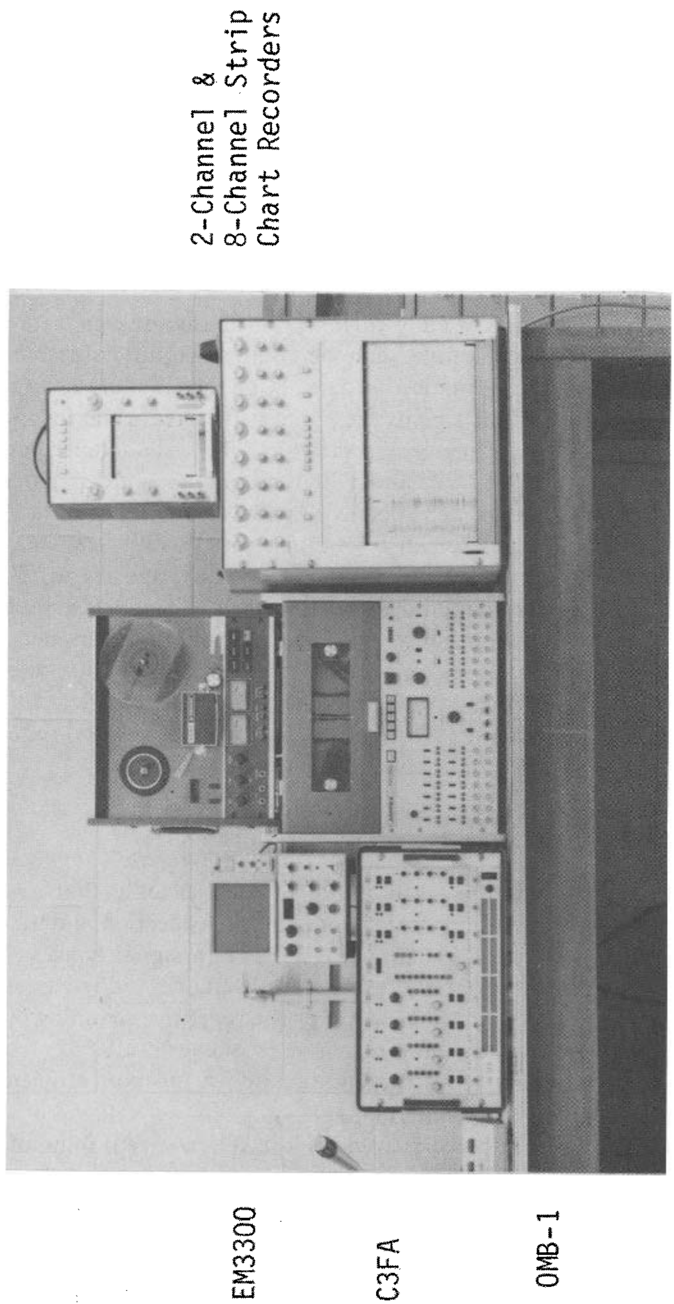

FIG. 1—*System configuration (magnetic tape recorders).*

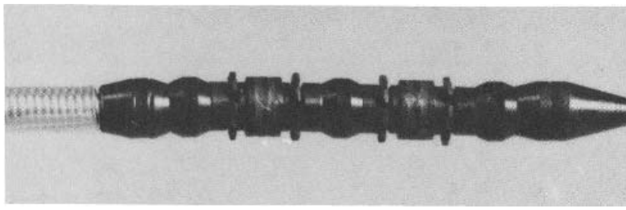

FIG. 2—*Typical dual coil.*

strument for the generation of eddy currents. In-phase and quadrature outputs from the frequency modules can be used as input data to mixing modules for the linear combination of data. A mixing module is an analog computer in which the input signals are combined in real time for the suppression of the desired extraneous test variable. The system generates three frequencies identified as F1, F2, and F3. A pseudo-absolute signal is also reconstructed from F3 and is identified as FA. The frequency of FA and F3 is thus always the same. F1, F2, and F3 are generated using fixed-frequency oscillator cards and, in general, can be selected over a range of 1 to 750 kHz. A maximum of three mixing modules can be utilized. These are identified as C1, C2, and C3. When the in-phase and quadrature signal components are taken into consideration, a maximum of fourteen information channels is available. An AMPEX PR-280 14-channel magnetic tape recorder is used for data storage, and an 8-channel Brush strip-chart recorder is used for the online monitoring of selected data channels.

Multifrequency Eddy-Current Benefits

MFEC benefits include the performance of parallel tests, that is, defect detection, sludge profiling, and dent sizing, and the collection of data at different frequencies for the characterization of certain signal types in which single frequency data is nonunique. A multifrequency eddy-current approach has been used in industry for years by the repetitive scanning of tubes using single-frequency instrumentation whose frequency is altered on a scan-to-scan basis. Multifrequency instrumentation allows for more efficient data collection in one pull through the tube.

Present RSG inspection practices require the selective reprobing of tubes to perform sludge profiling, dent sizing, and primary/secondary side tube inspection. With multifrequency coil excitation, appropriate selection of frequencies can allow these tests to be performed in one probing of the tube. In OTSGs, 400 kHz is the primary defect-detection frequency, with the selected reprobing of special interest tubes at 200 and 600 kHz. Again, with simultaneous multifrequency, the 200-400-600 kHz data set can be gathered in one pull through the tube.

Multiparameter Eddy-Current Benefits

The objective in using multiparameter eddy currents is the suppression of an extraneous test variable for the more reliable detection and characterization of steam-generator tube degradation. Typical extraneous variables that can be encountered in steam generator include tube supports, tube sheet, small dents/dings, and tube ID noise or chatter.

The suppression of an extraneous variable or variables is accomplished in the IC3FA with the use of mixing modules. Inputs to a mixer may be the outputs of the frequency modules F1, F2, and F3, or the outputs from the other mixers. The mixer can be visualized as a differential amplifier in which the extraneous variable is sampled at two different frequencies. Use of mixer-phase rotators and weighting resistors allow for the adjustment of similarly shaped inputs to the mixer amplifier. The amplifier output is then minimal with regards to the extraneous variable. Selection of initial mixing frequencies determines the resultant defect amplitude and phase-spread characteristics. The mixers may be also used in a series combination, and the output of a given mixer does not necessarily have to be adjusted in a minimal sense but may be used to transform the difference of two input signals to an output signal of desired shape.

Figure 3 illustrates the mixing module in schematic form. The extraneous variable to be minimized is sampled at two different frequencies and in-phase/quadrature components are fed to the mixer input terminals A and B.

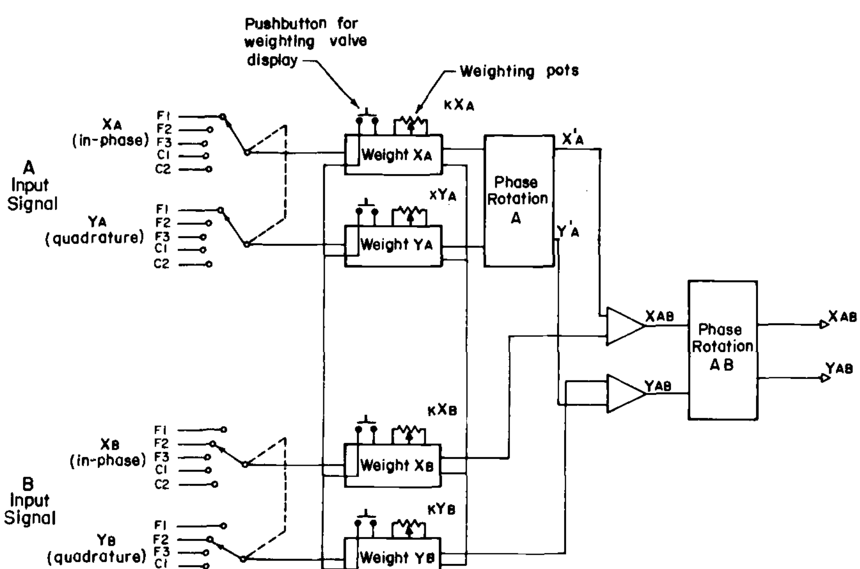

FIG. 3—*IC3FA mixing-module schematic.*

In general, the two signals will have different shapes, that is X-Y structure and different rotations. The phase rotator, A, and weighting resistors, K_{ax}, K_{ay}, K_{bx}, K_{by}, are used to orient the two inputs with the same phase and shape, namely, make the two congruent. The mixer output is then minimal with respect to the desired extraneous test variable. The mixer phase rotator, AB, is used for the adjustment of output reference phase, that is, wobble horizontal or whatever is desired.

Figure 4 illustrates a three-frequency support-plate mix, 100, 240, and 500 kHz, in which two series mixers are used. In the first mixer, C1, the input frequencies are 100 and 240 kHz. Using appropriate weighting and rotation, the C1 mixer output is adjusted to mimic a support plate at 500 kHz. The C1

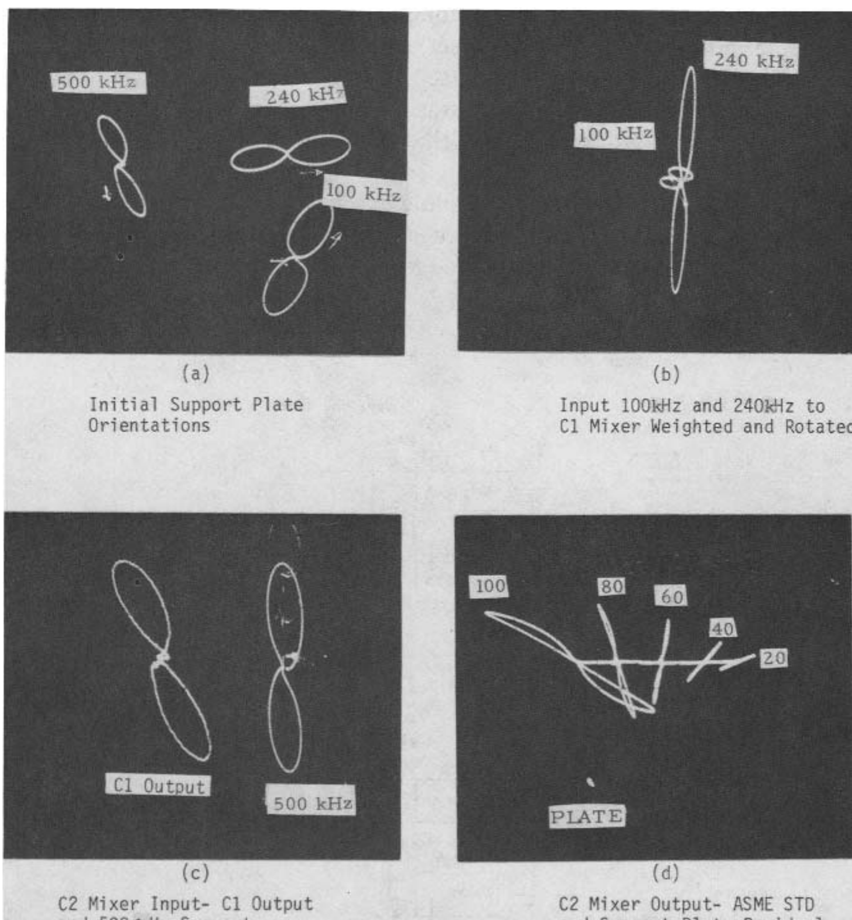

FIG. 4—*Three-frequency support-plate mix.*

output and 500 kHz plate signals are used as inputs to the C2 mixer. Again after appropriate weighting and rotation in the C2 mixer, the final plate residual and resultant ASME standard signal amplitude is shown. The phase-angle spread is approximately 120 deg, which is comparable to the conventional 400 kHz in 1.27 mm (0.05 in.) wall tubing.

The effectiveness of a particular mix can be assessed by comparing standard signals with and without the influence of the extraneous test variable. Figure 5 shows the mixed-output channel for an OTSG three-frequency support-plate mix. The mixing frequencies were 240, 400, and 500 kHz. The signals shown are derived from a typical OTSG eddy-current standard which contains a series of holes 1.5 mm (0.060 in.) in diameter at depths of 20, 40, 60, 80, and 100 percent of the tube wall. Figure 5*a* illustrates the mixed output for this series of holes without an extraneous broached support plate in proximity, and Fig. 5*b* shows the mixed output with a broached support-

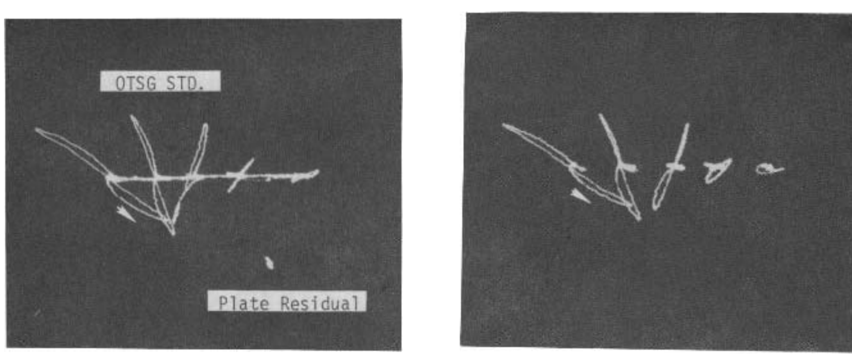

(a) Without Support Plate

(b) With Support Plate

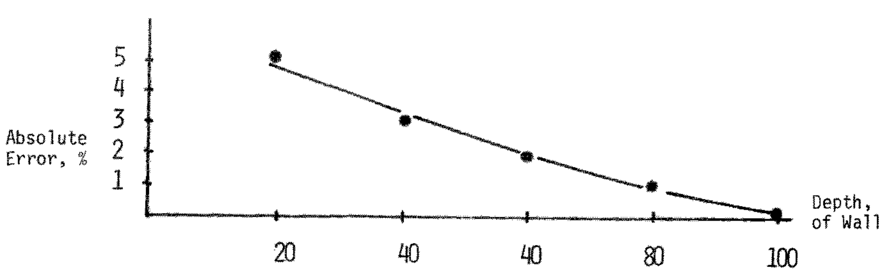

(c) Absolute Error Due to Mixing

FIG. 5—*OTSG three-frequency support-plate mixing error estimation.*

plate edge at each of the holes. As can be seen, the mix is not perfect, with the 20 and 40 percent hole depth Lissajous patterns rotated slightly. If a calibration curve is derived from Figure 5*a* and the angles from Fig. 5*b* are used to estimate depth, the error attributed to mixing can be estimated. Worse-case error is on the order of 5 percent, with a plot of error versus depth shown in Fig. 5*c*.

Multiparameter eddy currents can offer benefits in the more reliable detection and characterization of tube degradation in the presence of extraneous test variables. The real-time suppression of the desired variable can be achieved using a mixer or analog computer approach offering advantages over digital or computer subtraction techniques. These latter techniques cannot accommodate nondeterministic signals, such as tube ID noise, which can be readily handled using a simultaneous multifrequency approach.

EPRI MFEC/MPEC System Operational Experience

The EPRI system has been used in three steam generators during in-service inspection (ISI) outages. Experience with the system in two RSGs and one OTSG is summarized. Specific utility benefits are identified by a comparison of the MFEC/MPEC system results with conventional single frequency (400 kHz) and present inspection practices. Limitations of the system multiparameter aspects are also considered.

Multiparameter Aspects

Two basic support plate/tube sheet mixes were implemented for engineering evaluation: a two-frequency (100/240 kHz) mix and a three-frequency (100/240/500 kHz) mix. Both mixes have been used in RSGs and OTSGs, with necessary scaling of frequencies to accommodate differences in wall thickness, that is, 1.27 mm (0.050 in.) versus 0.94 mm (0.037 in.) nominal. Figure 6*a* illustrates distorted support-plate signals at three different frequencies from an RSG. Although the detection of a defect is possible, estimation of its depth cannot be made. Figure 6*b* illustrates the mixed-channel outputs for the two-frequency and three-frequency mix. Depth estimates for the defect are different for the two-frequency and three-frequency mixes. In all cases where both mixes have been available to estimate defect depth, the three-frequency mix has provided a greater depth estimate. The three-frequency mix has been found experimentally to be less influenced by the support plate than the two-frequency mix. This is due to more predominant use of a higher-mixing frequency in the three-frequency mix. The observed effect of the support on both mixes has been the rotation of the resultant signals in the nonconservative direction, with a greater rotation for the two-frequency mix. Hence the three-frequency mix provides a more accurate estimate of defect depth and the selection of mixing frequen-

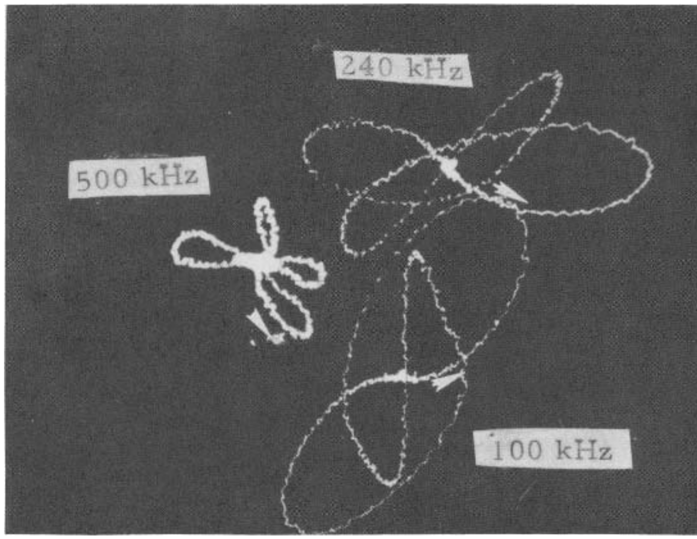

(a)

Distorted Support Plate Signals

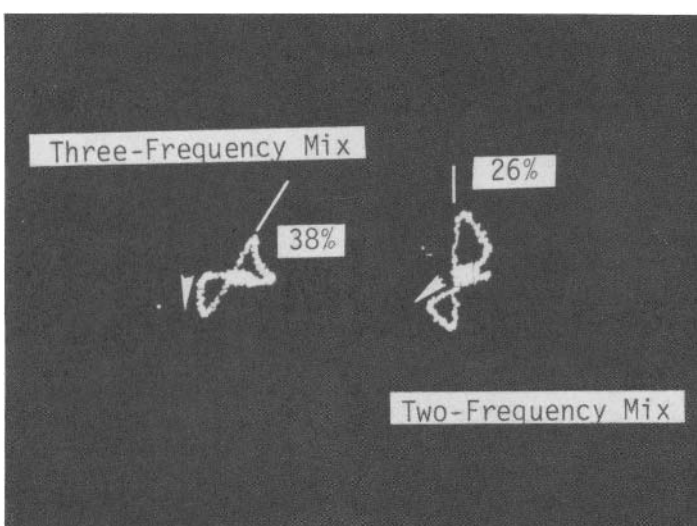

(b)

Mixed Channel Output

FIG. 6—*Defect detection/characterization using support-plate mix.*

cies should be chosen with some care. Without the use of a mixed-output channel for defect assessment, the tube would have been plugged, since the distortion caused by the support-plate signals prevents accurate sizing.

A limitation of mixing identified to-date is the presence of probable cold work in tubes resulting from vibration of the tube in the support plate/tube sheet intersection. Figure 7*a* illustrates a nonworked RSG tube support-plate signal (240 kHz) along with the two-frequency and three-frequency mix-plate residuals. Figure 7*b* shows an RSG tube, with cold working, at 100, 240, and 500 kHz, with the exit lobe showing the working effects. The effect of this cold working on the two mixes is shown in Fig. 7*c*. In general, the effect of the working is to "balloon" the mix residual, that is, the loop opening. Similar signals have been encountered in OTSGs.

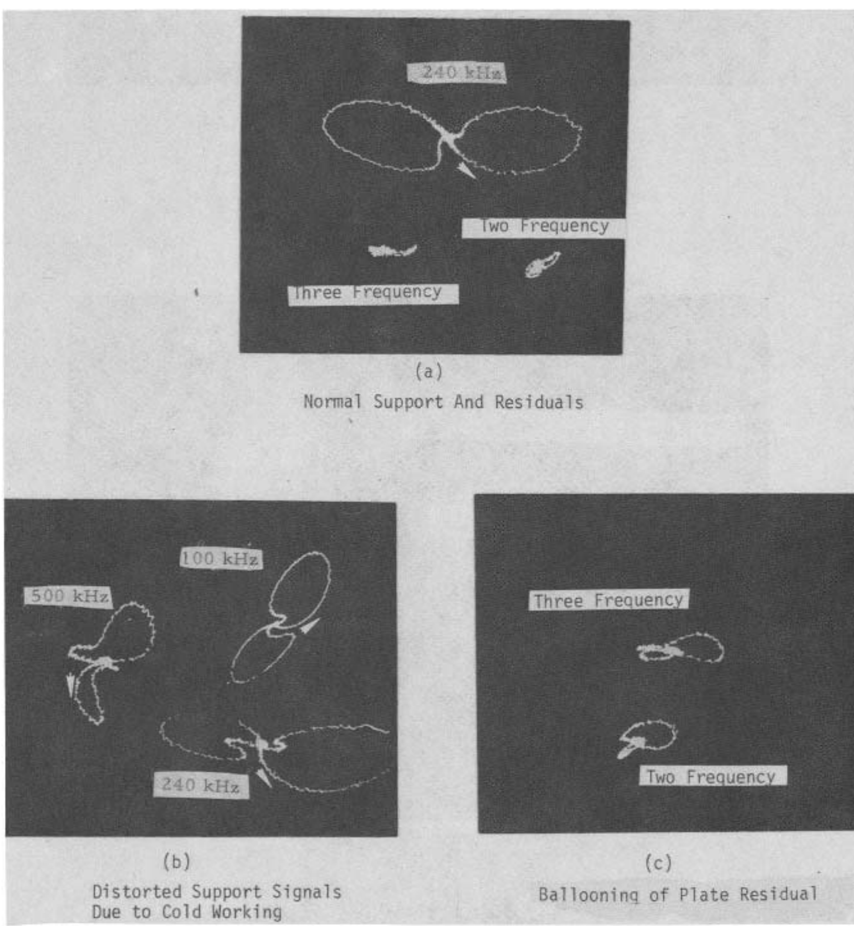

FIG. 7—*Effects of cold work on support-plate suppression.*

In-service experience with a dent-suppression mix is now considered. The nix evaluated was a three-frequency plate/dent mix and was utilized in an SG with minor denting at eggcrates. The effectiveness of the mix is illustrated in Fig. 8. Figure 8*a* shows the strip-chart recording of the 500 kHz

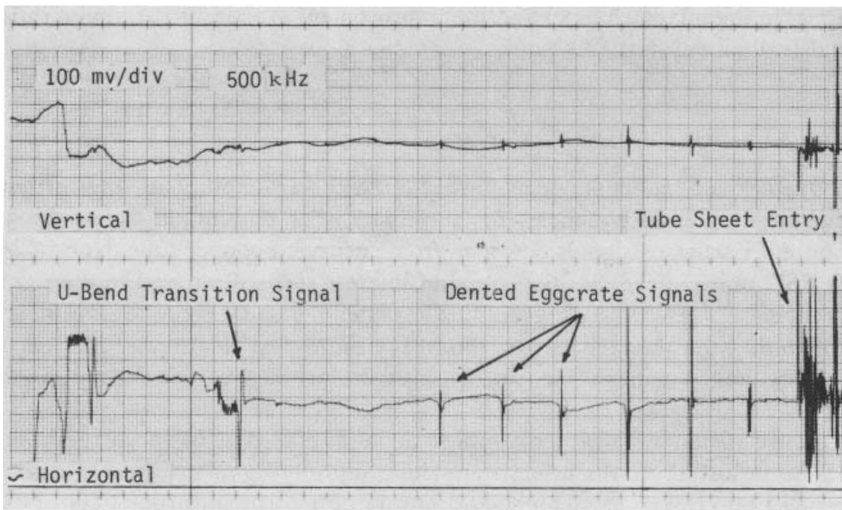

(a)
No Dent Suppression

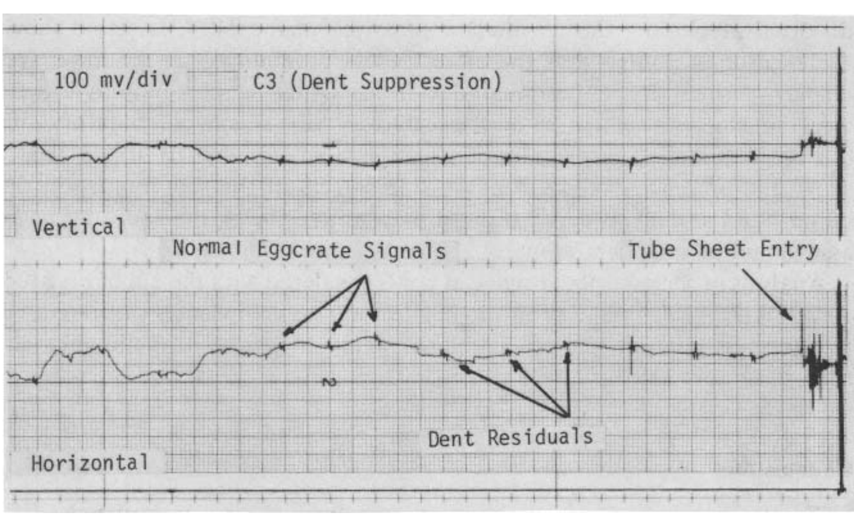

(b)
Dent Suppressed

FIG. 8—*Strip-chart traces illustrating dent suppression.*

eddy-current in-phase and quadrature signal components. Identified are the large dent signals, eggcrate signals only, and the horizontal offset that is obtained as the eddy-current probe transitions the U-bend tangent point. The mixed channel output is shown in Fig. 8*b*. The reduction or suppression of the dent signal is apparent. Also of interest is the elimination of the offset signal in the mixed channel and the improvement of the signal-to-noise ratio that is obtained in the U-bend.

Multifrequency Aspects

One of the benefits of MFEC inspection is the availability of eddy-current data at different frequencies for the analysis of nonunique signal types. Figure 9 illustrates signals obtained from suspected copper tube deposits in an RSG unit. In Fig. 9*a*, the signal of interest starts down and to the right mimicing an ID defect. Figure 9*b* illustrates the same signal at 240 kHz. Notice that the signal starts up and to the right. The rotation of this signal with frequency is inconsistent with legitimate primary or secondary side effects.

Figure 10*a* shows a rather complex signal at 500 kHz that occurred in an RSG unit just above the tube sheet. The composite signal of Fig. 10*a* can be resolved into two signals. These are shown in Figs. 10*b* and 10*c* at 500, 240, and 100 kHz. An examination of the Fig. 10*b* signal at 500 kHz shows the initial start of the signal is to the right, which from an impedance-plane analysis suggests a tube bulge. After initial bulge formation, the signal is distorted precluding further analysis. Analysis of the 240-kHz signal shows evidence of the bulge, but the effect is less pronounced at the lower frequency. A rotation of the remainder of the signal in the counterclockwise direction suggests something on the secondary tube side in combination with the bulge. Finally, an examination of the same signal at 100 kHz clearly shows the presence of the secondary side defect. At this low frequency, the bulge has basically become transparent, which allows the more accurate assessment of tube condition

Analysis of the associated signal is now considered with the aid of Fig. 10*c*. At 500 kHz, the signal lies on the horizontal and is obviously saturated. As frequency is lowered, the signal rotates, again suggesting something on the tube secondary side.

Conclusions

The following conclusions can be drawn from the accummulated EPRI system experience:

1. Multifrequency eddy-current offers benefits in increased test efficiency by the performance of parallel testing, namely, sludge profiling, code ISI,

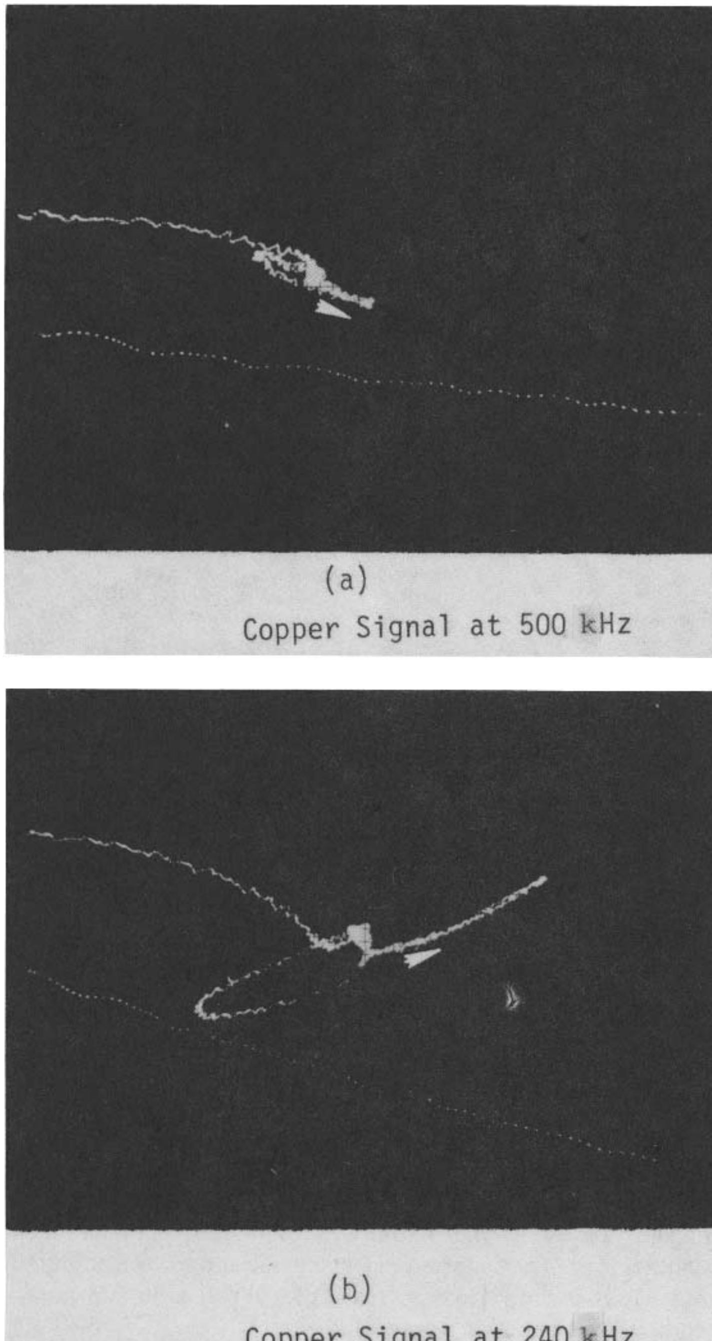

FIG. 9—*Multifrequency characterization of metallic tube deposits.*

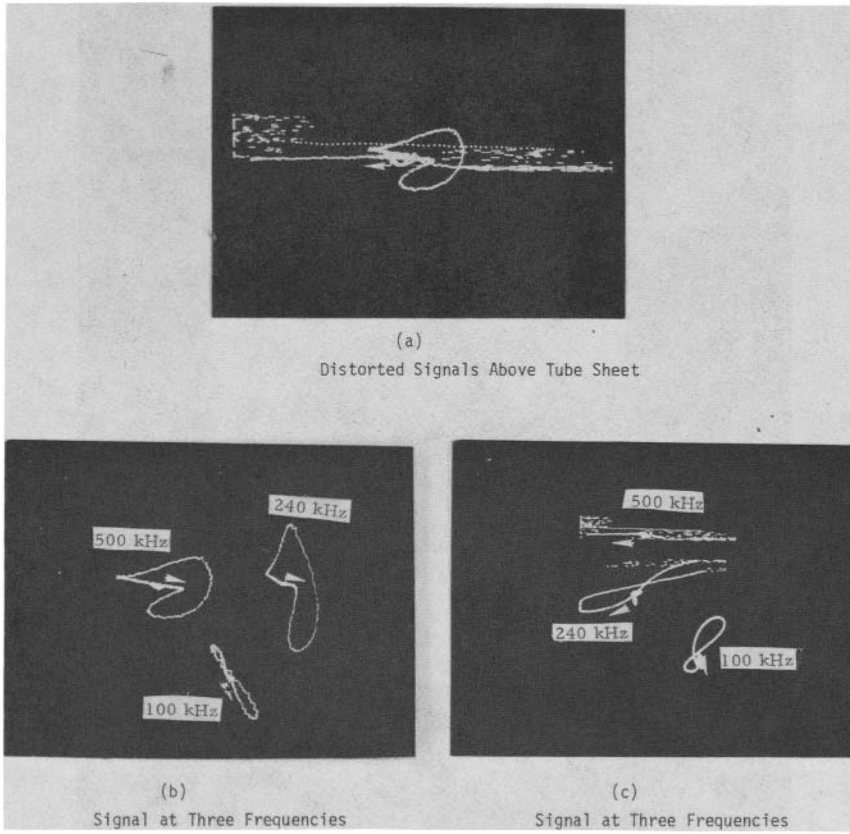

FIG. 10—*Multifrequency characterization of complex signals above tube sheet.*

and dent sizing. Data can be gathered in one pull through the tube. Eddy-current data at different frequencies are also beneficial in characterizing complex or nonunique signals that can occur during steam-generator tube inspection.

2. Multiparameter eddy-current approaches for the elimination of extraneous variables, such as support plates and dent signals, have been shown to offer advantages over conventional single-frequency methods. Specific benefits that are obtained include (*a*) the salvaging of tubes that may have been plugged because of the inability of single-frequency methods to accurately characterize the distorted defect signal, and (*b*) the ability to do the extraneous variable subtraction in real time, which offers advantages over digital/computer subtraction approaches.

3. A limiting factor in the characterization of identified multiparameter

diagnostics is the presence of cold-working in tubes at some support plate/ tube sheet intersections. Additional laboratory investigation of the parameter and of the ability to suppress it is necessary. Cold-working would also affect other support-plate subtraction schemes.

4. The introduction of more advanced eddy-current instrumentaion to in-service inspection personnel has gone very smoothly and has been aided by the development of system-operating and training manuals.

K. Betzold[1]

A Multifrequency Approach to Interpret Defect Signals Superimposed by Disturbing Signals According to the Causing Defect Type and Size

REFERENCE: Betzold, K., "**A Multifrequency Approach to Interpret Defect Signals Superimposed by Disturbing Signals According to the Causing Defect Type and Size,**" *Eddy-Current Characterization of Materials and Structures, ASTM STP 722,* George Birnbaum and George Free, Eds., American Society for Testing and Materials, 1981, pp. 204-212.

ABSTRACT: A multifrequency algorithm is applied to suppress the effects caused by disturbing signals. The remaining defect signals then exist in a scalar (one-dimensional) form. The defect indication can be assessed by using artificial reference defects of known depths giving equivalent indication peaks. It is not possible, however, to distinguish which type of defect has really caused the read-out value. Before the defect size can be determined it is necessary to know the defect type. A method of distinguishing the different types of defects has been developed. The multifrequency algorithm is applied twice by adding at least one additional measuring value (this can be the real part or the imaginary part of an additional testing frequency) or replacing the test frequencies by entirely new ones. In both parallel channels the indications of the disturbing parameters are suppressed. Provided that the two channels react in different ways to the different types of defects, one obtains a two-dimensional read-out value. Displaying the two channels on an oscilloscope achieves the following results: (*1*) the disturbing signals are suppressed and concentrated at the zero point of the screen, (*2*) the defects give indications with different phase angles corresponding to the different defect types, and (*3*) the heights of the defect indications are correlated with the defect size. Using a computer program based on the permutation principle, the angles between the phase directions of the defect types can be optimized. Results are presented for the testing of built-in heat-exchanger tubes and welded joints and claddings.

KEY WORDS: multifrequency evaluation, defect types, defect sizes, welded joints, claddings, built-in heat-exchanger tubes

In eddy-current testing the coil impedance can be affected by a large number of influencing parameters. When they occur separately the simple prob-

[1]Fraunhofer-Institut für zerstörungsfreie Prufverfahren, Saarbrücken, West Germany.

lem involved can be solved by single-frequency methods, but in general the coil impedance is influenced both by those parameters that are the goal of testing and by those that are not the subject of testing. One of the main aims in eddy-current testing, therefore, has been to separate the contributions of the different parameters to the impedance and to suppress the contributions caused by unwanted or disturbing parameters.

Our method of solving that problem is a so-called multifrequency or multiparameter approach based on the investigations of Libby [*1*].[2] A special field for the application of such methods is represented by the problems of nondestructive testing of nuclear components. When testing austenitic built-in heat-exchanger tubes, disturbing parameters are caused by the tube support plates and the tube sheet, while the effects of slits, pitting, holes, and changes of inside and outside diameter must be detected and assessed according to their size. Similar problems arise when testing the clad wall of a reactor pressure vessel; undesired effects are produced by the lift-off of the testing coil, by variations in the electrical and magnetic properties of the material, and by changes in the thickness of the welded layer. These influences have to be separated from those produced by surface cracks and holes as well as by cracks at the interface between cladding and base material. By the application of a multifrequency algorithm it is possible to suppress the aforementioned disturbing signals and to read out only the defect signals [*2,3*].

The results are given in a scalar (one-dimensional) form, for example, an A-scan. In the past the read-out values have been assessed by using artificial reference defects of known depths giving equivalent indication peaks [*4,5*]. In order to have exact results, however, it is necessary to know the defect type before determining the defect size. This report will outline a method for interpreting defect signals with disturbing signals superimposed according to the type and size of the defects producing them.

Methods

The information on defects can be increased by continuing with the evaluation just described, but applying in a second parallel channel an additional multifrequency evaluation process fed with new and different input information. This can be achieved by adding at least one additional measured value (this can be the real or imaginary part of a new testing frequency) or by replacing the test frequencies by entirely new ones. In both parallel channels the signals caused by the disturbing parameters are suppressed. By feeding the read-out values to the horizontal and vertical deflection circuits of an oscilloscope, we create a two-dimensional display in which various types of defects generally produce different phase angles. This means that the two sets of processed measured values react in a different manner to the types of

[2]The italic numbers in brackets refer to the list of references appended to this paper.

defects, while the disturbing signals are suppressed and concentrated at the zero point of the screen. The angles between the phase directions and the amplitudes can be influenced for each testing coil by the choice of the frequency combinations. A computer program has been written to perform a fast optimization in order to create large phase angles between the different types of defects. Based on a permutation method, the optimum frequency combinations are determined from a set of about 10 frequencies in the range of 30 to 500 kHz.

Especially for two-frequency testing there are $\binom{10}{2}$ possible combinations [*6*]. Each of them can be combined with another to create a two-dimensional display. The resulting 45 possibilities are reduced to a few good combinations by criteria for the amplitudes of the read-out values and for the angles between the various defect types. In the following section some results of the application of this method are described.

Experimental Work and Results

Testing of Welds and Clad Specimens

These tests were performed with an absolute pickup coil whose outside diameter was 5 mm. The apparatus [*4,5*] was calibrated to suppress the effects of variations of electrical conductivity, magnetic permeability, and lift-off of the test coil using the austenite state as a basis. The optimum frequency combination determined by the computer program was 40 and 200 kHz for one channel and 75 and 300 kHz for the other. Figure 1 shows the

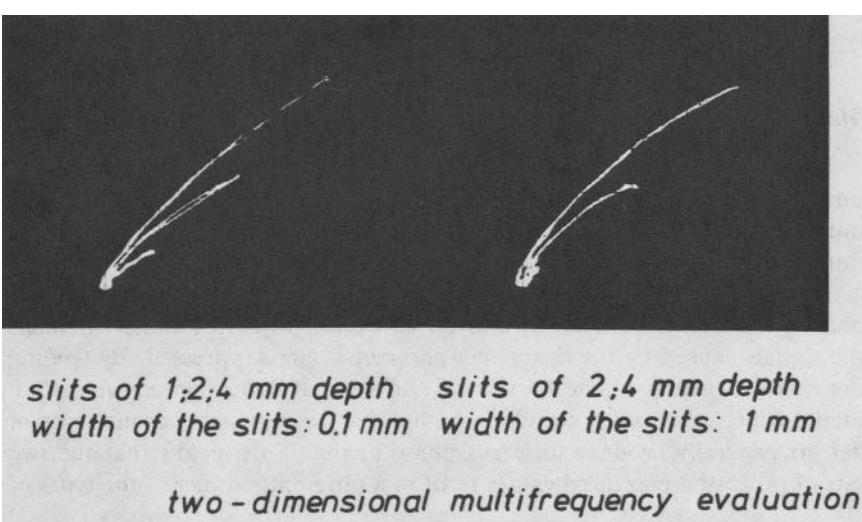

FIG. 1—*Inspection of saw cuts of different widths.*

results of testing an austenite plate in which three saw cuts with depths of 1, 2, and 4 mm were present; the width of the cuts was 0.1 mm. The pickup coil was moved over the slits in one pass. The corresponding two-dimensional display is shown on the left. When the plate was tested these saw cuts of the same type not only produced different amplitudes but also different phase angles; at the origin the signals come from the austenite plate where it is free of defects. The right half of the figure shows the signals for the same defect depth but with a width of 1 mm. There is a slight change in the curve but not in the end points. It is therefore possible to indicate the true defect depth irrespective of the defect width.

This combination of coil size and frequency is especially suitable for the detection of surface flaws. Yet a defect 2 mm below the surface can be detected. The two-dimensional signal for that defect is shown in the right half of Fig. 2 together with the indication of a 1-mm surface flaw. The amplitude is obviously small, but the phase direction is different from those of the surface cracks. In order to show that it is also possible to perform an optimization for cracks below the surface, the same procedure was carried out with a testing coil of greater diameter. The results are shown in the left half of the figure. The amplitude of the covered flaw is greater than that of a surface flaw of the same depth.

A typical problem is the inspection of welded joints. The specimen shown in the middle of Fig. 3 represents an austenite welded joint, where the properties of the weld material and the base material differ. The two pulsed fatigue cracks near the edges of the weld zone are measured by moving the coil over the specimen in several passes as indicated. The resulting coil impedance at each testing frequency is a function of the lift-off of the coil and of the

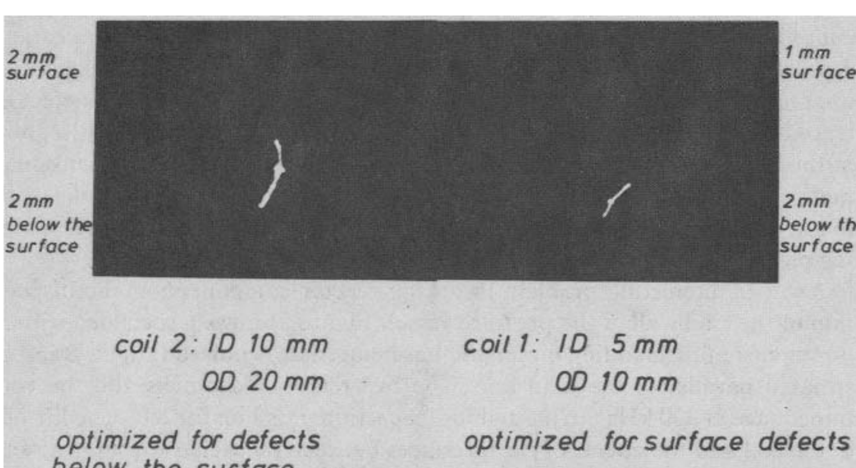

FIG. 2—*Multifrequency eddy-current testing; optimization for different types of defects.*

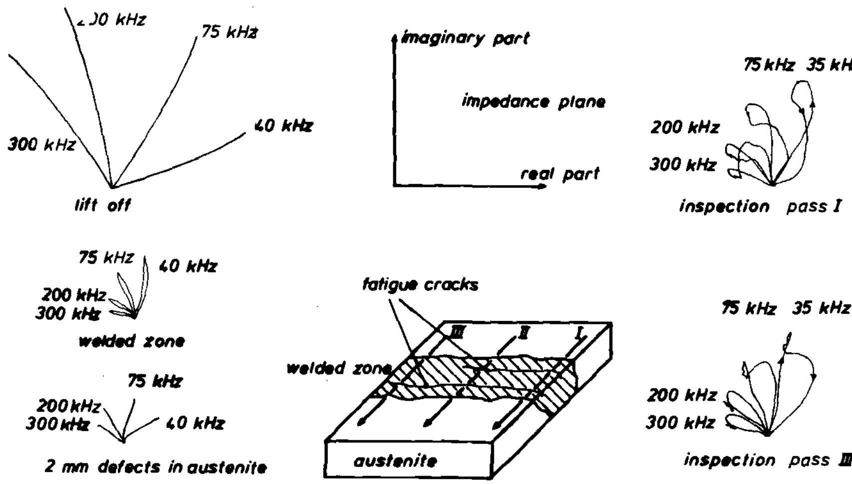

FIG. 3—*Inspection of an austenite weld.*

material properties of the weld and cracks. Some typical variations of coil impedance caused by these parameters are shown on the left. In each inspection pass all effects are superimposed at different intensities. The resulting impedances for two passes are shown on the right side. It is obviously impossible to recognize the contribution made by the defects. Figure 4 shows the two-dimensional measurement traces from the welded joint. The two upper plots show signals on the two read-out channels after two frequency evaluation. For comparison the real part of the coil impedance is shown in the lower plot. While the first signal on the left side in pass III derives from a lift-off of the coil it is suppressed in the other passes. The remaining disturbances caused by the weld zone are small. Near the end of the weld a large indication represents a fatigue crack. In the two-dimensional display all disturbances are reduced to a fat zero point, and only the signal representing the defect is traced out. In the second pass the amplitude of this first defect is smaller, but at the beginning of the weld there is a second defect. In the two-dimensional picture both defects are presented. The greater depth for the second defect is found in inspection pass I, while the first is still indicated. In the corresponding plot the first defect lies along the trace for the second.

Another interesting problem in testing reactor components is the inspection of the clad wall of the pressure vessel. Figure 5 shows a specimen with a 6-mm austenitic cladding on ferritic base material. A pulsed fatigue crack is situated parallel to the weld line. The two read-out channels and the coil impedance at 300 kHz are plotted for inspection pass I on the left. The lift-off of the coil and the effects of the interfaces between the welds are suppressed, and only the defect signal is read out. In the left photo the two-dimensional signal for this pass is shown with that for a second pass. Amplitude and phase angle have both changed to match the reduction in the depth of the defect. To find the depth, these signals can be compared with those from the austenite plate shown in the first figure; it is found to be 4 mm (shown in the right photo).

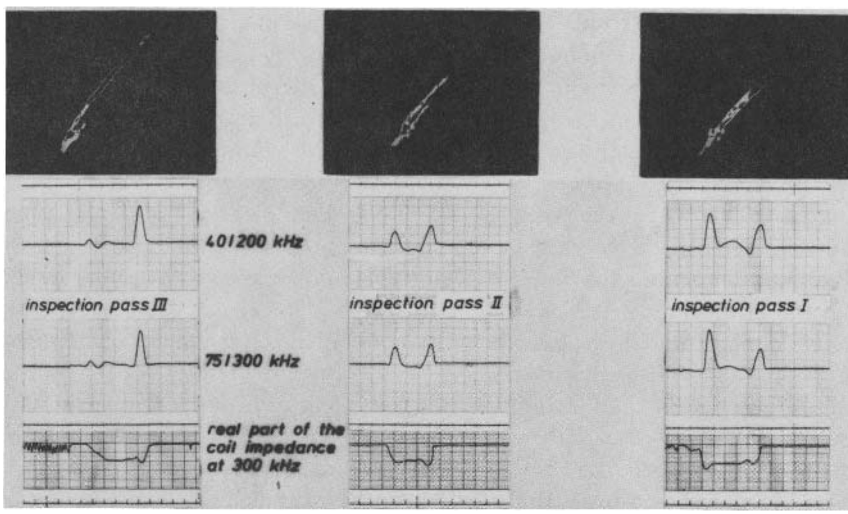

FIG. 4—*Inspection of a welded joint.*

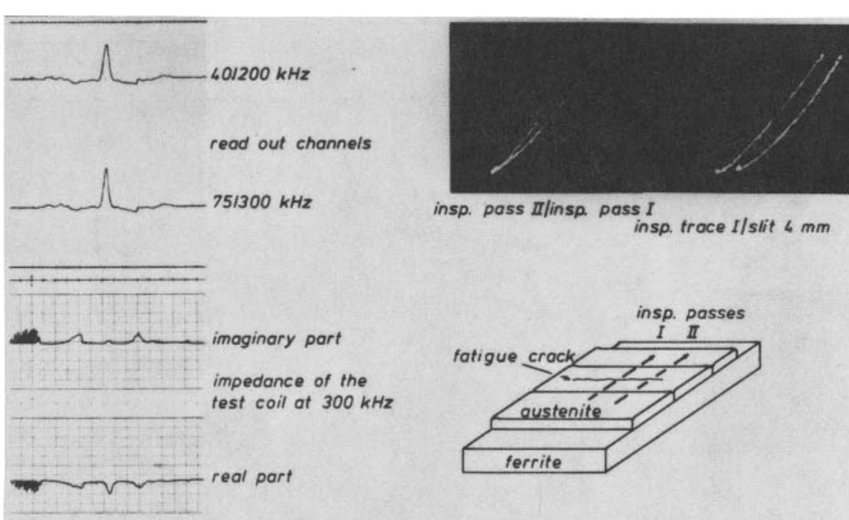

FIG. 5—*Inspection of a cladding surface.*

Testing of Built-in Heat-Exchanger Tubes

The testing was performed with an absolute coaxial inside coil that was moved through the tubes. A heat-exchanger tube with the tube sheet, the tube support plate, and several types of defects are shown in the center of Fig. 6. By using the method described previously and processing the two frequency combinations (200/340 and 100/200 kHz) one obtains the indications shown on the right of Fig. 6 caused by the named defect types. If both read-out values are displayed in the manner described on an oscilloscope, one obtains the deflections shown on the left of Fig. 6. The upper picture differs from the lower in the depth of the outside slit (60 and 90 percent of the wall thickness) and in the diameter of the hole (0.8 and 1.5 mm, both 100 percent of the wall thickness deep). In both cases the changes in the diameters are the same.

Figure 7 shows for the same test situations the indications for some other type of defect. In each case the plot and the picture beside it belong together. The phase directions for three inner and three outer axial slits are the same; the amplitude indicates the depth of the defects.

It is important to investigate the influence of disturbing effects on the phase angles in the two-dimensional display. As shown on the left side of Fig. 8, the fact of outer axial slits having the tube sheet and tube support plate superimposed on them does not change the phase direction. The amplitudes are slightly reduced as in the case of one-dimensional evaluation. The photos on the right side show the results from drilled holes and inner axial slits in the region of the tube sheet. By means of these investigations it is possible to get a general picture of the difference between real and measured defect depth.

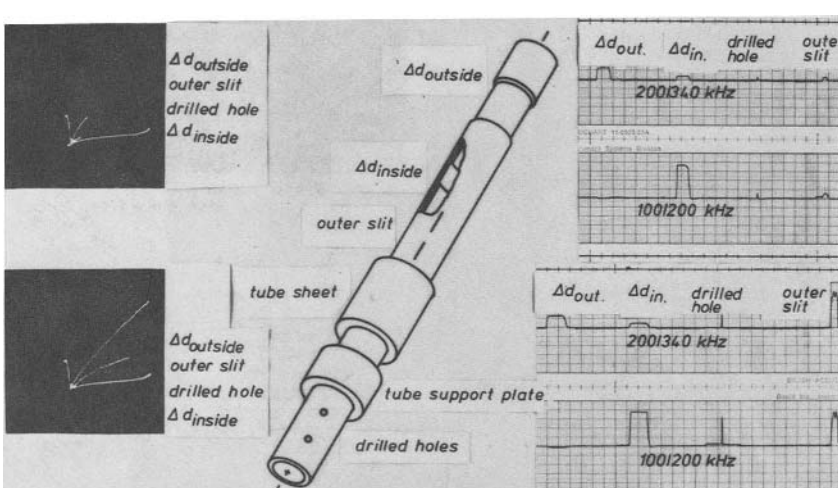

FIG. 6—*Interpretation of the defect signals after suppression of the disturbing effects.*

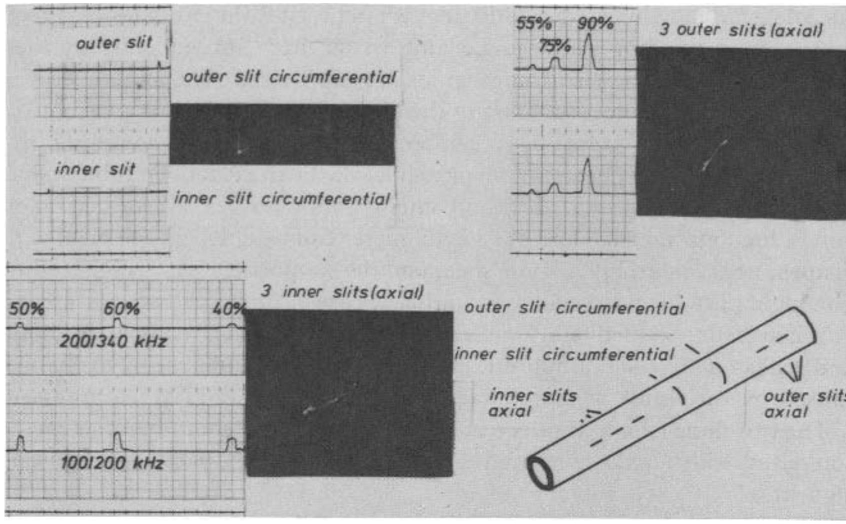

FIG. 7—*Interpretation of the defect signals after suppression of the disturbing effects.*

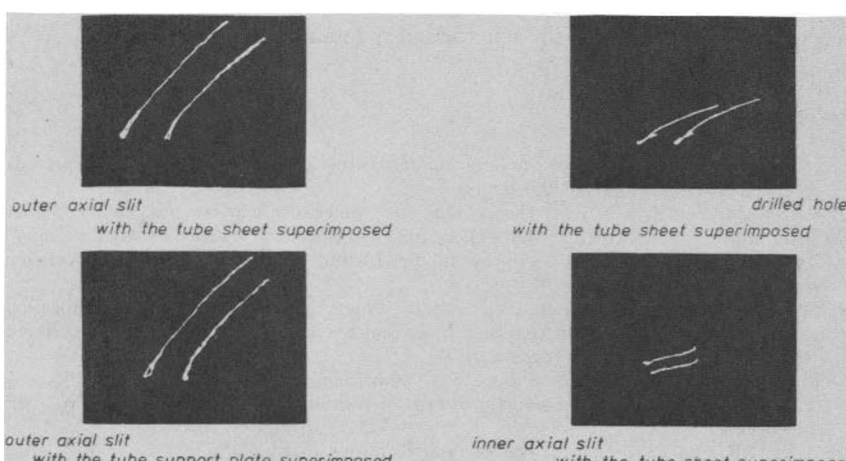

FIG 8—*Interpretation of the defect signals after suppression of the disturbing effects.*

Discussion

An evaluation procedure has been developed for interpreting the defect signals in multifrequency testing. It has been shown that a dual parallel application of the multifrequency algorithm provides additional phase information that enables a two-dimensional display. By means of this procedure we can avoid the need to assess the defect signals from the amplitude of reference defects; moreover, we can distinguish between different types of defects by the corresponding phase angle and assess them subsequently by their amplitudes, while the disturbing signals are suppressed. The angles between the defect types, being a function of the dimensions of the testing coil and of the combinations of frequencies, can be optimized by using a computer program based on the permutation principle. In heat-exchanger tube testing inner and outer axial slits, inner and outer circumferential slits, drilled holes, and reductions in inside and outside diameter can be detected irrespective of disturbances caused by the tube sheet and the support plates. A slight reduction in amplitude must be allowed for in the case of superposition.

When testing welded joints and clad specimens pulsed cracks can be found and assessed by their amplitude and phase angle while the disturbances caused by variations in the characteristics of the material are suppressed.

The two-dimensional results can be easily stored in a computer and can be compared with actual measured values by means of a pattern-recognition algorithm.

Acknowledgments

This work was supported by the German Ministry of Research and Technology within the scope of the reactor safety research program.

References

[1] Libby, H. L. in *Research Techniques in Nondestructive Testing,* Vol. 1, R. S. Sharpe, Ed., Academic Press, London, 1970, Chapter 7.
[2] Betzold, K. and Becker, R., "Theoretische und numerische Untersuchungen zur Wirbelstromprüfung geschichteter Materialien mit Abtastspulen gegebener Abmessungen," Technical Report No. 760501-TW, Fraunhofer-Institut für zerstörungsfreie Prüfverfahren (IzfP), Saarbrücken, 1976.
[3] Betzold, K., "Theoretische und numerische Untersuchungen zur Wirbelstromprüfung geschichteter Materialien mit koaxialen Innenspulen und Außenspulen," Technical Report No. 780725-TW, IzfP, Saarbrücken, 1978.
[4] Becker, R., Regneri, L., and Rüdiger, R., "Mehrfrequenz-Wirbelstromprüfung; Phase 1, Aufbau eines Mehrfrequenz-Geräteprototyps," Technical Report No. 780120-TW, IzfP, Saarbrücken, 1978.
[5] Becker, R. and Regneri, L., "Anpassung des Wirbelstromverfahrens für den Einsatz an Reaktoren," Technical Report No. 780832-TW, IzfP, Saarbrücken, 1978.
[6] Betzold, K. in *Proceedings,* First European Conference on Non-Destructive Testing, Mainz (West Germany), Vol. 1, 1978, pp. 189–198.

R. Becker[1] *and K. Betzold*[1]

Opitimization of a Multifrequency Eddy-Current Test System Concerning the Defect Detection Sensibility

REFERENCE: Becker, R. and Betzold, K., "**Optimization of a Multifrequency Eddy-Current Test System Concerning the Defect Detection Sensitivity,**" *Eddy-Current Characterization of Materials and Structures, ASTM STP 722,* George Birnbaum and George Free, Eds., American Society for Testing and Materials, 1981, pp. 213-228.

ABSTRACT: A multifrequency algorithm is applied to suppress signals caused by disturbing parameters. This procedure (based on the projection principle in a multidimensional vector space) and the electronics employed in prototype form are described. The prototype operates with up to four frequencies in a wide range (500 Hz to 1 MHz). The frequencies are continuously tunable and are fed into the coil one after the other by high-speed multiplexing. The multifrequency approach yields a read-out value affected only by defects. The defect signals then can be assessed by means of reference defects of known depths giving equivalent indication peaks. The elimination of the disturbing signals chiefly increases defect detection sensitivity. In general, however, the suppression is not total, and, additionally, the original defect signals are reduced to a greater or lesser degree by the application of the projection principle. The testing frequencies used have a strong influence on the projection losses and therefore on the defect detection sensitivity. A computer program system that allows the reaction of the impedance of the coil to be calculated as a function of the electric, magnetic, and geometrical properties of the specimens and the dimensions of the coil itself is used to determine an optimum frequency combination for the given test situation. This procedure is applied to the testing of heat-exchanger tubes, claddings, and welded joints. The results obtained with the optimized test system are presented.

KEY WORDS: multifrequency algorithm, projection principle, prototype, multiplexing of frequencies, testing frequencies, defect sensitivity, reference defects

The impedance of a coil conveys information about test parameters; it is measured and interpreted. The impedance is generally affected by several parameters at once, including some that are not the subject of the testing. The nature of the parameter that has caused the detected variation of the impedance cannot be recognized at once. Therefore, the first problem in applying the eddy-current test method is to isolate the contributions of the

[1]Fraunhofer-Institut für zerstörungsfreie Prüfverfahren, Saarbrücken, West Germany.

parameters to the impedance and to suppress the contributions caused by unwanted or disturbing parameters.

In this connection the detection limit for the different parameters is important. The detection limit indicates how large the defect must be for the variation in the impedance caused by the defect to be equal to the maximum level of the disturbing background. In principle the detection limit can be decreased to more advantageous small values by the suppression of the signals caused by the disturbing parameters. In general, however, the suppression is not completely successful, and, in addition, the contributions of the interesting parameters are not unaffected by the procedures applied in order to suppress the disturbing parameters. Therefore, the second problem is the optimization of the detection limit for the interesting parameters.

Finally, after the suppression of the disturbing signals, the third problem that remains is the classification and interpretation of the variations in the impedance. Especially when testing for defects, it is necessary to distinguish what type of defect caused the measured change of impedance before the defect size can be determined.

This report deals with work done towards solutions of the first and second problems; the third problem is the subject of a companion paper.[2]

Physical Basis

Starting from the results of the work done by Förster *[1]*[3] and the theoretical approaches going back to Dodd, Deeds et al *[2]*, we built up a computer program system that allows the numerical evaluation of those test situations where all bordering areas of the coils and the specimens correspond to coordinate planes of the cylindical coordinate system. Thus, the most important practical test situations can be dealt with: coaxial outside coil for a bar or a tube, coaxial inside coil in a tube, and pickup coil above a plate. The specimens may consist of one or two layers, with the electrical conductivity, the magnetic permeability, and the thickness of the layers constituting the input parameters of the program. The cross section of the tubular winding is assumed to be rectangular; its outer and inner diameter and height can be varied.

The numerical algorithm is based on the formulas published by Dodd, Deeds et al. The coil is composed of infinitesimal current loops. The Maxwell equations give the vector potential of the problem reduced to a single current loop. The vector potential of the real coil (and thus its impedance) is obtained by integrating the vector potential of the single current loop over the cross section of the coil.

Some results obtained by this method *[3,4]* are shown. Figure 1 is an impedance diagram related to the problem of testing the walls of a reactor

[2]This publication, pp. 204-212.

[3]The italic numbers in brackets refer to the list of references appended to this paper.

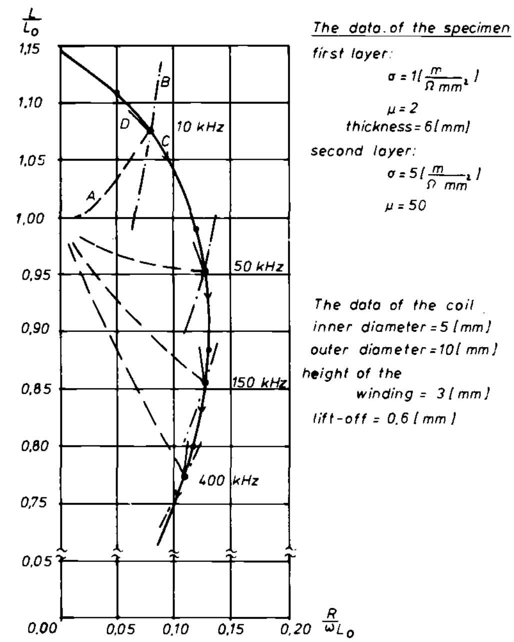

FIG. 1—*Impedance of a pickup coil above a two-layer specimen.*

pressure vessel. The thickness of the cladding is about 6 mm; the ferrite content of the cladding causes a magnetic permeability of 2; the base material is ferrite. The dimensions of the pickup coil are given on the right side of Fig. 1. The x- and y-axes represent the real and imaginary part of the coil impedance in the presence of the test specimen, normalized by the inductance of the coil in air. The tips of the impedance vectors progress a function of the test parameters along locus curves in the impedance plane. At 10, 50, 150, and 400 kHz the effects on the coil impedance caused by variations of the characteristics of the cladding material are calculated. The dotted lines (marked A) correspond to a lift-off of the coil; the lines marked B represent the variation in the magnetic permeability from 1 to 3; curve C shows the effect of the increase and decrease of the electric conductivity of the upper layer. In addition to these effects, the measured impedance of a slit in the surface of the plate is plotted (D). The upper starting point of the locus curve, representing low frequencies, is typical for the particular test configuration. Testing different specimens with the same coil at low frequencies therefore allows the y-value to be correlated with the magnetic permeability.

Figure 2 represents calculated results for a coil in the presence of an austenitic (lower curve) and a ferritic (upper curve) material. At the aforementioned frequency points the lift-off signals and the measured signals

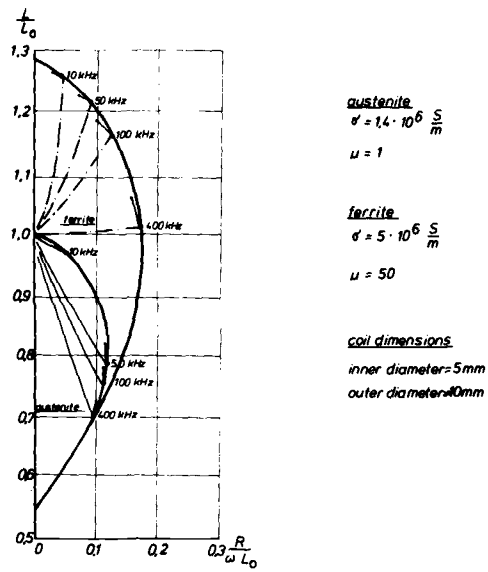

FIG. 2—*Impedance of a pickup coil; reaction on the test parameters.*

from defects are plotted. The low-frequency values on the y-axis are 1 for the austenitic specimen and about 1.28 for the ferritic material.

Figure 3 allows a comparison to be made between two different coils above a two-layer specimen. The increase in the coil diameter is correlated with greater real and imaginary parts of the impedance representing a stronger reaction between coil and material. There also arise other phase angles between the different test parameters. These phase angles are, as we can see, a function of the testing frequency and of the coil size; they are the basis of the multifrequency method explained in the following section. The eddy-current computer-program system provides a short and quick general picture of the effects and allows optimum frequencies to be selected.

Figures 4 and 5 demonstrate the penetration of eddy currents into the test specimen by showing the calculated amplitude of the eddy-current density of a pickup coil at two different depths. The winding of the coil lies above the maximum value. One can recognize that the decrease in the current amplitude in the radical direction of the coil is steeper near the surface than it is deeper below the surface.

Equivalent evaluations for coaxial outside coils are shown in Fig. 6. The lines marked A correspond to an austenitic tube with a wall thickness of 1.2 mm, and the curves marked B correspond to an austenitic bar. Thus, for the input data for the program, it follows that the electrical conductivity of region 1 in the upper part of Fig. 6 must be 0 in the first case (tube) and 1.1 $m/\Omega \cdot mm^2$ in the second (bar). At lower frequencies there is an obvious dif-

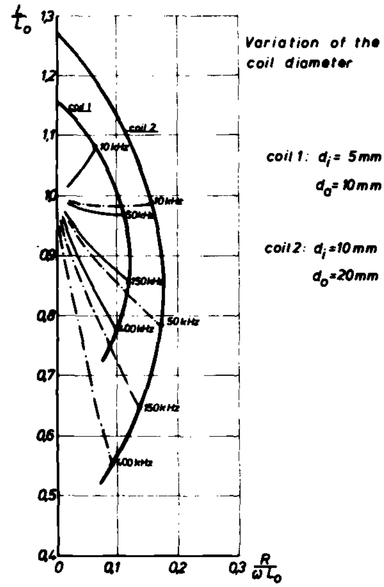

FIG. 3—*Impendance of two different pickup coils.*

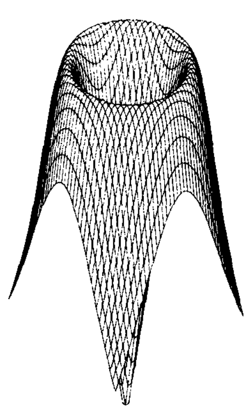

FIG. 4—*Amplitude of the eddy-current density of a pickup coil.*

ference between the eddy-current density in tubes and bars; the difference decreases with increasing frequency.

At least one representative plot given in Fig. 7 shows the effects and the problems involved in the testing of built-in heat exchanger tubes using inside coils. At six frequencies in the range of 30 to 400 kHz the changes of impedance caused by variations of the following parameters have been calculated: electric conductivity, magnetic permeability, and inside and out-

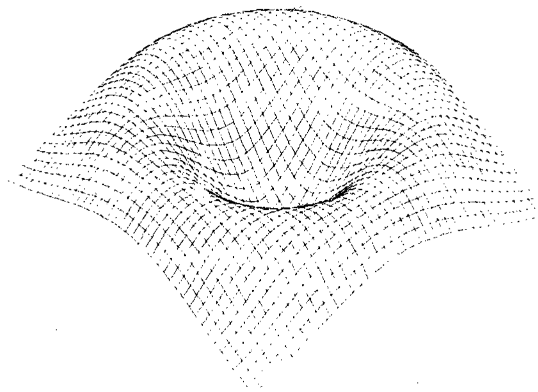

FIG. 5—*Amplitude of the eddy-current density of a pickup coil.*

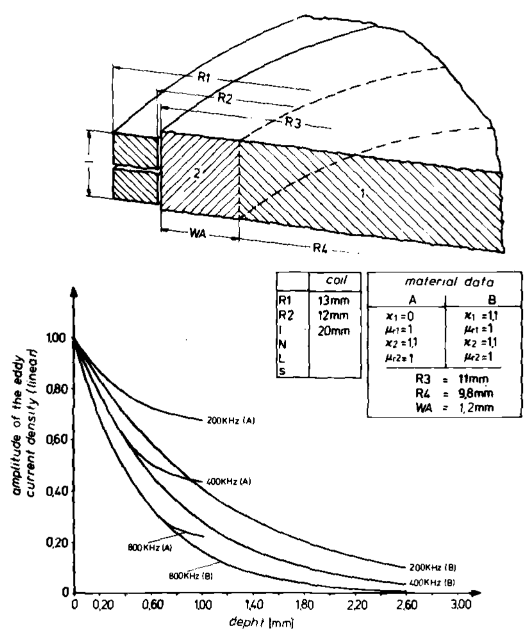

FIG. 6—*Amplitude of the eddy-current density in an austenitic tube and in an austenitic bar calculated for a coaxial outside coil.*

side diameters of the tubes. The effects of the ferritic tube sheet and of an annular austenitic tube support plate can be simulated in the computer program by the material data for a second layer. All parameters appearing in the list in the right half of Fig. 7 ($R1$, $R2$ = inner and outer radius of the coil; L = length of the coil; N = number of turns; L = inductance; s = diameter of

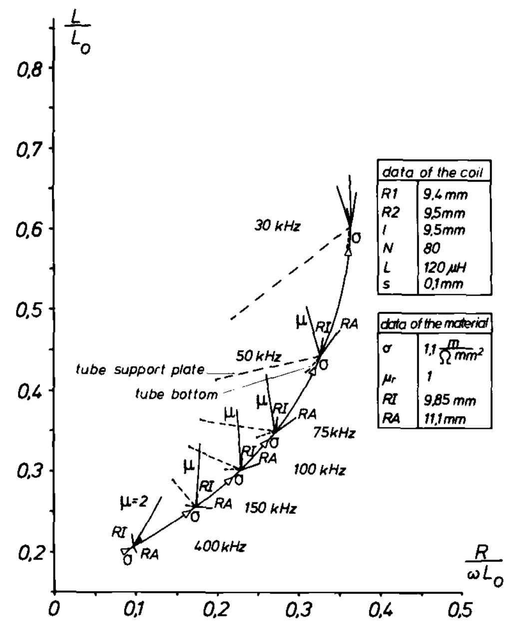

FIG. 7—*Impedance of a coaxial inside coil in an austenitic tube (calculated).*

the wire) are input parameters. They can be varied to gain a complete picture of static effects in tube testing.

Multifrequency Test Equipment [5]

To solve the aforementioned problems, we had to employ a multifrequency or multiparameter approach such as was originally published by Libby [6]. We therefore developed and built a set of multifrequency equipment. A fully developed prototype now exists that is suitable for field use (Fig. 8).

In contrast to the normal concept, where several test frequencies are fed into the coil simultaneously and processed in parallel channels, we have used a multiplexing concept. The principle is shown in Fig. 9. The frequencies are changed step-by-step in sequence with such rapidity that the time needed for one cycle is so short that, depending on the scanning speed, the test parameters remain unchanged. The lowest frequency limits testing speed.

Provided that the clock frequency is sufficiently high, both concepts yield the same results. But with regards to implementation and general flexible applicability the multiplexing concept has some advantages: (*1*) the cost of the electronics is independent of the number of frequencies, (*2*) the frequencies can be tuned continuously and over a wide range (there is no need for band filters), and (*3*) there is no crosstalk between the frequency channels.

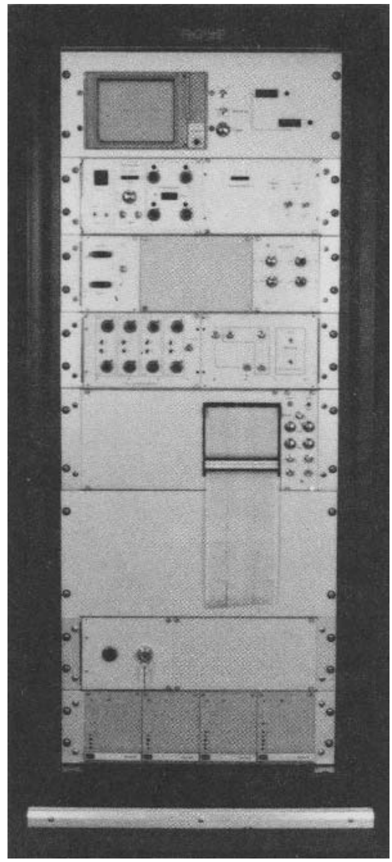

FIG. 8—*Multifrequency test equipment.*

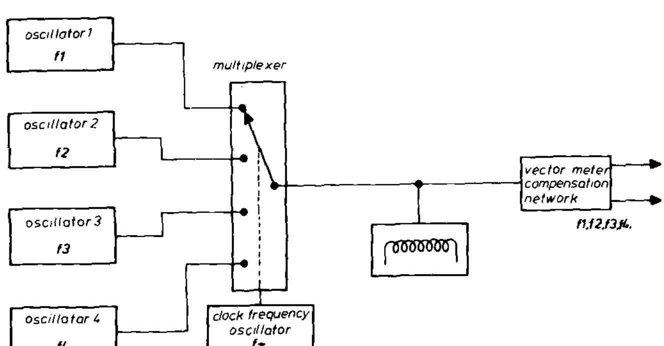

FIG. 9—*Multiplexing concept.*

Figure 10 shows a simplified block diagram of the prototype. In Fig. 11 the frequency control is shown separately. Four variable d-c voltages are fed into the VCO-input of a generator. By varying the voltages, the four testing frequencies can be adjusted in the range of 50Hz to 1 MHz. The testing frequency generator gives two output voltages with a phase shift of 90 deg to one another. The multiplexer is controlled by the clock frequency oscillator.

The output voltage of the testing frequency generator drives a current source that applies a constant current to the coil. The amplitude and phase of the voltage in the coil is affected by the properties of the specimen. The complex voltage at the coil is divided into a real and an imaginary part.

The further processing of the two components of the voltage in the coil is performed digitally. First, there is a network to compensate a given voltage at the coil and to set any zero point in the impedance plane. The network that

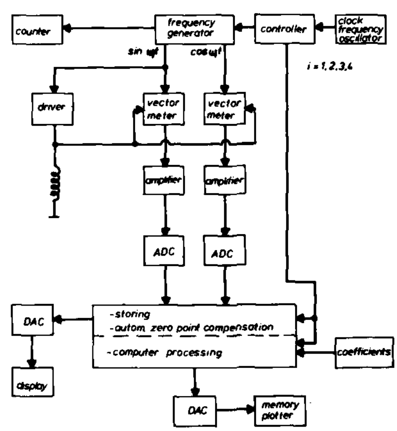

FIG. 10—*Block diagram of a multifrequency eddy-current system.*

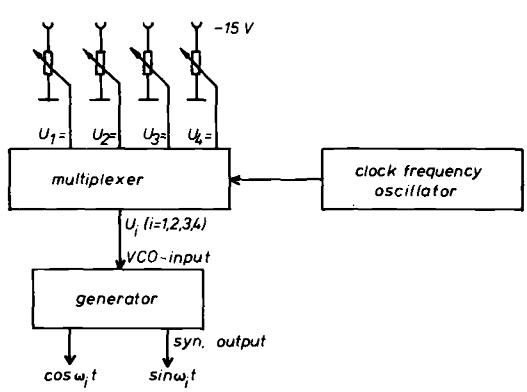

FIG. 11—*Frequency control.*

follows performs the suppression of the disturbing signals. This network is controlled by a micro-processor and is composed of fast computer modules that execute additions and multiplications.

Multifrequency Approach [7]

The algorithm applied to suppress the disturbing signals is illustrated in Fig. 12 with regards to a particular example. The task is the detection of defects in a heat exchanger tube. Disturbing signals are caused by the tube sheet and by variations in the diameter of the tubes. A general rule states that to suppress the signals of n disturbing parameters at least $n + 1$ independent measured values are necessary. In our example, therefore, we need three independent measured values which can be the real and imaginary part of the voltage at the first frequency and the real or imaginary part of the voltage at the second frequency. These measured values produce a three-dimensional vector space; its coordinates are plotted in Fig. 12. The calibration of the multifrequency system must be performed as a first step. The zero point for the measurement must be a specific point on the tube where no disturbances exist. Now the coil is brought to a position below the tube sheet outlined on the left of Fig. 12. The changes in measured values relative to the zero point form the three-dimensional vector $\vec{P}_R$. In the same way the measured values at a position shown at the top of Fig. 12, where the diameter of the tube is

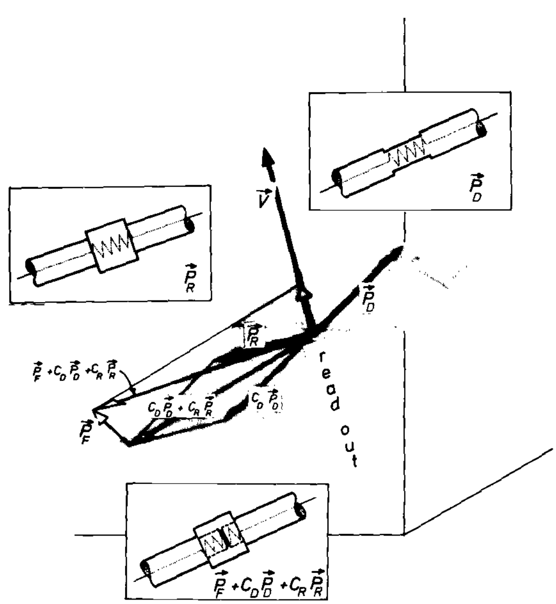

FIG. 12—*Principle of the multifrequency method.*

decreased, give the vector $\vec{P}_D$. The two vectors define in the three-dimensional space a plane colored gray in Fig. 12. In this plane lie all measured vectors that are caused by the two disturbing parameters in any combination and superposition. The size of the change in the disturbing parameters is expressed by the coefficients c_R and c_D. Obviously, the coefficient c_R can only have the two values 0 or 1. In a computing step consisting of solving a linear equation system, the read-out vector $\vec{V}$ is determined so that it is perpendicular to the plane of the disturbing parameters.

Once vector $\vec{V}$ is known the calibration stage is finished. Now testing can be carried out where the measured values obtained during the performance of the actual test are projected onto the read-out vector $\vec{V}$. In the worst case, at the bottom of Fig. 12, we have two disturbing signals superimposed on the defect signal $\vec{P}_F$ simultaneously. When performing the projection, however, the effects of the disturbing parameters are suppressed and only a defect signal is read.

Optimization of the Testing Frequencies [8]

It can be seen from Fig. 12 that the algorithm described not only suppresses the signals caused by the disturbing signals, but also reduces the defect signals to a greater or lesser degree. An indication of the projection losses is given by the angle α between the defect vector P_F and the read-out vector V. This angle is a function of the applied testing frequencies. A frequency combination is therefore optimum when the angle α is as different from 90 as possible. Since there are so many frequency combinations that must be examined, especially when a high number of frequencies is needed, we have developed a computer program that performs the choice of the frequencies automatically. By applying the method described previously, we determine numerically the relevant disturbing vectors as a function of the testing frequency and the coil dimensions. In this way, and by measuring a reference defect vector, the angle α is computed for all possible frequency combinations. Figure 13 shows the results for a particular example in the field of heat-exchanger testing. To suppress the disturbing signals caused by the tube plate and tube support plate and by variations in the conductivity of the tubes we must apply three frequencies. In the suitable frequency range of 30 to 400 kHz, we designate the nine possible frequencies (listed on the right of Fig. 13). Next to the frequency table are given the material properties and the coil data (σ = electric conductivity, μ = relative magnetic permeability, R_I and R_A = inside and outside diameters of the tubes, R_1 and R_2 = inside and outside diameters of the coaxial coil, l = length of the coil, N = number of turns, L = inductance, s = diameter of the wire). Diagonally across the figure are shown tables with squares. The trios of numbers in the squares characterize the frequencies of the corresponding combinations. The table at the left contains all combinations with the first frequency, the following table

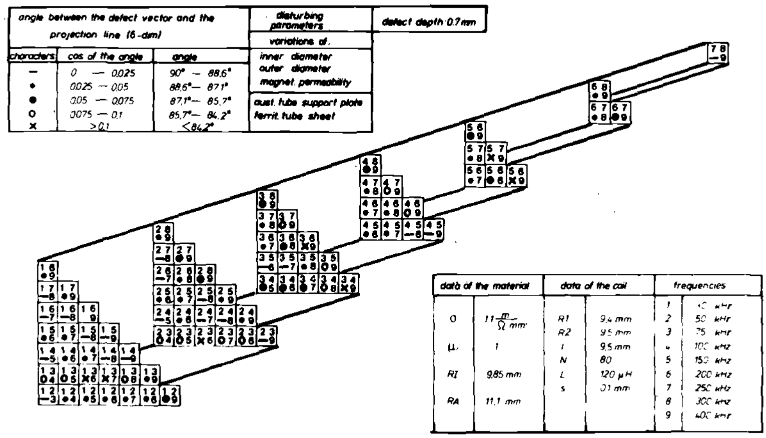

FIG. 13—*Valuation of the combinations of test frequencies in tube testing by means of inner coils (three frequencies).*

the combinations with the second frequency, etc. Beside the numbers in each square a sign appears which quantifies the ability of the relevant frequency combinations. The signs are set out on the left at the top in Fig. 13 and correspond to the angle α. The testing frequencies with the smallest projection losses and therefore with the best defect detection limit are marked by crosses. The result shown in Fig. 13 applies to an artificial slit on the outside of the tubes with a depth of 0.7 mm. The wall thickness of the tube is 1.3 mm.

Results and Discussion

Testing of Welds

A ferritic specimen clad with an austenitic steel is shown on the right-hand side of Fig. 14. Two pulsed fatigue cracks are present in the weld. At precisely these points, the distortions caused by changes in the material (σ and μ) and lift-off are especially pronounced. The testing is carried out with an absolute pickup coil which is moved over the surface in a number of passes.

The results of testing with one frequency (100 kHz) and with two frequencies (100 and 300 kHz) are compared on the left-hand side of Fig. 14. Slits of different depths are used to assess the depths of the defects. The signals caused by these slits are shown on the left of the plots, followed by signals that appear during an inspection pass over the actual specimen. It can be seen that at the bottom of the plot the disturbing signals are markedly reduced; the remaining signals have the same indication peak as a slit of 0.5 mm depth. The pulsed fatigue cracks give signals that correspond to a slit of 3 mm depth.

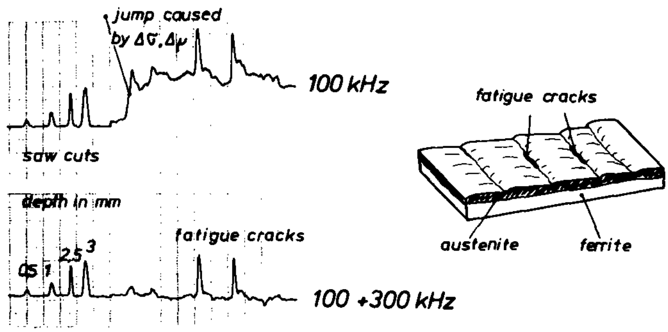

FIG. 14—*Inspection of a cladding surface.*

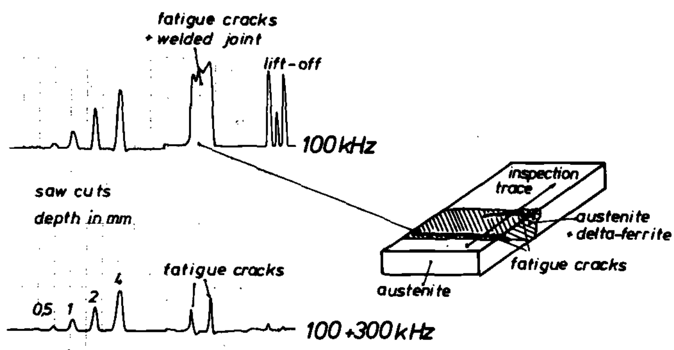

FIG. 15—*Inspection of an austenite welded joint.*

Figure 15 shows the results of testing an austenitic welded joint. The properties of the weld and the base material differ. The two pulsed fatigue cracks indicated in the welded joint are measured. The signals caused by saw cuts are first shown on the left of the plots, followed by signals in an inspection pass which crosses both cracks in the welded joint. The signals caused by the cracks are totally masked if the testing is performed with only one frequency (100 kHz), whereas they are clearly read out if the testing is performed with two frequencies (100 and 300 kHz). The disturbing signals caused by the weld are suppressed as well as those caused by lift-off. The remaining disturbing signals have the same indication peak as a saw cut of 0.5 mm depth. The pulsed fatigue cracks are indicated by signals of different heights related to their different depths; they produce the same signals as slits of 2 and 3 mm depth.

Figure 16 shows the results of testing a ferritic welded joint with two natural surface cracks. In the area of the weld the specimen is scanned in several passes. The plots show on the left the signals caused by the slits, followed at the top by the signals caused by defect 1, which is indicated four

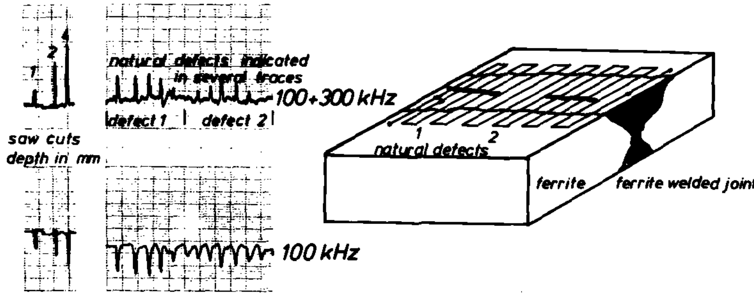

FIG. 16—*Inspection of a ferrite welded joint.*

times corresponding to the four passes that cross it. After this one can see defect 2, which is indicated at first with increasing and then with decreasing depth. The plot at the top is the result of testing with two frequencies. In contrast, if the testing is performed by means of one frequency, as shown at the bottom of the plots, incorrect defect depths are indicated and defect responses appear where no defects are present. Thus, defect 1 is indicated with the same height as a saw cut of 4 mm depth, whereas if two frequencies are used, it is assessed as a slit of 1.5 mm depth.

Testing of Heat-Exchanger Tubes

The testing is performed with an absolute coaxial inside coil which is moved through the tubes. Figure 17 shows the results obtained with frequencies of 75, 200, and 400 kHz. At the bottom of Fig. 17 the defect signals have superimposed on them disturbing signals caused by the tube sheet, the tube support plate, variations in the inside and outside diameters of the tubes, and coil wobble. After the processing of the signals obtained at the three frequencies, the upper plot in Fig. 17 indicates only defect signals. The indications of three slits (0.85, 0.7, and 0.4 mm depth, 0.5 mm width, 1.2-mm wall thickness of the tubes) located in the exposed part of the tubes and below the tube sheet and tube support plate appear three times.

Figures 18 indicates the defect detection limit in the same application. The plots show (*1a*)—disturbing signals caused by the tube sheet, the annular and the grid shaped tube support plate; (*1b*)—the residual background of disturbing signals after processing; (*2a*)—disturbing signals as in *1a*, but superimposed on defect signals; (*2b*)—the same signals as in *2a*, but after the suppression of the disturbing signals. The defects are outside slits lying in the axial direction of the tubes; their depth relative to the wall thickness is shown in Fig. 17; and (3)—defect signals from outside slits lying in the circumferential direction of the tubes. The results show that the 30 percent axial and the

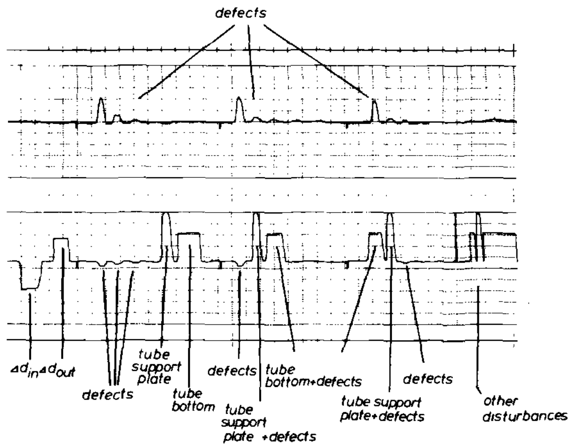

FIG. 17—*Testing of a heat-exchanger tube with absolute inner coil. Frequencies: 75, 200, and 400 kHz.*

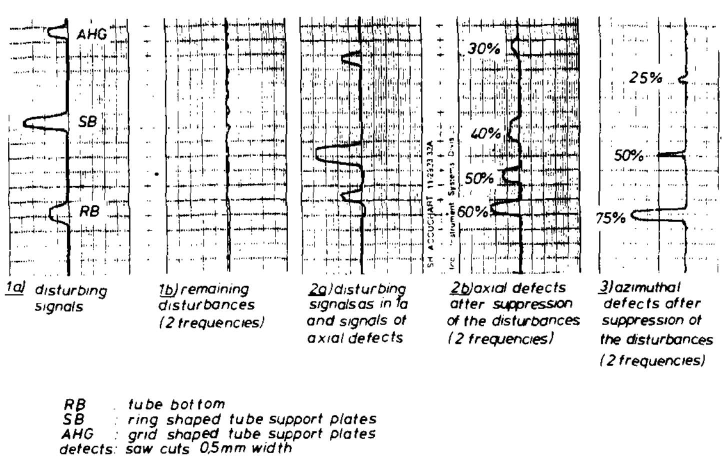

FIG. 18—*Detection limits in heat-exchanger tube testing with a multifrequency system.*

25 percent circumferential slits can be detected with certainty even when they are located below the tube sheet or tube support plate. It should be emphasized that in all cases an absolute coil is used.

Acknowledgments

This work is supported by the German Ministry for Research and Technology within the scope of the reactor safety research program.

References

[1] Förster, F. and Stambke, K., *Zeitschrift für Metallkunde,* Vol. 45, 1954, pp. 166–179.
[2] Dodd, C. V., *International Journal of Nondestructive Testing,* Vol. 1, 1969, pp. 29–90.
[3] Betzold, K. and Becker, R., "Theoretische und numerische Untersuchungen zur Wirbelstromprüfung geschichteter Materialien mit Abtastspulen gegebener Abmessungen," Technical Report No. 760501-TW, Fraunhofer-Institut für zerstörungsfreie Prüfverfahren (IzfP), Saarbrücken, 1976.
[4] Betzold, K., "Theoretische und numerische Untersuchungen zur Wirbelstromprüfung geschichteter Materialien mit koaxialen Innenspulen und Außenspulen," Technical Report No. 780725-TW, IzfP, Saarbrücken, 1978.
[5] Becker, R., Regneri, L., and Rüdiger, R., "Mehrfrequenz-Wirbelstromprüfung; Phase 1 Aufbau eines Mehrfrequenz-Geräteprototyps," Technical Report No. 780120-TW, IzfP, Saarbrücken, 1978.
[6] Libby, H. L. in *Research Techniques in Nondestructive Testing,* Vol. 1, R. S. Sharpe, Ed., Academic Press, London, 1970, Chapter 7.
[7] Becker, R. and Regneri, L., "Anpassung des Wirbelstromverfahrens für den Einsatz an Reaktoren," Technical Report No. 780832-TW, IzfP, Saarbrücken, 1978.
[8] Betzold, K. in *Proceedings*, First European Conference on Non-Destructive Testing, Mainz, 1978, Vol. 1, pp. 189–198.

C. V. Dodd[1] *and W. E. Deeds*[1]

In-Service Inspection of Steam-Generator Tubing Using Multiple-Frequency Eddy-Current Techniques

REFERENCE: Dodd, C. V. and Deeds, W. E., "**In-Service Inspection of Steam-Generator Tubing Using Multiple-Frequency Eddy-Current Techniques,**" *Eddy-Current Characterization of Materials and Structures, ASTM STP 722,* George Birnbaum and George Free, Eds., American Society for Testing and Materials, 1981, pp. 229–239.

ABSTRACT: Although a rapid, accurate, and easy-to-use inspection method for steam-generator tubes is clearly needed, it is not entirely provided by our present eddy-current tests. The signals from eddy-current tests are affected by changes in tube wall thickness, the location and size of defects, the electrical conductivity, the magnetic permeability, and the tube-to-tube support spacing and denting (which changes the probe-to-tube spacing). Simultaneous variations in these test properties produce signals that are ambiguous in present commercial eddy-current instruments.

However, this type of multiple-property eddy-current testing can be done using pulsed techniques or, as in this example, multiple frequencies. A systematic, automated process has been developed at Oak Ridge National Laboratory (ORNL) to allow rapid development of accurate multiple-property eddy-current tests. It consists of the following steps:

1. Using a computer to design the coil, instrument, and operating conditions that give the best determination of the desired properties from a nonlinear combination of instrument readings.
2. Constructing the coil and instrument and testing with calibration specimens.
3. Using a large digital computer to take on-line instrument readings and perform the nonlinear property calculations.
4. Programming the on-board microcomputer in the instrument to perform the property calculations in the field.

The system has demonstrated a considerable improvement in the ability to measure wall thickness, tubing inside diameter, defect size, and defect location even in the presence of severe denting using laboratory standards. We are now proceeding with field testing of the instrumentation.

KEY WORDS: eddy current, steam generator, tubing inspection, multiple frequency, defect detection, wall thickness, tube supports

Because the cost and demand for energy are increasing, we need to get as much use as possible from our steam generators by minimizing down time and loss of efficiency. A fast, accurate inspection method is needed that can be performed during normal plant maintenance. Of the presently available

[1]Physicist, Oak Ridge National Laboratory, Oak Ridge, Tenn. 37830.

methods of nondestructive testing, eddy-current inspection most nearly meets this need.

Eddy-current tests are affected by variations in a large number of the properties of the object being tested, such as material conductivity, permeability, geometry, thickness, and the presence of defects. Other variables in the test include the distance and orientation between the probe and test object. In order to perform accurate eddy-current measurements of a particular set of test properties, we must eliminate the effects of the other test property variations on this set. This can be done either by (*1*) controlling the variation of the undesired properties so that they do not cause any significant effects on the properties that we wish to measure or (*2*) measuring the effects of the undesired property variations and correcting the values of the desired properties for these effects. For steam generator inspection, we are not allowed to modify the design of the generators, so therefore we must accept all the unwanted property variations and measure the others in their presence.

At Oak Ridge National Laboratory (ORNL), we have developed a procedure for analyzing this type of multiple-property problem. It consists of the following steps:

1. Determine the best coil and instrumentation system using theoretical calculations of the instrument readings from the test properties.
2. Construct the system and verify the design calculations from actual readings on test standards.
3. Perform an inspection in the lab by use of a large minicomputer to calculate the test properties.
4. Program an on-board microcomputer and make the measurements in the field.

We are applying this method to the steam-generator inspection problem, which is a very severe example of multiple-property problems.

Test Property Variations in Steam-Generator Tubing

A number of variables in a steam generator produce signal changes in an eddy-current test. Some are shown in Fig. 1. The steam generator consists of many lengths of tubing that are fixed at the ends to a tubesheet and anchored (or restrained) at intervals by tube supports. The tubing is usually thin wall (less than 10 percent of its diameter) and can be inspected from the bore side when the generator head is removed. We shall limit ourselves to nonferromagnetic tubing with high electrical resistivity, such as Inconel 600 or Type 304 stainless steel. The properties that vary and can affect the readings are (*1*) defect size, (*2*) defect location in the tube wall, (*3*) tube wall thickness, (*4*) tube-to-tube-support distance, and (*5*) coil-to-tube distance. Generally, we are most concerned about measuring the properties at the beginning of this

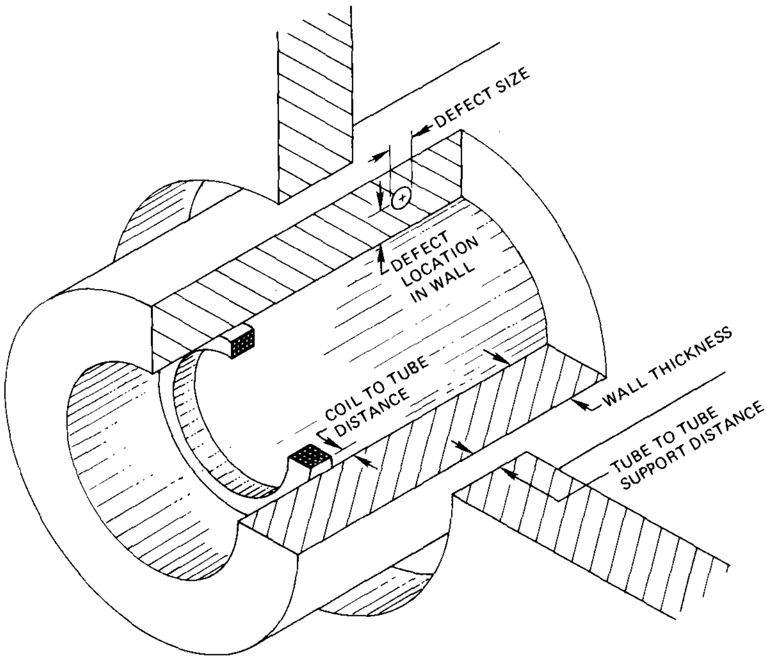

FIG. 1—*Test properties that vary during a steam-generator inspection.*

list, but the properties toward the end of the list produce the largest signal changes.

When the eddy-current coil is not close to the tube support or the tubesheet regions, the inspection is relatively easy. Unfortunately, it is in those very regions that defects are most likely to occur. A nonconductive ferromagnetic layer of iron oxide, or magnetite, may form between the tube support and tube. If this layer grows, it constricts the tube, producing dents, and this dented region beneath the tube support is very susceptible to cracks because of the increased stresses. Thus, the region of greatest concern is the region where all the test properties are varying.

Analysis of the Eddy-Current Problem

We are able to calculate the magnitude and phase of the eddy currents produced by a probe in the presence of multiple-cylindrical conductors [*1*],[2] as shown in Fig. 2. The general case shown in Fig. 2 can be reduced to a single absolute coil inside a steam generator tube, as shown in Fig. 1, with

[2]The italic numbers in brackets refer to the list of references appended to this paper.

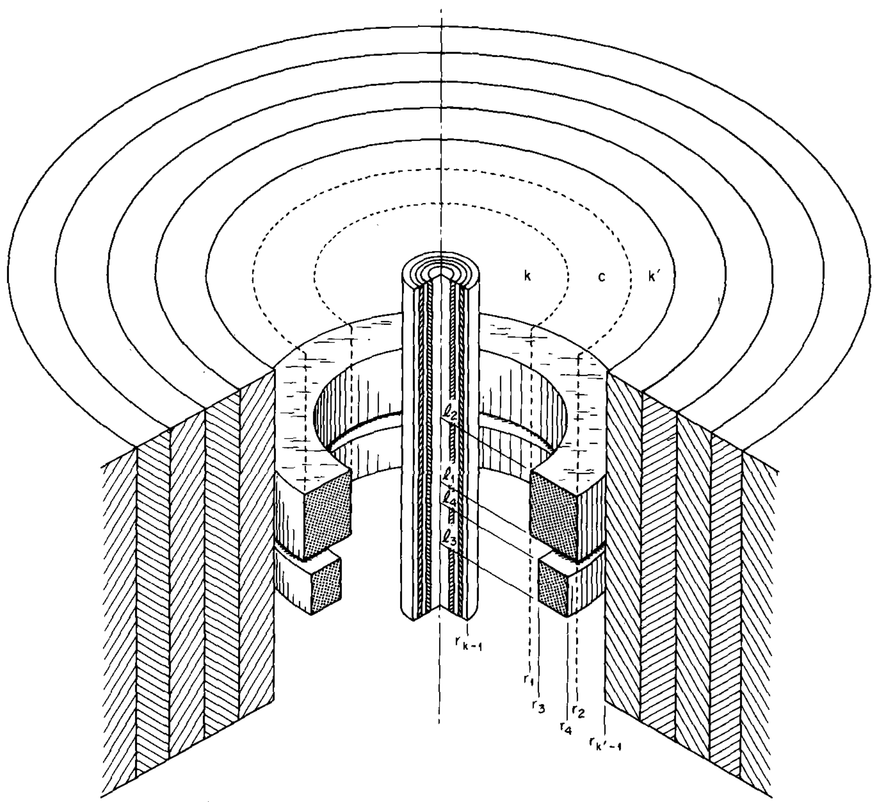

FIG. 2—*Multiple-cylindrical conductors encircling and encircled by two coils in the same radial region.*

one exception. The conductor boundaries can only run coaxial with the tube, not in a plane perpendicular to the tube axis. Therefore, the tube support or tubesheet must completely cover the coil or be entirely gone. Our calculation methods, as they now exist, cannot consider the "edge effect" as the tube support is moved over the coil. These effects are included in the experimental measurements. The effects of wobble of the probe in the tube and of the tube in the tube support have been experimentally shown to contribute no significant error. Our program, ENCIRM, can calculate the magnitude changes and phase shift of the voltage in an eddy-current coil to within about 0.01 percent for changes in the tube inside diameter, tube wall thickness, tube support dimensions, and electrical conductivity. The signal changes due to permeability changes of the tube support can be calculated to within about 1 percent and the effects of small defects to within 15 percent. It should be noted that small defects produce a small change in signal and are difficult to measure accurately. The signals from larger and irregularly shaped defects can be estimated by dimensional analysis.

By using these analytical techniques we are able to calculate the instrument readings for a given set of test properties. What we really desire, however, is the inverse of this, that is, to determine the test properties from our instrument readings. We shall now consider a least-squares technique that allows us to accomplish this.

Least-Squares Fit of Properties to Readings

If we have a series of independent equations containing unknowns, we can solve for the unknowns with standard algebraic techniques. If the relationship is between test properties, p_i, and instrument readings, r_j, the equations may appear as

$$r_1 = c_{11}p_1 + c_{12}p_2$$

$$r_2 = c_{21}p_1 + c_{22}p_2$$

We can solve for these two properties in terms of the two readings. The coefficients must be determined either by experimental measurements or theoretical calculations. This is done by varying the property over its expected range and calculating or measuring the readings. We may use the readings directly or use nonlinear functions of the readings, as well as various cross terms between the readings. The readings may be the magnitude and phase at each of several frequencies or the magnitude of a pulse at various time intervals. According to information theory, we have two independent readings for each separate frequency, and the information obtainable by using multiple-frequency and pulse techniques is the same with only the instrumentation being different. Pulse systems are simpler and cheaper, but noiser. We have had much more experience and done more independent development with multiple-frequency instrumentation, so we have concentrated on this type. The only actual requirements are that we have at least as many instrument readings as we have test properties and the frequencies are far enough apart so that the readings vary in a different manner with the properties.

We can represent the equations between the readings and the properties in matrix notation as

$$\bar{r} = \bar{\bar{c}}\,\bar{p}$$

and the notation for the solution as

$$\bar{p} = \bar{\bar{c}}^{-1}\,\bar{r}$$

where $\bar{\bar{c}}^{-1}$ denotes the inverse of the matrix $\bar{\bar{c}}$.

Generally, when we initially determine the coefficients, we have many more sets of equations between the readings and the properties than we actually need, resulting in an overdetermined system. The overdetermination allows us to minimize the errors caused by inaccuracies of measurement or calculation and by inaccuracy in the assumed functional dependence of the properties on the readings.

We shall consider the calculation of only one property at a time, the property p_n. This property will be determined while all of the other properties are varying over their entire range. We can write an equation for each of m sets of property values as

$$p_{nm} = \sum_{i=1}^{I} r_{mi} c_{in}$$

where we are summing the product of the r_i readings times the c_i coefficients for each set of m property values. If we have five properties, and take three values for each property (maximum, minimum, and nominal), m would be 3^5 or 243. The readings can be an actual reading, such as magnitude or phase, or "constructed" readings, consisting of polynomials of various functions of the readings, each with a different coefficient. Since our equation will not be exact, we shall rewrite it to include an error term, e_m, as

$$p_{nm} - \sum_{i=1}^{I} r_{mi} c_{in} = e_{mn}$$

or in matrix notation

$$\bar{p}_n - \bar{\bar{r}}\,\bar{c}_n = \bar{e}_n$$

This is the least-squares problem, and we wish to determine $\bar{c}$ *so that* $\bar{e}$ will be minimum. There are a number of standard computer programs to perform this calculation and determine the coefficients that give the least error [*2*].

This process may be repeated with different sets of readings constructed from the magnitudes and phases until the set of coefficients that best describes the property from the reading is determined. Many intermediate values of a given property can be taken, and one large range can be broken up into several smaller ranges to get a better fit. The response of an eddy-current instrument reading is quite nonlinear, and these techniques are often necessary to obtain a good fit. Our present computer programs will allow property sets as large as 1000 to be fitted although the round-off error increases as the number of property sets increases.

The least-squares fits have been applied first to the calculated readings in the design of the tests. The calculations were performed on a ModComp IV minicomputer using the program ENCIRM to calculate the readings from the properties for different coil and instrument parameters at three different frequencies chosen from eight in the range of 5 kHz to 1 MHz. The properties were then fitted to the readings using over 1000 different combinations of nonlinear functions of each of the 56 possible reading combinations. The program LSQENC performed these fits and printed out a summary of the results.

When an adequate design had been achieved according to the calculations, we constructed the needed instrumentation and repeated the tests using experimental measurements. We used the computer program TUBRDG [*3*] to make the experimental readings and the program TUBFIT to perform the fits. A summary of these results is presented in Table 1. We have also included an estimate of the present commercial capability made by Battelle Columbus Laboratories in the table for comparison [*4*]. The results obtained are very dependent on the range of property variations that is considered and get worse as the range is increased. The denting range was from 0.00 and 0.25 mm (0.01 in.) for the commercial measurements and 0.00 to 1.27 mm (0.050 in.) for the ORNL study. All the results have been "standardized" to a 4.76-mm (0.1875-in.)-diameter hole. The tubing in this study is Inconel 600 with 22.2-mm (0.875-in.) diameter and 1.3-mm (0.051-in.) wall thickness. The commercial measurements were performed at a single 400-kHz operating frequency, and the ORNL measurement used frequencies of 10 kHz, 100 kHz, and 1 MHz. The ORNL results are independent of probe motion and made with the probe directly over the defect. Some improvement in the detection of small defects may be achieved by including the effects of motion. The ORNL accuracy figures are the statistical root mean square error.

TABLE 1—*Accuracy of property measurements by eddy-current methods.*

Property Measured	Depth of 4.76-mm-diameter Flat-Bottomed Hole, mm (in.)	Tube Wall Thickness, mm (in.)	Tube ID (denting measurement), mm (in.)
Present commercial capability (approximate)	0.76 (0.030)	0.13 (0.005)	0.03 (0.001)
Total support-plate range			
ORNL calculated (standard deviation)	0.15 (0.006)	0.01 (0.0002)	0.01 (0.0002)
Measured (standard deviation)	0.18 (0.007)	0.01 (0.0002)	0.01 (0.0002)
Incremental support-plate range			
ORNL calculated (standard deviation)	0.02 (0.0006)	0.01 (0.0002)	0.01 (0.0002)
Measured (standard deviation)	0.03 (0.0012)	0.01 (0.0002)	0.01 (0.0002)

The design calculations were performed first with the tube support-plate inside diameter varying from a snug fit on the tube to completely away from the tube; that is, the range of clearances was from zero to infinity. Next the tube support-plate inside diameters were varied over several smaller partial ranges, particularly over limited ranges near the maximum and minimum clearances. The results for defect detection are considerably improved when the tube support plate is allowed to vary only over a limited range of inside diameters. This improvement is needed to allow more reliable detection of small defects. The measured results shown for the smaller "incremental" ranges were performed only for support-plate clearances near the maximum and minimum values because we do not have all the necessary standards yet, and these measurements require very careful positioning of the probe, defect, and tube support. We are constructing numerically controlled positioners to give more accurate and faster measurements.

We have also made a series of measurements as the tube support was moved past the probe for various combinations of wall thickness and tubing inside diameter (but not defects). The accuracy figures for wall thickness and tube inside diameter were the same as those in Table 1.

The measurements and back calculations of the properties from the readings were made with the ModComp IV minicomputer. It is impractical to use this system in the field. We shall now discuss the instrumentation designed for the field testing.

Instrumentation for Steam-Generator Inspection

The ideal instrument for inspection of steam-generator tubing should be accurate, reliable, lightweight, completely automatic, easily shipped, and low in power consumption. No instrumentation completely fills these needs, and none probably ever will, but we are constructing an inspection system at ORNL with these goals in mind. The system is based on the ORNL three-frequency eddy-current instrument [5], shown in the block diagram in Fig. 3.

The instrument drives a single absolute coil, through a dropping resistor, with three different frequencies. The output frequencies are separated by band-pass amplifiers. The magnitude at each frequency is measured to an accuracy of about 0.02 percent and the phase to about 0.01 deg. The demodulating computer, a microcomputer contained in the eddy-current instrument, is used to calculate the properties by evaluating an equation such as

$$\begin{aligned}\text{Prop} = C_0 &+ C_1 Ph_1 + C_2 Ph_1^2 + C_3 M_1 + C_4 M_1^2 + C_5 Ph_1 M_1 \\ &+ C_6 Ph_2 + C_7 Ph_2^2 + C_8 M_2 + C_9 M_2^2 + C_{10} Ph_2 M_2 \\ &+ C_{11} Ph_3 + C_{12} Ph_3^2 + C_{13} M_3 + C_{14} M_3^2 + C_{15} Ph_3 M_3\end{aligned}$$

where Ph_i is the phase and M_i is the magnitude at the ith frequency.

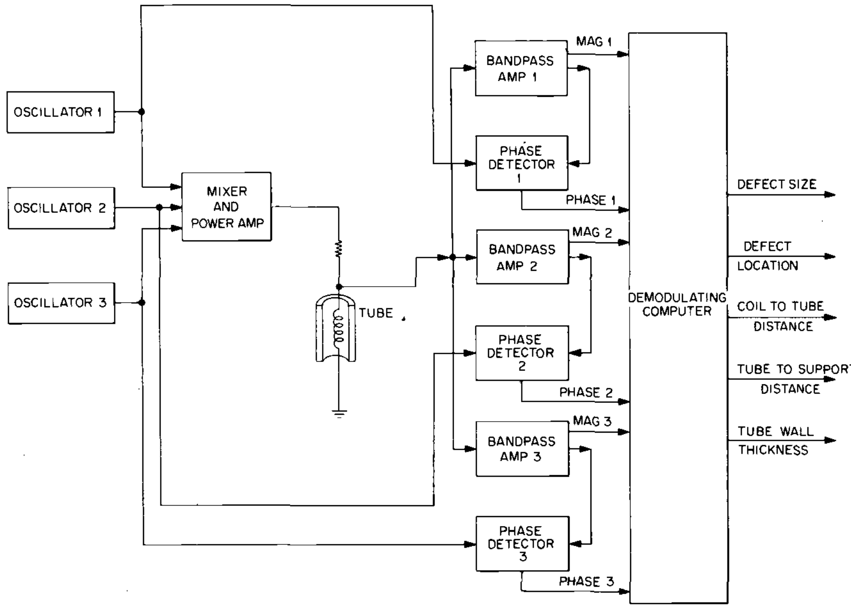

FIG. 3—*Block diagram of a three-frequency instrument.*

This equation with $C_0 = 0$ is the one most often used for the property evaluations. The coefficients are determined by the minicomputer from the least-squares fits of the readings to the standards and written into the programmable read-only memory of the microcomputer. The instrument also contains a calibrator, which consists of passive RLC networks that produce an accurate set of known magnitude and phase shifts. This network is switched into the circuit by the minicomputer, and a set of calibration readings is made before and after the measurements of the standard properties. These calibration readings are also stored in the microcomputer memory. The microcomputer has a program that will do a recalibration. It takes a set of calibration readings, calculates an offset and gain correction factor for each magnitude or phase data channel by a least-squares fit of the present calibration to the initial calibration, and stores this in the memory.

Each magnitude or phase is measured by the use of a separate 12-bit integrating analog-to-digital converter that has an adjustable conversion time. The converters are adjusted to 16.7 ms now to minimize any 60-Hz noise that the probe may pick up. The present microcomputer, an NDT-COMP9, designed and built at ORNL [*6*], can start a set of readings, perform three sets of property calculations, and store the data on magnetic tape in about 18 ms. Versions of the microcomputer components that work at twice the present clock speed are available, but the system noise may increase with the increased measurement speeds.

The data are recorded on digital magnetic tape, recorded on a strip-chart recorder, and can be sent to a serial terminal device (although the serial device will slow down the operation considerably). A variable-speed dc-motor-driven probe positioner is presently being used, but is being replaced with a stepping-motor system. The present system is shown in Fig. 4.

FIG. 4—*Eddy-current inspection system for steam-generator tubing.*

The microcomputer will insert the probe, do a recalibration, withdraw the probe from the tubing while making readings, make a final calibration reading, and store all the data on tape. We are continuing to make improvements by reducing the system weight and increasing the reliability, accuracy, and speed.

Summary and Conclusions

The inspection of steam-generator tubing with eddy-current techniques is a very difficult but important problem. The multiple-property design approach has the potential to solve this problem but introduces more complexity to the instrumentation. Any test properties that cause significant variations in the instrument readings will have to be included and eliminated. Unexpected property variations may cause significant errors in the results. Tests using the equipment should be performed in the field on used steam generators, and further suggestions should be solicited from other users.

Acknowledgments

This research was sponsored by the Office of Nuclear Regulatory Research, Nuclear Regulatory Commission, under Interagency Agreement No. DOE 40-551-75 with the U.S. Department of Energy under Contract W-7405-eng-26 with the Union Carbide Corporation.

References

[1] Nestor, C. W., Jr., Dodd, C. V., and Deeds, W. E., "Analysis and Computer Programs for Eddy-Current Coils Concentric with Multiple-Cylindrical Conductors," ORNL-5220, Oak Ridge National Laboratory, July 1979.

[2] Wampler, W. H., *Journal of Research*, National Bureau of Standards, Vol. 73B, No. 2, 1969, p. 59.

[3] Deeds, W. E. and Dodd, C. V., "Evaluation of Multiple-Property Variations in Coaxial Cylindrical Conductors with Multiple-Frequency Eddy Currents Using Experimental Measurements," ORNL/NUREG/TM-335, Oak Ridge National Laboratory, Nuclear Regulatory Commission, Nov. 1979.

[4] Brown, S. D. and Flora, J. H., "Evaluation of the Eddy-Current Method for the Inspection of Steam-Generator Tubing Denting," BNL-NUREG-50743, Brookhaven National Laboratory, Nuclear Regulatory Commission, 30 Sept. 1977.

[5] Dodd, C. V. and Chitwood, L. D., "Three-Frequency Eddy-Current Instrument for Multiple-Property Problems," ORNL-5495, Oak Ridge National Laboratory, March 1979.

[6] Dodd, C. V. and Cowan, R. F., "The NDT-COMP9 Microcomputer," (report, in preparation).

H. T. Yeh[1]

Transient Eddy Current in Magnet Structure Members

REFERENCE: Yeh, H. T., "**Transient Eddy Current in Magnet Structure Members,**" *Eddy-Current Characterization of Materials and Structures, ASTM STP 722,* George Birnbaum and George Free, Eds., American Society for Testing and Materials, 1981, pp. 240–254.

ABSTRACT: A computer program was developed to model transient eddy current in thin connected plates. Eddy current is deduced from the solution of an equivalent-network problem. Loop currents are introduced by a transformation as the unknown variables of the network equations (Kirchoff's laws). The network equations are solved numerically by the Runge-Kutta method. This program is quite efficient, allows for holes and multiple materials, and has built-in rotational symmetry options. In cases with known solutions, the model has been checked for both spatial and temporal profiles of the eddy current. Results are given for eddy-current profile and eddy-current loss in the magnet case, support plate, and several other magnet structure members.

KEY WORDS: eddy current, transient, eddy current loss, lumped circuit, network, magnet structure

Because a pulse field is present in tokamak-type fusion devices,[2] it is necessary to determine the eddy current induced in the magnet structure and vacuum vessel in order to ensure adequate coolant and mechanical support. The conductor generally comprises connected thin shells or plates with large-angle bends. There may be holes or multiple materials in the conductor.

In some of our earlier work,[3] we approached eddy-current determination with an integral equation formulation. The resulting computer program proved expensive to use, however, for applications such as eddy current loss in a magnet case because the program assumes eddy current to be constant in each element. To reveal a drastic local change in current, such as occurs when the current bends around a corner, small elements are required; thus,

[1] Research staff, Oak Ridge National Laboratory, Oak Ridge, Tenn. 37830.

[2] Roberts, M. and Bettis, E. S., "Oak Ridge Tokamak Experimental Power Reactor Study—Reference Design," ORNL/TM-5042, Oak Ridge National Laboratory, Oak Ridge, Tenn., November 1975.

[3] Yeh, H. T., "Computation of Transient 3D Eddy Current in a Nonmagnetic Conductor," *Proceedings,* Conference on the Computation of Magnetic Field, Grenoble, France, September 1978.

a large portion of the computational effort is spent to meet boundary condition requirements. This method would likely be much more efficient if linear or higher-order elements were used.

This paper discusses the use of a lumped circuit approach.[4,5] In this approach eddy current is assumed to flow in a network that is consistent with the conductor geometry. Because the construction of the network can be arbitrary, however, the network solution does not represent the actual eddy current in the conductor. The actual eddy current in each element must be interpolated from the current obtained through solving the equivalent-network problem. Our use of quadrilaterals in this paper makes this interpolation procedure particularly straightforward. Different network modelings are expected to lead to interpolated eddy currents that are very similar and thus to compensate for the arbitrary nature of the network construction.

The lumped circuit approach used will be explained in detail in the next section, followed by verification and application examples and further discussions.

Study Procedure

The procedure used in this study comprises three steps: (*1*) to establish an equivalent-network model, (*2*) to formulate the lumped circuit equations for the model, and (*3*) to introduce loop-current variables to simplify the numerical implementation of the equations.

Equivalent-Network Model

The conductor first is divided into quadrilateral elements. The boundaries of these elements form a wire-mesh network (Fig. 1). The current density $\vec{J}$ in each element is assumed to be constant and is deduced from the solution of the wire-mesh network problem by

$$\vec{J} = \frac{1}{2}(\vec{J}_1 + \vec{J}_3) + \frac{1}{2}(\vec{J}_2 + \vec{J}_4) \tag{1}$$

where $\vec{J}_i$ = current density in the ith wire. The factor of one half reflects the fact that there are two independent components in $\vec{J}$, each to be determined as the average of the current density in wires situated at opposing sides of the element.

[4]Turner, L. R. and Lari, R. J., "Development of the Eddy Current Program EDDYNET," *Proceedings*, Conference on the Computation of Magnetic Field, Grenoble, France, September 1978.

[5]Weissenburger, D. W. and Christensen, V. R., "Transient Eddy Currents on Finite Plane and Toroidal Conducting Surfaces," PPPL-1517, Plasma Physics Laboratory, Princeton University, Princeton, N.J., April 1979.

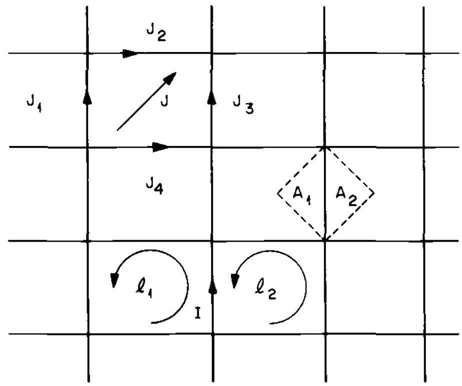

FIG. 1—*Network model.*

The cross-sectional area of each wire is determined from

$$A_c = (A_1 + A_2)T/D \tag{2}$$

where

T = thickness (assumed uniform) of conductor,
D = length of wire, and
A_i = area of the ith triangle.

For wires located at a boundary, only one triangle area enters into Eq 2.

Lumped Circuit Equations

Currents that flow in the network are determined by Kirchoff's laws. Let M be the number of elements, N the number of nodes, and L the number of lines in the wire-mesh model. It can be then shown that

$$M = L - (N - 1) \tag{3}$$

holds for the wire-mesh model of connected plates. If holes are present, M also includes the number of holes.

Kirchoff's laws give N node equations. The node equation states that at each node the net current that flows in equals the net current that flows out. Each line current flows from one node into another node. Thus, if we sum the $(N - 1)$ node equations and cancel out repetitive line currents, we get the node equation for the N's node. Hence there are only $(N - 1)$ independent node equations. From Eq 3 we need M independent-loop equations to uniquely determine the line currents. We shall choose the boundary of each element or hole as a loop. The loop equation states that the net voltage drop around each loop is zero. The resistive voltage must be balanced by the inductive voltage, or

$$\sum_{s=1}^{4} R_s I_s = -(\dot{B}_e + \dot{B}_i)A \tag{4}$$

where

R_s = resistance along the sth side of loop,
I_s = line current along the sth side of loop,
A = loop area,
$\dot{B}_e$ = rate of change (at centroid of loop) due to external field, and
$\dot{B}_i$ = rate of change (at centroid of loop) due to internal (eddy-current induced) field.

The resistance along each side of the loop is illustrated in Fig. 1 and is given by

$$\frac{1}{R} = \frac{1}{R_1} + \frac{1}{R_2} \tag{5}$$

where

$$R_1 = \rho_1 D/A_{c1}, \qquad R_2 = \rho_2 D/A_{c2} \tag{6}$$

and

$$A_{c1} = A_1 T/D, \qquad A_{c2} = A_2 T/D \tag{7}$$

Here ρ_1 and ρ_2, which represent the resistivities of adjacent elements, may be different. If the side is on a boundary, only one term contributes to R.

Transformation of Line Current to Loop Current

To reduce the number of independent unknowns, a loop current, l, is introduced for each loop (Fig. 1). To keep the algebra simple, the same convention (for example, right-hand rule) is used to fix the direction of the loop current. The node equation is automatically satisfied because the loop current that enters a node also leaves it. The line current, I, is related to the loop current (Fig. 1) and is determined by

$$I = l_1 - l_2 \tag{8}$$

where l_1, l_2 = loop currents in adjacent loops of I. It is clear that the M loop currents uniquely determine the M independent line currents.

In the centroid approximation (Fig. 2), the magnetic field B at centroid C by a line current I is given by

$$B = \frac{\mu_0}{4\pi} \frac{I}{r} \left(\frac{x_B}{r_B} - \frac{x_A}{r_A} \right) \tag{9}$$

where

$\mu_0 = 4\pi \times 10^{-7}$,
r_A, r_B = distance from centroid to end points of wire, and
x_A, x_B = projection of r_A and r_B along wire.

The field projects from, and is perpendicular to the plane of, the drawing.

To be compatible with Eq 4 and to improve the centroid approximation, a big hole or holes with irregular shapes should be divided into multiple quadrilateral elements. The resistivity of the hole is infinite, and loop currents of all loops in the hole are assigned to be the same. This ensures that no current will flow inside the hole.

Model Implementation

These equations were incorporated in five linked programs that constitute the equivalent-network model used in this study. The first program generates the mesh. The second computes the external field at the centroids of the elements. The third computes inductive and resistive matrix elements and obtains the inverse of the inductive matrix. The fourth solves the circuit equation using the Runge-Kutta method. The final program generates a plot of eddy-current profiles in the conductor. Rotational symmetry options are built into the composite program. The symmetry may be that of a single conductor or may be among multiple conductors.

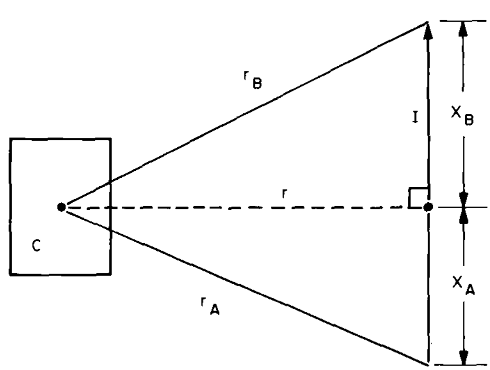

FIG. 2—*Centroid approximation for field computation.*

The composite program is run interactively on a time-shared PDP-10 (KL-10). A typical run for a case with 100 elements takes about 5 min of central processing unit (CPU) time, mostly for computing and inverting matrix elements. For cases involving multiple materials that vary greatly in resistivity (for example, steel and copper), several more minutes of CPU time may be required during the Runge-Kutta routine to compute the transients that follow a sudden pulse field.

Verification of Model Results

For shells and plates with cylindrical symmetry, the eddy-current problem has been solved by another lumped circuit approach—termed the "concentric-ring method"—that considers each element a coaxial circular ring. In order to verify our approach, we compared the results yielded by the equivalent-network model to those obtained by applying the concentric-ring method for several hypothetical examples.

Rings

Eddy current is induced in a circular ring by ramping the current linearly in a small coaxial circular coil that behaves like a dipole. The ring has an inner radius of 0.5 m, an outer radius of 0.75 m, and is 0.1 m thick. The resistivity of the ring is $2.4 \times 10^{-7}\ \Omega \cdot \text{m}$. The pulse coil is located 0.8 m away and has a 0.05 m inner radius, a 0.05 m radial thickness, and 0.1 m axial length. The current rises linearly to 0.5 MA at 1 s. Fourfold rotational symmetry is employed to solve this problem. One quarter of the ring is modeled by eight elements (four on the inner side and four on the outer side). One quarter of the hole inside the ring is modeled by six elements. The results are compared with the solution for three lumped circuits: the pulse coil, the inner ring, and the outer ring. Saturation is reached in 0.2 s and saturated eddy current agrees to within 0.4 percent. At 0.02 s the difference is 5 percent and decreases with time.

We have also checked the spatial distribution of the eddy current induced in a thin square plate by linear ramping of the current in a small coil aimed at the center of the plate. It is in good agreement with the concentric-ring solution for inner rings, in which the effect from the difference in boundary shapes is not important.

Tubes

The dipole field used in the previous example is used again with a coaxial circular tube. The tube is located 1.05 m from the pulse coil. It is 0.5 m long and 0.1 m thick, with an inner radius of 0.65 m and a resistivity of $2.4 \times 10^{-7}\ \Omega \cdot \text{m}$. The tube is divided axially into four sections. One quarter of each section is modeled by four elements. The computed eddy current is essentially the same whether the front end or the rear end of the tube is used for the hole loop. One quarter of the hole is modeled by six elements. The results agree well with the concentric-ring solutions. Figure 3 compares the temporal profiles for current density in the second and the fourth rings yielded by the two methods. The saturated eddy agrees to within 2 percent. As before, deviation is largest (15 percent) at the beginning of the transient.

Toroidal Vacuum Vessel with Plasma

Another determination that can be made using both the concentric-ring method and the wire-mesh network method is that of the eddy current induced in a toroidal vacuum vessel by plasma. The dimensions of the system are shown in Fig. 4. The cross section of the plasma is a square (1 by 1 m). It is ramped linearly to 7×10^4 MA at 1 s. The toroidal vessel has a major radius of 5 m and a cross section of 2 by 2 m. It is 0.1 m thick and has a resistivity of $5 \times 10^{-7}\ \Omega \cdot$ m (stainless steel). The eddy current is symmetrical about the torus midplane. In Fig. 4 only the upper-half cross section of the vacuum vessel is shown. It may be modeled either as eight concentric rings (circuits 1 and 2 for the inner side, circuits 3-6 for the top, and circuits 7 and 8 for the outer side). Alternatively, assuming fourfold rotational symmetry, one quarter of the upper half may be modeled by 64 elements, and one quarter of the center hole in the torus midplane may be modeled by 24 elements. The two solutions are compared in Fig. 4 for $t = 0.1$ s and $t = 1$ s. The differences are 15 and 4 percent, respectively. As expected, eddy current flows in the opposite direction of the plasma current.

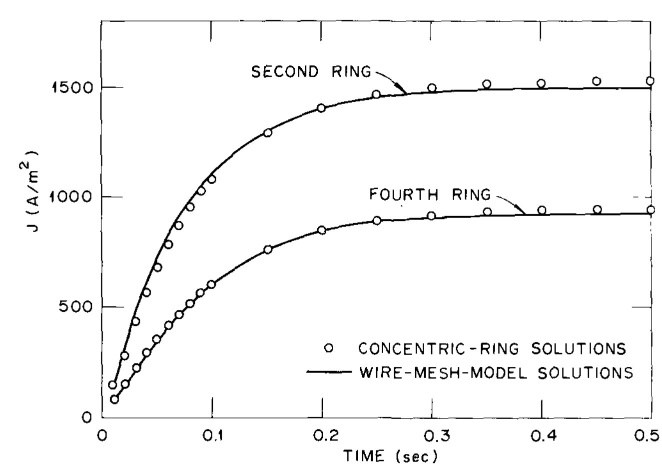

FIG. 3—*Temporary profiles of eddy-current density in tubular section computed as concentric rings (solid line) versus wire-mesh network (dots).*

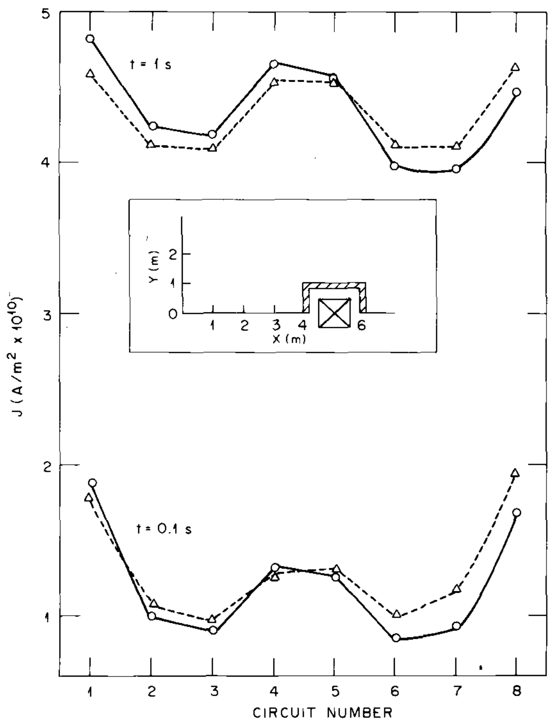

FIG. 4—*Spatial distribution of eddy-current density in toroidal vessel computed as concentric rings (circles) versus wire-mesh network (triangles).*

Model Applications

Once the equivalent-network model was verified through the aforementioned examples, it was applied to several other hypothetical cases, most of which could not be solved by the concentric-ring method.

Toroidal Vacuum Vessel with Equilibrium Field Coils

The vacuum vessel is used with two circular pulse coils with equal but opposing current to simulate the effect of equilibrium field coils. One pulse coil has a radius of 3 m, and the other has a radius of 7 m (Fig. 5); both have cross-sectional dimensions of 0.2 by 0.2 m. Their current is ramped linearly with time and reaches a magnitude of 4 MA at 1 s. Eddy-current density induced in the toroidal vessel is shown for 0.01 s, 0.1 s, and 1 s in Fig. 5. We noted that the longer the time, the more dominant the effect of the current in the outer coil, because most of the eddy current induced flows opposite to the current in that coil. This problem has also been solved using

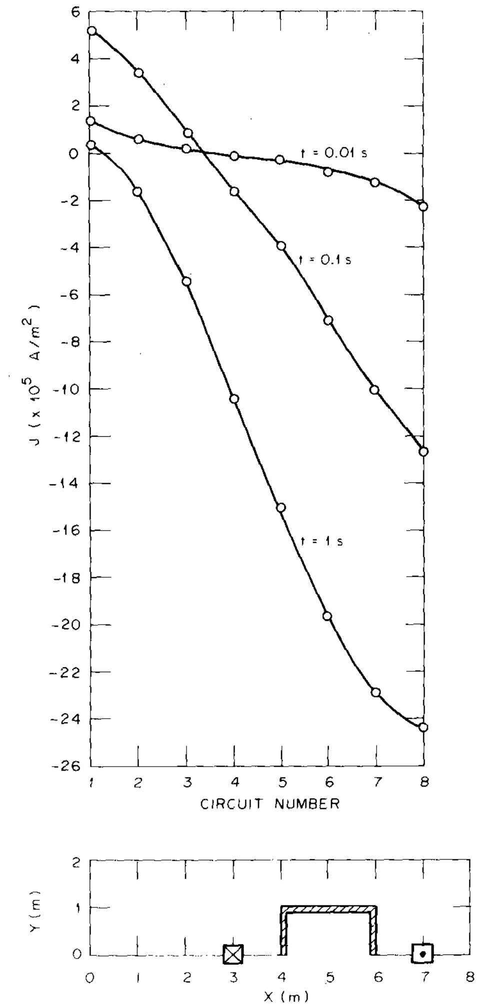

FIG. 5—*Eddy-current density induced in toroidal vessel by equilibrium field coils at 0.01, 0.1, and 1 s.*

the concentric-ring method, and the agreement is about the same as for the toroidal vacuum vessel with plasma.

Aluminum-Alloy Support Plate

A large magnet is made of laminated aluminum-alloy support plates that have a resistivity of $2.9 \times 10^{-8}\ \Omega \cdot m$ and that provide structural support for the embedded conductor. There is a high-resistance barrier between the upper half and the lower half of the magnet. A pulse coil is placed in the upper-half bore of the magnet (Fig. 6). The axis of the pulse coil lies on the midplane of the large magnet. The pulse coil has an inner radius of 0.2 m and a cross section of 0.38 by 0.51 m. Its current is ramped linearly, reaches 3 MA at 1 s, and then is held constant. Eighty-four elements were used to model the upper half of the outermost support plate. It is 0.32 m from the pulse coil and is parallel to the axis of the coil. The eddy-current profile induced in the support plate at 1 s is shown in Fig. 6. The length of each arrow in the figure is proportional to the magnitude of the local eddy-current density. Because of the resistive barrier, eddy-current density forms a closed loop in the upper half of the plate.

Stainless-Steel Support Plate

The pulse coil referred to in the support-plate determination is used with a thin, stainless-steel coil plate having a resistivity of $5 \times 10^{-7}\ \Omega \cdot \mathrm{m}$. The plate is placed 0.4 m from the pulse coil and parallel to its axis. The plate is 0.05 m thick and is modeled by 96 elements. The hole in the middle of the plate is modeled by 36 elements.

If two such pulse coils are placed symmetrically (Fig. 7) with their current flow in the same direction, the eddy current induced in the plate is broken into two separate loops as a result of the up-down symmetry. Figure 7 illustrates this result. The eddy loss is 9 J for the first 2 s. If the lower pulse coil is removed, eddy current (at t = 0.1 s) flows in big loops (Fig. 8), and the loss for the first 2 s jumps to 117 J.

Square Plate with Holes

The small dipole (see Rings) is used with a square plate 1 by 1 m. The dipole is 0.8 m from the plate and is aimed at its center. The plate is 0.1 m

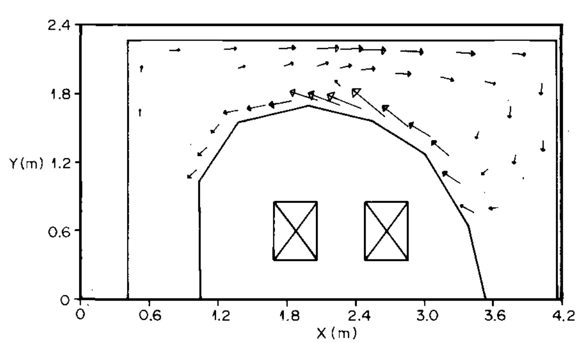

FIG. 6—*Profile of eddy-current density induced in an aluminum-alloy plate by a vertical pulse coil at* t = *1 s.*

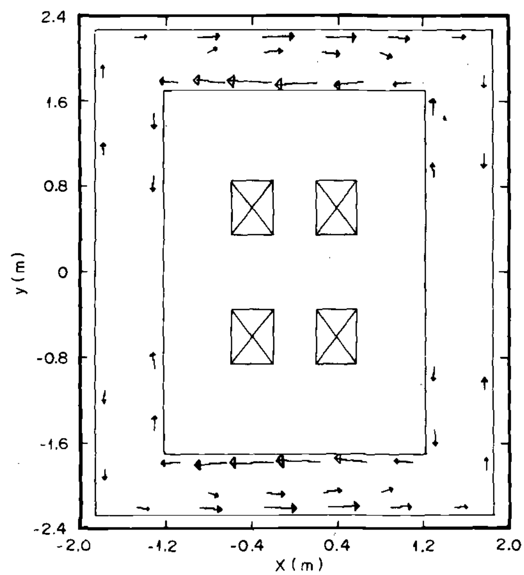

FIG. 7—*Profile of eddy-current density induced in a stainless-steel plate by two symmetrically placed pulse coils.*

thick and has a resistivity of $2.4 \times 10^{-7}\ \Omega \cdot m$. Fourfold rotational symmetry is used, and one quarter of the plate (conductor and holes) is modeled by 100 elements. The induced eddy-current density profile at $t = 0.1$ s is shown in Fig. 9.

Square Plate with Two Materials

The small dipole is again used with a square plate 1 by 1 m. The dipole is 0.8 m from the plate and is aimed at its center. The plate is 0.1 m thick and is made of materials with very different resistivities ($5.1 \times 10^{-5}\ \Omega \cdot m$ for the center and $2.4 \times 10^{-7}\ \Omega \cdot m$ for the outside). Fourfold rotational symmetry is again used, and one quarter of the plate is modeled by 64 elements. The induced eddy-current density profile at $t = 0.03$ s is shown in Fig. 10. Clearly, current prefers to flow in the lower-resistance region (outer plate). Because of the large difference in resistivity, about 3 min of CPU time is needed to obtain the Runge-Kutta solution for the $t = 0.03$-s profile.

Loss in Magnet Case

The two pulse coils (see Stainless-Steel Support Plate) are used with a stainless-steel magnet case 0.05 m thick and with a resistivity of 5×10^{-7} $\Omega \cdot m$. The dimensions of the case are shown in Fig. 11. The axial length

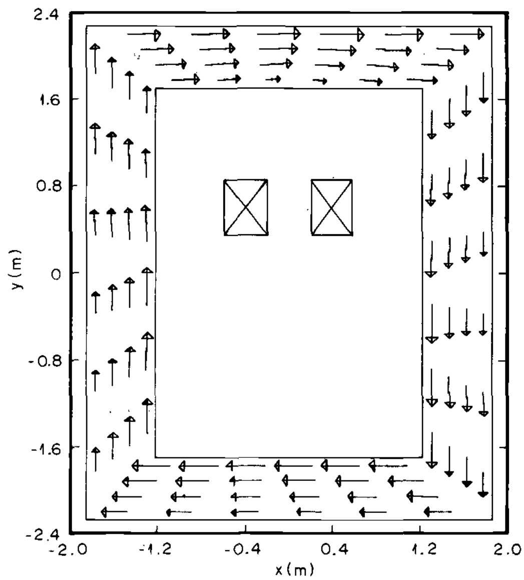

FIG. 8—*Profile of eddy-current density induced in a stainless-steel plate by a single pulse coil.*

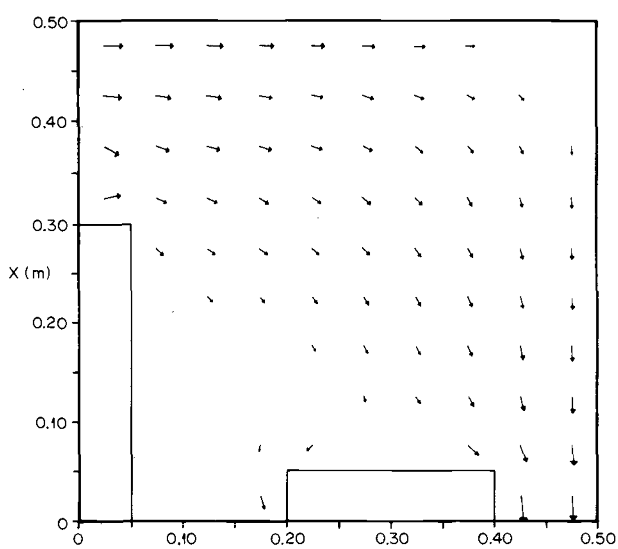

FIG. 9—*Profile of eddy-current density in one quarter of a square plate. Eddy current was induced in the plate by a dipole aimed at the center of the plate.*

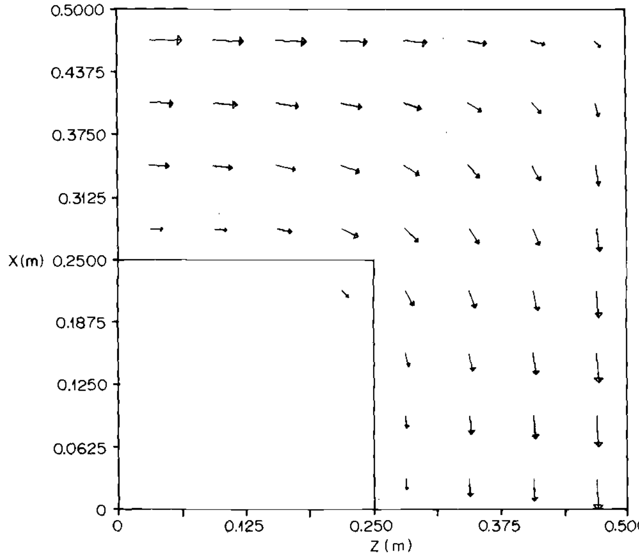

FIG. 10—*Profile of eddy-current density in one quarter of a dual-material plate. Eddy current was induced in the plate by a dipole aimed at the center of the plate.*

is 0.86 m. The axes of both pulse coils lie on the midplane of the magnet. The eddy-current loss in the whole case for the first 2 s is 722 J. If the pulse coil currents are reduced by one half, the loss for the first 2 s drops to 181 J. For both cases one half of the coil case is modeled by 136 elements. The hole intersected by the coil case and the torus midplane (x-z plane in Fig. 11) is modeled by four elements.

Current in Magnet Case

The magnet case is used with a linearly ramped line current, which passes through the center of the case. The resulting eddy-current profile in one of the endplates is shown in Fig. 12. As expected, the eddy current tends to wrap around the case in closed loops.

The profile in one of the endplates attributable to plasma current is shown in Fig. 13. The plasma current is linearly ramped to reach 7 MA at 1 s.

Discussion and Conclusions

In tokamak devices, where pulse currents and conductor geometry are usually symmetrical about the torus midplane, there will be no eddy current induced by pulse coils to flow across the torus midplane. Thus, for the toroidal vessel or the stainless steel support plate, there will be no loop

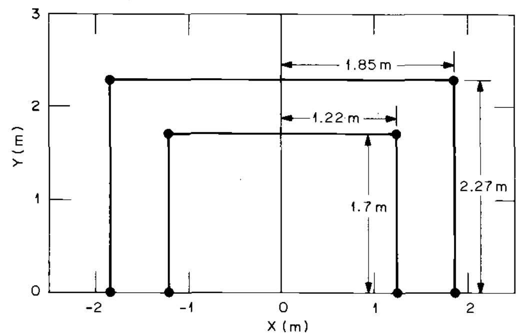

FIG. 11—*Magnet-case dimensions.*

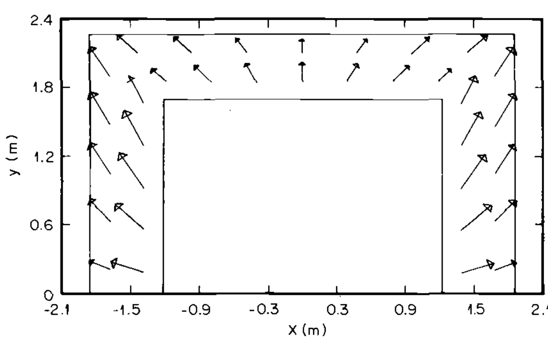

FIG. 12—*Eddy current in a magnet-case endplate. Eddy current was induced in the endplate by passing a linearly ramped line current through the center of the case.*

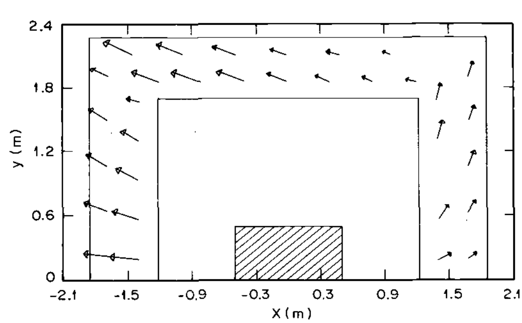

FIG. 13—*Eddy current in a magnet-case endplate. Eddy current was induced in the endplate by a linearly ramped plasma current.*

current to flow around the plasma, and the corresponding hole can be omitted from modeling.

In the cases discussed, eddy current is implicitly assumed to be uniform across the thickness of the conductor. Effects of thermal conduction and resistivity changes with temperature are ignored. These effects are estimated to be small for stainless steel, which is the primary candidate of magnet structural members.

In conclusion the equivalent-network method compares favorably with the concentric-ring method in those cases where the latter method is applicable. Since its development, the equivalent-network model has proved useful in studying eddy-current profiles and eddy-current losses in actual magnet designs.

Acknowledgments

I wish to thank L. Turner, D. W. Weissenburger, and U. R. Christensen for reprints and for very useful discussions. I am also indebted to K. H. Carpenter, S. S. Shen, and W. C. T. Stoddart for their helpful comments. Special thanks goes to S. S. Shen for reviewing the manuscript.

This research was sponsored by the Office of Fusion Energy, U.S. Department of Energy, under contract W-7405-eng-26 with the Union Carbide Corporation.

T. J. Davis[1]

Advanced Multifrequency Eddy-Current System for Steam-Generator Inspection

REFERENCE: Davis, T. J., "**Advanced Multifrequency Eddy-Current System for Steam-Generator Inspection,**" *Eddy-Current Characterization of Materials and Structures, ASTM STP 722,* George Birnbaum and George Free, Eds., American Society for Testing and Materials, 1981, pp. 255-265.

ABSTRACT: A research project conducted for the Electric Power Research Institute has resulted in substantial improvements in the assessment of steam-generator integrity. The objective of the work was to determine the maximum advantage of multifrequency methods for the inspection of steam generators. Advanced multifrequency technology has been developed under the program and has been implemented into a prototype system that uses both differential and absolute data simultaneously from four test frequencies. Multiparameter processing of the data results in very effective elimination of unwanted parameters such as support plates, probe wobble, dents, and other dimensional variations. The information of interest, flaw depth, is preserved in this process and is no longer masked or altered by the unwanted data. The availability of both differential and absolute multifrequency data significantly extends the range and accuracy of the flaw-sizing process, and enables the profiles or contours of larger volume flaws to be obtained.

KEY WORDS: multifrequency eddy currents, multiparameter processing, steam generator tubing, differential, absolute, mixing, dents, support plates

In-service inspection of steam-generator tubing is commonly performed with single-frequency eddy-current methods. Although this test has served well as the industry standard over the past ten years, it has not been able to deal effectively with the new types of generator anomalies that are becoming prevalent. These anomalies include denting, flaws in support and dented regions, cracked support plates, and conductive metal deposits. Additionally, the accuracy of the test for determining remaining tube-wall thickness is highly dependent on the geometry of the flaw or corroded area. Research project RP 403-2 was thus initiated at Battelle-Northwest by the Electric Power Research Institute (EPRI), Palo Alto, Calif., for the purpose of developing solutions to these inspection problems.

[1]Senior research engineer, Battelle-Northwest, Richland, Wash. 99352.

Technical Discussion

This section addresses two major areas: the test improvements obtained with the new system and a description of the system. As a matter of general familiarization with the test techniques employed by the new system, the following information is provided as an introduction to the discussion of test improvements.

The test system uses a total of four frequencies:

F1	25 kHz
F2	200 kHz
F3	400 kHz
F4	1.6 MHz

These are the frequencies used for Westinghouse generators 22.2 by 1.27 mm (0.875 by 0.050 in.) outside-diameter wall-tubing dimensions. Frequency F3 is changed to accommodate other tube dimensions. Both differential (two coil) and absolute (single coil) data are available from each frequency.

The test data may be examined either by the multifrequency method or the multiparameter method. For the multifrequency method, the data from each frequency may be treated as a separate single-frequency test, which permits comparison of test responses as a function of frequency. For the multiparameter method, data from individual frequencies is combined in real time by a vector addition process. This combination of data is referred to as mixing and is mathematically equivalent to simultaneous solution of multiple equations. This mixing process permits elimination of unwanted test parameters while those of interest are retained. Table 1 describes the system output data used for evaluation of most generator anomalies. As indicated in the table, three multiparameter mixes and an output from F4 (1.6 MHz) are used. Other mixes or data from individual frequencies may be employed, if necessary.

Test Improvements

Suppression of Unwanted Parameters

The primary advantage of multiparameter testing is the suppression of unwanted test variables that would normally mask or modulate a desired indication. In steam-generator inspection the desired information on tubing flaws can be masked by dents, support plates, probe wobble, and inside-diameter variations such as mandrel chatter or pilgering.

A unique mixing method for suppression of support-plate indications has been developed under the program. This method attains the maximum possible rejection and compensates for the fact that support signals from different frequencies are not always similar in shape.

TABLE 1—*System-output data commonly used for generator inspection.*

System Output	Parameters Detected	Parameters Suppressed	Frequencies Used	Test Mode (absolute or differential)
Mix A	wastage depth	supports, dents, ID variations, probe wobble	200 kHz, 400 kHz, 1.6 MHz	absolute
Mix B	pit and crack depth	supports, ID variations, probe wobble	200 kHz, 400 kHz, 1.6 MHz	differential
Mix C	support cracks, sludge, metallic deposits	dents, ID variations, probe wobble	25 kHz, 1.6 MHz	absolute
F4	dent size	(this test responds only to ID anomalies and throughwall flaws)	1.6 MHz	absolute

An example of support-plate suppression is shown in Fig. 1. Figure 1*a* shows a normal single-frequency response from a 60 percent flaw, and Fig. 1*b* shows the same response when the flaw is located under the edge of a support plate. In the latter case, the flaw can only modulate the support-plate signal to indicate the presence of a flaw, but flaw depth information is not available. Figure 1*c* shows the information resulting from a multi-parameter mix to suppress the support indication. Now an opposite condition exists wherein the support residue modulates the flaw indication only slightly, and flaw depth information is readily available.

The results of mixing data from three frequencies to simultaneously eliminate supports and probe wobble is shown in Fig. 2. This is Mix B (described in Table 1). The differential test data shown were generated by translating the probe through an American Society of Mechanical Engineers (ASME) calibration tube having a simulated support and five drill holes ranging from 20 to 100 percent of wall thickness. Data from single frequency testing and from Mix B are both recorded on a strip chart and plotted on the impedance plane using an X-Y oscilloscope.

Two major conclusions can be drawn from the data of Fig. 2. A high degree of support suppression is achieved in the mixed multifrequency data (namely, 95 percent for one channel and 90 percent for the other), and probe wobble (evidenced by baseline variation in Channel 2 single-frequency strip-chart data) is virtually eliminated in the mixed data, which results in an exceptionally clean impedance-plane pattern.

Another inspection problem that is aided by multiparameter testing is the detection of flaws in dented regions. The primary cause of dents (diameter reductions of tubing) is the growth of corrosion products from the supports that squeeze the tube down under the support. Dents can produce test

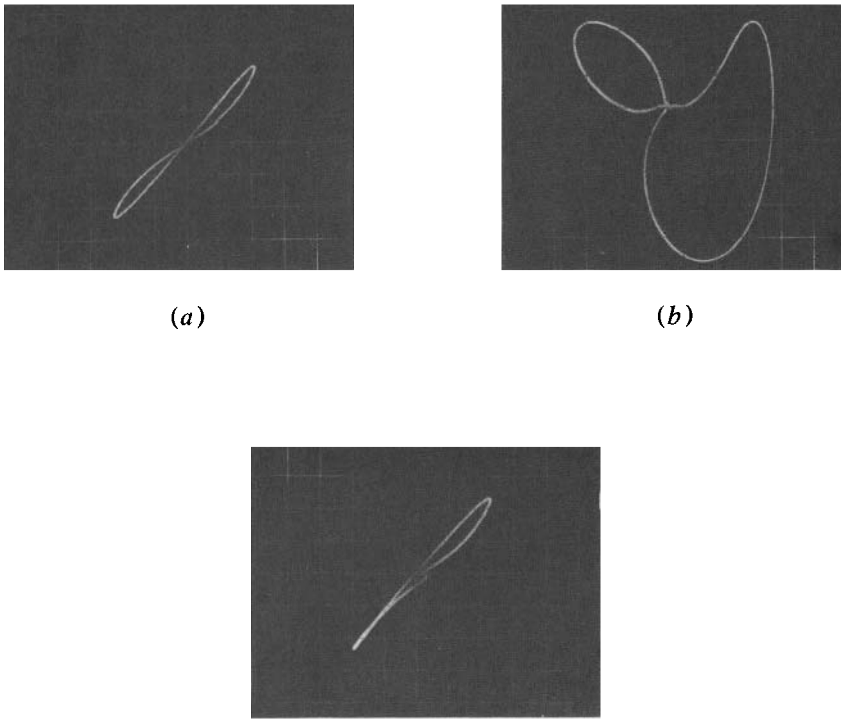

(a) (b)

(c)

(a) Single-frequency indication for 60 percent ASME flaw.
(b) Single-frequency indication for the 60 percent flaw when placed under a support.
(c) Three-frequency response of the flaw under a support.

FIG. 1—*Support-plate suppression.*

indications many times greater than flaw indications, which results in the inability to size a flaw or to even detect it using single-frequency methods.

The ability of multiparameter testing to suppress dent indications is shown in Fig. 3. Figure 3*a* compares single-frequency indications from a 40 percent wastage flaw and a 0.406 mm (0.016 in.) diameter reduction uniform dent. Figure 3*b* compares these same two indications after being processed by a three-frequency mix. This is Mix A (described in Table 1), which uses absolute testing wherein a unipolar response is derived. The mix results in a substantial reduction of signal-to-dent ratio and will permit reasonably accurate sizing of many flaws located in dented regions.

We have several techniques in mind to further improve the rejection of dents with multiparameter testing. One of these involves shielding of the test coils to eliminate variations in electrical capacitance about the test

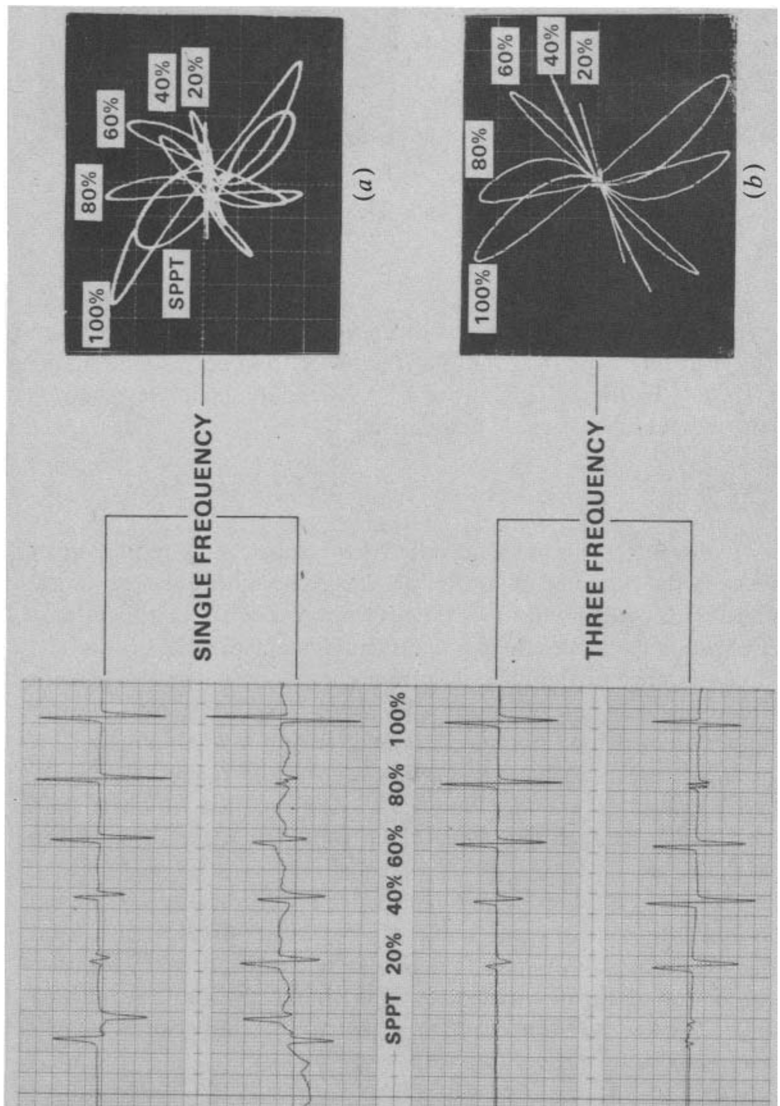

(a) Single-frequency test.
(b) Three-frequency test.

FIG. 2—*Comparison of single-frequency and three-frequency differential tests showing suppression of wobble and supports. The probe was translated through an ASME calibration tube with a simulated support plate.*

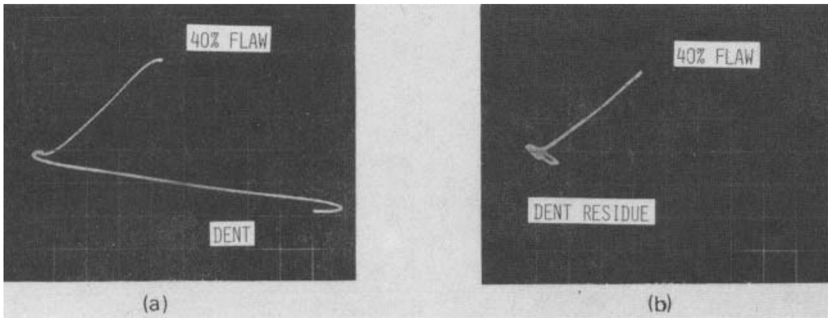

FIG. 3—*Comparison of* (a) *single-frequency and* (b) *three-frequency responses to a 0.406 mm (0.016 in.) diameter reduction dent.*

coils as they encounter a dent. This would render the dent response from the 1.6 MHz test more similar to those of the lower frequencies and enable better suppression in the mixing process. A Faraday shield designed to minimize eddy-current losses would be required.

Error Reduction

The use of absolute testing has resulted in a substantial reduction of error in assessing the depth of flaws that are large enough to be seen in the absolute mode. This category of flaws ranges from pits equivalent in volume to ASME calibration drill holes through uniform wastage existing around the complete circumference of the tube. Figure 4 compares the results of both differential and absolute inspection of a series of wastage defects. Almost a fivefold reduction of sizing error was obtained for uniform thinning defects using the multiparameter absolute test, while a threefold reduction of error was obtained for elliptical wastage flaws. The flaw set used for these data consisted of 12 flaws of each category, which ranged in depth from 20 to 90 percent wall thickness.

The main reason for the improved performance of the absolute test is that it generates a continuous measurement of the minimum wall thickness encountered in the tube. In contrast, the differential test is primarily sensitive to the edges of flawed regions where the wall thickness is undergoing an abrupt change. A gradual or tapered change in wall thickness can be missed or sized erroneously by the differential test.

Characterization of Supports

Laboratory results indicate that a two-frequency absolute mix (Mix C, described in Table 1) is capable of measuring both the degree of cracking in a support plate and the support-hole diameter. Figure 5 shows the results

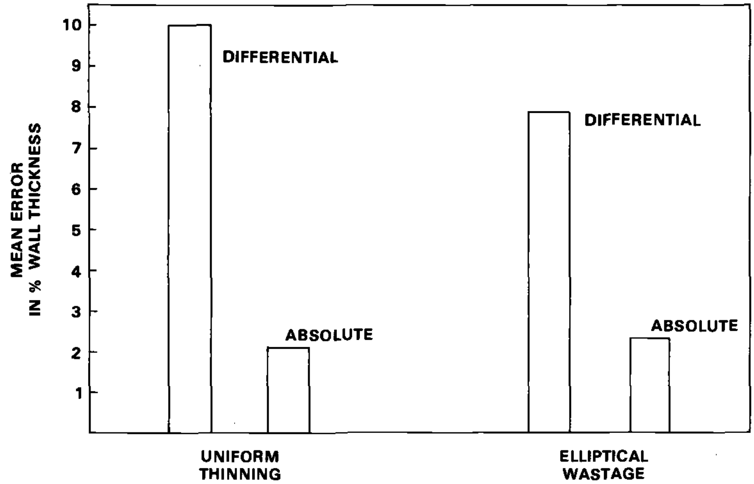

FIG. 4—*Comparison of flaw-depth sizing error for two types of flaws showing the reduced error available from absolute inspection methods.*

of inspecting a cracked and a noncracked support located over dents with the crevice being stuffed with magnetite powder. The support crack extended from one tubing hole to an adjacent hole. The differences in vertical components of the signals are quite dramatic and easily recognizable. Our work has also indicated that the horizontal component can be used as a measure of support-hole diameter.

More work needs to be done in this area to determine if actual support-corrosion products in the generators produce the same effect on this test as does magnetite powder used for the laboratory work.

Characterization of Dents

A vector component of the 1.6 MHz absolute data is taken at right angles to throughwall holes and used as an indication of dent size. Due to the high frequency and the phasing used, this channel responds to only inside-diameter information and is virtually independent of all other generator parameters. The response of this channel as the probe is translated through a series of simulated dents is shown in Fig. 6. Present indications are that this is a very accurate measure of dent size.

Profiling of Anomalies

Figure 6 demonstrates an important property common to all absolute testing used by the system. This is the ability to profile anomalies continuously along their length. As described previously, this can be a sub-

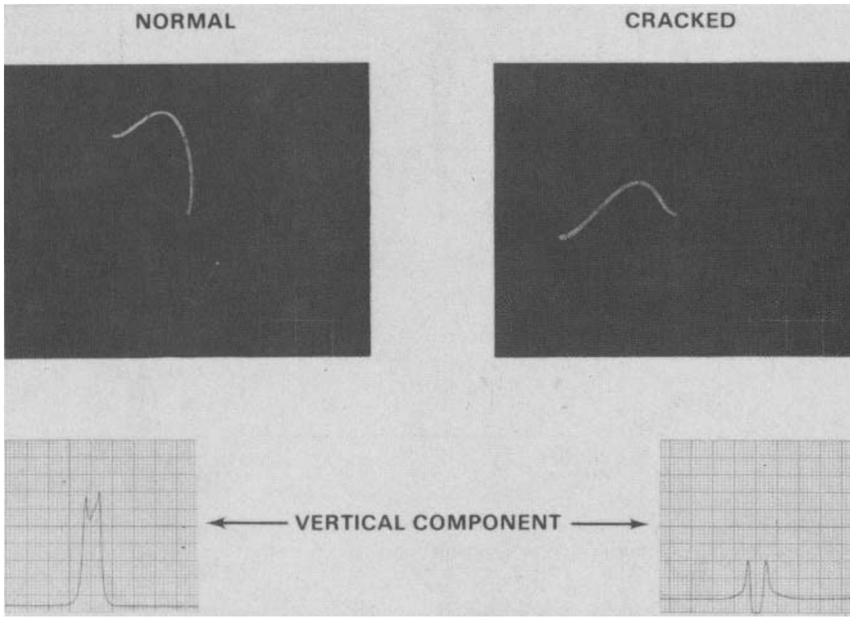

FIG. 5—*Absolute test for support-plate cracking. The response on the right was from a support with a complete crack between two tubing holes.*

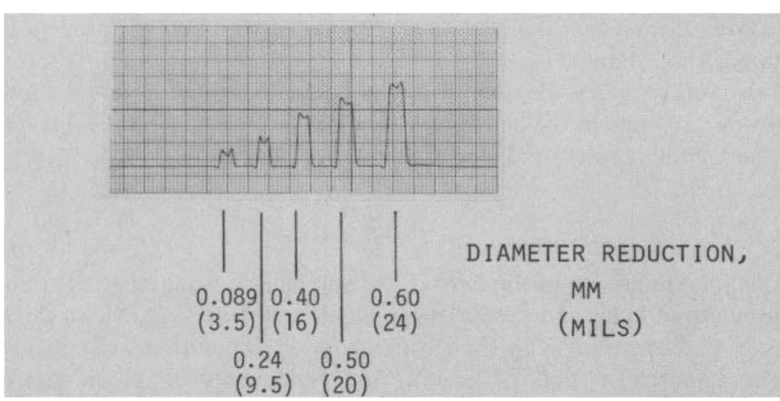

FIG. 6—*Response of system absolute dent size channel for a series of uniform dents.*

stantial advantage over the differential method, which responds primarily to the edges of the flaw and which could miss or erroneously size a tapered flaw. As an example of profiling capability, most of the dents used to generate the Fig. 6 data were found to have more diameter reduction at the edges than at the center using an inside-diameter micrometer. The eddy-current data shown verify this profile.

The ultimate improvement that could result from multiparameter absolute testing in the future is extended tube service resulting from being able to predict tube burst pressure. The detailed information on flaw geometry that is available from absolute inspection should provide quite adequate means for predicting burst strength. This information includes both flaw depth and flaw volume as a function of probe position.

Detection of Sludge and Conductive Metal Deposits

Magnetic sludge and conductive deposits both provide unique and distinctly recognizable indications on the system outputs. Mix C (absolute 25 kHz and 1.6 MHz) generates the information for distinguishing between the two types of deposits. Mixes A and B suppress deposit indications, which gives additional clues that the Mix C indication is from a deposit. In a single-frequency mode, for example, at 400 kHz, this descrimination is not possible and a conductive metal deposit can be mistaken for a flaw.

Test System

The prototype test system was developed with two primary objectives: (1) obtaining maximum information on steam generator integrity, and (2) providing an instrument design which, from a performance and economics standpoint, is highly attractive for commercialization by interested firms.

A photograph of the major components of the test system is shown in Fig. 7. These components are the multifrequency differential/absolute instrument (lower right), the multiparameter mixer (upper right), and a 16-channel FM-FM magnetic tape deck (left side). Other components required for tubing inspection include an oscilloscope, a strip-chart recorder, a probe, and a probe transport. These are not shown for purposes of simplicity.

The multifrequency instrument performs eight independent tests simultaneously: four frequencies of differential testing and four frequencies of absolute testing. The instrument uses a combination of multiplexing and frequency translation, which results in stable performance, simplified design, and minimized parts count. The multiplexing process places one frequency at a time on the search coils, which results in zero crosstalk between frequencies and eliminates the need for bandpass filters. The frequency-translation scheme uses phase-shift key modulation to translate the coil signals from each frequency to an equivalent waveform at a common intermediate frequency (25 kHz). A single channel of circuitry then performs final processing of data from all frequencies. This provides very substantial benefits in terms of stability and simplicity since the final channel must only accommodate one frequency.

The multiparameter mixer combines test signals in real time using analog computational processes. The major processes used are axis rotation of the

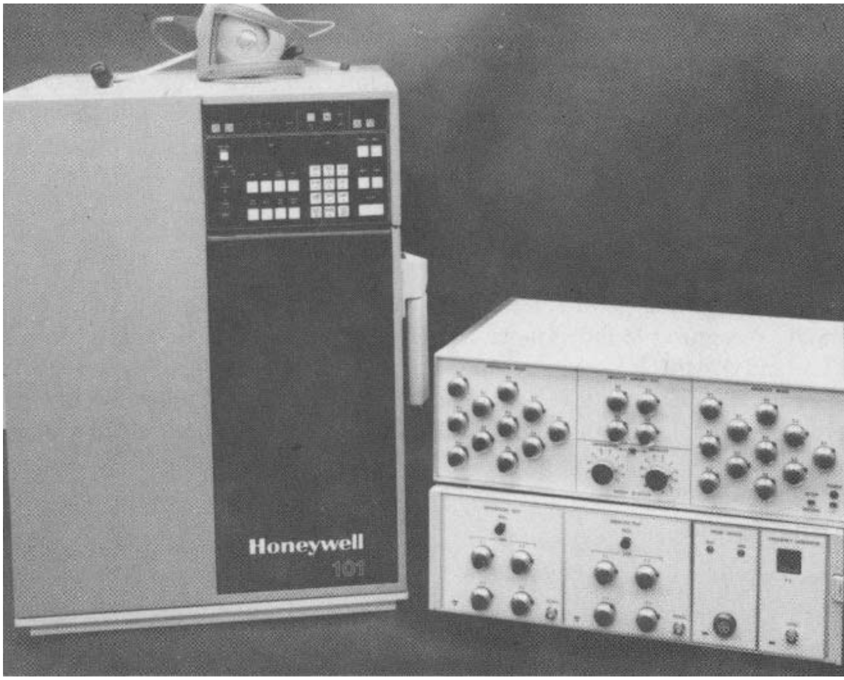

FIG. 7—*Major components of prototype test system. A conventional oscilloscope and strip chart recorder (not shown) are also used for data acquisition and analysis.*

impedance-plane data and vector summation with weighting. A unique feature of the mixer is the computational technique cited previously which obtains maximum possible suppression of support data.

A simplified block diagram of the test instrument and mixer appears in Fig. 8.

Summary

Multifrequency inspection methodology has been developed that provides substantial improvements in the assessment of steam-generator integrity. A prototype system using both differential and absolute tests at four frequencies has been developed to implement the new technology. The system was used recently to probe the EPRI steam-generator mockup and evaluation of the results is in progress. Some of the technology developed under the program has been incorporated into a new commercial multifrequency instrument manufactured by Zetec, Inc. under a transfer-of-technology arrangement.

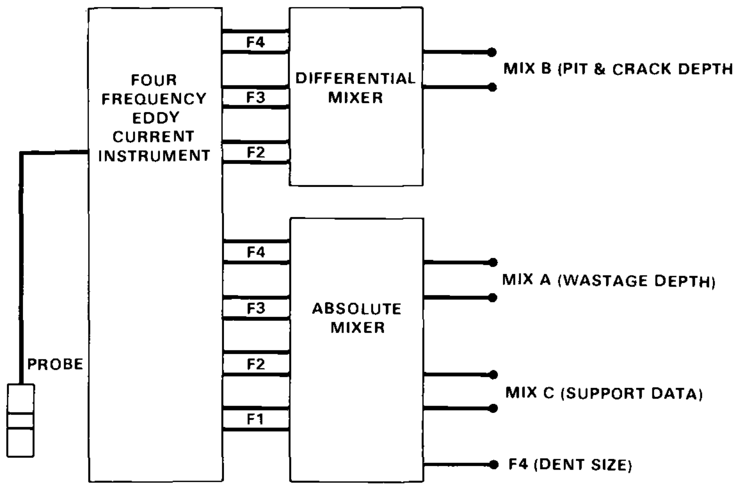

FIG. 8—*Simplified block diagram of the prototype test instrument and mixer.*

The prototype system developed under this program provides the following benefits for steam-generator inspection:

1. Detection of flaws in dented regions.
2. Detection of flaws under supports.
3. Rejection of inside-diameter variations and probe wobble.
4. Reduction of error in flaw sizing.
5. Characterization of supports and dents.
6. Profiling of anomalies with the absolute test.
7. Detection of sludge and conductive metal deposits.

Multifrequency data from the differential test are used for assessing the depth of small-volume flaws such as pits and cracks. Data from the absolute multifrequency test are used for larger-volume flaws and for the detection of support cracks and dent size.

Future Development

Additional technical areas which we feel are worthy of further investigation include:

1. High-speed helical scan testing.
2. Probe shielding to improve dent suppression.
3. Differential-absolute cross mixing to analyze compound flaws.
4. New probe designs that may be insensitive to flaw orientation.
5. Real-time correlation techniques for signal processing.

Theoretical Analysis of Fields, Defects, and Structures II

Amrit Sagar[1]

Multifrequency Eddy-Current Method and the Separation of Test Specimen Variables

REFERENCE: Sagar, Amrit, "**Multifrequency Eddy-Current Method and the Separation of Test Specimen Variables,**" *Eddy-Current Characterization of Materials and Structures, ASTM STP 722,* George Birnbaum and George Free, Eds., American Society for Testing and Materials, 1981, pp. 269–297.

ABSTRACT: The multifold accidental degeneracy present in eddy-current signals requires a multifrequency eddy-current examination of specimens to reduce the ambiguity in the determination of the nature of the source of the signals. The multiparameter technique for data analysis first developed by Libby is used for extracting information about multiple variables simultaneously present in the specimen. The effect of interaction between simultaneously present multiple variables on the results of the separation of these variables by this method of linear combination is discussed. It is suggested that the interactions between different regions of a discontinuity result in the lack of a unique relationship between the phase-amplitude characteristics and the depth of discontinuities of unknown geometry and orientation. The difficulty in the estimation of the diameter of the tube support-plate hole in the presence of magnetite (Fe_3O_4) in the crevice and methods for the determination of the inside dimensions of the tubing in regions with noncircular cross sections are discussed.

KEY WORDS: eddy current, discontinuity, Inconel, steel, signal phase, amplitude, flaw depth, flaw size, multifrequency, multiparameter, degeneracy

The eddy-current signals are generally characterized by their phase angle and amplitude in the complex impedance plane. The nature of a discontinuity responsible for an eddy-current signal is determined from these two signal characteristics. In fact the phase-angle information alone is often used for the evaluation of the discontinuity, the amplitude information analysis being too tedious and indeterminate. Unfortunately, the eddy-current signals often possess a multifold accidental degeneracy; that is, a signal characterized by phase angle and amplitude values only at the point of nearest approach between the coil and the discontinuity may result from many different types of sources. This degeneracy can often be removed by changing the test variables—for example, using multiple test frequencies, changing the coil geometry, using magnetic bias on the coil, etc. A careful analysis of the total signal from the point of entry of the discontinuity in the field of the coil to the point of its exit can result in a more complete characterization of the discon-

[1]Fellow engineer, Westinghouse Electric Corporation, Pittsburgh, Pa. 15230.

tinuity. It is a very tedious and difficult process, however, and is still in the realm of nondestructive testing (NDT) art rather than science.

The simultaneous presence of more than one type of specimen variable results in very complex eddy-current signals. Libby developed the multiparameter eddy-current technique for extracting the information about the specimen variables most relevant to the test from such complex signals [*1*].[2] The technique involves the solution of a set of simultaneous linear equations for the eddy-current signals at different test frequencies in terms of the parameters of the specimen variables. By this technique Libby was able to reduce the contribution of the various interfering signals resulting from some of the test variables not relevant to the characterization of the discontinuities in the specimen. For example, he was able to characterize the discontinuities on the wall of tubing in the presence of an interfering signal from such sources as the probe-wobble and the steel support plate surrounding the tubing. This technique was further developed at various organizations such as Battelle Pacific Northwest Laboratories (where Libby did his original work), Oak Ridge National Laboratories, and Commissariat a'l' Energie Atomique, France. The complete eddy-current systems based on the concepts developed by Libby have recently become commercially available.[3,4]

The work presented in this paper discusses the importance of the interaction among the multiple discontinuities that may be present in the specimen and deals with the phase and amplitude dependence of the signals on the geometry and orientation of the discontinuities. It is shown that no unique relationship between the depth of discontinuities of unknown geometry and the eddy-current signal characteristics, such as phase and amplitude, can be generated on account of the interactions between different regions of the discontinuities. The work reported here is especially relevant to the examination of the Inconel-600 tubing in the presence of interfering signals from such variables as carbon steel support plates surrounding the tubes, magnetite and metallic deposits on the outside diameter of the tubes, probe wobble and dents, etc. Some examples are given which point to the accidental degeneracy of the signals encountered in the evaluation of the Inconel-600 tubing. The evaluation of such specimen variables as the support plates, crevice between the tube wall and the support plate, and the changes in the tube cross section are also discussed.

Experimental

The specimens used in this work consisted of Inconel-600 tubing of 22.2-mm (0.875-in.) outside diameter and 1.27-mm (50-mil) nominal wall thickness. The discontinuities on the tubing wall and the tube support plate

[2]The italic numbers in brackets refer to the list of references appended to this paper.
[3]Technip International, distributors of Intercontrol Products, Kennewick, Wash.
[4]Zetec, Inc., P.O. Box 140, Issaquah, Wash.

were produced with the electrical-discharge machine. The tube support-plate samples consisted of 19.05-mm (0.75-in.)-thick carbon steel plates with approximately 22.86-mm (0.90-in.)-diameter circular holes. The magnetic oxide deposits on the outside diameter of the tubing were simulated by placing rings of iron oxide (Fe_3O_4) of different densities around the tubes. The metallic plating on the outside diameter of the tubing wall was simulated by using thin foils of copper or aluminum. The probes were inside-diameter type with circumferential coils mostly used in the differential mode. Most of the probes used in this study were obtained from Zetec, Inc.[4] (The coil dimensions will be shown in Fig. 11.) No corrections were made for possible nonlinearity of the bridge circuit of the instrument.

Results and Discussion

Interaction Between Specimen Variables

Figure 1 shows the configuration and geometry of four equally spaced axial slots on the tube wall. A set of specimens with 100 percent deep slots in this configuration but with different slot separations were prepared. Figure 2 shows the eddy-current signals at 400-kHz and 100 kHz test frequencies from these samples using a differential probe. Figures 3 and 4 show the phase and amplitude of the signals as a function of the slot separation taken from the data of Fig. 2. It may be observed that both the phase and the amplitude of the signals show a dependence on the slot separation although the depth of the slots and the volume of the metal involved in each set of slots is kept the same. Figure 5 shows the data on these specimens using an absolute probe. The noise from the probe wobble for these data was minimized by mechanical means. These data are presented in order to emphasize that the observed dependence of the eddy-current signal characteristics on the slot separation is not just an artifact of a differential probe. It may further be stated from the data of Fig. 5 that so long as the slots are far apart (separation of slots, $d \gg l$, the slot length), the resultant signal can be written as a simple sum of the signals from the individual slots, with the phase of the final signal identical to the phase of the individual signals. Although not shown here, this was also found to be the case for the data obtained using a differen-

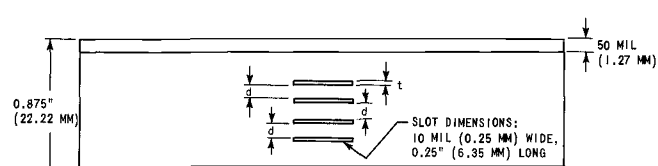

FIG. 1—*Four equally spaced axial slots around the circumference of a 1.27 mm (50 mil) wall, 22.2 mm (0.875 in.) outside-diameter Inconel-600 tube.*

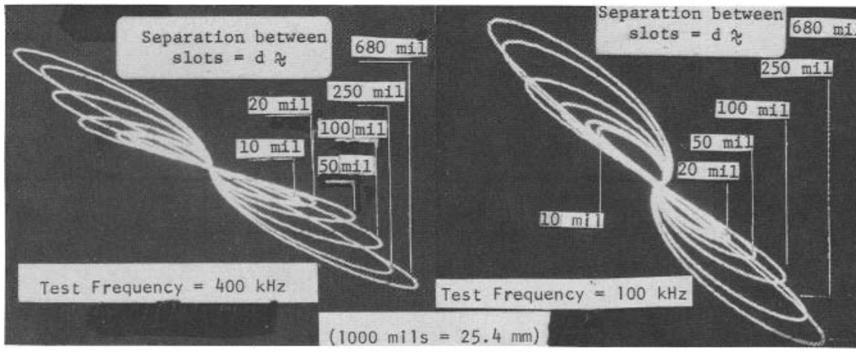

FIG. 2—*Eddy-current signals at 400- and 100-kHz test frequencies from four axially placed through-the-wall slots (length = 6.35 mm (0.25 in.), width = 0.25 mm (10 mil) around the circumference of a 22.2 mm (0.875 in.) outside-diameter, 1.27 mm (50 mil) wall Inconel-600 tube. The separation between the slots (denoted by* d*) for each signal is also shown.*

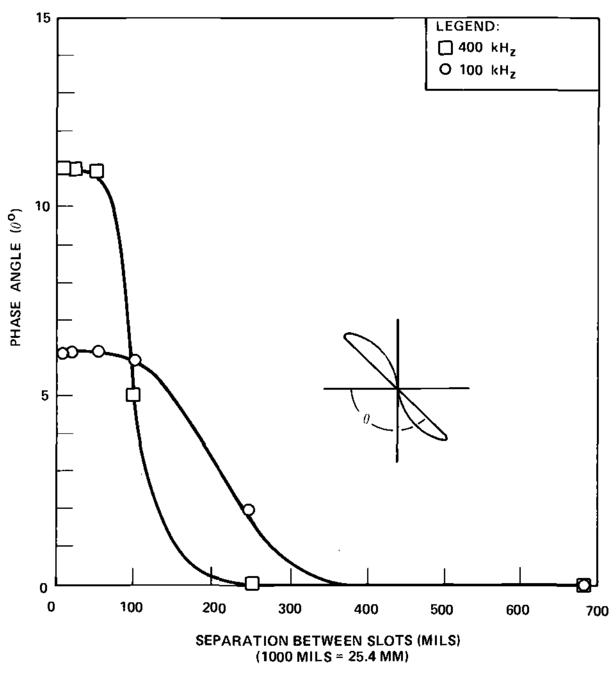

FIG. 3—*Phase of the eddy-current signal for 400- and 100-kHz test frequencies versus separation between four equally spaced 100 percent through-the-wall axial slots around the circumference of 22.2 mm (0.875 in.) outside-diameter, 1.27 mm (50 mil) wall Inconel-600 tube. Slot dimensions: 6.35 mm (0.25 in.) long, 0.25 mm (10 mil) wide. The phase angle for the signal from the slots spaced 17.27 mm (680 mil) was taken as 0 deg.*

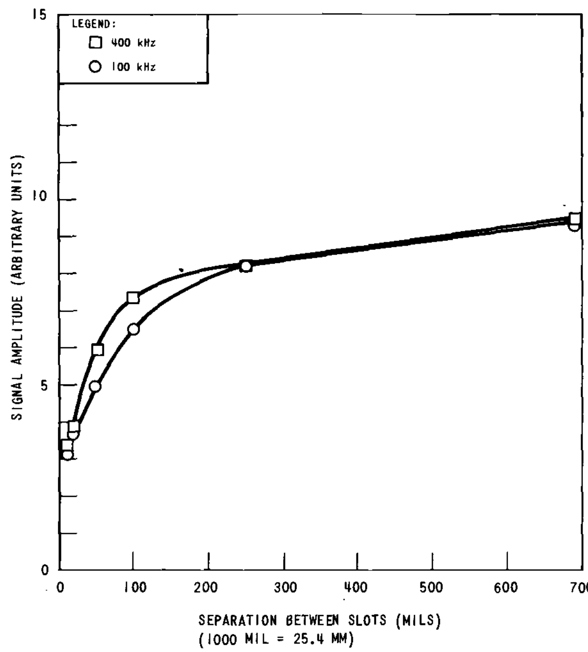

FIG. 4—*Amplitude of eddy-current signals for 400- and 100-kHz test frequencies versus separation between four equally spaced 100 percent through-the-wall axial slots around the circumference of a 22.2 mm (0.875 in.) outside-diameter, 1.27 mm (50 mil) wall Inconel-600 tube. Slot dimensions: 6.35 mm (0.25 in.) long, 0.25 mm (10 mil) wide.*

tial probe. The conditions for the validity of the simple additivity rule are (*1*) $d \gg l$ and (*2*) $d \gg \delta$, the skin depth. [The skin depth for Inconel-600 at 400 kHz is about 0.84-mm (33 mil).] In case either of the two conditions is not satisfied, the simple rule of additivity of signals breaks down. Another observation that can be made from the results shown in Figs. 3 and 4 is that whereas the amplitude versus slot separation curve shows a deviation from the additivity rule in the range of large values of slot separation $d \gtrsim 20\delta$, the phase versus separation data show detectable deviation from this rule in the range $d \gtrsim 5\delta$. Furthermore, the data on amplitude versus separation show a weaker frequency dependence (if any) than the data on phase versus separation. The results in Figs. 3 and 4 show the relevance of the interaction between discontinuities for any data analysis work.

Figure 6 shows the data on the 50 percent deep outside-diameter slots with a similar configuration to Fig. 1. Figure 7 shows the signal amplitude as a function of the slot separation obtained from these data at the two frequencies. Figure 8 shows the signal phase as a function of slot separation at 400-kHz test frequency. There may be some question about the precision of

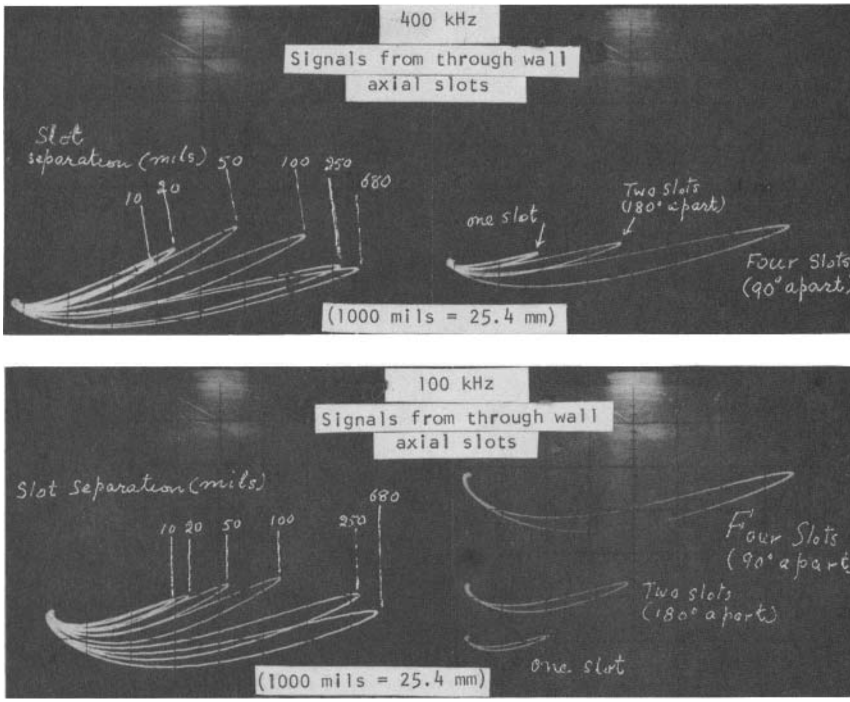

FIG. 5—*Eddy-current signals at different test frequencies from four 6.35 mm (0.25 in.) long, 0.25 mm (10 mil) wide equally spaced through-the-wall axial slots around the circumference of a 22.2 mm (0.875 in.) outside-diameter, 1.27 mm (50 mil) wall Inconel-600 tube using an absolute coil probe.*

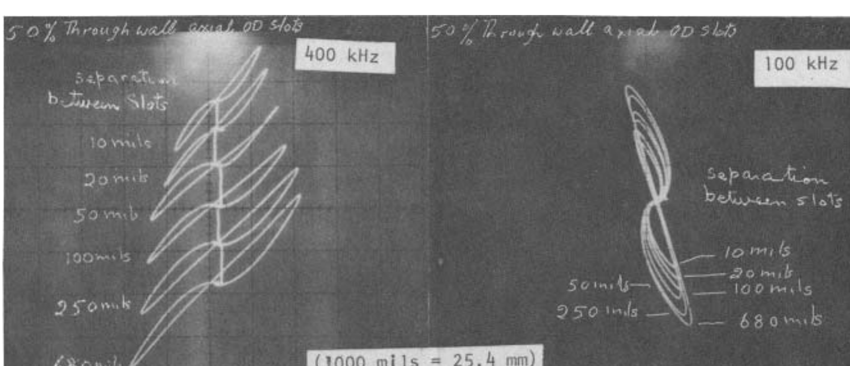

FIG. 6—*Eddy-current signals from four equally spaced 50 percent deep outside-diameter axial slots around the circumference of a 22.2 mm (0.875 in.) outside-diameter, 1.27 mm (50 mil) wall Inconel-600 tube. Slot dimensions: 0.25 mm (10 mil) wide, 6.35 mm (0.25 in.) wide.*

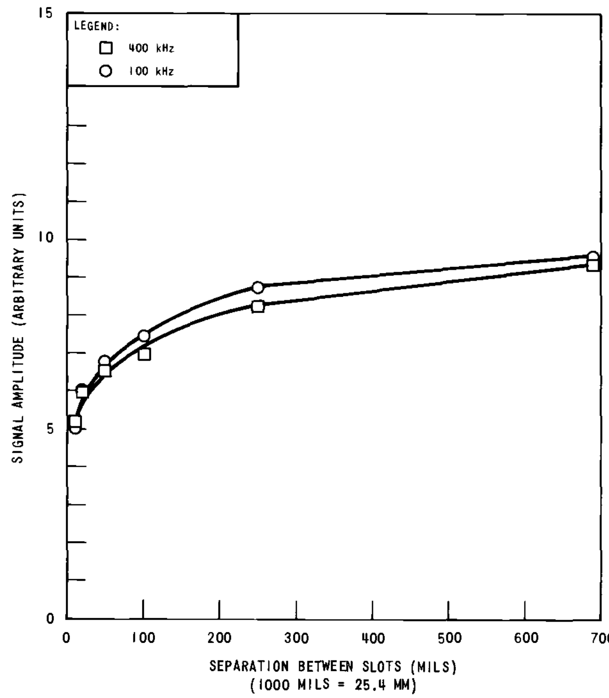

FIG. 7—*Eddy-current signal amplitude at 400- and 100-kHz test frequencies versus separation between four equally spaced 50 percent deep outside-diameter axial slots around the circumference of a 22.2 mm (0.875 in.) outside-diameter, 1.27 mm (50 mil) wall Inconel-600 tube. Slot dimensions: 6.36 mm (0.25 in.) long, 0.25 mm (10 mil) wide.*

machining identical slots in each case, but the amplitude of the oscillation observed in the phase versus separation data in Fig. 8 is quite large and seems beyond the possible errors in machining the slots. It may be noted that this effect was not noticeable in the data for 100 percent deep slots.

It is quite obvious from the aforementioned data that the construction of the eddy-current signal for a collection of slots by a simple summation of the signals from the individual isolated slots is not generally valid. It is, in fact, an approximation and its use is quite restrictive. The simple additivity rule cannot be assumed *a priori* even in the simple case, such as for the calculation of the effective d-c resistance from the collection of the slots in a thin metal plate. It is valid only where the spacing $d \gg l$. Thus, the interaction term may be quite significant in the range $d \sim l$ even though $d \gg \delta$; the interaction term will be independent of frequency in the region $d \gg \delta$.

This discussion emphasizes caution when using the simple additivity rule for the construction of the eddy-current signal for the case of multiple variables simultaneously present in the specimen. The indiscriminate use of a

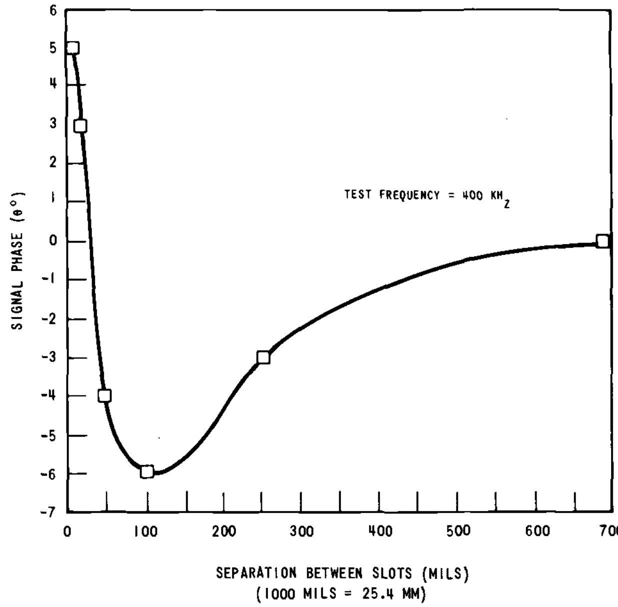

FIG. 8—*Phase of the eddy-current signal for 400-kHz test frequency versus separation between four equally spaced 50 percent deep outside-diameter axial slots around the circumference of a 22.2 mm (0.875 in.) outside-diameter, 1.27 mm (50 mil) wall Inconel-600 tube. Slot dimensions: 6.35 mm (0.25 in.) long, 0.25 mm (10 mil) wide. The phase angle for the signal from the slots spaced 17.27 mm (680 mil) was taken as 0 deg.*

simplistic model which ignores the interaction terms for any data analysis work can often lead to inaccurate results.

Theoretical Discussion

We will first establish the existence of the interaction term between neighboring discontinuities from first principles. Let us consider a conductor without any discontinuity with a current distribution $\bar{J}_0(r)$. In the presence of a cavity in the conductor, this current distribution will be perturbed. Let the perturbation in the current due to a cavity, C_1, located at r_1 be $\bar{J}_1(r)$. Similarly, let $\bar{J}_2(r)$ represent the current distribution due to a second cavity, C_2, located at r_2. Let the current distribution due to the simultaneous presence of the two cavities be $\bar{J}(r)$. We will show that $\bar{J}(r) = \bar{J}_0(r) + \bar{J}_1(r) + \bar{J}_2(r)$ will not do. From the boundary condition we have

$$[(\bar{J}_0 + \bar{J}_1)\cdot\hat{n}_1]_{r=r_1} = 0 \quad \text{and} \quad [(\bar{J}_0 + \bar{J}_2)\cdot\hat{n}_2]_{r=r_2} = 0$$

where $\hat{n}_1$ and $\hat{n}_2$ are unit normals to the surfaces of cavities C_1 and C_2, respectively [2]. If we assume $\bar{J} = \bar{J}_0 + \bar{J}_1 + \bar{J}_2$, then we have

$$[\bar{J}\cdot\hat{n}_1]_{r=r1} = 0 \quad \text{and} \quad [\bar{J}\cdot\hat{n}_2]_{r=r2} = 0$$

This will require

$$[\bar{J}_1\cdot\hat{n}_2]_{r=r_2} = 0 \quad \text{and} \quad [\bar{J}_2\cdot\hat{n}_1]_{r=r1} = 0$$

which is not true in general. It may be valid only for very large separation between cavities in which case $\bar{J}_1$ at r_2 and $\bar{J}_2$ at r_1 would vanish. We thus have to assume $\bar{J} = \bar{J}_0 + \bar{J}_1 + \bar{J}_2 + \bar{J}_{12}$, where $\bar{J}_{12}$ is the interaction term. This would give us

$$[(\bar{J}_2 + \bar{J}_{12})\cdot\hat{n}_1]_{r=r_1} = 0 \quad \text{and} \quad [(\bar{J}_1 + \bar{J}_{12})\cdot\hat{n}_2]_{r=r_2} = 0$$

These equations imply that the magnitude of the interaction term $\bar{J}_{12}$ at r_2 due to the cavity at r_1 is given by the current at r_2 due to the cavity at r_1. Similarly, the magnitude of the interaction term at r_1 due to the cavity at r_2 is given by the current at r_1 due to the cavity at r_2.

We will now try to understand the nature of this interaction term and its effects on the resultant signal generated in the presence of multiple discontinuities. We will not attempt a rigorous quantitative interpretation of these data because of the complex geometry of our experiment. An intuitive understanding of the phenomena, however, is in order. Let us consider the case of a conducting half space $0 \leq x \leq \infty$ with two identical cavities at a distance $x = x_1$ from the boundary and separated by a distance, d, from each other. The volume, ΔV, of each cavity is assumed small enough that the field within this volume is constant; that is, $\Delta V \ll \delta^3$. It is further assumed that $x_1 \gg \delta$ so that boundary effects are ignored. The current density at a distance x_1 from the boundary is given by

$$\bar{J}_y(x_1) = \bar{J}_y(o) \cdot e^{-x_1/\delta} \cdot e^{-jx_1/\delta}$$

where

$J_y(o)$ = current density at the boundary,
δ = $(2/\omega\mu\sigma)^{1/2}$,
σ and μ = conductivity and magnetic permeability of the conducting medium, and
ω = angular frequency of the excitation field [3].

Since no current is allowed across the cavity, we can visualize such a cavity at $x = x_1$ as a current source of volume ΔV and current density $-\bar{J}_y(x_1)$. We will be neglecting the effect of closure currents in this discussion with the understanding that such a treatment is at best approximate. Thus, we can treat the problem of two cavities separated by distance d and located in the conductor at the depth $x = x_1$ from the boundary as the case of two current sources of volume ΔV and current density $-\bar{J}_y(x_1)$ each and separated by d. The vector potential at a point located at a distance r from the current source of volume ΔV and current density $\bar{J}$ may be written as [2–5]

$$\bar{A}(r) \approx \frac{\mu}{4\pi} \cdot \bar{J} \cdot \Delta V \cdot \frac{e^{-r/\delta} \cdot e^{-jr/\delta}}{r}$$

We can thus write the vector potential at cavity 1 due to cavity 2 as

$$\bar{A}_{12} \approx -\frac{\mu}{4\pi} \cdot \bar{J}_y(x_1) \cdot \Delta V \cdot \frac{e^{-d/\delta} \cdot e^{-jd/\delta}}{d}$$

The perturbation of the current density at cavity 2 as a result of this contribution to the vector potential is given by

$$\bar{J}_{12} = \sigma \bar{E}_{12} = -\sigma \cdot \frac{d\bar{A}_{12}}{dt}$$

$$\approx \frac{j\omega\mu\sigma}{4\pi} \cdot \bar{J}(x_1) \cdot \Delta V \cdot \frac{e^{-d/\delta} \cdot e^{-jd/\delta}}{d}$$

The two cavities thus behave as a current source of current density $(-2\bar{J}_y(x_1) + 2\bar{J}_{12})$ in the conductor at $x = x_1$ from the boundary. This current source would produce a vector potential at the conductor surface given by

$$\bar{A}_s = \frac{\mu}{4\pi} \cdot (-2\bar{J}_y(x) + 2\bar{J}_{12}) \cdot \Delta V \cdot \frac{e^{-x_1/\delta} \cdot e^{-jx_1/\delta}}{x_1}$$

This vector potential, $\bar{A}_s$, in turn would produce a voltage at the sensing coil given by $e_i = -\oint dA_s/dt \cdot dl = -K_c \cdot dA_s/dt$, where the integration is taken around the coil and K_c represents the coil constant. We thus have

$$e_i = K_c \cdot \frac{j\omega\mu}{2\pi x_l} \cdot J_y(o) \cdot \Delta V \cdot e^{-2x_1/\delta} \cdot e^{-2jx_1/\delta}\left[1 - jk \cdot \frac{e^{-Q} \cdot e^{-jQ}}{Q}\right]$$

where

$Q = d/\delta$ and
$k = (1/2\pi) \cdot \Delta V/\delta^3$.

This equation leads to the relationship between phase angle θ and Q given by

$$-\theta = \tan^{-1}\frac{k\cdot(e^{-Q}/Q)\cdot\cos Q}{1-k\cdot(e^{-Q}/Q)\cdot\sin Q}$$

$$\approx \tan^{-1}(k\cdot(e^{-Q}/Q)\cdot\cos Q) \qquad \text{for } k \ll 1$$

This solution is an exponentially decreasing function of Q with an oscillatory term $\cos Q$. The function passes through zeros at $Q = 1.57, 4.71, \ldots$, and approaches zero for $Q \gg 1$. The relationship between the normalized amplitude A, with respect to the amplitude for the case when the spacing $d \rightarrow \infty$, and Q is given by

$$A^2 = 1 - 2k\cdot(e^{-Q}/Q)\cdot\sin Q + k^2\cdot\frac{e^{-2Q}}{Q^2}$$

which gives

$$|A| \approx 1 - k\cdot e^{-Q}\cdot\frac{\sin Q}{Q} \qquad \text{for } k \ll 1$$

This expression is an increasing function Q with an oscillatory term $\sin Q/Q$. The expressions for θ and A are valid for $d > \delta > (\Delta V)^{1/3}$, where $(\Delta V)^{1/3}$ may be considered as some characteristic slot dimension.

There is a general qualitative agreement between the experimental data and the aforementioned theoretical expressions for θ and A. When we ignore the data points in the range $d < \delta$ where these calculations are not quite valid, θ decreases exponentially with d for the data on 100 percent deep slots. This exponential dependence seems to extend even into the range $d < \delta$ for the data on 50 percent deep slots (Fig. 8). Again, for the 50 percent deep slots, θ crosses zero at $(d/\delta) \approx 1.5$ and suggests the presence of the oscillatory term, although the swing to negative value of θ is too large compared to that expected from theory. The data on 100 percent deep slots show no evidence of the oscillatory behavior in θ versus d. The data of Figs. 3 and 8 should show a linear relationship between $ln(\theta\cdot d)$ and d in the range where the calculations are valid, and the value of δ can be obtained from the slope $d(d)/d(\ln\theta\cdot d)$. Using the extrapolation of the limited data available, we find that 400-kHz data of Figs. 3 and 8 both yield a value for $\delta \approx 1.14$ mm (45 mil). The value of δ for Inconel-600 at 400 kHz calculated from the expression $\delta = (2/\mu\sigma\omega)^{1/2}$ is 0.84 mm (33 mil). Similar manipulation of the 100-kHz data yields a value for $\delta \approx 5.08$ mm (200 mil) that is in poor agreement with the value of $\delta \approx 1.68$ mm (66 mil) for Inconel-600 at 100 kHz. Of course, we had hardly any data points in the range of validity of the theory to justify a reliable estimate of the slope of the straight line drawn through the $ln(\theta \cdot d)$ versus d data at 100 kHz.

It may be mentioned that we did not expect a very good agreement between these limited experimental data and the results of such a simplistic calculation. The approximations made in this calculation were quite restrictive and may not be quite justifiable for our test conditions. We ignored, for example, the effect of closure currents when treating a cavity as a current source. This approximation is far from satisfactory for the case of long thin slots in the transverse field and was used only for simplicity of calculations. Furthermore, our calculations were for two interacting cavities only, whereas our experiment was performed on four slots. A complete calculation for more than two slots would require additional terms involving interaction terms between next-nearest neighbors etc., and would make the calculations more tedious without adding much to the understanding of the phenomena. We thus neglected these terms. Again, we had assumed $(\Delta V/\delta^3) \ll 1$ in our calculations, but for our experimental conditions $(\Delta V/\delta^3) \approx 5$ for the 100 percent deep slots at 400 kHz.

We have also ignored the effect of the field distortions from the sample boundary and from the presence of the slots in the conductor. The field distortions from the slots would contribute to the d-c resistance of the sample and would be reflected in the data on amplitude versus slot separation. This term would be also frequency independent. We will show in the following discussion that this is the dominant term in the data on the amplitude versus slot separation. The d-c resistance of slots in a conductor may be estimated by a graphical method, [*6, 7*]. Here, however, we will deal with the problem only qualitatively. Let us consider a thin rectangular metal sheet with the current in the direction of the long dimension of the sheet. We can divide this sheet into a uniform square grid pattern of orthogonal lines representing current and equipotential lines. When we take the resistance of one square as a convenient unit, the total resistance of the sheet can be calculated by using the series-parallel combination of unit resistances. The presence of a slot in the middle of the sheet will distort this uniform square grid pattern in the neighborhood of the slot. The field map for a narrow slot in a thin metal sheet is given in Ref *6* and can be used for computing the resistance of the slot. The resistance of two such slots in series and separated by a distance much larger than the slot length is just the sum of the resistances of the individual slots. An examination of the field map for the single slot, however, shows that so long as the slot length $\gg$ slot width is valid, the resistance of the slot is not changed significantly by change in the slot width [*6*]. The resistance of multiple slots in series would thus decrease with decreasing spacing between them. This decrease would be more rapid in the region $d < l$. In our experiment we have (slot length/slot width) $\approx$ 25. By merging the four slots together the value of this ratio becomes 6, which is still larger than unity, although the condition, slot length $\gg$ slot width, is not strictly valid now. Thus, the resistance of four merged slots of the dimensions used in our test would be near $1/4$ of the resistance of the slots when they are far apart; this is not too far from the value $1/3$ obtained from the data of Fig. 4 for the 100 percent deep slots. It may be noted that in this discussion we have not involved any a-c phenomena such as eddy-current and skin-depth. We are dealing strictly with the field distortions from the slot boundaries. This contributes a frequency-independent term to our results and should be noticeable in the amplitude data. The contribution from the frequency dependent term $A \approx 1 - k \cdot e^{-Q} \cdot (\sin Q/Q)$ does not seem to be dominant in the data on A versus d and results in the observed weak frequency-dependence of the amplitude data. No discussion of the amplitude data for the 50 percent deep slots is given here because of the complexity of this problem.

It is easy to see from this discussion that the often observed dependence of the phase of the signal on the size and geometry of a discontinuity (see the next two sections) may result in part from the interaction between different regions of a discontinuity. The simplistic phase versus depth relationship so often used for eddy-current data analysis is valid only for very small discontinuities where the fields within the volume of the discontinuity can be assumed as constant.

Phase Angle of the Signal versus Size of the Discontinuity

Figures 9 and 10 show the dependence of phase and amplitude of the eddy-current signals on the diameter of the circular holes 100 percent through the tube wall. The signal amplitude seems to follow an approximate linear dependence on the volume of the metal involved in the discontinuity. Although the geometrical shape and the depth of the discontinuity were kept the same, the data in this test show a strong dependence of phase angle on the size of the discontinuity.

Eddy-Current Signal versus Orientation of the Discontinuities

The data on the amplitude of the signals at 400-kHz test frequency as a function of the slot length for 100 percent deep longitudinal and the transverse slots are shown in Fig. 11. All these data were taken with a differential probe. The dimensions of the slots are shown in Table 1. The change in phase of the signals as a function of the slot length for the longitudinal slots is shown in Fig. 12. Similar data on amplitude versus slot length for the 50 percent outside-diameter slots are shown in Fig. 13. The physical reasons for such a difference in the characteristics of the curves for the axial slots of different depths is not clear. The general shape of the curves for the longitudinal slots can be understood as resulting from the use of a differential probe and is expected to be a function of the coil dimensions and the spacing between them. These data do emphasize, however, the ambiguity in the eddy-current results in terms of the nature of the discontinuity. The use of an absolute probe could, in principle, lead to a more complete evaluation of the nature of discontinuities encountered in the test, but the disadvantage of the low signal-to-noise ratio often resulting from the use of absolute probes makes it impractical for use in the detection of small discontinuities. The use of helical scans with small pancake coils is often useful for better characterization of the discontinuities; unfortunately, it is a tedious operation.

These data point to the fact that there are some uncertainties in the determination of the complete characteristics of a discontinuity in any practical eddy-current test. One can reduce the uncertainty, however, by performing multiple tests using different test variables.

Simultaneous Presence of Multiple Specimen Variables and the Multiparameter Technique

It is often required that one be able to evalute the condition of a tube in the region of support-plate intersection where the support-plate signal interferes with such an evaluation. The data in Fig. 14 show the effectiveness of the multiparameter technique in reducing the interference from the steel supports around the outside-diameter of the Inconel-600 tubing. Figure 14*a* shows the signals at 400-kHz test frequency from a calibration standard with machined discontinuities on the tube wall, and the signal from a simulation of a 19.05-mm (0.75 in.)-thick carbon steel support plate around the tube without any machined discontinuities. Figure 14*b* shows the signals at 100 kHz. Figure 14*c* shows the results of analysis of the two-frequency data. Defining the noise as the unwanted signal from the support plate and the signal as an indication from the 100 percent through hole, we find the best value of the signal-to-noise ratio in the single-frequency data is 1.3. The signal-to-noise ratio for the data in Figure 14*c* is about 13. There is thus an order of magnitude improvement in *S/N* ratio using the multiple-frequency data analysis. In order to understand the difficulty of achieving a further significant improvement in the *S/N* ratio, we may examine the electronically manipulated steel support signals at the two frequencies before they are finally combined in the analyzer. Figure 15 shows these shaped signals with the relative time sequence of their formation. Figure 16 shows the steel-support signals at the two frequencies without any electronic manipulation

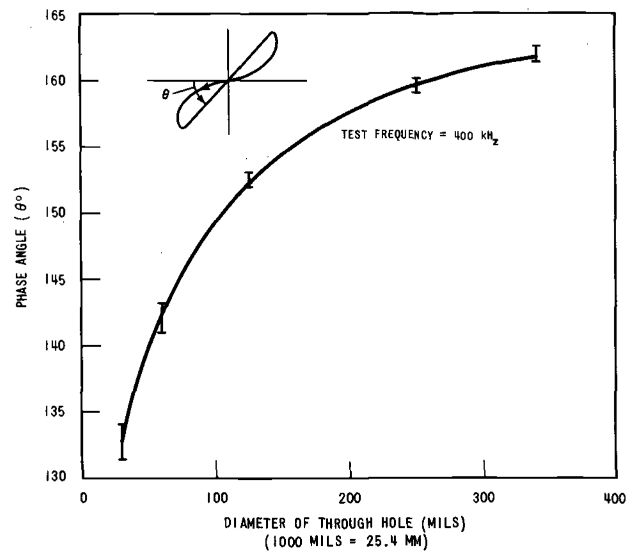

FIG. 9—*Phase of the eddy-current signals versus diameter of through holes in a 22.2 mm (0.875 in.) outside-diameter, 1.27 mm (50 mil) wall Inconel-600 tube.*

by the analyzer for a comparison. The signals in Fig. 15 also point to the limitation of this simple linear combination technique for obtaining the cancellation of such signals. Some further improvement in the results may be obtained by the use of probes with very well matched coils, judicious selection of frequencies, and perhaps more laborious manipulation of the signals with the analyzer.

This technique assumes linear conditions; that is, it assumes that the signal from a set of variables can be written as a linear sum of signals from individual isolated variables, and may be a good approximation for small signals [*1,5*]. This puts a limitation on the improvement of the S/N ratio that may be expected of the system. As shown in the section on Interaction Between Specimen Variables, the use of the simple rule of signal addition from different variables is quite restrictive. However, the use of a linear combination of signals in order to eliminate the unwanted signals produces acceptable, although not quite precise, results even where the interaction terms are quite significant. This is shown in the next section.

The multiparameter technique removes some of the signal degeneracies that one may encounter in a system of tubes and steel support plates. For example, in the results of the linear combination which reduces the interference of the steel-support signals, we automatically eliminate (or considerably attenuate) the signals from any discontinuities in the steel support-plate hole, thus eliminating the ambiguity of the support-plate discontinuity as being

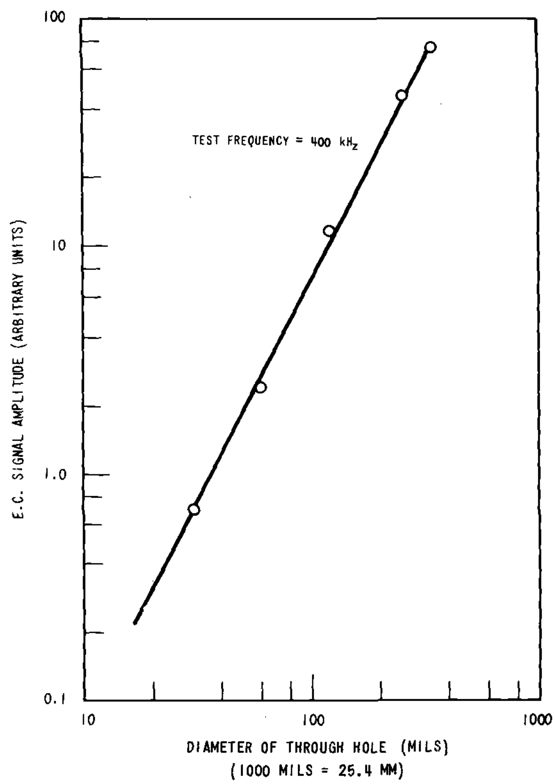

FIG. 10—*Eddy-current signal amplitude versus diameter of through holes in a 22.2 mm (0.875 in.) outside-diameter, 1.27 mm (50 mil) wall Inconel-600 tube.*

one of the causes of the signal seen in the single-frequency data. Such a solution will suffer from the deficiency that it would provide no information about the condition of the support plates. In case any information about the condition of the support plate is needed, one has to attempt a different linear combination or obtain the information from the data at individual frequencies by pattern recognition.

Influence of Interaction Terms Between Specimen Variables

Figure 17 shows the test specimen configuration where the interaction between two discontinuities was varied without varying their position with respect to the coil. The two specimen variables used in this test are an axial slot 100 percent through the tube wall and a carbon steel half-ring on the outside-diameter of the tube. The half-ring was rotated in order to change its position with respect to the slot without changing its position axially. The analyzer was first adjusted for the best cancellation of the signal from the steel support around a tube without any slot in its wall. The signals for the

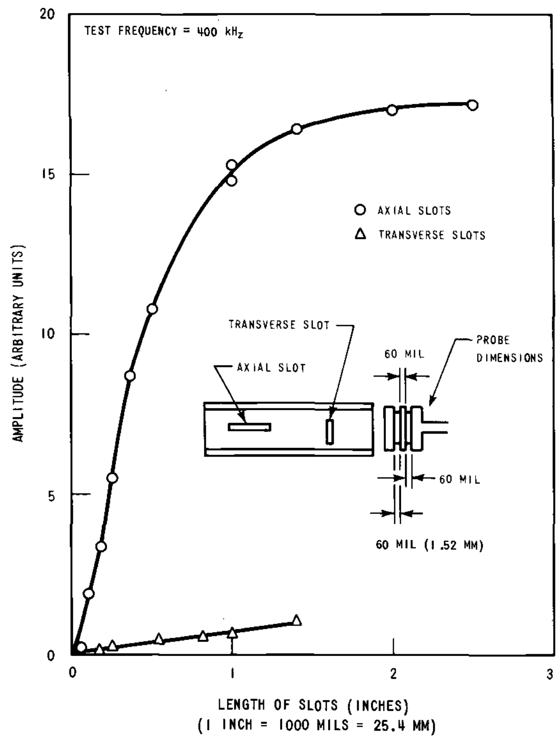

FIG. 11—*Eddy-current signal amplitude at 400-kHz test frequency versus length of through slots in a 22.2 mm (0.875 in.) outside-diameter, 1.27 mm (50 mil) wall Inconel-600 tubing. Slot width for longitudinal slots = 0.140 ± 0.013 mm (5.5 ± 0.5 mils). Slot width for transverse slots = 0.152 ± 0.013 mm (6.0 ± 0.5 mils).*

three configurations shown in Fig. 17 were then recorded. They are shown in Fig. 18. The interaction term is naturally more relevant when the half-ring covers the slot (Configuration #3).

Figures 19 and 20 show the results of the tests repeated with ferrite half-ring and copper foil, respectively. In each case the influence of the interaction is quite noticeable. The resulting signals after multiparameter analysis also indicate that this interaction is significant when the slot and the surrounding ring overlap.

These examples show that some errors in the results of this type of analysis may be expected on account of the interaction between neighboring discontinuities.

Signal Degeneracy

One often encounters accidental degeneracies in eddy-current signals. In the work reported here with Inconel-600 tubing of 1.27-mm (50 mil) wall, we

TABLE 1—*Dimensions of the slots in the tube wall used for the data of Fig. 11.*

Orientation of slot	Depth, %	Length, in.[a]	Width, mil[b]
Transverse	100	1.4	6
Transverse	100	1	6
Transverse	100	0.82	6
Transverse	100	0.55	6.5
Transverse	100	0.25	8
Transverse	100	0.18	6.5
Transverse	100	0.13	6.5
Longitudinal	100	2.5	5.5
Longitudinal	100	2	6
Longitudinal	100	1.5	5
Longitudinal	100	1	5.5
Longitudinal	100	1	6
Longitudinal	100	1/2	6
Longitudinal	100	3/8	6
Longitudinal	100	1/4	6
Longitudinal	100	3/16	6
Longitudinal	100	1/8	5
Longitudinal	100	1/16	5

[a]1 in. = 25.4 mm.
[b]1000 mil = 25.4 mm.

have often come across multifold degeneracies in the signals. For example, a low depth discontinuity involving wall reduction originating from the outside diameter and a dent on the tube wall results in signals with nearly the same phase at a 400-kHz test frequency. This degeneracy can be easily removed by performing the test at another frequency. At about 100 kHz, for instance, the phase separation between the two signals becomes almost 90 deg (Fig. 21*a*). The situation can become quite complicated in some cases. As an example, at 400-kHz test frequency, the signals from metallic plating on the outside diameter of the tube, a discontinuity originating from the inside diameter of the tube wall, a slight variation in the magnetic permeability of the Inconel-600, local enlargement of the tube inside diameter, and some magnetic oxide deposit on the tube inside diameter, all lead to signals with about the same phase. Obviously, one has to perform many tests to remove this degeneracy. The use of a different test frequency can discriminate between the signal sources originating from the outside diameter and the ones located on the inside diameter of the tube. Some examples of removing the degeneracy by this method are shown in Fig. 21. (The degeneracy of the signals from a dent and from magnetite on the outside diameter of the tube at the 100-kHz test frequency may be noticed from Figures 21*a* and 21*d*.) However, a magnetic bias on the coil has to be used to remove the degeneracy of the signals resulting from magnetic sources (such as magnetite on the inside diameter or magnetic permeability variations of Inconel-600) and other

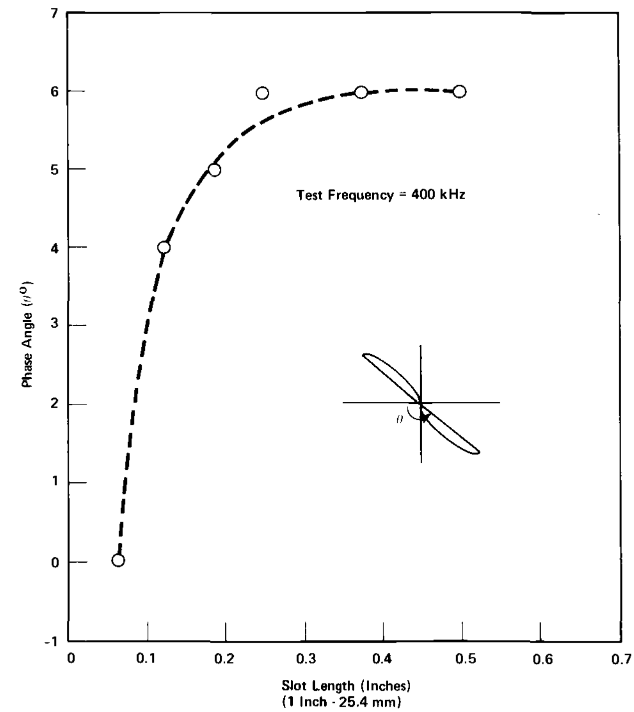

FIG. 12—*Change in the phase of the eddy-current signals at 400-kHz test frequency versus the length of the 100 percent through-the-wall axial slots on the 22.2 mm (0.875 in.) outside-diameter, 1.27 mm (50 mil) wall Inconel-600 tube.*

sources (such as localized enlargement of the tube diameter and discontinuities originating from the inside diameter of the tube.) Signals from the magnetic sources can easily be attenuated by many orders of magnitude when using a magnetic bias on the coil. The remaining degeneracy between the signals from inside diameter discontinuities and the localized enlargement of the tube diameter may finally be removed by measuring the tube inside diameter, using perhaps an absolute probe or a multicoil probe.

Tube Support-Plate Evaluation

In the absence of interference signals from any other test variables, an estimate of the diameter of the tube support-plate hole surrounding the tube can be readily obtained using calibration curves such as the ones shown in Fig. 22. These curves were generated using a differential probe. In case the high-frequency test shows any evidence of tube-wall discontinuities (including deformation) at the support-plate intersections, one would need the

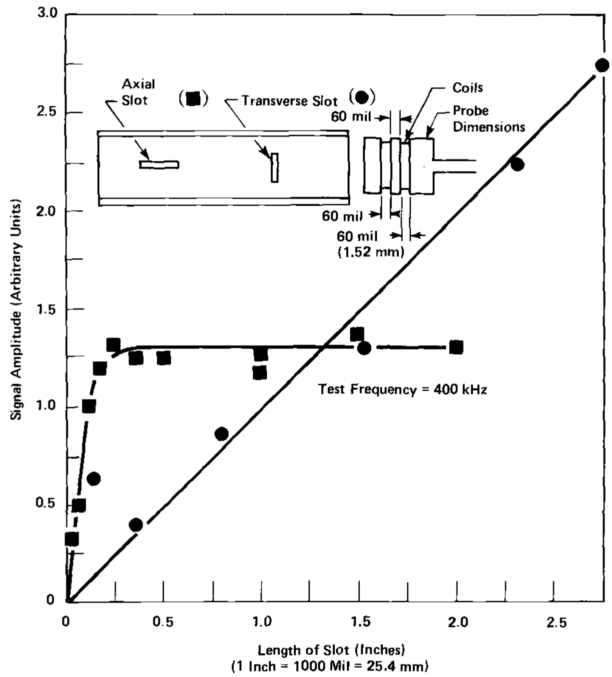

FIG. 13—*Eddy-current signal amplitude at 400-kHz test frequency versus the slot-length for 50 percent deep, 0.13 mm (5 mil) wide, outside-diameter slots on 22.2 mm (0.875 in.) outside-diameter, 1.27 mm (50 mil) wall Inconel-600 tube.*

low-frequency test data (below 10 kHz) for support-plate evaluation since the eddy-current system becomes relatively insensitive to the tube-wall discontinuities at lower frequencies. This results in a support-plate signal unperturbed by any contributions from the discontinuities in the tube wall. There is also considerable degeneracy between the signals from the tube-wall discontinuities and from the discontinuities in the tube support-plate; one usually needs to analyze the multifrequency data in order to evaluate the origin of the signals in such regions.

The calibration curves shown in Fig. 22 are valid only when the corrosion products that may be present in the crevice do not create any interfering eddy-current signals, and when the variations in the electrical and magnetic properties of carbon steel samples in question are quite small and can be ignored. If the crevice is filled with magnetite, for example, the calibration curves of Fig. 22 become less applicable. Figure 23 shows the support-plate signals in the absolute and differential mode with and without the magnetite in the crevice keeping the diameter of the support-plate hole the same. These data show that the presence of magnetite in the crevice decreases the loss and increases the reactive component of the coil impedence, which results in a

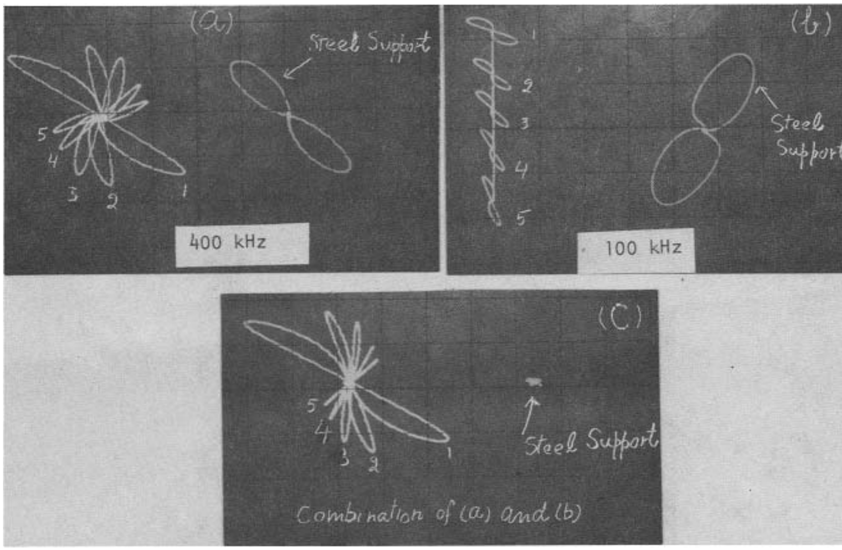

FIG. 14—*Eddy-current signals from machined outside-diameter discontinuities in the tube wall and a carbon steel support around the as-manufactured tube at* (a) *400-kHz and* (b) *100-kHz test frequencies, and* (c) *a linear combination of* (a) *and* (b). *Signals 1 to 5 on the left represent the following discontinuities machined on the tube wall: #1—1.52 mm (60 mil) diameter through hole; #2—1.98 mm (78 mil) diameter, 80 percent deep outside-diameter; #3—2.77 mm (109 mil) diameter, 60 percent deep outside-diameter; #4—4.76 mm (187.5 mil) diameter, 40 percent deep outside-diameter; and #5—four 4.76 mm (187.5 mil) diameter, 20 percent deep outside-diameter co-planar discontinuities 90 deg apart.*

counterclockwise rotation of the signal. It is quite obvious that one needs to know the density profile of Fe_3O_4, if present in the corrosion products, in order to estimate the diameter of the tube support hole. A simple detection of any significant amounts of Fe_3O_4 in the crevice could possibly be accomplished by signal-pattern recognition. In fact the presence of nonuniform deposits of magnetite, which results from corrosion of the support-plate inner diameter, enhances the detectability of localized corrosion of the support-plate hole. The detection of axial slots running through the entire 19.05 mm (0.75 in.) length of the support-plate ligaments may also be accomplished by the examination of the support-plate signals. Figure 24 shows some data at 7 kHz in differential and absolute mode for different combinations of support-plate samples and magnetite. The data show that the signals from a support plate with slotted ligaments can be distinguished from a normal support-plate signal even in the presence of Fe_3O_4 in the crevice. In the case of a support plate without slotted ligaments, the reactance of the coil shows an initial drop as the support-plate enters the field of the coil, whereas for the support plates with slotted ligaments this initial drop in the coil reactance does not occur.

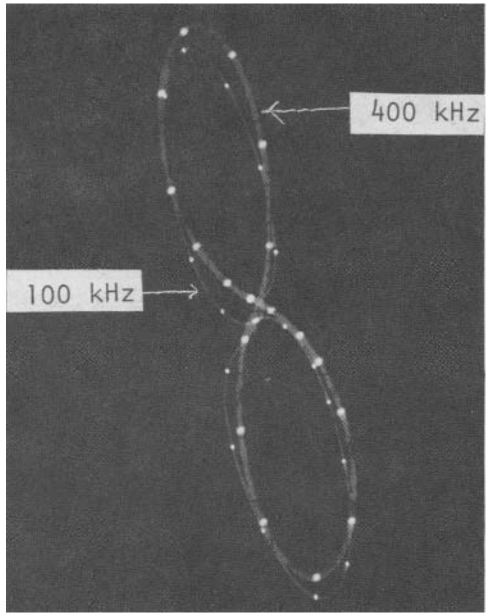

FIG. 15—*Steel-support signals at the two test frequencies shaped by the analyzer before combining in order to obtain results shown in Figure 14c.*

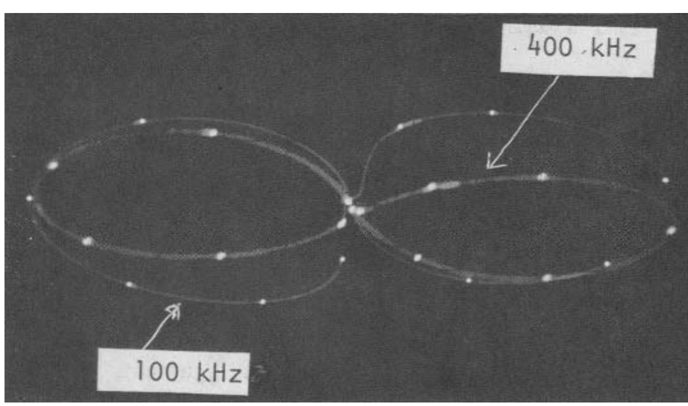

FIG. 16—*Steel-support signals at the two test frequencies without any shaping by the analyzer.*

Determination of the Tube Inside Diameter

Any variation in the inside diameter of the tubing can be easily detected from the high-frequency eddy-current data using a differential or absolute circumferential probe. A precise estimate of the tube inside diameter can be made from such data so long as the tube maintains its circular cross section. This can be accomplished by using calibration curves generated with a calibration standard consisting of a tube with regions of different inside diameters but still maintaining a circular cross section. In the event the tub-

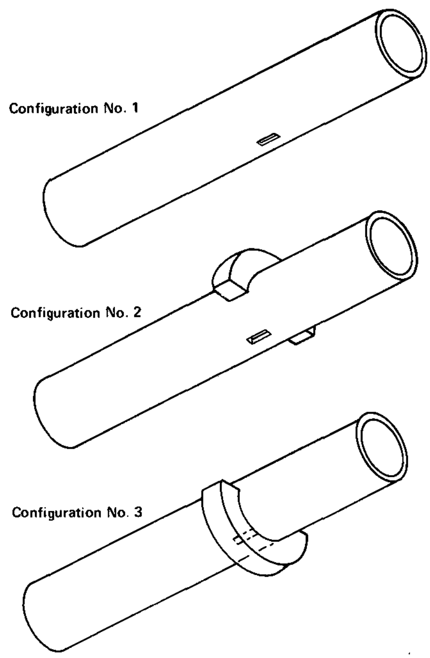

FIG. 17—*Drawing showing the position of the half-ring relative to the machined slot in the tube wall used for the data shown in Figs. 18 to 20.*

FIG. 18—*Eddy-current signals for the specimen configurations (shown in Fig. 17) consisting of a tube with a 100 percent through-the-wall axial slot and a half-ring of carbon steel at 400- and 100-kHz test frequencies and the resulting signals after the combination of the two frequency data.*

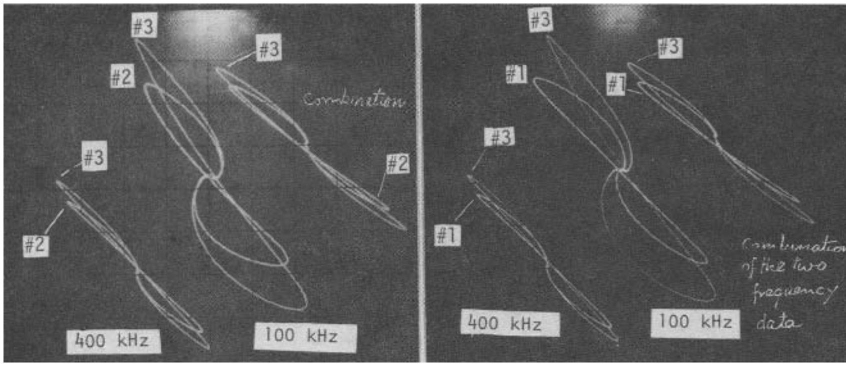

FIG. 19—*Eddy-current signals for the specimen configurations (shown in Fig. 17) consisting of a tube with a 100 percent through-the-wall axial slot and a half-ring of ferrite at 400- and 100-kHz test frequencies and the resulting signals after the combination of the two frequency data.*

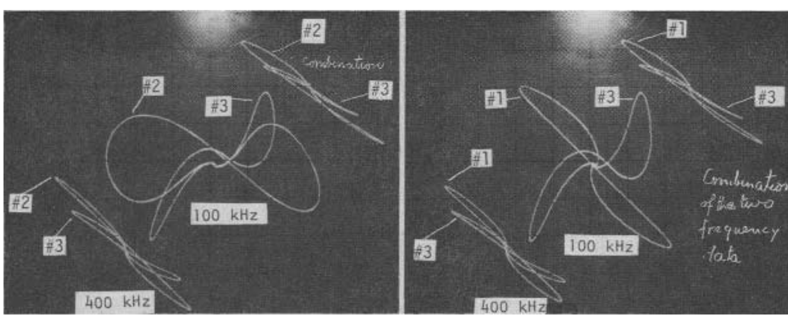

FIG. 20—*Eddy-current signals for the specimen configurations (shown in Fig. 17) consisting of a tube with 100 percent through-the-wall axial slot and a thin copper foil at 400- and 100-kHz test frequencies and the resulting signals after the combination of the two frequency data.*

ing may have regions of noncircular cross sections, eddy-current data obtained by using a circumferential coil obviously becomes less relevant to the determination of the inside dimension of the tube. In order to determine the inside dimensions of the tube in regions of noncircular cross section one can use a probe with multiple pairs of small pancake coils with the two coils of each pair placed 180 deg apart and facing the tube inside surface. The response of the two coils to the lift-off is first made linear and identical electronically. A summation of the response of the two coils placed 180 deg apart and the distance between the two coils would then give the tube dimension in that local region. The summation can be easily accomplished electronically. The response of a set of such coil pairs placed around the cross section of a cylindrical probe would then give the profile of the tube cross section. A high-

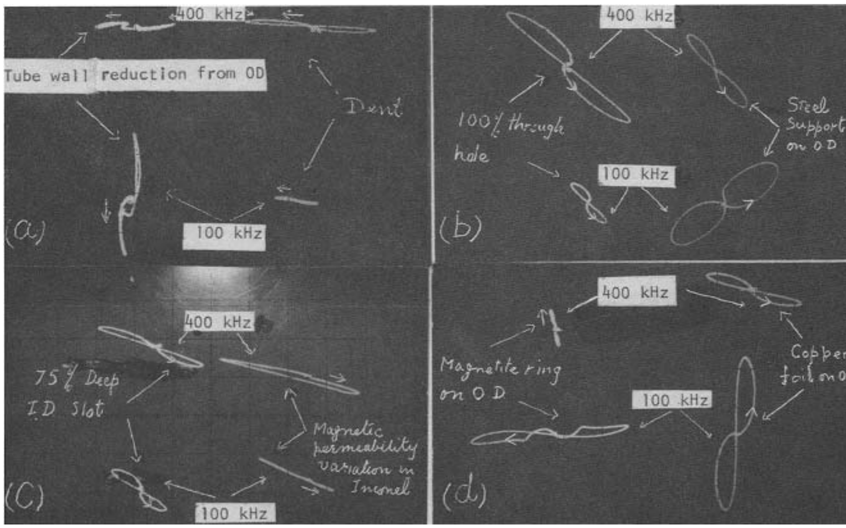

FIG. 21—*Some examples of the degeneracies in the single test frequency eddy-current signals and the removal of such degeneracies by two-frequency eddy-current testing.*

excitation frequency needs to be used in order to eliminate the interference from sources such as the tube support-plate, the possible tube-wall reduction, and the presence of corrosion products in the crevices. The results of our laboratory tests with such a probe using 1-MHz excitation frequency suggest that such a device can measure variations in tube dimensions on the order of 0.013 mm (0.5 mil).[5]

One can also use capacitive displacement sensors in place of the coils for such measurements. These sensors have the advantages of easy manufacture and of the response being unaffected by any change in the electrical and magnetic properties of the alloy of the tubing. Such probes, however, have the disadvantage of being sensitive to the electric properties of the medium between the sensors and the tube wall (for example, water, dirt, etc.). This factor would limit its use to situations with controlled environments.

Summary

1. The multifold degeneracy of the eddy-current signals requires a multifrequency eddy-current test for reducing the ambiguity in the evaluation of the signals.

2. The interaction between different regions of a discontinuity results in the lack of a unique relationship between the phase-amplitude charac-

[5]The probe and the electronics used for this work were fabricated by KAMAN Sciences Corporation, Colorado Springs, Colo. Since the completion of this work, an eddy-current instrument capable of on-line display of tubing cross section has been developed by Zetec, Inc., Issaquah, Wash.

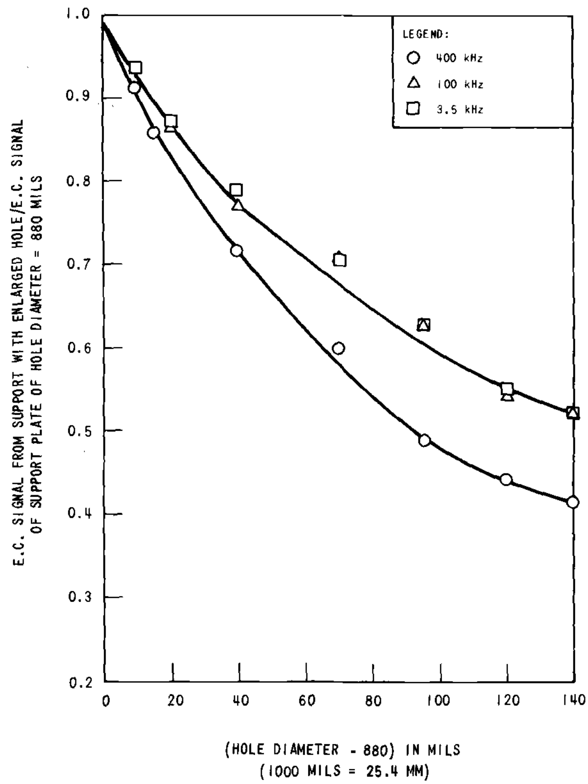

FIG. 22—*Amplitude of the eddy-current signals from the carbon steel tube support with enlarged holes relative to the signal from the support plate of inside-diameter = 880 mil versus (hole diameter − 880) in mil (1000 mil = 25.4 mm).*

teristics and the depth of discontinuities of unknown geometry and orientation.

3. Some knowledge of the geometry and the size of a discontinuity may be needed in order to precisely estimate the depth from the phase-angle information.

4. In the case of simultaneous presence of multiple variables, such as tube support and tube-wall discontinuity, the method of linear combination of multi-frequency data improves the ratio of the signal from the wall discontinuity to the unwanted signal from the tube support by an order of magnitude when compared with the single-frequency data.

5. The interaction between closely spaced variables is significant and may interfere with the precise determination of the characteristics of the discontinuities when the method of linear combination of multifrequency data is used. Although this method ignores the non-linearities in the system, it yields

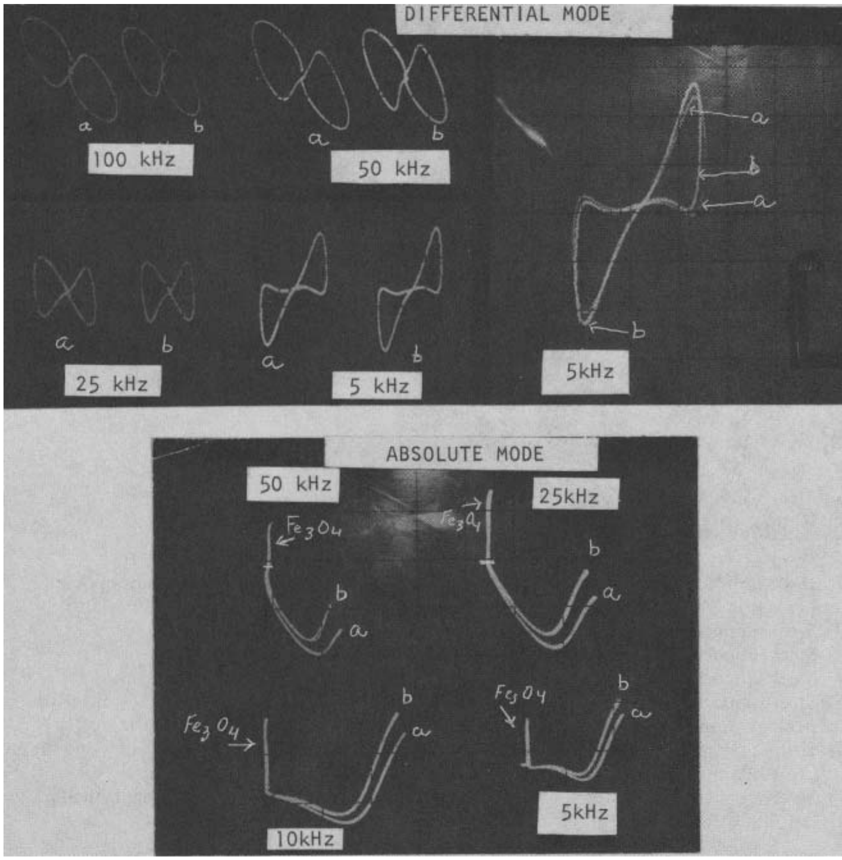

FIG. 23—*Eddy-current signals in differential and absolute modes at various test frequencies from carbon steel support and an Inconel-600 tube. Signals marked* (a) *represent the case without* Fe_3O_4 *in the 0.30 mm (12 mil) radial crevice. Signals marked* (b) *represent the case of the crevice filled with* Fe_3O_4 *powder of unknown density.*

acceptable results. If a more precise determination of the sample discontinuities is required, the non-linearities will have to be taken into account by tedious numerical methods.

6. The presence of Fe_3O_4 in the crevice between the tube and the tube support-plate may lead to some uncertainty in the determination of the diameter of tube support-plate hole.

7. Estimates of the variations in the inside dimensions of the tubing in regions with noncircular cross sections can be made within ±0.013 mm (0.5 mil) using specially designed cylindrical probes with multiple pairs of pancake coils placed 180 deg apart about the probe circumference.

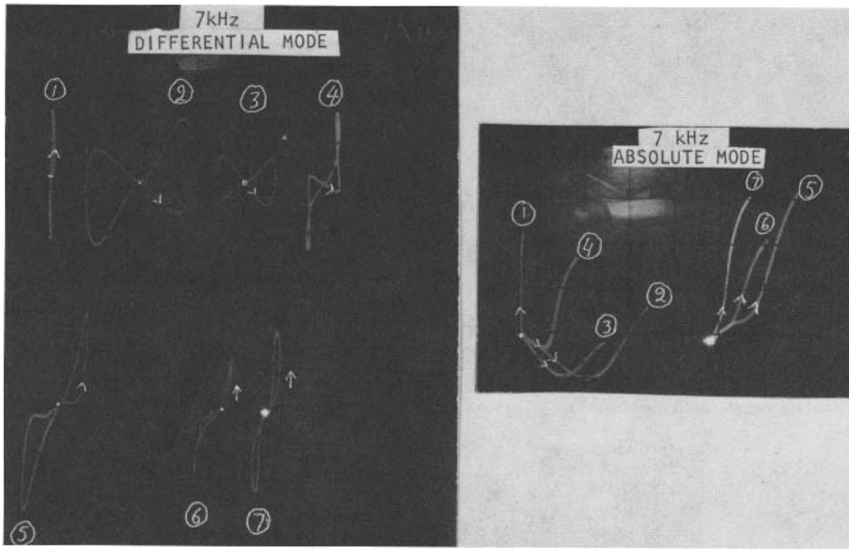

(*1*) 19.05 mm (0.75 in.) long, 1.02 mm (40 mil) thick, Fe_3O_4 cylinder (density approximately 50 percent.
(*2*) Steel-support inside-diameter = 22.35 mm (0.880 in.).
(*3*) Steel-support inside-diameter = 25.91 mm (1.020 in.).
(*4*) Steel-support inside-diameter = 25.91 mm (1.020 in.), surrounding Fe_3O_4 ring.
(*5*) Steel-support inside-diameter = 22.35 mm (0.880 in.), with a 0.25-mm (10-mil)-wide 100 percent through slot along the entire 19.05 mm (0.75 in.) length of the ligament.
(*6*) Steel-support inside-diameter = 26.31 mm (1.036 in.), with a slotted ligament along the entire 19.05 mm (0.75 in.) length.
(*7*) Steel-support inside-diameter = 26.31 mm (1.036 in.), with a slotted ligament surrounding the Fe_3O_4 ring.

FIG. 24—*Eddy-current signals at 7-kHz frequency in differential and absolute mode from different combinations of steel support and Fe_3O_4 ring surrounding an Inconel-600 tube.*

Conclusions

The work presented in this paper emphasizes the importance of understanding the mutual interactions taking place between various discontinuities during the time the coil is interrogating them collectively in order to precisely characterize them. We often do not have the option of interrogating the discontinuities separately and have to contend with their ability of mutual communication before we receive their final signal. Our work leads us to conclude that these interactions result in a somewhat higher phase angle and lower amplitude of the final signal compared to the situation where these interactions may have been ignored as insignificant.

References

[*1*] Libby, H. L., *Introduction to Electromagnetic Nondestructive Test Methods*, Wiley-Interscience, New York, 1971, pp. 214–257
[*2*] Panofsky, W. K. H. and Phillips, M., *Classical Electricity and Magnetism*, Addison-Wesley, Reading, Mass., 1955, Chapter 7.
[*3*] Libby, H. L., *Introduction to Electromagnetic Nondestructive Test Methods*, Wiley-Interscience, New York, Chapters 5 and 6.
[*4*] Burrows, M. L., "A Theory of Eddy-Current Flaw Detection," Ph.D. dissertation, University of Michigan, 1964.
[*5*] Libby, H. L., BNWL-953, Battelle-Northwest, Richland, Wash., 1 Jan. 1969.
[*6*] Moon, P. and Spencer, D. E., *Field Theory for Engineers*, Van Nostrand, New York, 1961, Chapter 7.
[*7*] Rogers, W. E., *Introduction to Electric Fields*, McGraw-Hill, New York, 1954, Chapter 4.

A. H. Kahn[1] *and R. Spal*[1]

A Boundary Integral Equation Method for Calculating the Eddy-Current Distribution in a Long Cylindrical Bar with a Crack

REFERENCE: Kahn, A. H. and Spal, R., "**A Boundary Integral Equation Method for Calculating the Eddy-Current Distribution in a Long Cylindrical Bar with a Crack,**" *Eddy-Current Characterization of Materials and Structures, ASTM STP 722*, George Birnbaum and George Free, Eds., American Society for Testing and Materials, 1981, pp. 298-307.

ABSTRACT: We report calculations of the impedance of a long solenoid which surrounds a cylinder of conducting material containing a crack. The calculation is approached by expressing the eddy-current problem as an integral equation for the normal derivative of the magnetic field on the boundary of the conductor. This method is generally applicable to any cylindrical problem, regardless of the cross-sectional shape of the conductor. The boundary integral equation is solved in the case of the crack problem by discretizing and converting to a system of linear algebraic equations for the normal derivative of the field. The complex impedance is thereby obtained for a wide range of values of the ratio of crack depth to radius to skin depth. The results are displayed in graphical form, which gives the fractional changes of the real and imaginary parts of the impedance caused by the presence of the crack.

KEY WORDS: crack detection, eddy currents, nondestructive evaluation

Interest in electromagnetic methods of nondestructive evaluation has led us to examine methods for calculation of the distribution of eddy currents in the vicinity of a crack in conducting material. In a previous paper we considered the problem of a surface crack in a plane slab subjected to a uniform magnetic field [*1*].[2] In that work we found solutions for the eddy currents in the vicinity of the corners and the tip of the crack. For cracks deeper than four times the electromagnetic skin depth, the two solutions could be joined to give the full eddy-current pattern. We then went on to give an analytic solution to a problem more closely related to testing conditions, that of a cylinder with a uniform radial crack, surrounded by a solenoid [*2*]. For this case the modification of the impedance of the solenoid, caused by the crack,

[1] Physicist, National Bureau of Standards, Washington, D.C. 20234.
[2] The italic numbers in brackets refer to the list of references appended to this paper.

was calculated from an eigenfunction expansion devised for the particular geometry of the problem.

In this paper we offer another method of calculating the impedance in two-dimensional cylindrical problems, an application of the boundary integral equation (BIE) method [*3-7*; but see also *8*]. This procedure has the advantage of being tractable in cases of cylindrical geometry where the core of the solenoid and the defect may have arbitrary cross-sectional shape. It also serves as a check on calculations performed by other methods. Lastly, we review the results for the crack in the cylinder, show the impedance diagram for a typical case, and offer an intuitive understanding of the results.

The BIE method in the present approach may be contrasted with the finite-element approach to similar problems [*9,10*] presented previously by Chari and Kincaid.[3] The BIE method seeks the eddy-current density at the boundary of the core of the solenoid; the finite-element method solves directly for the field distribution throughout the core. We view the two approaches as complementary.

Statement of the Problem

Consider an infinitely long solenoid that surrounds a cylindrical conducting core of arbitrary cross-sectional shape. We shall develop a method of calculating the contribution of the core to the impedance of the solenoid. Particular attention will be given to the case in which the core consists of a circular cylinder with a uniform, tight radial crack, in which case the contribution of the crack will be isolated.

Let the solenoid be excited by a sinusoidally varying current so that the magnetic field in the open space between it and the core is given by the real part of $H_0 e^{-i\omega t}$, where the amplitude H_0 is spatially uniform and in the direction of the axis of the solenoid, the z-axis. The configuration is shown in Fig. 1.

To obtain the impedance of the coil we shall need the inward flux of the complex Poynting vector through the solenoid. The time average of the complex power per unit length of the coil is given by

$$\begin{aligned}\overline{P} &= (1/2)\left(\int_{\text{coil}} \mathbf{E} \times \mathbf{H}^{*} \cdot dA\right)\\ &= (1/2)\left(\int_{\text{coil}} \mathbf{E} \times \mathbf{H}_0{}^{*} \cdot \mathbf{dl}\right)\\ &= (1/2)\left(H_0{}^{*} \int_{\text{coil}} \mathbf{E} \cdot \mathbf{dl}\right) \qquad (1)\end{aligned}$$

[3]Chari, M. V. K. and Kincaid, T. G., this publication, pp. 59-75.

where the lateral area integration over dA has been converted to a line integral on dl around the cross section of the coil. From the Maxwell equation which holds in the open area between the coil and core

$$\nabla \times \mathbf{E} = -\dot{\mathbf{B}} = i\omega\mu_0\mathbf{H}_0 \tag{2}$$

we obtain, by application of Stokes' theorem,

$$\int_{\text{coil}} \mathbf{E}\cdot dl = \int_{\text{core}} \mathbf{E}\cdot \mathbf{dl} + i\omega\mu_0 H_0 \times (\text{unfilled area}) \tag{3}$$

which will be used for the evaluation of $\overline{P}$. The value of $\mathbf{E}$ at the surface of the core is obtained from the appropriate Maxwell equation in the core (with neglect of displacement current)

$$\nabla \times \mathbf{H} = \sigma\mathbf{E} \tag{4}$$

where σ is the electrical conductivity.

Since $\mathbf{H}$ has only a z-component we obtain, again by Stokes' theorem,

$$\int_{\text{core}} \mathbf{E}\cdot \mathbf{dl} = -1/\sigma \int_{\text{core}} \partial H/\partial n_o dl \tag{5}$$

where n_0 is in the direction of the outward normal on the surface of the core.

Connection with the impedance, z, per unit length is made by utilizing the expression for the average complex power

$$\overline{P} = 1/2(II^*Z) \tag{6}$$

where I is the current in the coil. The field in the unfilled area is

$$H_0 = n'I \tag{7}$$

where n' is the number of turns per unit length of the coil. Putting together Eqs 1, 3, 5, 6, and 7 we obtain the impedance per unit length of the coil

$$Z = \frac{n'^2}{\sigma} 1/H_0 \left(\int_{\text{core}} \partial H/\partial n_o dl\right) - in'^2\omega\mu_0 \times (\text{unfilled area}) \tag{8}$$

Thus the problem is reduced to finding the normal derivative of the field on the surface of the core. This normal derivative is proportional to the eddy-current density at the surface of the core. The second term on the right of Eq

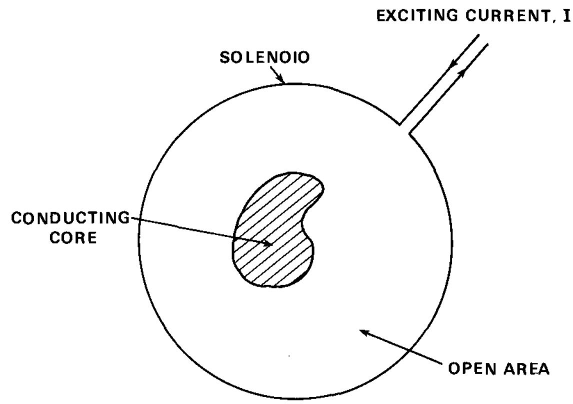

FIG. 1—*Cross-section of solenoid containing a cylindrical core of arbitrary shape. The contribution of the core to the impedance per unit length of the solenoid is given by Eq 8.*

8 gives the contribution to the inductance by the flux in the unfilled area. (Making the substitution $j = -i$ in Eq 8 will yield the usual positive imaginary quantity for inductive reactance.) To find the value of $\partial H/\partial n_o$ on the surface of the core it is necessary to obtain a solution of the eddy-current equation [*1,2*]

$$(\nabla^2 + k^2)H(\mathbf{r}) = 0 \tag{9}$$

where k, the complex propagation constant, is related to the skin depth, δ, by

$$k^2 = 2i/\delta^2$$

and

$$\delta = \sqrt{\frac{2}{\sigma\omega\mu_o}}$$

This task is treated in the following section.

Boundary Integral Equation

We follow the standard application of Green's theorem to convert the differential equation, Eq 9, to an integral equation on the boundary [*7*]. To do this we utilize the Green's function satisfying

$$(\nabla^2 + k^2)G(\mathbf{r}, \mathbf{r}') = 4\pi\delta(\mathbf{r} - \mathbf{r}') \tag{10}$$

The solution we select is the outgoing waveform

$$G(\mathbf{r}, \mathbf{r}') = i\pi H_o^{(1)}(k\,|\mathbf{r} - \mathbf{r}'|) \tag{11}$$

where $H_o^{(1)}$ is the Hankel function of the first kind. Applying Green's theorem to $H(\mathbf{r})$ and $G(\mathbf{r}, \mathbf{r}')$, we find for the field at any point in or on the surface of the core, the representation

$$H(\mathbf{r}) = (1/4\pi) \int_{\text{core}} G(\mathbf{r}, \mathbf{S}_0)\partial H/\partial n_o d\mathbf{S}_0 - (1/4\pi) \int_{\text{core}} \frac{\partial G(\mathbf{r}, \mathbf{S}_0)}{\partial n_o} H(\mathbf{S}_0) d\mathbf{S}_0 \tag{12}$$

This expression gives the field in terms of its value and normal derivative on the boundary. The symbols under the integral indicate that the line integrations are to be performed on the surface and the faces of the crack. It is understood that if interior point $\mathbf{r}$ is moved to the surface at location $\mathbf{S}$, the integrations on the right hand side of Eq 12 are to be performed *before* taking the limit $\mathbf{r} \rightarrow \mathbf{S}$.

For our crack problem, Eq 12 simplifies considerably. We take $H(S_0) = 1$, a normalized value of the uniform applied field on S_0. Also, the part of the second integration over the crack vanishes because the normal derivatives of the Green's function have equal values but opposite signs on the two sides of the crack.

Since we are concerned with the changes due to the crack, we set down the same equation for the "uncracked" cylinder:

$$H_0(\mathbf{r}) = (1/4\pi) \int_{\text{circle}} G(r, S_0)\partial H_0/\partial n_o dS_0 - (1/4\pi) \int_{\text{circle}} \partial G/\partial n_o H_0(S_0) dS_0 \tag{13}$$

where again $H_0(S_0) = 1$. In this case, $H_0(\mathbf{r})$ is given by the well-known Bessel function solution [*11,12*]

$$H_0(r) = J_0(kr)/J_0(ka) \tag{14}$$

We now let

$$H(r) - H_0(r) = \Delta H(r) \tag{15}$$

where Δ symbolizes the change induced by the crack at any point $\mathbf{r}$. By subtracting Eq 13 from Eq 12 we obtain

$$\Delta H(\mathbf{r}) = (1/4\pi) \int_{\text{circle+crack}} G(r, S_0)\Delta \partial H/\partial n_o dS_0 \tag{16}$$

Finally, we let r approach the surface, S, where ΔH is known, and obtain

$$(1/4\pi) \int_{\text{circle+crack}} G(S, S_0)\Delta \partial H/\partial n_o dS_0 = \begin{cases} 0, & S \text{ on surface} \\ 1 - J_0(kr)/J_0(ka), & S \text{ on the crack} \end{cases}$$
$$\equiv \phi(s) \tag{17}$$

This last result, Eq 17, is a Fredholm equation of the first kind for the change of the normal derivative of the field induced by the crack. When this is solved the impedance is obtained from Eq 8, and the change of field in the interior may be obtained from Eq 16.

At this point we discuss a difference between our treatment and that used most frequently in BIE applications. According to our use of Eq 13, the left-hand side approaches the field on the surface as $\mathbf{r} \rightarrow \mathbf{S}$ from the interior, and vanishes outside the core. This recipe will be correct if the integrations of the right-hand side are performed before letting $\mathbf{r} \rightarrow \mathbf{S}$. This choice, favored by Morse and Feshbach [*13*], is arbitrary. An immediate simplification resulting from this choice is the vanishing of the integrals of $\partial G/\partial n_o$ over the crack surfaces by virtue of symmetry. In the more usual method [*3*], $\mathbf{r}$ is moved to the surface first, and the integrals are evaluated as Cauchy principal values. Then the left-hand side of Eq 13 assumes the value $H(S)/2$, the mean of the interior and the exterior limits, when $\mathbf{r} \rightarrow \mathbf{S}$. Careful examination shows that the physical results obtained are the same by either method.

Numerical Solution

The integral equation for the unknown normal derivative of the field on the boundary of the cylinder with a crack is solved by numerical techniques that were originally devised for potential problems [*6*]. The path of integration in Eq 17 is broken into segments, ΔS_i; the values of the functions in each interval are replaced by values at the midpoints. The integral equation is then replaced by the algebraic system

$$\phi_i = (1/4\pi) \sum_j \left(\Delta \frac{\partial H}{\partial n_o}\right)_j \int_j G(S_i, S_0) dS_0 \tag{18}$$

The segment integrals over the Green's function are approximated by assuming straight line paths, and integration by the midpoint rule if $i \neq j$, or by using the small argument expansion of the Hankel function if $i = j$. The integrals are abbreviated by $G_{ij}\Delta S_j$, where ΔS_j is the length of the j^{th} interval. Then the system to be solved by standard computer routines is

$$(1/4\pi)\sum_j G_{ij}\Delta S_j\left(\Delta\frac{\partial H}{\partial n_o}\right)_j = \phi_i \tag{19}$$

This discretization is illustrated in Fig. 2.

The change of impedance due to the crack can be expressed, using Eq 8, as

$$\Delta Z = \frac{n'^2}{\sigma}(1/H_0)\sum_j\left(\Delta\frac{\partial H}{\partial n_o}\right)_j \Delta S_j \tag{20}$$

We found that the impedance converges rapidly, with the solution stable to better than one percent with fewer than 100 collocation points. This problem was also solved by the authors by an independent method [2]. The results of the two methods are in agreement to within one percent.

For problems where the crack has an open shape or for a cylinder of arbitrary cross section these same methods could be applied to Eq 12.

Discussion of Results

We performed numerical calculations for the ratio of crack depth, d, to cylinder radius, a, in the range $0.1 \leq d/a \leq 1.0$, with the ratio of radius to skin depth, δ, in the range $0.2 \leq a/\delta \leq 4.0$. Figures 3 and 4 show respectively the fractional change in the real and imaginary parts of the impedance

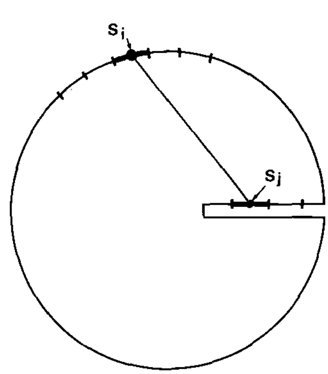

FIG. 2—*Illustration of the discretization used for the numerical solution of the integral equation for the eddy-current density on the surface and in the crack of the core. The functions of Eq 17 were approximated as constant over each subinterval. The calculations were performed as if the opening of the crack were infinitesimally small.*

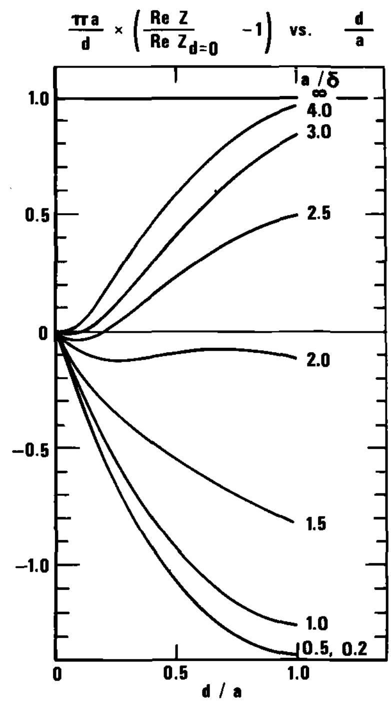

FIG. 3—*Fractional change, due to the crack, of the real part of the impedance as a function of* d/a *for selected values of* a/δ.

multiplied by $\pi a/d$. This multiplying factor gives the limiting normalized impedance a value of unity for $a/\delta \rightarrow \infty$.

We have prepared the impedance diagram for a demonstration case in which the crack depth is equal to one half the radius ($d/a = 0.5$). In Fig. 5 the solid curve is a plot of the impedance for the "uncracked" cylinder. The arrows indicate the changes of the complex impedance, induced by the crack, for several selected values of the ratio of cylinder radius to electromagnetic skin depth. We observe that the shape of the impedance curve is changed only slightly by the crack, and that the shift of the a/δ points is mainly along the curve, as if the resistivity were increased.

The results may be understood qualitatively. Consider the effect of the crack on the real part of Z. For small a/δ, the effect is to decrease Re Z; the loss is diminished, analogous to the way transformer core lamination reduces penetrating eddy currents. For large a/δ, Re Z is increased; here the skin effect is dominant, and the crack increases the surface area, which increases the loss. On the other hand, Im Z is always increased by the presence of the crack. This corresponds to the fact that the crack always allows an increased penetration of magnetic flux into the core, which leads to increased induc-

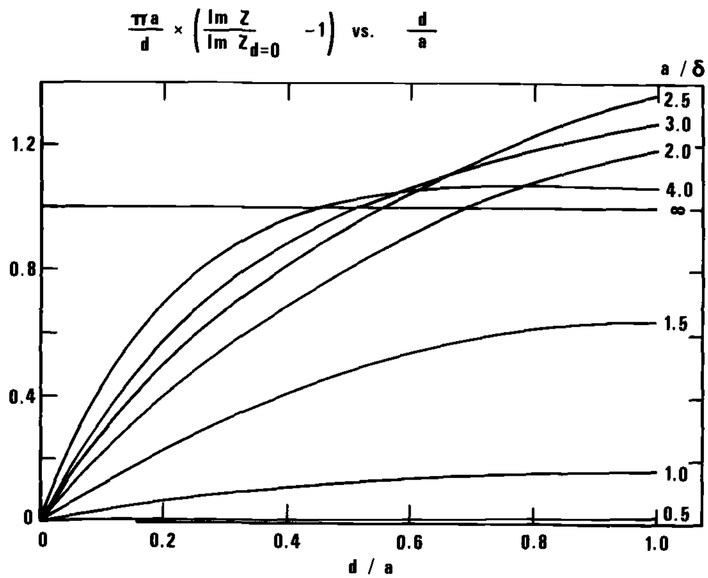

FIG. 4—*Fractional change, due to the crack, of the imaginary part of the impedance as a function of* d/a *for selected values of* a/δ.

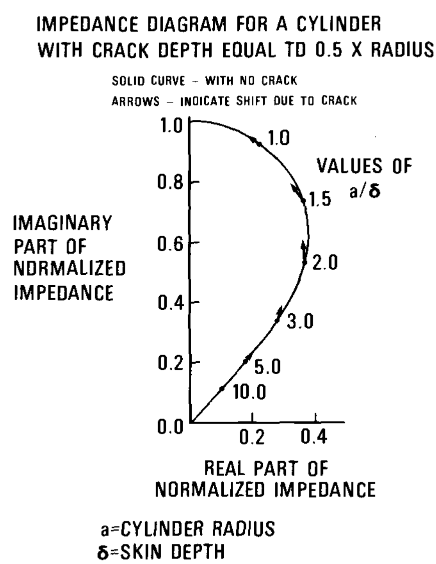

FIG. 5—*Impedance diagram for a demonstrative case for which the crack depth is one half of the radius. Arrows, drawn to scale, show the shifts of selected* a/δ *points induced by the presence of the crack.*

tance. The greatest sensitivity of the impedance to the crack is near the maximum of the loss, and the change there is almost purely inductive.

In conclusion, we believe that the numerical results and plots of relative impedance changes should be of direct use in determining the sensitivity of surround coil apparatus to crack depth. The BIE method should be applicable to defects other than tight radial cracks.

Acknowledgments

We are grateful to numerous persons at NBS, particularly Dr. S. Haber and M. Cordes for advice concerning numerical analysis and computation, and to Dr. T. Kincaid and his colleagues at the General Electric Company for valuable and stimulating discussions.

References

[1] Kahn, A. H., Spal, R., and Feldman, A., *Journal of Applied Physics*, Vol. 48, No. 11, Nov. 1977, p. 4454.
[2] Spal, R. and Kahn, A. H., *Journal of Applied Physics*, Vol. 50, No. 10, October 1979, p. 6135.
[3] Jaswon, M. A. and Ponter, A. R., *Proceedings*, Royal Society of London, Vol. A273, No. 1353, 7 May 1963, p. 237.
[4] Jaswon, M. A., *Proceedings*, Royal Society of London, Vol. A275, No. 1360, 20 Aug. 1963, p. 23.
[5] Symm, G. T., *Proceedings*, Royal Society of London, Vol. A275, No. 1360, 20 Aug. 1963, p. 23.
[6] Jaswon, M. A. and Symm, G. T., *Integral Equation Methods in Potential Theory and Elastostatics*, Academic Press, London, 1977.
[7] Rizzo, F. J. in *The Boundary-Integral Equation Method: Computational Applications in Applied Mechanics*, T. A. Cruse and F. J. Rizzo, Eds., American Society of Mechanical Engineers, 1975, p. 1.
[8] Morse, P. M. and Feshbach, H., *Methods of Theoretical Physics*, McGraw-Hill, New York, 1953, p. 1136.
[9] Chari, M. V. K. and Kincaid, T. G., *Transactions on Magnetics*, Institute of Electrical and Electronics Engineers, Vol. MAG-15, No. 6, November 1979, p. 1956.
[10] Kincaid, T. G., Chari, M. V. K., Fong, K., Czendes, E. J., and McCary, R. O., ARPA/AF Review of Progress in Quantities NDE, San Diego, 8-13 July 1979, (to appear).
[11] Landau, L. D. and Lifshits, E. M., *Electrodynamics of Continuous Media*, Addison-Wesley, Reading, Mass., 1960, p. 194.
[12] Libby, H. L., *Introduction to Electromagnetic Nondestructive Test Methods*, Wiley-Interscience, New York, 1971.
[13] Morse, P. M. and Feshbach, H., *Methods of Theoretical Physics*, McGraw-Hill, New York, 1953, p. 805.

Measurement Methods II: Microwave and Pulsed Techniques

A. J. Bahr[1]

Microwave Eddy-Current Techniques for Quantitative Nondestructive Evaluation

REFERENCE: Bahr, A. J., "**Microwave Eddy-Current Techniques for Quantitative Nondestructive Evaluation,**" *Eddy-Current Characterization of Materials and Structures. ASTM STP 722,* George Birnbaum and George Free, Eds., American Society for Testing and Materials, 1981, pp. 311-331.

ABSTRACT: The objectives of this work were to develop an electromagnetic scattering model that can be used to predict the scattering from a crack in a conducting surface and to evaluate the feasibility of using this model in conjunction with microwave-measurement techniques to determine the dimensions of such a crack. Such a theory has been developed, and its derivation is presented. Theory and experiment are compared for rectangular slots measured at 100 GHz, and the agreement is found to be good. The necessary measurement protocol for determining the dimensions of a crack is discussed, and an example of inverting the measured data to determine the dimensions of a rectangular slot is presented.

KEY WORDS: eddy current, microwave, surface cracks, quantitative nondestructive evaluation

In the low-frequency eddy-current testing of metals, currents are caused to flow in a specimen by placing it in a magnetic field of an induction coil. The flow of currents is affected by the electrical properties and shape of the specimen and by the presence of discontinuities and defects. In turn, these currents react on the exciting coil and affect its impedance. Thus, the presence of a defect is determined by monitoring the test-coil impedance.

Such eddy-current tests are typically conducted at frequencies of less than 1 MHz where induction fields predominate and the electromagnetic wavelength is greater than 300 m. In quantitative nondestructive evaluation (NDE), however, where it is desired to obtain the defect dimensions from an analysis of the measured data, the use of such low frequencies does not provide the degree of sensitivity to changes in defect dimensions that is necessary for obtaining an accurate determination of these dimensions from an inversion of the eddy-current data. The problem of obtaining sufficient accuracy becomes more difficult as the flaws of interest become smaller.

This problem would be alleviated if higher frequencies were to be used in

[1]Senior research engineer, SRI International, Menlo Park, Calif. 94025.

eddy-current inspection. Thus, the work reported here addresses the possibility of conducting eddy-current measurements in the microwave-frequency regime (1 to 100 GHz). Previous work [*1,2*][2] using frequencies in the range of 10 to 30 GHz has shown that good sensitivity to small cracks can be obtained, and that there is a clear correlation between crack depth and the detected signal.

In using microwave frequencies, the radiation fields associated with the sensors become an important consideration, and the physics involved is best described in terms of fields and waves. For example, a defect should be thought of as producing a change in the scattering of electromagnetic waves from the metal surface. It should be also noted that, since the use of microwave frequencies causes the currents induced in the test object to flow essentially on the surface (that is, the skin depth is typically less than 1 μm at 100 GHz), microwave eddy-current techniques are limited in metals to surface inspection, for example, to the detection and characterization of surface-breaking cracks.

In order to invert the measured microwave eddy-current data to obtain crack dimensions, it is necessary to have a theoretical model that relates the electromagnetic scattering from a crack to the crack dimensions. The requisite theory should be variational so that approximate solutions for irregular crack geometries can be obtained. In addition, the theory should not be restricted to any particular frequency range so it can be used to clarify any distinctions between conventional (low-frequency) and microwave (high-frequency) eddy-current techniques. Finally, such a model would be useful for establishing an optimum measurement protocol.

A suitable general theory has been developed, and its derivation is outlined next. Then, as an example, the theory is applied to cross-polarized backscattering of a plane wave from a rectangular slot in an aluminum plate, and the measurement protocol necessary to determine the slot dimensions is discussed. The results of this theoretical example are compared with experimental results obtained at 100 GHz and are found to be in good agreement. Finally, graphical inversion of the theoretical electromagnetic scattering from the slot is performed to illustrate the process of obtaining the slot dimensions from the measured data.

A Theoretical Model for Electromagnetic Scattering from Surface-Breaking Cracks in Metals

A general electromagnetic scattering-measurement system is shown schematically in Fig. 1, which illustrates the general bistatic case where the transmitter and receiver are separated. The probes, *a* and *b*, are arbitrary, but it is assumed that a single electromagnetic mode propagates at some

[2]The italic numbers in brackets refer to the list of references appended to this paper.

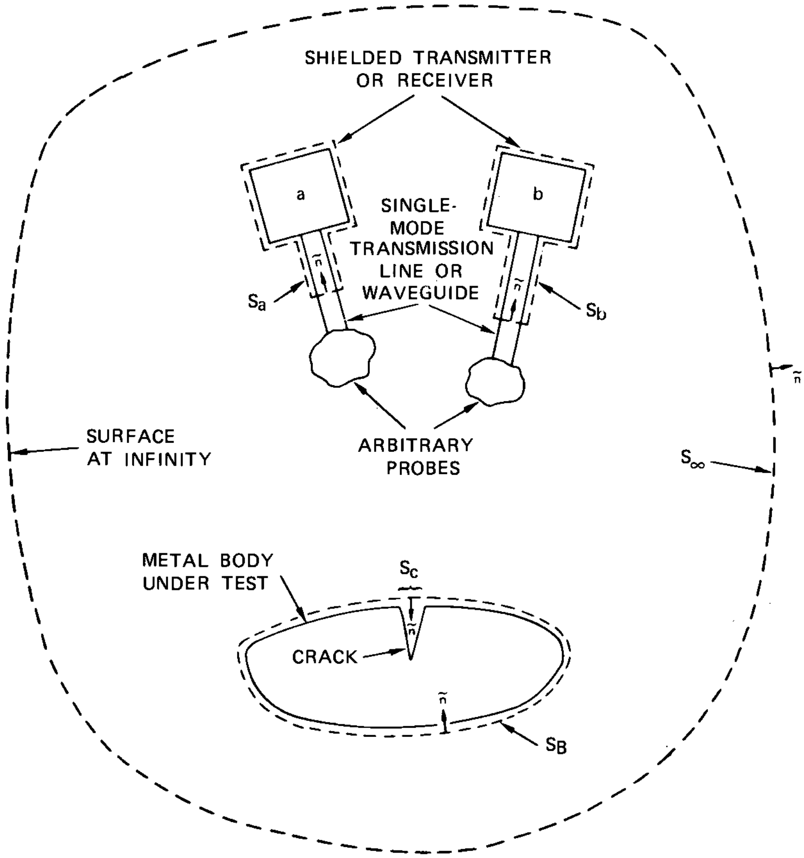

FIG. 1—*General electromagnetic scattering-measurement system.*

point in the transmission line(s) (waveguide(s)) that connect the probe(s) to the transmitter and receiver. It is also assumed that the metal shields and test body exhibit finite conductivity.

The starting point of the theory is the Lorentz reciprocity theorem [3], which involves an integral over the closed surface, S, equal to $S_a + S_b + S_B + S_c + S_\infty$. If there are no sources enclosed within the volume defined by S, the theorem takes the following form

$$\int_S\!\!\int (\vec{E} \times \vec{H}' - \vec{E}' \times \vec{H}) \cdot \tilde{n}\, dS = 0 \qquad (1)$$

where $\tilde{n}$ is a unit vector that points outward from the enclosed volume. The quantities $\vec{E}$ and $\vec{H}$ are the electric and magnetic fields, respectively, that exist on the surface S. The unprimed and primed fields are defined by the following conditions: (*a*) Unprimed field—no crack is present, *a* is a receiver, *b* is a transmitter; and (*b*) Primed field—a crack is present, *a* is a transmitter, *b* is a receiver. In addition, if gyromagnetic media exist within the closed volume, all d-c magnetic fields within the volume must be reversed in the two cases [4].

The evaluation of the surface integral in Eq 1 requires a knowledge of the fields on the various parts of the surface S. First, on all the metal surfaces the tangential electric field can be related to the surface magnetic field by means of a surface impedance, Z_s

$$\vec{E}_t = -Z_s(\hat{n} \times \vec{H}) \tag{2}$$

For plane waves, Z_s is related to the skin depth, δ_s, by the well-known formula

$$Z_s = (1 + j)/(\sigma\delta_s) \tag{3}$$

where σ is the conductivity of the metal. Second, on the surface at infinity the following radiation condition exists

$$\vec{E} = j\omega\hat{n} \times (\hat{n} \times \vec{A}) \tag{4a}$$

$$\vec{H} = -j\,\frac{\omega}{\eta_0}\,(\hat{n} \times \vec{A}) \tag{4b}$$

where ω is the radian frequency, η_0 is the intrinsic impedance of free space, and $\vec{A}$ is the vector potential. Third, since single modes are assumed to propagate in the transmission lines, it can be shown [5] that the integrals over the transmission-line cross sections reduce to the following form

$$\int_{S_a}\int (\vec{E} \times \vec{H}' - \vec{E}' \times \vec{H})\cdot\hat{n}\, dS = -4P_A\Gamma_a \tag{5a}$$

$$\int_{S_b}\int (\vec{E} \times \vec{H}' - \vec{E}' \times \vec{H})\cdot\hat{n}\, dS = 4P_A\Gamma_b' \tag{5b}$$

where P_A is the power available from the transmitter and Γ is the reflection coefficient of the propagating mode in the transmission line. Finally, the unknown electric field in the crack mouth can be expressed as a fictitious magnetic current, $\vec{M}'$, namely,

$$\vec{M}' \triangleq \hat{n} \times \vec{E}' \tag{6}$$

By using Eqs 2, 4, 5, and 6, we can convert Eq 1 into the following form

$$4P_A(\Gamma_b' - \Gamma_a) = -Z_s \int_{S_c}\int (\vec{H}_t' \cdot \vec{H})\, dS + \int_{S_c}\int (\vec{M}' \cdot \vec{H})\, dS \tag{7}$$

Equation 7 expresses the difference between the scattering coefficients measured with probes a and b in terms of fields that exist in the crack mouth when it is either open or covered by a conductor having surface impedance Z_s. Hence, to relate this theoretical result to an experimental measurement, the measurement system must be capable of measuring this difference in scattering coefficients.

In conventional eddy-current systems, we usually measure the change in impedance, $Z' - Z$, of a probe as it passes over a crack, rather than the change in scattering coefficient. In the case where the same probe is used both for excitation and detection, the distinction between a and b disappears, and we find from transmission-line theory that the change in scattering coefficient and the change in impedance are related by

$$4P_A(\Gamma' - \Gamma) = II'(Z' - Z) \tag{8}$$

where I and I' are the total currents flowing in the transmission line without and with a crack present, respectively. We will retain the scattering coefficients in the present development however, because they are more fundamental to a wave analysis.

Equation 7 is a linear integral equation that relates the unknown reflection coefficient, Γ_b', to the unknown tangential magnetic field, $\vec{H}_t'$, and magnetic current, $\vec{M}'$, in the crack mouth. The quantity $\vec{H}$ is the magnetic field that exists on the surface of the metal test object in the absence of a crack. One way of solving this equation is to use the method of moments [*6*]. Such a solution possesses the variational characteristics [*7*] that are desired.

Following the method of moments, we expand $\vec{M}'$ in a set of basis functions, $\vec{M}_n$

$$\vec{M}' = \sum_{n=1}^{N} V_n \vec{M}_n \tag{9}$$

The only conditions on the $\vec{M}_n$ are that they be linearly independent, and that their superposition approximate $\vec{M}'$ "reasonably well" (herein lies the "art" in the method of moments). Also, we invoke the necessary condition that the tangential magnetic field be continuous across the crack mouth, that is,

$$\vec{H}_t' = \vec{H}_t^i + \vec{H}_t^r(\vec{M}') = \vec{H}_t^c(-\vec{M}') \tag{10}$$

where $\vec{H}_t^i$ is the incident magnetic field, $\vec{H}_t^r(\vec{M}')$ is the induced magnetic field just outside the crack mouth, and $\vec{H}_t^c(-\vec{M}')$ is the induced magnetic field just inside the crack mouth. $\vec{H}_t^c$ is a function of $-\vec{M}'$ rather than of $\vec{M}'$ because of the equivalence principle [*6*]. Also, because the $\vec{H}_t$ operators are linear, Eq 9 can be substituted into Eq 10 to give the result

$$\sum_{n=1}^{N} V_n \vec{H}_t^r(\vec{M}_n) + \sum_{n=1}^{N} V_n \vec{H}_t^c(\vec{M}_n) = -\vec{H}_t^i \tag{11}$$

Next, we choose a set of testing functions, $\vec{W}_m$, that are similar (but not necessarily equal) to the $\vec{M}_n$. By taking the dot product of each $\vec{W}_m$ with Eq 11 and integrating that product over the crack mouth, we obtain the following result

$$\sum_{n=1}^{N} V_n \int_{S_c}\int \vec{W}_m \cdot \vec{H}_t^r(\vec{M}_n)\, dS + \sum_{n=1}^{N} V_n \int_{S_c}\int \vec{W}_m \cdot \vec{H}_t^c(\vec{M}_n)\, dS = -\int_{S_c}\int \vec{W}_m \cdot \vec{H}_t^i\, dS \tag{12}$$

Thus, Eq 10 has been converted into a set of scalar inhomogeneous linear equations, which thus can be solved for the unknown coefficients, V_n.

The result of eliminating the V_n in Eq 9 and substituting the result into Eq 7 is best expressed in matrix form

$$\Gamma_b' - \Gamma_a = (F_{\mathrm{LF}} F_{\mathrm{CO}}/\eta_0)\{-Z_s\{C_c + \underline{\tilde{y}}[Y_r + Y_c]^{-1} C^i]\} + \underline{C}[Y_r + Y_c]^{-1} C^i]\} \tag{13}$$

where the normalized coefficients and matrix elements are given by

$$F_{\mathrm{LF}} F_{\mathrm{CO}} \triangleq \eta_0 \frac{\int_{S_c}\int (\tilde{a}_M \cdot \vec{H})(\tilde{a}_W \cdot \vec{H}_t^i)\, dS}{4P_A} \tag{14a}$$

$$C_c \triangleq \frac{\int_{S_c}\int (\vec{H}_t^i \cdot \vec{H})\, dS}{\int_{S_c}\int (\tilde{a}_m \cdot \vec{H})(\tilde{a}_W \cdot \vec{H}_t^i)\, dS} \tag{14b}$$

$$\tilde{y}_n \triangleq \frac{\int_{S_c}\int \vec{H}_t^r(\vec{M}_n) \cdot \vec{H}\, dS}{\sqrt{\int_{S_c}\int (\tilde{a}_M \cdot \vec{H})(\tilde{a}_W \cdot \vec{H}_t^i)\, dS}} \tag{14c}$$

$$Y_{mn}{}^{r} \triangleq -\int_{S_c}\int \vec{W}_m \cdot \vec{H}_t{}^{r}(\vec{M}_n)\, dS \tag{14d}$$

$$Y_{mn}{}^{c} \triangleq -\int_{S_c}\int \vec{W}_m \cdot \vec{H}_t{}^{c}(\vec{M}_n)\, dS \tag{14e}$$

$$C_m{}^{i} \triangleq \frac{\displaystyle\int_{S_c}\int (\vec{W}_m \cdot \vec{H}_t{}^{i})\, dS}{\sqrt{\displaystyle\int_{S_c}\int (\tilde{a}_M \cdot \vec{H})(\tilde{a}_W \cdot \vec{H}_t{}^{i})\, dS}} \tag{14f}$$

and

$$C_n \triangleq \frac{\displaystyle\int_{S_c}\int (\vec{M}_n \cdot \vec{H})\, dS}{\sqrt{\displaystyle\int_{S_c}\int (\tilde{a}_M \cdot \vec{H})(\tilde{a}_W \cdot \vec{H}_t{}^{i})\, dS}} \tag{14g}$$

Here $\tilde{a}_M$ and $\tilde{a}_W$ are unit vectors pointing along $\vec{M}$ and $\vec{W}$, respectively.

Equation 13 applies to all electromagnetic eddy-current measurements of cracks. At this stage, no restrictions have been made on the operating frequency or the distance between the probe(s) and the specimen. The first term in the equation, that is, the one involving Z_s, can be interpreted as the change in scattering caused by removing a small volume (the crack) of metal that has finite conductivity. The second term can be interpreted as the change in scattering caused by energy being stored in the crack and being reradiated. The coefficient $F_{LF}F_{CO}$ contains the effects of changing the distance between the probe and the specimen surface (liftoff), and of crack orientation. At low frequencies, we find that the finite-conductivity term dominates; at high frequencies, where the crack becomes resonant, the effects of energy storage become predominant. The theory thus provides a clear distinction between conventional and microwave eddy-current techniques.

Example

To illustrate how Eq 13 can be evaluated in a specific case, consider the simple case of perpendicular plane-wave excitation of a rectangular slot cut in a perfectly conducting plane. The geometry of such a slot is shown in Fig. 2. Assuming the receiver is cross-polarized to the transmitter, $\Gamma_a = 0$ and Eq 13 becomes

$$\Gamma_b{}' = F_{LF}F_{CO}C_1C_1{}^{i}\,[1/\eta_o Y_s)] \tag{15}$$

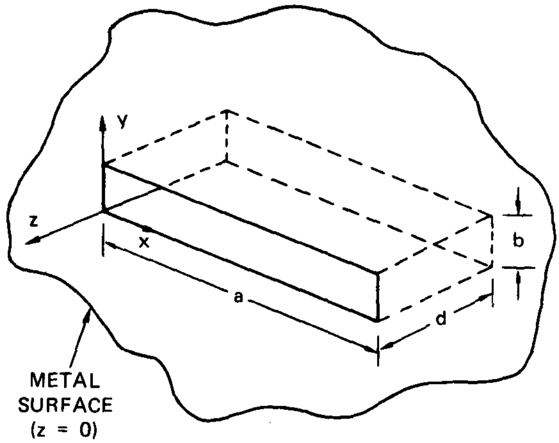

FIG. 2—*Rectangular slot geometry.*

where the slot admittance is $Y_s \triangleq Y_r + Y_c$ and only one basis function has been used to approximate the fields in the slot mouth.

In this case, we can take advantage of the knowledge that exists concerning the solution for the fields in the aperture of a narrow-slot antenna [*8*]. This solution should provide a good resonance-region[3] approximation to the fields in the mouth of a slot that is deeper than it is wide. Hence, we take the basis function and test function to be

$$\vec{M}_1 = \tilde{a}_x(1/b)\sin\left[k\left(\frac{a}{2} - \left|x - \frac{a}{2}\right|\right)\right] = \vec{W}_1 \tag{16}$$

where $\tilde{a}_x$ is a unit vector along the x-axis, k is the wave number, and the slot dimensions and coordinate system are as defined in Fig. 2. Use of this approximate function converts the moment-method solution to a perturbation solution.

Now, for a plane incident wave with magnetic field H_0, we have

$$\tilde{a}_x \cdot \vec{H}_t^{\,i} = 2H_0 \cos\theta \tag{17}$$

and

$$\tilde{a}_x \cdot \vec{H} = 2H_0 \sin\theta \tag{18}$$

where θ is the angle between $\vec{H}_t^{\,i}$ and the x-axis, and it has been assumed that there are no reflections from the probe. Using Eqs 16, 17, and 18 the coefficients of the normalized slot impedance $(1/\eta_0 Y_s)$ in Eq 15 become

[3]The term "resonance region" refers to frequencies where the slot length is equal to or greater than one-half wavelength.

$$F_{\text{LF}} = (\eta_0 H_0{}^2 ab)/(P_A) \tag{19a}$$

$$F_{\text{CO}} = (1/2)\sin 2\theta \tag{19b}$$

$$C_1 = \sqrt{\tan\theta}\,\frac{4}{k\sqrt{ab}}\sin^2(ka/4) \tag{19c}$$

and

$$C_1{}^i = \frac{1}{\sqrt{\tan\theta}}\,\frac{4}{k\sqrt{ab}}\sin^2(ka/4) \tag{19d}$$

Here, the quantity $C_1 C_1{}^i$ is a slot coupling factor that gives the frequency dependence of the coupling between the slot and the incident field. The normalized slot admittance, $\eta_0 Y_s$, is a slot parameter that is independent of the excitation. It is important to note that Y_s is the sum of a radiation admittance, Y_r, that depends on the boundary conditions external to the slot, and a cavity admittance, Y_c, that depends on the geometry inside the slot. Thus, if the geometry of the slot cavity changes, but not the geometry of the slot mouth, only the cavity admittance needs to be recalculated.

To calculate the cavity admittance for a rectangular slot, we can expand $\vec{H}_t{}^c(\vec{M}_1)$ in transverse-electric waveguide modes. Then Eq 14e becomes

$$Y_c = -(8j/\eta_0)(a/b)(ka)\cos^2(ka/2)\sum_{q\,\text{odd}} ctnh(\Gamma_q d)/(\Gamma_q a)^3 \tag{20}$$

where

$$\Gamma_q{}^2 = (q\pi/a)^2 - k^2 \tag{21}$$

This result differs slightly from that obtained in Ref *5* because of a difference in the definition of slot voltage.

The radiation admittance (Eq 14d) can be calculated by expanding the aperture fields in the plane-wave spectrum [*9,10*]. Assuming $kb \ll 1$, we have

$$\begin{aligned}\text{Re}(Y_r) = {} & (1/\pi\eta_0)\{\text{Cin}(ka) \\ & + [\text{Cin}(ka) - 1/2\,\text{Cin}(2ka)]\cos ka \\ & - [\text{Si}(ka) - 1/2\,\text{Si}(2ka)]\sin ka\}\end{aligned} \tag{22a}$$

and

$$\begin{aligned}\text{Im}(Y_r) = {} & (1/\pi\eta_0)\{\text{Si}(ka) + [\text{Si}(ka) - 1/2\,\text{Si}(2ka)]\cos ka \\ & + [\text{Cin}(ka) - 1/2\,\text{Cin}(2ka) - \ln(e^{3/2}a/2b)]\sin ka\}\end{aligned} \tag{22b}$$

where

$$\text{Cin}\,(x) \triangleq \int_0^x [(1 - \cos u)/u]\, du \tag{23a}$$

and

$$\text{Si}\,(x) \triangleq \int_0^x (\sin u/u)\, du \tag{23b}$$

Equations 19, 20, and 22 show explicitly how slot coupling and slot admittance depend on the frequency and the dimensions of the slot. In order to show explicitly how the liftoff factor (Eq. (19a)) depends on these parameters, it is necessary for us to relate H_0 and P_A. For example, if the source antenna were equivalent to an electric dipole located at a large distance, R, from the slot, we would have

$$F_{\text{LF}} = (-3/4\pi)(ab/R^2)e^{-j2kR} \tag{24}$$

Hence, if k is large (wavelength is small), the dominant effect of changing R will be to change the phase of the reflection coefficient. Thus, the locus of the reflection coefficient in the reflection-coefficient plane as R is changed will be a nearly circular arc. This behavior can be used to discriminate between the signals produced by variations in liftoff and by a bonafide crack.

Having obtained Eqs 19, 20, and 22, it is now possible to calculate the cross-polarized scattered power given by

$$P_{HV} = |\Gamma_b'|^2 P_A \tag{25}$$

as a function of the frequency and slot dimensions. It is convenient, however, to normalize the scattered power first to suppress the dependence of the result on the characteristics of the probe and slot orientation, namely,

$$P_{HV}\,[P_A/(\eta_0{}^2a^2b^2\,|H_0{}^4|\,\sin^2 2\theta)] = \frac{[64/(k^4a^2b^2)]\sin^8(ka/4)}{|\eta_0 Y_s|^2} \tag{26}$$

The right-hand side of this equation is plotted (in dB) in Fig. 3 as a function of the product of frequency and slot length, with the ratios of slot width and depth to slot length as parameters. In this figure, $ka/\pi \geq 1$ defines the resonance region where electromagnetic energy can propagate into the slot with low attenuation. In this region, the scattering is seen to be a strong function of slot depth, which is a desirable characteristic from the standpoint of obtaining an accurate determination of depth from a scattering measurement. For frequencies below the resonance region, the fields inside the slot are evanescent, and so the sensitivity of the scattering to changes in slot depth decreases rapidly as the slot approaches one slot length in depth. Thus, eddy-current measurements for determining slot depth quantitatively

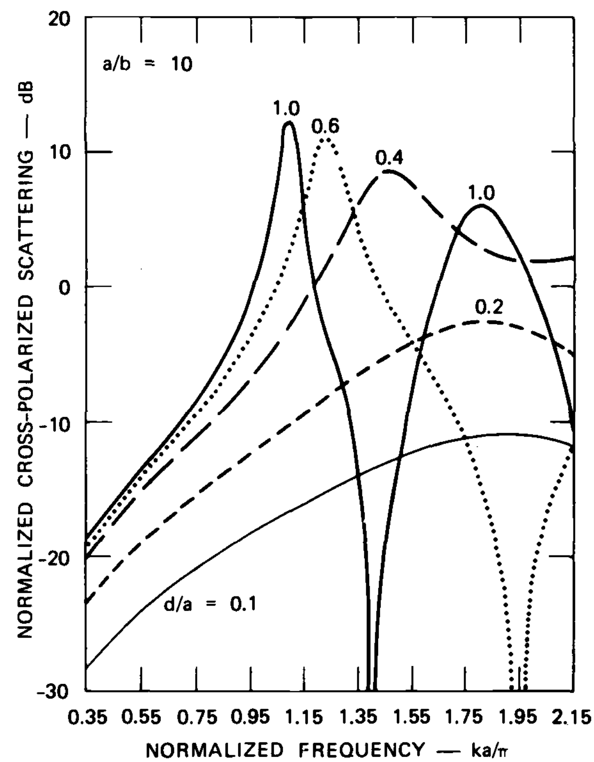

FIG. 3—*Normalized cross-polarized power scattered from a slot as a function of normalized frequency.*

are best conducted in the resonance region. It should be noted, however, that more than one slot depth can give the same value of scattered power in this frequency region, and so it may be necessary to conduct measurements at more than one frequency to resolve this ambiguity.

So far, this example has neglected the contribution of the surface-impedance term to the scattering. Indeed, in the cross-polarized case, $C_c = 0$ in Eq 13, and the other term containing Z_s is small for most metals. On the other hand, in the copolarized case, $C_c = 1$, and $F_{CO} = \cos^2\theta$. At very low frequencies, $1/Y_s \rightarrow 0$, and the quasi-static scattered power, P_Q, is determined entirely by the surface impedance

$$P_Q\,[P_A/(\eta_0{}^2 a^2 b^2\,|H_0{}^4|\;4\cos^4\theta)] \cong |Z_s|^2/(4\eta_0{}^2) \tag{27}$$

Of course, as the frequency is increased from zero, the energy stored in the slot also contributes to the scattering. For a deep slot ($d/a \sim 1$), the Rayleigh scattering term, P_R, can be approximated by expanding Eq 15 for small ka. The result is

$$P_R\,[P_A/(\eta_0{}^2 a^2 b^2 \,|H_0{}^4|\, 4\cos^4\theta)] \cong (\pi^6/16^4)(ka)^2 \tag{28}$$

These two normalized scattering powers are plotted as functions of frequency in Fig. 4. In making the computations, it was assumed that $a = 2.5$ mm, and that the material was aluminum with $Z_s = 3.26 \times 10^{-7}\sqrt{f}(1 + j)$ Ω, where f is the frequency. This figure clearly shows the dominance of the surface-impedance term (quasi-static term) at low frequencies, and the dominance of the energy-storage term (Rayleigh term) at high frequencies. The crossover occurs in this example at about 10 kHz. It is important to note that neither of these low-frequency approximations to the slot scattering contains any depth information. Hence, we conclude that eddy-current measurements of crack depth are best conducted at frequencies where the wavelength is commensurate with the crack length.

An Idealized Measurement Protocol

Equation 13 provides the basis for defining an idealized eddy-current measurement protocol for determining crack dimensions. This protocol can be divided into four main steps:

1. Calibrate the system at each measurement frequency using a "standard crack" to determine the lift-off factor.
2. Detect the real crack while keeping the distance between the probe and the specimen the same as in the calibration.
3. Measure the crack in at least two different orientations to determine the orientation factor (assuming the crack length is much larger than the crack width).
4. Collect sufficient data to permit unambiguous inversion using the model to obtain the crack dimensions. (Ideally, a minimum data set would consist of amplitude and phase at two frequencies; the use of more frequencies may be required in the resonance region in order to resolve ambiguities.)

Since the data will not be perfectly accurate and the crack geometry will not be known precisely, it is likely that statistical techniques, adaptive learning techniques, or both, will be required to obtain sufficient accuracy for crack dimensions determined from eddy-current measurements. In any case, Eq 13 should provide a useful basis for designing experiments.

Experiment

The amplitude and phase of the cross-polarized backscattering from a series of rectangular slots in a flat aluminum plate were measured using the

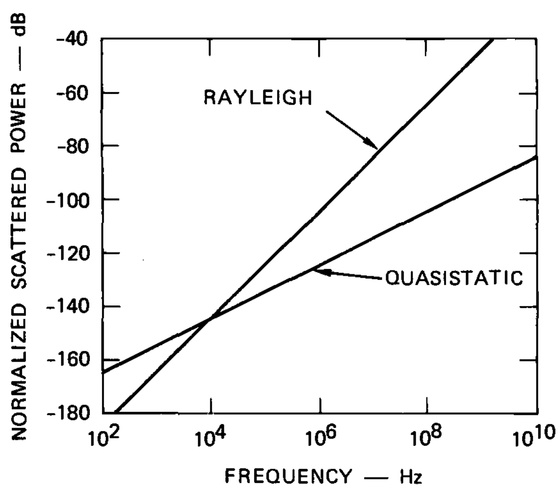

FIG. 4—*Comparison of Rayleigh and quasi-static scattering for a deep slot.*

microwave system whose schematic diagram is in Fig. 5. This system uses an orthomode coupler to discriminate against copolarized backscatter, and a homodyne detection system to provide in-phase (I) and quadrature (Q) output signals. The sensitivity of this system is currently about −75 dBm; this sensitivity is determined by the degree to which the transmitting and receiving portions of the system can be isolated in the absence of a crack by the orthomode coupler. The antenna used in the system is a lens-focused horn with a beamwidth at its focal point of about 3.5 mm at the operating frequency of 100 GHz.

An aluminum plate with six slots of different sizes electrodischarge-machined into its surface was prepared according to the layout shown in Fig. 6.[4] Slots one, two, and three have a cross section ($a \times b$) of 2.54 × 0.25 mm; Slots four, five, and six have a cross section of 1.27 × 0.25 mm. Thus, a/b = 10 for the first set of slots, and a/b = 5 for the second set of slots. Also, at 100 GHz, ka/π = 1.7 for the first set, and ka/π = 0.85 for the second set. Finally, Slots one and four were specified to be 0.25 mm deep, Slots two and five, 0.5 mm deep, and Slots three and six, 1.0 mm deep.

The measured in-phase and quadrature voltages obtained at 98 GHz by translating the slots through the microwave beam are shown in Fig. 7. The plate was aligned perpendicularly to the microwave beam and was positioned so that a linear translation of the plate caused the centers of the slots to pass through the center of the beam, thereby maximizing the peak signal obtained from each slot. The slots were aligned with their lengths at an angle of about

[4]This test plate was prepared under the direction of Dr. O. Buck of Rockwell International Science Center, Thousand Oaks, Calif.

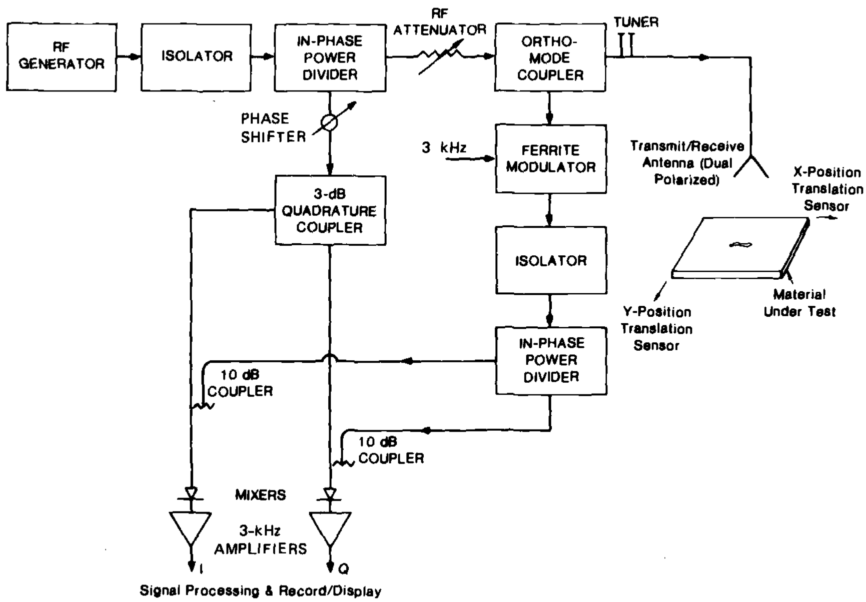

FIG. 5—*Microwave system for measuring cross-polarized backscatter using homodyne detection.*

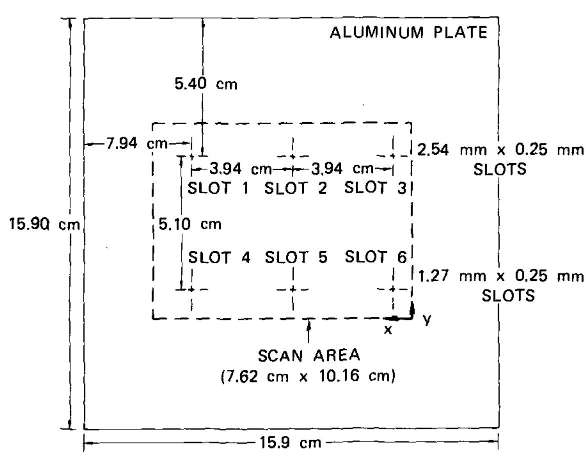

FIG. 6—*Layout of slotted aluminum plate (slots are aligned in the* x *direction).*

60 deg to the electric polarization vector, thus ensuring that some of the incident energy would be coupled into the cross-polarized mode by each slot.

The in-phase and quadrature voltages were combined to form a polar display on a storage oscilloscope (common practice in low-frequency eddy-

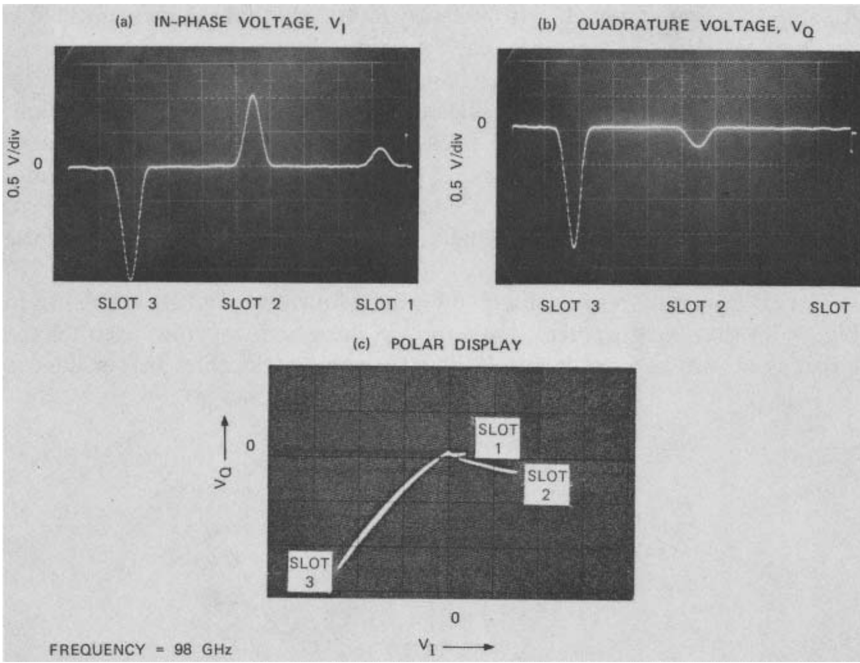

FIG. 7—*Measured slot response for Slots 1, 2, and 3.*

current work). The corresponding polar display for Slots one, two, and three (the 2.5-mm-long slots) is shown in Fig. 7(*c*). This type of display clearly shows the differences in the amplitudes and phases of the scattered signals produced by the different-depth slots. In this case, the signal produced by Slot three (1.0 mm deep) is very different from the signals produced by the other slots. All three signals, however, are clearly distinguishable.

The approximate model (described previously) that assumes a sinusoidal distribution of electric field in the slot mouth can be used to calculate the theoretical slot response for the parameters used in the experiment. For a focused microwave beam, the change in excitation of the slot caused by moving the slot through the beam can be approximated by setting

$$F_{\mathrm{LF}} \propto e^{-jkx'^2/R_0}\,[2J_1(kx'/2)]/(kx'/2) \tag{29}$$

where

k = wave number,
x' = distance along the scanning direction measured from the center of the slot,
R_0 = distance between the microwave lens and the aluminum plate, and
J_1 = Bessel function of first kind and first order.

Also, in this simple model, it is necessary to assume that the incident field is constant over the slot mouth for each position x'.

The result of the calculation for Slots one, two, and three is shown in Fig. 8. The absolute amplitude and phase is undetermined in this calculation; therefore, the theoretical plot has been normalized so that the peak response for Slot three matches the experimental value for that slot. The experimental peak values of each slot response are indicated by *X*s. A comparison of Figs. 7*c* and 8 shows remarkable agreement, when the approximate nature of the model is considered.

The experimental results obtained for Slots four, five, and six are shown in Fig. 9. In that measurement, the gain was increased over that used for the larger slots and, as a result, liftoff effects became noticeable, as is evidenced

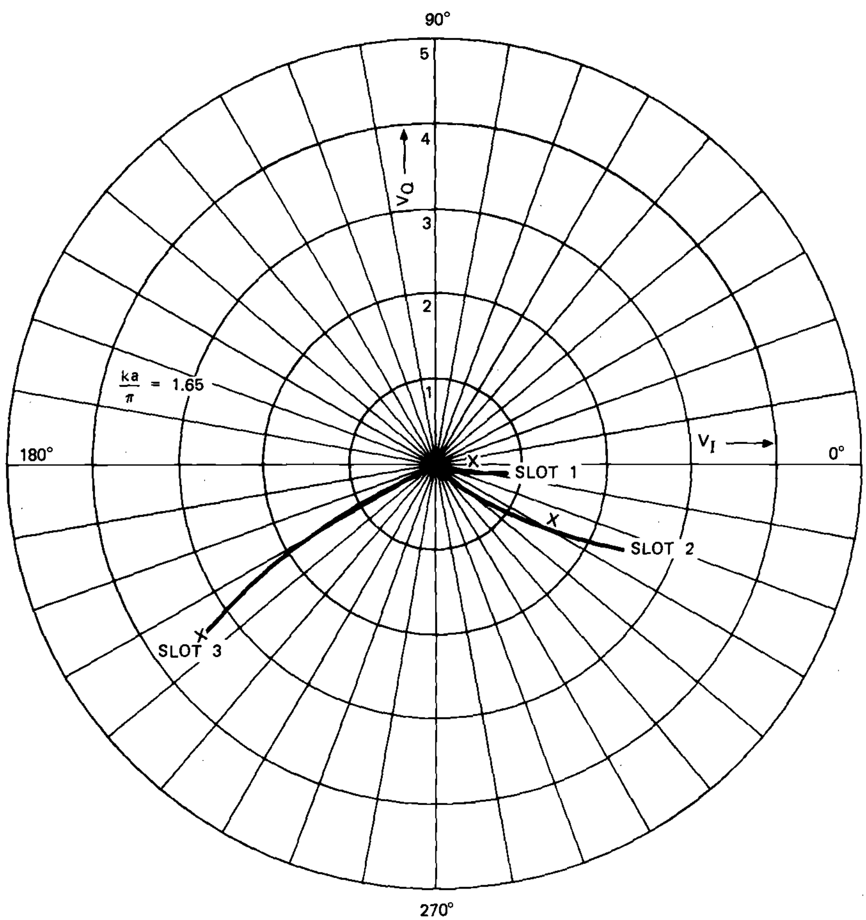

FIG. 8—*Theoretical slot response for Slots 1, 2, and 3 (x indicates measured peak value).*

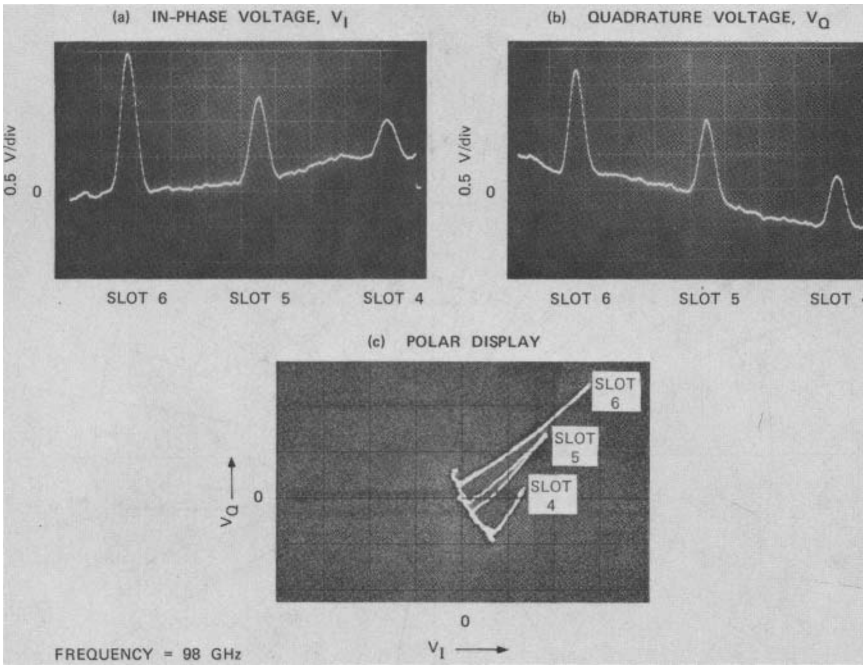

FIG. 9—*Measured slot response for Slots 4, 5, and 6.*

by the high background or clutter in Figs. 9*a* and 9*b*. As expected, however, the polar display (Fig. 9*c*) allows the slot signals to be clearly distinguished from the liftoff signal because the two types of signals are nearly orthogonal.

In this case, the length of the slots (1.27 mm) causes the operating frequency of 98 GHz to lie below the resonance region, with the result that changes in slot depth produce relatively little change in the phase of the scattered signal.

The corresponding theoretical response for these smaller slots is shown in Fig. 10. In this case, the theoretical plot was normalized to the experimental peak value for Slot six after the clutter (liftoff signal) had been subtracted. Again, agreement between theory and experiment is fairly good.

Inversion

In view of the good agreement between theory and experiment, it appears worthwhile to examine the measurement-error sensitivity of an inversion process that is based on the simple model. Since all the slots were located at the same distance from the microwave lens and had the same orientation relative to the polarization of the incident wave, it was simplest to use one of the slots (Slot three) as a reference slot for calibrating the system via the model. Slot

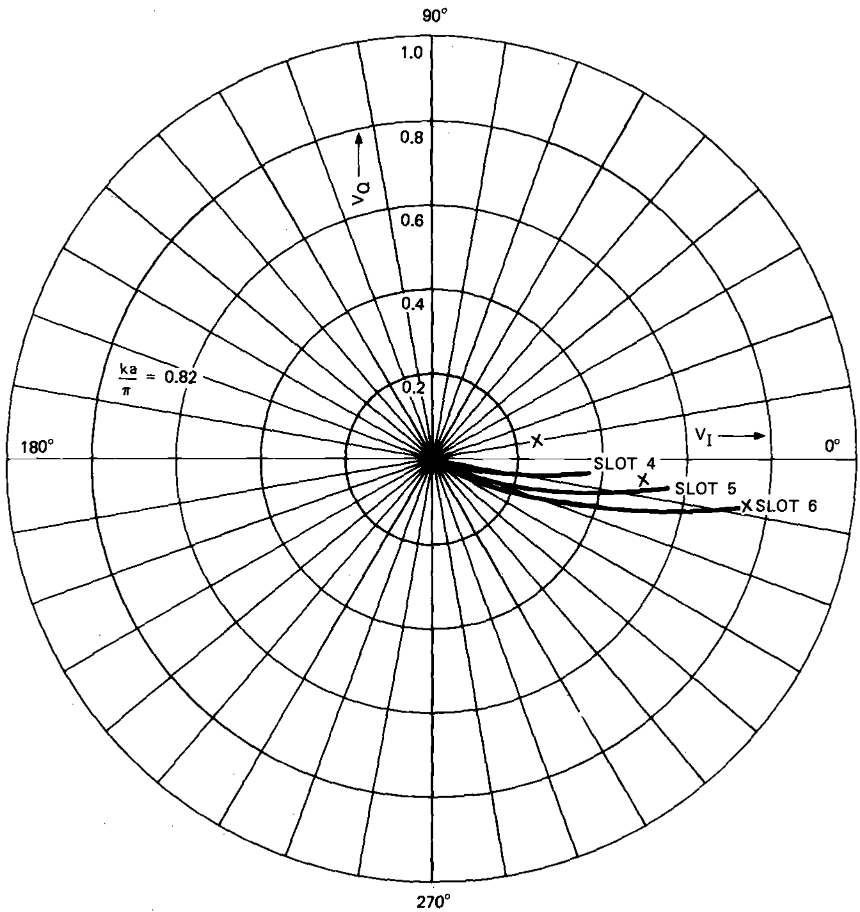

FIG. 10—*Theoretical slot response for Slots 4, 5, and 6 (x indicates measured peak value).*

two was chosen as the unknown slot whose dimensions were being sought. Hence, the ratio of the measured complex signal for Slot two to that for Slot three was compared to the same ratio obtained from theory.

Ideally, measurements at two frequencies that are far enough apart to produce measurable changes in scattering are needed in order to determine all three dimensions of a slot, as was mentioned in the section on measurement protocol. The existing experimental system, however, did not permit significant changes in operating frequency to be made; therefore, it was necessary to assume that one of the slot dimensions was known. The slot length, *a*, was chosen for this dimension, as it is the most likely to be known.

The amplitude and phase of the relative scattering from Slot two at 99.9 GHz are shown in Fig. 11 as functions of slot depth, with slot width as a

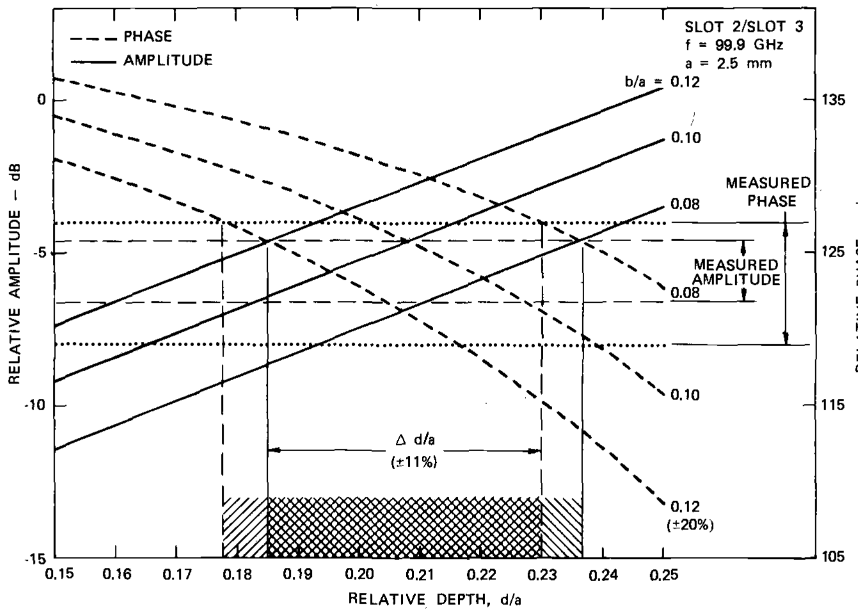

FIG. 11—*Amplitude and phase of the scattering from Slot 2 (relative to Slot 3) as Functions of Slot Depth.*

parameter. It is assumed that $a = 2.5$ mm. Also indicated in the figure are the estimated ranges for the measured data. The measurement errors corresponding to these ranges are amplitude, ± 1 dB; phase, $\pm 4°$. We see from the figure that, if the slot width can be estimated to within ± 20 percent, the measured data determine the slot depth to within ± 11 percent (the cross-hatched area).

It is interesting to note that, in this case, the use of amplitude data alone would only increase the uncertainty in the depth determination by a small amount, namely to ± 14 percent. The slot depth measured from a scanning electron micrograph of a rubber replica of Slot two is $d/a = 0.21$. This value lies approximately in the center of the cross-hatched slot-depth range shown in Fig. 11.

If the cross-sectional dimensions of a crack cannot be obtained by microscopic examination or by some other means, all three of the crack dimensions must be obtained from the eddy-current measurement alone. The accuracy of the required inversion solution will depend on how sensitive the scattering is to changes in each crack dimension. Calculations using the model developed here show that this sensitivity depends on the product of crack length and operating frequency, with maximum sensitivity obtained in specific portions of the resonance region. Thus, obtaining maximum accuracy in determining crack size will necessitate the use of a frequency that is appropriate to the size range being measured.

Summary

A general theory for the electromagnetic scattering from a surface-breaking crack in a conducting material has been developed. The theory is valid for any frequency and provides a basis for defining a measurement protocol for the purpose of determining crack dimensions from eddy-current measurements. The theory also shows that, at low frequencies, eddy-current measurements of cracks are dominated by effects of finite conductivity while, at high frequencies, the measured signals are determined mostly by energy storage in the crack.

Approximate numerical results have been obtained for the case of a rectangular slot. This example reveals all of the essential characteristics of the backscattering as a function of frequency and slot dimensions, and gives insight into what can be expected for the behavior of a signal scattered by a real crack. For example, when the slot length is greater than one-half wavelength, resonances can occur; these resonances make the determination of slot depth from measured scattering accurate but introduce ambiguities. For smaller slot lengths, there is a one-to-one relation between slot depth and scattered signal, but the amplitude of the scattered energy is smaller and slot depths that are greater than one slot length are not well resolved. The effects of liftoff and slot orientation are also elucidated in the example.

Experimental results obtained at 100 GHz using electrodischarge-machined slots in an aluminum plate were found to be in good agreement with theory. The smallest available slot, which was 1.27 mm long, 0.25 mm wide, and 0.25 mm deep, could be distinguished from clutter (liftoff) by using phase-sensitive detection and a polar display. An example of using the measured data and the theoretical model to determine slot depth was given.

We can conclude that it should be possible to obtain an accurate determination of the dimensions of a surface-breaking crack from microwave scattering measurements. Future work should be concerned with improving the theory and with answering questions concerning the practical and economic realization of the technique.

Acknowledgments

Technical discussions with Dr. B. A. Auld of Stanford University and Dr. R. B. Thompson of Rockwell International Science Center were most helpful in this work. Thanks are also due to Dr. A. C. Phillips of SRI for designing the 3-kHz portion of the phase-sensitive detection system used in the measurements.

This work was sponsored by the Center for Advanced NDE operated by Rockwell International Science Center under Contract F33615-74-C-5180.

References

[1] Hruby, R. J. and Feinstein, L., *The Review of Scientific Instruments*, Vol. 41, May 1970, pp. 679-683.
[2] Hussain, A. and Ash, E. A., *Proceedings*, 5th European Microwave Conference, Hamburg, Germany, Sept. 1975, pp. 213-217.
[3] Collin, R. E., *Field Theory of Guided Waves*, McGraw-Hill, New York, 1960.
[4] McIsaac, P. R., *Transactions on Microwave Theory and Techniques*, Institute of Electrical and Electronics Engineers, Vol. MTT-27, Apr. 1979, pp. 340-342.
[5] Bahr, A. J., *Transactions on Antennas and Propagation*, Institute of Electrical and Electronics Engineers, Vol. AP-27, Nov. 1979, pp. 738-746.
[6] Harrington, R. F. and Mautz, J. R., in *Electromagnetic Scattering*, P. L. E. Uslenghi, Ed., Academic Press, New York, 1978, pp. 429-470.
[7] Harrington, R. F., *Field Computation by Moment Methods*, Macmillan Company, New York, 1968.
[8] King, R. W. P. and Harrison, C. W., Jr., *Antennas and Waves: A Modern Approach*, Massachusetts Institute of Technology Press, Cambridge, Mass., 1969.
[9] Rhodes, D. R., *Proceedings*, Institute of Electrical and Electronics Engineers, Vol. 52, Sept. 1964, pp. 1013-1021.
[10] Rhodes, D. R., *Transactions on Antennas and Propagation*, Institute of Electrical and Electronics Engineers, Vol. AP-14, Nov. 1966, pp. 676-683.

B. A. Auld[1]

Theoretical Characterization and Comparison of Resonant-Probe Microwave Eddy-Current Testing with Conventional Low-Frequency Eddy-Current Methods

REFERENCE: Auld, B. A., **"Theoretical Characterization and Comparison of Resonant-Probe Microwave Eddy-Current Testing with Conventional Low-Frequency Eddy-Current Methods,"** *Eddy-Current Characterization of Materials and Structures, ASTM STP 722,* George Birnbaum and George Free, Eds., American Society for Testing and Materials, 1981, pp. 332-347.

ABSTRACT: During the past two years small ferromagnetic resonators (FMR) operating at frequencies above 1000 MHz have been shown to offer promise as a new type of eddy-current probe for surface-breaking cracks in metals. Strong signals have been obtained from both electrical discharge machining (EDM) notches and actual fatigue cracks, and the FMR probes have been shown to have lift-off discrimination capability. Since the skin depth at these microwave frequencies is of the order of microns, the surface currents must penetrate the crack and, in order to detect its presence, the flaw detection mechanism must be necessarily somewhat different in detail than for conventional low-frequency eddy-current methods, where the flaw has dimensions typically of the order of the skin depth. A general theory, based on the Lorentz reciprocity relation and applicable to all types of detection systems, is reviewed and used as a vehicle for comparing microwave with low-frequency eddy-current techniques. In the microwave case, the FMR resonator is emphasized but other probe geometries are also considered.

KEY WORDS: flaw detection, low frequency probes, microwave probes, Lorentz reciprocity relation, microwave resonators, ferromagnetic resonance, cracks, inclusions, skin depth, waveguides

The purpose of this paper is to review some recent developments in eddy current flaw-detection analysis and to use this theory as a framework for characterizing and comparing resonant microwave probes, discussed in more detail in the companion paper, and conventional low-frequency probes. This formulation of the theory was first developed for microwave ferromagnetic resonance (FMR) probes [*1*][2] in either one-terminal or two-terminal con-

[1] Adjunct professor, Ginzton Laboratory, Stanford University, Stanford, Calif. 94305.
[2] The italic numbers in brackets refer to the list of references appended to this paper.

figurations (that is, using either a single coil for excitation and detection, or separate coils for these two functions). In contrast with the analysis in Ref *2*, however, the formulation presented here is not restricted as to probe geometry and applies not only to microwave probes such as the FMR probe, the microwave antenna probe [*3*], or a conventional resonator probe [*4*], but also to inductive and capacitive[3] probes operating in the frequency range (below 10 MHz) of standard eddy-current practice.

It should be noted that the term "microwave" in electrical engineering designates primarily a particular range of the frequency spectrum (≈ 1000 MHz to 20 000 MHz), but has also taken on the sense of a particular approach to the analysis of circuit problems. This has occurred because analysis of microwave waveguide and resonator problems requires that equivalent voltages, currents, and impedances be defined directly in terms of the electromagnetic fields, since distinct physical terminal connections do not exist as they do in low-frequency circuits. Because of this, there has developed in microwave-circuit theory a general field approach to circuit problems that is also applicable to low-frequency circuits, where it has the advantage of permitting the derivation of general formulas that can be subsequently specialized to particular cases. As will be seen, the approach allows one to derive a completely general eddy-current detection formula in a direct manner. Although the treatment is completely general, attention is directed here to probes and flaws that are small compared with the electromagnetic wavelength in air. The probe and flaw system, that is, constitutes a near-field (or quasistatic) problem, where radiation effects are unimportant. Interactions of flaws with microwave radiation fields are discussed in Ref *3*.

Derivation of the Basic Probe Response Formula

The analysis begins with the Lorentz reciprocity relation, which takes the form

$$\nabla \cdot [(H_1 \times E_2) - (H_2 \times E_1)] = 0 \tag{1}$$

for a system that does not contain ferromagnetic resonant (or gyromagnetic) media and

$$\nabla \cdot [(H_1 \times \hat{E}_2) - (\hat{H}_2 \times E_1)] = 0 \tag{2}$$

for a system that does [*5*]. Here, the subscripts 1 and 2 refer to two possible solutions of Maxwell's equations for a given electromagnetic system, and the

[3] Only one reference to this type of probe has been located in the literature: Decker, W. A. and Waidelich, D. L., "Nondestructive Testing Using an Electric Field Probe," *Proceedings*, 7th International Conference on NDT, Paper D-02, Warsaw, 1973.

carat in Eq 2 indicates that the d-c magnetic field, which must always be applied to realize a ferromagnetic resonant medium in practice [*6*], is reversed for the 2-solution. For simplicity, only the one-terminal probe is considered here. The case of a two-terminal FMR probe is treated in Ref *1*.

One begins with the construction of Fig. 1, where the probe is shown in block form to emphasize that its particular geometry is unimportant for the general derivation. It may, for example, be any of the geometries shown in Fig. 2. For all of these cases, except the ferromagnetic resonator, Eq 1 is applicable. In the ferromagnetic resonator a d-c magnetic field, shown by the light arrow external to the sphere, is present, and the magnetization of the ferrite sphere, shown by the dark arrow, performs a resonant precessional motion about the field in the manner illustrated. The second form of the reciprocity relation must be used here. To simplify the notation in what follows the carat on the 2-solution will be suppressed, with the understanding that this solution corresponds to a reversed d-c field in cases where this field is required. Furthermore, the 2-solution will be supposed to apply when the flaw is present in Fig. 1 and the 1-solution when it is not. The following notation is then adopted

$$E_1, H_1 \rightarrow E, H$$

$$E_2, H_2 \rightarrow E', H'$$

where the prime designates perturbation of the system by the presence of a flaw.

It should be noted that Eqs 1 and 2 are valid at every point where the

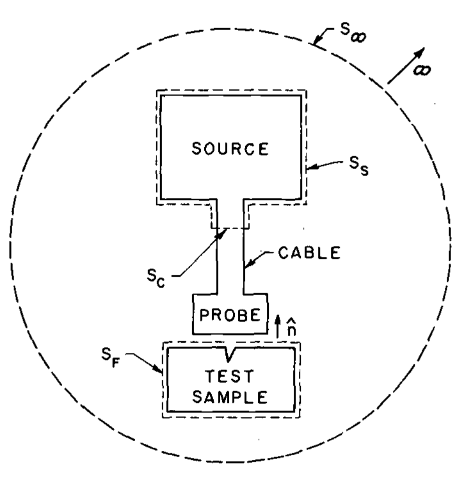

FIG. 1—*General construction for reciprocity theorem analysis of a one-terminal probe.*

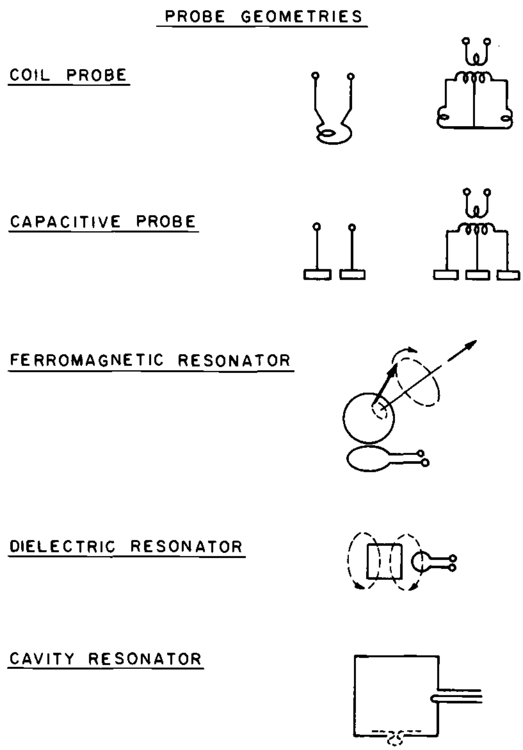

FIG. 2—*Different types of probe geometries.*

material parameters are the same for both solutions. The reciprocity relation is therefore valid at all points within the volume enclosed by the surfaces S_S, S_C, S_F, and S_∞ in Fig. 1, since the flaw itself is excluded. One can therefore integrate over this volume and, applying Gauss's theorem, convert the integral to an integral over the enclosing surface S

$$\int_S [(H \times E') - (H' \times E)] \cdot \hat{n}\, dS = 0 \tag{3}$$

In the quasistatic approximation the fields go to zero at infinity sufficiently rapidly that the contribution of S_∞ vanishes.[4] If the shielding around the source is considered to be perfectly conducting, the contribution of S_S also vanishes, and one is left with contributions from S_C, over the transmission line feeding the probe, and S_F, surrounding the test piece. By expressing the primed and unprimed fields within the transmission line in terms of an

[4] This integral can be also shown to vanish when radiation is taken into account.

incident and a reflected wave, with reflection coefficients Γ' and Γ, respectively, one can manipulate the reduced form of Eq 3 into

$$\Delta\Gamma = \Gamma' - \Gamma = \frac{1}{4P}\int_{S_F} [(\dot{E} \times H') - (E' \times \dot{H})] \cdot \hat{n}\, dS \tag{4}$$

where P is the power flow in the incident wave. Details of the algebra, which are straightforward and follow exactly the analogous problem in ultrasonic nondestructive examination NDE [7], are presented in Ref *1* and will not be repeated here. If it is noted, then, that

$$\Gamma = \frac{Z_{IN} - Z_0}{Z_{IN} + Z_0} \tag{5}$$

and that the current I at the input plane (S_C in Fig. 1) is

$$I = (1 - \Gamma)(2P/Z_0)^{1/2} \tag{6}$$

Eq 4 can be reduced to a more useful form [8]

$$\Delta Z = \frac{1}{I^2}\int_{S_F} [(E \times H') - (E' \times H)] \cdot \hat{n}\, dS \tag{7}$$

giving the first-order change in the impedance of the probe due to the presence of a flaw. The first-order restriction means that the formula is applicable to small impedance changes, which is what one wishes to detect in practice.

For a surface-breaking crack in a perfectly conducting specimen, the boundary conditions on S_F in Fig. 1 require that

$$\hat{n} \times E = 0$$

everywhere on S_F and that

$$\hat{n} \times E' = 0$$

everywhere except on the crack opening. Under these circumstances Eq 7 reduces to

$$\Delta Z = \frac{1}{I^2}\int_{\text{crack opening}} (E' \times H) \cdot \hat{n}\, dS, \tag{8}$$

Approximate evaluations of this integral have been reported for a near-field microwave FMR probe [1] and for a microwave antenna probe, including the effect of finite specimen conductivity [3].

Equation 8 is a particular version of the ΔZ formula applicable to a surface-breaking crack in a perfectly conducting specimen. The fact that the surface S_F is completely arbitrary, as long as it encloses the flaw itself, permits many other modifications of the basic formula. Figure 3 gives some of the possibilities. In the upper schematic S_F is shrunk to enclose the contour of the crack itself. This permits incorporation of the detailed physics of the flaw-field interaction into the ΔZ calculation. For example, it is known for a specimen of finite conductivity that the surface perturbation of the fields extends outside the opening of the crack. Furthermore, the perturbed fields have a singularity at the crack tip [9], just as in the ultrasonics case, and it has been stated that conductivity changes in the plastic zone around the crack tip sometimes play an important role in the flaw response. By defining the surface S_F so as to closely surround the flaw, one can incorporate these phenomena directly into the ΔZ calculation and study their effect on the flaw response. Since the theory presented here is not restricted to the microwave case, where the skin depth is very small and the technique is essentially limited to surface-breaking cracks, one may also consider

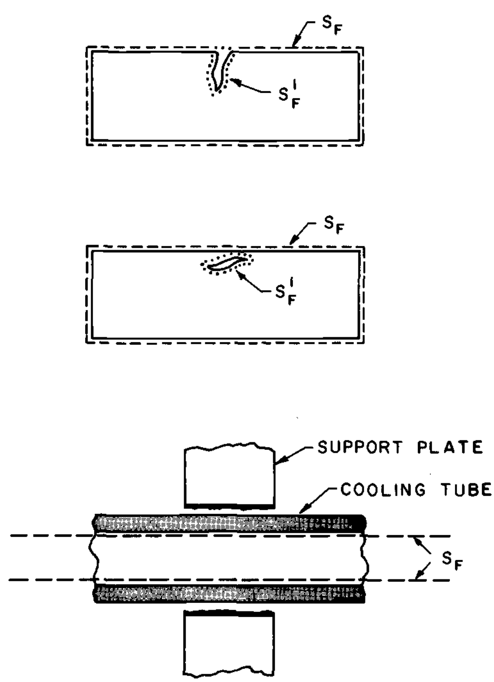

FIG. 3—*Various allowable choices for the surface* S_F *in Eq 7.*

buried cracks and again shrink S_F to the surface of the crack (Fig. 3). Alternatively, it may be convenient to remove S_F entirely from the surface of the specimen nearest the flaw. An illustration is given at the bottom of Fig. 3, which illustrates the cooling tube support region of a PWR steam generator. In this case the flaw consists of a buildup of corrosion products between the tube and the support plate. For this geometry there is an advantage in taking S_F to be on the inner surface of the tube and closing it at infinity with the source and the probe inside. Equation 7 can be then written in terms of the perturbed and unperturbed surface impedances seen looking from S_F into the layered structure consisting of tube wall, the air gap, the corrosion layer, and the support plate [8].

Another important category of flaw is the buried inclusion (Fig. 4), consisting of a region having different electromagnetic parameters than the host material (for example, a metallic inclusion in a structural ceramic). In this geometry Eq 7 is applied with S_F shrunk to enclose the surface of the inclusion, as shown in the figure. However, since the flaw in this situation consists of a perturbation $\delta\mu$, $\delta\epsilon$ of the material parameters, where

$$\delta\epsilon \rightarrow \delta\epsilon + \delta\sigma/i\omega$$

for a medium with conductivity, it is often desirable to modify the ΔZ formula so as to display these perturbations explicitly. This is accomplished by rewriting Eq 7 as a volume integral

$$\Delta Z = \frac{1}{I^2}\int_{V_F} \nabla \cdot [(E' \times H) - (E \times H')]dV \qquad (9)$$

and then using the identity

$$\nabla \cdot (A \times B) = B \cdot \nabla \times A - A \cdot \nabla \times B$$

plus Maxwell's equations, to recast in the form

$$\Delta Z = -\frac{i\omega}{I^2}\int_{V_F} [(\delta\mu H \cdot H') - (\delta\epsilon E \cdot E')]dV \qquad (10)$$

Note that, up to this point, the shape of the inclusion has not been specified. The difficulty in evaluating all of the above formulas consists primarily in calculating the perturbed fields at the flaw. One approach to Eq 10 for the case of a weak perturbation is the Born approximation, which has been widely applied to ultrasonic scattering NDE [10]. In this method, the perturbed fields are only weakly perturbed and, for a first-order evaluation of ΔZ, can be taken as equal to the unperturbed fields in evaluating the integral of Eq 10. Since the unperturbed fields are unaffected by the shape of the

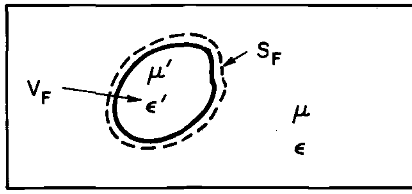

FIG. 4—*Flaw geometry for a general inclusion.*

inclusion, this approximation is readily applicable to inclusions of arbitrary shape. For inclusions that are of ellipsoidal shape and small compared with the spatial variations of the unperturbed field, the quasistatic approximation may be used [*2*]. Here, the inclusion is analyzed as an element polarized by a spatially uniform applied field, and the perturbed fields within the flaw are simply proportional to the unperturbed field applied by the probe. In the case of a spherical inclusion [*11*], then

$$H' = \frac{3\mu}{\mu' + 2\mu} H \qquad E' = \frac{3\epsilon}{\epsilon' + 2\epsilon} E \tag{11}$$

Applying this approximation to a two-terminal version of the general theory presented here, one obtains Burrows's result [*12*]. The development of his theory, however, is restricted from the beginning to ellipsoidal flaws that are small compared with a skin depth. Figure 5, an adaptation of his construction to a one-terminal probe geometry, illustrates this point for the case of a magnetic inclusion. The dipole moment induced in the inclusion by the probe coil is replaced by the current loop shown. Then, the reciprocity relation in circuit form is applied to the back emf $V_{2,m}$ induced in the probe coil by I_1, and to the emf V_1 induced in the "dipole" loop by the excitation current I_2 in the probe coil. Faraday's law gives another expression for V_1 in terms of the flux density produced at the dipole loop by the excitation current. Equating these two expressions for V_1, one obtains an expression for the back emf $V_{2,m}$ terms of the normalized test field at the inclusion and the polarizability of the inclusion. From this the change in the probe input impedance ΔZ can be calculated. This argument, restricted to low-frequency inductive probes and small flaws, is not directly transferable to some of the other geometries in Fig. 2 or to, for instance, the Born approximation for flaws of arbitrary shape. An illustration of the application of the more general theory to the analysis of larger flaws and of its advantages for numerical calculation is given in Ref *13*.

In all forms of the ΔZ formula it will be noted that the fields appearing in the integrals are, in fact, normalized with respect to the current I appearing at the test-probe terminals. This is true for all probe geometries and shows that the field per unit current is an appropriate figure of merit for the

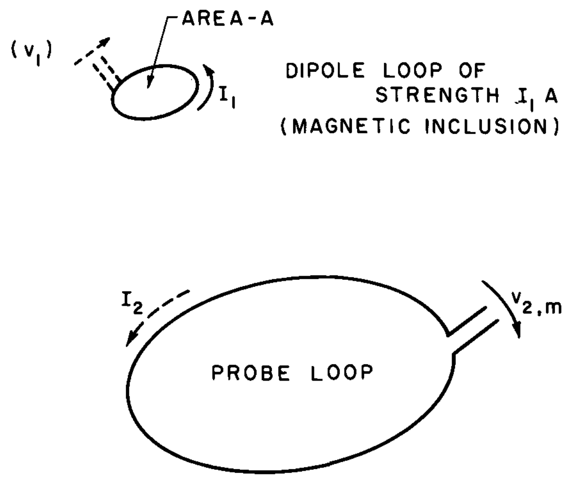

FIG. 5—*General construction for Burrows's analysis of a one-terminal low-frequency eddy-current probe.*

sensitivity of a probe. Evaluation of these normalized probe fields in terms of the probe geometry constitutes the second principal difficulty of eddy-current theory, the first being the perturbed-field problem noted above. Detailed calculations of field distributions around eddy-current coils of various shapes have been reported in the literature [*14,15*]. However, order of magnitude calculations of the normalized fields can be also usefully employed in comparing the sensitivities and optimum operating conditions for various types of probes: microwave versus low frequency, inductive versus capacitive, etc. Figure 6, for example, shows order-of-magnitude figures of merit for detecting changes in conductivity with low-frequency inductive and capacitive probes. These results, obtained from simple circuit and field considerations, show clear distinctions in frequency and dimensional dependence that need to be evaluated in defining optimum conditions for applying these types of probes to practical problems.

Comparison of Microwave and Low-Frequency Probes

The previous discussion shows that there is really no basic difference between a microwave near-field probe and a conventional low-frequency probe insofar as the general theory is concerned. Because of the large difference in operating frequency, however, there is a very significant difference in the parameters entering into the theory. First of all, because the skin depth varies as (frequency)$^{-1/2}$, the penetration of the field into the specimen is very much less at microwave frequencies, implying that only surface-breaking cracks can be examined by eddy-current techniques in this frequency range. Table 1 compares the penetration depths at two typical frequencies for several common structural materials. It can be seen from this that the interaction of a microwave test field with a crack must take place as a result of the surface currents propagating down into the crack, as if into a small electromagnetic waveguide. Some analyses have been made of microwave crack response (Eq 8) on the basis of this waveguide model [*1,3,4*]. For a very small crack, equivalent to a waveguide below cutoff, depth information is generated by the exponential decay of the waveguide mode fields as they penetrate into the crack. Beyond a certain depth ΔZ becomes independent of depth because the fields do not reach the bottom of the crack. At very high frequencies and large cracks, the flaw may actually support an electromagnetic resonance, giving a very large response and high sensitivity to depth variations [*3*]. By contrast, the depth response in low-frequency testing, where the crack depth is comparable to a skin depth, arises from

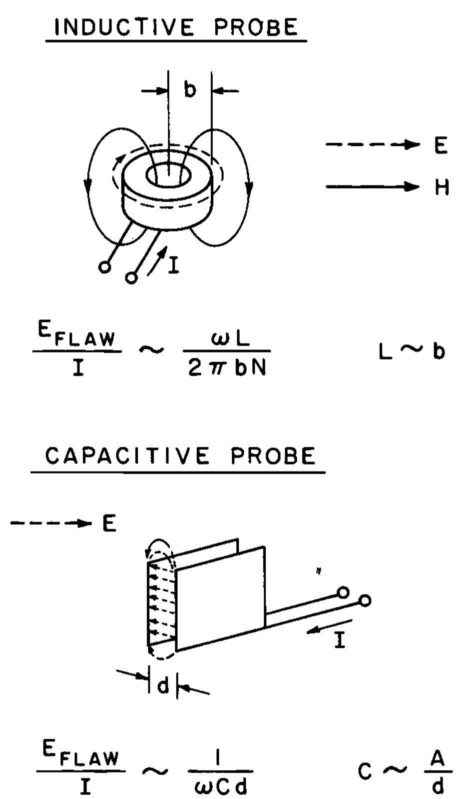

FIG. 6—*Qualitative comparison of figures of merit for inductive and capacitive probes. Coil inductance is* L *and the number of turns is* N. *The capacitive probe has capacitance* C *and area* A.

TABLE 1—*Skin Depth and Surface Resistivity for Typical Materials and Frequencies.*

Material	Frequency, ω, MHz	Skin Depth, δ, mil	Surface Resistivity, R_S
Aluminum	1	3.25	3.25×10^{-4} ohm
	1000	0.103	1.03×10^{-2} ohm
304L Stainless	1	16.8	1.69×10^{-3} ohm
	1000	0.532	5.34×10^{-1} ohm
6-4 Titanium	1	26.0	2.52×10^{-3} ohm
	1000	0.823	7.96×10^{-1} ohm
	for air, $Z_0 = 377$ ohm		

the phase variation of the r-f field as it penetrates the test piece. This leads to a phase angle change with crack depth, which may be understood by picturing the surface integral over surface $S_F{}^I$ at the top of Fig. 3 and which is small because the fields penetrating the specimen die away to very small amplitude before the phase angle reaches π. Another effect of increasing the frequency is to increase the surface impedance of the specimen (R_S in Table 1). This impedance change plays a role in determining the ΔZ produced by lift-off. The table shows, however, that the surface impedance is quite close to a short circuit compared with Z_0, even for the lowest conductivity material in the table at 1000 MHz. This becomes less and less true, however, at the higher microwave frequencies.

A change in operating frequency also influences the choice of probe circuit parameters. For an inductive probe, the inductance must be decreased with increasing frequency if the probe impedance is to be maintained at some suitable level, and Fig. 6 shows that this may influence the sensitivity, since the figure of merit depends on both the inductance L and the number of turns N. At microwave frequencies, resonant probes (such as the ferromagnetic resonance probe) can be compact and rather easily fabricated. Referring to the figure-of-merit for sensitivity discussed above, one notes that this resonant operation increases the sensitivity by increasing the ratio of E_{FLAW} to the drive current I and is probably the preferred type of operation for a microwave probe. Such a resonant probe requires only a one-turn coupling coil (Fig. 7), relying on the resonance effect for sensitivity, rather than the multiturn coils used at low frequencies.

The circuit differences noted also cause significant differences in operating characteristics and adjustment between low-frequency and microwave probes. Figure 8 shows the standard equivalent circuit model of a low-frequency eddy-current probe [*16*]. Here, the mutual inductance M represents the coupling of the test coil to the specimen and is the parameter related to lift-off effects. The resistance R, on the other hand, describes the influence of resistance changes and flaws in the specimen. This simple circuit allows one to predict the general behavior of such a probe, that is, the

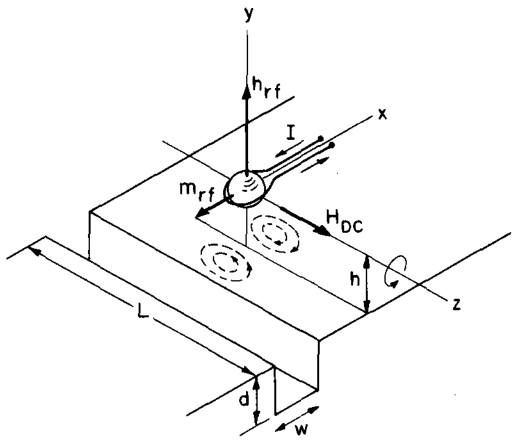

FIG. 7—*Microwave ferromagnetic resonance (FMR) probe.*

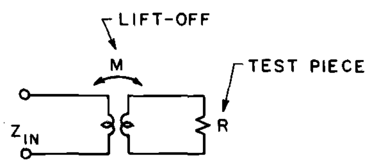

FIG. 8—*Equivalent circuit representation of a standard low-frequency probe.*

variation of complex Z_{IN} as a function of liftoff or the presence of a flaw. Figure 8 in the paper by Auld and Winslow[5] indicates the lift-off effect in the complex impedance plane as a dashed line and the flaw signal as a solid line.

In the microwave ferromagnetic resonance probe, a loop excited by the input current drives the magnetization of the ferrite sphere (in practice, pure or doped single crystal yttrium iron garnet) in a resonant precessional motion about the applied d-c field. This is illustrated by the dark precessing arrow in Fig. 2 and the transverse r-f magnetization m_{rf} shown rotating about the d-c field in Fig. 7. This rotating magnetization couples to the surface of the specimen by inducing eddy or surface currents. It is the reaction of the r-f fields generated by these currents upon the precession motion of the magnetization that causes a change in the frequency and quality factor Q of the ferromagnetic resonance. The resonant behavior of the probe can be represented by a loop-coupled series resonant circuit (Fig. 9) and, as in the conventional probe, interaction with the specimen is represented by mutual inductance coupling to a resistance load. Since lift-off and flaw variations

[5]Auld, B. A. and Winslow, D. K., this publication, pp. 348-366.

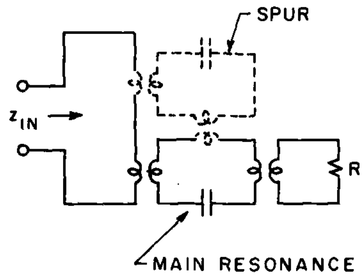

FIG. 9—*Equivalent circuit representation of the FMR probe.*

induce both reactive and resistive changes into the resonant circuit of the figure, both the resonant frequency f_0 and Q are changed and neither of these parameters individually provides the necessary separation of lift-off and flaw responses. This is not a complete picture, however, of the physical behavior of a ferromagnetic resonator. The resonance described previously, in which the magnetization of the sphere is uniformly distributed as it precesses about the d-c field, is only one of many possible modes of ferromagnetic resonance. For each of the other modes the magnetization is spatially distributed in a characteristic manner and has a frequency variation with H_{dc} that differs from mode to mode [6]. These spurious modes or spurs may be coupled directly to the input loop or indirectly through the main resonance (or uniform precession mode). Consequently, the complete equivalent circuit is as illustrated in Fig. 9, where a representation of one of the spurs is shown in dashed outline.

As is discussed in Auld and Winslow, coupling to the ferromagnetic resonator may be adjusted so as to excite one or more spurs to varying degrees. Experiments performed using a microwave network analyzer to display an oscilloscope presentation of the complex input impedance of the probe have shown that discrimination between liftoff and flaw signals exists (Fig. 8 of Auld and Winslow) if the probe is adjusted for suitable coupling to one of the spurs. At the present time this adjustment is largely empirical, but the nature of the interaction between the two modes can be somewhat clarified by reference to the equivalent circuits. Figure 10 shows the equivalent circuit of the main resonance in the standard form corresponding to an inductively coupled series resonant circuit. The bottom of the figure gives, in the complex-impedance plane, the resonance circle describing its impedance versus frequency characteristic. Each spurious mode coupled directly to the input loop has a similar representation, all of the parallel resonant elements appearing in series. The left side of Fig. 11 illustrates a case with direct coupling to one spurious mode and, below it, the general form of the resulting variation of impedance with frequency. On the right side, Fig. 11 presents the equivalent circuit for a single spur coupled in-

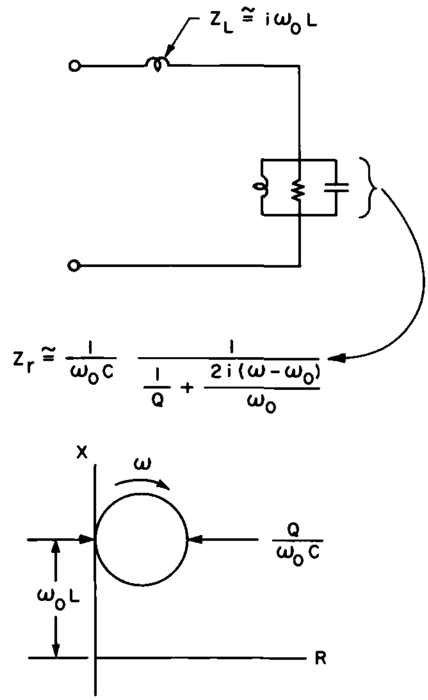

FIG. 10—*Detailed equivalent circuit and complex impedance versus frequency plot for the main resonance of an FMR probe.*

directly through the main resonance (or uniform precession (UP)). As is shown in Auld and Winslow, this gives the form of curve that is observed experimentally, and this is the form of equivalent circuit to be compared with the standard probe in Fig. 8. Determining optimum conditions for operating the FMR probe will depend upon correctly identifying the best choice of spurious mode and understanding the relationship of the various circuit parameters to the experimental variables.

Summary and Conclusions

A general theory of electromagnetic flaw-detection probes, applicable to both resonant and nonresonant probes operating either at low or microwave frequencies, has been described and compared with earlier work. Because of its generality, this approach is useful for comparing the performance of different probe geometries and the response of a probe to different types of flaw. It has also been shown to have the potential for reducing the cost of numerical calculations for certain types of flaws.

In this paper the theory has been used as an organizational basis for the

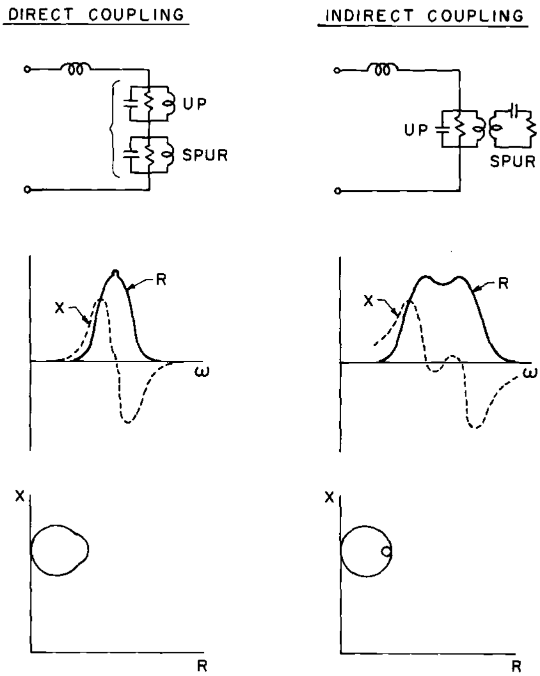

FIG. 11—*Comparison of direct and indirect coupling to a spurious mode.*

comparison of conventional low-frequency probes with microwave-frequency probes. There is essentially no difference in the functioning of these two types of probe, but the wide spread in operating frequencies leads to considerable differences in the physical characterization of the flaw and in optimum circuit parameters of the probe. At low frequencies the behavior of a surface-breaking flaw is dominated by skin effect, and at microwave frequencies it is dominated by waveguide effects inside the flaw. The theory leads to a simple figure of merit for probe sensitivity, useful for studying and comparing probe adjustment and performance in the two cases. Note added in proof: Use of a ferromagnetic resonance probe for measuring the spatial variation of the magnetic properties of materials was reported by Soohoo [*17*].

Acknowledgments

Discussions with R. A. Craig and C. M. Fortunko on ferromagnetic resonators, with M. Riaziat on the reciprocity formulation of probe theory, and with A. J. Bahr on the waveguide representation of a surface crack at microwave frequencies were most useful and are greatly appreciated.

This work was supported by the NSF-MRL Program through the Center for Materials Research, by Electric Power Research Institute Contract No. RP 1395-3, and by the Center for Advanced NDE, operated by the Rockwell International Science Center for the Advanced Research Projects Agency and the Air Force Materials Laboratory under Contract F33615-74-C-5180.

References

[*1*] Auld, B. A., "Theory of Ferromagnetic Resonance Probes for Surface Cracks in Metals," Ginzton Laboratory Report No. 2839, Stanford University, Stanford, Calif., July 1978.
[*2*] Burrows, M., "A Theory of Eddy Current Flaw Detection," Ph.D. thesis, University of Michigan, 1964, University Microfilms International, Ann Arbor, Mich.
[*3*] Bahr, A. J., this publication, pp. 311-331.
[*4*] Hussain, A. and Ash, E. A., *Proceedings*, 5th European Microwave Conference, Hamburg, Germany, Sept. 1975, pp. 213-217.
[*5*] Harrington, R. F. and Villneuve, A. T., *Transactions*, Institute of Radio Engineers, Vol. MTT-6, July 1958, pp. 308-310.
[*6*] Lax, B. and Button, K. J., *Microwave Ferrites and Ferrimagnetics*, McGraw-Hill, New York, 1962.
[*7*] Auld, B. A., *Wave Motion*, Vol. 1, Jan. 1979, pp. 3-10.
[*8*] Auld, B. A., "Quantitative Modeling of Flaw Responses in Eddy Current Testing," Fourth Monthly Report, Electric Power Research Institute Contract No. RP 1395-3, Ginzton Laboratory Report No. 2926, Stanford University, Stanford, Calif., Feb. 1979.
[*9*] Kahn, A. H., Spal, R., and Feldman, A., *Journal of Applied Physics*, Vol. 48, Nov. 1977, pp. 4454-4459.
[*10*] Gubernatis, J. E., Domany, E., Krumhansl, J. A., and Huberman, M., *Journal of Applied Physics*, Vol. 48, July 1977, pp. 2812-2819.
[*11*] Stratton, J. A., *Electromagnetic Theory*, McGraw-Hill, New York, 1941, pp. 211, 258.
[*12*] Riaziat, M., unpublished notes.
[*13*] Kincaid, T. G. and Chari, M. V. K., this publication, pp. 59-75.
[*14*] Dodd, C. V. and Deeds, W. E., *Journal of Applied Physics*, Vol. 39, May 1968, pp. 2829-2838.
[*15*] Szabo, T. L., Frost, H. M., and Sethares, James C., *Transactions*, Institute of Electrical and Electronic Engineers, Vol. SU-24, Nov. 1977, pp. 393-406.
[*16*] Libby, H. L., *Introduction to Electromagnetic Nondestructive Test Methods*, Wiley-Interscience, New York, 1971.
[*17*] Soohoo, R. F., *Journal of Applied Physics*, Vol. 33, March 1962, pp. 1276-1277.

B. A. Auld[1] *and D. K. Winslow*[1]

Microwave Eddy-Current Experiments with Ferromagnetic Resonance Probes

REFERENCE: Auld, B. A., and Winslow, D. K., "**Microwave Eddy-Current Experiments with Ferromagnetic Resonance Probes,**" *Eddy-Current Characterization of Materials and Structures, ASTM STP 722,* George Birnbaum and George Free, Eds., American Society for Testing and Materials, 1981, pp. 348-366.

ABSTRACT: Experimental results obtained with the ferromagnetic resonance probe described in the companion paper by B. A. Auld are presented for a variety of real and fabricated flaws. Details of the apparatus are given with a brief explanation of the measurement technique used. Particular reference is made to the important property of discrimination between flaw and liftoff signals. An illustration of the edge-discrimination characteristics of the ferromagnetic resonance probe is shown.

KEY WORDS: eddy current testing, ferromagnetic resonance, microwave frequencies, surface cracks, liftoff discrimination, aluminum, titanium alloy, fatigue cracks

In the companion paper by Auld[2] the general principles of ferromagnetic resonance (FMR) flaw detection were presented and compared with those of standard low-frequency eddy-current testing. Also given were the essentials of a general theory applicable both to FMR probes operating at microwave frequencies (approximately 1000 MHz and above) and to standard probes operating at low frequencies (approximately 2 MHz and below). Although the skin depth at microwave frequencies is less than 0.0254 mm (1 mil), it has been found that even tightly closed fatigue cracks in aluminum are detectable with FMR probes. This new type of probe has the advantage of being smaller than conventional probes, yet our experiments show that it can detect all surface breaking flaws we have detected by conventional eddy current methods. A quantitative comparison of sensitivities has not yet been made, nor is there yet a good understanding of the interaction of microwave fields with tightly closed cracks. It has been found, however, that such flaws can be detected and that they give signals which can be distinguished in the complex impedance plane from liftoff signals.

[1]Adjunct professor and research engineer, respectively, Stanford University, Stanford, Calif. 94305.
[2]Auld, B. A., this publication, pp. 332-347.

Experimental Procedure

A ferromagnetic resonator is a small sphere of ferromagnetic crystal placed in a d-c magnetic field and excited by a microwave frequency current flowing in a wire loop encircling the sphere. The resonance phenomenon is a precessional motion of the crystal's inherent magnetic moment about the direction of the d-c magnetic field. This precessing magnetic moment induces surface currents in the metallic specimen, and it is the disturbance of these currents by a surface flaw that produces a detectable flaw signal at the electrical terminals of the wire loop. Since the surface currents at microwave frequencies are confined to a skin depth of less than 0.0254 mm (1mil), this new technique is restricted to surface-breaking flaws. A ferromagnetic resonator, unlike other types of electromagnetic resonators, has the property of its resonant frequency being independent of its dimensions. The resonant frequency depends solely on the strength of the applied d-c field and can be tuned by varying the field. Typically, the resonator (Fig. 1) has a diameter less than 0.762 mm (30 mil) but it can be adjusted to resonate at 1000 MHz, where the electromagnetic wavelength is of the order of 254

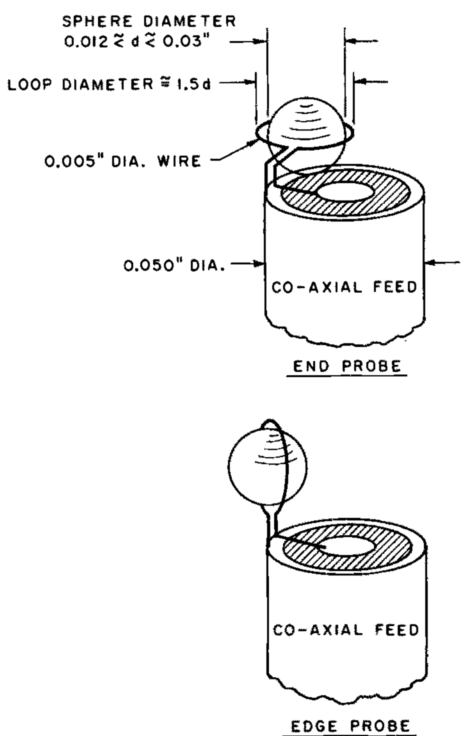

FIG. 1—*Detail of currently used probes.* (a) *End probe;* (b) *Edge probe.*

mm (10 in.). The material usually used for such resonators is pure or doped yttrium iron garnet (YIG). A resonator quality factor of 1000 is achievable in a YIG resonator, which provides high sensitivity for flaw detection. It was estimated by Auld[3] that a surface crack 0.508 mm (2 mil) in length should be detectable.

In addition to its potential advantages with regard to sensitivity the YIG probe, because of its very small size, promises to provide excellent spatial resolution, discrimination against edge effects, and accessibility to restricted corners. Figure 1 illustrates the geometries of our present generation of probes, one for surface probing and the other for the interiors of holes and corners. Our current philosophy is to apply the d-c magnetic field from a separately mounted samarium-cobalt permanent magnet having dimensions on the order of a fraction of an inch. This technique, illustrated in Fig. 2, allows accessibility to flaws to be determined by the probe size rather than by the magnet. Figure 3 shows an actual probe with a separate magnet. Other probes have a smaller piece of permanent magnet mounted near the resonator directly on the probe.

Unlike lower-frequency eddy-current probes, the coil in Fig. 1 requires only a single turn, which simplifies fabrication in miniature sizes. YIG

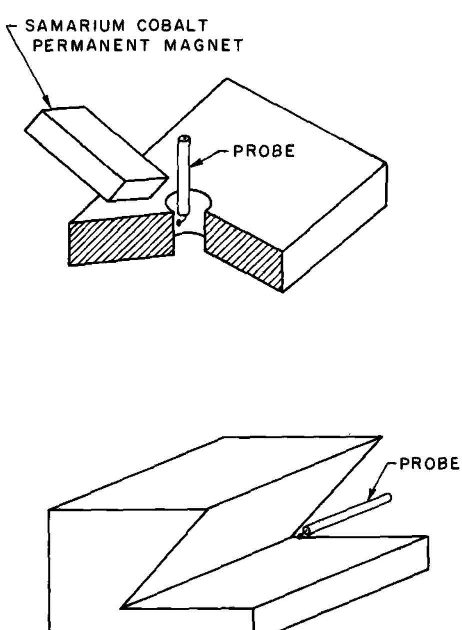

FIG. 2—*Typical positioning of the edge probe relative to a specimen.*

[3]Auld, B. A., "Theory of Ferromagnetic Resonance Probes for Surface Cracks in Metals," Ginzton Laboratory Report No. 2839, Stanford University, Stanford, Calif., July 1978.

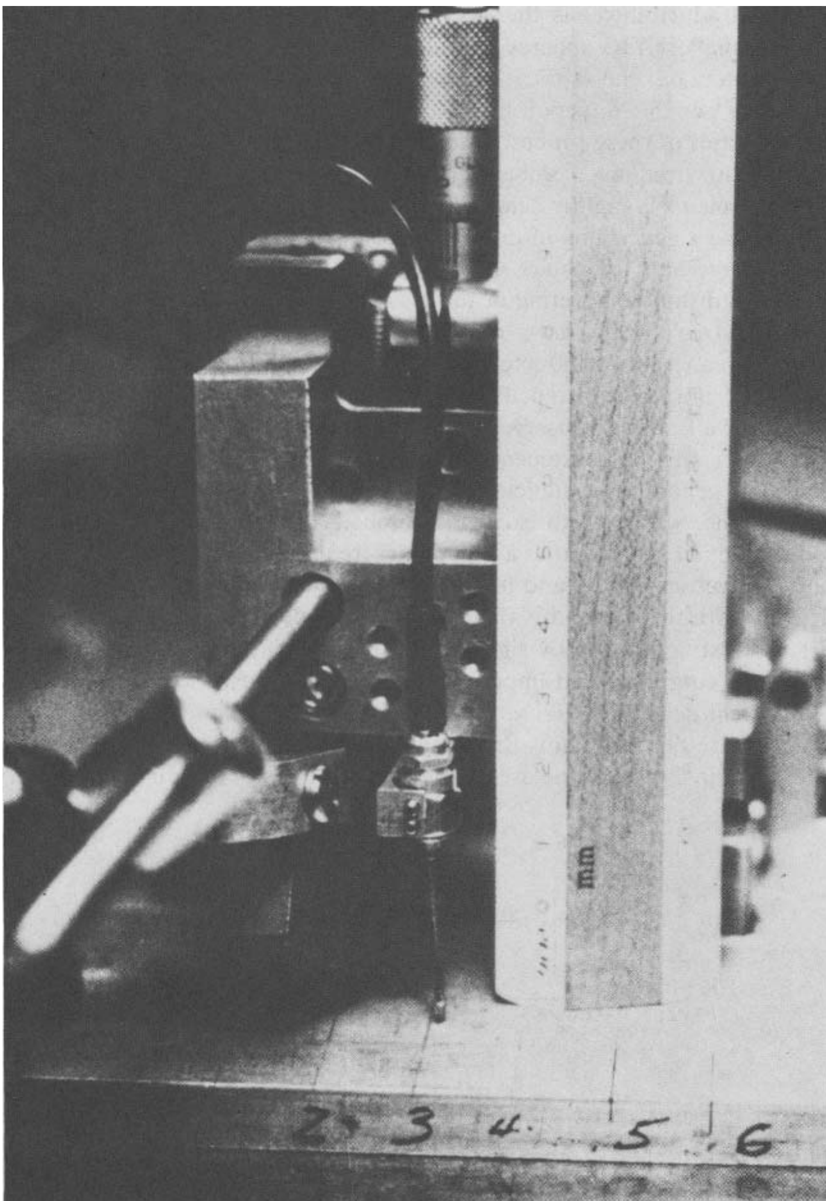

FIG. 3—*End probe with a separately supported samarium cobalt magnet. The operating frequency is between 800 and 1000 MHz, depending on the magnet positioning.*

resonator technology has been an established industrial process for many years, having been used for tunable microwave filter and oscillator applications. Reproducibility has therefore already been realized. At the present time the smallest YIG spheres available commercially are 0.305 mm (0.012 in.) diameter, but the fabrication of even smaller spheres appears feasible. This is one possible direction for further improving the edge discrimination characteristics of these probes. Another is the use of shielding, as currently applied in low-frequency probes. The lowest operating frequency in our current experiments is slightly below 800 MHz; this is not a limit, however, even for the present generation of probes. Also, the use of resonator shapes other than a sphere and the choice of other magnetic materials offer possibilities for a very substantial lowering of the resonant frequency.

Figure 11 in Auld[2] shows the equivalent circuit representing the YIG probe resonance, and inductor in-series with a parallel resonant circuit. Clearly the simplest way to detect changes in the probe impedance due to the presence of a flaw is to observe the shift in resonant frequency.[4] In our first experiments this measurement was carried out as shown in Fig. 4. A microwave generator, producing a voltage whose frequency was swept linearly in time, was used to excite the probe. An oscilloscope display of the probe reflection coefficient as a function of frequency then permitted observation of the resonance dip and its shift produced by scanning over a flaw. The difficulty with this method is that liftoff variations also produce a frequency shift. To distinguish a flaw signal from liftoff variations, it is necessary to observe the complex input impedance of the probe, just as in low-frequency eddy-current detection. Figure 5 shows a standard microwave circuit, called a polar-phase discriminator, that may be used for this purpose. It presents on the X- and Y-axis of the oscilloscope screen the real and imaginary parts

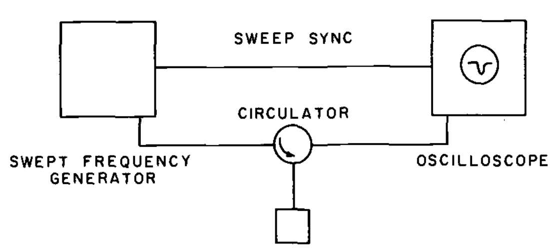

FIG. 4—*Detection circuit used in early experiments for measuring the ferromagnetic resonance line shift due to the presence of a flaw.*

[4]Auld, B. A., Elston, G., and Winslow, D. K., "A Novel Ferromagnetic Resonance Probe for Eddy Current Detection of Surface Flaws in Metals," *Proceedings*, 8th European Microwave Conference, Paris, Sept. 1978.

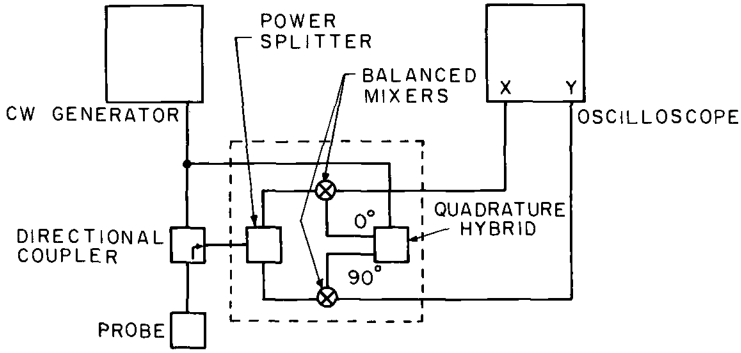

FIG. 5—*Detection circuit currently used for measuring the complex input impedance of the FMR probe.*

of the complex reflection coefficient Γ at the probe terminals. This quantity is related to impedance by the elementary formula

$$\frac{Z}{Z_o} = \frac{1 + \Gamma}{1 - \Gamma}$$

where Z_o is the characteristic impedance of the electrical transmission line feeding the probe. Since the oscilloscope display in Fig. 5 is a polar representation of the complex number Γ, the real and imaginary parts of the impedance must be obtained from the transformation noted previously. This generates the contours shown on the right-hand side of Fig. 6, where the dashed lines represent constant resistance (or real part of impedance) and the solid lines constant reactance (or imaginary part of impedance).

Figure 6 also shows a trace representing the main resonance circle (frequency response) of the probe, with a secondary circle due to coupling with one of the spurious magnetostatic modes mentioned in Auld[2]. By suitably adjusting the position and direction of the permanent magnet on the left-hand side of Fig. 3, one can couple to many of these spurious modes (Fig. 7). It has been found that coupling to a spurious mode produces a flaw-response curve in the complex impedance plane that is partially orthogonal to the liftoff curve. The principle behind the probe adjustment required to achieve this desirable condition, commonly used in conventional systems, is not yet well understood. Observations have shown that not all spurious modes are effective in providing liftoff discrimination, and a systematic study will be required to identify the optimum conditions.

As a comparison of low-frequency and microwave-frequency probes, Fig. 8 shows liftoff discrimination in the complex impedance plane for three types of probes: a low-frequency single (or absolute) coil, a low-frequency differen-

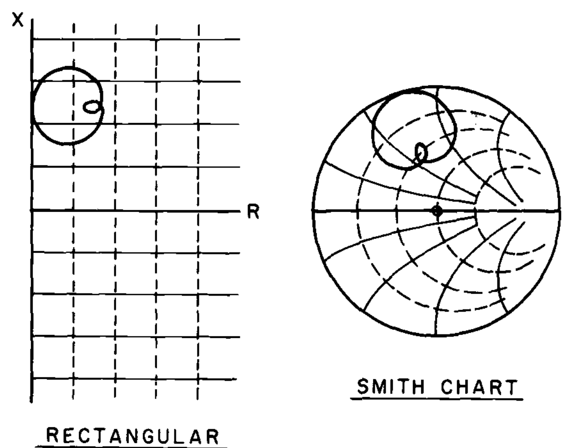

FIG. 6—*Comparison of rectangular and Smith Chart displays of complex input impedance.*

tial coil, and a ferromagnetic resonance (FMR) probe using a YIG sphere at microwave frequencies. In the latter case it should be recalled that the actual experimental results appear on a Smith Chart display, as in Fig. 6. All of the figures show flaw signals as a solid line and liftoff signals as a dashed line. For the single and differential coils the liftoff curves trace the trajectory of the impedance change obtained as the mutual inductance of Fig. 8 in Auld[2] is changed. The liftoff curve for the FMR probe arises from the detuning of a resonator excited at a constant frequency and follows the resonance circle in Fig. 11 in Auld[2]. It was noted above that liftoff discrimination in this case appears to require coupling to one of the spurious modes of the probe. This does not, however, necessarily have to be a strongly coupled secondary mode, as shown in Fig. 6. Good liftoff discrimination has been also achieved with a probe frequency-response curve that is almost a perfect circle, with only a small dimple or flattening to indicate the presence of a second mode.

Results

The first complex impedance plane measurements of flow and liftoff signals for a microwave FMR probe were made using a commercial network analyzer, a precision instrument built around the basic circuit of Fig. 5. Some of the measurements obtained for the flaws of Table 1 are exhibited in Fig. 9, where the liftoff and flaw signals may be distinguished by comparing with Fig. 8 and noting that the oscilloscope gives a Smith Chart rather than a rectangular impedance display. The fatigue crack in (*h*) was in a compact tension specimen of stainless steel. It had a length of about 12.7 mm (1/2 in.) and extended completely through the specimen in the other dimension. Probe signals were observed right out to the tip of the crack.

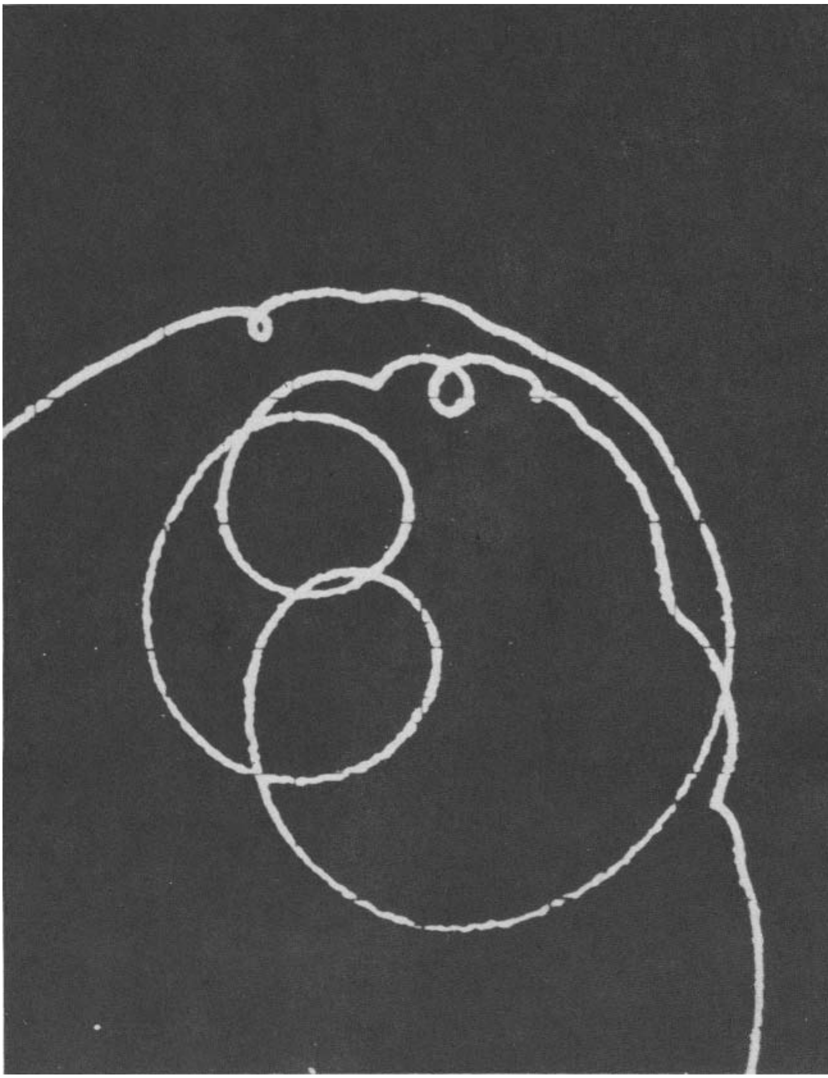

FIG. 7—*Smith Chart display of probe input impedance adjusted to show many spurious mode couplings. The trace shows impedance versus frequency for a probe placed in proximity to the specimen surface.*

Subsequently, a portable dedicated network analyzer with only the necessary features for nondestructive evaluation (NDE) work was fabricated, incorporating some of the features (display rotation, offset, and magnification) commonly used in conventional eddy-current instruments. The X- and Y- outputs of this instrument were fed into a storage oscilloscope for recording the data. Figure 10 illustrates the test bench layout, using a small end-

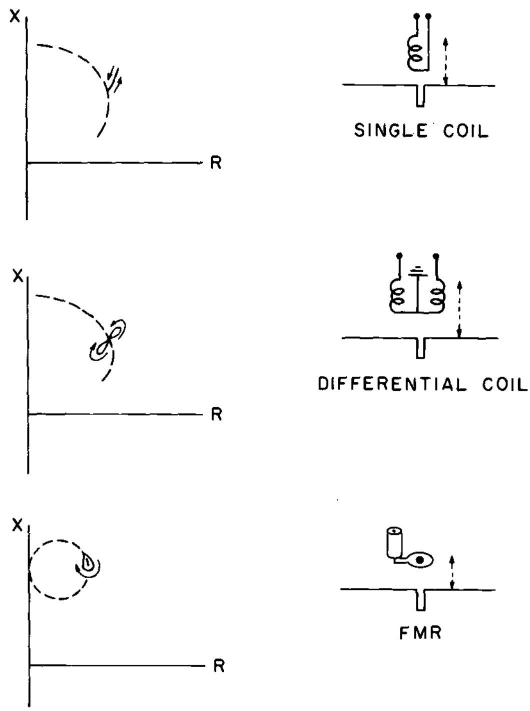

FIG. 8—*Discrimination between liftoff responses and flaw response in* (a) *standard absolute coil probe;* (b) *standard differential coil probe;* (c) *FMR probe.*

type probe (Fig. 1) with an integral samarium-cobalt magnet. Figure 10 shows a measurement being made on a series of saw cuts in an aluminum plate. These were cut with a 25.4-mm (1-in.) diameter by 0.127-mm (0.005-in.) thick jeweller's saw to depths from 0.051 to 0.51 mm (0.002 in. to 0.020 in.) in 0.051-mm (0.002-in.) steps and were spaced by 4.76 (3/16 in.). Figure 11 is the oscilloscope display obtained by first orienting the complex impedance curves so the flaw signal tear drop lies along the X-axis, then disconnecting the network analyzer signal from this axis and replacing it with a very slow internal sweep. The specimen was then slowly drawn by hand under the probe, so that it passed over each slot in turn. Note that even the 0.051-mm (0.002-in.)-deep slot was clearly resolved. Figure 12 shows the result of performing the same manual scan with both outputs of the network analyzer connected to the oscilloscope. In this case a tear drop is traced out as the probe passes over each slot, and the various tear drops nest inside each other as the slot size varies. It should be remarked that during these measurements the FMR probe, supported by the micromanipulator, was not in contact with the specimen. In spite of this there was no problem with table vibrations.

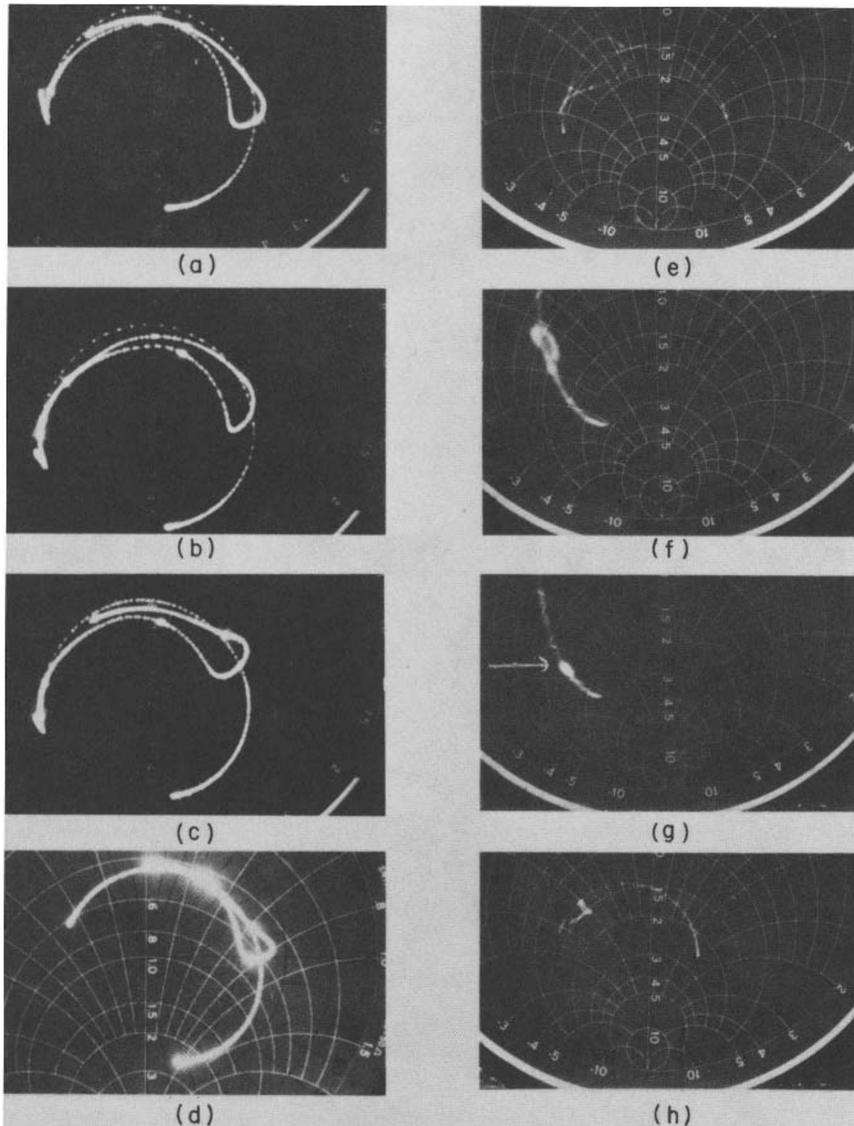

FIG. 9—*Displays of liftoff and flaw curves in the complex impedance plane for the flaws listed in Table 1.*

To test the instrument under more realistic conditions and to begin a joint investigation with Professor J. Shyne and M. Resch of the Stanford Material Science Department into the eddy-current behavior of aluminum tight fatigue cracks under load, measurements have been started on cracked

TABLE 1—*Representative test flaws.*

	Material	Length, in.	Depth, in.	Width, in.
	IDENTIFICATION MACHINED SLOTS			
(*a*) SB-1	aluminum	2	0.005	0.013
(*b*) SB-3	aluminum	2	0.015	0.012
(*c*) SB-5	aluminum	2	0.150	0.012
(*d*) SB-6	aluminum	2	0.200	0.012
	EDM NOTCHES			
(*e*) RA	titanium	0.105	0.024	0.010
(*f*), (*g*) NB	titanium	0.030	0.030	0.0027
	FATIGUE CRACKS			
(*h*) 316-L	stainless			

NOTE—1 in. = 25.4 mm

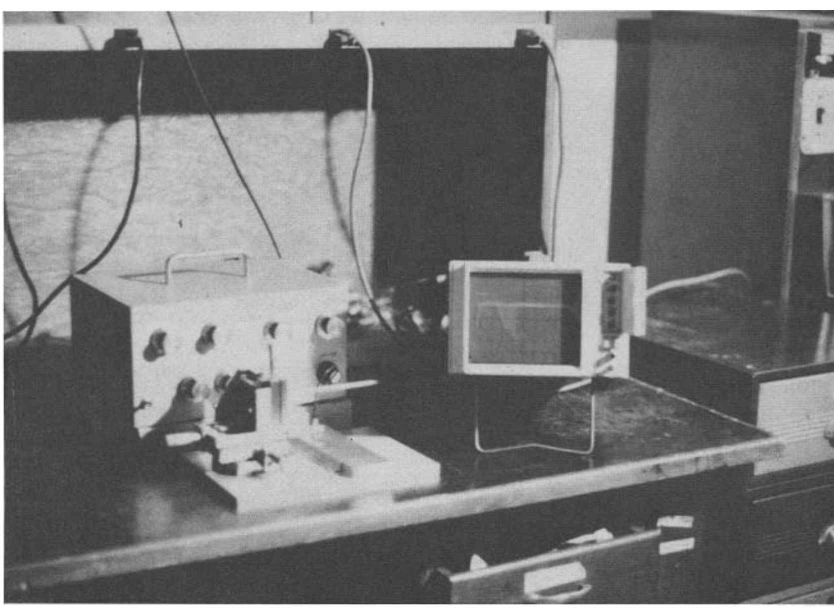

FIG. 10—*Test setup, showing probe with integral magnet, dedicated network analyzer, and storage tube for recording data. The probe operates at 900 to 1000 MHz.*

aluminum specimens subjected to bending in an MTS machine. Figures 13 and 14 show the general instrument arrangement and a closeup of the probe and specimen, respectively. Displays obtained in an initial run are shown in Figs. 15 and 16, the first being under zero load and the second under approximately 80 percent yield stress.

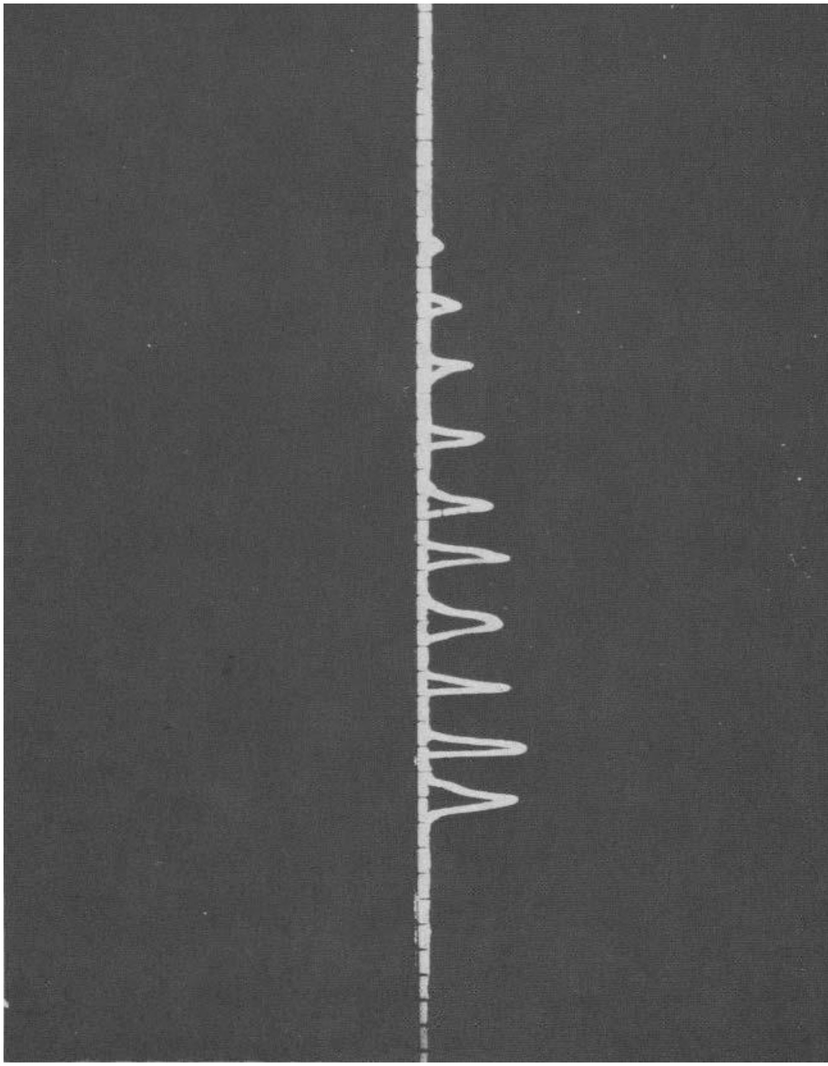

FIG. 11—*Oscilloscope recording of the orthogonal flaw signal obtained by manually scanning over a series of saw cuts in aluminum (0.051 to 0.51 mm (0.002 to 0.020 in.) in depth and approximately 0.13 mm (0.005 in.) opening width). The horizontal oscilloscope axis (oriented vertically here) is internally swept during the scan.*

Measurements of the spatial resolution of the probe, which determines its ability to discriminate between closely spaced flaws and between a flaw and a nearby edge, have also begun. Figure 17 illustrates measurements made by scanning a special 2200 MHz probe, with d-c field normal to the specimen,

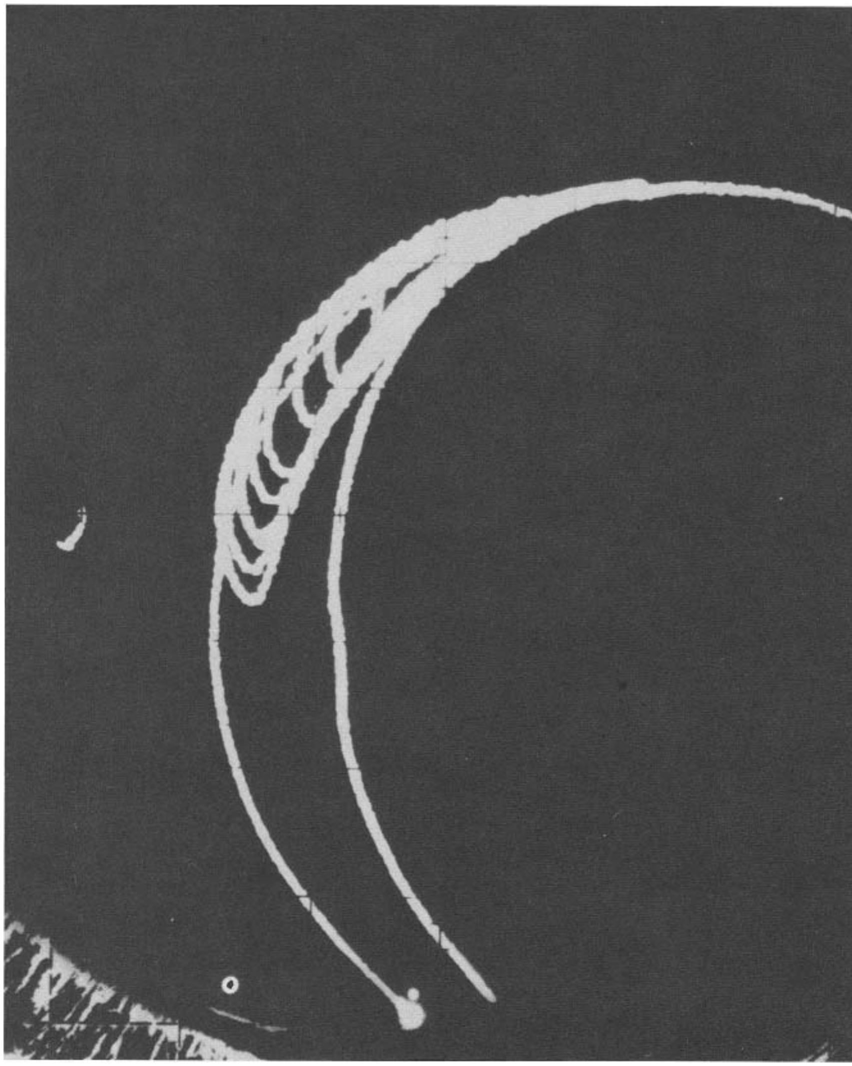

FIG. 12—*Recording of complex impedance data produced by manual scanning over the same slots as in Fig. 11.*

over a machined slot 0.13 mm (0.005 in.) in width in a steel plate.[5] The spatial resolution is seen to be on the order of the diameter of the spherical ferromagnetic resonator (0.38 mm (15 mil) in this case). Another illustration of the spatial resolution capability of these probes is given by Fig. 18. The

[5]Auld, B. A., Winslow, D. K., Elston, G., and Fortunko, C. M., "Detection of Surface Flaws with Microwave Ferromagnetic Resonators," Special Report on the Fourth Year Effort under the Interdisciplinary Program for Quantitative Flaw Definition, Rockwell International Science Center (Contract F33615-74-C-5180), 1 July 1977–30 June 1978, pp. 153–162.

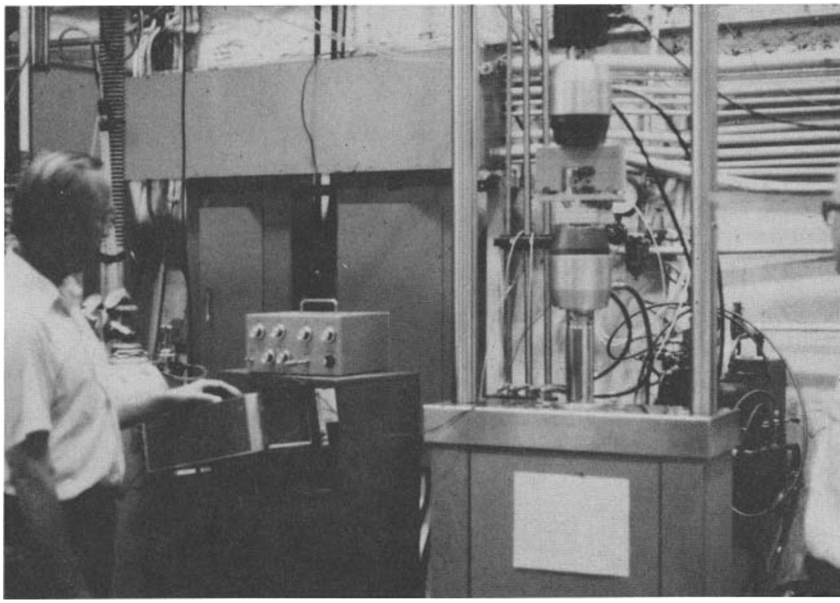

FIG. 13—*Measurement of the eddy current response under load of a fatigue crack in aluminum.*

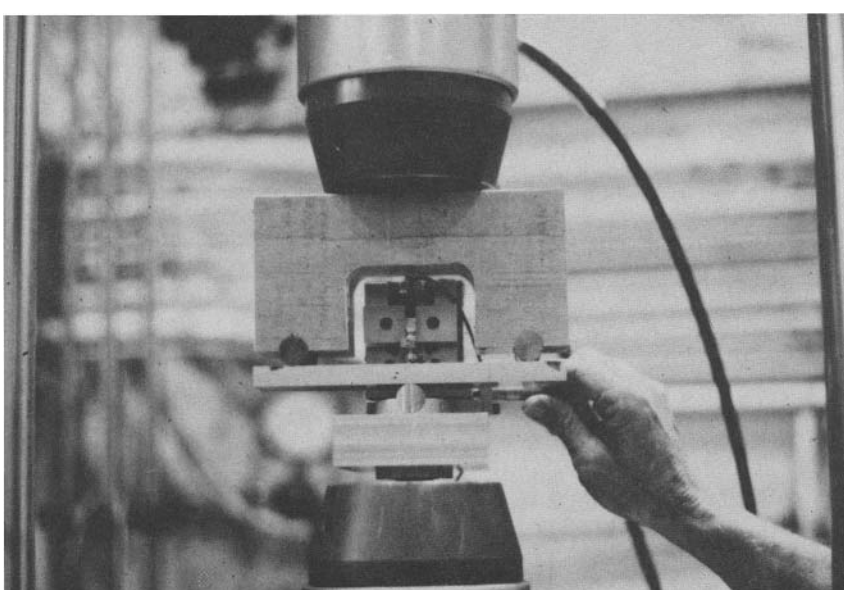

FIG. 14—*Closeup of the probe and specimen.*

FIG. 15—*Complex impedance plane signal from fatigue crack under zero load.*

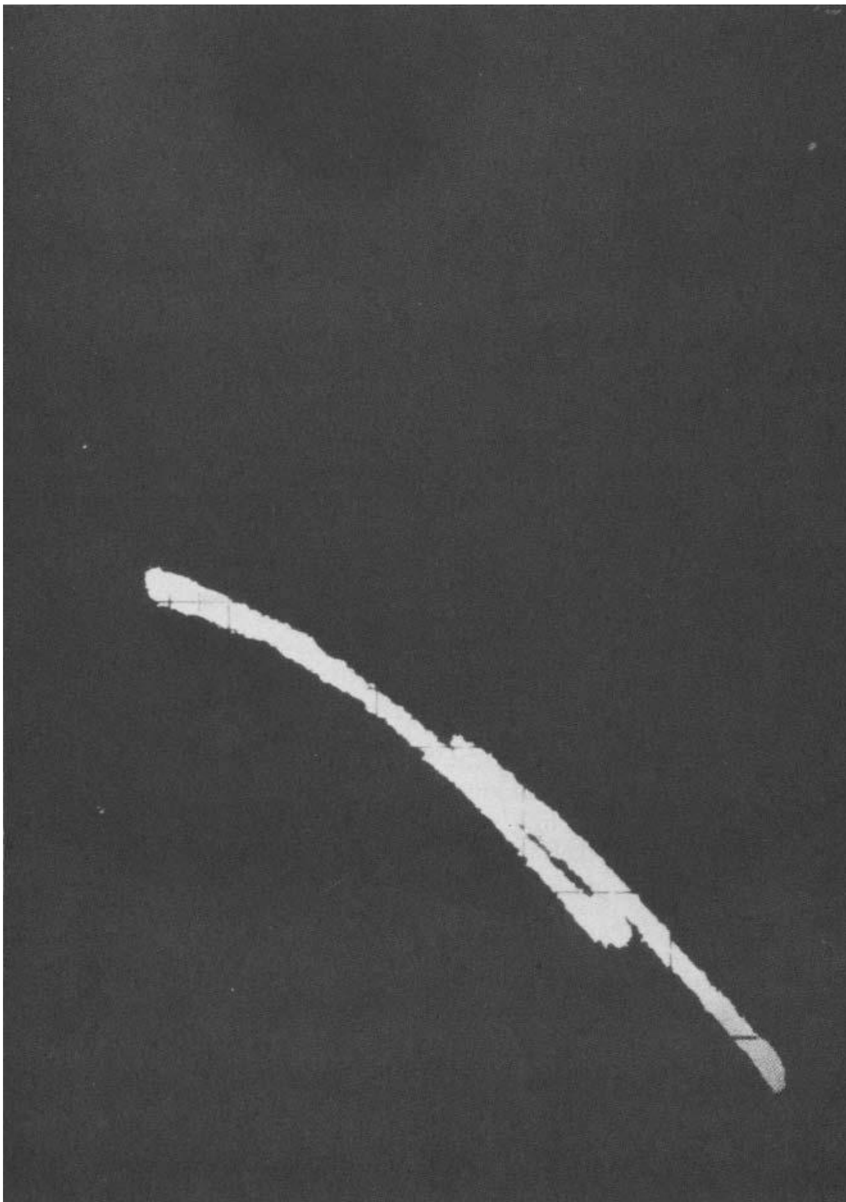

FIG. 16—*Same as Fig. 15, but at loading to 80 percent yield strength of aluminum.*

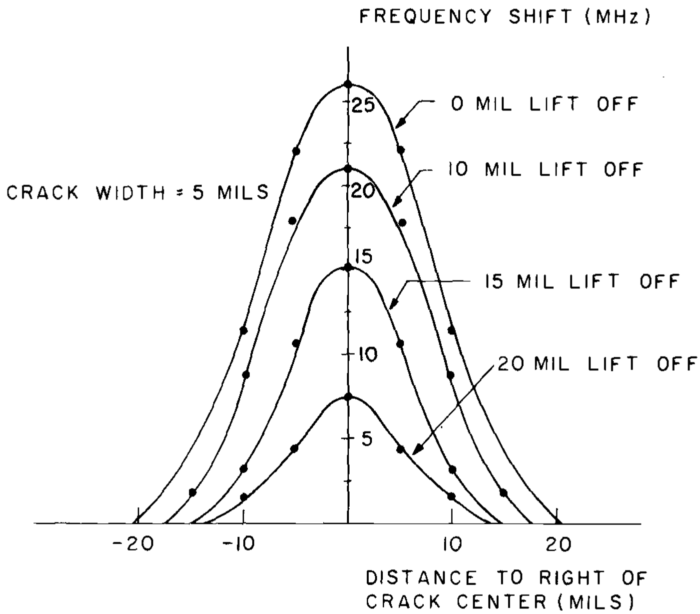

FIG. 17—*Shift of the ferromagnetic resonance frequency as a function of liftoff and lateral displacement from a machined crack or slot.*

smooth curve represents the liftoff effect taken at a point removed from both the saw cut and the edge, while the S-shaped curve represents a perpendicular scan over the saw cut and the plate edge. Scanning over an unflawed portion of the edge results in a smooth curve, clearly distinguishable from that produced by the flaw. These curves were taken with the 900- to 1000-MHz probe shown in Fig. 10, using the setup shown in the figure.

Conclusions

The feasibility of using ferromagnetic resonance probes operating in the microwave frequency range as detectors of surface-breaking flaws in metals has been demonstrated experimentally. Despite the very small skin depth at these frequencies, a variety of real and fabricated flaws have been detected with good sensitivity. These probes are capable of discriminating between liftoff or edge signals and flaw signals, and they have good spatial resolution because of their small size. In some potential applications such as thickness measurement of metal films the very small skin depth should be an advantage, permitting the measurement of thinner layers than with conventional eddy-current probes.

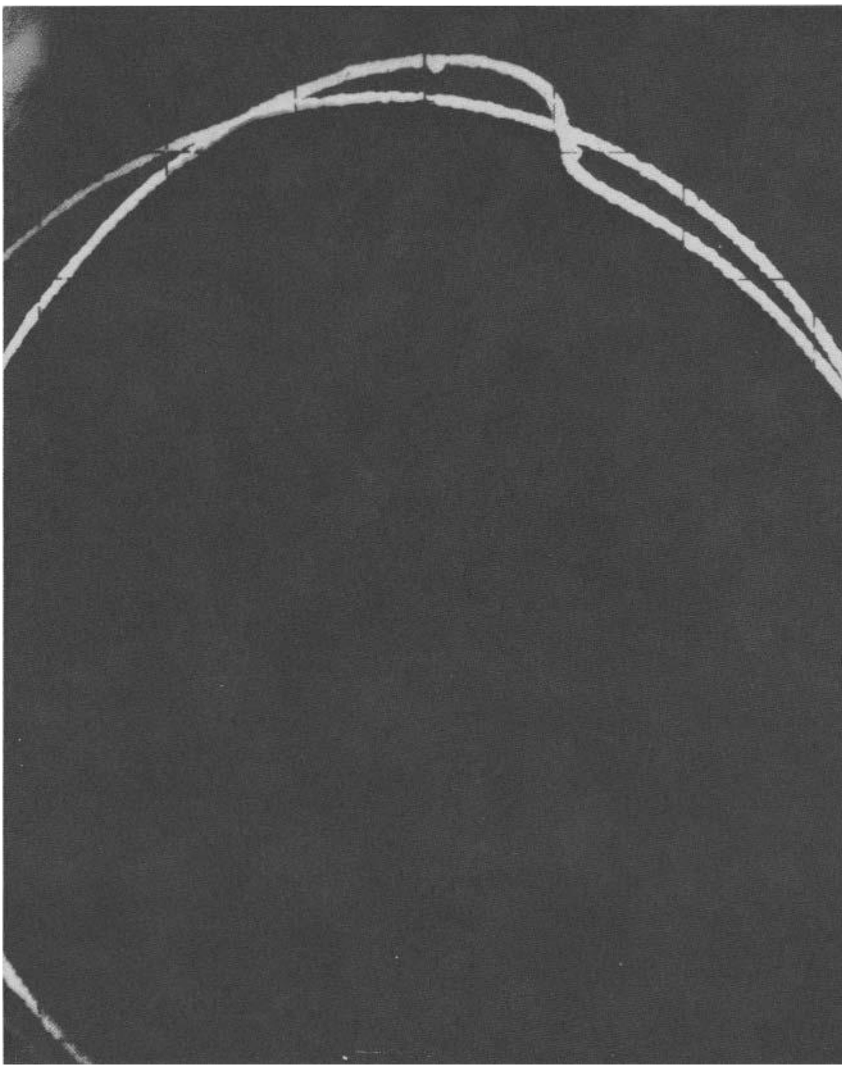

FIG. 18—*Complex impedance plot obtained by scanning normal to the edge of an aluminum plate with a saw cut (0.152 mm (0.006 in.) depth, 0.152 mm (0.006 in.) width, 6.35 mm (0.250 in.) surface length) 0.51 mm (0.020 in.) from the plate edge.*

Acknowledgments

We wish to express our appreciation to R. A. Craig and C. M. Fortunko for their advice and suggestions, to D. Walsh for probe fabrication, and to J. James, D. Pettibone, and A. Ezekiel for the electronics.

This work was sponsored by the Center for Advanced NDE, operated by Rockwell International Science Center for the Advanced Research Projects Agency and the Air Force Materials Laboratory under Contract F33615-74-C-5180.

D. L. Waidelich[1]

Pulsed Eddy-Current Testing of Steel Sheets

REFERENCE: Waidelich, D. L., **"Pulsed Eddy-Current Testing of Steel Sheets,"** *Eddy-Current Characterization of Materials and Structures, ASTM STP 722,* George Birnbaum and George Free, Eds., American Society for Testing and Materials, 1981, pp. 367-373.

ABSTRACT: This is a brief report on some early work on the testing of steel sheets using pulsed eddy currents. Penetration up to about 10 mm has been achieved and some artificial defects have been observed. Longer pulses are to be employed for deeper penetration, and more work done on the observation of defects. Some theoretical work is also reported. An indication is given of further work and the preparation of computer programs to produce a calculated output pulse where the input pulse shape is known.

KEY WORDS: nondestructive testing, steel sheets, pulsed eddy currents, analysis

Almost all of the nondestructive evaluation work done so far with pulsed eddy currents has been concerned with nonferromagnetic metals 2 mm or less in thickness.[2] Recent testing to a depth of 9 mm has been reported.[3] A recent paper gives results of work on aluminum sheets up to about 100 mm in thickness.[4] Some work on steel sheets and some analytical work concerned with the penetration of the electromagnetic waves into the metal will be reported here.

Experimental Work

The equipment employed consisted of a pulse unit driving a probe coil that transmitted the pulsed electromagnetic waves into the steel sheet. On the other side of the sheet was another probe coil that received the waves and converted them into an electric voltage observed on an oscilloscope. The

[1] Professor of Electrical Engineering, University of Missouri, Columbia, Mo. 65211.

[2] Waidelich, D. L. in *Research Techniques in Nondestructive Testing,* R. S. Sharpe, Ed., Vol. 1, Academic Press, New York, 1970, pp. 383-416.

[3] Reimann, K. J. and Sather, A., "Evaluation of a Pulsed Eddy Current System for Subsurface Flaw Detection," Report ANL/MSD-78-1, Argonne National Laboratory, December 1977.

[4] Waidelich, D. L. and Lahmeyer, C. R., "The Testing of Thick Sheets of Metal Using Pulsed Eddy Currents," *Proceedings,* Ninth World Conference on Nondestructive Testing, Melbourne, Australia, 18-23 Nov. 1979, paper 4B-3.

transmitting and receiving probe coils have been also used on the same side of the steel sheet.

The pulse unit employed a 3C45/6130 hydrogen thyratron to drive the transmitting probe coil. The grid of the thyratron in turn was driven by a driver stage using a transistor. The driver stage itself was either coupled to a multivibrator that was free-running or to an external generator. The discharge circuit supplying the transmitting probe has the probe coil, a capacitor, and the thyratron in series. The capacitor is charged slowly from a high direct-voltage source and then is discharged suddenly when the thyratron conducts. The voltage across the probe coil rises very fast, varies sinusoidally until the thyratron ceases to conduct, and finally decays exponentially towards zero. The resulting current in the probe coil produces a pulsed electromagnetic field that penetrates into the steel sheet. The transmitting probe coil consisted of a coil of about 500 turns wound on a rod of ferrite ceramic; the receiving probe coil had about 2000 turns of wire on a similar ferrite rod.

The output pulse voltage of the receiving probe coil was observed on an oscilloscope screen. A typical pulse shape is shown in Fig. 1 with the voltage as the ordinate and time, *t*, as the abscissa. Two of the important characteristics of the output pulse are the height of the peak voltage and the time delay from the beginning of the pulse to the peak of the pulse. In the case of the aluminum sheets these two quantities were measured from thicknesses of about 0.3 to about 9 cm. It was found that the peak volts varied approximately inversely as the fourth power of the thickness of the metal.[4] In a similar fashion it was found that the time delay of the output pulse peak varied approximately as the 1.6 power of the thickness of the aluminum.

Similar tests were made on steel sheets, but it was found that the pulses would only penetrate through about 1 cm of steel with sufficient strength to be above the noise level. These pulses appeared to have the same behavior for the steel sheets as for the aluminum sheets when the variation of the peak voltage and the time delay of the peak pulse voltage was observed. The range in thickness available for the steel sheets was not sufficient for good obser-

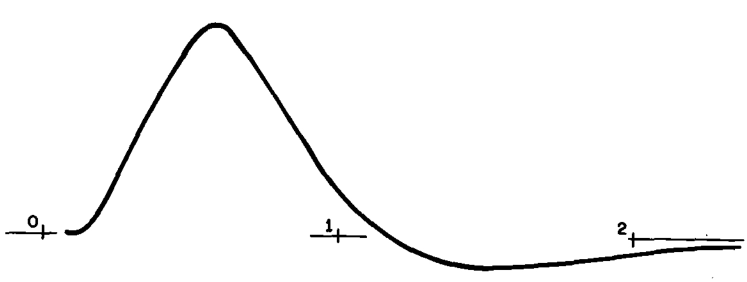

FIG. 1—*Output pulse showing the time in milliseconds.*

vation of these quantities. It is believed that a new pulse unit producing longer pulses would enable the penetration of much greater thicknesses of steel sheets and thus give results for steel sheets similar to those obtained for the aluminum sheets.[4] An idea of the difficulty of working with the steel sheets in comparison with the aluminum sheets may be gained from the fact that for a given experimental setup it was found that the peak pulse voltage for a 6-mm-thick aluminum sheet was 13 V, while for a steel sheet of the same thickness it was 20 mV, a ratio of 650.

Some tests were made to see if artificial defects could be observed using this method. Some holes were drilled in one sheet, and this sheet was sandwiched in between two other sheets without holes. By moving the probe coils over the surfaces of the sheets and observing the behavior of the tail of the output pulse, the positions of the defects could be found. Information about the depth of the defects could be also obtained from the changes in the tail of the pulse. It should be mentioned that piling one sheet on top of another does not affect the penetration or the output of the electromagnetic waves in comparison with one sheet of the same thickness as that of the pile. More work is needed in determining the position, depth, size, and type of defects from the information contained in the output pulse.

Analytical Work

An analysis of the penetration of the electromagnetic pulse into the steel sheets and of the output pulse voltage is needed to understand the experimentally obtained results. It was decided to work first in two dimensions for simplicity, but to switch to an analysis in three dimensions later. The origin and the x-y plane are taken in the surface of the metal sheet with the positive z-axis extending down into the metal. The metal is assumed to be linear again with the expectation that the nonlinearities of hysteresis may be added later. It is also assumed that there is no variation with y.

The transmitting probe coils used consisted of a solenoid wound on a ferrite core and had up to 500 turns of wire. The vertical component of the magnetic flux density, B_z, under the probe was measured in the x-direction for $z = 0$ (surface of the steel sheet). It was found that B_z varied from a maximum B_0 immediately under the probe to zero at $|x| = x_0$, reversed, and then approached zero as $|x|$ became very large. To simulate this variation and at the same time to use a moderately simple mathematical expression, it was decided to treat B_z as a product of $[1 - |x/x_0|]$ for the zero and $e^{-|x/x_0|}$, so B_z would approach zero as $|x|$ became large and the integrated flux for all of the x-range would be zero. For the time variation a step function would be simple, and by the use of a convolution integral later the response to an input pulse of any shape could be simulated as long as the system is assumed linear. Since the Laplace transform of the unit step is $(1/s)$, the transform of B_z was assumed as

$$L[B_z]_{z=0} = (B_0/s)[1 - |x/x_0|]e^{-|x/x_0|} \tag{1}$$

It is assumed that the thickness of the steel sheet is z_0 and that the receiving probe coil is placed on the surface of the sheet ($z = z_0$). The receiving probe coils were made similar to the transmitting probe coils, except that the number of turns was approximately ten times greater in number. It was also assumed that the receiving probe was directly below the transmitting probe. By use of Maxwell's equations the electric and magnetic field intensities in the steel sheet are

$$\begin{aligned} E_y &= \int_0^\infty (Ae^{-\alpha z} + Be^{\alpha z}) \sin \beta x \, d\beta \\ H_x &= \frac{1}{s\mu} \int_0^\infty \alpha(-Ae^{-\alpha z} + Be^{\alpha z}) \sin \beta x \, d\beta \\ H_z &= -\frac{1}{s\mu} \int_0^\infty \beta(Ae^{-\alpha z} + Be^{\alpha z}) \cos \beta x \, d\beta \end{aligned} \tag{2}$$

where

$\alpha^2 = \beta^2 + s\mu\sigma$,
μ = magnetic permeability of the steel,
σ = electrical conductivity of the steel,
β = integration variable with dimensions of (metres)$^{-1}$, and
A and B = constants.

By employing Eqs 1 and 2 and $B_z = \mu_0 H_z$ at $z = 0$, where μ_0 is the magnetic permeability of air,

$$A + B = -\frac{4\beta\mu B_0}{\pi\mu_0 x_0[\beta^2 + (1/x_0{}^2)]} \tag{3}$$

In a similar fashion in the air below the steel sheet

$$\begin{aligned} E_y &= \int_0^\infty Ce^{-\gamma z} \sin \beta x \, d\beta \\ H_x &= -\frac{1}{s\mu_0} \int_0^\infty C\gamma e^{-\gamma z} \sin \beta x \, d\beta \\ H_z &= -\frac{1}{s\mu_0} \int_0^\infty C\beta e^{-\gamma z} \cos \beta x \, d\beta \end{aligned} \tag{4}$$

where

$\gamma^2 = s^2\mu_0\epsilon_0 + \beta^2$,
ϵ_0 = electrical permittivity of the air, and
C = constant.

At the lower boundary ($z = z_0$) of the steel sheet, the boundary conditions on the electric and magnetic field intensities from Eqs 2, 4, and 3 give

$$C = -\frac{4\mu\beta B_0 e^{\gamma z_0}}{\pi\mu_0 x_0[\beta^2 + (1/x_0^2)][\cosh\alpha z_0 + (\mu\gamma/\mu_0\alpha)\sinh\alpha z_0]} \tag{5}$$

From Eqs 4 and 5 the Laplace transform of the time derivative of the magnetic flux density at the receiving probe is

$$L[sB_z]_{z=z_0} = \frac{4\mu B_0 z_0}{\pi\mu_0 x_0}\int_0^\infty \frac{w^2 f(p, w)dw}{[w^2 + (z_0/x_0)^2]^2} \tag{6}$$

where

$p = z_0^2 s\mu\sigma$,
$w = \beta z_0$, and

$$f(p, w) = (\cosh\sqrt{p + w^2} + R\sinh\sqrt{p + w^2})^{-1} \tag{7}$$

R is a reflection coefficient at the lower surface ($z = z_0$) of the metal sheet and

$$R = \frac{\mu\sqrt{p(s\mu_0\epsilon_0/\mu\sigma) + w^2}}{\mu_0\sqrt{p + w^2}} \tag{8}$$

The phenomenon desired is observable in the tail of the pulse, so the time t is fairly large; consequently s and p must be small, so it is assumed that $|p(s\mu_0\epsilon_0/\mu\sigma)| \ll |w^2|$ and then

$$R = \mu w/\mu_0\sqrt{p + w^2} \tag{9}$$

and

$$f(p, w) = \frac{\sqrt{p + w^2}}{\sqrt{p + w^2}\cosh\sqrt{p + w^2} + (\mu w/\mu_0)\sinh\sqrt{p + w^2}} \tag{10}$$

When $\sqrt{p + w^2} = jv$, where $j^2 = -1$, the denominator of Eq 10 becomes

$$\nu \cos \nu + (1/k) \sin \nu \tag{11}$$

where $k = (\mu_0/\mu w)$. The roots of Eq 11 may be found by putting Eq 11 equal to zero and solving $\tan \nu + k\nu = 0$ for its roots. These roots are shown in Fig. 2 as a function of k.

When the Laplace transform of Eq 6 is inverted, the result is the time rate of change of the magnetic flux density at the lower surface ($z = z_0$) of the metal sheet; this would be proportional to the voltage developed in the receiving probe coil.

The resulting computed pulse is shown in Fig. 3 as a function of the dimensionless quantity $\tau = (t/\sigma\mu z_0^2)$. A log scale was employed in plotting τ so that more features of the pulse could be shown. The pulse rises very rapidly and then decays quite slowly with a long tail. To obtain a computed pulse similar to Fig. 1 it would now be necessary to use the input driving pulse wave shape in a convolution integral along with the pulse of Fig. 3.

The aforementioned work was done to determine the steps necessary for the solution in two dimensions. It is intended now to develop the similar

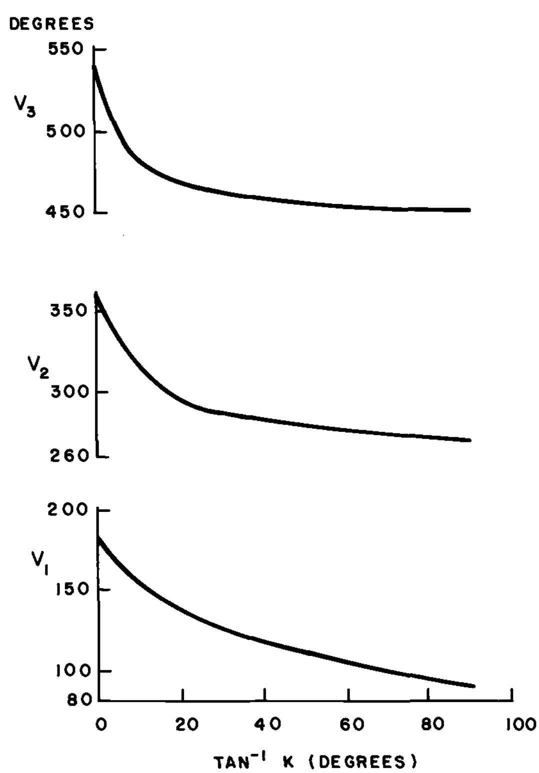

FIG. 2—*The roots,* ν_1, ν_2, *and* ν_3, *in degrees, as a function of* k.

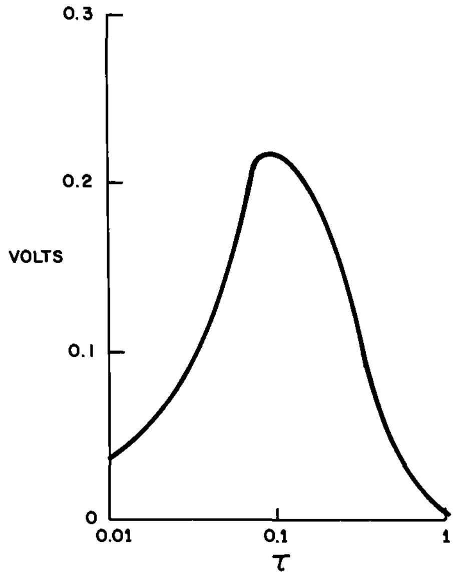

FIG. 3—*The computed output pulse voltage is shown as a function of the dimensionless quantity* $\tau = (t/\sigma\mu z_0{}^2)$.

solution in three dimensions with rotational symmetry and program the solution on a computer. This will allow a given input driving pulse wave shape to be placed in the program; the computed output pulse will then be available for comparison with the experimentally obtained output pulse. Later it is expected that the effects of magnetic hysteresis will be added to the computer program. With these computations it should be possible to obtain values of the peak pulse voltage and time delay of the peak for any thicknesses of the steel sheets. These values may be then compared to the experimentally obtained values. This type of analysis should be also adaptable for predicting other results, such as the responses of defects and the effects of lift-off.

Conclusion

This paper has presented a brief report on some of the experimental and theoretical work that has been lately done on the testing of steel sheets. On the experimental side, longer pulses should be used for deeper penetration and the observation of defects studied in more detail. On the theoretical side, an analysis in three dimensions and the accompanying computer program should be developed along with extensions of the analysis to predict results such as the response of defects and the effects of lift-off.

Allen Sather[1]

Investigation into the Depth of Pulsed Eddy-Current Penetration

REFERENCE: Sather, Allen, "**Investigation into the Depth of Pulsed Eddy-Current Penetration,**" *Eddy-Current Characterization of Materials and Structures, ASTM STP 722,* George Birnbaum and George Free, Eds., American Society for Testing and Materials, 1981, pp. 374-386.

ABSTRACT: Pulsed eddy-currents have been used successfully for a number of years to measure the wall thickness of thin-wall tubing. In studies of 88.9-mm (3.50-in.)-diameter stainless-steel tubing, wall thicknesses in the 0.254 to 0.762 mm (0.010 to 0.030 in.) range have been measured with an accuracy of ±10%. This paper describes an investigation of the relationship between the pulse length and depth of electromagnetic plane-wave penetration. Long pulses contain lower-frequency components than pulses of shorter duration. Therefore, longer pulses will penetrate much more deeply into a conductive material, assuring a 90 percent confidence level in the measurement of thicker materials. The pulsed eddy-current equipment used at Argonne National Laboratory (ANL) employs sampling of the detector waveform at discrete time intervals. Optimization of field-coil design for larger thicknesses of conductive material necessitates an increase in the pulse length. With a preliminary coil design, a penetration of 9 mm into stainless steel was achieved.

KEY WORDS: pulsed eddy current, electromagnetic plane wave, electromagnetic penetration, field coil, pickup coil

The eddy-current method is commonly used for volumetric examination of metallic components. The need to monitor an increasing number of parameters such as defect size, location, and probe liftoff during inspection has resulted in the introduction of the multifrequency or pulsed eddy-current (PEC) system. The theory of such systems is well documented in the literature.[2,3,4] A prototype PEC system was developed at Argonne National Laboratory (ANL) for the examination of stainless-steel breeder-reactor fuel cladding; at present, PEC systems are not commercially available. The system is modular in construction (Fig. 1) and contains two current-pulse generators and eight adjustable sampling units for data retrieval or parameter sepa-

[1]Engineering assistant, Argonne National Laboratory, Argonne, Ill. 60439.
[2]Libby, H. L. in *Research Techniques in Nondestructive Testing*, R. S. Sharpe, Ed., Academic Press, London, 1970, Chapter 11.
[3]Waidelich, D. L. in *Research Techniques in Nondestructive Testing,* R. S. Sharpe, Ed., Academic Press, London, 1970, Chapter 12.
[4]Cox, C. W. in *Research Technique in Nondestructive Testing*, R. S. Sharpe, Ed., Academic Press, London, 1970, Chapter 7.

ration. In general, two-point probes of different construction are used, one for wall-thickness measurements and the other for defect detection. These point probes can be interchanged with circumferential probes, if desired.

The PEC system was chosen because of some unique advantages over conventional equipment. Commercial systems apply continuous sine waves to a driver coil. The number of separate parameters that can be detected in a multifrequency eddy-current test is twice the number of test frequencies used, assuming small signals and linear approximation. Thus, a system with three discrete frequencies can yield information on six parameters. On the other hand, a pulsed system contains all frequencies within a reasonably broad band, which permits the determination of a large number of parameters. The signal in the receiving coil is sampled at adjustable delay times to obtain the desired information. Various frequency components will affect different portions of the received waveform. A sampling point at a particular time is therefore comparable to one frequency in the multifrequency system, and two parameters can be resolved.

From these considerations, the following unique advantages of the ANL PEC system become apparent:

(*a*) The system, with eight available sampling points, is comparable to an eight-frequency system with respect to parameter determination.

(*b*) The electronics are much simpler, that is, crystal-controlled oscillators and accurate frequency discriminators are not needed.

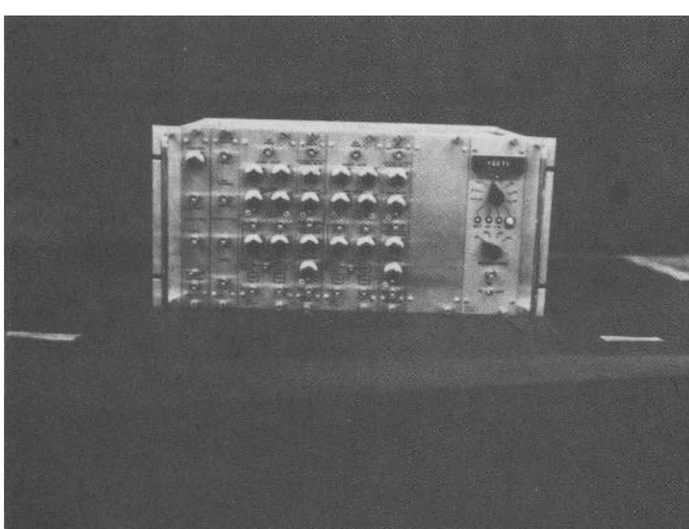

FIG. 1—*ANL pulsed eddy-current equipment.*

(c) Selection of sampling times makes the instrument versatile and easily adaptable to particular problems.

The advantages of the PEC system suggest a much wider area of application than is being realized at present. The system could be used, for example, to test for subsurface voids in stainless-steel components. The objective of the present investigation was to evaluate the penetration depth of PEC systems as a function of driving-pulse duration.

Laboratory Evaluation

ANL PEC equipment was evaluated, with modification of the probes only, in order to determine its penetration capabilities. All probes had the same configuration, with the energized (driver coil) perpendicular to the sample surface. A single pickup coil was zero-balanced at the electromagnetic center of the driver coil, at 90 deg to the driver-coil axis.

A stainless-steel test block with side-drilled 3-mm (0.125-in.)-diameter holes at various distances from the upper and lower surfaces (Fig. 2) was supplied by KWU (Kraftwork Union, West Germany) for use in evaluating the detection capability of the PEC system. In the first test, the block was hand-scanned with a standard driver coil of the type used for nuclear applications, mounted in a square trifluoroethylene resin block. The standard coil has a 1.6-mm (0.063-in.)-diameter ferrite core wrapped with ~200 turns of No. 38 wire, for a total coil length of 3 mm (0.125 in.). The output of the PEC instrument (~ 1-μs pulses, yielding a minimum frequency of ~ 150 kHz) was recorded on a strip chart. As shown in Fig. 3, holes 1 to 3 mm (0.04 to 0.125 in.) below the surface were detected with this coil. No indications, however, were obtained from holes more than 3 mm below the surface. This was anticipated, since the standard coil was designed for thin-walled tubing. A rough calculation of the penetration depth for a $\geq$ 150-kHz signal in material with conductivity = 1.4×10^6 S/m and permeability = $4\pi \times 10^{-7}$

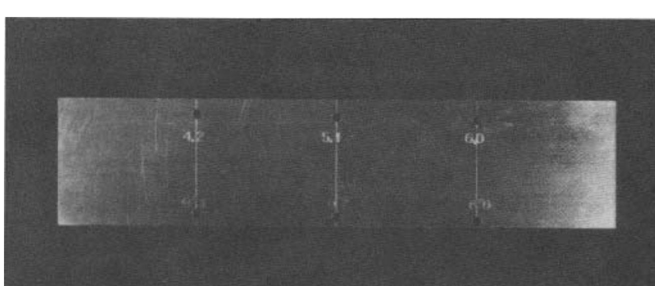

FIG. 2—*Side view of Type 304 stainless steel test block showing 3-mm-outside diameter side-drilled holes at various distances from upper and lower surfaces.*

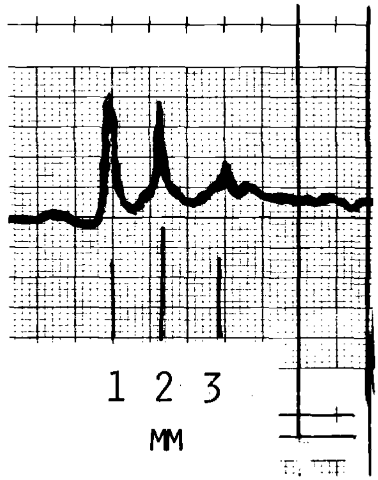

FIG. 3—*Strip-chart recording of scan over side-drilled holes 1 to 3 mm (0.004 to 0.125 in.) below surface of stainless-steel test block, using standard driver coil with ~ 1-μs pulses.*

A/m, yields a value of $\delta = 1$ mm, assuming that the lowest-frequency component of the pulse provides the deepest penetration. At a depth of 3 mm (0.125 in.) in our specimen, the intensity of the signal used is $e^{-3} \simeq 0.05$, which is the limit of detectability for the instrument.

An increase in penetration depth can be, theoretically, achieved by lengthening the pulse duration, which decreases the lowest-frequency components present in the pulse. Since the driving pulse in the instrument is generated by discharging a capacitor through the driver coil, the discharge time will be determined by the impedance of the coil. It was therefore necessary to construct a new probe to achieve the desired pulse length.

A driver coil was fabricated with the same size ferrite core as the standard 200-turn coil, but with 600 turns of wire and a total coil length of 6 mm (0.25 in.). The current (bottom curve) was approximately the same as for the standard coil, and both coils had a peak pulse power of 2500 W when energized by ANL's equipment (see Fig. 4). However, increasing the number of turns to 600 increased the pulse length (Fig. 5) and slightly lowered the frequency spectrum (Fig. 6).

The ability of the longer pulse to penetrate more deeply into the stainless-steel test block is demonstrated in Fig. 7. Sampling time was initially set at 6 μs and adjusted for linear response. With a sampling time of 8 μs, and without any increase in power output, we were able to detect a side-drilled hole 5 mm (0.200 in.) below the surface.

The results indicate that an increase in the pulse duration (by increasing coil windings and length), without a change in the ferrite core diameter or peak pulse power, yields the following:

(*a*) Lower-frequency components.
(*b*) Deeper penetration into the material.
(*c*) More driver-coil heat dissipation.

To obtain an even deeper penetration capability, a larger-diameter driver coil was fabricated. Standard pickup coils were balanced on driver coils with

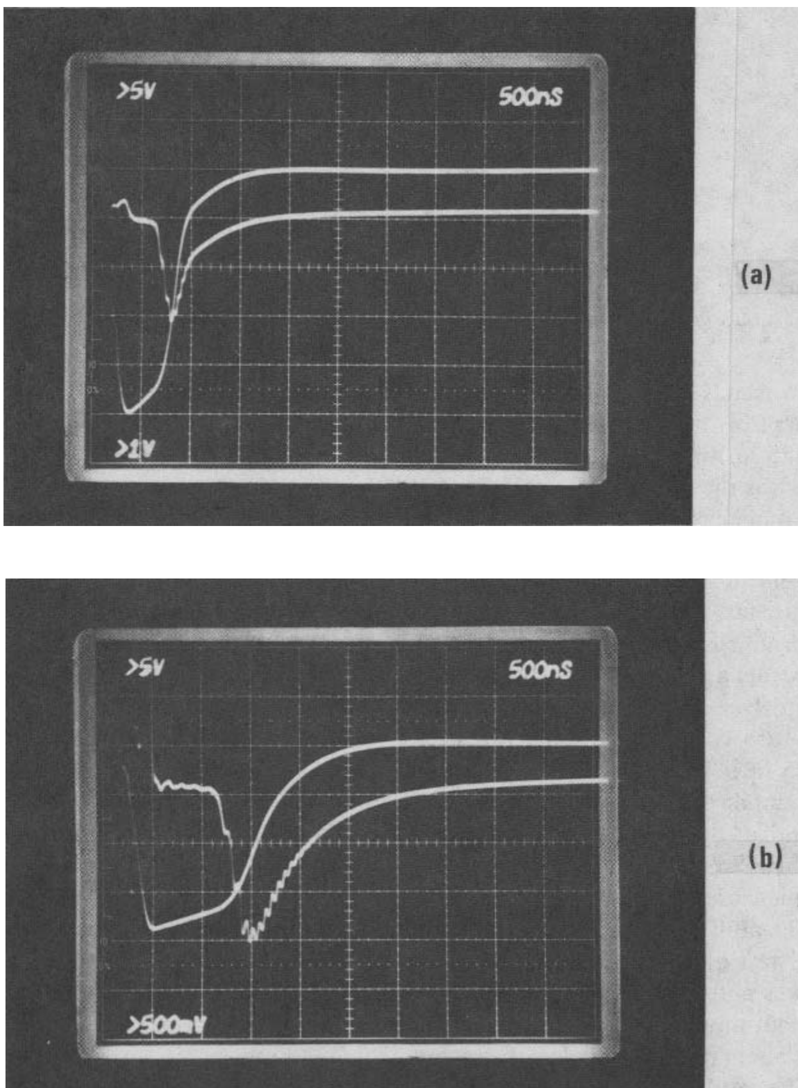

FIG. 4—*Current and voltage pulses of* (a) *standard (200-turn) driver coil; and* (b) *600-turn driver coil at 2500 peak watts.*

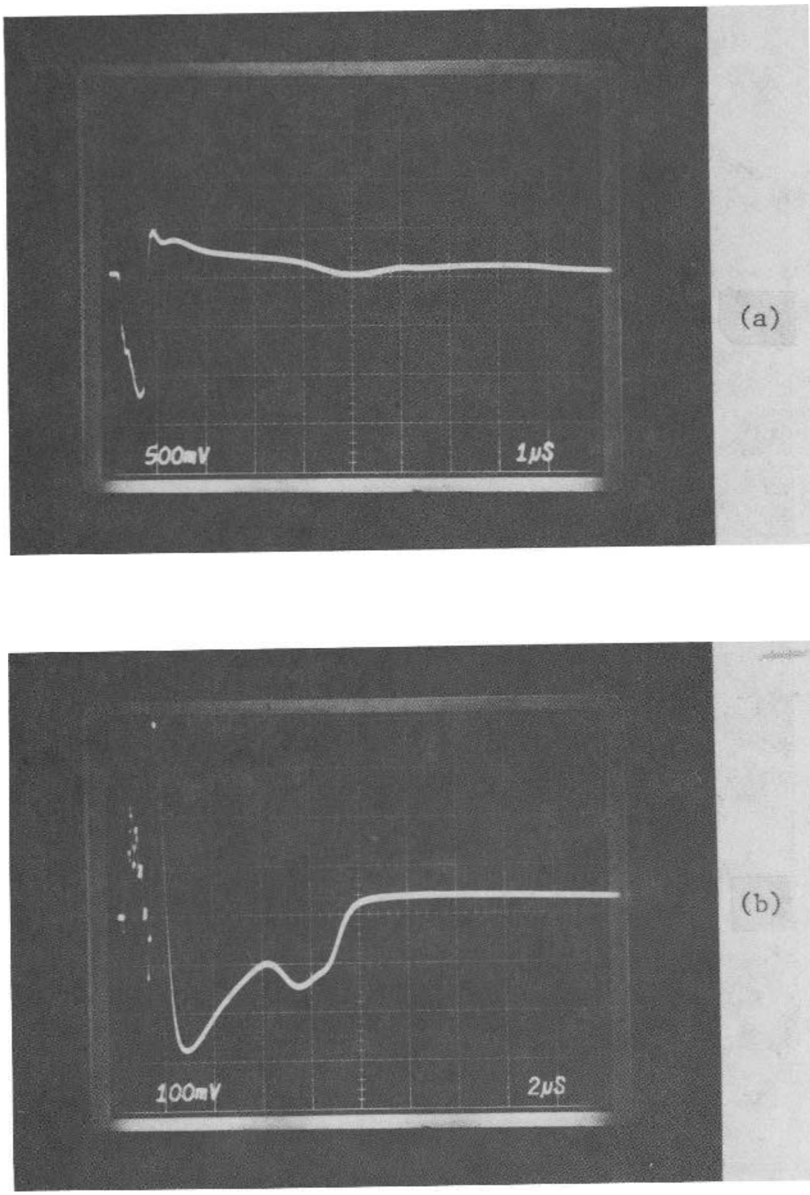

FIG. 5—*Pickup coil pulse with* (a) *200-turn driver coil and* (b) *600-turn driver coil.*

500 turns of No. 38 copper wire, wound on 4-mm (0.187-in.)-diameter ferrite cores. The peak pulse power developed in the new coil with ANL PEC equipment was very close to 2500 W. A peak of 0.6 A (top curve) was measured at 400 V (Fig. 8). The frequency spectrum (Fig. 9) shows an increase

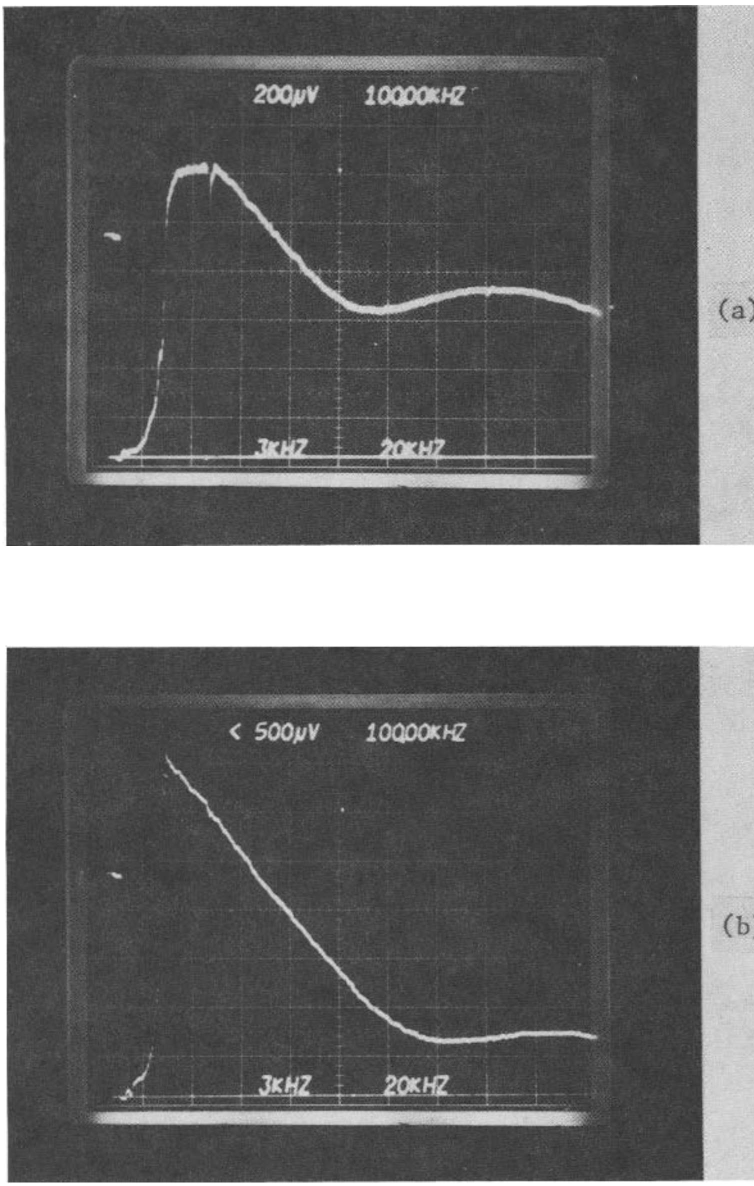

FIG. 6—*Frequency spectra of pickup coil pulses shown in* (a) *Fig. 5a and* (b) *Fig. 5b.*

in low-frequency components with a peak very close to the 20-kHz point. Pulse lengths of 25 μs were obtained (Fig. 10). An increase in the core diameter helps to dissipate heat, but increases the effective field area coverage and decreases selectivity. Two sets of test blocks were procured; one of

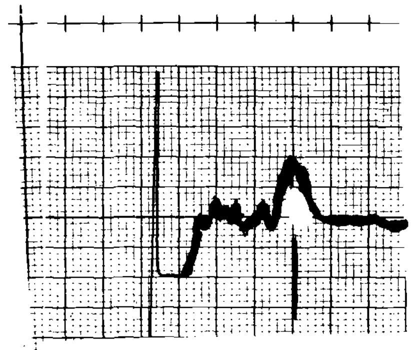

FIG. 7—*Strip-chart recording of scan over side-drilled hole 5 mm (0.200 in.) below surface, using 600-turn driver coil with 8-μs pulse.*

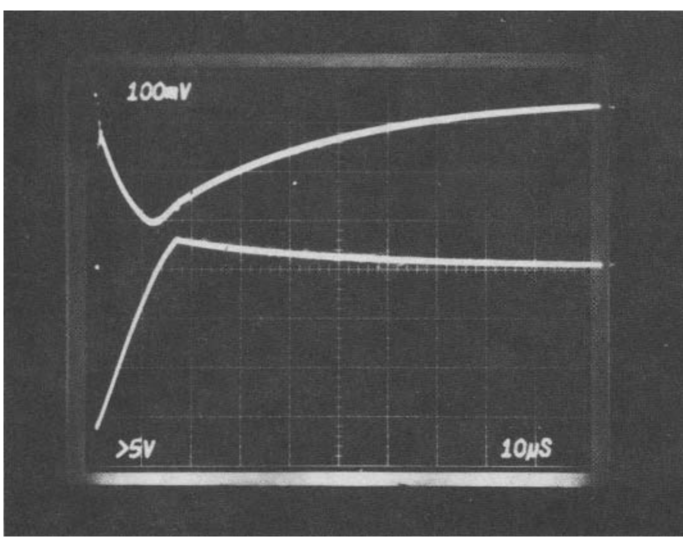

FIG. 8—*Current and voltage pulses of larger-diameter driver coil at 2500 peak watts.*

6061-aluminum and one of Type 304 stainless steel. Each set consisted of sixteen 76 by 76-mm (3 by 3-in.) blocks ranging in thickness from 1.6 to 25.4 mm ($^1/_{16}$ to 1 in.), increasing in steps of 1.6 mm ($^1/_{16}$ in.).

The larger-diameter driver coil was tested on the two sets of blocks to determine penetration depth. Output signals were obtained for all the blocks in both sets. The measurements on the stainless steel blocks showed a non-linear increase in the output voltage with increasing thickness (Fig. 11).

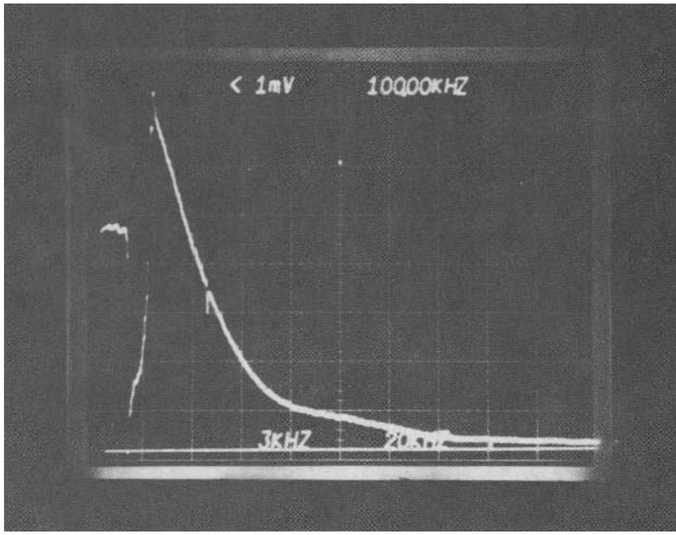

FIG. 9—*Frequency spectrum of pickup-coil pulse shown in Fig. 10.*

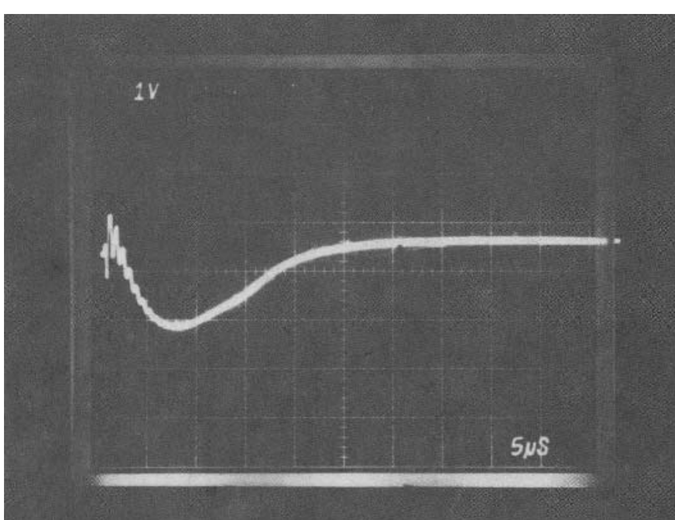

FIG. 10—*Pickup-coil pulse with larger-diameter driver coil.*

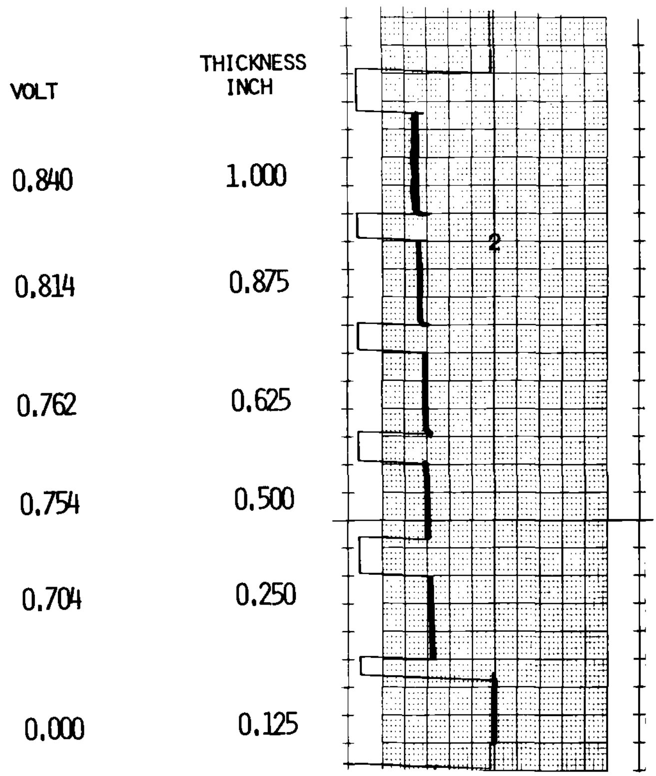

FIG. 11—*Strip-chart recording for PEC scan of Type 304 stainless steel test blocks using larger-diameter driver coil.*

Results obtained with the aluminum blocks showed a different trend (Fig. 12): The output voltage did not increase with increasing thickness, but oscillated around a mean value. The PEC output voltages obtained from the stainless-steel and aluminum blocks are plotted in Fig. 13. This difference in the behavior of stainless steel and aluminum with regard to PEC thickness measurements is probably due to the difference in the conductivity between aluminum and stainless steel.

Conclusions

The present evaluation of the ANL PEC system indicates a wider range of possible applications than previously considered, such as measurements of thick specimens. Optimizing probe design to fit a specific test should give better linearity in results. The results of thickness measurements on stainless

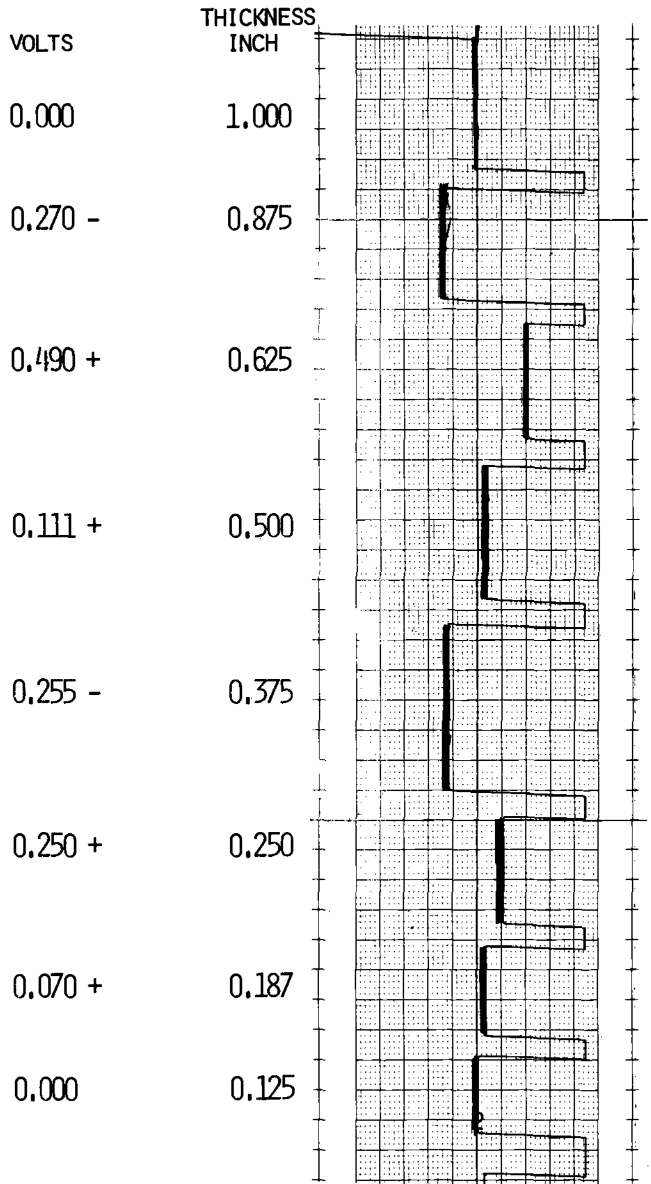

FIG. 12—*Strip-chart recording for PEC scan of aluminum test blocks using larger-diameter driver coil.*

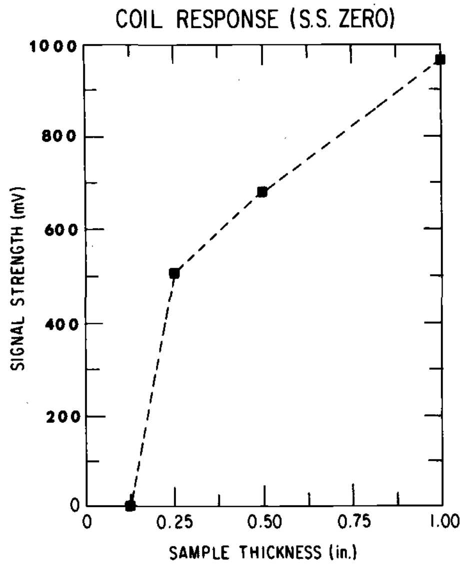

(a)

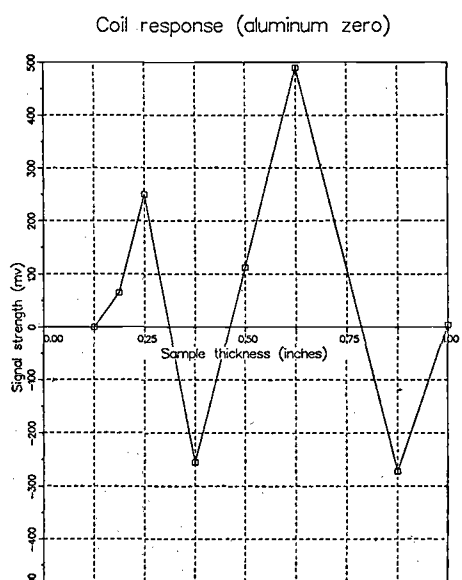

(b)

FIG. 13—*Computer plots of PEC output voltages obtained with* (a) *Type 304 stainless steel and* (b) *aluminum test blocks as a function of thickness.*

steel and aluminum show that each material and thickness range has to be appraised on an individual basis.

The amount of peak pulse power one is able to generate and use is an important factor. The equipment used in these experiments was not designed to deliver a lot of power; to achieve even deeper penetration, it will require further modification.

Acknowledgments

The author is thankful for the support of the U.S. Department of Energy.

G. Wittig[1] *and H.-M. Thomas*[1]

Design of a Pulsed Eddy-Current Test Equipment with Digital Signal Analysis

REFERENCE: Wittig, G. and Thomas, H.-M., "**Design of a Pulsed Eddy-Current Test Equipment with Digital Signal Analysis,**" *Eddy-Current Characterization of Materials and Structures, ASTM STP 722,* George Birnbaum and George Free, Eds., American Society for Testing and Materials, 1981, pp. 387-397.

ABSTRACT: Test equipment was designed for investigations on the application of the pulsed eddy-current method on the detection of subsurface defects in thicker components or layers. The evaluation of the signals delivered by the coil system is performed in four single channels with different sampling delays or by plotting the signal time shape. The measured values are digitized and stored within the memory of a minicomputer for data processing. The coil systems are dimensioned in such a manner that the desired sensitivity was obtained for a defect depth range of about 10 mm in austenitic materials. The determination of the time of the signal zero crossing gives information concerning the defect distance from the surface.

KEY WORDS: pulsed eddy current method, time sampling, coil systems, test blocks, artificial defects, defect depth, data acquisition and processing, austenitic components, welded claddings

The main work on the development of a pulsed eddy-current method for application in nondestructive testing has been carried out in the United States of America. There has been, to mention a few, the theoretical and experimental investigations by Waidelich, Renken, Cox, and their collaborators [*1-6*].[2] The design of test equipment, however, was mainly restricted to the examination of thin-walled tubes of materials that are usually used in nuclear plants. Applications of the method were performed on irradiated fuel rods and cladding tubes with 0.38 and 0.6-mm wall thickness [*7,8*].

The results of these investigations and applications have served as a foundation for expansion of the field of application. The use of the method on thick-walled components or thicker layers of materials with low electrical conductivity to detect subsurface defects is the objective of this work. Preliminary investigations made by means of simple laboratory apparatus

[1]Bundesanstalt für Materialprüfung, Berlin, Germany.
[2]The italic numbers in brackets refer to the list of references appended to this paper.

confirmed, that there were no fundamental difficulties in realizing this objective [9]. Extensive design, development, and investigations were started. This report attempts to give a preliminary account of this work, which is still in progress. The design and use of the equipment is described, and questions related to possible applications are discussed.

Pulsed Eddy-Current Test Equipment

The requirements for the examination of components with thicknesses up to 10 mm and more, the results of the preliminary investigations, and the inspection system described in Ref *6* were used as foundations for a design concept of pulsed eddy-current test equipment. As a guideline in developing the system, a wide range of applications should be provided.

The structure of the built-up system is shown in the block diagram of Fig. 1. Within the control unit (CU), from a stable oscillator frequency of 1 MHz, all the signals are generated that are needed for the control of the time sequence. This rigid coupling avoids the disadvantages which may arise in

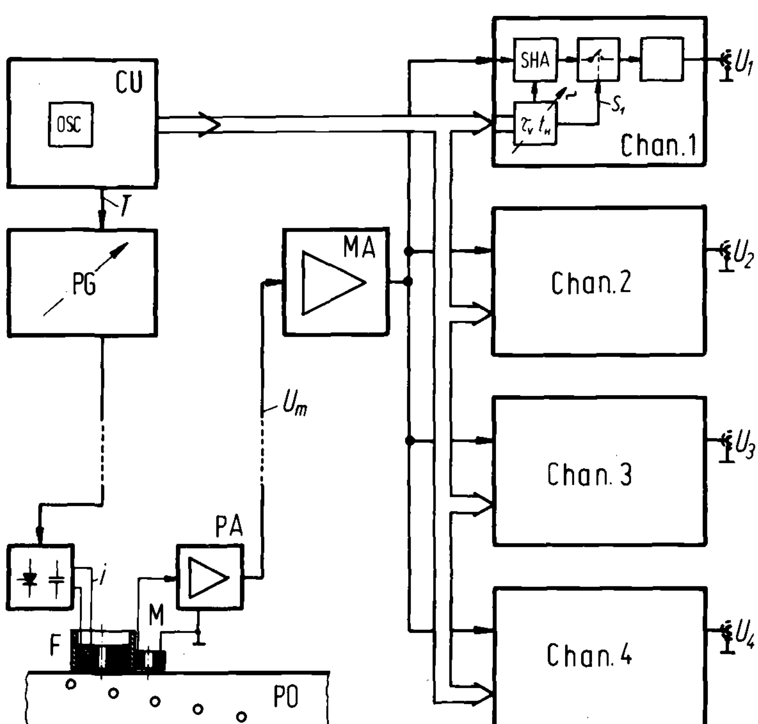

FIG. 1—*Block diagram of pulsed eddy-current test equipment.*

freely oscillating circuits as the result of drift phenomena. The clock or pulse frequency is 1 kHz.

The field coil F and a capacitor form a resonant circuit for the generating of the pulse current i. By means of a thyristor circuit, pulses with the shape of a sinusoidal half-wave with the clock frequency of 1 kHz are supplied. The required electronic components are housed in a small box, which is fixed directly beside the field coil. The supply voltages and the control signals are fed by means of cables from the pulse generator PG in the apparatus. The pulse current flows within the short wires of the resonant circuit. A maximal amplitude of 10 A may be set. The pulse duration is determined by the values of the inductance of the field coil and the capacity. The range of variation is between about 5 to 75 μs. This variation provides the flexibility for dealing with special test problems.

The measuring coil system, M, delivers a signal voltage to the low noise preamplifier, PA, which is also connected to the coil by short wires. A cable leads to the main amplifier, MA, in the apparatus. The overall gain may be chosen in stages between 10 and 60 dB. The circuits are resistant to overload. Signals that are going partially into the overload state may thus be evaluated after recovery without any restriction.

The evaluation of the signals is carried out by measuring the amplitudes in fixed moments. This means the information is extracted by a sampling technique. The signal of the main amplifier is fed to a sample-and-hold circuit. After an adjustable delay time, τ_v, the status is changed from sample to hold. During the hold time, t_H, the signal amplitude, U_m, present at the time τ_v is stored. A low pass filter is used for smoothing. A voltage proportional to the signal amplitude at τ_v is available as an output.

The delay time, τ_v, is digital adjustable in 1 μs-stages up to 200 μs. The clock frequency of 1 MHz supplies the needed reference signal. This frequency also controls the hold time t_H. The block diagram shows that this part of the instrument consists of four identical sections. There are four analog outputs $U_1 \ldots U_4$ concerned with four independent delay times $\tau_1 \ldots \tau_4$.

The timing diagram (Fig. 2) shows the most important control and signal voltages. T is the amplitude of internal 1 kHz clock frequency, i is the pulse current in the field coil, and U_m is the measuring signal. Signals S_1 and S_3, with delay times τ_1 and τ_3, respectively, and the hold time t_H of the sample-and-hold circuits are indicated. The output signals of the channels 1 and 3 are proportional to the amplitudes at τ_1 and τ_3.

During the scanning of a specimen, the output voltages of the four channels are simultaneously recorded. Since the visual observation of the traces permits only a coarse survey of the defects present, the evaluation of the signals should be accomplished by means of a data processing system. The extraction of the extensive information content for classifying and description of defects is only done in this way.

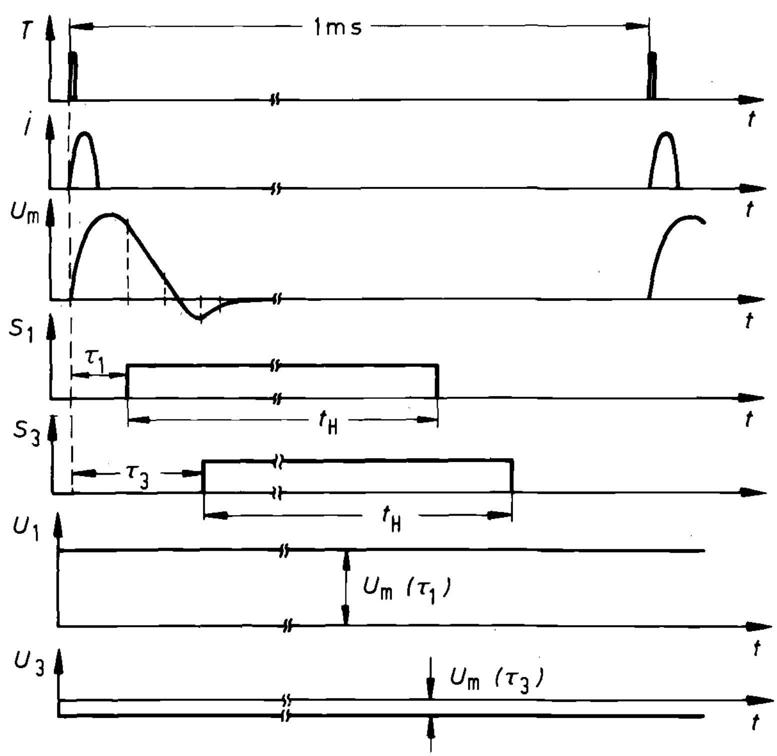

FIG. 2—*Time diagram of pulsed eddy-current test equipment.*

The block diagram (Fig. 3) shows the connection of the test equipment with a minicomputer system. The four analog outputs or the output of the sample-and-hold circuit are joined with a multiplexer. The signals are digitized by a 12-bit analog-to-digital converter. The data word is stored in the core memory of the computer by using the universal interface.

There are two methods applied for the acquisition of data. The first provides a quasi-simultaneous collection of the four data words from the channels concerned with the different delay times. That means that between two current pulses, which arise in intervals of 1 ms, the four analog signals are digitized and stored in the memory. This process is controlled by software and the scanning unit. This procedure permits a scan velocity up to 100 mm/s with a local resolution of 0.1 mm/pulse.

The second data acquisition method is used for the registration of the complete measured pulse shape or a part of it. In this case the signal of the first channel is sampled in intervals of 1 μs. Only one data word is stored from each pulse. The control is performed by software and hardware. A low scan velocity of 1 mm/s is therefore allowed.

Design of Coil Systems

The efficiency of an eddy-current test equipment strongly depends on the properties of the coil system. For the present test problems the coil arrangement should be designed in such a manner that the required information concerning a specimen is transmitted to the electronic circuits as optimally as possible. Contrary requirements are frequently encountered; for example, a high depth of penetration of the magnetic fields demands a large-area coil whereas a high resolution is achieved with a small coil. Between these two opposing conditions a compromise has to be chosen.

A schematic sketch (Fig. 4) illustrates the design of the coil systems used for several applications; the dimensions are entered into the short table. The aperture ring was not used with systems 1, 3, and 5. In these cases the winding forms slide down within the shield. The measuring coils in differential connection are situated beside the field generating system. The axes are parallel. As a result of preliminary investigations it was discovered that this type of coil system has advantages in defect sensitivity in comparison with other arrangements.

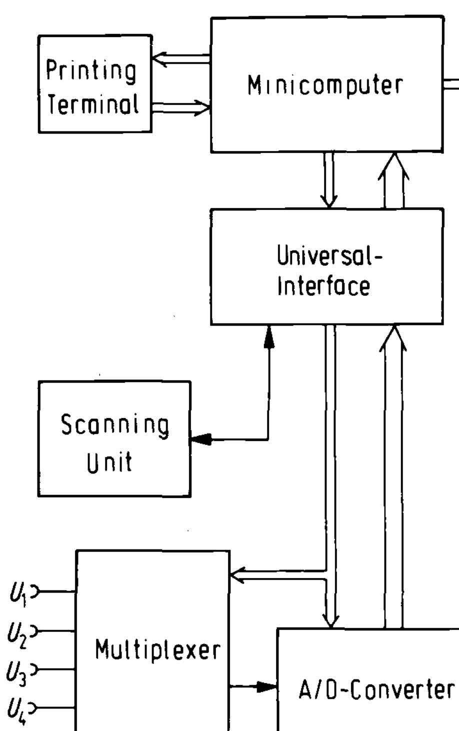

FIG. 3—*Block diagram of data acquisition and processing.*

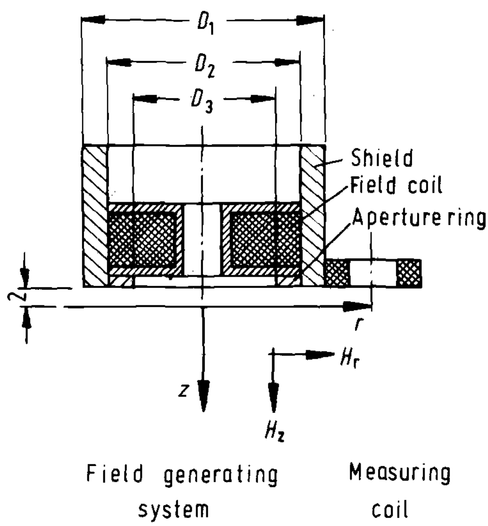

No	D_1 mm	D_2 mm	D_3 mm
1	25	20	—
2	25	20	15
3	20	15	—
4	20	15	11,25
5	15	10	—

FIG. 4—*Coil systems.*

The efficiency of the coil systems are investigated by measurement of the magnetic field distribution of the generating system and by measurement on test blocks with artificial defects.

An example shall demonstrate the procedure. Figure 5 shows the measured normal component, H_z, of the field strength dependent on the distance to the base line of the system. The amplitudes of the pulse currents are chosen for equal numbers of ampere turns. The current in system No. 5 produced the maximum thermal loading. A further attempt was performed on an austenitic test block with side-drilled holes of 3 mm diameter at various distances from the surfaces. By scanning this specimen, the signals of the several field coil systems (all with identical measuring coils) were recorded. The evaluation of the maximum amplitudes yields a defect depth of $h = 7$ mm at a signal-to-noise ratio of 20:1 for the coil system No. 5, which is the smallest one. This point is marked by a circle in Fig. 5. The signal-to-noise ratio of 20:1 is required for further data processing. That means that the defect depth of 7 mm is the application limit of the coil system No. 5 related to holes with 3 mm diameter.

By determining the field distribution and making measurements on the test specimen, information was obtained that was applied to the design of the coil systems.

Another aspect concerning the characteristics of the coil systems is the influence of lift-off. Measurements are made by scanning the test specimen with lift-off spacing between 1 = 0.1 and 1.0 mm. The amplitudes of the defect signals are reduced by about 4 dB in this range, but the shapes of the signals remained the same. The zero-crossing points were time-invariant within a small region of measuring uncertainty. This behavior was independent of the size of the coil system (Fig. 6). The time, t_n, of the zero-crossing point, measured from the start of the generating pulse, is plotted as a function of the defect depth range from 1.0 to 8.9 mm. Only a constant displacement of about 2 μs is seen between the two systems.

Examples of Data Acquisition and Processing

The acquisition of data during the scan of a test specimen has been explained in the description of the eddy-current test equipment. In the simplest case the stored measured values are put into a plotter for evaluation. The visual observation of the plotted shape of the four channels yields only a qualitative assessment. This may serve, for example, to give some information regarding the influence of noise sources. Also an optimization of the setting of the sampling points for further evaluation may be done by means of this plotting.

As an example, the results of a measurement on an original welded cladding of a pressure vessel are shown in Fig. 7. In this cladding are side-drilled

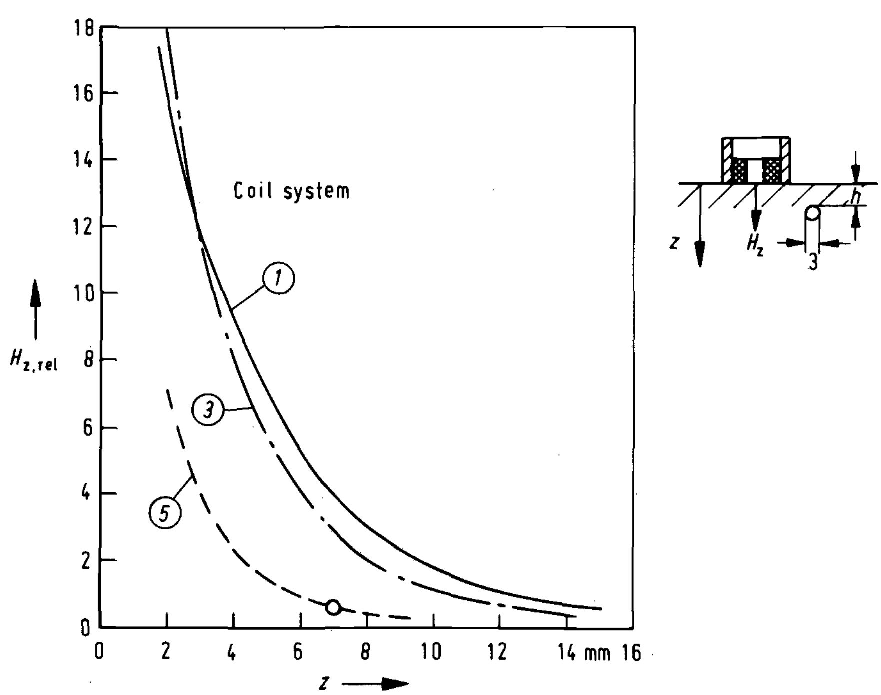

FIG. 5—*Magnetic field strength of coil systems.*

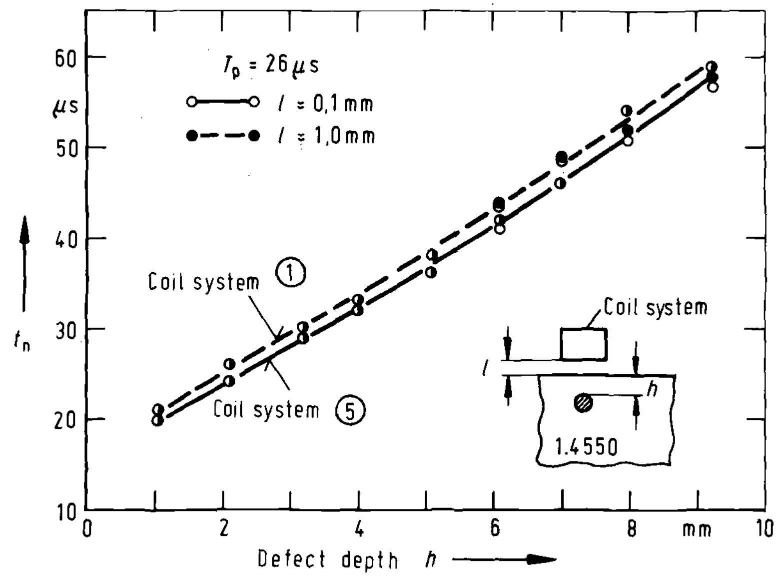

FIG. 6—*Influence of coil system lift-off; zero-crossing time,* t_n, *versus defect depth.*

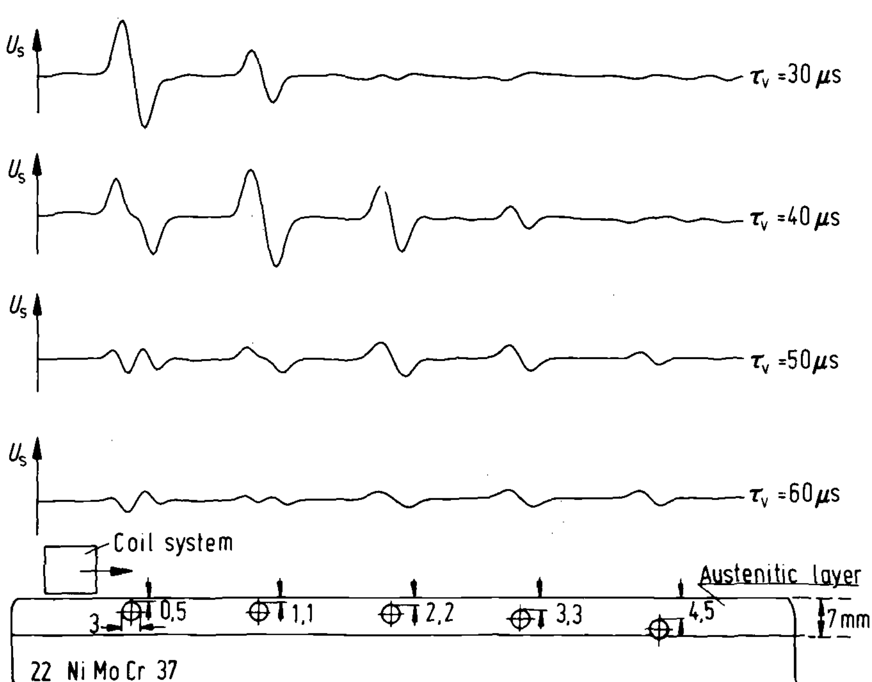

FIG. 7—*Scan of an austenitic welded cladding.*

holes with 3 mm diameter as artificial defects. The pulse length was $T_p = 26\ \mu s$. Since the movement of the coil system took place in the direction of the welding line, noise voltages were small. These are present mainly at delay times below 30 μs.

When the test objects are scanned, a high occurrence of data is noted if the measuring points are picked each 0.1 mm. A distance of 100 mm requires about 4 k-words in the core memory. Therefore it is advantageous to suppress such data that contain no information. For this purpose a program was developed that eliminates measured values with zero amplitude and with small amplitude variations compared with the adjacent measuring point. This is done between two clock pulses. The requirement for core memory capacity is reduced in this manner.

The objective of a digital signal evaluation is to deliver statements for classifying or describing the defects present. As a great deal of information is necessary to discover the appropriate correlations, it is necessary that within the signals the needed information is included.

An example may serve to illustrate the mentioned dependence of the time of the zero-crossing point of the signal upon the distance of the defect from the surface [*10*]. This value is evidently influenced in a slight manner by noise parameters. The scan of a test block (Fig. 8) shows that the zero-crossing point of the 7-mm-deep defect is situated in the vicinity of about 50 μs. The recording of the time shapes during the approach of the coil system to this defect allows a more accurate statement (Fig. 9). Signal amplitudes are plotted as a function of the sampling delay. The distance of the main axis of the coil system to the defect coordinate is a parameter. The measure of the zero-crossing and the defect depth is determined by software from the stored values.

During the approach of the zero-crossing point to its minimum value, a characteristic shape is noted, which allows the discrimination against noise signals.

Conclusions

Other authors have already pointed up the advantages of the pulsed eddy-current method for tube testing. The results of this investigation show that there are possibilities for applications of this method on thicker layers or components. Materials with low electrical conductivity should preferably be used.

When compared to the continuous-frequency eddy-current method applied to austenitic steel test blocks [*11*], it seems that the penetration depth of the pulsed fields leads to an increased sensitivity for the detection of deeper defects. Investigations will be performed, in the frame of a common program of several institutions, to compare single-frequency, multifrequency, and pulsed eddy-current methods.

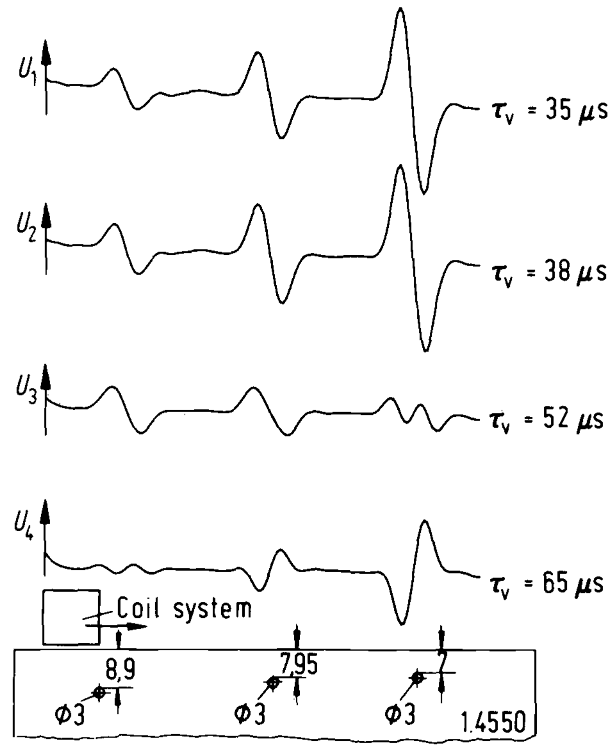

FIG. 8—*Scan of an austenitic test block.*

Further work on pulsed eddy currents will be devoted to different applications and to the extension of signal processing procedures. Here pattern recognition methods will need to be considered.

Acknowledgments

The authors wish to thank D. Maser and W. Grigulewitsch for their contributions in detailed development of the test equipment and in carrying out the measurements. This research was sponsored by the German Minister of Research and Technology under Project No. RS 299.

References

[1] Waidelich, D. L. in *Research Techniques in Nondestructive Testing*, R. S. Sharpe, Ed., Academic Press, London and New York, 1970, Chapter 12, pp. 383–416.

[2] Chan, S. B. and Waidelich, D. L. in *12e Colloque de Metallurgie Juin 1968*, Nondestructive Testing and Control in the Field of Nuclear Metallurgy and Technology, Presses Universitaire de France, 1969, pp. 111–117.

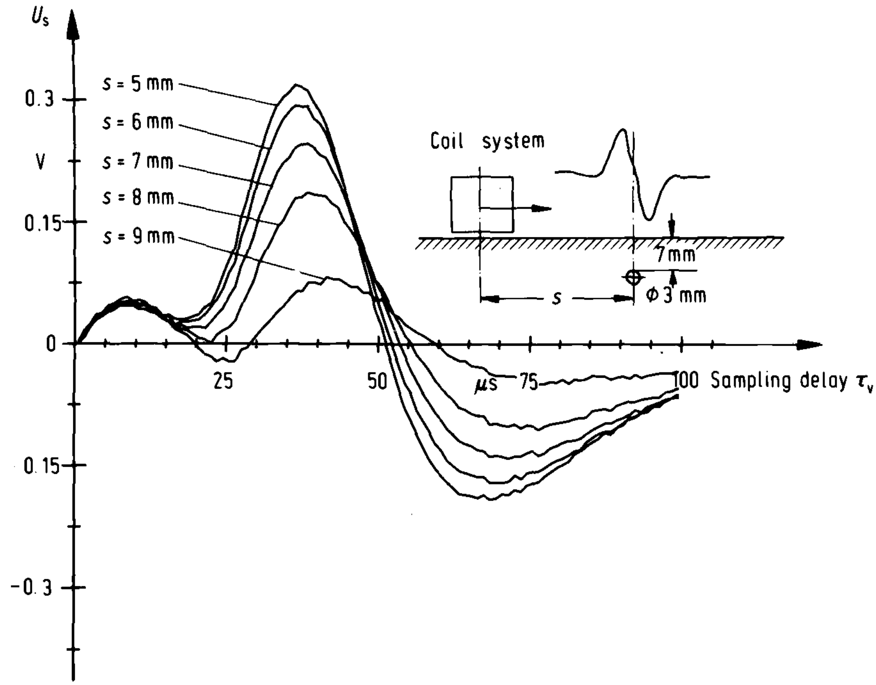

FIG. 9—*Signal versus approach to a defect.*

[*3*] Waidelich, D. L. and Huang, S. C., *Materials Evaluation,* Vol. 30, No. 1, 1972, pp. 20-24.
[*4*] Renken, C. J. and Selner, R. H., *Materials Evaluation,* Vol. 24, No. 5, 1966, pp. 257-262.
[*5*] Cox, C. W. and Renken, C. J., "The Use of the Conducting Mask in Pulsed Electromagnetic Testing," Report ANL-7172, Argonne National Laboratories, Argonne, Ill., 1969.
[*6*] Renken, C. J. and Sather, A., "Pulsed Eddy Current Test System for Hot-Cell Use—Manual of Operation," Report ANL-7973, Argonne National Laboratories, Argonne, Ill., 1973.
[*7*] Asamoto, R. R., Bacon, R. F., Conti, A. E., and Wozadlo, G. P., *Materials Evaluation,* Vol. 31, No. 4, 1973, pp. 67-72.
[*8*] Martin, M. R. and Francis, W. C. in *Proceedings,* 23rd Conference on Remote Systems Technology, 1975, pp. 316-328.
[*9*] Wittig, G. and Grigulewitsch, W. in *Proceedings,* First European Conference on Non-Destructive Testing, 1978, pp. 165-172.
[*10*] Wittig, G. and Grigulewitsch, W., *Materialprüfung,* Vol. 20, No. 12, 1978, pp. 449-454.
[*11*] Meier, W., *Materialprüfung,* Vol. 20, No. 2, 1978, pp. 57-62.

Measurement Methods III

W. D. Dover,[1] *F. D. W. Charlesworth,*[1] *K. A. Taylor,*[1] *R. Collins,*[1] *and D. H. Michael*[1]

The Use of A-C Field Measurements to Determine the Shape and Size of a Crack in a Metal

REFERENCE: Dover, W. D., Charlesworth, F. D. W., Taylor, K. A., Collins, R., and Michael, D. H., **"The Use of A-C Field Measurements to Determine the Shape and Size of a Crack in a Metal,"** *Eddy-Current Characterization of Materials and Structures, ASTM STP 722,* George Birnbaum and George Free, Eds., American Society for Testing and Materials, 1981, pp. 401–427.

ABSTRACT: An instrument designed to measure the a-c field accurately has been built and fully tested on steel, aluminium, and titanium. These field measurements can be interpreted in terms of crack size, which provides a new technique for nondestructive testing (NDT) that requires no prior calibration. This paper describes the basic electronic measuring system, theoretical derivations of the electrical-field distribution, and application to industrial problems such as crack measurement in threads, shafting, welded connections, etc.

KEY WORDS: cracks, measurement, depth, shape, nondestructive testing, alternating current, field measurements, field solutions, surface cracks

The occurrence of fatigue and stress-corrosion cracks in large structures has led to the demand, over the last ten years, for a device that could detect and size surface cracks. Early attempts to satisfy this need employed d-c field measurements (a technique found to be reasonably successful for simple laboratory specimens), but the fact that large structures need a very heavy current imposes a considerable restriction on the use of that method.

An alternative approach is to use ac where the current flows in a thin skin at the metal surface. Compared to dc, a much smaller ac is needed for a given voltage drop across the metal surface. For a given alternating current of frequency, f, the current flows in a skin whose depth is of order δ, where

$$\delta = (\mu \mu_o \sigma \pi f)^{-1/2}$$

[1]Reader in mechanical engineering, research assistant in mechanical engineering, lecturer in mechanical engineering, senior lecturer in mechanical engineering, and reader in mathematics, respectively, University College London, England.

where:

μ = relative permeability of metal,
μ_o = permeability of free space, and
σ = conductivity of metal.

If one used an ac of 5 kHz frequency on mild steel, for example, the skin depth would be about 0.13 mm. It can be seen from this that ac would be preferable to dc and that the skin depth could be controlled by varying the frequency. It would still be desirable, however, to keep the ac down to as low a value as possible. Thus, any technique developed would have to be capable of accurately measuring very small voltages.

One of the difficulties in using ac is that the impedance of the electrical circuit is sensitive to mechanical stress, chemical composition, etc.; this means that the use of some remote calibration device could lead to unacceptable errors. In applying this approach it would be preferable to make all the field measurements directly on the metal under test. This is only possible if all stray voltages are eliminated from the measuring system so that the local measure of voltage is the true voltage at the metal surface. These ac field measurements could then be interpreted in terms of the crack depth and shape.

A device meeting these requirements has been developed *[1]*[2] and is now being manufactured commercially for nondestructive testing (NDT) and laboratory work.

This instrument was used initially in situations where the a-c electrical-field distribution could be predicted very easily, but service experience proved so successful that it encouraged work *[2]* on theoretical solutions, especially the semielliptical crack problem.

This paper describes some of the activities in three areas: the basic measurement system, theoretical estimates of the electrical-field distribution, and applications to industrial problems.

Alternating-Current Field Measurement (ACFM) System

Figure 1 shows the NDT version of the instrument, known as the Crack Microgauge. It consists of a stable constant-current a-c source and a sensitive a-c voltmeter, with a digital display located on the front panel. The electronic system needed for a-c field measurements is shown in block-diagram form in Fig. 2.

A thermistor-stabilized Wien bridge oscillator is used, which provides good amplitude and frequency stability. The output from the oscillator feeds a constant-current power amplifier, which drives current through the specimen or structure under test; connection may be made via, for example, small magnets, screw connections, or clamps. The amplifier can drive loads

[2]The italic numbers in brackets refer to the list of references appended to this paper.

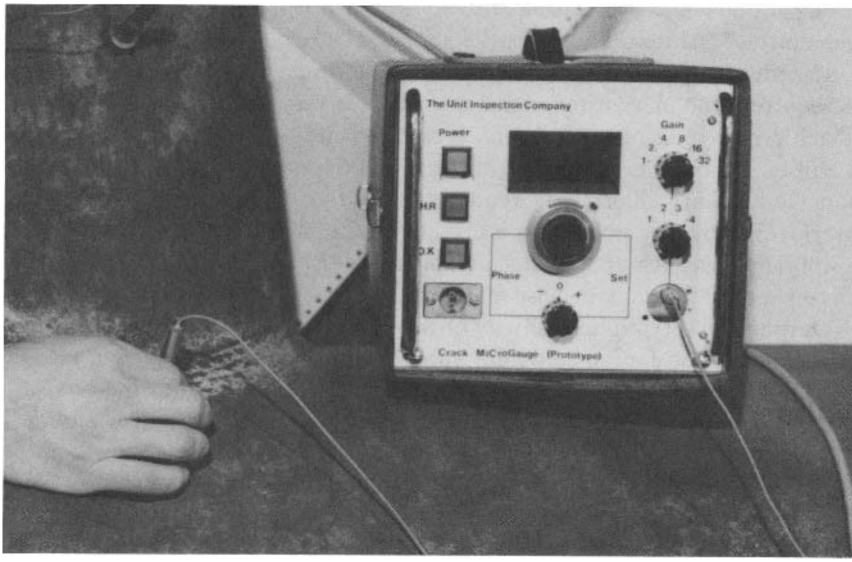

FIG. 1—*General view of Crack Microgauge manufactured by the Unit Inspection Co., Sketty Hall, Swansea SA2 8QE, U.K.*

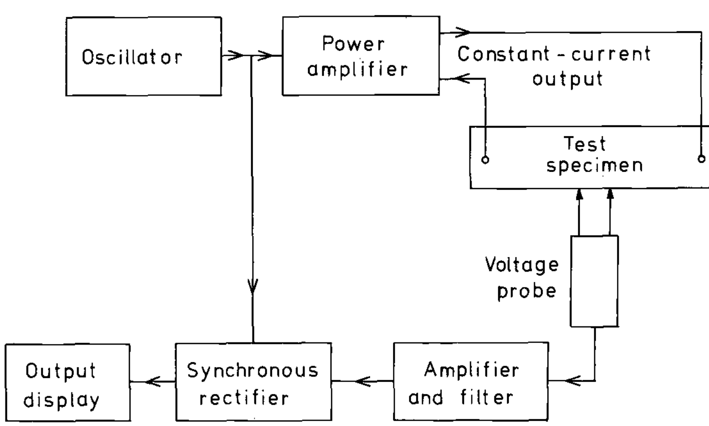

FIG. 2—Block diagram showing main elements of the a-c resistance for crack measurement.

up to about 3.5 Ω. A sensing circuit causes a warning lamp on the front panel to light if the load circuit resistance is too high, for example, due to a faulty connection to the specimen.

The field voltage at any point on the metal surface is sampled using a voltage probe that has two contact points a set distance apart. This separation distance is the probe length Δ. The input to the probe is typically of the order of a few microvolts, but can vary widely according to the material and geometry of the item under test.

In order to reduce the effects of random noise, particularly when high gain is required, the measuring circuit must have a very narrow bandwidth. This is achieved by use of a synchronous rectifier circuit. For good linearity and stability, the rectifier is situated at the end of the measurement chain, so that some additional filtering is required earlier in the amplifier to prevent overloading by any interference present at the input and (at high gain) by amplifier noise. An active filter arrangement [*3*] based on the Wien bridge circuit is used to promote close matching and tracking of oscillator and filter.

Despite the very high sensitivity of the measuring circuit, the complete instrument may be contained within a single portable box (as shown in Fig. 1). This is achieved by careful positioning of the circuitry within the box, appropriate use of magnetic and electrostatic shielding, and careful attention to power-supply decoupling and isolation.

ACFM Uniform Field

One of the simplest and commonest situations in which to use the a-c resistance techniques is where the electric field can be arranged so that the gradient of potential does not vary. Consider the example displayed in Fig. 3. This shows part of an infinite plate containing an infinitely long surface crack of uniform depth b. If the current connections are at 1 and 2, the field would be expected to spread out as indicated by the dashed lines. If, however, the distance between 1 and 2 is large compared with both b and AC, line ABC will be one where the potential gradient is constant. Thus, if the voltage is measured by a probe of length Δ at any point between A and C but excluding bridging the crack, the value would be constant. If the crack is bridged, then the effective probe length, or distance between measuring points, is $\Delta + 2b$ (note that both faces of the crack are included). If the

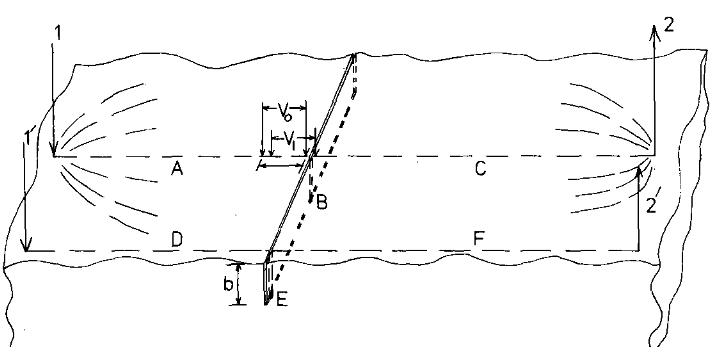

FIG. 3—*General arrangement for crack-depth measurement in a uniform a-c field.*

measured voltage is solely dependent on the path length between the probe tips, then the crack depth can be estimated by comparing the voltage measured off and on the crack. The following equation can be used to calculate the crack depth:

$$b = \left[\frac{V_1}{Vo} - 1\right]\frac{\Delta}{2} \tag{1}$$

It can be seen that this approach does not require any prior calibration of the instrument.

The accuracy of this estimate of crack depth is dependent upon the instrument being capable of measuring the true voltage on the metal surface. The Crack Microgauge was the first instrument designed to work in this mode and has been successfully applied to many service problems, some of which are described later. Most of these early applications have been in situations where the cracks were fatigue cracks. These cracks were surface-breaking semielliptical cracks of high aspect ratio; that is, the ratio of the surface-crack length to the depth is large (10 or more). For this type of crack the field can be arranged so that Eq 1 applies.

Consider again the physical arrangement shown in Fig. 3. Here the current connections are placed across the crack so that the current flow is perpendicular to the plane of the crack, and the probe is aligned parallel to *ABC*. If all the measurements are taken close to line *AC*, the crack-depth prediction will be accurate. If measurements are taken on line *DEF*, *however*, the assumption of a constant gradient of potential would no longer be valid and Eq 1 would not apply.

If one wished to measure along line *DEF*, it would be necessary either to determine the field distribution at this section or, alternatively and much more simply, move the current connections to 1′ and 2′.

To illustrate this point consider the results taken on a T-butt weld, fabricated from 50-mm steel plate, known to possess a fatigue crack at the weld toe. These are shown in Fig. 4. For this example the current connections were placed on the centerline about 100 mm each side of the weld and kept there for all of the measurements. A series of readings were taken just off and just over the crack so that the crack depth could be calculated, using Eq 1, for any point across the section. Subsequently the specimen was fractured at low temperature and the crack depth measured optically. The two sets of results, measured and predicted depth, are shown in Fig. 4.

It can be seen that in the center region the predictions are accurate, and that the error is not significant for at least 40 mm each side of the centerline. Outside of this region the field was not uniform and use of Eq 1 produced considerable errors. If the current input points had been positioned closer to the fatigue crack, again the field would not have been uniform and errors

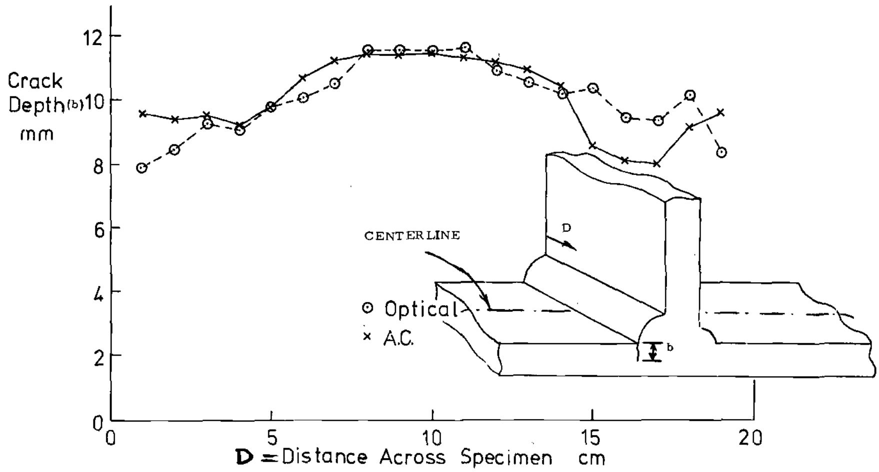

FIG. 4—*Comparison of a-c predicted depth with optical measurements for a T-butt weld.*

would have occurred in the crack-depth prediction (using Eq 1). It is most important in practice to arrange for the field to be as uniform as possible.

As the concept of this uniform or one-dimensional field was rapidly assimilated by users of the a-c resistance technique, it was decided that the analysis of more complex fields would be interpreted by means of modifying factors to be applied to the estimate using Eq 1. In the following sections Eq 1 will be referred to as the one-dimensional solution.

ACFM, Theory of the Field

Formulation

Consider the electromagnetic-field distribution surrounding a surface crack in a highly conducting metal specimen, subject to the restriction that the metal surface apart from the crack is a single plane for which the incident current stream may be taken as uniform. The electromagnetic field in the metal is described by Maxwell's equations [*4*], which are as follows

$$\text{Curl}\,\mathbf{H} = \mathbf{j} + \frac{\partial \mathbf{D}}{\partial t} \tag{2}$$

$$\text{Curl}\,\mathbf{E} = -\frac{\partial \mathbf{B}}{\partial t} \tag{3}$$

$$\text{Div}\,\mathbf{D} = \rho \tag{4}$$

$$\mathrm{Div}\,\mathbf{B} = 0 \tag{5}$$

In addition Ohm's Law can be written as

$$\mathbf{j} = \sigma \mathbf{E} \tag{6}$$

In these equations **H** and **B** are the magnetic field and induction vectors, and **E** and **D** are the electric field and electric displacement vectors. It is assumed, also, that there exist linear isotropic constitutive relations $\mathbf{D} = \epsilon\mathbf{E}$, $\mathbf{B} = \mu\mathbf{H}$, where ϵ and μ are the permittivity and magnetic permeability; ϵ, μ, and the electrical conductivity, σ, are taken to be constant. The current-density vector is $\mathbf{j}$ and the charge density ρ.

The equation of charge conservation that follows from Eqs 2 and 4 is

$$\mathrm{Div}\,\mathbf{j} + \frac{\partial \rho}{\partial t} = 0 \tag{7}$$

Equations 4, 6, and 7 may then be combined to give the equation of charge relaxation

$$\frac{\partial \rho}{\partial t} + \frac{\sigma}{\epsilon}\rho = 0 \tag{8}$$

This equation shows that the charge density has a relaxation time, ϵ/σ, that is exceedingly small in the problems of interest here. Thus, there can be no background charge distribution in the interior of these metals, and in the present context of an alternating-current flow where ρ would be proportional to $e^{i\omega t}$, where ω is the angular frequency, then $\rho = 0$. Free charge is therefore confined to a surface distribution only. Equations 2, 3, and 6 can be used to give the following equation for **E**

$$\mathrm{Curl}\ \mathrm{Curl}\ \mathbf{E} = -\ \mu\sigma \frac{\partial \mathbf{E}}{\partial t}$$

for the electric field in the metal interior when the displacement current in Eq 2 is neglected. In addition, since $\mathrm{Div}\ \mathbf{E} = 0$, this can also be written as

$$\nabla^2\, \mathbf{E} = \mu\sigma \frac{\partial \mathbf{E}}{\partial t} \tag{9}$$

When Cartesian coordinates are used, $\nabla^2\,\mathbf{E}$ may be taken as the Laplacian operating on the components of **E**. Thus, assuming an alternating-current flow in which all quantities vary with time t like $e^{i\omega t}$, this equation may be written in Cartesian coordinates (x,y,z) as

$$\frac{\partial^2 \mathbf{E}}{\partial x^2} + \frac{\partial^2 \mathbf{E}}{\partial y^2} + \frac{\partial^2 \mathbf{E}}{\partial z^2} = k^2 \mathbf{E} \tag{10}$$

where $k^2 = i\mu\sigma\omega$. For sufficiently large values of ω, in a specimen with length scale ℓ, $k\ell$ will be large, and the effect of this is to confine the electromagnetic field into a thin surface layer. If we take axes O-x-y in the plane of the metal surface and O-z normally out of the surface, a solution of Eq 10 representing the electric field in the surface layer is

$$\mathbf{E} = \mathbf{E}\ (x,y)\ e^{mz}$$

where the real part of m is positive and the time dependence $e^{i\omega t}$ is omitted throughout. $\mathbf{E}\ (x, y)$ evidently satisfies the equation

$$\frac{\partial^2 \mathbf{E}}{\partial x^2} + \frac{\partial^2 \mathbf{E}}{\partial y^2} = (k^2 - m^2)\, \mathbf{E}\,(x,y) \tag{11}$$

In the cases of interest $\mathbf{E}$ will be a vector parallel to the surface, that is, $\mathbf{E} = (E_x, E_y)$, and using Eq 6 one may integrate the current-density components j_x, j_y to give the total current $\mathbf{i}\ (x,y)$ flowing in the surface layer in terms of the surface value of $\mathbf{E}$ which is $\mathbf{E}\ (x,y)$. The present discussion is confined to problems in which there is an incident uniform surface current $\mathbf{i}_o$. The x–y axes are chosen such that the incident current flows along O-y in the negative sense so that $\mathbf{i}_o = -(\sigma/m)\ E_o\ \mathbf{j}$ at incidence and $\mathbf{E}\ (x,y) = -E_o\ \mathbf{j}$. It can be seen from Eq 11 that the field satisfying this incidence condition must have $k^2 = m^2$, at least in the plane of incidence, and the surface distribution of $\mathbf{E}$ in this case satisfies Laplace's equation

$$\frac{\partial^2 \mathbf{E}}{\partial x^2} + \frac{\partial^2 \mathbf{E}}{\partial y^2} = 0 \tag{12}$$

Consider the way in which the surface distribution of $\mathbf{E}$ is altered by the presence of a symmetrical surface crack, whose geometry is illustrated in Fig. 5. In order to predict the crack depth from the surface measurements it is necessary to find the surface distribution of $\mathbf{i}$ or $\mathbf{E}$ over the plane of the surface, O-x-y, and the plane of the crack, O-x-z. In the plane O-x-y, $\mathbf{E} = [E_x(x,y),\ E_y(x,y)]$ satisfies Eq 12. A stream function $\psi_1(x,y)$ may be introduced for the current distribution since Div $\mathbf{E} = 0$, so that

$$E_x = \frac{\partial \psi_1}{\partial y} \quad \text{and} \quad E_y = \frac{-\partial \psi_1}{\partial x}$$

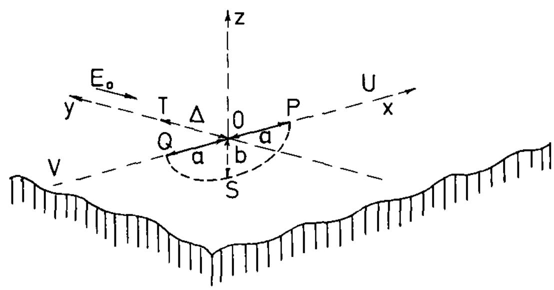

FIG. 5—*Perspective view of a plane crack in a plane surface.*

Then $(\partial/\partial x)\ \nabla^2\psi_1 = 0$, and $(\partial/\partial y)\ \nabla^2\psi_1 = 0$, and $\nabla^2\psi_1 =$ constant. Since "upstream" $\partial\psi_1/\partial y = 0$ and $\partial\psi_1/\partial x = E_o$, the constant on the right hand side of this equation must be zero and

$$\nabla^2\psi_1 = 0 \tag{13}$$

The symmetry of the solution about the y-z plane is ensured by taking ψ_1 to be an odd function of x.

In the plane of the crack O-x-z one can assume a similar form of the surface field $E_x(x,z)$, $E_z(x,z)$ given in terms of the stream function $\psi_2\ (x,z)$, where $E_x = \partial\psi_2/\partial z$, $E_z = -\partial\psi_2/\partial x$, and

$$\nabla^2\psi_2 = \text{constant} \tag{14}$$

$\psi_2\ (x,y)$ is evidently also an odd function of x, and we shall assume the current distribution to be symmetric about the center-line *VQSPU*. The resulting boundary conditions and continuity conditions between the two domains have been written in Fig. 6 and are as follows:

(*a*) On *UP* and *QV* $\partial\psi_1/\partial y = 0$; otherwise there would be a jump in the tangential components of **E** on these lines which would imply from Eq 3 a singularity in the magnetic field.

(*b*) The tangential components of **E** on approaching points such as *R* at the interior edge of the crack from either side are taken to be continuous so that by symmetry they are zero and $\partial\psi_2/\partial n = 0$, n being the normal to *PSRQ* at *R*.

(*c*) (*i*) At the interface *POQ* between the two domains it is necessary to have continuity of current flow across the edge. This requires the perpendicular component of **E** to be continuous so that $\partial\psi_1/\partial x = \partial\psi_2/\partial x$. (*ii*) As in (*b*) we take the tangential component of **E** approaching the edge from either side to be continuous, so that $\partial\psi_1/\partial y = \partial\psi_2/\partial z$.

Note that in (*b*) and (*c*) further calculations are required to find the exact distribution of the field at distances of order $1/k$ around *R* and *POQ* respectively. When the skin depth is very small, however, these edge corrections produce only very small changes in the surface distribution of ψ_1 and ψ_2 and are neglected here.

Since $\psi_1 = \psi_2 = 0$ on $x = 0$ it follows from (*c*)(i) that $\psi_1 = \psi_2$ and that $\partial^2\psi_1/\partial x^2 = \partial^2\psi_2/\partial x^2$ on *POQ*. Also, since $\partial^2\psi_1/\partial y^2$ and $\partial^2\psi_2/\partial y^2$ are zero on $x = 0$, it can be seen from Eq 13 that $\partial^2\psi_1/\partial x^2 = 0$ at O. Thus $\partial^2\psi_2/\partial x^2$ is also zero at O; therefore, the constant on the right hand side of Eq. 14 is zero. The continuity conditions (i) and (ii) then ensure that derivatives of ψ_1 and ψ_2 of all orders are continuous across *POQ*; therefore, ψ_2 is the analytic continuation of ψ_1 into the domain *PSRQ*. Thus, provided one neglects the edge corrections, the solution may be regarded as the solution of $\nabla^2\psi = 0$ in the entire domain above *UPSRQV* in Fig. 6, with the given incident value of ψ upstream and $\partial\psi/\partial n = 0$ everywhere along *UPSRQV*. The problem of a plane symmetrical crack in a plane surface thus may be solved by "unfolding" the field so as to produce a two-dimensional Laplace field.

The problem may also be expressed in terms of the conjugate function $\phi(x,y)$, where, from the Cauchy-Riemann equations

$$\frac{\partial\phi}{\partial x} = \frac{\partial\psi}{\partial y} = E_x$$

$$\frac{\partial\phi}{\partial y} = -\frac{\partial\psi}{\partial x} = E_y$$

Thus $\nabla^2\phi = 0$ with $\phi = 0$ on *UPSRQV* and $\phi \rightarrow E_o\, y$ as $y \rightarrow \infty$. This representation is useful since practical measurements of the field are in the form of differences of voltage between two points which are represented by the difference in ϕ.

Derivation of Two-Dimensional Solutions

When the crack geometry is of circular arc form the field problem may be solved exactly by standard techniques. This solution gives the true depth from two measurements of voltage on the sample. Figure 5 shows the geometry of the system in hidden perspective; the crack width at the surface is $2a$ and the maximum depth is b, while Δ denotes the distance *OT*, which is the distance between the contacts of the probe used to detect differences in the potential ϕ. Figure 7 shows the unfolded field problem which results from the consideration of the previous section. It is mathematically equivalent to the problem of irrotational flow of a stream over a plane containing a circular arc indentation, and the solution for the crack problem may thus be obtained by suitable adaptation of the known hydrodynamic solution. That adaptation consists of interpreting hydrodynamic streamlines as lines of constant electric

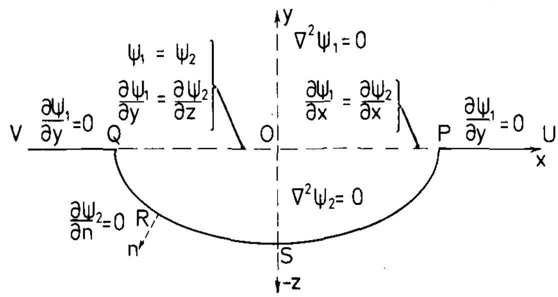

FIG. 6—*The unfolded field problem, general.*

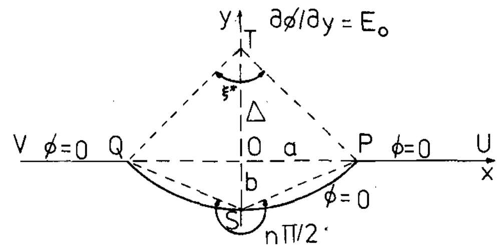

FIG. 7—*The unfolded field problem, circular-arc cracks.*

potential so that, on adopting Milne-Thomson's form [5] working with a complex potential function $w = \phi + i\psi$, one obtains

$$w = \phi + i\psi = \frac{2aE_o}{n} \cot \frac{\zeta}{n} \tag{15}$$

with

$$z = ia \cot \frac{1}{2} \zeta \tag{16}$$

Here z and ζ are complex variables ($z = x + iy$ and $\zeta = \xi + i\eta$), and ξ and η are coaxal coordinates of a point. In particular $\xi = 0$ defines those parts of the x-axis for which $|x| > a$, and for $n > 2$, $\xi = n\,\pi/2$ defines a circular arc depression PSQ of width $2a$ and depth $b = a \cot n\,\pi/4$. The x-axis between P and Q corresponds to $\xi = \pi$, while the y-axis is given by $\eta = 0$. It may be readily confirmed that the solution satisfies the boundary conditions indicated in Fig. 7 by examining the equation for the potential obtained from Eq. 15 which is

$$\phi = \frac{2a}{n} E_o \frac{\sin 2\,\xi/n}{\cosh 2\eta/n - \cos 2\,\xi/n} \tag{17}$$

The geometrical aspect ratio, $|2a/b|$, is determined by the value assigned to the parameter, n, since

$$|2a/b| = 2\tan n\pi/4 \tag{18}$$

A semicircular crack has $n = 3$, while the crack depth becomes vanishingly small if $n \rightarrow 2$.

Consider a probe of length Δ placed on the y-axis which measures the difference in potential between T and O in Fig. 5. It is convenient to work with ξ^*, the coaxial coordinate of T, so that

$$\Delta = a \cot {}^1\!/_2\, \xi^* \tag{19}$$

Since the coordinates of O are $\xi = \pi$, $\eta = 0$, the difference in potential recorded is

$$\phi_T - \phi_o = \frac{2a}{n} E_o \left[\cot \frac{\xi^*}{n} - \cot \frac{\pi}{n}\right] \tag{20}$$

If moved an infinitesimal distance along the y-axis so as to cross the crack, the probe reading will increase by an amount

$$2\phi_o = \frac{4a}{n} E_o \cot \frac{\pi}{n} \tag{21}$$

the potential being zero at the bottom of the crack. If the readings are interpreted on a one-dimensional basis, which ignores the distortion of the field produced by the crack presence, then the depth so indicated, b_i, is

$$\frac{b_i}{\Delta} = \frac{\phi_o}{\phi_T - \phi_o} = \frac{\cot \pi/n}{\cot \xi^*/n - \cot \pi/n} \tag{22}$$

whereas, from Eqs 19 and 18 the real depth, b, is given by

$$\frac{b}{\Delta} = \frac{\cot n\pi/4}{\cot (1/2)\, \xi^*} \tag{23}$$

Thus, one can obtain

$$\frac{b_i}{b} = \frac{\cot \pi/n \cot (1/2)\, \xi^*}{\cot n\pi/4[\cot \xi^*/n - \cot \pi/n]} \tag{24}$$

Equation 24, together with Eqs 18 and 19, provides the means of determining the true depth on the centerline from two voltage measurements in the field. The parameters n and ξ^* may be formally eliminated to give

$$b_i/b = f\,(b_i/2a,\ \Delta/2a) \tag{25}$$

shown plotted in Fig. 8.

No exact solution in closed form in yet available for the problem of an elliptical crack. Instead, two approximate solutions have been developed from the circular-arc results. The first represents an asymptotic solution to the problem valid for $2a/b \rightarrow \infty$ that is applied to slender cracks of large aspect ratio, and the second takes the circular-arc solution and reinterprets it by applying it to an equivalent arc that approximates the elliptical crack at its bottom. The result is qualitatively similar to that shown in Fig. 8 and can be found in Ref *2*.

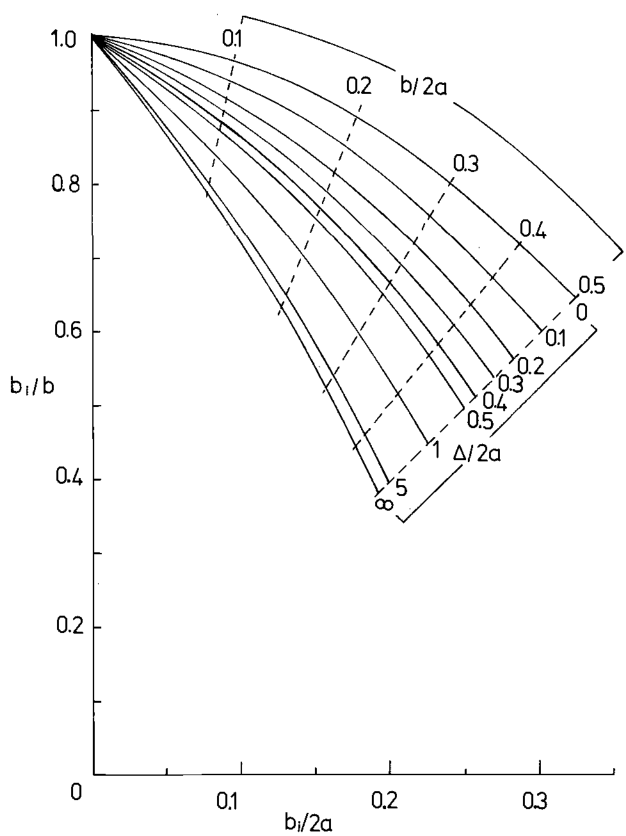

FIG. 8—*Solution for circular-arc cracks.*

Experimental Results

It can be seen from Fig. 8 that the one-dimensional solution will underestimate the real crack depth for circular-arc cracks; this is also true for semielliptical cracks. This underestimate can be as much as 50 percent and cannot be ignored. A series of tests has been conducted on circular-arc and semielliptical cracks in order to check the theoretical analysis presented in this section.

Natural cracks seldom grow in the form of a circular arc unless they are very small when compared to the specimen cross section and are growing under the action of a uniform tensile stress. Thus, the only reasonable way to produce a set of circular-arc cracks is by machining. Several large mild-steel plates, 450 by 200 by 25 mm, were machined using slitting saws to give a range of aspect ratios, slot sizes, and crack depths. The slot depths were measured optically and then measured again using the Crack Microgauge with a range of probe sizes. The comparison of the ACFM predicted depths and the optical readings of depth is shown in Fig. 9. In the figure both one-dimensional and two-dimensional interpretations are shown, the latter using the data given in Fig. 8. It can be seen that with a one-dimensional interpretation the errors can be as much as 40 percent, whereas with the two-dimen-

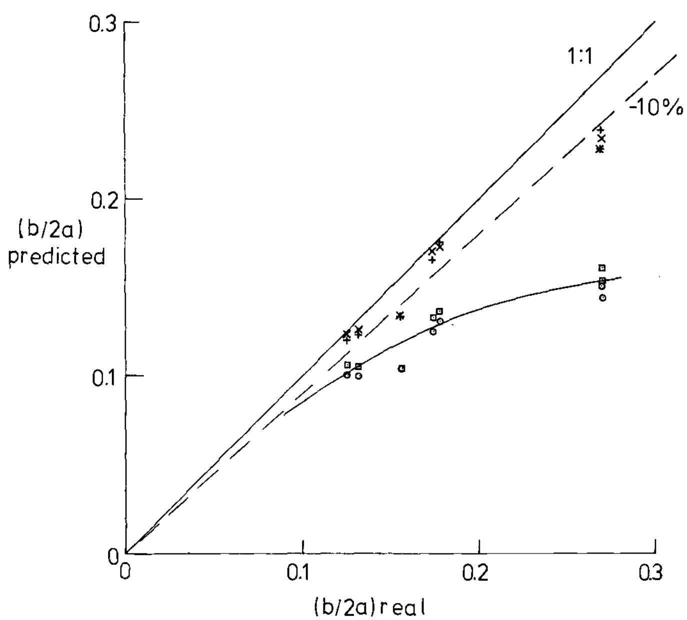

FIG. 9—*Predicted depth of machined circular-arc cracks;* ○, □, *one-dimensional interpretation;* +, ×, *two-dimensional interpretation;* □, ×, *20-mm probe length;* ○, +, *40-mm probe length.*

sional interpretation most of the predicted errors seem to be about the 10 percent error line.

Approximate solutions for semielliptical cracks are also available [*2*]. Most fatigue cracks grow in the shape of a semiellipse except for small cracks growing in a uniform tensile-stress field. Consequently it was possible to monitor a growing fatigue crack with ACFM and to predict depths using Ref *2*. In these tests the fatigue-crack front position was marked by changing the loading periodically so that after failure these crack shapes could be measured optically. The results for this series of tests are shown in Fig. 10. It can be seen that, using the two-dimensional elliptical solution, the error has been reduced from about 30 percent to about 10 percent.

In all applications the two-dimensional solutions given here and in Ref *2* have been found to reduce the errors in the predicted depth to about 10 percent and are a valuable contribution to the use of this technique in crack-size measurement. It is hoped that further theoretical solutions will become available in the near future for fields such as those associated with corner cracks etc.

Applications

Tubular Welded T-joints

A large fatigue-test program on tubular welded T-joints is currently being undertaken in Europe. One of the aims of this program has been to validate the fracture mechanics approach to fatigue life prediction. In order to do this it is necessary to measure the shape and size of the surface fatigue cracks that are the principal form of damage in these structures. This has been done in several cases by using the Crack Microgauge and has revealed some interesting information on the mechanisms of load transfer within these structural models. Figure 11 shows the crack-depth measurements taken at five sites during a random-load fatigue test on a 450-mm-diameter tubular welded T-joint. One can see that the growth rate is not uniform along the crack front; this is further illustrated by the alternative plot of those data shown in Fig. 12. The crack front looks highly irregular in the diagram, but it must be noted that the scales are distorted. Nevertheless, the crack front is not a simple curve and the rate of growth does seem to vary from point to point. This type of growth was confirmed on an H-type tubular specimen, of 1800 mm diameter, where both ACFM and acoustic emission (AE) monitoring was undertaken [*6*]. In this work the ACFM results showed again that the crack front was irregular. In addition the AE results showed that the greatest acoustic activity came from the deepest parts of the crack and that the crack growth was not continuous. Instead, the active region of crack growth appeared to be changing from one part of the front to another.

Of interest in a more general sense is that using this instrument without

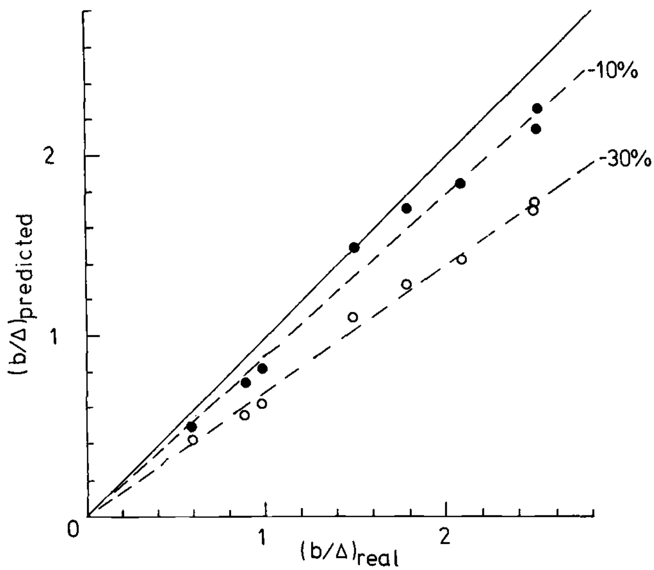

FIG. 10—*Predicted depth of naturally growing elliptical cracks;* ○, *one-dimensional interpretation;* ●, *two-dimensional interpretation.*

any prior calibration it was possible to estimate the crack depth at any point around the intersection to within 10 percent. Several operational points are worth mentioning, however. Although the crack site is at the junction of weld metal and parent plate, the crack grew predominantly in the parent plate. Consequently, the initial value (V_o) was taken in the parent plate as close to the weld toe as possible. Also, the aspect ratio from these cracks was high so that the one-dimensional solution could be used. The current connection points were carefully chosen so that the potential field was uniform, and several current-input sites were used to get the accuracy required around a large part of the circumference. These factors combined to give the levels of accuracy quoted earlier. Fortunately, in many large metal structures these conditions frequently occur and this simple approach is successful.

The T-joints in these tests are fabricated from steel and the initial crack sites are often easy to predict. The Crack Microgauge can be used on any metal, however, and can also be used for detecting the crack and sizing, as shown in the next application.

Titanium Bolt

This application arose during some contract work conducted earlier this year for an aircraft company. In this work a forged titanium bolt of 30 mm diameter was subjected to a sequence of loading comprising preloads and flight loading. After each preload and flight loading the bolt was to be inspected, and the test was to proceed until a crack depth of 0.5 mm was reached.

A special-purpose jig was designed for the inspection (Fig. 13). The probe was built into a part section of a plastic nut and arranged to be held by spring loading to the top surface of the test bolt. The probe contacts were arranged so that the distance apart was the thread pitch; they were held in contact with the crowns of adjacent threads. Rotation of the bolt caused the part nut to

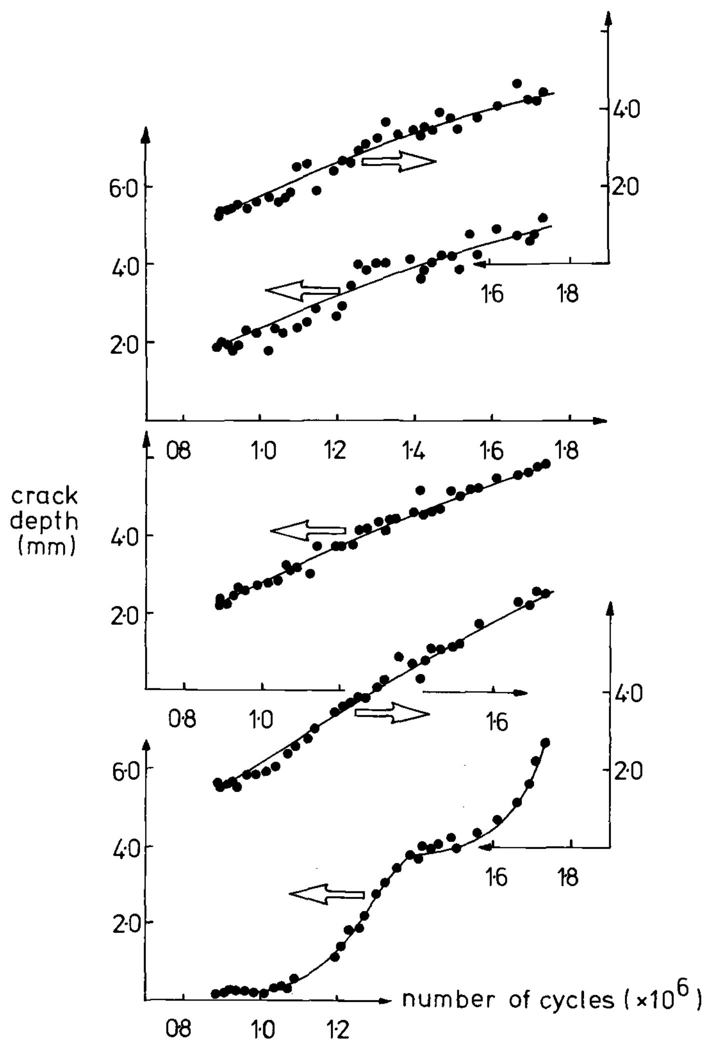

FIG. 11—*Fatigue-crack growth curves at adjacent sites around a tubular welded T-joint.*

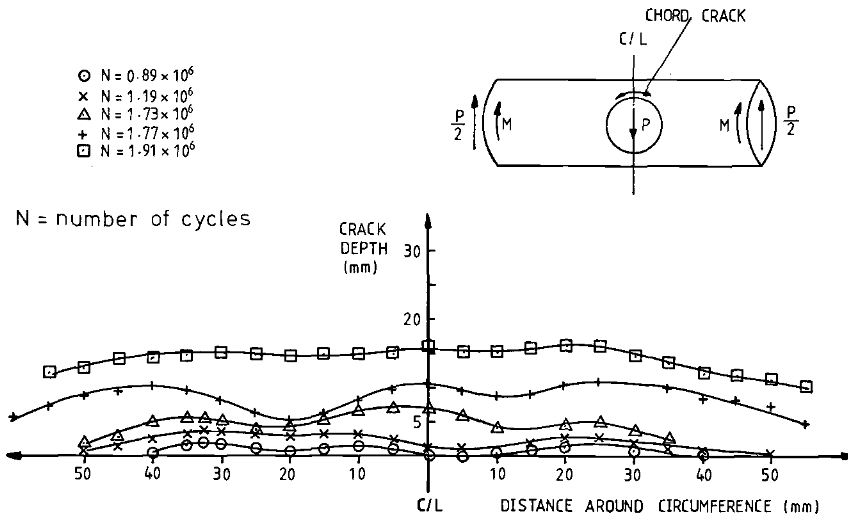

FIG. 12—*Fatigue-crack shapes during a fatigue test on a tubular welded T-joint.*

traverse along the thread so that the voltage difference across any adjacent thread crowns could be measured. The output from the Crack Microgauge was linked to a chart recorder to give a continuous record of the voltage. A displacement transducer was also attached to the jig and the part nut so that any movement of the nut would be related to the transducer output. This output was connected to the x-axis of the chart recorder. The trace on the chart was thus a permanent record of the voltage drop across the thread at any position along the bolt. Shortly after the start of the test two cracks were noted (shown on the chart record reproduced in Fig. 14). The crack depth was estimated from this record by means of a calibration from a second bolt possessing an artificial flaw. The crack-growth plot for these two cracks is shown in Fig. 15.

Several interesting points emerged from this test. The cracks were at a site close to the back face of the test nut and were high up on the flanks of the notch. Despite this unexpected site the cracks were easily detected using the special-purpose jig. Also, the crack-growth curve appears to have increments of growth followed by periods where the crack depth appears to be decreasing. Further examination of the test bolt provided possible interpretations of these measurements. Optical examination using a stereomicroscope showed that the two cracks that had been followed throughout the test were the sites indicated by the Crack Microgauge. Similarly, the thread form was also measured using a profile projector. Figure 16 shows the profile recorded near the completion of the test. Two features are significant. First, the thread crown region has experienced considerable plastic deformation, which causes the cracks to occur high on the flank of the thread. Second, the repeated applica-

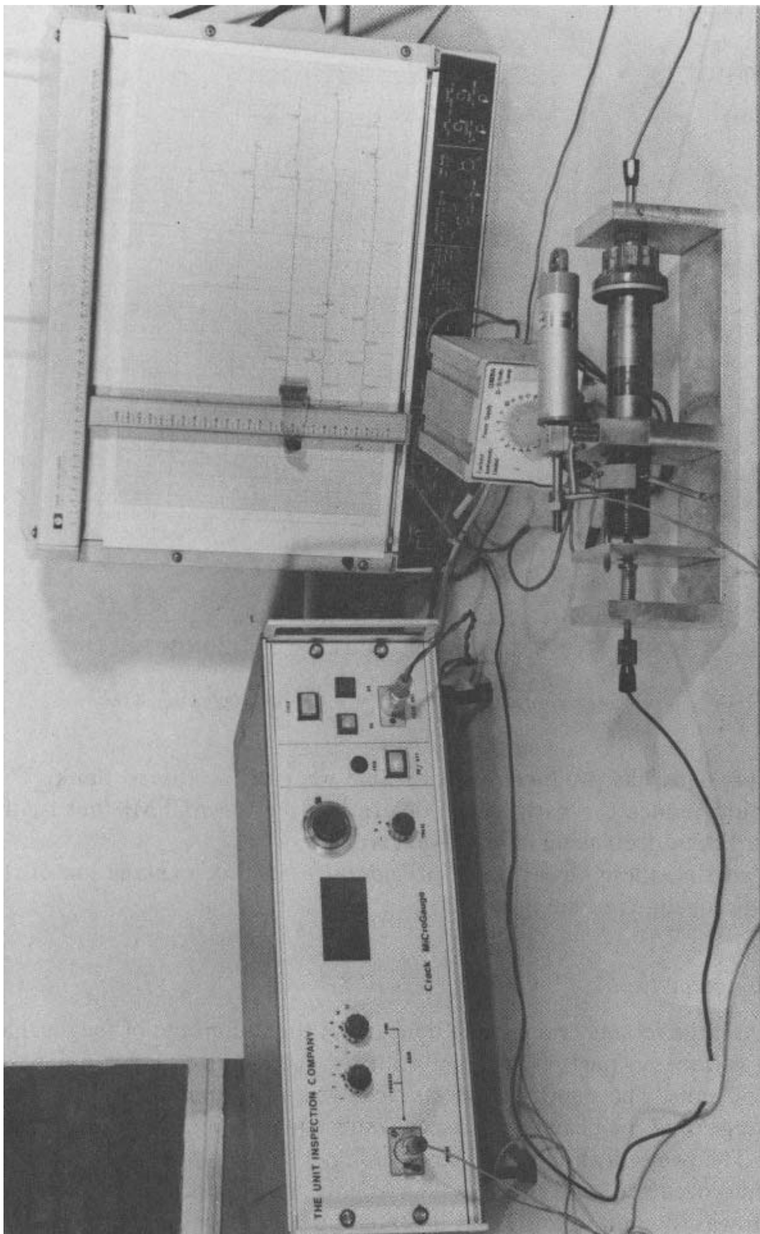

FIG. 13—*General view of crack-detection system for titanium bolts.*

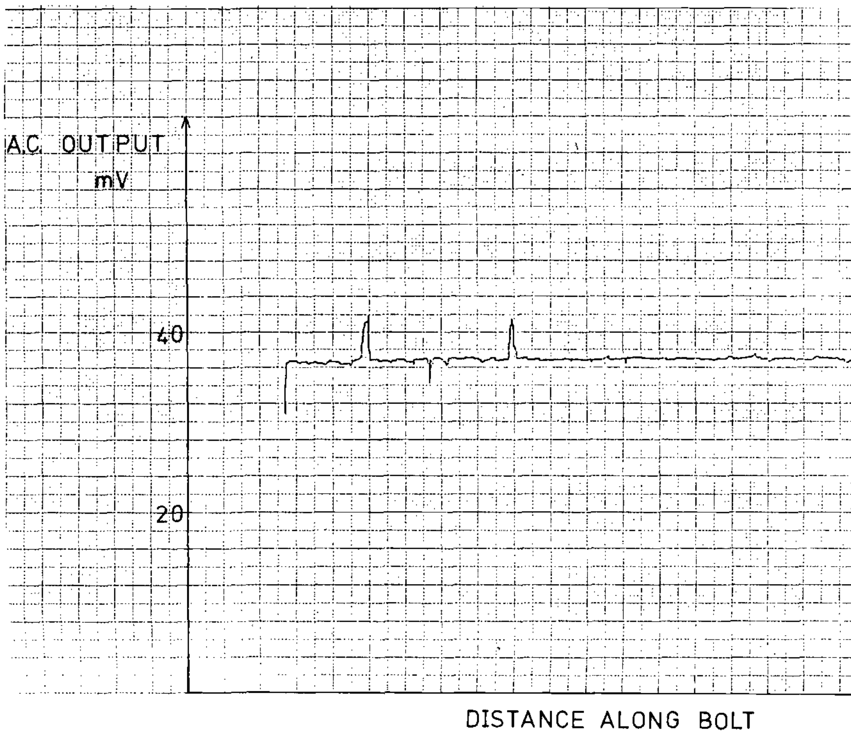

FIG. 14—*Chart record of initial cracks in a titanium-bolt fatigue test.*

tion of preloads has produced considerable wear of the thread flank. This wear would reduce the path length determined by the ACFM; that is, the crack had been decreasing in size as recorded.

It is felt that these observations provide a reasonable explanation of the Crack Microgauge recordings.

Steel Elongator Roll

Several large fatigue cracks were detected at the radius end of the journal-bearing surface on part of a rolling mill; the section size at this point was about 300 mm. The depth of these cracks was measured using the Crack Microgauge, and the bearing surface was subsequently sectioned as shown in Fig. 17. The two sets of data are shown in Fig. 18. It can be seen that several cracks had occurred, and that the ACFM gave an overestimate of the crack depth. It was thought initially that this might be due to the inclination of the crack to the surface; that is, the sectioning technique only determines the net section penetration not the real crack length. The angle between the crack plane and the surface was not 90 deg, but the difference was insufficient to

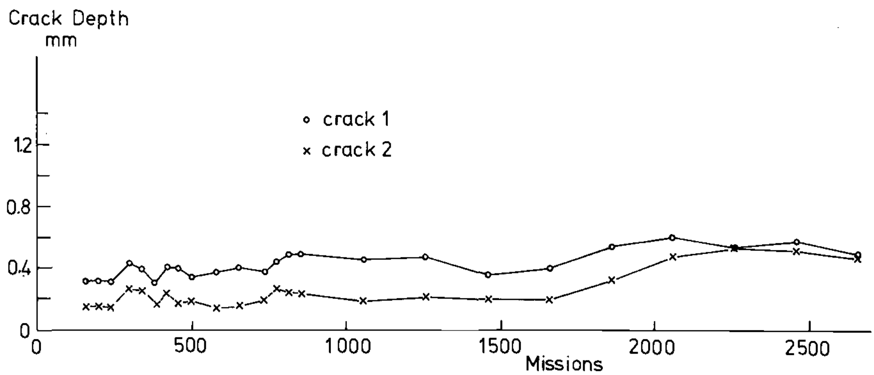

FIG. 15—*Fatigue-crack growth curves for the two cracks monitored during the titanium-bolt fatigue test.*

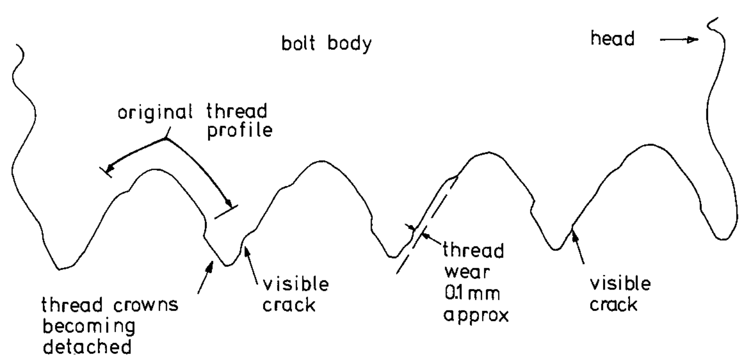

FIG. 16—*Thread profile of the titanium bolt after the fatigue test.*

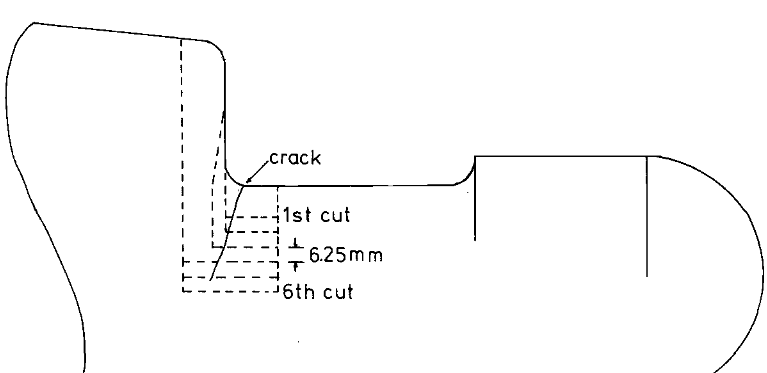

FIG. 17—*Sectioning details of the elongator roll.*

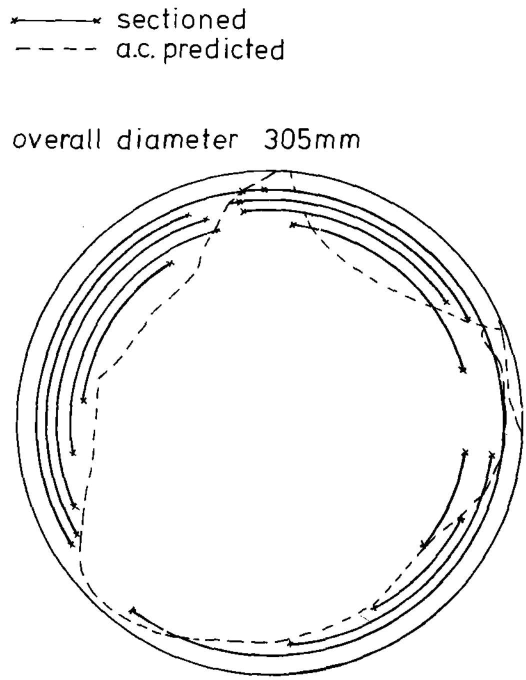

FIG. 18—*Predicted and measured crack profiles for the elongator roll.*

account for all of this error. A second possibility is that the reduction in that section locally made the a-c field nonuniform. This could have a much larger effect and can be approximately estimated as follows.

Consider a constant alternating current, I, flowing along a rod of radius r_o. The surface current density, i, is given approximately by $i = (Ik/2\pi r_o)$ $e^{-k(r_o-r)}$ where r is the radial coordinate measured from the axis of the cylinder. In this expression the surface is treated as locally plane, and the small effect of curvature on the skin-depth profile is neglected. If the current encounters an axisymmetric circumferential groove that preserves the symmetry of the current flow about the axis of the rod, the current density will not change until the groove is reached. On the face of the groove the continuity of current flow shows that the current density will be radially $(Ik/2\pi r)$ e^{-kz}, where z here measures the depth from the surface of the groove in the axial direction. Thus, if E_o is the surface value of the incident electric field the value at radius r on the groove face is $E_o r_o/r$. If V_c and V_o are the voltages measured across the groove and adjacent to it we have

$$V_c - V_o = 2\int_{r_i}^{r_o} E_o \frac{r_o}{r} dr \qquad (26)$$

where r_i is the inner radius of the groove and $r_i = r_o - d$, where d is the depth of the groove. From this we deduce that

$$d = r_o \left\{1 - \exp\left[-\left(\frac{V_c}{V_o} - 1\right)\frac{\Delta}{2r_o}\right]\right\} \tag{27}$$

A further consideration is necessary if the groove has a finite width, h, since the probe reading when straddling the crack will include a contribution from the length h in which the axial electric field is enhanced in the ratio r_o/r_i. From this we deduce

$$d = r_o \left\{1 - \exp\left[-\frac{\Delta}{2r_o}\left(\frac{V_c}{V_o} - 1 - \frac{dh}{\Delta(r_o - d)}\right)\right]\right\} \tag{28}$$

which may be solved by an iterative procedure. Equation 28 can be used to calculate the notch (crack) depth and should give a more accurate answer than the one-dimensional solution given earlier.

In order to check this analysis an experiment was conducted on a steel bar of 37 mm diameter and 262 mm length. A circumferential groove was machined into the bar and the values of V_c, V_o, and d recorded. This was repeated several times for different values of d and the results are shown in Fig. 19. It can be seen that the one-dimensional solution overestimates the depth while Eq 28 produces an answer within 10 percent irrespective of the value of d. The elongator roll does not have a uniformly decreasing net section at all points, but if one assumes an average crack depth of about 30 mm this theory suggests that using a one-dimensional interpretation would lead to an overestimate of about 11 percent. If one used the two-dimensional interpretation of the field measurements, represented by Eq 28, and took into account the orientation of the crack, the discrepancy between the predicted and measured crack depths would be considerably reduced.

Monitoring of Fatigue Cracks

A slightly different application for the a-c technique is that of continuous monitoring of fatigue or stress-corrosion cracks in the laboratory. This version is being developed by Instron Ltd. so that it can be incorporated into their test systems. Some of their results are included here [7].

The commonest type of fatigue or fracture specimen is the compact-tension specimen; fatigue tests have been conducted on this type of specimen using both steel and aluminum. Figure 20 shows some typical results for the steel specimen. It can be seen that the scatter is extremely small and that linearity is excellent. It should be noted that the crack length was determined optically, and that the very small scatter is quite probably due to difficulties

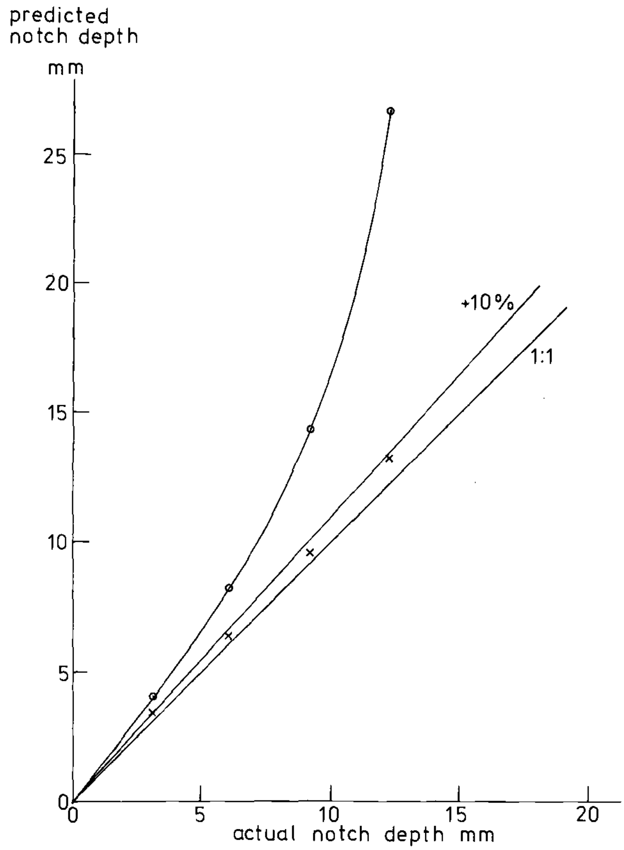

FIG. 19—*Predicted depth of a circumferential groove in a round bar;* O, *one-dimensional interpretation;* X, *two-dimensional interpretation; (see Eq 28).*

with optical measurements rather than the a-c instrument. The reproducibility found in these tests and the complexity of the field suggest that a calibration technique would be most suitable for compact-tension specimens, but for other specimen forms this would not be desirable or possible. Figures 21 and 22 show two more crack-growth curves for a T-butt weld specimen and a surface-cracked specimen. Calibration of these specimens would be very difficult and instead the modifying factors described in the section on ACFM theory were used. These specimen forms were much closer to the in-service conditions and can correctly match the interaction effects expected in corrosion fatigue and random-load fatigue. Now that cracks of this shape can be accurately monitored, these types of specimen will become more widely adopted and prove to be very useful in providing the information needed for service-life prediction.

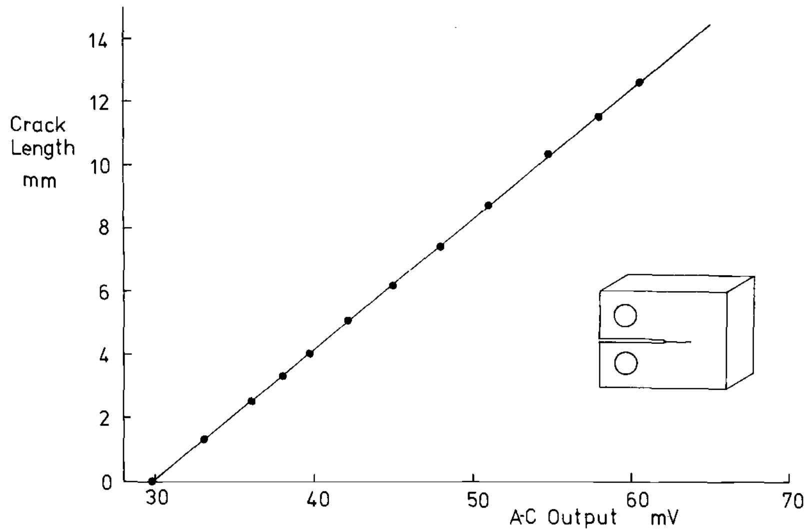

FIG. 20—*Fatigue-crack growth data recorded during a fatigue test on a compact-tension specimen made from steel.*

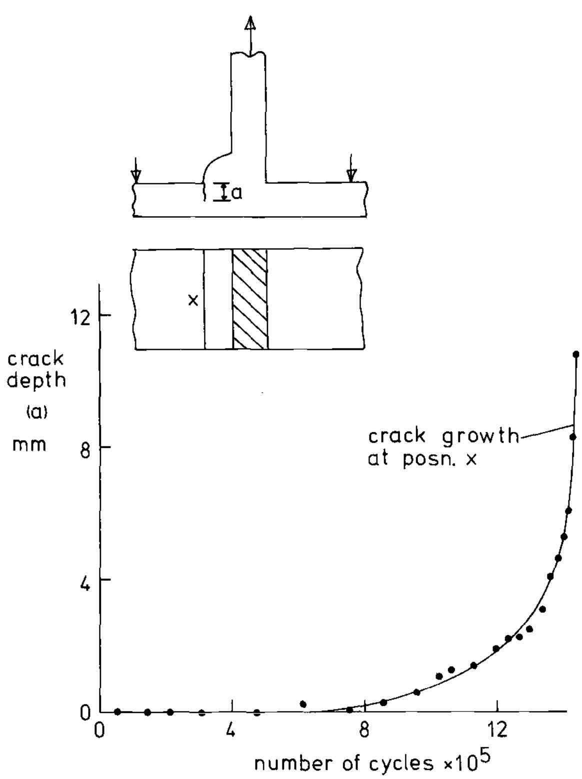

FIG. 21—*Fatigue-crack monitoring of a T-butt weld specimen.*

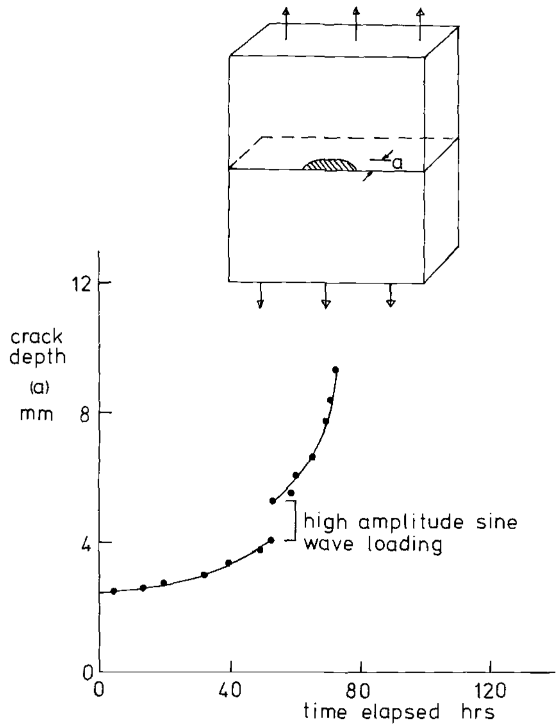

FIG. 22—*Fatigue-crack monitoring of a surface-cracked specimen.*

Conclusions

1. A new electronic instrument for making a-c field measurements has been described and shown to be suitable for predicting crack depths of surface cracks found in structures in service.
2. It has been shown that for uniform fields and circular-arc or semielliptical cracks no prior calibration of the instrument is needed in order to predict the crack depth.
3. The theoretical solution for the a-c field around a circular-arc crack has been derived.
4. The instrument can be used on any conducting material or geometry, and the accuracy of the predicted crack depth is generally on the order of 10 percent.
5. The instrument can also be used for crack detection even where the crack depth is less than 0.5 mm.
6. Growing fatigue cracks can be monitored successfully using ACFM.

References

[1] Dover, W. D., Charlesworth, F. D. W., and Taylor, K. A., "Crack measurement using the a-c resistance technique," U.K. patent application.
[2] Michael, D. H. and Collins, R., "The assessment of crack depth from measurements of the electrical potential field on metal surfaces," Internal Report UIC/Tech 2005, Unit Inspection Co., Swansea, U.K.
[3] Williams, P., *Electronic Letters*, Vol. 6, No. 6, March 1970, pp. 186–187.
[4] Bleaney, B. I. and Bleaney, B. *Electricity and Magnetism*, Oxford University Press, Third ed., 1976.
[5] Milne-Thomson, L. M., *Theoretical Hydrodynamics*, 4th ed., Macmillan, London, 1962, p. 172.
[6] Rogers, L. M., Hansen, J. P., and Webborn, T. J. C., "Acoustic emission during the fatigue testing of tubular welded joints of BS 4360-50 D," Technical Report ATP 3/2, Unit Inspection Co., 1979.
[7] Private communication, Instron Ltd., High Wycombe, Bucks., U.K.

R. E. Beissner,[1] *C. M. Teller,*[1] *G. L. Burkhardt,*[1] *R. T. Smith,*[1] *and J. R. Barton*[1]

Detection and Analysis of Electric-Current Perturbation Caused by Defects

REFERENCE: Beissner, R. E., Teller, C. M., Burkhardt, G. L., Smith, R. T., and Barton, J. R., "**Detection and Analysis of Electric-Current Perturbation Caused by Defects,**" *Eddy-Current Characterization of Materials and Structures, ASTM STP 722,* George Birnbaum and George Free, Eds., American Society for Testing and Materials, 1981, pp. 428–446.

ABSTRACT: The electric-current perturbation technique consists of establishing an electric-current flow in the material to be examined and then detecting localized perturbations of this current flow at inhomogeneities such as inclusions or cracks. The current perturbation is sensed by using a small noncontacting probe to detect the associated magnetic-flux perturbation at the surface of the specimen. In the work reported here, analysis of the electric-current perturbation signals was based on an analytic solution for the change in current density caused by a slot of infinite length and finite depth. Comparisons were made with experimental data for electric-discharge machining (EDM) slots of various depths in Incoloy 901 where the electric current was introduced by ohmic contact. Excellent agreement between theory and experiment was obtained for deep slots, although the model predicts a more rapid decrease in signal amplitude with decreasing slot depth than is experimentally observed. Additional measurements made with fatigue cracks show that cracks as small as 0.45 mm in length are easily detected. It was concluded that the technique is not only a sensitive method for flaw detection, but also offers the possibility of determining flaw characteristics through analysis of signal shapes and amplitudes.

KEY WORDS: electromagnetic testing, nondestructive tests, surface defects, fatigue cracks

The purpose of this paper is to present the results of recent experimental and analytical research pertaining to the detection and characterization of notches and fatigue cracks by the electric-current perturbation (ECP)

[1]Staff scientist, Southwest Research Institute, San Antonio, Tex. 78284.

method.[2,3] The experimental measurements, which will be described first, were intended to provide preliminary data on the sensitivity of the method in the detection of small fatigue cracks while at the same time providing a basis for judging the adequacy of analytical models of the ECP process. The analytical phase involved the development of a simple mathematical expression for the change in flux density associated with a cracklike defect and comparisons with experiment. This phase of the work was intended as a first step in the development of methods for relating ECP signal characteristics to crack geometry.

The principle on which the ECP method is based is illustrated in Fig. 1. The drawing on the left represents a specimen with no flaw in which there exists an unperturbed current density $\vec{j}_0$ and a corresponding magnetic flux density $\vec{B}_0$, just above the surface of the specimen. When a flaw is introduced, the distribution of current density is perturbed, as indicated on the right side of Fig.1, and the flux density changes from $\vec{B}_0$ to $\vec{B}_0 + \Delta\vec{B}$. The ECP method consists of measuring $\Delta\vec{B}$ as a function of position and, ultimately, relating the resulting signal to flaw geometry.

Experimental Method and Results

The apparatus used in one set of experiments is shown in Fig. 2. In this case, the specimens were small disks fabricated from the iron-nickel base superalloy, Incoloy 901, and slots of various sizes were produced in the surface to be inspected by electric-discharge machining (EDM). Current was injected directly into the specimen through contacts on opposite sides of the

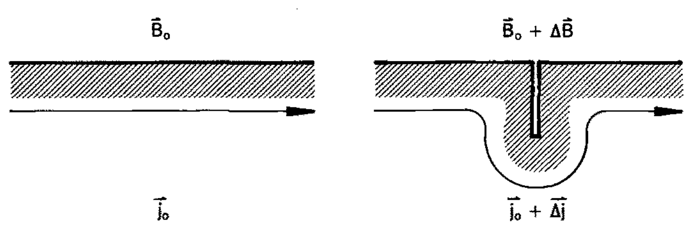

FIG. 1—*Electric-current perturbation principle.*

[2]Kusenberger, F. N., Francis, P. H., Leonard, B. E., and Barton, J. R., "Nondestructive Evaluation of Metal Fatigue," AFOSR 69-1429TR, 1969. (Available from Defense Documentation Center to qualified requestors as AD 688 892; available to the public from Clearinghouse for Federal Scientific and Technical Information.)

[3]Gardner, C. G. and Barton, J. R., "Recent Advances in Magnetic Field Methods of Nondestructive Evaluation for Aerospace Applications," *Proceedings*, Advisory Group for Aerospace Research and Development Conference, No. 64 on Advanced Technology for Production of Aerospace Engines, 1970, pp. 18-1-18-9. Available from National Technical Information Service, Springfield, Va.

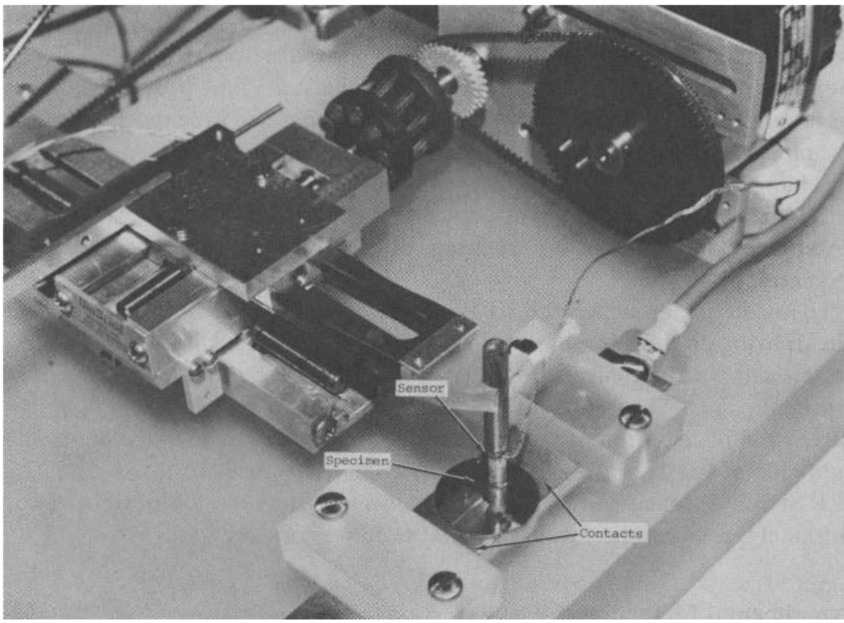

FIG. 2—*Experimental apparatus.*

disk. Frequencies were in the range of 1 to 100 kHz; the skin depths at these frequencies are 17 to 1.7 mm, much greater than the depths of the EDM slots.

Because the unperturbed current density produced a strong, but slowly varying, magnetic field in the region to be inspected, a differential sensor arrangement was used to enhance the signal caused by the defect. The sensor consisted of two magnetometers separated by a small distance, and the signal recorded was the difference in output signals of the two sensors.

A schematic illustration of the differential sensor and slot geometry is presented in Fig. 3. For all of the measurements reported here, the magnetometers were oriented as shown in this figure so as to measure the x component of the field. The unperturbed current density was in the x direction, normal to the plane of the slot, and most scans were made in the x direction at various values of z. The y position of the center of the sensor, the liftoff distance, was 0.43 mm.

The signal recorded with this arrangement is proportional to the difference in the flux-density perturbations at the sensor positions if the unperturbed flux density varies by a negligible amount over the distance between sensors. This is because the signal produced by the unperturbed field then cancels when signals are subtracted.

Figure 4 shows data typical of those obtained from cracklike defects.

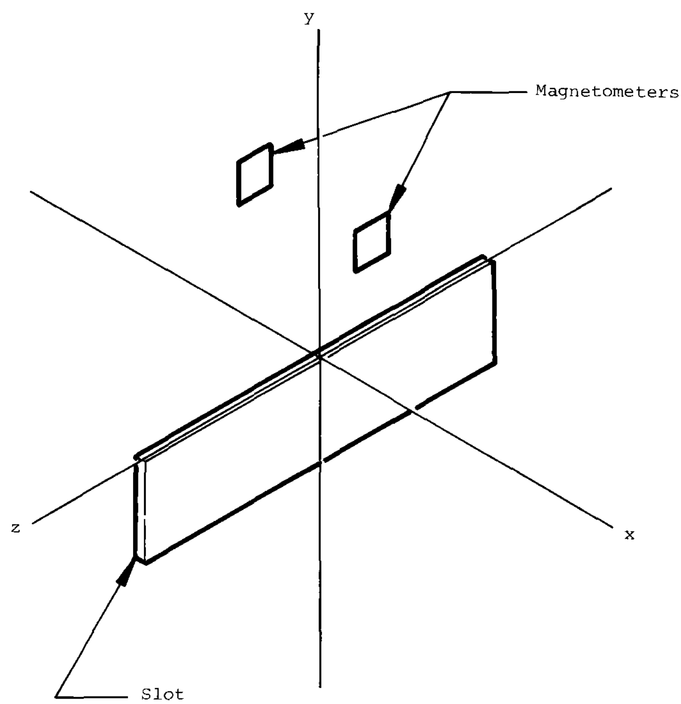

FIG. 3—*Schematic illustration of magnetometer arrangement.*

These are plots of the differential signal generated by scanning across an EDM slot 0.48 mm long by 0.40 mm deep with a surface opening width of 0.15 mm. The numbers on each curve are the distances from the approximate center of the slot to the scan line.

Two features are worthy of note at this point. The first is that the flux-density perturbation can be detected at positions well beyond the extremities of the slot, and the second is that the polarity of the signal is reversed as the scan position is moved from one end of the slot to the other. Thus, the scan at $z = 0.5$ mm, for example, shows a negative peak followed by a positive peak while the signal at $z = -0.5$ mm is first positive and then negative. Further examples of this signal sequence are provided by ECP data for fatigue cracks, some of which will be presented next.

Specimens used for initial fatigue-crack studies were tiebolt-hole segments from a third stage TF-33 gas-turbine engine disk (Incoloy 901). One such specimen is shown in Fig. 5. Fatigue cracks were observed in several of the specimens by optical microscopy. In general, the cracks were oriented approximately along the axis of the tiebolt hole although there was some branching at angles to the hole axis. Surface lengths of the cracks varied from approximately 0.5 to 2.0 mm.

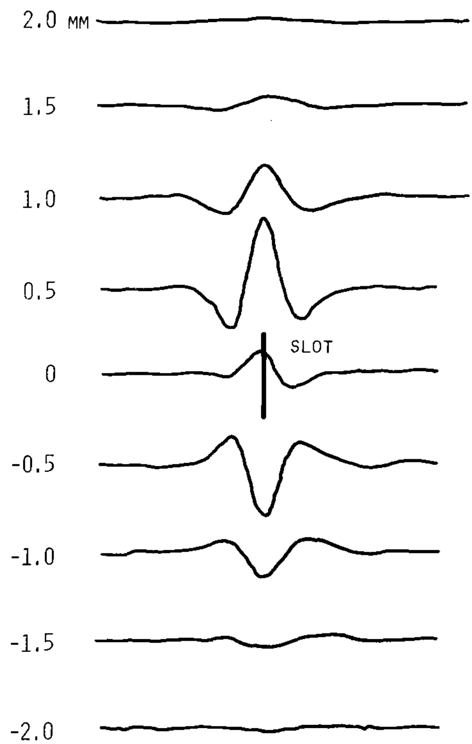

FIG. 4—*Map of an EDM slot.*

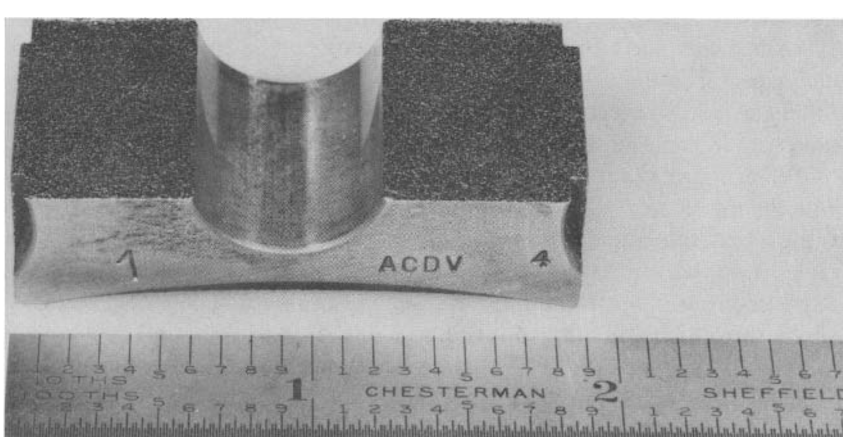

FIG. 5—*Tiebolt hole segment from a TF-33 jet-engine turbine disk (Incoloy 901).*

Figure 6 is a plot of data obtained from one of the larger fatigue cracks. The ECP "map" of the flux-density perturbation is, in general, similar to that for EDM notches, although the irregular path of the crack causes a significant asymmetry in the signal.

Figure 7 is a preliminary result for a much smaller crack, in this case about 0.45 mm in length. A more careful mapping of the field associated with this crack is planned, and these results are, therefore, presented only as evidence that small cracks are easily detected.

Finally, Fig. 8 shows signals obtained from a tiebolt hole in an actual retired gas-turbine aircraft-engine disk (TF 33, third stage) containing several small, low-cycle fatigue cracks, along with a scanning electron microscope (SEM) photomicrograph of the area inspected. The major peak

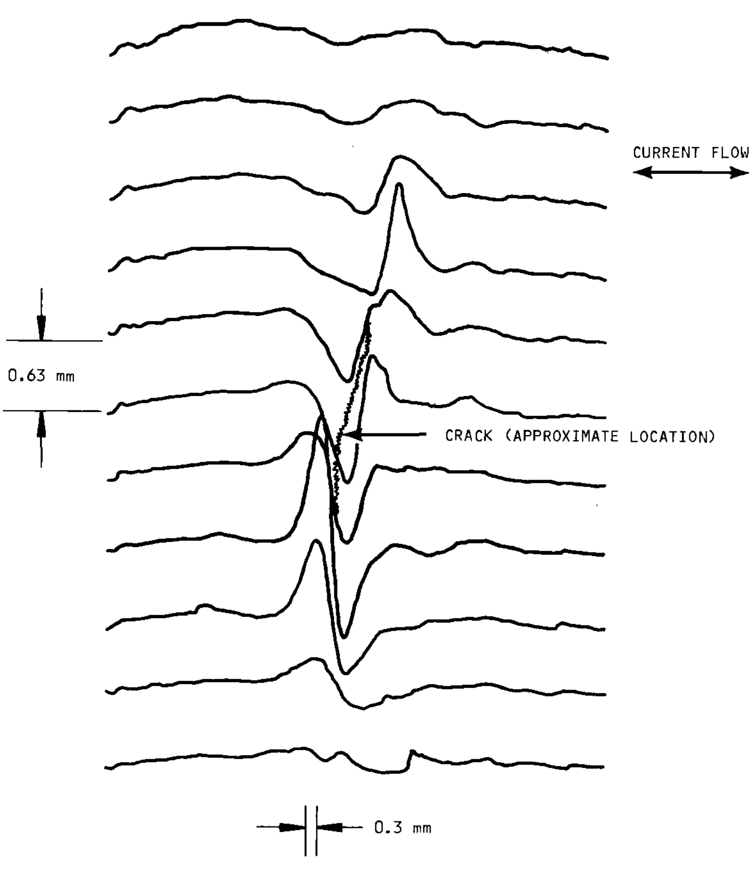

FIG. 6—*Electric-current perturbation signals from a 1.8-mm fatigue crack.*

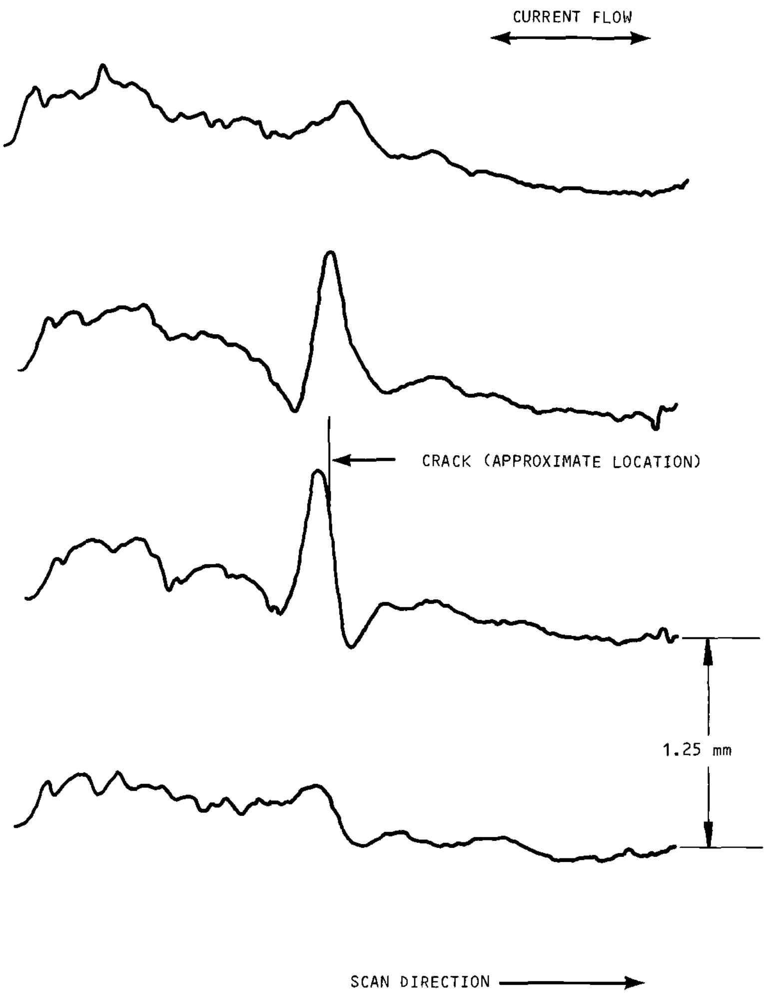

FIG. 7—*Electric-current perturbation signals from a 0.45-mm fatigue crack.*

in the upper trace, which corresponds to a scan line above the upper end of the crack near the top center of the photograph, is negative, while the major peak in the third trace, well below the lower end of this crack, is positive. This positive signal polarity persists in scans across the lower part of the area although there is a tendency toward another polarity reversal in the scan shown at the bottom of the figure.

Comparison of this sequence of signals with similar maps of larger, isolated EDM slots and fatigue cracks (Figs. 4 and 6) shows that in the present case the spatial dependence of the peak structure is more complex. While it is not yet possible to unambiguously associate certain features of this

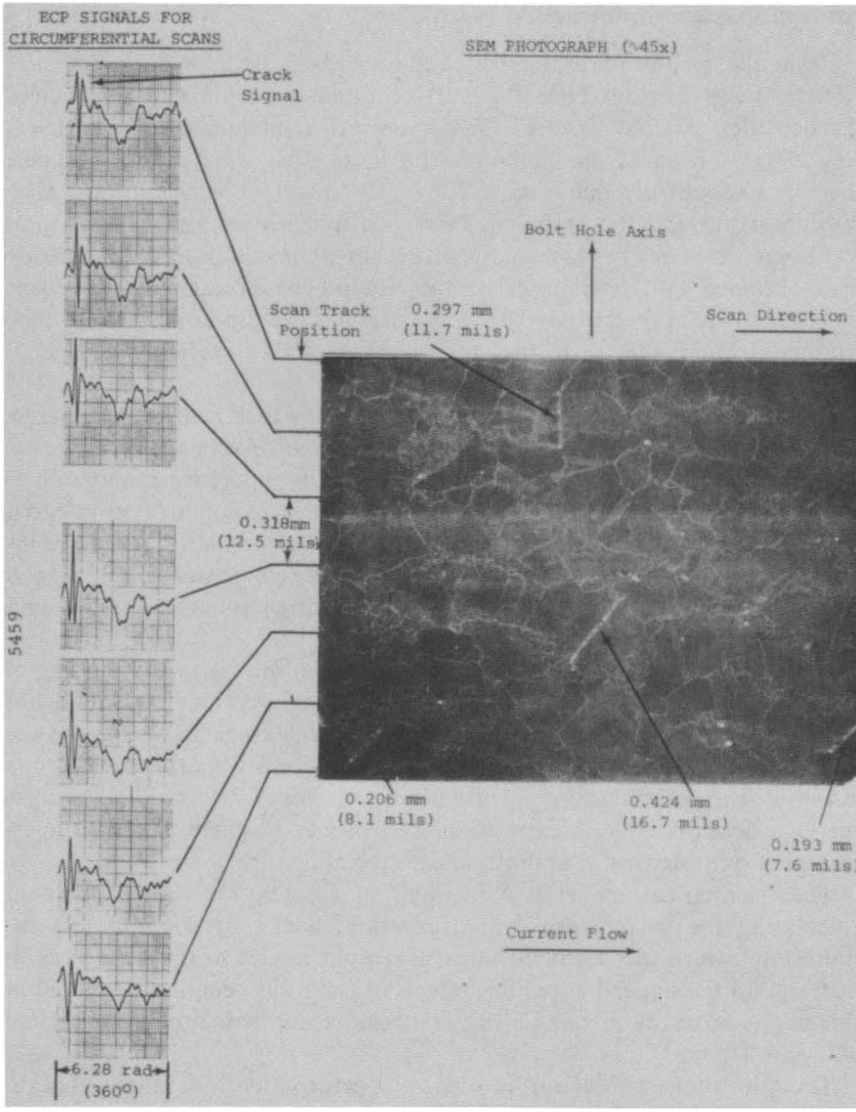

FIG. 8—*Electric-current perturbation signals from an area containing several small fatigue cracks.*

sequence of signals with the presence of multiple cracks, it is encouraging to note that there are very pronounced qualitative differences in the signal structures of single-crack and multiple-crack data. This suggests that, with further development, the ECP method may be capable of distinguishing relatively large, isolated cracks from smaller, closely spaced cracks.

An Approximate Mathematical Model

From the results of exploratory experiments like those described previously, it was concluded that the ECP technique is a promising approach to the detection of small cracks in materials with moderate-to-high electrical conductivity. Because the method is still in an early stage of development, there is undoubtedly much room for improvement in sensitivity and flaw resolution through the optimization of instrumentation and experimental technique. Even so, the fact that good sensitivity to small flaws has already been obtained with available laboratory equipment indicates that excellent flaw sensitivity is realizable. The next question, therefore, pertains to flaw characterization, that is, to the determination of flaw geometry from ECP signal characteristics.

Even at this early stage in the development of the ECP method, there are a number of indications that there are strong correlations among signal characteristics and crack geometry. From Figs. 6 and 7, for example, it is evident that the spatial extent of the ECP signal is closely related to crack length, as one would expect. Figure 6 also provides an indication of the influence of crack geometry on the symmetry of the signal, and, finally, Fig. 8 illustrates how multiple-crack signal sequences differ from those for isolated cracks.

As a first step towards developing a better quantitative understanding of such relationships, an attempt was made to develop an analytical model of the ECP process. In this initial effort an idealized crack geometry was assumed to keep the mathematics as simple as possible while still retaining the essential features of current perturbation by a planar defect. Also, because the skin depth is large in cases of interest, it was assumed that the unperturbed current density is uniform and constant in time.

The geometrical model is illustrated in Fig. 9. For the purpose of calculating the current-density perturbation, a slot of depth d and infinitesimal width was assumed to exist at right angles to the surface as illustrated in the upper figure. The effects of finite slot length are ignored at this stage so that the current perturbation can be approximated by a function of x and y only.

This two-dimensional current-density perturbation was then used to calculate an approximate change in magnetic flux density by integrating over a slot of length l as indicated in the lower figure.

The method of complex potentials[4,5] was used to calculate the current-density perturbation $\Delta\vec{j}(x,y)$. Briefly, this amounts to finding a complex analytic function

[4] Panofsky, W. K. H. and Phillips, M., *Classical Electricity and Magnetism*, Addison-Wesley, Reading, Mass., 1955.

[5] Binns, K. J. and Lawrenson, P. J., *Analysis and Computation of Electric and Magnetic Field Problems*, Pergamon, New York, 1973.

$$W(\omega) = \phi(\omega) + i\psi(\omega)$$

that satisfies appropriate boundary conditions on the surface of the conducting medium. Here ω is the complex variable

$$\omega = x + iy$$

where x and y are the coordinates shown in Fig. 9. Because $W(\omega)$ is analytic, it can be shown that the family of curves

$$\phi(\omega) = \text{constant}$$

can be interpreted as curves of constant potential, while family of curves

$$\psi(\omega) = \text{constant}$$

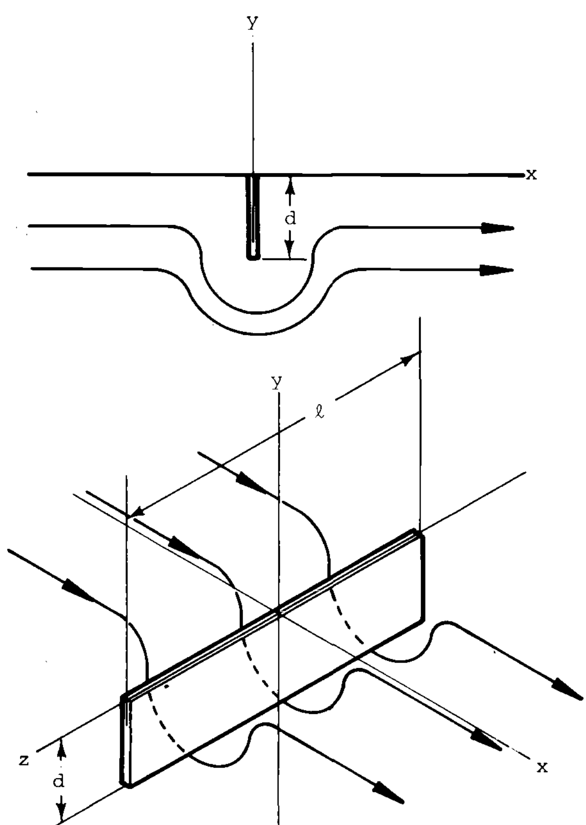

FIG. 9—*Geometry for the calculation of electric-current perturbation signals.*

which are orthogonal to the equipotential curves, can be interpreted as electric-field lines. It can be also shown that the components of the electric field strength can be expressed in terms of $W(\omega)$ as

$$E_x = -\mathrm{Re}\frac{dW}{d\omega}$$

$$E_y = \mathrm{Im}\frac{dW}{d\omega}$$

where Re and Im stand for the real and imaginary parts, respectively. Because the change in current density caused by the slot is equal to the conductivity multiplied by the change in field strength, calculation of $W(\omega)$ with and without the slot determines the change in current density.

From the theory of complex potentials we know that if one can find a transformation of variables that maps the geometry of the problem of interest into a simpler geometry, then the solution for W in the case of interest is determined by first finding W in the simpler geometry and then substituting the inverse transformation of variables. In the present case, the transformation is that illustrated in Fig. 10.[5] With this change of variables the boundary in the ω_2 plane, which is the real axis, is mapped into the real axis with a cut of length d along the negative imaginary axis of the ω_1 plane, and all points in the upper half of the ω_2 plane are mapped into points in the lower half of the ω_1 plane.

The complex potential for a uniform field $\vec{E}_0$ in the positive x-direction in the ω_2 plane is

$$W(\omega_2) = -E_0\omega_2$$

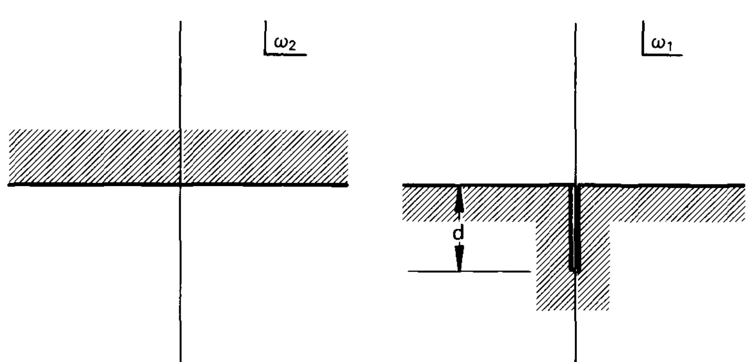

$\omega_1 = d\sqrt{(\omega_2^*)^2 - 1}$

FIG. 10—*Complex-variable transformation.*

The potential in the ω_1 plane obtained by substituting the inverse transformation is

$$W(\omega_1) = -E_\infty \sqrt{(\omega_1{}^*)^2 + d^2}$$

where E_∞ is the field strength at large distances from the perturbing slot. This determines the electric field and current density in the ω_1 plane. If the unperturbed current density is subtracted, the resulting expressions for the changes in the x and y components of the current density are

$$\Delta j_x = j_0 \operatorname{Re}\left[\frac{\omega_1{}^*}{\sqrt{(\omega_1{}^*)^2 + d^2}} - 1\right] \tag{1}$$

$$\Delta j_y = -j_0 \operatorname{Im}\frac{\omega_1{}^*}{\sqrt{(\omega_1{}^*)^2 + d^2}} \tag{2}$$

where j_0 is the unperturbed current density. An alternative form of this solution is the following expression for the streamlines of current-density change

$$\operatorname{Im}[\sqrt{(\omega_1{}^*)^2 + d^2} - \omega_1{}^*] = -\frac{\Delta j_i}{j_0} = -C_i$$

The parameter, C_i, on the right side is the fractional change in current density caused by the slot; each value of this parameter determines a curve of constant current-density change. The current per unit length normal to the ω_1 plane that flows between two curves Δj_i and Δj_{i+1} is $\Delta j_{i+1} - \Delta j_i$.[4] A contour plot of the streamline function for various values of C_i, therefore, provides a useful visual display of the changes in current flow caused by the slot.

Figure 11 shows this streamline function in terms of the dimensionless coordinates x/d and y/d and the fractional current density changes C_i. The important point illustrated here is that the change in current density caused by the slot is highly concentrated at the tip of the slot. This result will prove useful in developing an approximate expression for the corresponding change in the magnetic field.

The geometry for the calculation of the flux density change is illustrated in Fig. 12. The surface of the material is the x-z plane and the slot lies in the y-z plane. The unperturbed current density is directed along the positive x axis.

The change in the vector potential caused by the slot is

$$\Delta\vec{A}(\vec{r}) = \frac{\mu_0}{4\pi}\int \frac{\Delta\vec{j}(\vec{r}\,')}{|\vec{r} - \vec{r}\,'|}\, d^3r\,'$$

The vector $\vec{r}\,'$ from the origin to a general point inside the material can be written

$$\vec{r}' = \vec{z}' + \vec{d} + \vec{\rho}$$

where $\vec{z}'$ is the displacement along the z axis, $\vec{d}$ is the constant vector from the x-z plane to the tip of the slot and $\vec{\rho}$ is a vector in the x-y plane. Because the current density change is highly localized at the tip of the slot, $\Delta\vec{j}(\vec{r}')$ is negligible for large values of $\vec{\rho}$. If the distance from the tip of the slot to $\vec{r}$ is large compared to values of $\vec{\rho}$ for which $\Delta\vec{j}$ is significant, then

$$\frac{1}{|\vec{r} - \vec{r}'|} \sim \frac{1}{|\vec{r} - \vec{z}' - \vec{d}|} + \frac{(\vec{r} - \vec{z}' - \vec{d})\cdot\vec{\rho}}{|\vec{r} - \vec{z}' - \vec{d}|^3} \tag{3}$$

Because $|\vec{r} - \vec{z}' - \vec{d}| \geq d$ this approximation involves less error for large d (deep slots) than for small d. If it is further assumed that the z dependence of $\Delta\vec{j}$ can be ignored (that is, end effects are negligible) then the integral of the first term vanishes because $\Delta\vec{j}$ forms closed loops (see Fig. 11). This leaves

$$\Delta\vec{A}(\vec{r}) = \frac{\mu_0}{4\pi}\int \vec{F}(\vec{r})\cdot\vec{\rho}\Delta\vec{j}(\vec{\rho})d^2\rho$$

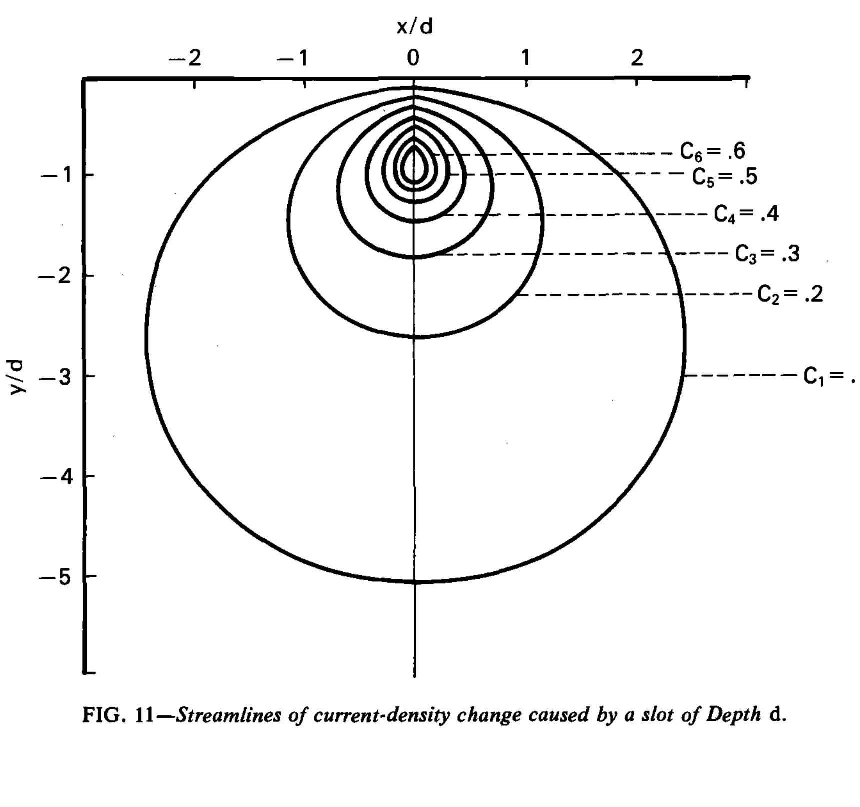

FIG. 11—*Streamlines of current-density change caused by a slot of Depth* d.

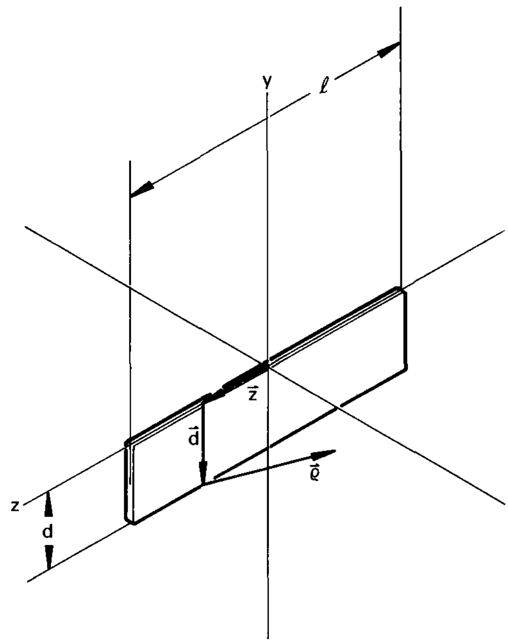

FIG. 12—*Detailed geometry for flux-density calculation.*

where

$$\vec{F}(\vec{r}) = \int_{-l/2}^{l/2} \frac{\vec{r} - \vec{z}\,' - \vec{d}}{|\vec{r} - \vec{z}\,' - \vec{d}\,|^3} dz\,'$$

and $d^2\rho$ is an element of area in the x-y plane. By means of vector manipulations similar to those outlined by Panofsky and Phillips,[6] the following form is obtained

$$\Delta\vec{A}(\vec{r}) = \vec{M} \times \vec{F}(\vec{r})$$

where

$$\vec{M} = \frac{\mu_0}{8\pi} \int \vec{\rho} \times \Delta\vec{j}(\vec{\rho}) d^2\rho$$

Because both $\vec{\rho}$ and $\Delta\vec{j}$ are parallel to the x-y plane, only the z component of $\vec{M}$ is nonvanishing. If the integral for M_z is written in terms of the dimen-

[6]Panofsky, W. K. H. and Phillips, M., *Classical Electricity and Magnetism*, Addison-Wesley, Reading, Mass., 1955, p. 120.

sionless variables $\xi = x/d$ and $\eta = y/d$, with Δj_x and Δj_y given by Eqs 1 and 2, then it is easily seen that

$$M_z = M_0 d^3 \tag{4}$$

where M_0 is a constant that depends only on the unperturbed current density.

The remainder of the calculation, which involves the evaluation of the integral that determines the components of $\vec{F}(\vec{r})$ and calculation of the curl of $\Delta\vec{A}$, is straightforward. The resulting expressions for the components of the change in flux density caused by the slot are as follows

$$\Delta B_x(\vec{r}) = xM_z[f(x,y,z - l/2) - f(x,y,z + l/2)] \tag{5}$$

$$\Delta B_y(\vec{r}) = (y + d)M_z[f(x,y,z - l/2) - f(x,y,z + l/2)] \tag{6}$$

$$\Delta B_z(\vec{r}) = M_z[(z - l/2)f(x,y,z - l/2) - (z + l/2)f(x,y,z + l/2)] \tag{7}$$

where

$$f(x, y, z) = [x^2 + (y + d)^2 + z^2]^{-3/2}$$

Comparison with Experiment

To assess the usefulness of this simple model, Eqs 5 to 7 were used to calculate the differential flux-density perturbation for comparison with experimental data for EDM slots. One such comparison is shown in Fig. 13. These data are the x-component of the differential field produced by an EDM slot 0.48 mm long by 0.40 mm deep by 0.15 mm wide. The scan direction in this case is along the z-axis of Fig. 3.

To determine the value of the constant M_0 defined by Eq 4, the calculated curve was normalized to the experimental trace at the position of the largest positive peak. This value of M_0 was then used in all subsequent calculations.

As can be seen from this comparison, the calculated distance between the larger peaks agrees almost exactly with the experimental result. However, the theoretical curve fails to account for the secondary peaks that are observed in the experimental data, immediately adjacent to the larger peaks. It is possible that the secondary peaks are an artifact of the signal-processing method used to suppress the strong unperturbed field gradient in this particular experiment. On the other hand, if the disagreement in signal shape is attributed to the theoretical model, then the failure of the model is probably caused by the dipole approximation (Eq 3) used in the derivation. This is because the calculated curve is typical of dipolar fields, and the extra structure in the experimental curve is therefore indicative of higher-order effects. There are, however, other possible reasons for the disagreement shown here

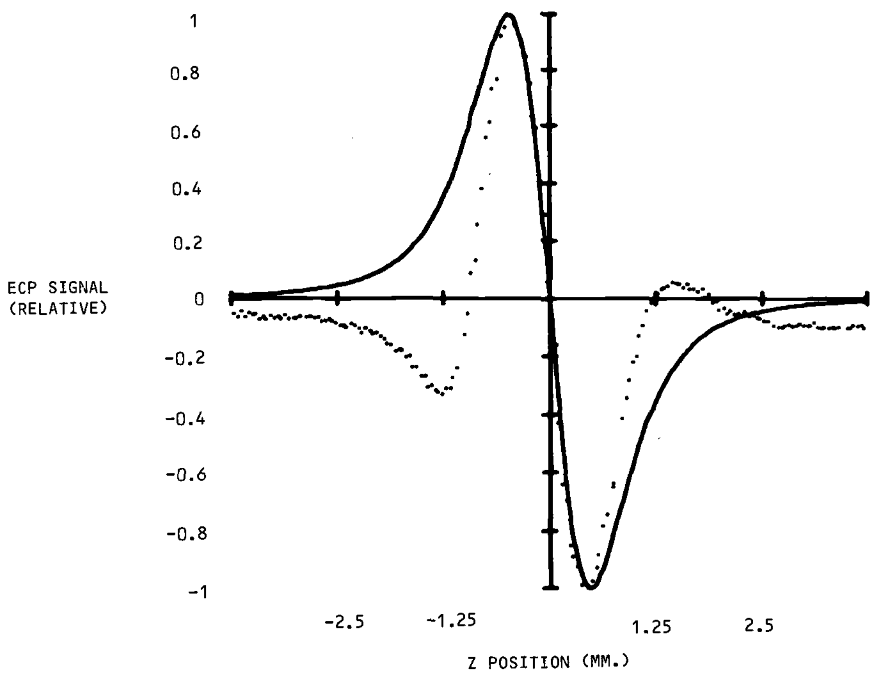

FIG. 13—*Calculated and measured flux-density changes along an EDM slot.*

including the assumption of uniform unperturbed current density and negligible slot width.

Figure 14 is a plot of calculated and measured peak-to-peak amplitudes obtained from x-direction scans at various z positions along the slot, normalized to unity at the center of the slot. In this case agreement is excellent, indicating that the model does correctly account for variations in the amplitudes of the major peaks as a function of position. This, in turn, tends to support the assumption that the effects of finite slot length on the current distribution can be neglected except near the ends of the slot.

A similar plot is shown in Fig. 15 for a slot of approximately the same length but roughly one fourth as deep. The normalization factors for the experimental and calculated data shown here were the same as those used in Fig. 14. Thus, the fact that calculated amplitudes are much smaller than the experimental values shows that the model fails to account for the observed depth dependence of signal amplitude. Another such comparison for a smaller slot shows much the same trend and will not be presented here.

This deficiency in the model is illustrated in another way in Fig. 16. Here the data are peak-to-peak amplitudes as a function of the area of the slot. The experimental data reported here, as well as earlier unpublished data, show an approximately linear dependence of amplitude on flaw area alone,

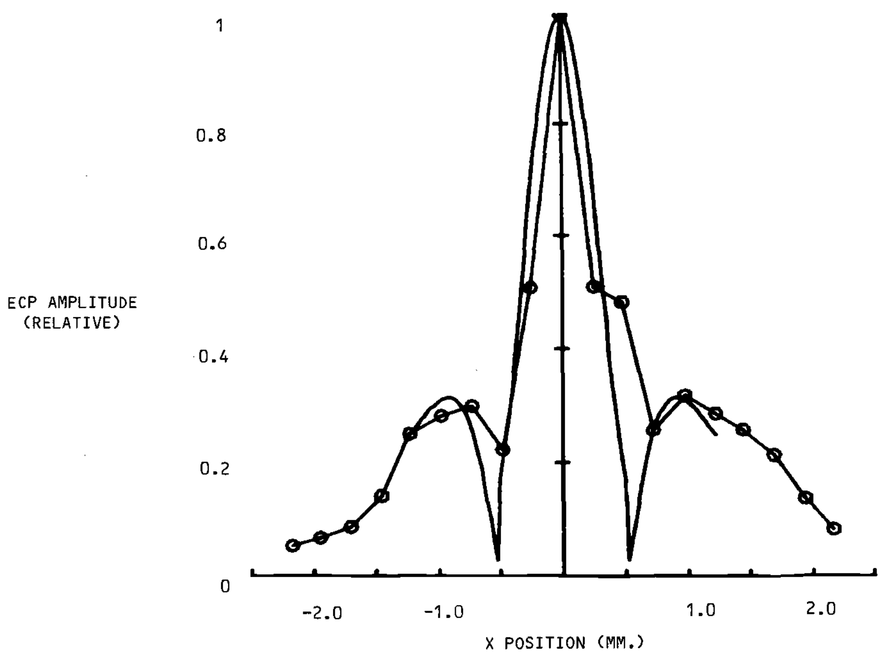

FIG. 14—*Calculated and measured peak amplitudes as a function of distance from a 0.4-mm-deep EDM slot.*

and the solid line in Fig. 16 is an approximation to this empirical relationship. The theoretical model, on the other hand, shows a more complicated dependence on slot length and width, as evidenced by the family of calculated curves presented here. Once again, one might suspect that the failure of the dipole approximation is responsible for the disagreement with experiment, in this case because the approximation is expected to become less reliable with decreasing slot depth and agreement with experiment does indeed worsen as the slot depth becomes smaller. Still, the effects of the dipole and other approximations employed in the development of the model have not yet been investigated in detail, and reasons why the model fails, therefore, remain an open question.

Conclusion

The principal conclusion drawn from this work is that the ECP method shows considerable promise as a sensitive technique for detecting and, eventually, characterizing small, cracklike defects. The signal amplitudes observed in exploratory measurements were, in fact, surprisingly large, especially in view of the fact that no attempt was made to optimize the experimental equipment or technique. The observed dependence of signal-

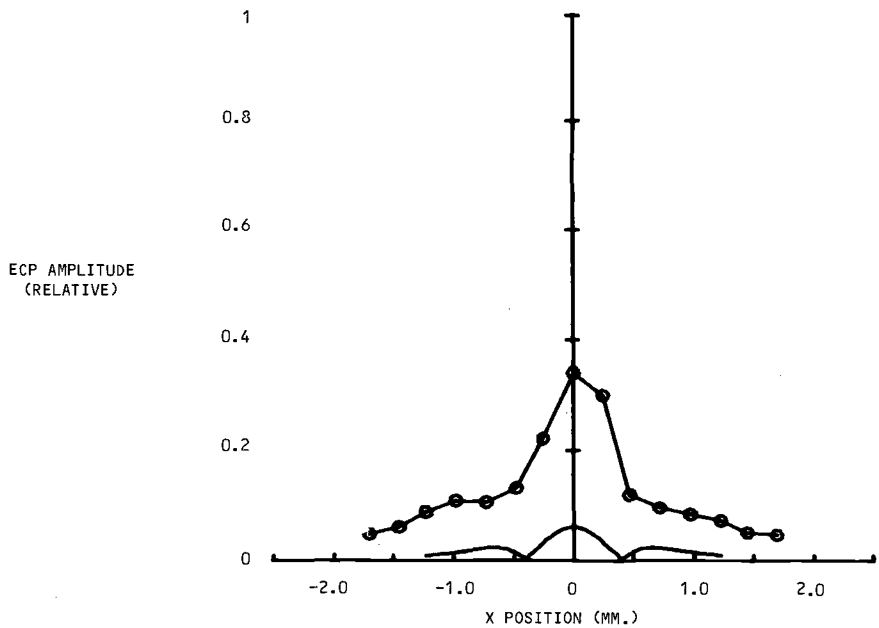

FIG. 15—*Calculated and measured peak amplitudes as a function of distance from a 0.1-mm-deep EDM slot.*

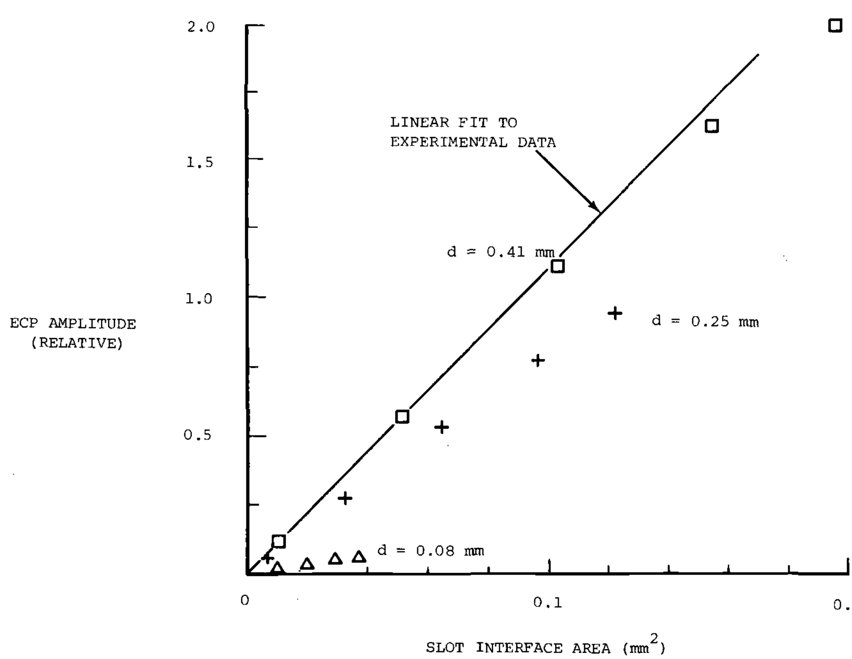

FIG. 16—*Calculated and measured peak amplitude as a function of slot area.*

shape characteristics on crack and slot geometry is also encouraging, as this dependence suggests that one might hope to derive quantitative flaw-geometry information from analyses of ECP signals. On the theoretical side, however, it is evident from the comparisons between theory and experiment presented here, that improvements in the existing theoretical model are needed before theory can be used in the quantitative interpretation of signals from unknown flaws. Nevertheless, it is encouraging to note that even this very simple model provided qualitative agreement with most experimental results. There is, therefore, reason to anticipate that an adequate theory of ECP signal analysis is mathematically tractable. Successful development of the analysis could not only aid in flaw characterization, but could also provide guidance for optimizing the ECP method.

Acknowledgments

The authors are pleased to acknowledge the able assistance of Tom Doss and Ron McInnis in the experimental work reported here. Partial support was provided by the Air Force Materials Laboratory.

Automation, Data Analysis, and Display

J. M. Feil[1]

Eddy-Current Testing of Thin Nonferromagnetic Plate and Sheet Materials Using a Facsimile-Recording Data Display Method

REFERENCE: Feil, J. M., **"Eddy-Current Testing of Thin Nonferromagnetic Plate and Sheet Materials Using a Facsimile-Recording Data Display Method,"** *Eddy-Current Characterization of Materials and Structures, ASTM STP 722,* George Birnbaum and George Free, Eds., American Society for Testing and Materials, 1981, pp. 449–463.

ABSTRACT: The wide-spread use of eddy-current testing of thin flat plates or sheet materials has been hampered by the difficulty of test signal interpretation and the problem of locating the discontinuity when the test has been completed. These drawbacks could be reduced by a simple facsimile-recording system that displays the test-signal amplitude changes as changes in the darkness of the facsimile recording. The interpretation of the facsimile recording is very similar to the interpretation of standard radiographic films or ultrasonic C-scan data. The location of the discontinuity on the specimen is directly related to the discontinuity indication on the facsimile recording, again analogous both to radiography and ultrasonic C-scan. This technique of data presentation also allows for the differentiation between discontinuities that extend through the full thickness of the specimen and the discontinuities that extend only partially through the full thickness. Small-diameter discontinuities can be also detected and displayed by this system.

KEY WORDS: eddy current nondestructive testing, facsimile recording, test automation, nonferromagnetic materials

Eddy-current inspection has several major advantages over other nondestructive testing (NDT) methods for the rapid automatic inspection of thin flat plates or sheets: (*1*) eddy-current inspection is a noncontact inspection method in comparison with ultrasonic inspection, (*2*) it does not require special facilities, such as radiography does, (*3*) there is no residual material, such as liquid penetrant developer, left on the material being inspected, and (*4*) eddy-current inspection may be done continuously over a large area. The limitations of the eddy-current inspection technique that have been the most restrictive to the wide-spread application of the test technique for flat plate and sheet have been (*1*) the difficulty of interpreting the test signal, (*2*) de-

[1]NDE Level III test examiner and welding engineer, United Engineers and Constructors, Inc., Philadelphia, Pa. 19101.

fining the discontinuity, and (*3*) determining the exact location of the discontinuity on the material being inspected when the inspection is completed.

These difficulties and limitations may now be significantly reduced or eliminated entirely by the use of a facsimile-recording system that is used in conjunction with an automated two-dimensional scanning carriage for eddy-current inspection. The inspection system that was developed (shown in Figs. 1 and 2) has the capability of detecting linear and small-diameter discontinuities as small as 0.64-mm (0.025-in.) in-plane dimension and displaying the discontinuities on electrosensitive paper as a facsimile C-scan. This form of data presentation is analogous to the ultrasonic inspection C-scan presentation where the specimen is displayed in a plan view and any discontinuities are shown in their respective locations on the specimen. The size of the discontinuity may be also determined with respect to the length or the width of the discontinuity and, in certain instances, the depth of the discontinuity.

System Theory and Operation

Facsimile recording is a technique of displaying data signals as a raster of lines that have varying levels of blackness that correspond with the variation of the data-signal voltage changes. Facsimile recordings are generally used to form a picture (C-scan) by displaying the data on a line-by-line procedure. If no data were transmitted, then the result would be a uniformly-light or

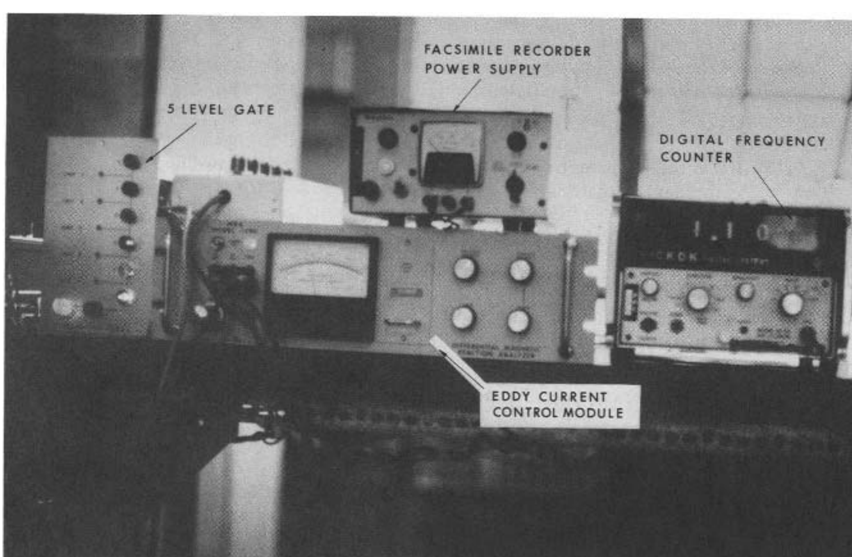

FIG. 1—*Electronics for inspection system.*

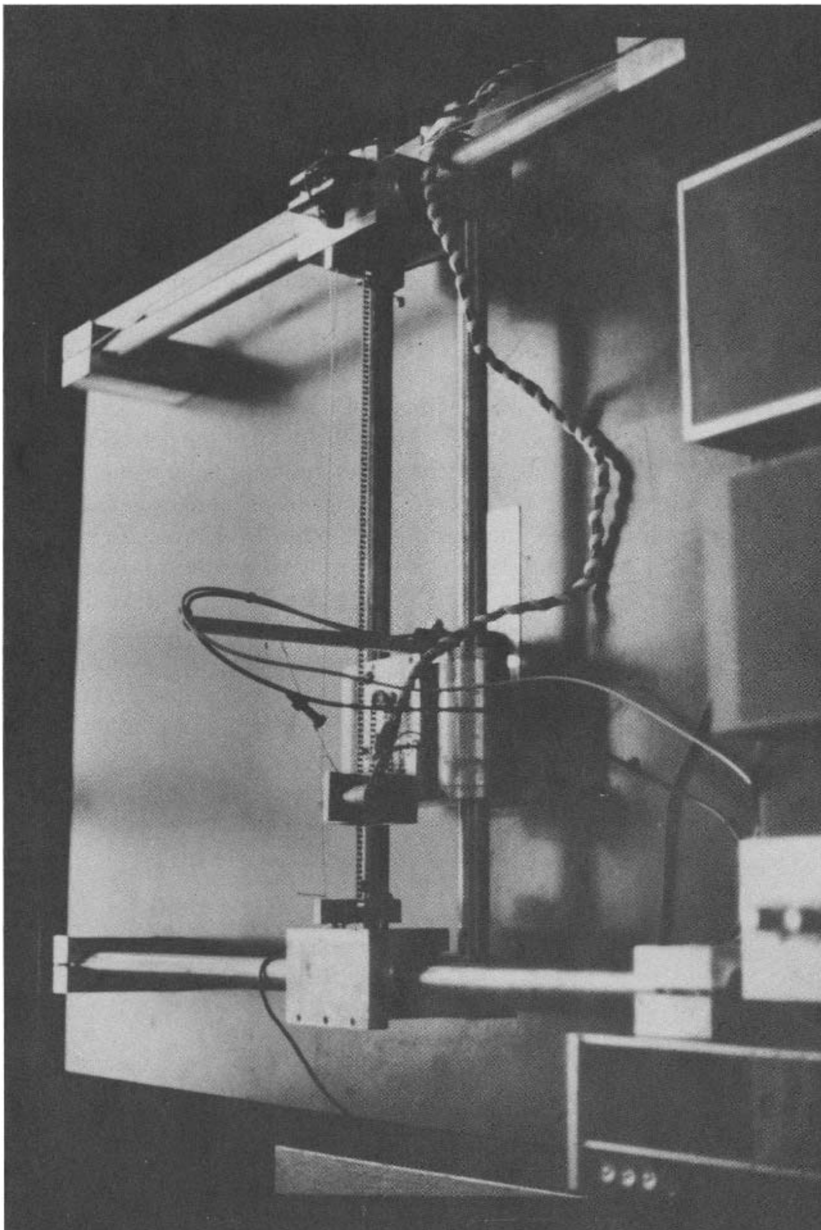

FIG. 2—*Scanning carriage for inspection system.*

uniformly-dark (dependent upon the facsimile polarity) raster pattern. If data were transmitted, then there would be areas of different darkness, the darkness dependent upon the amplitude of the incoming data signal, and the location of the dark areas would be dependent upon the location of the recording stylus when the data signal was received.

The theory of eddy-current inspection has been well described in the literature for most coil and semiconductor detection systems [*1-7*].[2] The new system uses two semiconductor detectors arranged in a differential configuration within a single test-probe assembly. Also contained within the test-probe assembly is the circular magnetizing coil that is used to induce the eddy currents. A block diagram of a typical differential semiconductor detector probe and the associated electronic systems is shown in Fig. 3. The dimensions of the semiconductor elements are 0.76 mm (0.030 in.) in length, 0.38 mm (0.015 in.) in width, and 0.05 mm (0.002 in.) in thickness. The center-to-center separation distance is approximately 3.2 mm (0.125 in.). The close spacing of the two detectors is the key to the sensitivity of the detection system to discontinuities. When the differential test probe (magnetizing coil and dual semiconductor detectors) is over homogeneous material, the signals from each detector are equal and cancel each other, which results in a zero-difference signal. A differential probe is relatively insensitive to conditions to which a single, or absolute, test probe would react. Changes in conductivity, relative permeability, test frequency, and test-material thickness, unless exceedingly rapid, are detected equally by both detectors simultaneously and are cancelled out. The eddy-current density around any discontinuity is a function of the geometry of the magnetizing coil and the discontinuity, and

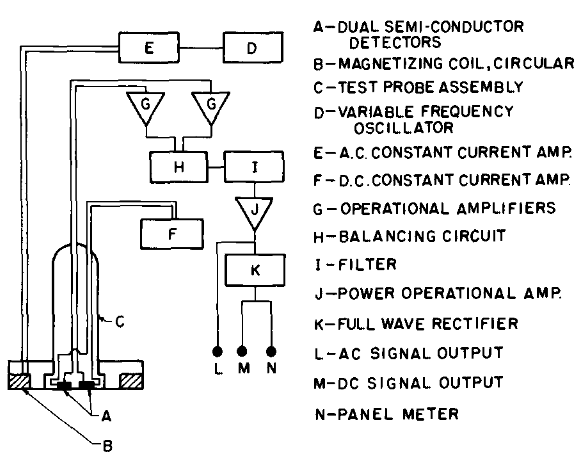

FIG. 3—*Test-system block diagram.*

[2]The italic numbers in brackets refer to the list of references appended to this paper.

also a function of the location of the discontinuity within the specimen. The difference signal generated by the differentially arranged test probe is double peaked. There is one peak generated as each detector passes over the discontinuity, and a central valley in the difference signal due to the balancing effect achieved when the two detectors are exactly equidistant on each side of the discontinuity. This difference signal may be presented either as an a-c or a d-c voltage, or as a meter deflection. The magnitude of the a-c or d-c output voltage is proportional to the magnitude of the difference signal. The meter deflection is also proportional to the magnitude of the difference signal.

In the new inspection system, a varying d-c voltage is used to trigger a multilevel gating system that controls the current applied to the facsimile-recording stylus. The differential eddy-current inspection unit that was used had a 0 to 2 V dc full-scale output-voltage capability; the multilevel gate had five available gate levels. The voltage ranges for each gate and the facsimile-recording current levels for each gate are given in Table 1.

These current levels for the facsimile recorder were chosen so that there were five distinctive black levels on the facsimile recordings. The facsimile recorder was created by modifying a Hewlett-Packard Mosley 7005-B *X-Y* recorder by the addition of a conductive plate on the recording surface and an insulated stylus in place of the recording pen. The recorder was also modified so that the facsimile stylus was in the down position for one scanning direction (the recording direction) and was lifted for the scan return. This procedure was done so that any backlash in the two-dimensional eddy-current scanning carriage and the positioning system could be eliminated.

The automatic eddy-current scanning carriage had a set of precision potentiometers installed as *X*- and *Y*-position sensors. These position sensors, by applying their output voltages to the appropriate axis of the *X-Y* recorder, allowed the facsimile recorder to mimic the motions of the eddy-current scanning carriage as a specimen was being inspected. This positioning system ensured that the image of the specimen that was produced would be proportional to the plan view of the specimen.

Test Procedures

The specimens were all 1.625-mm (0.064-in.)-thick 7075-T6 aluminum plate grouped into three categories. The first category had only a single plate which had six 0.35-mm (0.014-in.)-wide saw cuts made in it oriented at various angles (Fig. 4*b*). The second category consisted of a set of seven plates that had holes of various diameters drilled through the plate and a single 0.35-mm-wide slot milled across the width of the plate. The location of each hole and the diameter of the holes were identical for each plate; the depth of the saw cut, however, was different for each plate. A drawing of a typical plate in this category is shown in Fig. 4*a* and the data relating hole diameter and slot depth are given in Table 2. The third category of specimens had

TABLE 1—*Voltage ranges and facsimile-recording current levels for each gate.*

Gate No.	Meter Range, %	Voltage Range, V	Facsimile Current, mA
1	0 to 25	0.0 to 0.5	5.1
2	25 to 50	0.5 to 1.0	7.1
3	50 to 75	1.0 to 1.5	12.4
4	75 to 95	1.5 to 1.9	18.5
5	95 to 100	1.9 to 2.0	20.0

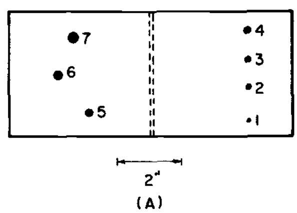

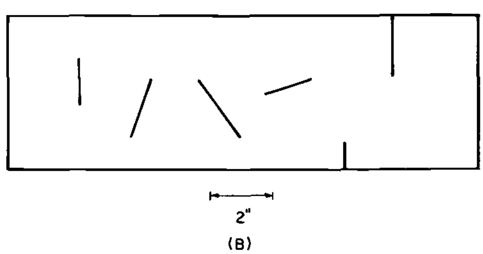

FIG. 4—*Standard test specimens.*

three fatigue-cracked plates. Drawings of two of the plates are shown in Figs. 5*a* and 5*b*.

These plates were inspected using a standardized procedure composed of the following routines. The dual semiconductor detector signals were balanced with the probe away from any conductive material (balanced in air). Then the plate that was chosen as a reference standard (homogeneous and without any discontinuities) was inserted under the test probe. The lift-off (the air gap between the top of the specimen and the bottom of the detector elements) was adjusted to 0.254 mm (0.010 in.) using feeler gages. With the test probe and reference plate in this position, the gain of the eddy-current inspection unit was set for 20 percent of the full-scale meter deflection. The frequency of the test unit was set at 1.0 kHz and then the scanning of the specimens was started. The actual scanning movement consisted of three separate motions: (*1*) the inspection motion started at the extreme left-hand

TABLE 2—*Data relating hole diameter and slot depth.*

Hole No.	Hole Diameter, mm	Test Plate No.	Slot Depth, mm
1	1.27	2-1	0.254
2	1.90	2-2	0.381
3	2.59	2-3	0.508
4	3.17	2-4	0.635
5	3.83	2-5	0.762
6	4.44	2-6	1.016
7	5.23	2-7	1.270

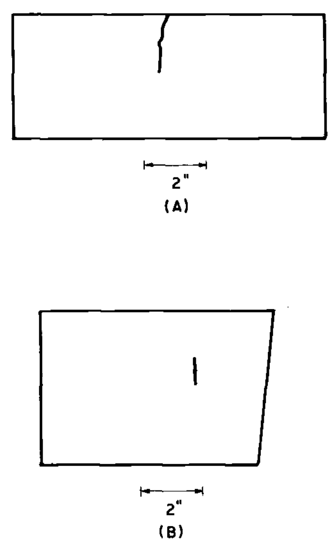

FIG. 5—*Fatigue-cracked specimens.*

position of the transverse carriage and moved from left to right, (*2*) the return motion moved the transverse carriage back to the extreme left-hand position, and (*3*) the longitudinal indexing motion moved the longitudinal carriage 0.4 mm in preparation for the next inspection motion (see Fig. 6). This single-scan procedure was continuously repeated until the entire longitudinal width of the specimen had been inspected. This close line-by-line inspection provides the basic characteristic raster pattern of the "C" scan.

Test Data and Results

The results that were obtained for small-diameter discontinuities were graphed as shown in Fig. 7. The minimum detectable discontinuity diameter

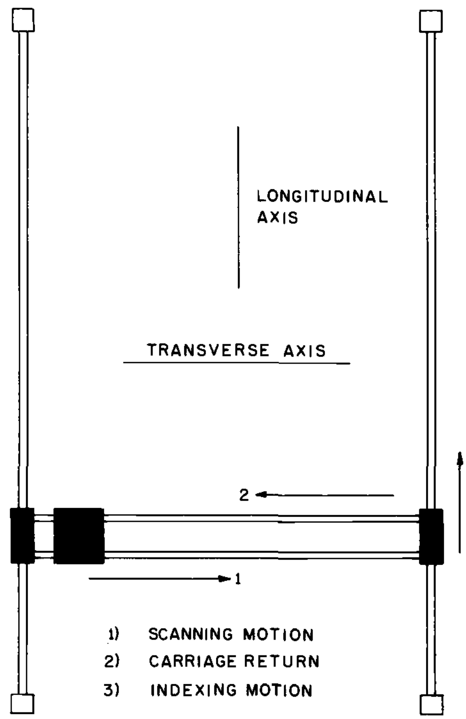

FIG. 6—*Pictorial of single-line scanning motions.*

was 1.27 mm (0.050 in.) at a gain setting of 20 percent of full-scale deflection. At a gain setting of 50 percent, a discontinuity of 0.64 mm (0.025 in.) was reliably detected; however, other nonrelevant indications that are related to the residual stress state of the test material also are detected. This condition is typified in Fig. 8, where cold-working of the specimen occurred during the slot milling and hole drilling operation. The results for detection of linear discontinuities that extend only partially through the full thickness of the specimen and are located on its back side (the side opposite the test probe) are graphed in the sensitivity curve shown in Fig. 9. The gain setting for this curve was also 20 percent of full-scale deflection. Increasing the gain setting would also allow the detection of shallower back-side discontinuities or larger discontinuities at greater depths. When the partial-thickness discontinuities were on the side being inspected, there was no detectable difference between the partial-thickness and full-thickness discontinuities.

The facsimile recording of the specimen with the saw cuts is shown in Fig. 10. The two dark indications that extend the full width of the plate are the end indications caused by the test probe passing over the end of the plate and the change of conductivity from air to aluminum. The saw-cut indications

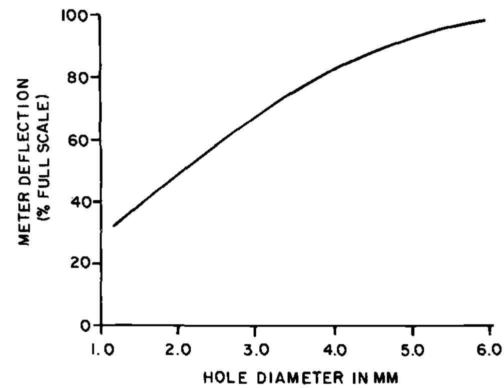

FIG. 7—*Meter response for various hole diameters.*

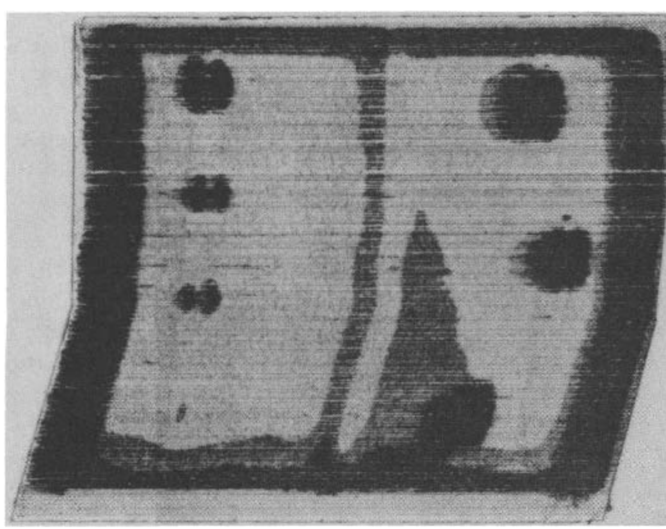

FIG. 8—*Scan with calibration set at 50 percent.*

are very clear; the width of the indication, however, is several times the actual width of the discontinuity. This is due to the double-peaking phenomenon that was mentioned previously. The orientation of the saw cuts has very little effect on the detection of the discontinuity. If the discontinuity were exactly parallel to the direction of travel of the test probe, the only indication of the discontinuity would be two points at the extreme ends of the discontinuity. This would be owing to the fact that over the majority of the length of the discontinuity the two detectors would be receiving the same signal. This is the reason that the ends of the specimens that are perpendicular to the direction

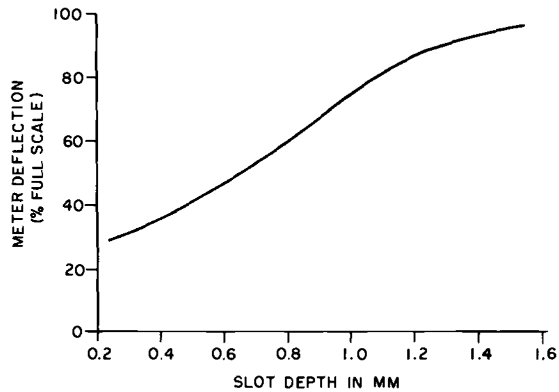

FIG. 9—*Meter response for various slot depths (far surface).*

of travel for the test probe show clearly while the edges of the plate which are parallel to the direction of travel do not show at all on the scan.

The facsimile recordings shown in Figs. 11 and 12 are recordings of tests on the plates with the drilled holes and the milled slot that extended partially through the thickness of the specimen. In these tests the milled slot was located on the back side of the specimen. In Fig. 11 the depth of the milled slot was the minimum depth tested, 0.254 mm. The indication is distinctly different from the indications of the through saw cuts shown in Fig. 10. In this specimen there was 1.37 mm (0.054 in.) of material remaining between the bottom of the milled slot and the side of the plate that was being inspected. In the facsimile recording shown in Fig. 12, which was also a specimen with drilled holes and a milled slot, the thickness of material between the bottom of the milled slot and the side of the plate being inspected was only 0.355 mm (0.014 in.) (the slot depth was 1.27 mm). The line discontinuity is again very clearly indicated, but the intensity of the indication is between the intensity of the through saw cuts and the intensity of the 0.254-mm milled slot. For the other specimens with milled slot depths between these two extremes, the intensity of the line discontinuity indications varied in direct proportion with the slot depth, the deeper slots having a darker indication and the shallower slots having lighter indications. In both cases shown, and in the other tests, the smallest-diameter drilled hole (1.27 mm) was clearly visible. The ability of the system to detect small-diameter discontinuities is shown by the detection of the location and relative diameters of all the drilled holes in all of the specimens.

The facsimile recordings shown in Figs. 13 and 14 are the test results from the fatigue-cracked plates that are shown in Figs. 5*a* and 5*b*. The plate in Fig. 14 had the fatigue crack initiated at the edge of the plate and the crack propagated towards the center of the plate. The plate shown in Fig. 13 had

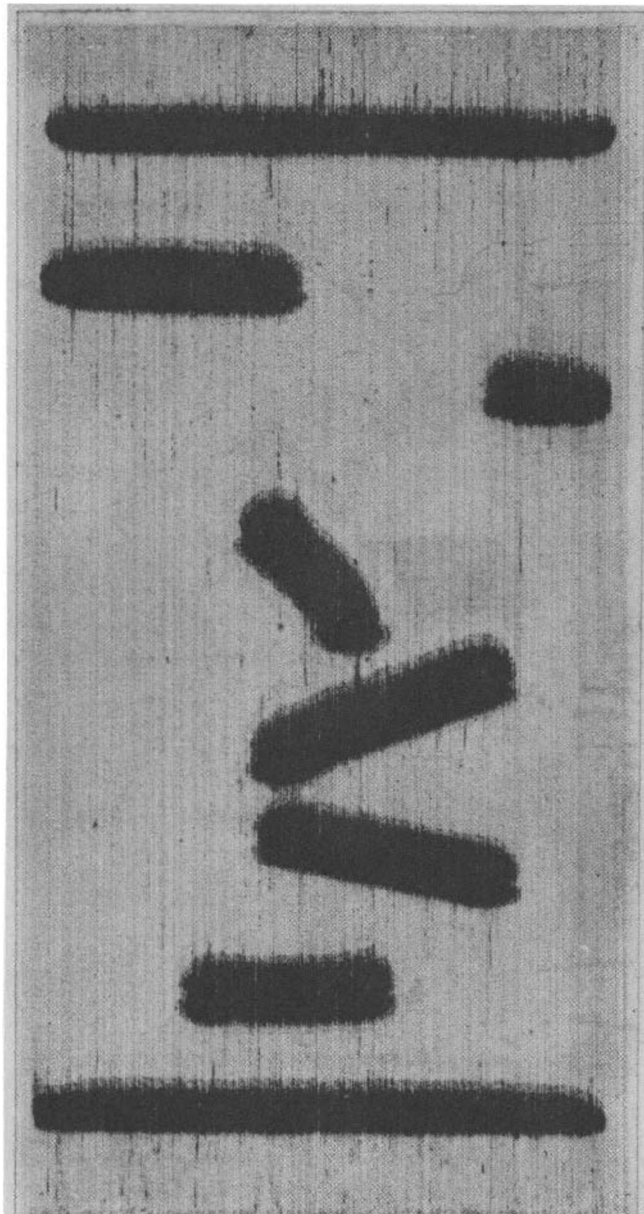

FIG. 10—*Scan of saw-cut specimen.*

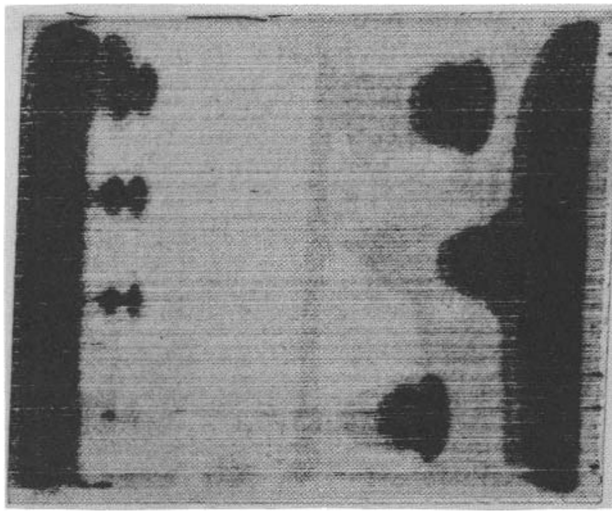

FIG. 11—*Scan of standard specimen (slot depth 0.254 mm).*

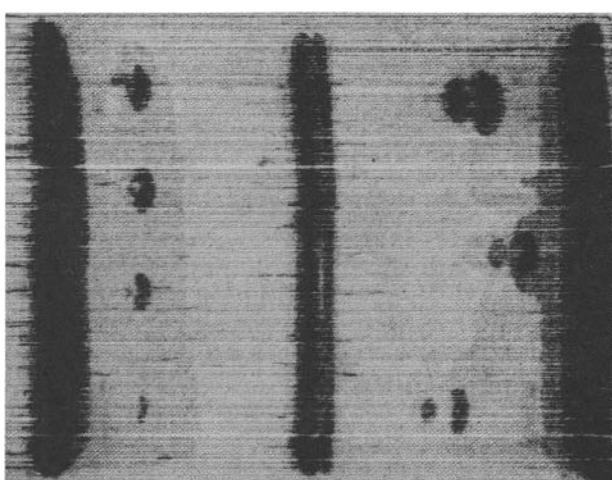

FIG. 12—*Scan of standard specimen (slot depth 1.27 mm).*

the fatigue crack initiated by a 1.27-mm drilled hole, and the crack then propagated from both sides of the hole towards the edges of the plate. Since the cracks extended through the full thickness of the material, the resulting indications are very similar to the indications obtained on the plate with the saw cuts. In Fig. 14 only one end of the specimen is shown on the facsimile recording owing to the positioning of the plate during the inspection. The

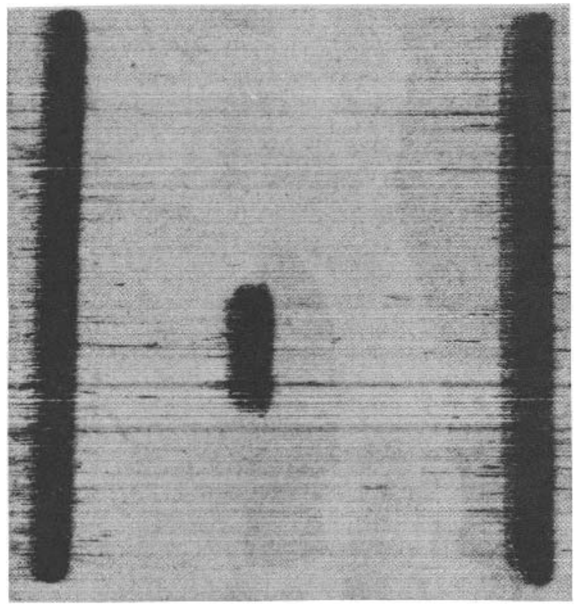

FIG. 13—*Scan of fatigue-cracked specimen.*

lengths of the cracks were determined and verified by two other nondestructive tests (liquid penetrant and radiography). For both specimens the lengths indicated on the facsimile recordings were longer than those determined by visual inspection. In Fig. 14, for example, the crack length was indicated to be 45.7 mm (1.8 in.); however, only 39 mm (1.5 in.) was visually detectable. A similar situation existed for the plate shown in Fig. 13. In addition, the initiating hole for the fatigue crack in the plate shown in Fig. 13 was not shown on the facsimile recording owing to geometric considerations affecting the eddy-current density distribution.

The interpretation of the test data obtained using the facsimile-recording technique is very analogous to the interpretation of radiographic films or ultrasonic C-scan recordings. A discontinuity is shown as a dark line or a dark point. The darkness of the indication is proportional to the intensity of the eddy-current difference signal. The difference signal is a function of the magnetizing coil geometry, the geometry and location of the discontinuity, and the orientation of the discontinuity. The interpretation of any particular indication may be aided by the presence or absence of the double-peaking phenomenon being clearly visible. The phenomenon was exhibited only by discontinuities which extend only partially through the specimen thickness or by small-diameter discontinuities. The widths of the indications have not been shown to be reliable criteria for the determination of the true discon-

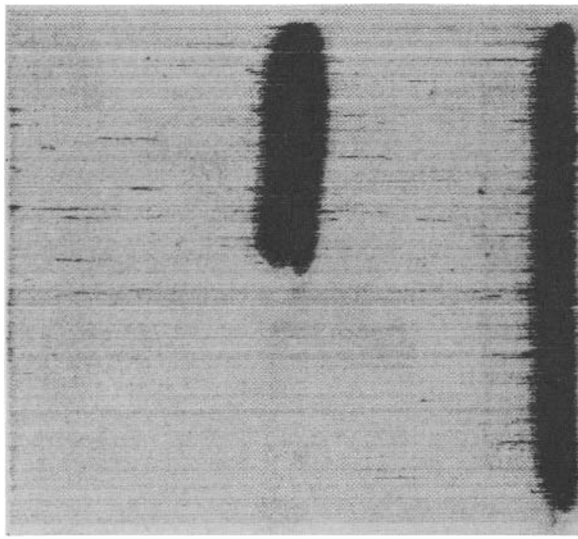

FIG. 14—*Scan of fatigue-cracked specimen.*

tinuity widths. The indications obtained from the fatigue cracks and the through saw cuts showed very little difference, whereas the actual widths of the two types of discontinuities differed greatly. The diameter of the drilled-hole discontinuity indications, though, may be used as a guide to determine the relative diameter of the discontinuities. The determination of the location of the discontinuities with respect to the widths of the indications is as follows. For line discontinuities, the location of the discontinuity is approximately at the center of the indication. For small-diameter discontinuities, the location is at the center of the valley due to the double-peaked indications obtained from these discontinuities. For the specimens that were used, the determination of the location of the discontinuity from the facsimile recording was not more than 0.254 mm in error.

Conclusions

The use of facsimile recording as a means of data presentation for eddy-current inspection of flat plate and sheet materials has several advantages over other techniques of eddy-current inspection. These advantages are (*1*) the ease of interpretation of the test signal, (*2*) the exact determination of the discontinuity location, and (*3*) a permanent record of the test results.

There are several additional refinements that could be made to the system that would enhance the performance and sensitivity of the system significantly. One is the use of a solid-state gating system that has a much smaller overlap voltage response than the relay-operated gating system that was used in the research. In addition, having a larger number of gates available would enable the system to have several more distinct indication darkness levels with which to display more detailed data. The third major refinement that would enhance the system would be a differential test probe that had a smaller center-to-center separation distance between the two semiconductor detectors. This would allow a sharper indication for either a line or a small-diameter discontinuity on the facsimile recording.

References

[1] Smith, G. H. and McMaster, R. C., "Current Aerospace Applications Using MRA Eddy Current Test Systems," paper presented at the Spring National Meeting of the American Society for Nondestructive Testing, Los Angeles, Calif. 1967.
[2] Smith, G. H. and McMaster, R. C., "The Magnetic Reaction Analyzer—A New Tool for Maintenance Inspection and Control," paper presented at the Plant and Maintenance Conference, American Society of Mechanical Engineers, April 1966.
[3] McMaster, R. C., "The Magnetic Reactor Analyzer—A New Eddy Current Nondestructive Test," paper presented at the 1965 Metals/Materials Conference, American Society for Metals, Detroit, Mich., October 1965.
[4] McMaster, R. C., *Nondestructive Testing Handbook,* Vol. 2, Sections 36 to 42, Ronald Press, New York, 1963.
[5] Hochschild, R., "The Theory of Eddy Current Nondestructive Testing in One (Not-So-Easy) Lesson," *Nondestructive Testing,* Vol. 12, No. 5, September-October, 1954.
[6] Jones, A. L. and Pezdritz, K. F., "Nondestructive Eddy Current Testing," *Transactions on Instrumentation and Measurement,* Institute of Electrical and Electronics Engineers, Vol. IM-21, No. 4, February 1972.
[7] Libby, H. L., *Introduction to Electromagnetic Nondestructive Test Methods,* Wiley-Interscience, New York, 1971.

P. G. Doctor,[1] *T. P. Harrington,*[1] *T. J. Davis,*[1] *C. J. Morris,*[1] *and D. W. Fraley*[1]

Pattern-Recognition Methods for Classifying and Sizing Flaws Using Eddy-Current Data

REFERENCE: Doctor, P. G., Harrington, T. P., Davis, T. J., Morris, C. J., and Fraley, D. W., **"Pattern-Recognition Methods for Classifying and Sizing Flaws Using Eddy-Current Data,"** *Eddy-Current Characterization of Materials and Structures, ASTM STP 722,* George Birnbaum and George Free, Eds., American Society for Testing and Materials, 1981, pp. 464–483.

ABSTRACT: This paper extends the work of Shankar et al to the classification of three types of machined defects in Inconel 600 steam-generator tubing: electrodischarge machined slots, uniform thinning, and elliptical wastage. Three different pattern-recognition techniques were used for classification: (*1*) an empirical Bayes procedure, (*2*) a nearest-neighbor algorithm, and (*3*) a multicategory linear discriminate function. The three types of defects were classified correctly with an overall accuracy of 96 to 98 percent depending on the technique used. Two pattern-recognition algorithms, least squares and nearest neighbor, were used to size uniform-thinning defects in steam-generator tubing. All of the defects were between 25 and 75 percent of the wall in depth. With the least-squares algorithm, we achieved a fit correlation of 0.99 with a 95 percent confidence interval of (0.98, 1.00).

KEY WORDS: pattern-recognition, eddy current inspection, classification, nondestructive evaluation, signal analysis, Inconel 600 steam generator tubing, clustering

Pattern recognition is the generic term for statistical techniques that classify objects described by multiple parameters. For some nondestructive evaluation (NDE) technologies (including eddy current), the basic datum is a time-varying waveform; this type of data has been a barrier to statistical analysis in the past, since a waveform cannot be described by a single numeric value. A waveform can be described simultaneously with a number of parameters (features in pattern-recognition terminology). In the time domain they include peak amplitude, rise time, and moments. In the frequency domain they include maximum frequency response, energy in selected bandwidths, power-spectrum parameters, and, by further transformation,

[1] Senior research scientist, senior research scientist, senior research scientist, research scientist, senior research scientist, respectively, Battelle, Pacific Northwest Laboratories, Richland, Wash. 99352.

cepstrum parameters. For eddy-current signals additional parameters, such as cross correlations and properties of the impedance-plane response, can be used as features.

Pattern recognition has several advantages in the detection and sizing of flaws:

1. More relevant flaw information can be obtained from the signal than from the customary visual inspection.
2. It is less dependent on the operator so the results are reproducible and hence more reliable.
3. These techniques are microprocessor-implementable, which permit real-time automated inspection decisions.

This paper focuses on the application of pattern-recognition analysis techniques to eddy-current inspection of steam-generator tubes.

The steam generator in a nuclear reactor is made up of thousands of thin-walled tubes that provide the heat-transfer area for the transfer of thermal energy from primary reactor coolant to secondary working fluid. Since these tubes form over half of the boundary between the contaminated and the non-contaminated fluid, their integrity is vital to the economic and safe operation of the pressurized water reactor (PWR).

The currently accepted method of determining the integrity of steam-generator tubing is by the use of nondestructive eddy-current inspection techniques. The major problems with eddy-current inspection are (*1*) the interpretation of a particular signal will vary among any group of experts, (*2*) the interpretation can be affected by various human factors, such as experience, concentration, and fatigue, and (*3*) flaw geometry strongly affects flaw-depth interpretation. Since pattern-recognition techniques are computer-based, they produce results with a minimum of operator assistance.

Pattern-recognition techniques have recently been applied to eddy-current inspection of steam-generator tubing. Shankar et al used a pattern-recognition technique referred to as adaptive learning networks (ALN) to classify and size two types of defects machined into Inconel[2] tubing [*1*].[3] Brown used two pattern recognition techniques, clustering and ALN, to analyze eddy-current data from tube samples that contained both artificial defects and nondefects [*2*]. (Nondefects are tube anomalies that affect eddy-current measurements but not the integrity of the tube.)

We extended the work of Shankar et al to the classification of three types of machined defects: electrodischarge machined slots, elliptical wastage, and uniform thinning. We used three pattern recognition techniques to classify the defects: Bayes procedure, the K-nearest-neighbor algorithm, and a multicategory linear discriminant function. Our flaw-sizing results for

[2] Registered trademark of the International Nickel Co., Inc.
[3] The italic numbers in brackets refer to the list of references appended to this paper.

uniform-thinning defects are also presented. A *P*-percent nearest-neighbor algorithm and a least-squares procedure were the two pattern recognition algorithms used to size the defects. We also discuss the use of cluster analysis as a means of investigating the structure of the data.

The pattern recognition and clustering methods discussed in this paper are a portion of a general-purpose interactive pattern recognition/data analysis capability being developed at Pacific Northwest Laboratory (PNL), operated by Battelle Memorial Institute for the Department of Energy. This capability includes ten pattern-recognition algorithms (including the Adaptive Learning Network), three clustering algorithms, four feature reduction algorithms, and a variety of display techniques. This capability also includes the general-purpose interactive statistical packages: MINITAB, P-STAT, and SPSS.

The data for this investigation were gathered during the first phase of a multiyear, multiphase study to establish a data base that will define the integrity of PWR steam-generator tubing. The study is being performed by PNL for the Nuclear Regulatory Commission [*3*].

The study includes the nondestructive eddy-current examination of steam-generator tubing specimens with machine-induced flaws of different types and severities. In addition, destructive data from burst and collapse testing of the tubing are also being collected.

Eddy-Current Data

Three basic types of flaws were machined into the steam-generator tubes: electrodischarge machined (EDM) slots, elliptical wastage, and uniform thinning. These particular defect geometries were chosen because they simulate service-induced flaws.

A standard EDM slot was selected as the best simulation of tight cracks (which are indicative of stress-corrosion and fatigue flaws) that can be constructed by mechanical methods. The dimensions of the slots in the data set were 6.35, 12.7, 25.4, 38.1 mm (0.25, 0.50, 1.00, and 1.50 in.) in length; 55 to 60 percent, 85 to 90 percent, and 100 percent of the wall thickness in depth; and 0.08 to 0.25 mm (0.003 to 0.010 in.) in maximum width.

Elliptical-wastage flaws are representative of wastage-type flaws that occur at the tube-support plates or antivibration bars. The elliptical-wastage flaws were machined with a specially made cutter. Each flaw is defined by the radius of the cutter, the required depth of the flaw, and the wrap angle. The depths of the elliptical-wastage flaws were in the ranges of 25 to 30 percent, 55 to 60 percent, and 85 to 90 percent. Wrap angles of 0, 45, and 135 deg were used to partially extend the wastage around the tube circumference.

Uniform-thinning defects are representative of the type of wastage experienced near the tube sheet where chemical impurities build up to form a sludge layer. These caustic impurities attack and corrode the tubing. This type of flaw was machined on a lathe, while the inside of the tube was supported so that no deformation of the inside surface could occur. The lengths of the machined flaws were 4.77, 9.55. 19.0, and 38.1 mm (0.188, 0.376, 0.750, and 1.50 in.). The depths of the uniform thinning were 25 to 30 percent, 55 to 60 percent, and 75 to 80 percent of the wall thickness.

All of the data available for this study, summarized in Table 1, were obtained with the single-frequency eddy-current technique using a two-coil differential probe. The procedure for obtaining the data involves translating the conducting coils through the tubing under inspection. When the coils are excited with a sinusoidal current, eddy currents are induced in the material. The presence of a flaw in the material disrupts the flow of the eddy currents. This change in the eddy currents can be detected by test equipment and translated into vertical and horizontal output voltages corresponding to the Fourier amplitude coefficients of the eddy currents. These voltages can be monitored at the instrument output terminals. The instrumentation was adjusted during data collection so that the wobble, associated with lateral movement of the coil through the tube, resulted in voltage changes primarily in the horizontal channel. For a complete discussion of single-frequency eddy-current theory, see Ref *4*.

During the tests, the voltage levels produced by each flaw were recorded on an FM tape recorder. A specially designed digitizer converted the analog recordings to digital form at a digitization rate of 400 Hz. The digitized data were temporarily stored on magnetic tape and transferred to a minicomputer where the pattern recognition analyses were performed. Before analysis, the flaw data for both the horizontal and the vertical channels were processed to remove the means and any linear trends.

Figures 1, 2, and 3 show examples of the type of data available for this study. The figures show the horizontal and vertical voltage levels, and the Lissajous pattern plotted on the impedance plane. The Lissajous pattern is obtained by plotting the vertical output against the horizontal output. This pattern is used in eddy-current inspection procedures to estimate flaw type and size. Estimations of flaw type are based on the size and shape of the two lobes of the Lissajous pattern. Flaw-depth estimates can be made by measuring the angle of the lobes with respect to the horizontal axis.

Feature Generation

Waveform parameterization, or feature generation in pattern-recognition terminology, is the process of defining a set of parameters that describe the waveform. In this study we had to identify two such sets of parameters: one set that contained sufficient information to separate the waveforms into three discrete flaw categories (EDM slots, uniform thinning, and elliptical wastage), and a second set that contained sufficient information to size the

TABLE 1—*Eddy-current data available for the pattern-recognition investigation.*

Defect Type	20 to 30 %	50 to 60 %	70 to 90 %	100 %	Total
EDM slots	...	7	11	16	34
Uniform thinning	13	13	14	...	40
Elliptical wastage	9	14	4	...	27
Total	22	34	29	16	101

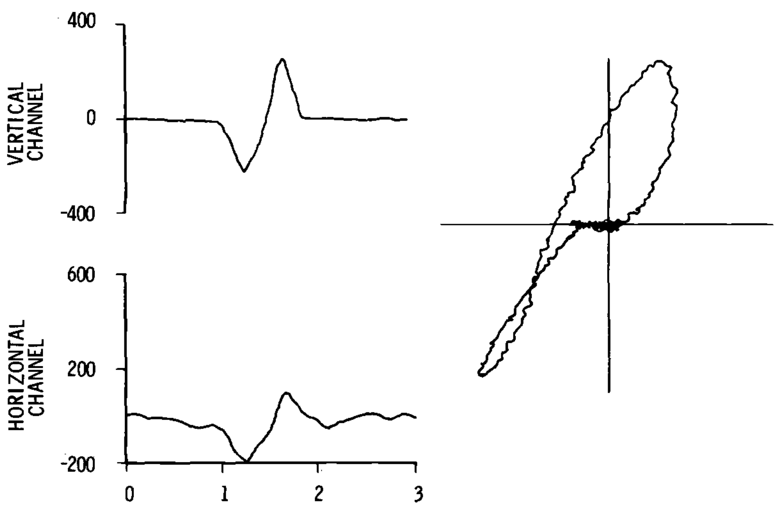

FIG. 1—*Eddy-current data from an EDM slot 82 percent of the wall in depth.*

uniform-thinning defects. The procedure for finding the first of these two sets of features is discussed in this section and Feature Analysis. A similar procedure was used to develop the second set for sizing flaws.

At the outset of a pattern-recognition investigation, we do not know which features (parameters) will provide the most information for the particular objective; we usually do know, however, which features have historically played a valuable role. Both Shankar et al and Brown have described sets of features that they have found useful in applying pattern recognition to eddy-current data.

For this investigation we selected features from both of these sets and added several additional features that we felt would have applications in our particular investigation. These features are listed in Table 2. The features we have chosen can be divided into three groups: shape parameters, autocorrelation (time series) parameters, and frequency-domain parameters.

The purpose of the shape features is to describe the Lissajous pattern in detail. The features that we have placed in the shape category and their

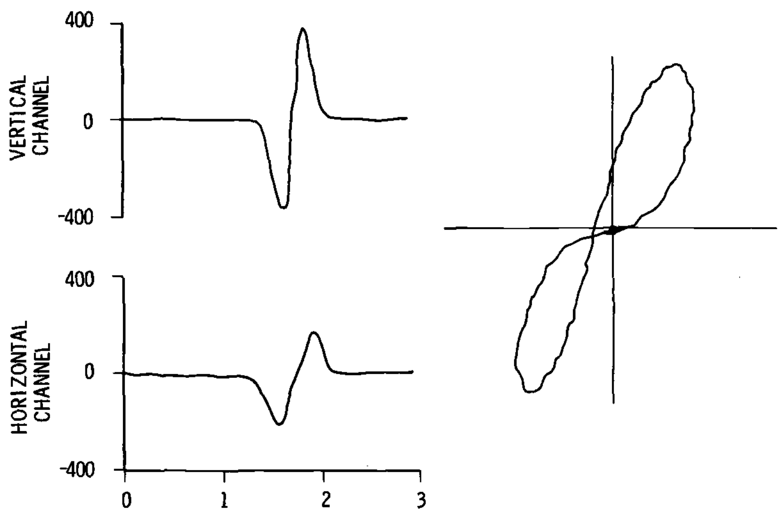

FIG. 2—*Eddy-current data from a uniform-thinning flaw 58 percent of the wall in depth.*

defining equations are Features 1 to 19 in Table 2. Figure 4 identifies several of the terms used in the definition of the shape parameters.

The second group of features is based on the autocorrelation function. It is defined as

$$C_k = \frac{\sum_{l=1}^{N} (v_{k+l} - \bar{v})(v_l - \bar{v})}{\sum_{l=1}^{N} (v_l - \bar{v})^2}$$

$$k = 0, 1, \ldots$$

where

k (called the lag) = separation between two points of the digitized waveform,
v = voltage level,
$\bar{v}$ = average voltage, and
N = number of voltage values.

The feature C_k is simply the correlation between all of the values of the waveform that are k units apart. The mathematical properties of C_k are $C_0 = 1$ and $-1 \leq C_k \leq 1$.

For the vertical channel we computed the autocorrelations through Lag 100 for all of the waveforms and then selected the three lags that produced

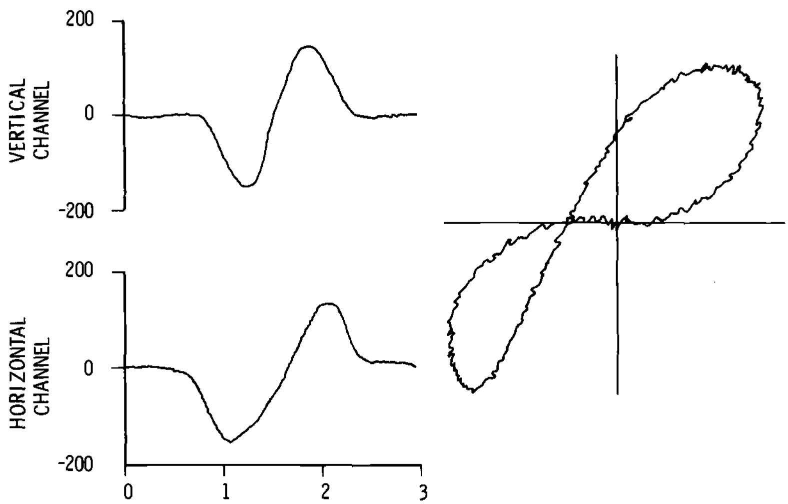

FIG. 3—*Eddy-current data from an elliptical-wastage flaw 55 percent of the wall in depth.*

TABLE 2—*Features used in pattern-recognition study.*

Feature	Definitions	Description
1	$C_{HH} = 1/N\ \Sigma h_i^2$	Power in horizontal channel
2	$C_{VV} = 1/N\ \Sigma v_i^2$	Power in vertical channel
3	C_{VV}/C_{HH}	Ratio of power
4	$\sqrt{C_{VV}C_{HH}}$	Geometric mean of power
5	$C_{HV}/\sqrt{C_{HH}C_{VV}}$	Correlation
6	λ_1	Maximum eigenvalue of the power matrix
7	λ_2	Minimum eigenvalue of the power matrix
8	$\lambda_1 \lambda_2$	Product of eigenvalues
9	$\angle \lambda_1$	Angle of eigenvector corresponding to the maximum eigenvalue
10	$(H_{max} - H_{min})/\sqrt{C_{HH}}$	Horizontal voltage (peak-to-peak)
11	$(V_{max} - V_{min})/\sqrt{C_{VV}}$	Vertical voltage (peak-to-peak)
12	$\lvert r \rvert$	Length of the radial vector
13	$\angle r$	Angle of the radial vector
14	...	Area of Lissajous pattern above the horizontal axis
15	...	Area of lower lobe of Lissajous pattern below the horizontal axis
16	$\lvert r_1 \rvert$	Length of upper lobe
17	$\angle r_1$	Angle of upper lobe
18	$\lvert r_2 \rvert$	Length of lower lobe
19	$\angle r_2$	Angle of lower lobe
20	...	Vertical-channel autocorrelation at Lag 40
21	...	Vertical-channel autocorrelation at Lag 60
22	...	Vertical-channel autocorrelation at Lag 87
23	...	Vertical-channel maximum frequency response
24	...	Vertical-channel frequency of maximum response
25	...	Vertical-channel total power
26	...	Vertical-channel first moment
27	...	Vertical-channel second moment

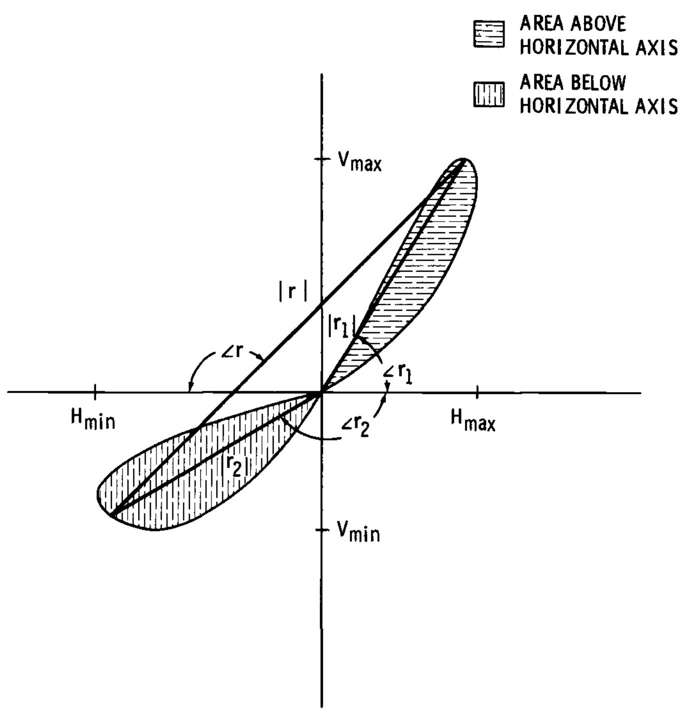

FIG. 4—*Definitions of selected shape parameters.*

the best separation between the three categories of defects by computing the t statistic for the difference between the means for each pair of categories. These three lags were C_{40} for EDM slots and uniform thinning, C_{60} for EDM slots and elliptical wastage, and C_{87} for uniform thinning and elliptical wastage. These three autocorrelation coefficients are Features 20 to 22 in Table 2.

Features from the frequency domain were obtained using the fast Fourier transform (FFT) algorithm. For each flaw indication we performed an FFT on the vertical channel. We then calculated five frequency-domain features: the maximum frequency response, the frequency of the maximum response, and ratios of the first three moments of the frequency distribution.

The moments in the frequency domain are defined by the following formulas

$$M_0 = \int_0^\infty p(w)dw \qquad (1)$$

$$M_1 = \int_0^\infty wp(w)dw \qquad (2)$$

$$M_2 = \int_0^\infty w^2 p(w) dw \tag{3}$$

where $p(w)$ is the power spectral density.

The zeroth moment, M_0, is equivalent to the total power. From Fourier transform theory it is easy to show that the first and second moments are related to the total power of the first and second derivatives (with respect to time) of the original time-domain waveform. For this study we took the ratio of the moments in the frequency band from 0 to 2.5 Hz to the corresponding moments computed in the frequency band from 0 to 5 Hz. The moments were obtained by using the trapezoidal rule to integrate Eq 1, 2, and 3. Features 23 to 27 in Table 2 are the frequency-domain features.

The set of features just discussed form together the pattern used to describe each flaw. Table 2 is a complete list of the features chosen for this study.

A convenient way to examine the separation capacity of an individual feature is to plot its histogram. For a feature with ideal separation capacity, the feature values corresponding to different categories would occupy different intervals on the horizontal axis. Figures 5 and 6 give histograms for the total power, Feature 25, and the product of the eigenvalues, Feature 8. The histogram of total power (Fig. 5) shows fair separation capacity. For this feature the values of elliptical wastage are generally larger than those of EDM slots and uniform thinning. The EDM slot values fall in the middle of the interval while those of the uniform thinning are generally smaller.

Feature Analysis

Once an initial set of features has been defined, several preliminary feature-analysis steps should be performed before the pattern-recognition techniques are applied. In this section we will discuss four of these procedures: constructing training and test sets, scaling, feature reduction, and clustering.

The goal of pattern-recognition analysis is to predict the property of interest solely on the basis of the features. To reach this goal it is necessary to first divide the data into a training set and a test set. As the name implies, the training set is used to produce the best prediction for the property. Since this prediction must hold for future data as well, it is validated on the test set. For this procedure to be reasonable the test and the training sets should be as similar as possible; that is, they should differ only randomly.

A stratified sampling procedure was used to divide the data into the training and test sets for flaw classification and sizing. The stratification for classification was based on these flaw characteristics: flaw type (EDM slot, uniform thinning, and elliptical wastage), flaw depth, and flaw length. Fifty-one flaws were randomly assigned to the training set and 50 to the test set.

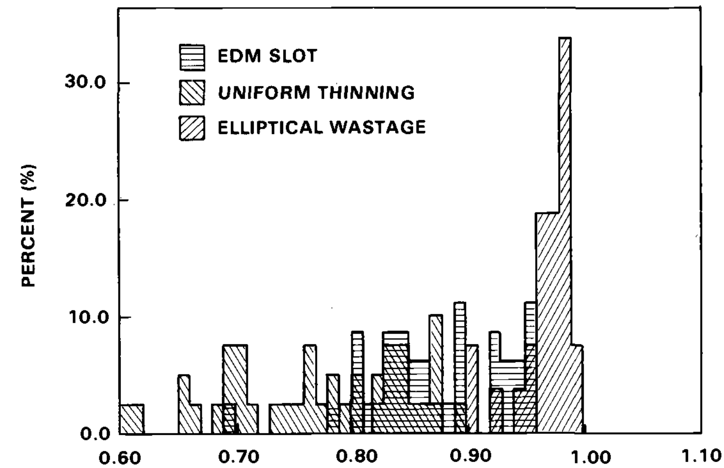

FIG. 5—*Histogram of total power (Feature 25).*

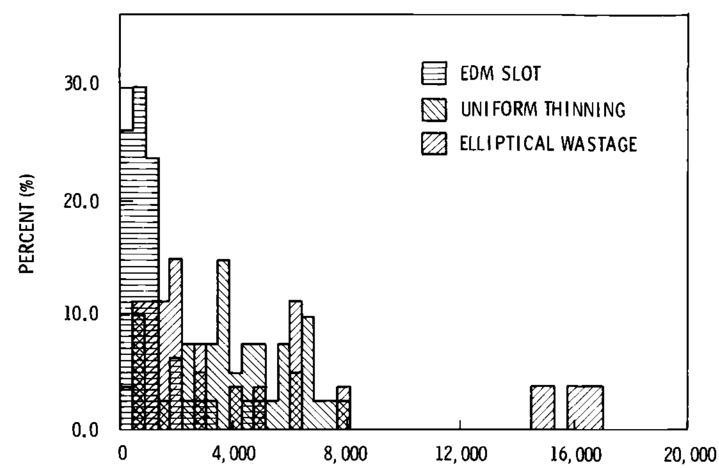

FIG. 6—*Histogram of product of eigenvalues (Feature 8).*

There were 40 uniform-thinning flaw waveforms available for sizing. Twenty waveforms were randomly assigned to the training set and 20 to the test set. An equal number of flaw depths and flaw lengths were included in each set. Analyses of the training and test sets for both classification and sizing showed that they were basically similar.

The second step in feature analysis is to scale the features. The original features frequently have different physical units and may be vastly different in magnitude. The goal of scaling is to obtain a transformed set of features that are all of approximately the same magnitude. The method used to scale the eddy-current data produced features with zero mean and unit variance.

The pattern selected to represent the flaws may contain features that are highly correlated. This correlation between features indicates that the pattern contains redundant information. Prior to the actual pattern-recognition analysis, it is often necessary to reduce the pattern to include only the features or the functions of the features that contain the best separation information; this is necessary to avoid numerical problems in the classification algorithms.

The feature-reduction algorithm used on the training set produces a set of linearly independent features that are ordered in accordance with a criterion called Fisher weighting, which is a measure of a feature's ability to discriminate categories. The Fisher weight of Feature j for three categories is defined as

$$W(f)_j = \left(\frac{1}{3}\right) \sum_{m=1}^{2} \sum_{n=m+1}^{3} \frac{(\overline{X}_{m,j} - X_{n,j})^2}{N_m s_{j,m}{}^2 + N_n s_{j,n}{}^2}$$

where

$\overline{X}_{m,j}$ = mean of the jth feature in Category m,
$s_{j,m}{}^2$ = variance of the jth feature in Category m, and
N_m = number of patterns in Category m.

Based on the Fisher weighting, the five features that contained the most information for identifying the three types of flaws were selected. They are, in order of importance,

25. Vertical-channel total power.
8. Product of eigenvalues.
13. Angle of radial vector.
12. Length of radial vector.
4. Geometric mean of the power.

The criterion for feature reduction for sizing the uniform-thinning flaws was correlation to property, which is defined as

$$W(P)_j = \frac{\sum_k (X_{j,k} - \overline{X}_j)(p_k - \overline{p})}{\sum_k (X_{j,k} - \overline{X}_j)^2 \sum_k (p_k - \overline{p})^2}$$

where

$\overline{X}_j$ = average value of Feature j,
p_k = property value for Pattern k, and
$\overline{p}$ = average property value for all of the patterns in the training set.

In this case four of the features seemed to contain the relevant information for flaw sizing. They are

13. Angle of the radial vector.
5. Correlation.
14. Area of upper lobe of Lissajous pattern.
20. Vertical-channel autocorrelation at Lag 4.

We used cluster analysis to verify the ability of the reduced set of features to predict the property. Clustering consists of grouping patterns that are similar. An obvious measure of the similarity of two patterns, and hence of two defects, is the distance between them. Although this distance may be computed by a variety of metrics, the most appealing is probably the euclidean norm. This metric assumes that a good measure of the similarity between Patterns i and j is

$$d_{ij} = \sqrt{\left[\sum_{l} (X_i - X_j)^2\right]}$$

where the summation is over all features (l). Ideally, for classifying the eddy-current data, we would like to obtain three clusters: one containing the EDM slots, one containing the uniform-thinning defects, and the third containing the elliptical-wastage defects. If we were able to obtain these three clusters, we could determine the characteristics of each of the three clusters and use them as templates for classifying unknown waveforms, or we could classify an unknown waveform on the basis of the category of its nearest neighbors. We will elaborate on the latter of these two techniques in Pattern Recognition.

The clustering technique that we used is called the K-means algorithm. Basically, this algorithm attempts to minimize a performance index, which is defined as the sum of the squared distances from each pattern associated with a cluster to the center of the cluster. The general procedure is to move a pattern from one cluster into another if this movement will reduce the performance index. After a pattern has been moved, new cluster centers must be computed for the cluster that loses the pattern and the cluster that gains the pattern. In this algorithm the cluster center is computed as the mean of all the patterns that are assigned to the cluster, hence the name K-means. To add a new cluster, the algorithm searches the existing clusters to locate the one with the maximum variance. This cluster is replaced by two new clusters; their centers are the average feature values for features greater than, and less than, the original cluster center. The algorithm that we used to perform the cluster analysis is one given by Hartigan [5].

The results of applying the K-means algorithm to the combined training and test sets are shown in Table 3. To produce this table the algorithm was instructed to cluster the patterns into eight groups. In this method the

TABLE 3—*Sequential* K-*means clustering results for one to eight clusters.*

Number of Clusters	Pattern Count							
	1	2	3	4	5	6	7	8
1	101	...	...	...	...	...	...	...
2	61	40	...	...	...	...	...	...
3	64	15	22	...	...	...	...	...
4	49	13	34	5	...	...	...	...
5	41	13	30	5	12	...	...	...
6	26	13	25	5	12	20	...	...
7	26	12	11	5	12	22	13	...
8	26	12	11	5	12	12	13	10

algorithm first defines a single cluster consisting of all of the patterns. This cluster is divided into two clusters using the procedure described previously, and the patterns are moved to minimize the performance index. The algorithm continues to add clusters and to minimize the performance index until eight clusters have been defined. Table 3 shows the number of patterns that were grouped into each of the eight clusters at the completion of the run. The pattern counts for the intermediate clusters formed by the algorithm are also shown in Table 3.

An examination of Table 3 does not reveal the three distinct clusters that we would like to have seen. When considering the pattern counts for three or more clusters, however, we found that Clusters 2, 4, and 5 remained stable. This suggests that some internal structure exists within the data. In order to investigate this internal structure, we expanded Table 3 to show the pattern breakdown for the six-cluster case. This expanded representation is presented in Table 4.

The cluster structure shown in Table 4 verifies the hypothesis that internal structure in the data is partially responsible for the pattern counts given in Table 3. Cluster 1 in Table 4 is composed primarily of patterns from elliptical-wastage defects. Cluster 2 consists mainly of patterns from uniform-thinning defects. Cluster 3 is a combination of patterns from uniform-thinning and EDM-slot defects. An interesting characteristic of Cluster 3 is that the shallow uniform-thinning defects are clustered with the deeper EDM slots. One possible reason may be that three of the selected features (Features 4, 8, and 12) are directly related to the amplitude of the flaw signal. Clusters 4, 5, and 6 are each composed of a different type of defect. Cluster 4 consists entirely of elliptical-wastage defects that are 50 to 60 percent of the wall in depth; Cluster 5 is composed of 100 percent throughwall EDM slots; and Cluster 6 contains only shallow uniform-thinning defects. Since we wanted to size the defects, it was encouraging that a large percent of the uniform-thinning defects split into two clusters (Clusters 2 and 6) as a function of flaw depth.

TABLE 4—*Cluster structure for six clusters.*

		Defect Size			
Cluster No.	Defect Type	20 to 30 %	50 to 60 %	70 to 90 %	100 %
1	EDM slot	...	...	5	...
	Uniform thinning	...	...	...	...
	Elliptical wastage	9	9	3	...
2	EDM slot	...	...	...	...
	Uniform thinning	...	...	12	...
	Elliptical wastage	...	...	1	...
3	EDM slot	...	7	6	4
	Uniform thinning	4	2	2	...
	Elliptical wastage	...	...	...	...
4	EDM slot	...	...	...	...
	Uniform thinning	...	...	...	...
	Elliptical wastage	...	5	...	...
5	EDM slot	...	...	...	12
	Uniform thinning	...	...	...	...
	Elliptical wastage	...	...	...	...
6	EDM slot	...	...	...	...
	Uniform thinning	9	11	...	...
	Elliptical wastage	...	...	...	...

Pattern Recognition

In this section we discuss the pattern-recognition techniques that actually make the classification decision from the reduced set of features. There are many classification techniques available, and each one is based on a different set of mathematical assumptions. For example, not all of the classification algorithms can be used for both category (flaw type) and continuous property (flaw size) data. The best technique for a particular situation is not chosen solely on the basis of theoretical considerations; in many cases, information about the behavior of the phenomenon is insufficient to determine the best classification algorithm. For these reasons we compared the results of three different classification algorithms that were used to categorize the flaw type and two algorithms that were used to size the uniform-thinning flaws. The algorithms are an empirical Bayes procedure, two nearest-neighbor algorithms, a least-squares procedure, and a multicategory linear discriminant algorithm.[4]

Empirical Bayes Procedure

In terms of statistical theory the empirical Bayes procedure is perhaps the most sophisticated of the classification techniques that are discussed here. It

[4]The algorithms used are contained in the pattern-recognition computer package ARTHUR [*6*].

is often used as the standard of comparison for other classification techniques and is appropriate for category data.

The original Bayes rule classification requires a functional form for the n-dimensional joint probability of the features. It also requires a quantification of the risks and costs of misclassification. A flaw is assigned to the category to which it has the greatest probability of belonging (see Mendel and Fu [7] for a detailed derivation). In practice the n-dimensional probability distribution is usually not known, so a functional form of the probability must either be assumed or estimated empirically. An empirical approach uses the histogram of each feature for each category or property value interval and then combines the histograms to approximate the n-dimensional probability. The probability of an Observation j on Feature i, given that it belongs to Category 1, is denoted by

$$P(X_{ij}\,|\,\text{Category 1}) \tag{4}$$

This probability can be estimated from the histogram (for example, Figs. 5 and 6). What we really want to know is the reverse of this probability: the probability of Category 1 for Feature i given Observation j. This probability is a function of Eq 4, the misclassification risk for Category l, (R_l), and the *a priori* probability of the l^{th} category (q_l). It is given by the equation

$$P(\text{Category 1}\,|\,X_{ij}) = \frac{q_1 R_1 P(X_{ij}\,|\,\text{Category 1})}{\sum_l q_l R_l P(X_{ij}\,|\,\text{Category } l)}$$

Since these probabilities are for each feature separately, they must somehow be combined to approximate the joint probability distribution function for all of the features. Because the probability densities are estimated with histograms that can have empty cells, problems can occur if they are simply multiplied together; a strictly empirical approach is to add a function of the probabilities

$$P(\text{Category 1}\,|\,\text{Observation}\,j) = \sum_i f[P(\text{Category 1}\,|\,X_{ij})]$$

where f is either a positive power or the natural logarithm. In practice the choice of f is based on the function that best predicts the property for a particular data set.

For these data we chose $q_1 = q_2 = q_3$, since the numbers and sizes of flaws of each type were chosen arbitrarily and do not necessarily reflect real-life experience. Also, in lieu of assessing and quantifying the relative consequences of misclassification, R_1 was chosen equal to R_2 and R_3.

Nearest Neighbor

These classification algorithms, one for category data and one for continuous data, assign patterns in the test set to the category or property value to which the majority of its K- (or P-percent) nearest neighbors in the training set belong. "Nearest" is defined in terms of a measure in n-space; we used the euclidean distance measure described in Feature Analysis.

The K-nearest-neighbor classification technique for category data has several desirable statistical properties. Firstly, it is a nonparametric technique; this means that no distributional assumptions are required on the feature space. Secondly, it can be shown to have the same asymptotic misclassification rate as Bayes procedure if K is chosen to be a certain function of sample size. See Cover and Hart [*8*] and Freidman [*9*] for a more complete discussion of this classification rule.

Least Squares

When applying the least-squares procedure we assume that a continuous or dichotomous property can be expressed as a linear function of the features. We let Y be the property value and then search for a linear function of the features that estimates Y as accurately as possible. This relationship can be expressed formally as a decision function

$$Y = a_0 + a_1X_1 + a_2X_2 + \cdots + a_mX_m$$

where m is the number of features, and a_i, $i = 0, \ldots, m$, are coefficients that are estimated from the training set data by least-squares minimization. When the estimated coefficients and the feature values are used, a decision function value, $\hat{Y}$, can be calculated for each pattern. This value is also called the predicted value of the property for the pattern. See Draper and Smith [*10*] for a general discussion of least-squares regression analysis.

Multicategory Linear Discriminant Function

As the name implies, this decision algorithm is appropriate for data with more than two categories. The algorithm constructs hyperplanes in n-space that separate the patterns contained in one category from those of the other categories. It is an iterative procedure that continues until it achieves a perfect classification for the patterns in the training set. The discriminant function for Feature k and Category c is given by the equation

$$D_{k,c} = b_{o,c} + \sum_{i=1}^{n} b_{i,c}X_{i,k}$$

where the coefficients $b_{i,c}$, $i = 0, \ldots, n$, are estimated by an iterative procedure. A pattern, k, is assigned to the category with the largest $D_{k,c}$ value.

Results

Flaw-Type Classification

The classification algorithms used for the discrimination of the three types of flaws were the empirical Bayes procedure, the K-nearest-neighbor algorithm, and the multicategory linear discriminant procedure.

For the empirical Bayes procedure, $\beta = 0.5$ produced the best discrimination. For the training set the classification was perfect, and the test set produced an overall correct classification rate of 96 percent. All of the uniform-thinning flaws were classified correctly, but one EDM-slot flaw was misclassified as elliptical wastage and one elliptical-wastage flaw was misclassified as an EDM slot.

The correct classification rate for the multicategory linear discriminant procedure for the test set was 96 percent. All of the uniform-thinning flaws were correctly classified. Two elliptical-wastage flaws were misclassified as EDM slots; one of them was that misclassified by the Bayes procedure.

The results for the nearest-neighbor algorithm are more striking. Based on the category of its closest neighbor in the training set, all of the flaws in the test set were correctly classified. Classification rates based on the algorithm for the 3- to the 10-nearest neighbors for the test set ranged between 92 and 98 percent. Five flaws were misclassified by at least one of these nearest-neighbor algorithms; three of these were the flaws misclassified either by the Bayes procedure or the linear discriminant function algorithm. The misclassification results show that one uniform-thinning flaw was misclassified as an EDM slot, two elliptical-wastage flaws were misclassified as EDM slots, one EDM slot was misclassified as uniform thinning, and one EDM slot was misclassified as elliptical wastage.

The successful classification rates for the test set using the Bayes rule, the linear discriminant function, and one of the nearest-neighbor algorithms are summarized in Table 5.

TABLE 5—*Test set identification success rates (%) for three flaw types using three classification rules.*

	EDM Slots	Elliptical Wastage	Uniform Thinning	Overall
Empirical Bayes procedure	94	92	100	96
Multicategory linear discriminant function	100	85	100	96
6-nearest neighbor	100	92	100	98

The three classification algorithms gave very consistent and accurate results under the controlled conditions of the experiment. In this case there were three misclassified flaws. Uniform-thinning flaws were categorized perfectly; elliptical-wastage flaws were the most often missed flaws; they were always misclassified as EDM slots. The misclassified EDM slot was misclassified as elliptical wastage. Further study will be required to explain the reasons for this pattern.

A comparison of the clustering results with the classification results for the test set helped explain the misclassified flaws. Recall that Clusters 1, 2, and 3 each contained a mixture of two flaw types. All five of the flaws that were misclassified in the test set were contained in Clusters 1 and 3. In the training set six of the eight flaws that were misclassified by at least one of the nearest-neighbor algorithms (the success rate was 100 percent for the other two procedures) were contained in Clusters 1, 2, and 3. These results suggest that mixed clusters are the places to look for flaws that may be misclassified. Just because a flaw is contained in a mixed cluster, however, does not mean that it will be misclassified. Misclassified flaws accounted for only 20 percent of the flaws in Clusters 1 and 3.

Flaw Sizing for Uniform Thinning

The purpose of in-service inspections is to size flaws. The classification of flaw type (geometry) is a necessary first step to sizing because flaw geometry affects the angle of the Lissajous figure, which is the basis of the conventional eddy-current inspection method. Flaw typing before sizing is a means to correct for this effect. Since what is reported here is work in progress, sizing results will be given for only one flaw type. Sizing results for the other two flaw types will be reported later.

We used the least-squares algorithm and the nearest-neighbor algorithm to size the uniform-thinning flaws. The depths of these flaws were between 25 and 75 percent of the wall.

The results in terms of fit correlation, that is, the correlation between the actual and estimated flaw depths for the two procedures, are very close. The techniques, their fit correlations, their 95 percent confidence intervals, and the maximum absolute difference between the actual (Y) and the estimated ($\hat{Y}$) flaw depths (max $|Y - \hat{Y}|$) for the training set are given in Table 6.

TABLE 6—*Summary of flaw-depth size fits for uniform thinning in the training set.*

	Fit Correlation (confidence interval)	Max $\|Y - \hat{Y}\|$ (% of wall)
Least squares	0.99 (0.98, 0.99)	6 %
20 % nearest neighbor	0.95 (0.88, 0.98)	13 %

The 20 percent nearest-neighbor algorithm produced less accurate results than the least-squares algorithm. It had two deviations larger than 10 percent in the training set. The results for the test set are even worse; the largest deviation was 20 percent and five deviations were over 10 percent. This algorithm appears to be too strongly influenced by outliers for it to size flaws reliably.

Of the two algorithms, the least-squares algorithm produced smaller deviations in the test set. The estimated flaw depths for the test set are plotted against the actual flaw depths in Fig. 7. The average deviation was 2.33 percent with a maximum of 6.4 percent. The estimated flaw depths using the conventional eddy-current method (produced by visually interpreting the angle of the Lissajous figure) are also shown in Fig. 7. The average deviation using the conventional eddy-current method was 9.4 percent with a maximum of 13.9 percent.

Discussion

Several obstacles must be overcome before pattern-recognition techniques can be accepted for inservice inspection: (*1*) a data base containing the types of flaws encountered in the field must be developed and used to train the

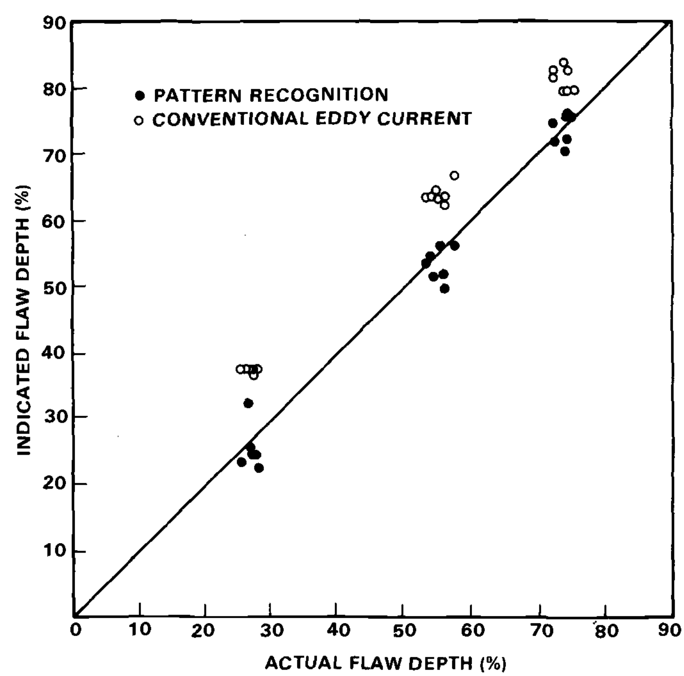

FIG. 7—*Results of sizing the uniform-thinning flaws using the least-squares decision rule.*

techniques, (*2*) the data for this training set must be collected under realistic in-field conditions, and (*3*) the techniques must be extensively tested to validate their reliability.

Current microprocessor technology would permit the development of instruments that can implement these pattern-recognition techniques. The recent introduction of 16-bit microprocessors and high-speed multiplier/accumulator integrated circuits makes possible the development of an instrument that can automatically classify and size defects in steam-generator tubing with a minimum of operator assistance.

References

[*1*] Shankar, R., Brown, C. L., Mucciardi, A. N., and Davis, T. J., "Feasibility of Using Adaptive Learning Networks for Eddy-Current Signal Analysis," NP-723, Electric Power Research Institute, Palo Alto, Cal., 1978.

[*2*] Brown, R. L., "Investigating the Computer Analysis of Eddy Current NDT Data," HEDL-SA-1721, Hanford Engineering Development Laboratory, Richland, Wash., Feb. 1979.

[*3*] Morris, C. J., Lyon, G. H., and Alzheimer, J. M., "Steam-Generator Tube Integrity Program—Phase I Eddy-Current Test and Evaluation of Inconel-600 Pressurized Water Reactor Tubes," NUREG-CR-0419, PNL-2961, Pacific Northwest Laboratory, Richland, Wash., 1979.

[*4*] Flora, J. H. and Brown, S. D., "Evaluation of the Eddy-Current Method of Inspecting Steam-Generator Tubing," BNL-NUREG-50512R, U.S. Nuclear Regulatory Commission, Washington, D.C., Sept. 1976.

[*5*] Hartigan, J. A., *Clustering Algorithms*, Wiley, New York, 1975.

[*6*] Duewer, D. L., Koskinen, J. R., and Kowalski, B. R., "ARTHUR," available from B. R. Kowalski, Laboratory for Chemometrics, Department of Chemistry BG-10, University of Washington, Seattle, Wash.

[*7*] Mendel, J. M. and Fu, K. S., *Adaptive Learning and Pattern Recognition Systems*, Academic Press, New York, 1970.

[*8*] Cover, T. M. and Hart, P. E., *Transactions on Information Theory*, Institute of Electrical and Electronics Engineers, Vol. IT-13, No. 1, Jan. 1967, pp. 21-27.

[*9*] Friedman, J. H., *Transactions on Computers*, Institute of Electrical and Electronics Engineers, Vol. C-26, No. 4, April 1977, pp. 404-408.

[*10*] Draper, N. R. and Smith, B., *Applied Regression Analysis*, Wiley, New York, 1966.

C. L. Brown,[1] D. C. Defibaugh,[1] E. B. Morgan,[1] and A. N. Mucciardi[1]

Automatic Detection, Classification, and Sizing of Steam-Generator Tubing Defects by Digital Signal Processing

REFERENCE: Brown, C. L., Defibaugh, D. C., Morgan, E. B., and Mucciardi, A. N., "**Automatic Detection, Classification, and Sizing of Steam-Generator Tubing Defects by Digital Signal Processing,**" *Eddy-Current Characterization of Materials and Structures, ASTM STP 722,* George Birnbaum and George Free, Eds., American Society for Testing and Materials, 1981, pp. 484–493.

ABSTRACT: An eddy-current analysis system is being developed for the inspection of steam-generator tubing that provides automatic interpretation of eddy-current signals. The microprocessor-based system realizes real-time analysis capability through a programmed probe controller, on-line data conversion, and high-speed digital signal processing. In a fully automatic mode, a wide variety of anomalies can be detected by appropriate enhancement of their characteristic wave shapes. Each detected signal is transformed and parameterized to yield a set of representative features that are used to classify the type of anomaly. An additional feature set is then extracted for estimating the depth of the discontinuity. Classification and sizing capabilities are provided by adaptive learning networks that were trained on a data base of simulated-defect waveforms. Machined defects were utilized in training to simulate as much as possible the most prevalent problems of stress-corrosion cracking, pitting, wastage (wall thinning), and denting of steam-generator tubing. The data base includes combinations of these defect types as well. The range of depth estimation is from 10 to 100 percent of the tube-wall thickness. The system has been designed to interface with either single-frequency or multifrequency devices.

KEY WORDS: eddy current analysis, automatic interpretation, on-line data conversion, digital signal processing, parameterization, feature extraction, classification, adaptive learning networks, stress corrosion cracking, pitting, wastage, phase plane pattern, nondestructive evaluation, Inconel 600 tubing, program controlled devices, spectral measurements, incremental encoder.

Traditional eddy-current analysis has focused on the visual interpretation of a phase-plane pattern to identify and size discontinuities in steam-generator tubing. The success of this approach has been limited by the wide variety of complex signals due to the presence of tube support plates, often with accompanying denting of the tube, low sensitivity to circumferential

[1]Scientist/engineer, engineering aide, engineering aide, and vice-president, respectively, Adaptronics, Inc., McLean, Va. 22102.

cracking, and the occurrence of more than one type of anomaly at the same location in the tube. The approach taken by Adaptronics in this project involves the use of signal-processing techniques applied to the in-phase and quadrature components of the phase plane followed by characterization of the signals. The conditioned signals are then used for synthesizing individual adaptive learning network (ALN) models to classify and size each flaw type.

Four major objectives have been established in this program to provide faster, more reliable, complete, and accurate analysis of expected tubing conditions during in-service inspections (ISI):

1. On-line detection capability is being developed to locate any known type of discontinuity regardless of the presence of tube sheet, support plate, or other interfering phenomena.
2. Each detected signal will be classified by type as axial crack, circumferential crack, pitting, wastage, denting, or combinations of these types.
3. The depth of each detected anomaly will be estimated in through-wall percentages.
4. The results from four single-frequency data sets (100, 200, 400, and 600 kHz) will be compared to determine the optimum carrier frequency or frequency combinations for identification of each defect type.

A portable microprocessor-based system, the ALN 4000 Multi-Purpose Processing System (MPPS), has been designed to incorporate these objectives. This system will provide a real-time, automatic analysis capability which may sufficiently overcome some of the present eddy-current nondestructive evaluation (NDE) problems.

Equipment

The eddy-current data collection system that was used for recording the simulated-defect responses in this study consists of commonly utilized field equipment (Fig. 1). A two-coil differential probe was pulled by a Zetec pusher-puller through a mockup of Westinghouse Inconel 600 tubes with a 22.2 mm (7/8 in.) outer diameter. The signals to the coils were transmitted and received by an Automation Industries EM-3300 eddyscope employing a carrier frequency of 400 kHz. The two analog data channels were recorded on a Zetec FM tape recorder. This type of system typically requires replay of the tapes through the eddyscope at a later time for visual interpretation of the signal responses.

By contrast, the Adaptronics ALN 4000 MPPS developed for this work utilizes a standard probe and eddyscope but replaces the other items with program-controlled devices (Fig. 2). A new probe controller has been designed to eliminate the problems of speed variation during a tube scan. Any change in the speed of the probe scanning past a defect causes any time or

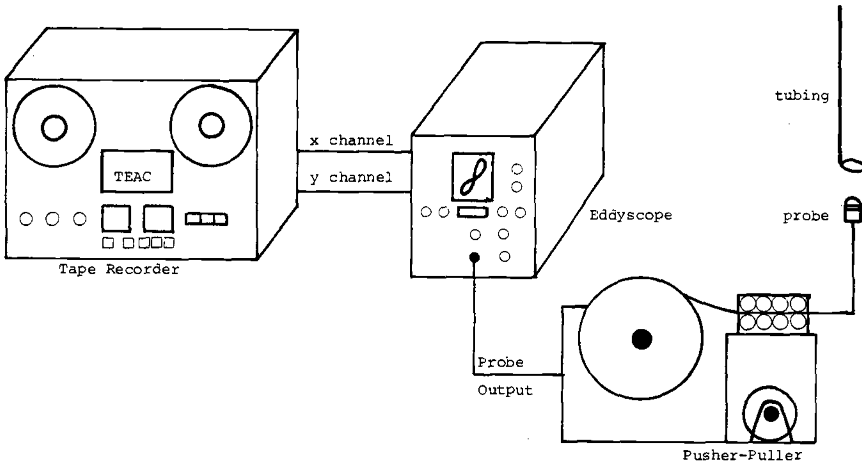

Equipment: 720 LC standard differential encircling probe
Zetec pusher-puller
Automation Industries EM-3300 Eddyscope
Zetec FM 2300 Tape Recorder
Tubing: Westinghouse Inconel 600 tubes (22.2 mm) with 1.27 mm wall thickness

FIG. 1—*Standard data collection system.*

spectral measurements of the individual in-phase and quadrature components to be unreliable and nonrepeatable. In-house measurements of a constant-speed motor on a probe pusher-puller showed a variation of 2.8 to 5.8 cm/s over a time interval of 2 s. This was a cyclic pattern that occurred as a result of oscillations in the feedback circuit of the motor assembly. Since a nominally constant speed motor can actually fluctuate by a factor of two over small distances, an unacceptable error occurs in many signal features computed for ALN's. To guarantee a solution to this problem, an incremental encoder is attached to the front end of the pusher-puller. The digital output pulses serve to clock the analog-to-digital conversion of the data, thereby achieving a sampling by unit distance rather than time and making speed variations irrelevant.

The most significant contribution of the ALN 4000 system lies in its ability to digitize, process, and analyze the eddy-current responses in the time it takes to perform a tube scan. The controller/processor unit controls the probe speed, direction, and position through commands sent to the pusher-puller controller. The two data channels are fed continuously to the unit but digitized only when clocked by the encoder pulses. All defectlike signals are stored on minicartridge tapes, and all results are displayed immediately on a miniprinter mounted in the storage/display unit. The signal detection function is performed in real-time during the probe pull through the tube. Classification and sizing of the suspected defect are performed during the

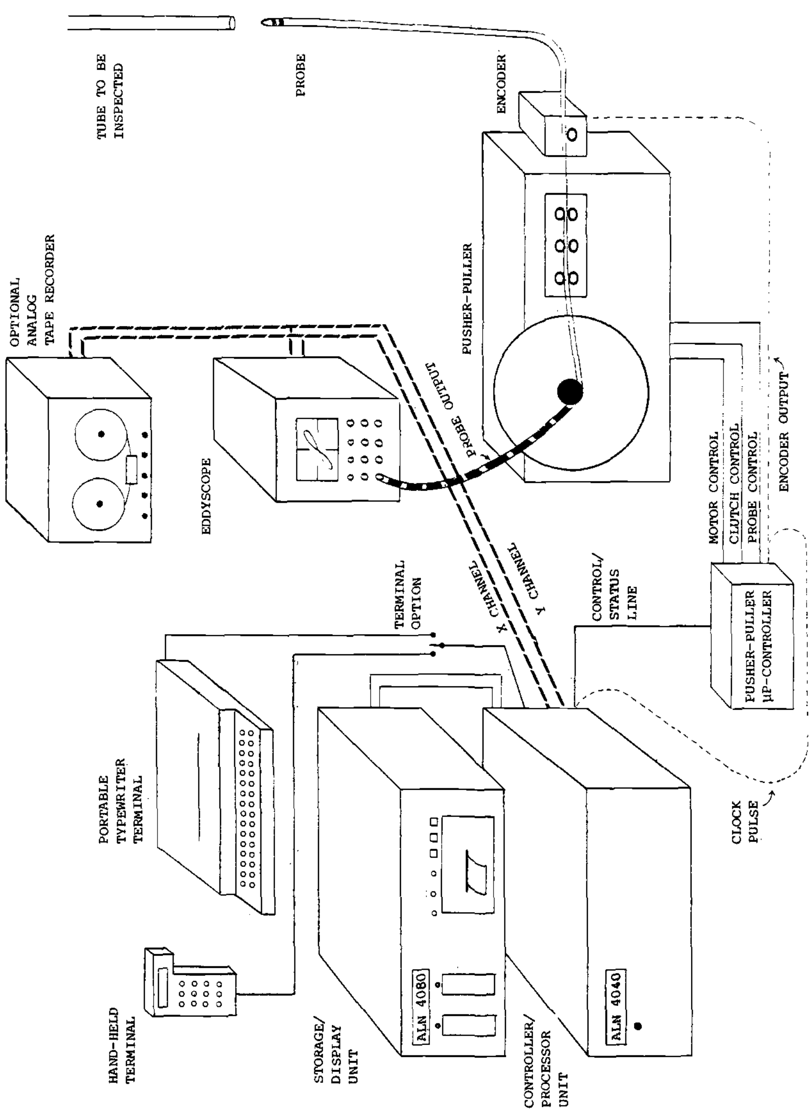

FIG. 2—ALN 4000 eddy-current analysis system.

repositioning of the probe in the next tube to be scanned. Operator communication and interruption of the device is allowed at any time. For normal situations, however, the system is designed to function automatically with little or no operator intervention necessary.

Defect Data Base

In order to represent the most prevalent flaws currently encountered in steam generators, a training base of machined defects was prepared. The types included are electrical-discharge machine (EDM) notches, flat-bottom and tapered holes, wall thinning (both alone and combined with axial and circumferential notches), and axisymmetric dents (alone and combined with notches or wall thinning) (Fig. 3). The notches, holes, and wall thinning were provided in a range of depths from 10 to 100 percent thru-wall (wall thickness = 1.27 mm). The dents ranged from 0.025 to 0.46 mm (1 to 18 mil) in diametral reduction. Since denting is caused by the buildup of the corrosion product magnetite (Fe_3O_4) in the crevice between tube and support plate, the dent specimens were packed with magnetite and covered with a simulated support plate. All other discontinuities were scanned under three conditions: with no support plate, under the edge of a support plate, and centered under a support plate. The total data base for training models contained 725 simulated-defect waveforms.

Signal Processing Procedure

Research has been concentrated in three main areas: detection of flawlike signals, classification of each detected signal into one of six types of tubing defects, and estimation of the anomaly depth.

The detection process is implemented on a continuous stream of incoming data on a point-by-point basis. A detection function is computed from an enhanced version of the y-channel signal plus a baseline noise level and serves as the criterion for identifying defectlike waveforms. All data from defect-free sections of tubing are discarded immediately. All "suspicious" signals are stored in memory or on tape with their corresponding location coordinates.

The process of classification requires generating a feature vector for each simulated-defect waveform. The necessary descriptive features are extracted from the signal response in both the time and frequency domains. All amplitude-dependent features are normalized by the response from a calibration defect so that changes in sensitivity settings of the instrument will not affect the magnitude of the feature values. The classification logic is illustrated in Fig. 4. Each decision box signifies a nonlinear ALN mathematical model that has been trained adaptively on the available data base to identify a given type of anomaly from its feature set. Separate paths are required for

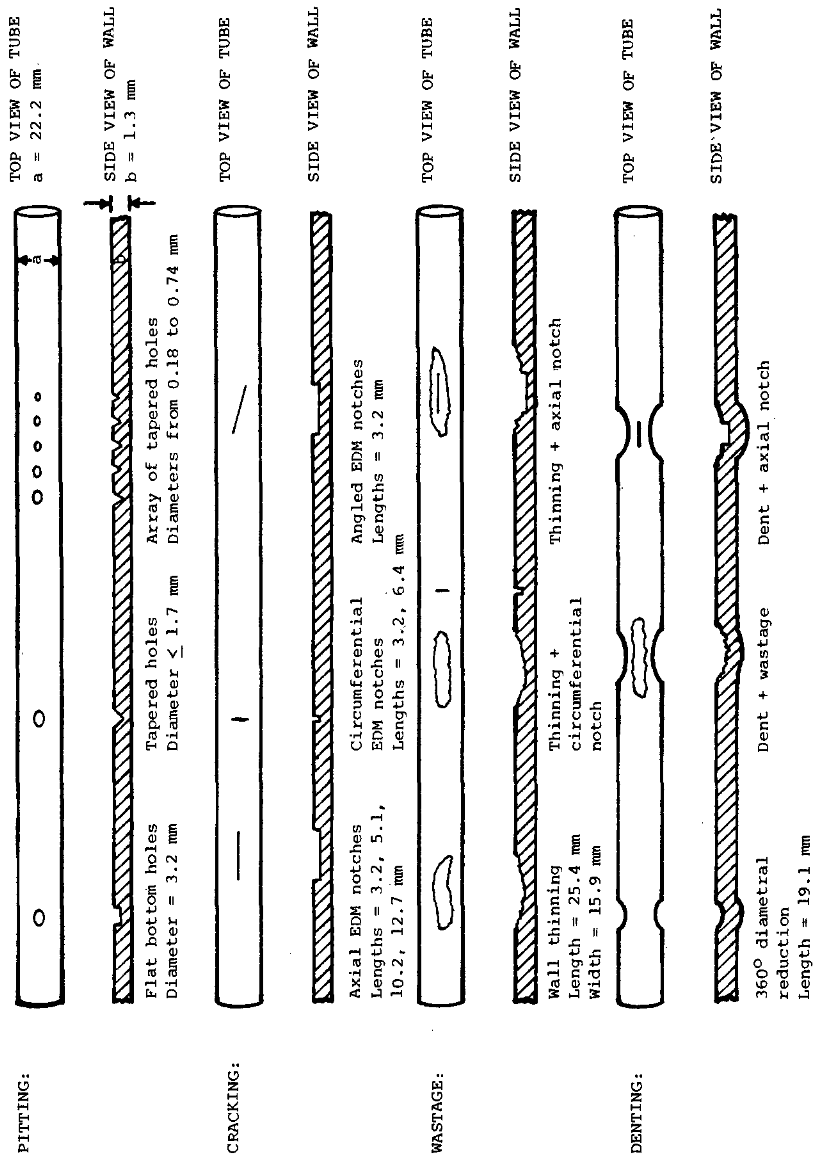

FIG. 3—*Simulated-defect geometries.*

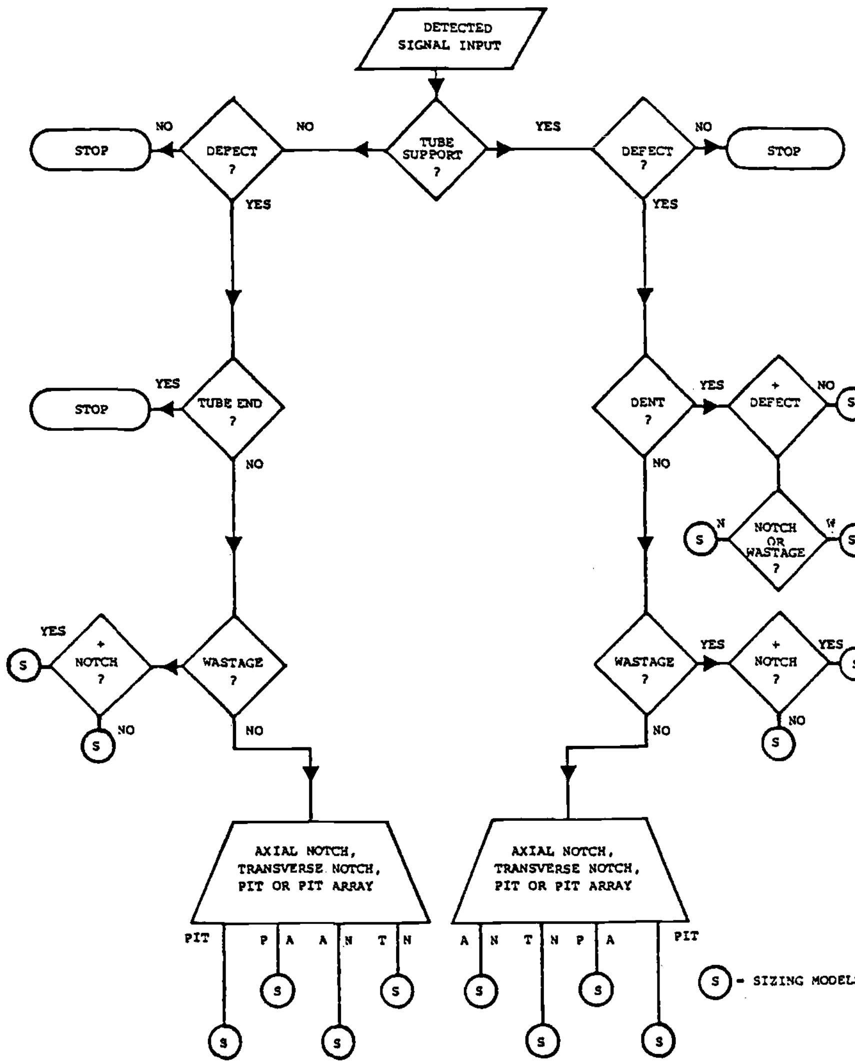

FIG. 4—*Classification logic.*

anomalies occurring alone and those occurring under a tube support. It was found that tube-support cancellation techniques provided results that were no better than results obtained without eliminating the support response. Therefore, all models were trained on the original data. The training algorithm, however, typically chose different sets of features for the tube support and nonsupport cases.

A similar approach was taken for estimating the depth of each discontinuity. Sizing models were trained separately on each type of simulated defect. Again, the results after tube-support cancellation did not improve the accuracy of depth estimation, so no such techniques were used.

Results and Discussion

The signal-detection algorithm was tested on the training base of mockup data. The detection rates were above 95 percent for simulated defects not under supports with false dismissals limited to holes and notches less than 20 percent through-wall. Signals from anomalies under tube supports could be detected clearly in all cases due to the large amplitude response of the support.

Using this mockup data as a test bed for the signal detector proved to be a worst-case test. In the field, all tubes in a generator are manufactured to the same specifications and are a continuous 18.3 m (60 ft) long. In the mockup, however, several short sections of tubing, made by different manufacturers, are stacked together in a column. This situation creates a wide disparity in baseline noise levels in scanning from one tube section to the next. In addition, some machined defects were placed close to one another or to the end of a tube causing difficulty in automatically separating waveforms when each defect was under a 19 mm (3/4 in.) support plate. The end of each tube also created a large signal that delayed updating of the baseline noise estimate at the beginning of each tube. Despite all these difficulties, which would not exist in actual ISIs, the automatic signal detector performed quite well.

In terms of classification and sizing results, the speed variations in the data used for training the ALN models must be considered. Since a large number of the computed signal features are dependent upon the probe speed, this variability will set a lower bound on the errors in the model predictions. Nevertheless, the classifier models yielded correct calls on 91 percent of the isolated signals and 86 percent of the signals under tube supports. Each classifier and its correct classification rate are listed in Table 1.

The defect versus false-alarm classifier is certainly the most important one since an incorrect call here could falsely dismiss a defect. With the exception of the dent classifier, it has the highest rate of correct classification both for signals alone and under supports. Considering the magnitude of the support response, which can be ten times larger than that of a small discontinuity, these percentages are indeed impressive. In fact, only one 10 percent through-wall simulated defect was falsely dismissed in the defect under tube-support class.

For combinations of anomalies, that is, where two or more anomalies occur at the same location, the complexity of the resultant signal often obscures the type and size of the discontinuity in the phase-plane representation. However, a network model, trained to identify the presence of any additional defectlike signals under a dent-plus-tube support, achieved 95 percent

TABLE 1—*Classification-model results.*

Class	Isolated Defects		Defects Under Tube Support	
	No. of Defects	% Correct	No. of Defects	% Correct
Defect versus false alarm	261	97	506	99
Dent	5	100	147	98
Wastage	51	93	159	90
Axial crack	37	85	79	77
Circumferential crack	26	85	57	74
Pit	93	90	80	78
Pitting array	8	95	21	72

correct discrimination on 147 waveforms, consisting of dents only, dents plus wall thinning, and dents plus circumferential notches. A second model was trained to discriminate between the wall thinning and EDM notches in this category, again with a 95 percent correct rate.

The results obtained for models trained to estimate the depth of each class of defect are summarized in Table 2. The root mean square (RMS) error listed refers to percentage points of the true through-wall depth. In any given model, the error was about equally distributed between overprediction and underprediction. The errors under tube supports are larger for the smaller volume discontinuities, as could be expected.

In view of the inconsistencies in the data base due to probe speed and tube variations, these results are very encouraging. When the ALN 4000 system is used to collect the data, the situation should be markedly improved since the features will be more stable and repeatable.

Conclusions

The performance of the automatic signal detector has demonstrated that reliable and automatic detection can be obtained for simulated defects deeper than 20 percent through-wall. This is an appropriately satisfactory limit since the Boiler and Pressure Vessel Code of the American Society of Mechanical Engineers (ASME) specifies that defects less than 20 percent need not be reported during ISIs.

For the purposes of classification and sizing of defects, it seems clear that successful models can be generated to estimate these defect characteristics even in the presence of large-amplitude distorting factors. The accuracy and reliability of the models, however, could be increased substantially by the use of scanning techniques that provide consistent time waveforms.

An examination of the features selected by each of the ALN models leads to further insights into the problems of eddy-current analysis. Although most

TABLE 2—*Sizing-model results.*

Class	Isolated Defects RMS Error (% through-wall)	Defects Under Tube Support RMS Error (% through-wall)
Dent	...	2
Wastage	9	9
Axial crack	6	12
Circumferential crack	8	20
Pit	10	16
Pitting array	6	17

depth-estimation techniques use a single calibrated curve to relate the phase-plane angle to the defect depth, this feature was chosen by only three of the 22 nonlinear models trained here. In fact, no single feature was selected for more than seven sizing models. Across the board, a total of 39 features were selected in training all the classification and sizing models. These results indicate that no one feature and no single calibration curve will be as informative of defect characteristics as a full set of measurements and nonlinear functions applied specifically to each type of defect.

Acknowledgments

The enthusiastic support and guidance of Dr. G. J. Dau, EPRI project manager, is gratefully acknowledged. This work is supported by the Electric Power Research Institute under Contract No. RP1125-1-1.

Summary

Summary

Conference Papers

The broad range of subjects covered in this symposium can be fitted into the following categories: theoretical analysis of fields, measurement methods (including the use of multifrequencies, microwaves, pulsed fields, and other approaches), automation and data processing, material properties, applications to specific inspection problems, and standards for the improvement of instrumentation calibration.

The presentation of the papers in this volume follows the same order as that in the symposium. In the discussion that follows, the papers are categorized by their major themes. In several cases papers are discussed in categories that differ from those of the symposium presentation, since the need for this change was obvious only after reading the complete paper.

The solutions of electromagnetic field problems are of several types. In an approach taken by Kahn and Spal, the problem is formulated analytically (exactly) and numerical methods are used to obtain final results. Due to the complexity of the boundary conditions in most eddy-current problems, however, very few lend themselves to analytical-type solutions. To deal with complex geometries, Lord and Palanisamy, Demerdash and Nehl, and Chari and Kincaid use finite-element analysis, where the electromagnetic field in discrete areas is found by minimizing its energy. A third approach by Turner et al, Yeh, and Herman and Prodan transforms Maxwell's equations into electrical circuit equivalents, and the problem is then solved using generalized circuit theory. These various methods applied to the same problem can sometimes be used to examine the validity of various approximations. In one case, where such a comparison was made by Chari and Kincaid, the close fit of the results of the two methods was encouraging.

Three major measurement methods (multifrequency, pulsed, and microwave) study different aspects of the eddy-current phenomena. Microwaves are better suited for precise measurement of surface defects because of the higher frequency. Multifrequency techniques provide information helpful for interpretation, simply because more information is available. Pulsed systems are most advantageously applied to detect defects below the surface. These methods complement each other in expanding the range of application of eddy-current nondestructive evaluation (NDE).

The characteristics of commercially available multifrequency equipment are discussed by Brown and by Davis, who analyze their performance and present various techniques to optimize performance in specific tests. The use of an algorithm for processing multifrequency test data is presented in papers by Betzold and by Becker and Betzold. This algorithm is designed to suppress spurious signals due to probe wobble, tube supports, etc., while enhancing the signals due to defects. A detailed example of the use of this algorithm is presented. The design and development of a multifrequency system from the initial theoretical calculations to the final application are discussed by Dodd and Deeds, who also deal with the maximization of system performance and treatment of test data. Sagar discusses the theoretical assumptions underlying the design and application of most multifrequency test systems. His analysis of the electromagnetic field interaction between closely spaced defects shows the possible erroneous conclusions that may be reached if a linear model is used for the interpretation of data.

Microwave testing has been used in past years, but the method has usually been considered too complex and esoteric for most applications. However, several papers indicate a renewed interest in this technique, and present possibilities for simple industrial applications. Papers by Auld and by Bahr dealing with the theory of microwave testing show that it may be regarded as an extension of the normal coil test configurations and can be used in certain cases with superior results. Theoretical models are presented which are generalized to all eddy-current testing; these can be fruitfully used to test the results expected from a microwave measurement and to interpret data in specific applications. Auld and Winslow discuss a unique microwave system using a spherical ferrite probe for surface-crack detection, and present results obtained with this apparatus.

Pulsed eddy-current systems extract information about the test material by analyzing the shape of the transient waveform. Such testing is important because it may be applied to the detection of defects at depths below the surface of metals not readily detectable with continuous-wave techniques. Both Waidelich and Sather discuss the theory and design of equipment to achieve maximum penetration into the metal, and the resultant sensitivity to defects. Wittig and Thomas treat the total design and analysis of a pulsed system. Hendrickson and Hansen show how a pulsed system may be used to investigate defects in the lower layers of a multilayered metal structure.

Other methods include the sizing of surface cracks of measuring the a-c potential drop between two probes contacting the metal on either side of the crack. The results of this measurement are fitted to a theoretical model to determine crack dimensions. Although present practice uses an algorithm based on linear relations to correlate the signal with crack size, nonlinear algorithms are developed by Dover et al to deal with certain crack geometries. The use of fringe flux measurements in a new application is discussed by Beissner et al. The feasibility of testing the integrity of composite materials is discussed by Anderson.

It is well known that a variety of material properties can be monitored by eddy-current techniques. Hartwig deals with the determination of the phase boundary in dilute aluminum-gold aluminum alloy and the changes in residual resistivity using an eddy-current decay method. Wallace et al study the motion of the solid-liquid interface in several solidifying metals. From such studies one may learn how to control the solidification process to achieve the desired results.

Computer technology has been applied to eddy-current testing in two areas: automation of experiments and analysis of test data. The advent of high-speed data acquisition systems and more powerful computers makes it feasible to analyze a large number of data points from a single output signal as well as the signals from multiple probes. A method of modifying test data from flat plates for video display by relating changes of signal amplitude to changes in video beam intensity is discussed by Feil. The use of statistical models to interpret test signals makes possible the extraction of useful information from signals containing a high degree of spurious information. The adaptive learning techniques of Brown et al and the pattern-recognition technique of Doctor et al are used with data obtained from a typical single eddy-current coil to interpret heretofore ambiguous data and correlate it with real defects. These methods have produced a high degree of accuracy in the sizing of defects.

The accuracy of eddy-current material testing and defect characterization is dependent in all cases on the accuracy with which the test standards are known. As long as theoretical developments lag behind experimental techniques, it is important to have well-characterized standards for instrument calibration. Jones presents a detailed analysis of the long-term stability of eddy-current conductivity standards, both the primary standards used to establish the unit of conductivity and the secondary standards that are used for the calibration of eddy-current conductivity meters. Free discusses a variable-frequency bridge method for the calibration of secondary standards which greatly reduces the number of primary standards ordinarily required. Wittig et al discuss the development of a defect standard that can be used for all types of metal tubing and that will be incorporated into testing procedures in West Germany.

Comments

The vast majority of the papers are concerned with the detection of defects in materials or in metal structures rather than with the determination of metal properties. However, as industry becomes concerned with more precise design criteria, one may expect to see greater emphasis in the further development of eddy-current techniques for measuring various metal properties.

Present work places much greater emphasis on determining the physical nature of the defect along with a quantitative assessment of its size and shape. Concern with quantitative defect evaluation instead of just detection is one indication of the method "coming of age" not only as a quantitative NDE method but also as a scientific discipline.

If a single application were to be chosen as the most significant from the number of papers presented, it would be detection of defects in tubing, especially as the problem relates to the nuclear industry. Approximately one third of the papers presented at the symposium deals with this problem. Theoretical models of these defects, instrumentation to detect them, and methods of data acquisition and analysis to quantify the defects have reached a surprisingly high degree of sophistication.

Regarding the theoretical advances, it is clear that finite-element analysis for modeling of eddy-current problems is a very powerful and flexible method that is coming into wider use. The technique is not limited by material nonlinearities or awkward defect geometry but rather by the core storage that is presently available in computers. It may be noted that the successful application of the technique requires some knowledge of the physics of the problem.

Multifrequency techniques seem to hold the greatest immediate promise for improved measurement results. There are several reasons for this. These techniques benefit from recent advances in single-frequency analysis, and by their nature present a greater number of measurement variables for use in data analysis. The increased degrees of freedom allow for the elimination of unwanted test variables (probe wobble, for example) while maximizing those variables related to the characteristics of interest. Microwave testing, although restricted to the study of surface defects due to the limitations imposed by skin depth, promises great resolution. Pulsed techniques, although clearly valuable for the detection of deep defects, are limited at present by insufficient theoretical development.

Although multifrequency techniques are being established on a firm basis, the limitations on their accuracy due to the interactions of closely spaced defects deserve further study. Regarding the pulsed eddy-current method, the use of finite-element analysis would seem to be a natural way to provide the required theoretical foundations that this measurement requires.

Although there is little doubt that the advances mentioned here will make eddy-current testing faster, more reliable, and more quantitative, the need for further work is clear. In the area of theoretical analysis, calculations of more realistic defect geometries are needed. The incorporation of varying material properties in the region of the defect would be useful, since such variation is difficult to investigate experimentally. The quantitative verification of theoretical predictions by precise experiments is also lacking in a number of cases.

Several obstacles must be overcome before pattern recognition can be widely accepted for in-service inspection. A sufficiently extensive data base containing the types of flaws encountered in the field must be developed and used to train the system, and the data for this training set must be collected under realistic field conditions. To further develop the method, the parameters used to recognize patterns should have a physical basis, as far as this is possible.

The success of any eddy-current approach depends upon the quality of available standards. While a few eddy-current standards are well characterized, improvements in this area would be beneficial. Finally, the correlation between defect standards and real defects has received little attention, and is an area that should be studied to enhance the performance of all eddy-current methods.

George Birnbaum

National Bureau of Standards, Washington, D.C. 20234; co-chairman and co-editor

George Free

National Bureau of Standards, Washington, D.C. 20234; co-chairman and co-editor

Index

V

W